Doctoral Dissertation
Doctoral Program in Energy Engineering (38th Cycle)

Shallow Geothermal Energy in Urban Environment

Innovative solutions for sustainable cities

Alessandro Berta
* * * * * *

Supervisors
Prof. Glenda Taddia, Supervisor
Prof. Vittorio Verda, Co-Supervisor

Politecnico di Torino
October 31, 2025

I hereby declare that, the contents and organisation of this dissertation constitute my own original work and does not compromise in any way the rights of third parties, including those relating to the security of personal data.

…….....

Alessandro Berta

Turin, October 31, 2025

Summary

The present doctoral thesis sets out a comprehensive, data-driven methodological framework for evaluating and designing low-enthalpy geothermal solutions for heating and cooling applications in urban environments. This framework is systematically structured to address the fundamental challenges of energy transition implementation in complex urban settings. The research workflow, depicted in Figure 1, comprises an exploration of contemporary energy transition definitions. In this phase, the thesis examines how geothermal energy contributes to renewable energy systems and investigates the key challenges of integrating thermal energy sources within urban settings. The contemporary energy transition signifies a substantial structural transformation in energy supply and consumption systems, effecting a fundamental shift from fossil fuel reliance towards sustainable energy sources.

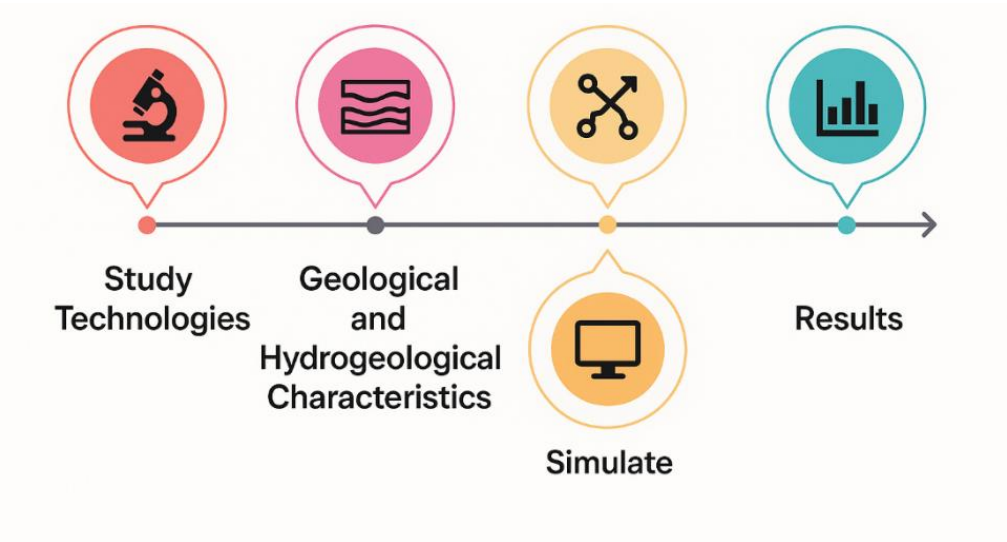

Figure 1. Schematic workflow of the thesis.

Geothermal energy is of particular significance in this transition, as it provides a constant power source that can offset the intermittent nature of other renewables, such as solar and wind energy. This contributes to the creation of more stable and dependable energy systems. However, integration in urban areas presents significant challenges due to thermal interference, spatial constraints, and regulatory frameworks, all of which must be carefully managed to ensure successful deployment. Subsequent to this exploratory phase, the thesis undertakes a comprehensive evaluation of low-enthalpy geothermal solutions, assessing their efficacy under diverse geological and hydrogeological conditions. The work specifically addresses which geothermal technologies are most effective by examining vertical borehole arrays, groundwater doublets, and subsurface thermal storage systems within the urban context of Turin. The influence of geological and hydrogeological conditions on technology selection is systematically investigated using publicly available datasets from regional geoportals, including stratigraphic profiles and piezometric data. The methodological steps essential for comprehensive evaluation are formalised through the integration of QGIS (©1989, 1991 Free Software Foundation, Inc.) for spatial data analysis, MODFLOW (U.S. Geological Survey Software) for groundwater flow modelling, FEFLOW (© DHI A/S) for coupled heat and mass transport simulations, and PEST for automated parameter calibration. This integrated approach facilitates the construction of spatially explicit conceptual models that capture the complexity of Turin's alluvial shallow aquifer system, which serves as a valuable resource for low-enthalpy geothermal energy exploitation.

The application phase of the thesis is centred on the maximisation of simulation accuracy through the implementation of advanced numerical methods and model calibration procedures. The research explores the potential of simulation methods to enhance the precision of results by implementing rigorous uncertainty quantification strategies. In this context, PEST is integrated within automated inversion loops to condition hydraulic and thermal parameters to observable data or literature benchmarks. In cases where observational constraints are limited, the calibration strategy prioritises the production of posterior parameter ranges as opposed to deterministic best-fit solutions.

The final phase of the research synthesises the key outcomes of the study and their implications for the deployment of geothermal systems in urban environments. The thesis presents spatial suitability maps for closed-loop versus open-loop solutions under documented stratigraphy and hydrogeology, operational guidelines for extraction and reinjection rates and borehole spacing requirements. The research implications for geothermal system deployment encompass practical guidance for

urban implementation, including design heuristics for borefield sizing and layout, reinjection and monitoring requirements for piezometry and temperature, data standards for improving open databases, and policy measures to streamline permitting while protecting groundwater quality. The methodological framework is characterised by open datasets and numerical experimentation, ensuring transparency and reproducibility while positioning the approach as a transferable, low-cost decision-support tool for planners, utilities, and regulators. This comprehensive approach provides a pragmatic roadmap for the scaling of low-enthalpy geothermal solutions in urban areas. This is achieved by the use of reproducible, open-data modelling methods, which ultimately support the broader energy transition towards sustainable urban energy systems.

Acknowledgment

I would like to acknowledge the Supervisor and Co-Supervisor, as well as all my colleagues and friend in Polito, NTNU, and Iren with whom I shared this journey.

I would like to dedicate this thesis to my loving parents and partner

To my mother and father, who taught me the value of curiosity, integrity, and hard work, and who supported every step of this long academic path.

To Alessandra, for your unwavering support, for believing in this work even when I doubted it, and for filling this demanding journey with kindness and laughter.

Contents

List of Tables

List of Figures

Chapter 1

Context Overview

"[...] We may brave human laws, but we cannot resist natural ones"

Jules Verne (1870)[1]

The concept of energy transition has become a fundamental pillar for achieving sustainable economic development and building resilient societies in the face of climate and environmental challenges. Growing awareness of the energy sector's impact, responsible for about 75% of global greenhouse gas emissions, has made the deep transformation of energy systems toward renewable and low-carbon sources an urgent priority. This transformation is framed within the "World Energy Trilemma," which balances environmental sustainability, energy security, and energy equity, highlighting the need for integrated governance and coherent policy frameworks. The rapid expansion of renewable technologies, particularly solar and wind, is accompanied by advances in smart grids, energy storage, and building energy management systems. However, the thermal energy sector remains a critical frontier, accounting for half of global final energy consumption and a substantial share of CO_2 emissions. Integrating renewables into heating systems, through heat pumps, solar thermal, and biomass, is therefore essential for effective decarbonization. Italy's 2024 Integrated National Energy and Climate Plan (PNIEC) outlines an ambitious 2030 strategy aligned with EU climate neutrality goals, including the expansion of geothermal energy. Geothermal resources, due to their reliability and continuous baseload capacity, represent a strategic asset for the thermal energy transition, particularly within densely populated urban contexts such as the Metropolitan City of Turin, which serves as the focus of this thesis.

[1] *Twenty Thousand Leagues Under the Seas, Part 2, Chapter 15, Jules Verne, (1870).*

1.1 Role of Renewable in the Energy Transition

Energy systems have been identified as a fundamental component for ensuring economic advancement and social welfare, whilst concurrently maintaining sustainable development pathways [1]. This understanding has gained global institutional recognition, with international authorities acknowledging energy's critical importance to the extent that the United Nations has established access to affordable, sustainable, and modern energy as a fundamental global priority for all citizens [2,3]. In this context, the concept of sustainability signifies the necessity for economic growth to remain compatible with both socio-economic development and environmental preservation [4]. Within this framework, the theme of sustainable or clean energy transition has emerged as a dominant paradigm, driven by mounting concerns regarding climate change, global warming, and energy security challenges that societies worldwide must address [5–7].

The World Energy Trilemma, as conceptualised and assessed by the World Energy Trilemma Index [8], encapsulates the three core dimensions that define global energy system performance: environmental sustainability, energy security, and energy equity (Figure 2). The term 'environmental sustainability' is defined as the responsible stewardship of natural resources and the mitigation of greenhouse gas emissions, with a particular emphasis on the transition to low-carbon energy sources and the minimisation of ecological impacts [9]. Energy security is defined as the reliability and resilience of energy supply chains, including the capacity to meet current and future demand, even in the face of geopolitical, technological, or climate-related disruptions [10]. The concept of energy equity pertains to the universal accessibility and affordability of energy, thereby ensuring that all populations have fair and reasonable access to modern energy services that support socio-economic development [11]. The trilemma posits the notion that the attainment of progress in a particular dimension frequently gives rise to trade-offs in other dimensions. This observation underscores the imperative for integrated governance and balanced policy design as indispensable components of the pursuit of just, secure, and sustainable energy systems on a global scale [12].

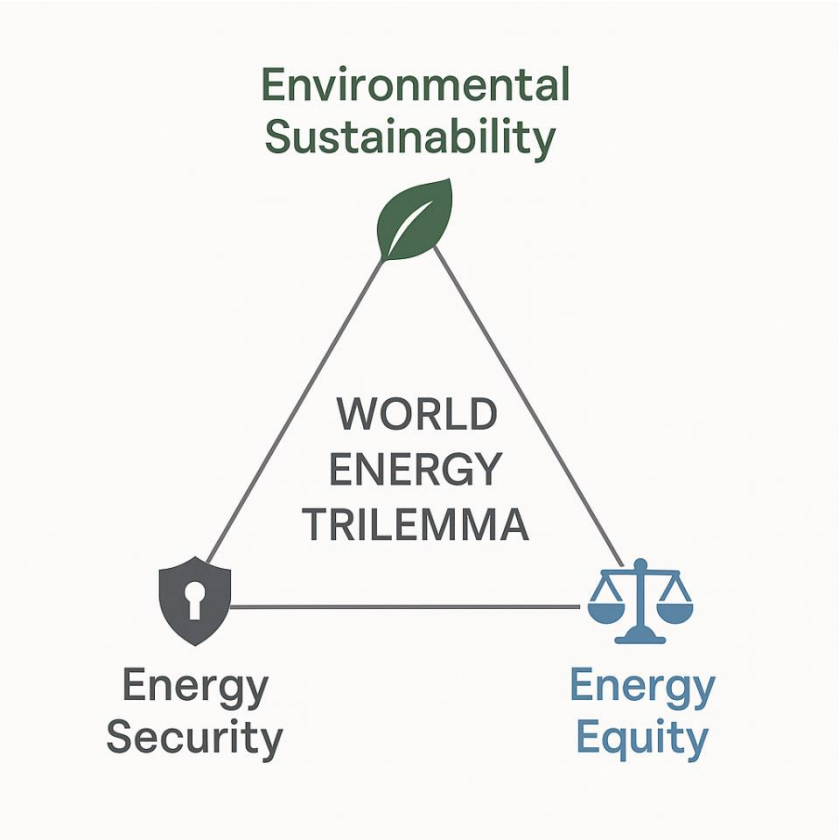

Figure 2. World Energy Trilemma (modified from [13]).

The necessity for rapid transformation of energy systems has been explicitly stated in scientific literature, with researchers emphasising that current energy systems are unsustainable from social, economic, and environmental perspectives.

The urgency of this transformation has increased in line with the findings of scientific research, which demonstrates that the energy sector is responsible for approximately 75% of global greenhouse gas emissions, with fossil fuels providing 79% of the total energy supply as of 2022 [14]. This dependency on carbon-intensive energy sources has necessitated a radical rethinking of energy systems, catalyzing what researchers define as the contemporary energy transition toward renewable and sustainable energy sources [15]. Current energy systems demonstrate substantial momentum toward renewable energy deployment, with global renewable energy capacity experiencing exponential growth from 2.1 TW in 2015 to 5.2 TW in 2025 (Figure 3), representing a compound annual growth rate of 10.5% [16]. This expansion has been particularly pronounced in variable renewable energy technologies, with solar photovoltaic capacity increasing from 233 GW to 2,450 GW over this period, while wind energy capacity expanded from 433 GW to 1,250 GW [17]. It is evident that these growth trajectories are indicative of both technological advancement and supportive policy frameworks. Indeed, it is demonstrable that renewable energy technologies are achieving competitive levelised costs of electricity in a number of global markets [18].

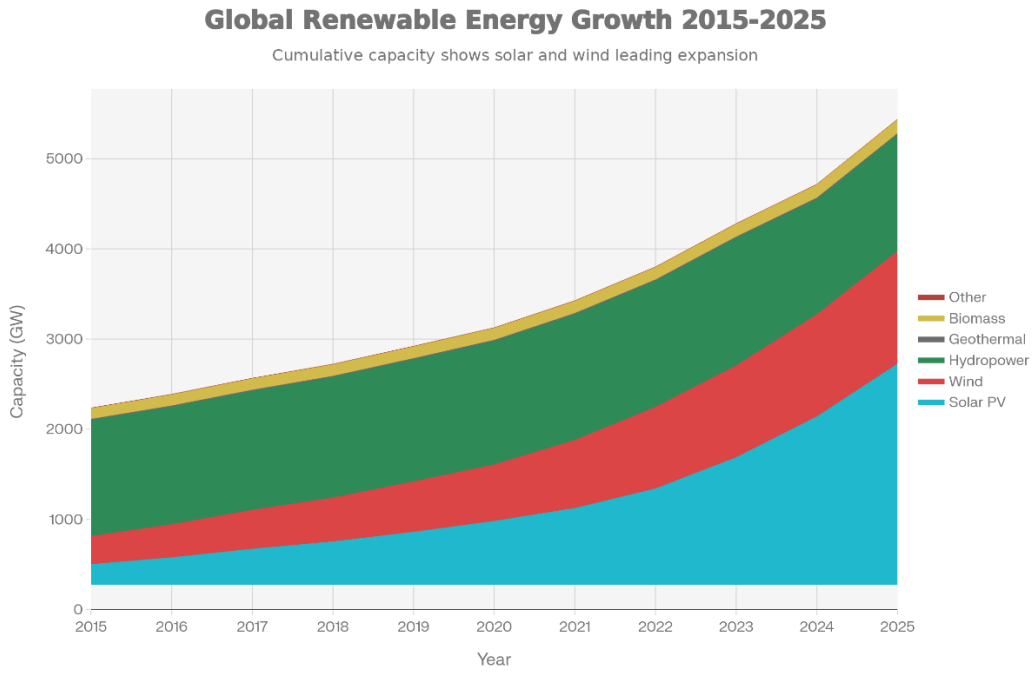

Figure 3. Global renewable energy capacity (data derived from [14,17,19]).

The European Union has established ambitious targets, including the achievement of climate neutrality by 2050, with interim emission reduction targets of 55% by 2030 [20,21].

International cooperation and policy coordination represent fundamental requirements for achieving global energy transition objectives [22,23]. The Paris Agreement has established frameworks for coordinated action, with countries developing nationally determined contributions and long-term strategies for achieving net-zero emissions [24,25]. The success of energy transition efforts depends on effective policies, cooperation between public and private stakeholders, and coordination across diverse territorial and institutional scales from local to international levels. Only through comprehensive coordination can the benefits of energy transition overcome existing challenges and achieve the transformative changes necessary for sustainable energy future.

The thermal energy sector is a significant part of the global renewable energy transition, accounting for about 50% of final energy consumption and 38% of energy-related CO_2. Despite this substantial environmental impact, modern renewable sources currently supply only 13% of global heat consumption, representing a critical gap in climate mitigation efforts that demands urgent technological and policy intervention [26]. The sectoral distribution of thermal demand indicates that industrial process heat constitutes 50% of total demand, with building applications (space and water heating) accounting for 47%. The discrepancy between the emissions of the thermal sector and the penetration of renewable energy sources highlights the necessity for the accelerated deployment of renewable heating technologies and the integration of these technologies into comprehensive systems [27].

Heat pumps are the primary means of decarbonising space and water heating in buildings. The heat pump itself consists of a compressor, which moves a refrigerant through a refrigeration cycle, and a heat exchanger, which extracts heat from the source. The heat is then passed on to a heat sink through another heat exchanger. It extracts heat from a source, such as the surrounding air, geothermal energy stored in the ground, or nearby sources of water or waste heat from a factory. It then amplifies and transfers the heat to where it is needed (Figure 4). The energy performance of heat pumps is commonly expressed through the coefficient of performance (COP), defined as the ratio between the useful heating output and the electrical energy input, and, in cooling mode, through the energy efficiency ratio (EER), defined as the ratio between the delivered cooling capacity and the corresponding electrical power input. Ground-source heat pumps (GSHPs) have been shown to demonstrate exceptional efficiency, with COP ranging from 3.5 to 6.0 [28]. This results in energy efficiency levels of 300-600%, whilst concurrently reducing CO_2 emissions by 50-70% in comparison with conventional fossil fuel systems [29]. Air-source heat pumps offer deployment options with greater accessibility, exhibiting COP values ranging from 2.8 to 3.6 [30].

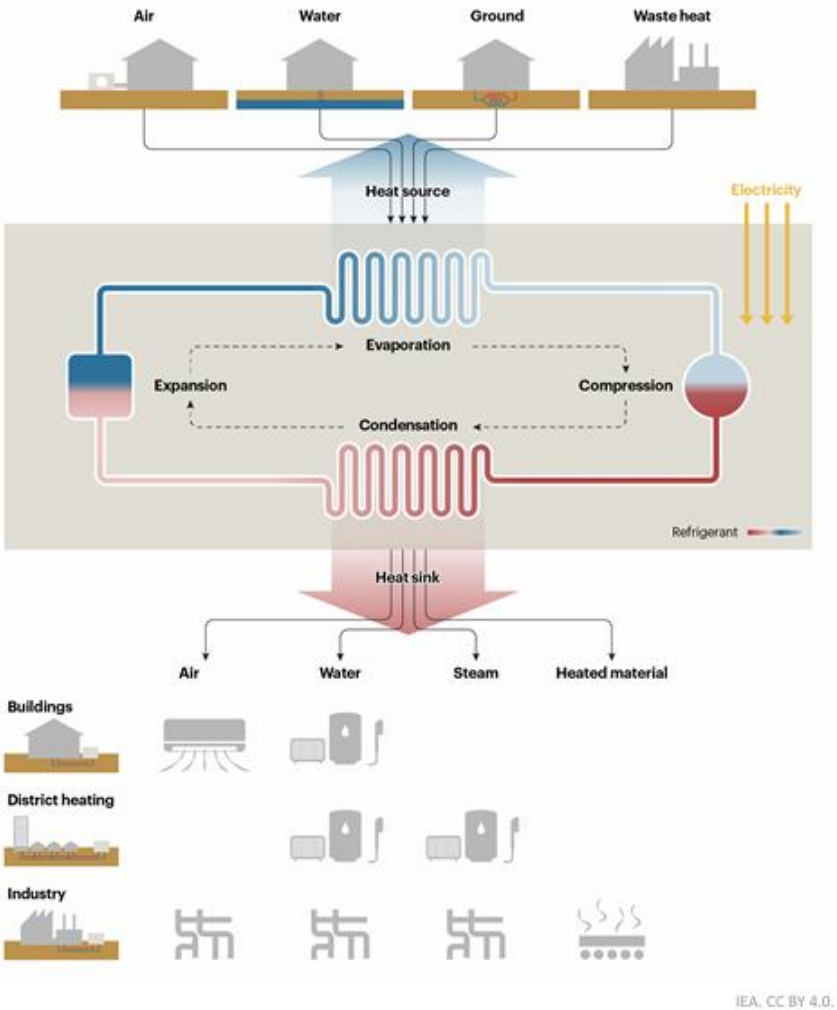

Figure 4. Workflow of a typical residential heat pump (from [31]).

A total of 2.3 million heat pumps were installed in the European Union by 2024 (the data cover 19 Member States). While deployment experienced a significant increase in 2022, with 2.8 million heat pump units installed, it exhibited a decline to 2.7 million units in 2023 and 2.3 million units in 2024 (Figure 5). The most significant growth in air-water heat pumps has been observed within the European Union over the past two decades. The number of air-water heat pumps sold increased from 216,000 in 2015 to 809,000 in 2024, representing an increase of 275% (Figure 6). The number of geothermal heat pumps (ground source/water-water heat pump, as illustrated in Figure 7) sold increased from 79,000 in 2015 to 87,000 in 2024, marking an increase of approximately 10% [32].

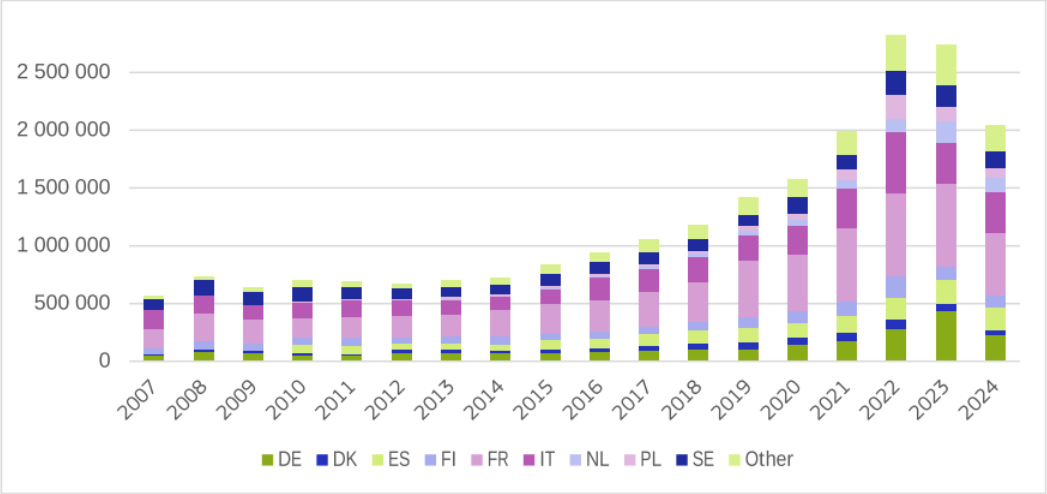

Figure 5. Annual sales of heat pumps, per Member State [32].

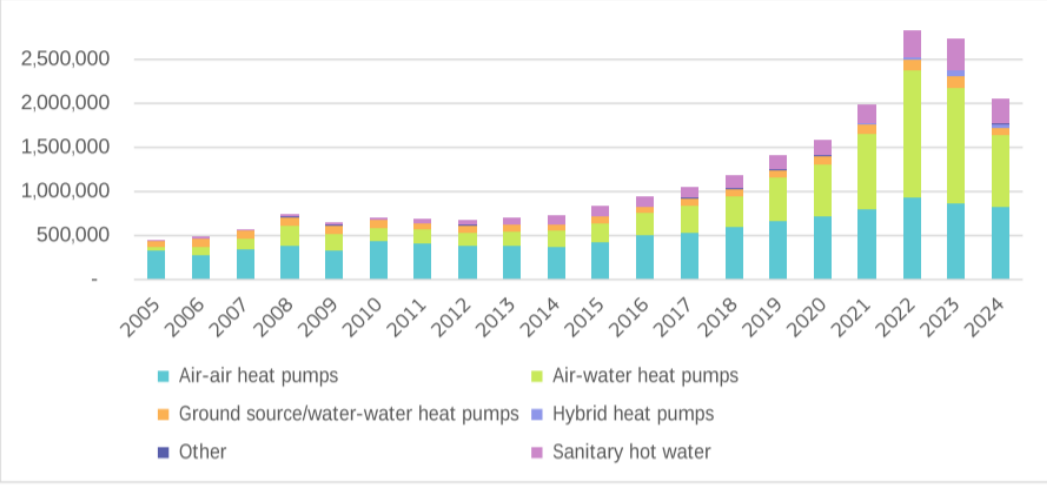

Figure 6. Annual sales of heat pumps, per type in 19 European Country [32].

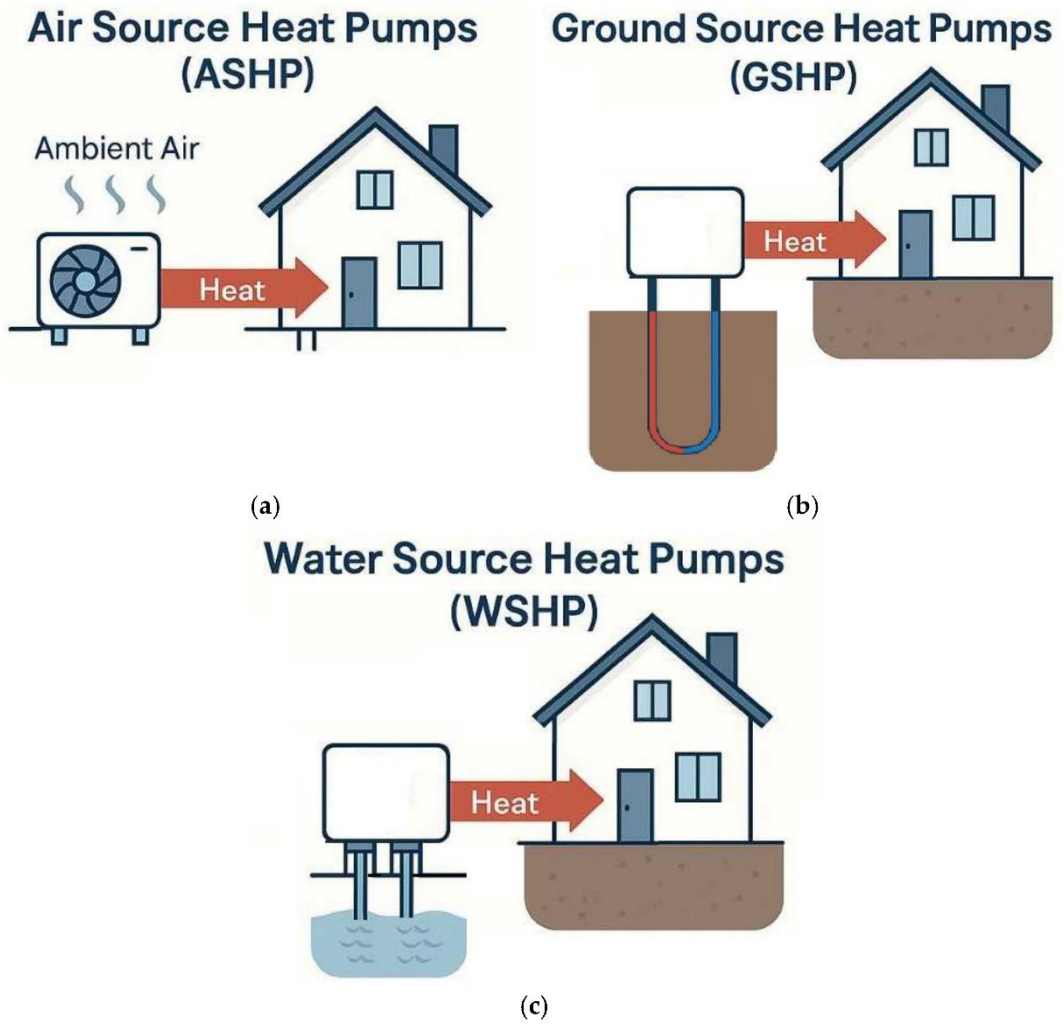

Figure 7. Types of heat pumps due to the source of heat: (a) ASHP, (b) GSHP, (c) WSHP. (from [33]).

Market dynamics and technological advancement trends demonstrate accelerating deployment in specific segments while revealing persistent systemic barriers. In 2023, global sales of heat pumps experienced an increase of 11%, with a particularly notable 47% growth observed in European markets (Figure 8). This growth can be attributed to concerns regarding energy security and the presence of supportive policy frameworks [34,35]. Globally, solar thermal capacity reached 542 GWth in 2022, with an annual generation of 442 TWh [36]. District heating networks demonstrate increasing renewable integration, with advanced systems achieving high percentage of renewable shares through biomass, geothermal, and waste heat utilisation [37,38]. Nevertheless, the deployment of such systems remains constrained by high upfront costs, inadequate infrastructure, and regulatory barriers, particularly for heat pumps and solar thermal systems [39].

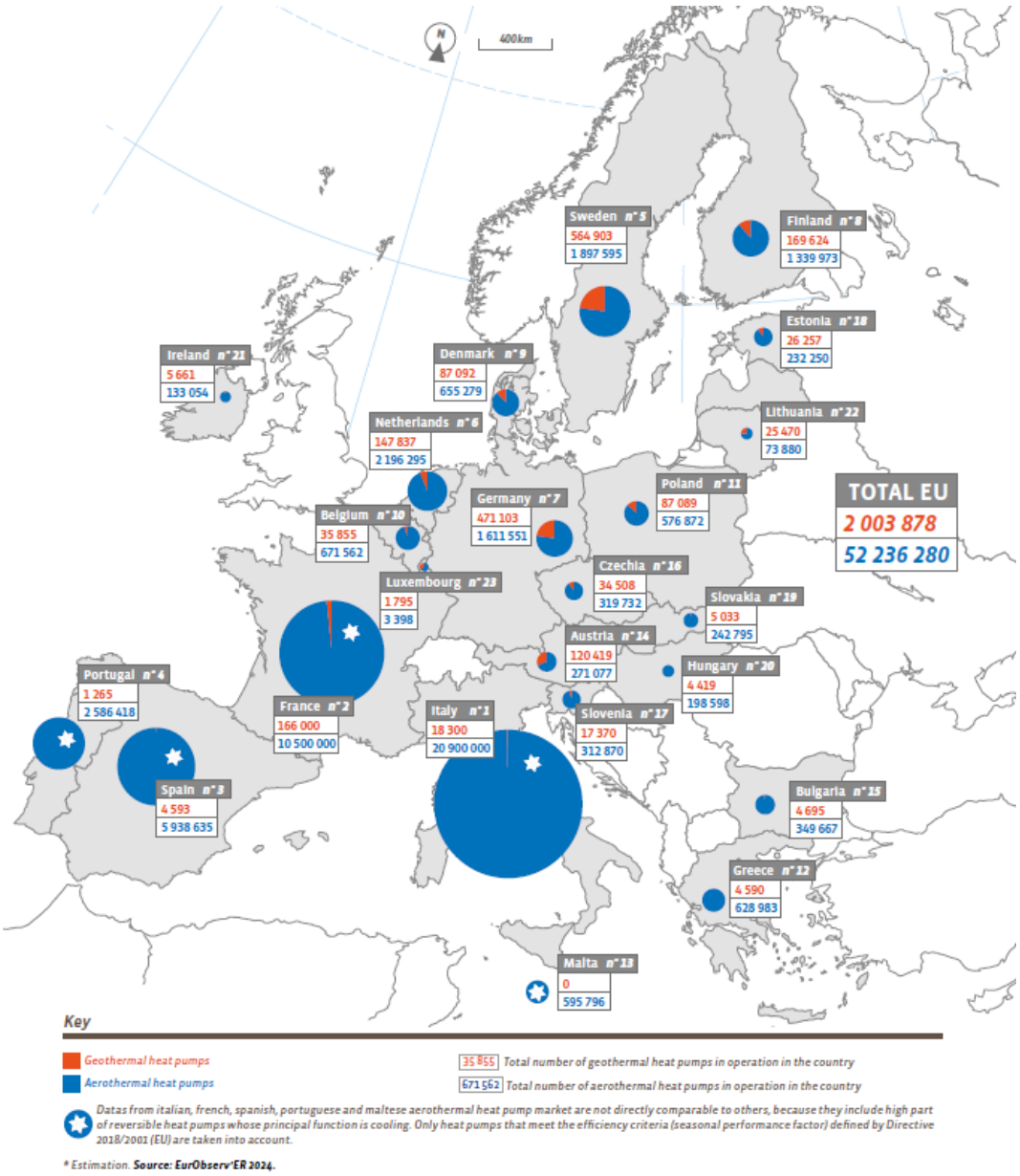

Figure 8. Air-source and ground-source heat pumps in the European market in 2023 (from [35]).

Power-to-heat systems facilitate the flexible utilisation of surplus renewable electricity through the use of electric boilers and heat pumps, thereby engendering beneficial grid interactions that enhance stability while reducing thermal sector emissions [40,41]. Seasonal thermal energy storage technologies, including aquifer thermal energy storage (ATES, chapter 4), borehole thermal energy storage (BTES, chapter 5), address the fundamental temporal mismatch between renewable energy availability and heating demand patterns [42]. These storage solutions facilitate the capture of heat during periods of renewable abundance, thereby ensuring its utilisation during times of peak demand [43]. This approach achieves round-trip efficiencies ranging from 60% to 80%, while concurrently providing load balancing capabilities that enhance system reliability [44,45].

1.2 Geothermal Energy

Geothermal energy is defined as *the natural heat stored in the rocks and water that is found within the Earth*. A geothermal resource is defined as a reservoir of heat located within the Earth, which can be extracted and utilised economically for the generation of electric power or for any other suitable industrial, agricultural or domestic application [46]. The phenomenon of geothermal energy derives from two fundamental sources: deep radioactive decay and residual planetary heat. These sources are responsible for the generation of hot rock, steam, or hot water at depth. From a thermodynamic perspective, enthalpy H (per unit mass) is defined as the heat content of the fluid and can be expressed as follows:

Equation 1

$$H = U + P \cdot V$$

where U is the internal energy, P is the pressure and V is the volume of the reservoir fluid. The classification of geothermal resources is typically based on the temperature (or enthalpy) of the reservoir fluid [47]. Low-enthalpy (or low-temperature) resources are defined as those with temperatures below approximately 90°C, medium/intermediate-enthalpy resources are characterised by temperatures ranging from 90 to 150°C, and high-enthalpy resources are classified as those with temperatures above 150°C (Table 1).

Table 1. Overview of the main geothermal energy type characteristics.

Type	Temperature Range (°C)	Depth (m)	Primary Applications	Technology	Geological Setting	Environmental Impact
High Enthalpy	>150	1000-4000+	Electricity Generation	Steam/Flash Turbines, EGS	Volcanic/ Tectonic	Low-Medium
Medium Enthalpy	100-150	500-2000	Electricity & District Heating	ORC, Binary Cycles	Sedimentary Basins	Very Low
Low Enthalpy	<100	10-400	Space Heating/ Cooling	GSHP, BTES, ATES, Energy Piles	Shallow Subsurface	Minimal

These categories correspond to different technologies and applications: low-enthalpy systems typically serve building-scale heating and cooling via heat pumps and shallow wells, medium-enthalpy systems can supply district heating or small power via binary (Organic Rankine Cycle, ORC) plants, and high-enthalpy systems yield electricity or large-scale heat via steam turbines or flash plants. In contrast to intermittent energy sources that are contingent on meteorological conditions, geothermal energy offers a consistent baseload thermal capacity with exceptional reliability and minimal environmental impact.

Low-enthalpy geothermal resources are defined as those with a temperature of approximately 90°C [48]. The primary technology employed is the ground-source heat pump (GSHP), which utilises either a closed-loop or open-loop system to facilitate heat exchange with the ground or groundwater [49–51].

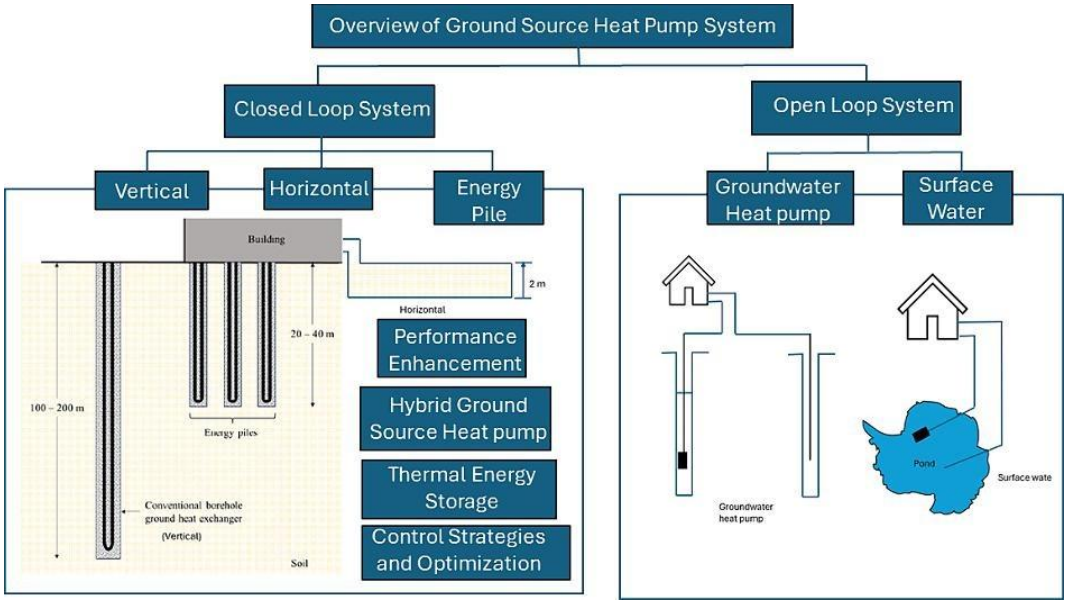

Figure 9. Overview of GSHP System [50].

In heating mode, heat pumps elevate the moderately warm ground heat (frequently ranging from 5 to 15°C during winter months) to a temperature suitable for building heating [52]. Despite the low source temperature, contemporary heat pumps yield high COP [53,54]. In practice, seasonal performance factors (SPF) for ground-coupled systems frequently range around 4.0–5.5 (meaning 4–5 times as much heat is delivered as electric input) [55]. Low-enthalpy systems encompass vertical borehole fields, horizontal loops, groundwater well doublets, and surface heat exchangers (e.g. rivers or lakes). These systems are employed for the provision of space heating, cooling, and domestic hot water in buildings, with a growing trend of integrating these systems into low-temperature district heating networks [56,57]. In Italy, geothermal heat pumps are the dominant form of low-enthalpy generation, with an installed capacity of over 1,300 MWth by 2020 [58]. It is estimated that approximately 50% of Italy's geothermal heat is utilised for building heating, with an annual growth rate of approximately 3% [58]. Regulatory frameworks mandate meticulous environmental management practices, such as the reinjection of cooled water to avert water depletion, and thereby ensure the preservation of groundwater, a particular concern in open-loop systems [59]. The integration of geothermal energy with broader renewable thermal strategies positions this resource as a cornerstone technology for comprehensive sector decarbonisation [60]. Geothermal baseload characteristics complement intermittent renewable sources, while direct thermal applications maximise energy efficiency in comparison to electricity-based heating approaches [61]. The integration of advanced storage systems facilitates the dynamic allocation of energy resources, thereby ensuring the optimal functioning of the grid [62–64]. Community-based deployment models have been shown to

maximise local economic benefits while ensuring sustainable resource management [65,66]. The confluence of technological maturity, economic competitiveness, environmental benefits, and scalability potential positions geothermal energy as a pivotal component of renewable thermal energy transition strategies, which are imperative for achieving global climate objectives while ensuring the maintenance of energy security and economic development goals [67–69].

The thesis will focus on an Italian case studies applied to the metropolitan city of Turin, and will explore how multiple solutions of shallow geothermal energy as a renewable source can be integrated into a densely populated urban context for a successful thermal energy transition (**Figure 10**).

The chapter 2 addresses groundwater heat pump systems (open-loop), examining regulatory frameworks at European, national, and regional levels, developing the Geothermal Aquifer Potential (GAP) methodology for spatial assessment, and employing MODFLOW and FEFLOW numerical models to predict groundwater flow and thermal plume evolution in some case studies in Turin.

The chapter 3 investigates borehole heat exchanger systems (closed-loop), establishing design parameters through analytical methodologies based on international standards, examining borehole spacing and thermal interference prevention, and presenting case studies demonstrating technology applicability in building-scale applications under specific hydrogeological conditions.

The chapter 4 explores Aquifer Thermal Energy Storage (ATES) systems, demonstrating innovative well positioning strategies that enable seasonal thermal energy storage in high-velocity aquifer systems, examining hybrid sequential, seasonal reversible, and cascaded recovery configurations through numerical modelling and case studies.

The chapter 5 conducts comprehensive global analysis of Borehole Thermal Energy Storage (BTES) installations, characterizing critical design parameters including borehole spacing, grout thermal properties, array geometry, and groundwater flow influence, and presenting numerical modelling case studies validating system performance and thermal impact containment.

Figure 10 outlines the key questions that prompted this research and analysis. The first of these is the fundamental question underlying this PhD: *is it possible to deploy geothermal energy, a renewable thermal resource, as a viable and sustainable solution in densely populated urban environments?* The chapters that follow provide a comprehensive scientific and practical response to this central inquiry through systematic examination of diverse low-enthalpy geothermal technologies, numerical modelling validation across case studies in the Metropolitan City of Turin, comparative technology assessment to guide informed decision-making, and evidence-based policy recommendations for streamlined permitting and cumulative impact management. This research, developed in close collaboration with IREN S.p.A. Company (Prot. n° 49626 del 2023) and supported through academic partnership with Politecnico di Torino, aims to provide both rigorous scientific analysis and actionable guidance addressing a critical challenge

of our historical period: the decarbonisation of thermal energy systems in urban contexts aligned with European climate neutrality objectives.

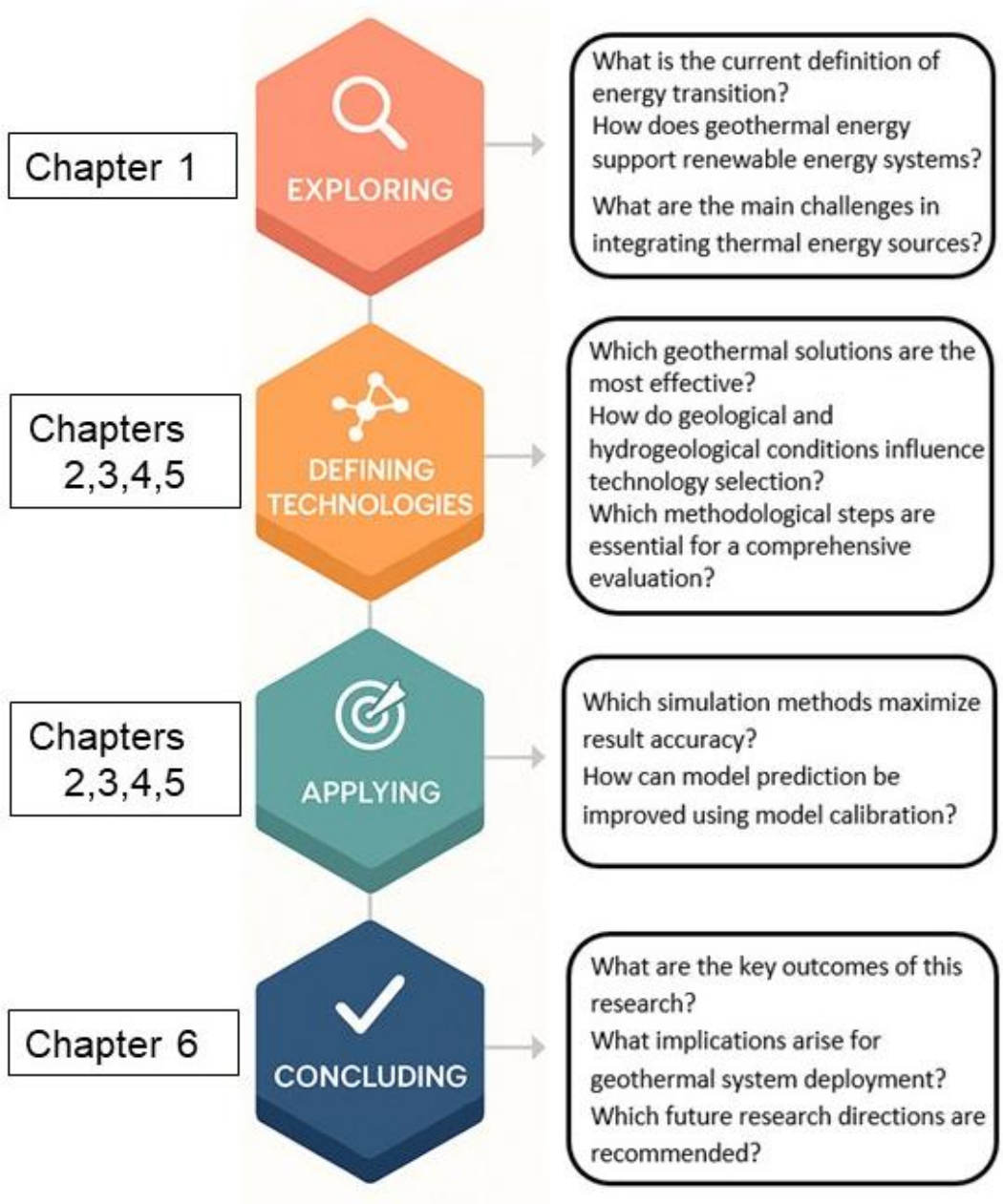

Figure 10. Summary of the thesis and main questions.

Chapter 2

Open-loop

"[…] I believe that when the deposits of coal are exhausted, we shall heat and warm ourselves with water. Water will be the coal of the future"

Jules Verne (1874)[2]

Low-enthalpy geothermal systems using shallow groundwater are an important part of urban energy strategies. Open-loop groundwater heat pump systems use the thermal stability and high heat capacity of shallow aquifers to meet space heating and cooling demands while maintaining high performance compared to conventional air-source systems. However, the operational viability and environmental sustainability of such systems are contingent upon the rigorous integration of three interdependent knowledge domains. Firstly, there is the need for multilayered regulatory frameworks governing groundwater protection and energy development at European, national, and regional scales. Secondly, there is the need for the hydrogeological characterisation of shallow aquifer systems and their capacity to support sustainable groundwater extraction and reinjection. Thirdly, there is the need for predictive capabilities to model the spatio-temporal evolution of thermally altered zones (TAZ) that arise from temperature perturbations in the thermal plume during long-term operation. This chapter synthesises current European directives and Italian national and regional legislation governing open-loop geothermal systems. It also presents a computationally efficient screening methodology (Geothermal Aquifer Potential – GAP) for spatially distributed assessment of geothermal potential in shallow aquifers. Furthermore, it documents rigorous numerical modelling approaches utilising finite-difference (MODFLOW) and finite-element (FEFLOW) techniques coupled with advanced parameter estimation methodologies for prediction of coupled groundwater flow and heat transport dynamics. The application to the Turin metropolitan area shows that scientifically-guided modelling, integrated with regulatory frameworks and design protocols, enables sustainable deployment of open-loop systems at various organisational scales.

[2] *The Mysterious Island, Part 2, Chapter 11, Jules Verne, (1874).*

2.1 Overview

Declaration: The topic described in this chapter was previously published in the following publications:

- Berta, A.; Gizzi, M.; Taddia, G.; Russo, S.L. (2024) The role of standards and regulations in the open-loop GWHPs development in Italy: The case study of the Lombardy and Piedmont regions. *Renew. Energy*, 223, 120016. https://doi.org/10.1016/j.renene.2024.120016.
- Berta, A., Taddia, G., (2024). Exploring Urban Sustainability: The Role of Geology and Hydrogeology in Numerical Aquifer Modelling for Open-Loop Geothermal Energy Development, the Case of Torino (Italy). *Geosciences* (2024), Vol. 14, Page 180 14, 180. https://doi.org/10.3390/GEOSCIENCES14070180
- Gizzi M, Berta A, Vagnon F, et al. (2024) Groundwater heat pumps diffusion in the Turin City urban area: modelling for the thermally affected zone analysis of an open-loop geothermal system. *Italian journal of engineering geology and environment* 165–173.
- Gizzi M, Berta A, Vagnon F, et al. (2024) Geothermal Technologies: Progress Through Examples of Sustainable Applications in an Urban Context. *Geoingegneria Ambientale e Mineraria* 51–57.

Open-loop groundwater heat pump (GWHP) systems represent a category of low-enthalpy geothermal applications that leverage the relatively stable and high heat capacity of shallow aquifers to facilitate space heating and cooling in buildings. This process involves the extraction of groundwater, the exchange of heat through a heat pump, and the subsequent discharge of thermally-altered water back into the aquifer or to surface receivers. This operational principle has been demonstrated to facilitate elevated COP and diminished primary energy consumption in comparison to air-source systems. Nevertheless, it concomitantly engenders a discrete array of hydrogeological, thermal, regulatory and planning challenges that must be addressed when deploying GWHPs at the building and urban scales [70–72]. The classification of groundwater and aquifers is pivotal for site selection, particularly the distinction between shallow, unconfined aquifers that receive direct infiltration and are hydraulically connected to surface water and deeper, slower-turnover aquifers with distinct properties. Shallow aquifers are typically preferred for open-loop applications, while deeper aquifers should generally be excluded from direct exploitation for thermal use to preserve water resource quality and quantity. It is imperative to recognise that the initial and indispensable step in conducting feasibility studies and planning procedures, particularly within the context of Italian legislation, which explicitly delineates groundwater categories and stipulates the protection of deep aquifers, is the hydrogeological characterisation of parameters such as grain size, hydraulic conductivity, transmissivity, natural hydraulic gradient, groundwater temperature, and the connectivity with surface waters.

Relevant legal references include Legislative Decree No. 152/2006 and Regional Law 22/1996, as amended by Regional Law 6/2003 [70,73].

The principal environmental concern of GWHP operation is the formation and evolution of TAZ or thermal plume arising from the reinjection of water at temperatures differing from the natural condition. The TAZ propagates under the influence of advection, dispersion and conductive exchange with the solid matrix. It has been demonstrated that this may produce upstream thermal recycling or thermal breakthrough at extraction wells. Furthermore, it has been observed that the TAZ can interact adversely with neighbouring groundwater users and ecosystems. This interaction can produce hydraulic and thermal interferences that have the capacity to degrade heat pump performance (by reducing COP through warmer abstraction temperatures during cooling, or colder temperatures during heating) and impair downstream abstractors such as drinking-water wells or other GWHP installations [70,74–76]. Consequently, the ability to predict TAZ dimensions and temporal evolution is a pivotal requirement for sustainable design and approval. Analytical solutions (e.g. those developed by Banks and subsequent analytical formulations) offer rapid, low-complexity tools for estimating plume extent in simplified, homogeneous, steady-state conditions. However, their applicability is limited by the common violation of underlying assumptions in urban settings (e.g. heterogeneous stratigraphy, anisotropic hydraulic conductivity, variable pumping/injection schedules, and complex boundary conditions). In contrast, numerical groundwater and heat-transport models, despite being more computationally intensive and necessitating detailed site parameterisation, facilitate a realistic evaluation of plume dynamics, inter-system interference, and long-term impacts. These models are now extensively utilised in both individual plant design and urban-scale planning, where the assessment of cumulative effects is imperative [71,76,77].

Sensitivity analyses reported in the literature, indicate that thermal plume dimensions are most responsive to hydraulic parameters, particularly hydraulic conductivity and regional hydraulic gradient, and to a comparatively lesser degree to thermal parameters (specific heat capacity, thermal conductivity) and operational variables (pumping and reinjection rates, temperature differential). These findings underscore that the feasible and sustainable GWHP deployment in urban areas depends critically on accurate hydrogeological data and on the inclusion of realistic temporal horizons in modelling exercises, because short-term simulations can underestimate long-term plume migration and feedback phenomena [76]. Regulatory frameworks and administrative workflows thus become pivotal factors in determining the pace and pattern of GWHP adoption. Permit regimes must achieve a balance between the need for rapid diffusion of efficient heating and cooling technologies and the obligation to protect groundwater resources and public water supplies.

The ramifications of GWHP proliferation for urban planning necessitate a strategic approach by municipal and regional authorities, as opposed to a mere project-by-project basis. In order to avoid negative interference and to enable synergistic use of distributed GWHP resources, it is necessary to undertake city-

scale inventories of subsurface hydrogeology, strategic zoning for well fields, the development of thermal budgets for aquifers, the installation of monitoring networks and data repositories, and the adoption of rules governing minimum well separations, maximum allowable reinjection temperatures and cumulative thermal loads. Moreover, the implementation of educational initiatives targeting drillers, designers and permitting officers, in conjunction with the establishment of certification schemes, is imperative to ensure the technical competence of installations and the adherence to environmental safeguards during drilling, operation and decommissioning [75,78,79].

In order to reduce the adverse thermal impacts, the following mitigation strategies should be considered:

- Discharging to surface water bodies should be given priority, where hydrogeological assessments demonstrate acceptability;
- Indirect heat exchangers should be used to avoid direct groundwater contact with building systems;
- Well doublets should be designed with optimised spacing and flow regimes based on site-specific modelling;
- Adaptive operational strategies such as seasonal flow modulation or cascade use between heating and cooling loads should be implemented;
- Thermal recycling should be exploited deliberately as part of an integrated design when space constraints preclude large separations.

The selection of modelling approach is congruent with the prevailing decision context and analytical formulae and reduced-order models are valuable screening tools. They can be applied where assumptions are approximately met and where rapid estimates are required. However, detailed numerical models are indispensable for definitive design, regulatory compliance and urban planning. This is because they can represent heterogeneous stratigraphy, anisotropy, transient operation and interactions with multiple users. Such models should be calibrated where possible against field observations and extended over decadal operating horizons [71,76,77,80].

2.2 Regulatory Framework

This section synthesises the regulatory architecture that frames the deployment of open-loop GWHP systems in the Piedmont Region. The policy is derived from the European policy context through national transposition to the regional and municipal instruments that directly determine permitting, monitoring and operational constraints in the Metropolitan Area of Turin. The regulatory framework must be interpreted as a multilevel governance cascade, in which European directives and political priorities establish objectives and constraints for water protection and renewable energy promotion. These objectives are then transposed into substantive environmental and administrative requirements by national legislation. As specified by regional and municipal instruments, technical thresholds, authorisation classes and operational monitoring obligations are binding for project proponents and permitting authorities. A geothermal project must comply with a number of main regulatory references, concerning the in-force national, regional, and municipal regulations (i.e. geothermal wells drilling authorization requests and plant final testing operations). These references were considered and summarised through a schematic approach (**Figure 11**).

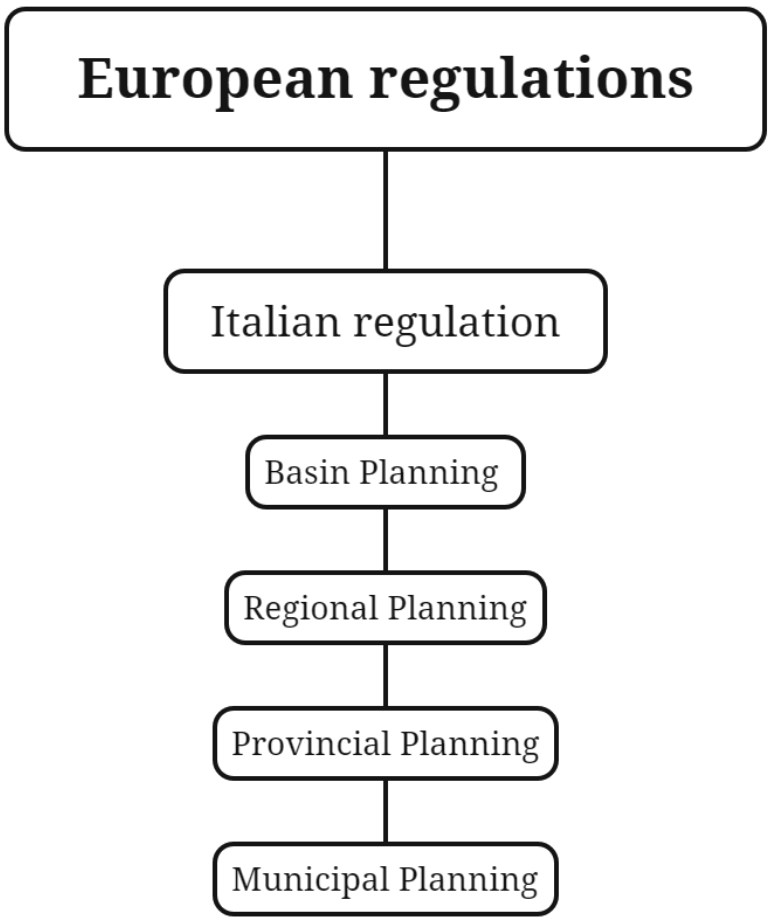

Figure 11. Flowchart illustrating the regulatory tools analysis that was performed at differing levels.

2.2.1 European Regulations

The regulatory framework of the European Union for open-loop geothermal systems is derived from a complex network of legislation pertaining to climate, energy, and water protection. This network is fundamentally anchored by the European Green Deal's commitment to achieve climate neutrality by 2050 [81]. The European Green Deal, a comprehensive initiative spearheaded by the European Commission, entails a series of policy recommendations aimed at reshaping the EU's climate, energy, transport, and taxation agendas [82]. The overarching objective of the European Green Deal is to curtail net greenhouse gas emissions by a minimum of 55% by the year 2030, in comparison to 1990 levels. Italy's commitment to promoting the European Green New Deal, conceptualised as a green pact with businesses and citizens that positions the environment as the country's economic driver, exemplifies national-level implementation through measures such as Law No. 160 of 27 December 2019 [83], and the transformation of the Interministerial Committee for Economic Planning (CIPE) into the Committee for Sustainable Development (CIPESS) under Law No. 141 of 12 December 2019 [84], pursuing sustainable development objectives aligned with UN Resolution A/70/L.1 [85]. This overarching policy context provides the foundation for a multi-layered regulatory approach that governs open-loop geothermal systems through both renewable energy promotion and groundwater protection mechanisms.

The primary renewable energy framework is established by Directive (EU) 2018/2001 (RED II), which sets a binding 32% share of renewables in EU final energy consumption by 2030 and explicitly mandates that Member States assess and support innovative heating and cooling technologies, including low-enthalpy geothermal systems and heat pumps [86]. Article 18(3) of RED II stipulates that Member States must ensure the provision of certification or equivalent qualification systems for installers of small-scale biomass boilers and stoves, solar photovoltaic and solar thermal systems, shallow geothermal systems, and heat pumps, with specific reference to the systems delineated in Annex IV. The directive also accelerates deployment through Article 16e, which establishes that permit-granting processes for heat pumps below 50 MW must not exceed one month, and a three-month maximum timeline is granted for ground-source geothermal heat pumps. It is imperative that grid connection procedures for heat pumps with an electrical capacity of 12 kW or less are authorised within a period of two weeks from the date of notification. However, this timeframe may be extended in the event that justified safety concerns are raised.

Directive (EU) 2023/2413 (RED III), which entered into force on 20 November 2023, has substantially expanded these requirements by increasing the 2030 renewable energy target to a binding 42.5% with an aspiration of 45% [87]. The RED III Directive establishes annual increases in the renewable share of building heating and cooling of 0.8% through 2026 and 1.1% from 2026 to 2030, creating direct market demand for geothermal systems. The directive introduces a series of measures designed to facilitate the process of obtaining permits, including the designation of "renewables acceleration areas" within Member States. In these

designated areas, Member States are required to establish locations that are particularly conducive to the installation of renewable energy infrastructure, with the objective of reducing the environmental assessment requirements typically associated with such projects. The Article 15c imposes obligations on Member States to designate these acceleration areas for at least one renewable technology, while the Article 16e specifically reduces permitting timelines for geothermal installations and requires Member States to give priority to projects recognized as being of overriding public interest.

The Energy Efficiency Directive (EU) 2023/1791 establishes a binding target of 11.7% reduction in final energy consumption by 2030, accompanied by specific provisions pertaining to geothermal deployment [88]. Article 14 imposes an obligation on Member States to ensure the provision of financing facilities for energy efficiency improvement measures. The term "efficient district heating and cooling" is defined as systems utilising a minimum of 50% renewable energy, 50% waste heat, 75% cogenerated heat, or 50% of a combination thereof. The directive promotes local heating and cooling plans in municipalities exceeding specified population thresholds and progressive increases in efficient energy consumption in heat supply systems, including district heating networks that can integrate geothermal sources. The Article 7(3) stipulates that ambient and geothermal energy utilised for heating and cooling through heat pumps may be categorised as renewable energy, contingent upon the heat pump's efficiency exceeding the stipulated performance thresholds.

In the context of open-loop geothermal systems, the fundamental regulatory instrument is the Water Framework Directive 2000/60/EC, which establishes a comprehensive framework for Community action in the domain of water policy protection [89]. At the European level, the Article 1 promotes the sustainable utilisation of water resources, with a focus on ensuring long-term protection and the progressive reduction of pollution, thereby preventing further contamination. The Article 2 provides crucial definitions: the term "groundwater" is defined as *'all water that is located beneath the surface of the ground within the saturation zone and that is in direct contact with the ground or subsoil'*. Conversely, the term "water use" is understood to encompass water services in addition to any other activity that exerts a substantial influence on the status of water. The Article 4 establishes environmental objectives that require Member States to take measures to prevent deterioration of groundwater status, ensure a balance between abstraction and recharge, and achieve "good groundwater status" within 15 years of the directive's entry into force.

The most direct provisions of the Water Framework Directive for geothermal systems are contained in the Article 11, which establishes the requirements for programmes of measures. The Article 11(3)(e) stipulates the implementation of "regulations pertaining to the abstraction of groundwater, encompassing the establishment of a register or registers documenting water abstractions, in addition to a prerequisite requirement for prior authorisation for both abstraction and impoundment activities." It is noteworthy that exemptions may be granted for abstractions that demonstrate no substantial impact on the status of the water. It is

imperative to note that the Article 11(3)(f) delineates the requirement for prior authorisation for artificial recharge or augmentation of groundwater bodies. However, the provision is further qualified by the stipulation that Member States may authorise reinjection into the same aquifer of water utilised for geothermal purposes. This provision establishes the fundamental legal basis for open-loop geothermal operations, provided that the reinjected water does not compromise the environmental objectives of either the source or the recharged aquifer, and provided that controls are periodically reviewed and updated.

The Article 11(3)(j) deals with the matter of direct discharges to groundwater, and, in general terms, it prohibits such discharges. However, it provides for specific exemptions, including the reinjection of geothermal water into the same aquifer and the injection of water for technical reasons into geological formations that are permanently unsuitable for other purposes, provided that such injections contain only substances resulting from hydrocarbon extraction, mining, or geothermal operations. The Annex V establishes detailed technical criteria for determining "good quantitative status" and "good chemical status" of groundwater bodies, requiring monitoring of groundwater level regimes, conductivity, and pollutant concentrations. These technical standards establish the framework within which open-loop systems must demonstrate compliance through environmental impact assessments and ongoing operational monitoring.

The implementation of these directives varies significantly across Member States, creating a complex regulatory landscape that affects open-loop geothermal development. Water acts are typically concerned with the regulation of measures impacting groundwater temperature changes, groundwater use (including extraction and reinjection), and groundwater contact through drilling operations. In contrast, mining and construction acts primarily govern drilling works and environmental protection. However, none of these instruments specifically considers or regulates the geothermal energy stored in the geological environment. In the context of open-loop systems, water authorities generally mandate licensing for groundwater usage in accordance with national water framework legislation. This requirement holds particular relevance for groundwater heat pumps, given the consideration that even borehole heat exchangers are regarded as utilizing groundwater when physical properties undergo alteration. Areas of regulatory concern include groundwater pollution during drilling operations, potential connection of different aquifers, and antifreeze leakage from borehole heat exchangers.

Recent policy developments demonstrate an increasing recognition of the strategic importance of geothermal energy within the European Union. The Council Conclusions on the Promotion of Geothermal Energy, adopted on 16 December 2024, acknowledge geothermal energy as a vital renewable resource for enhancing energy security, sustainability, and decarbonisation, particularly in reducing emissions within the building sector [90]. These findings necessitate the formulation of a comprehensive strategy for decarbonising heating and cooling, encompassing the development of an European Geothermal Action Plan to expedite deployment, the establishment of an European Geothermal Alliance to facilitate

collaboration among stakeholders, and the streamlining of regulatory procedures for geothermal energy production, encompassing infrastructure, drilling, mining, and environmental processes. The conclusions specifically address open-loop systems by calling on Member States to '*encourage the application of an integrated approach to subsurface pore-space activities in order to harmonise geothermal energy usage with the protection of groundwater as well as with other uses of the subsurface pore-space activities such as carbon capture and storage, and hydrogen storage*'.

The establishment of environmental protection requirements gives rise to the introduction of additional regulatory layers, the impact of which is felt by open-loop systems. Directive 2018/2001 acknowledges the importance of geothermal energy as a local renewable energy source, noting that it typically results in significantly lower emissions when compared with fossil fuels [86]. However, the directive also acknowledges the potential for geothermal energy production to result in greenhouse gas emissions and the release of other substances from underground fluids and geological formations, which have the potential to be harmful to human health and the environment, depending on the specific geological characteristics of the area in question. The directive stipulates that the deployment of geothermal energy must be facilitated, provided that it exhibits a low environmental impact and results in greenhouse gas emissions savings when compared to non-renewable energy sources. This necessitates the implementation of comprehensive environmental impact assessments, geological risk evaluations, and long-term monitoring protocols for open-loop installations.

Member States are obliged to integrate these multiple regulatory streams into coherent national frameworks that address permit procedures, environmental assessments, technical standards, and monitoring requirements. The requirements for re-injection vary by country but generally permit re-injection into the same aquifer or aquifer of the same use, provided that the re-injected fluid maintains equivalent quality and does not impact groundwater quality [86].

The development of national dynamic inventories of geothermal energy resources and reserves designed to register annual changes and allow country-scale modelling is increasingly recommended to ensure compatibility at the pan-European level through common basic methodologies.

The harmonisation efforts concentrate on the development of best available technique reference documents for geothermal applications under the industrial emissions directive, the establishment of common EU methodologies for geothermal resource inventories, and the alignment of financial incentives and funding mechanisms to eliminate economic discrepancies across Member States. The ongoing revision of groundwater protection legislation is intended to provide more detailed prescriptions on surface discharge and reinjection criteria for used geothermal waters. The present regulatory developments, when considered in conjunction with targeted EU funding availability through programmes such as InvestEU and the Innovation Fund, create an evolving framework [90,91]. The purpose of this framework is to ensure that open-loop geothermal systems contribute effectively, sustainably and uniformly to Europe's clean energy

transition. In addition, the framework is designed to maintain rigorous protection of groundwater resources and environmental integrity.

2.2.2 National and Regional regulations

The Italian regulatory framework for open-loop geothermal systems reflects a complex, multi-layered governance structure that integrates national energy policy objectives with regional water protection mandates and local territorial planning requirements. A national reorganisation of regulations concerning geothermal resource exploration and exploitation was proposed through Legislative Decree No. 22 of 11 February 2010, which established the foundational framework for geothermal development in Italy [92]. In accordance with the Article 10 of Legislative Decree No. 22, the definition of small local utilisation of geothermal heat is as follows: thermal power below 2 MW, obtained from geothermal fluid at the conventional effluent temperature of 15 degrees Celsius and the drilling of wells up to 400 metres deep for the exploration, extraction, and utilisation of geothermal fluids or hot waters, including those from springs. In addition to the aforementioned applications, minor local uses of geothermal heat have been achieved through the installation of closed-loop systems. These systems were subsequently regulated by the Legislative Decree issued on 30 September 2022 [93], known as the "*Decreto sonde*" or Probe Decree (described in Chapter 3.2).

Administrative streamlining for small and medium-sized enterprises was subsequently achieved through Presidential Decree No. 59 of 13 March 2013, which established the Single Environmental Authorisation (*Autorizzazione Unica Ambientale* - AUA) system [94]. This decree integrated multiple environmental authorisations previously obtained separately by companies, including wastewater discharge authorisation, atmospheric emissions permits, noise pollution notifications, simplified waste treatment authorisation procedures, and related environmental compliance requirements. The AUA system requires submission of application forms to the Single Desk for Productive Activities (Sportello Unico per le Attività Produttive - SUAP) via designated online platforms, with competent authorities typically being provinces unless regional laws allocate competence to different governmental levels.

In the context of open-loop systems, the regulatory framework for groundwater protection is characterised by significant variations across different Italian cities and regions, governed by national, regional, and local regulations. Legislative Decree No. 152 of 3 April 2006 [95], specifically Title III concerning "Regulations on soil protection and combating desertification, protection of water against pollution and management of water resources," is the national regulatory reference point. This decree transposes the Water Framework Directive 2000/60/EC for Community action on water and water bodies through restoration, recovery, and improvement of aquatic ecosystems, sustainable use of surface and groundwater resources, implementation of specific measures to reduce discharges and emissions into water bodies, and mitigation of flood and drought effects [89].

At the basin level, the Po River Basin District Management Plan is the operational tool required by Directive 2000/60/EC, as implemented nationally through Legislative Decree No. 152/06. This plan defines a coherent and sustainable policy for community water protection through an integrated approach to different management and ecological aspects at the river basin district scale. The plan constitutes a comprehensive framework that coordinates water resource management across the Po River basin, which encompasses significant portions of northern Italy, including the Piedmont region where intensive shallow geothermal development is occurring. The basin-level approach recognises that hydrological systems transcend administrative boundaries and require coordinated management strategies that consider cumulative impacts across jurisdictional lines

At the regional level in Piedmont, the Water Protection Plan (*Piano di Tutela delle Acque* - PTA) establishes criteria for the prevention and control of groundwater pollution through continuous monitoring [96]. The Plan stipulates that the good quantitative status of groundwater is achieved when available groundwater resources exceed abstractions in long-term quantitative balance analysis and anthropogenic changes in groundwater levels do not damage surface waters and related ecosystems.

The PTA was most recently updated in 2021 through Regional Council Decision No. 179-18293 [96], with the aim of protecting and valorising surface and groundwater within the framework of sustainable community development and achieving the environmental objectives prescribed by the Water Framework Directive 2000/60/EC. The plan is also instrumental in enhancing the resilience of aquatic environments and connected ecosystems, while addressing the ongoing effects of climate change.

This approach is fundamentally grounded in Regional Law No. 22 of 30 April 1996 concerning research, use, and protection of groundwater, which mandates that geothermal installations avoid communication between superficial and deep aquifers [97]. The establishment of technical criteria for identifying the base of superficial aquifer systems was codified through Regional Decision No. 34-11524 of 3 June 2009 [98], supported by appropriate cartographic tools for application of protective dispositions. This hierarchical protection strategy recognises that deep aquifers typically provide higher quality groundwater resources with longer recharge times, necessitating their preservation for drinking water supplies, while superficial aquifers can accommodate geothermal utilisation provided that appropriate safeguards are implemented to maintain their quantitative and qualitative status [99].

The Provincial Territorial Coordination Plan (*Piano Territoriale di Coordinamento Provinciale - PTC2*) is a key factor in achieving the desired qualitative and quantitative levels for groundwater and surface water [100]. This is achieved through a well-articulated strategy of behaviours aimed at controlling point and diffuse pollution. The strategy is designed to ensure the preservation of minimum naturalness levels in water bodies and the surrounding areas, as identified by the PTA. It entails the introduction of urban planning regulations and guidelines within General Town Planning instruments, with the objective of constraining soil

impermeabilization phenomena. The process of soil impermeabilization can be defined as *the loss of water absorption capacity of natural terrain due to human interventions*. Such interventions may include urbanization, surface paving, and the construction of buildings, roads, parking areas, and other infrastructure. These interventions can completely prevent or limit water absorption into soil. This phenomenon is associated with a number of deleterious effects on the environment and water resources. These include increased surface runoff, leading to local flooding, and accelerated soil erosion. In addition, decreased aquifer recharge results in lower piezometric levels, and increased temperatures due to lack of surface recharge (urban heat island).

At the municipal level, the Metropolitan General Territorial Plan (*Piano Territoriale Generale Metropolitano - PTGM*) promotes the protection and sustainable use of water resources as both heritage and a common right of humanity and all living species [101]. Furthermore, this Plan recognises water as an essential public good for the environment and economic and social development. The deep aquifer system must be protected and preserved in view of its priority use for human consumption, with exploitation of only the superficial aquifer permitted for geothermal purposes. This hierarchical approach to aquifer protection is predicated on the understanding that deeper groundwater resources typically provide higher quality drinking water and require longer recharge times, necessitating their preservation for essential human needs while permitting geothermal utilisation of more readily renewable shallow groundwater resources.

The Article 29 of the Plan Regulations of Piedmont Region's PTA stipulates that, in derogation from the prohibition on discharging into groundwater and subsoil as outlined in the Article 104 of Legislative Decree No. 152/2006, the competent authorities may authorise discharge into the same aquifer solely in the absence of technically and economically feasible discharge or reuse alternatives. The second paragraph of the Article 29 stipulates that such authorisations are issued subsequent to investigations with the aim of verifying the geometry and hydrochemical characteristics of the receptor water body, modifications induced on piezometric surface morphology, changes in aquifer chemistry through assessment of thermal and hydrochemical status effects, and overlapping effects of other geothermal plants operating on groundwater bodies in the investigation area. These requirements are indicative of the recognition that multiple geothermal installations have the potential to generate cumulative thermal and hydraulic impacts, which must be meticulously assessed and managed in order to ensure the integrity of the aquifer is maintained.

Region requires a range of technical documentation, depending on the discharge capacity assumed in projects (articles no. 10, 12, and 13 of Regional Presidential Decree no. 7/R of 25/06/2007 [170]). Small installations are defined as those with a discharge of up to 2 l/s, medium installations as those with a discharge between 2 and 10 l/s, and large installations as those with a discharge exceeding 10 l/s (**Table 2**).

Table 2. *Installation Classification by Discharge Capacity [170].*

Installation Category	Discharge Capacity	Documentation Level
Small	≤ 2 l/s	Basic
Medium	2–10 l/s	Enhanced
Large	> 10 l/s	Comprehensive

In the context of large-scale installations, the technical documentation must encompass reports that demonstrate the absence of reuse or discharge alternatives. This documentation should also include cartographies and settlement and project plans, as well as technical reports and graphic diagrams of plant circuits. These diagrams should provide maximum wastewater discharge temperatures and ensure that there is no interference between discharge and neighbouring building structures. Furthermore, the documentation must include the implementation of at least one control piezometer downstream of the discharge, as well as technical reports on water table characteristics. Finally, the documentation must predict the temporal evolution of heat/cold plume propagation in aquifers, simulating amplitude, duration, and propagation modes. The utilisation of predictive models for a minimum of three years of geothermal plant activity is mandatory, though not subject to stringent regulation. Numerical simulations must consider boundary conditions, natural aquifer conditions, geothermal plant parameters, and operating regimes, including monthly average temperature and flow rates. Furthermore, it is imperative to substantiate the absence of interference between extraction and discharge wells, as well as to demonstrate the absence of overlap with other neighbouring facilities.

The authorization procedures for industrial effluents mandate the installation of flow rate, temperature, and volume measuring and recording instruments at both the intake and discharge points. These instruments must comply with the technical characteristics stipulated in Articles 10, 12, and 13 of Regional Presidential Decree No. 7/R of 25 June 2007 [102]. The monitoring of piezometers situated downstream of wells must be equipped with multi-parameter probes that provide continuous measurements of groundwater level, temperature, and electrical conductivity, with appropriate records being maintained. In order to facilitate a more effective comprehension of the regulatory framework, **Table 3** provides a concise overview of the fundamental characteristics that are necessary in order to obtain authorisations, systematically categorised according to the size of the plant.

Table 3. *Technical Documentation Requirements by Installation Category.*

Technical Documentation Requirements	**Small (≤ 2 l/s)**	**Medium (2–10 l/s)**	**Large (> 10 l/s)**
Hydrogeological investigations of receptor aquifers (geometry, hydrochemistry, piezometry)	Basic assessment	Enhanced assessment	Comprehensive investigation
Thermal plume simulations for at least three years of operation	Not required	Simplified modelling	Required (minimum 3 years)
Demonstration of absence of technically and economically feasible reuse/discharge alternatives	Not required	Basic demonstration	Required
Plant layouts, hydraulic circuits, and maximum discharge temperature specifications	Required	Required	Required
Proof of no interference between abstraction and reinjection wells, and no overlap with existing installations	Basic verification	Detailed verification	Required
Installation of at least one downstream control piezometer for continuous monitoring	Not required	Recommended	Required

It is mandatory for the relevant parties to prepare and submit annual reports that present monitoring results through graphs and tables showing temporal trends and revised thermal plumes based on monitored data. The establishment of these monitoring requirements is indicative of the prevailing understanding that open-loop geothermal systems have the potential to induce substantial thermal perturbations in groundwater. It is essential to ensure the continuous monitoring of these perturbations to avert potential adverse environmental impacts and to prevent interference with other users of groundwater.

The regulatory framework under discussion here addresses both environmental protection and energy development objectives through integrated approaches that balance the promotion of renewable energy with the protection of groundwater resources. Recent studies of groundwater heat pump diffusion in Turin demonstrate the efficacy of urban-scale numerical modelling in assessing the cumulative impacts of multiple open-loop geothermal systems [74]. The findings of these studies suggest that installations managed in an appropriate manner can operate without creating significant hydraulic or thermal disturbances over multi-year operational periods. However, maximum flow rate scenarios with extended cooling and heating operating seasons have the potential to create thermal interference, which can have a detrimental effect on downstream systems. This emphasises the importance of careful design and construction precision, particularly in areas with complex extraction systems.

Authorisation processes generally necessitate comprehensive environmental impact assessments that address geological and hydrogeological site characterisation, thermal plume modelling, interference analysis with existing installations, monitoring system design, and long-term operational management plans. The regulatory framework, with its multiple layers, serves to ensure that open-loop geothermal development occurs within the confines of frameworks that protect water resources. Concurrently, it facilitates the deployment of renewable energy, in a manner that is consistent with both national and European climate objectives. This regulatory evolution is indicative of a growing recognition of geothermal energy's strategic importance for decarbonisation, whilst maintaining rigorous environmental protection standards that are essential for sustainable groundwater resource management.

The implementation of these complex regulatory requirements poses challenges for developers, while providing necessary safeguards for groundwater protection and sustainable energy development. The AUA process, despite being formulated to facilitate streamlined authorisation procedures, continues to necessitate comprehensive technical documentation and environmental assessments, particularly in the context of larger installations, which have the potential to impact regional groundwater systems. This regulatory complexity reflects the inherent tension between accelerating renewable energy deployment and maintaining stringent environmental protection standards. Achieving both objectives requires ongoing refinement of authorization procedures and improved harmonization across jurisdictional levels, particularly in coordinating national directives with regional implementation frameworks.

2.3 Methodology

The design of open-loop geothermal systems relies on several key factors that must be carefully balanced to ensure both technical feasibility and environmental compliance. The current regulatory framework is of particular importance, as it governs the approval procedures and ultimately determines the practical implementation of such systems. Equally important is the availability and assessment of the geothermal groundwater resource, since only when these two conditions are simultaneously met can the actual design phase be effectively initiated. At present, no standardized or rapid mapping approach capable of estimating the geothermal potential of groundwater that combines open-access GIS tools, scientific robustness, and computational simplicity. For this reason, chapter 2.3.1 Geothermal Aquifer Potential (GAP) introduces this innovative methodology. This methodology provides a scientifically rigorous and computationally efficient framework for the spatial assessment of geothermal potential. It ensures full compliance with environmental directives and promotes the sustainable use of geothermal resources.

A shallow aquifer suitable for geothermal exploitation is typically an unconfined or semi-confined groundwater body located within the first few tens of meters below ground level, characterised by sufficient permeability and yield to allow for sustainable groundwater extraction and reinjection. Such aquifers represent an effective low-enthalpy geothermal resource when paired with open-loop GSHP systems.

The approach adopted to estimate the open-loop thermal potential is based on the amount of heat that can be exchanged by a given volume of groundwater passing through a heat exchanger. Its estimation is determined by a combination of geological, thermogeological, hydrogeological, economic, and legal constraints. For GWHP systems, the amount of heat that can be extracted from the aquifer is directly related to the flow rate, the temperature variation induced in the water, and its volumetric heat capacity, as described by the following equation:

Equation 2

$$G = Q \cdot \Delta T \cdot S_{VCwat} \quad (1)$$

where G is the thermal power expressed in MW, Q is the flow rate extracted from the aquifer (m^3/s), ΔT is the difference in temperature between the inlet water temperature from the aquifer and the outlet water temperature to the source (K), finally S_{VCwat} is the volumetric heat capacity of the water equal to 4.18 MJ/Km^3. Since ΔT is typically legally defined with limitations on the maximum and minimum reinjection temperatures, resulting in a maximum allowable induced thermal disturbance [70], the key parameter that strongly influences the thermal potential is the flow discharge (Q). Its accurate estimation is essential for sustainable water resource management.

Furthermore, to ensure the long-term functionality and sustainability of an open-loop geothermal system, understanding aquifer behaviour and assessing the thermo-hydraulic dynamics resulting from pumping is essential. In the context of a shallow aquifer, hydraulic flow refers to the movement of water through underground water-bearing layers. Still, it can also describe sustainable extraction and reinjection rates that the aquifer can support without causing excessive drawdown, piezometric rise, or violating regulatory thresholds. This depends on key hydrogeological parameters such as transmissivity, aquifer thickness, well spacing, and the operational configuration of the system.

Thermal feedback describes the phenomenon whereby the thermal plume generated by the reinjection of used groundwater migrates toward the extraction well, potentially reducing the effective temperature gradient over time. This effect is influenced by groundwater flow direction and velocity, well doublet orientation, thermal dispersion, and aquifer heterogeneity. If not adequately accounted for, thermal feedback can lead to performance degradation and reduced efficiency of the heat pump system.

Together, the above-described factors define the technical potential of a site for geothermal exploitation and must be incorporated into any reliable assessment method for open-loop systems.

Over the past two centuries, a wide range of analytical methods has been developed to characterise aquifer properties through pumping tests. These methodologies have progressively evolved, from fundamental principles of fluid flow to more advanced transient solutions, enhancing the accuracy and applicability of groundwater assessments [103]. Among the earliest steady-state approaches (**Table 4**), the Thiem equation (Thiem, 1906), based on the principles of radial flow in porous media, remains widely used for confined and unconfined aquifers under equilibrium conditions. For unconfined aquifers, the Dupuit assumption (Dupuit, 1857) provides a simplified steady-state model by neglecting vertical flow components. To address transient behaviour, the Theis solution (Theis, 1935) introduced a time-dependent analytical framework for confined aquifers, later simplified by Cooper and Jacob (1946) through a semi-logarithmic approximation valid for late-time drawdown data. For leaky or semi-confined aquifers, the Hantush and Jacob method (1955) extended the Theis approach to account for leakage through semi-pervious confining layers. These methods have provided the theoretical basis for estimating key hydrogeological parameters, such as transmissivity and storativity, and remain essential for defining sustainable pumping rates in groundwater management and geothermal applications.

Table 4. Different methods for the analytical evaluation of flow discharge.

Method	Equation	Parameter	Strong Points	Limitations
Thiem-Dupuit for confined aquifer	$Q = 2.73 \cdot K \cdot b \cdot \frac{(h_1 - h_2)}{log_{10}\left(\frac{r_2}{r_1}\right)}$ (2)	h_i = hydraulic head at radial distance from the well (m) r_i = radial distance from the well (m)	Under the hypothesis of horizontal hydraulic gradient, the radial flow problem is treated as one-dimensional. Robust tool for estimating groundwater flow in steady-state conditions.	In the presence of a non-negligible vertical flow, the equation may lead to errors in parameter estimation. The aquifer is assumed to be infinite in the area surrounding the well. The aquifer must exhibit uniform properties. The analysis is valid once the flow at the well has reached a steady state. The well must fully penetrate the aquifer and be pumped at a constant flow rate.
Thiem-Dupuit for unconfined aquifer	$Q = 2.73 \cdot k \cdot b \cdot \frac{(s_{c1} - s_{c2})}{log_{10}\left(\frac{r_2}{r_1}\right)}$ (3)	S_{c1} = correct drawdown at radial distance r_1		
Cooper and Jacob	$s = \frac{Q}{4\pi \cdot T} log_{10}\left(\frac{2.25 \cdot T \cdot t}{S \cdot r^2}\right)$ (4) $T = \frac{2.3 \cdot Q}{4\pi \cdot \Delta s}$ (5) $u = \frac{r^2 \cdot S}{4 \cdot T \cdot t}$ (6)	T = aquifer transmissivity (m^2/s) Δs = gradient of a straight line fit on the semi-log plot of drawdown against time between a 1 log cycle S = storativity (dimensionless) t = pumping duration (s) C = well-loss coefficient reflecting non-linear losses. If i) C < 1200 s^2/m^5: properly designed and developed well, ii) 1200 < C > 2300 s^2/m^5: Mild deterioration, iii) C > 2300 s^2/m^5: severe clogging and efficiency loss.	A practical graphical method to estimate aquifer parameters from pumping test data.	The method is valid for u<0.02. Need to pre-define S and T. The fixed quadratic dependence of well loss is not universally valid.

The GAP method proposed builds on the advantages of the Dupuit formulation for modelling groundwater flow in unconfined aquifers and integrates spatially distributed hydrogeological data with regional regulatory constraints and thermo-hydraulic constraints. It estimates the extractable geothermal potential at high spatial resolution and is designed to reflect site-specific conditions. The method can effectively support both energy planning and feasibility assessments at the single-plot or district scale.

The utilisation of numerical modelling in the context of groundwater flow and coupled hydrogeological processes has become an indispensable methodology for the assessment of geothermal systems. This is particularly evident in the characterisation of fluid dynamics and thermal responses within complex aquifer architectures. The mathematical representation of three-dimensional saturated groundwater flow is governed by the governing partial differential equation, which describes fluid conservation within porous media. In order to solve this equation, it is necessary to discretise it and use numerical solutions derived from simulation codes that are specifically designed for this purpose. The selection of an appropriate numerical method and software platform is a fundamental decision that directly influences both model accuracy and the feasibility of representing site-specific hydrogeological heterogeneity.

The present chapters employ a dual-modelling strategy that utilises both MODFLOW (based on finite-difference discretisation, chapter 2.3.2) and FEFLOW (based on finite-element discretisation, chapter 2.3.3). This approach is justified by established standards and supported by professional practice in complex hydrogeological applications. The ASTM D5447-17 [104] standard guide for the application of numerical groundwater flow models establishes a comprehensive procedural framework applicable to any quantitative groundwater modelling investigation (**Figure 12**A). This standard delineates the essential steps required for defensible model development, encompassing problem definition, conceptual model formulation, computer code selection, model construction, calibration and sensitivity analysis, predictive simulations, documentation, and post-audit evaluation. The underlying principles embedded in ASTM D5447 provide a universally accepted protocol that transcends specific software platforms, ensuring that modelling efforts maintain scientific rigor regardless of whether finite-difference or finite-element discretization is employed. In addition, a comprehensive suite of companion ASTM standards addresses specific technical aspects of model construction. ASTM D5979-96 [105] provides a framework for the conceptualisation and characterisation of groundwater systems through iterative hypothesis refinement (**Figure 12**B). ASTM D5609-16 [106] stipulates the definition of boundary conditions (Dirichlet, Neumann, Cauchy, free-surface, and seepage-face types). ASTM D5610-94 [107] deals with the establishment of initial conditions, which are critical for transient simulations. ASTM D5981/D5981M-18 [108]offers guidance on calibration methodology for both manual and automated inverse approaches. ASTM D5490-93 [109] establishes quantitative and qualitative criteria for comparing model simulations with site-specific data. ASTM D5611-94 [110] specifies procedures for conducting sensitivity analyses to identify critical

model parameters. Finally, ASTM D5718-13 [111] specification stipulates comprehensive documentation requirements, with the objective of ensuring reproducibility and transparency.

In the field of complex hydrogeological characterisation, professional practice is increasingly acknowledging the value of dual-model applications. These applications leverage the strengths of finite-difference and finite-element frameworks to enhance the analysis of complex geological systems. Rather than regarding these methodologies as competing alternatives, this study employs both approaches in a complementary manner, assigning MODFLOW to the representation of large-scale, city-wide open-loop systems and FEFLOW to the detailed simulation of site-scale configurations characterised by strong structural and parametric heterogeneity. This hierarchical strategy facilitates the testing of alternative conceptualisations at the regional scale, while site-specific finite-element analyses refine the understanding of local flow and heat-transport processes around individual installations. In the context of geothermal system characterisation, where coupled fluid flow and heat transport occur at multiple spatial scales, the integration of both platforms provides a more rigorous assessment of renewable resource potential and improves the reliability of predictions of system response to anthropogenic stresses.

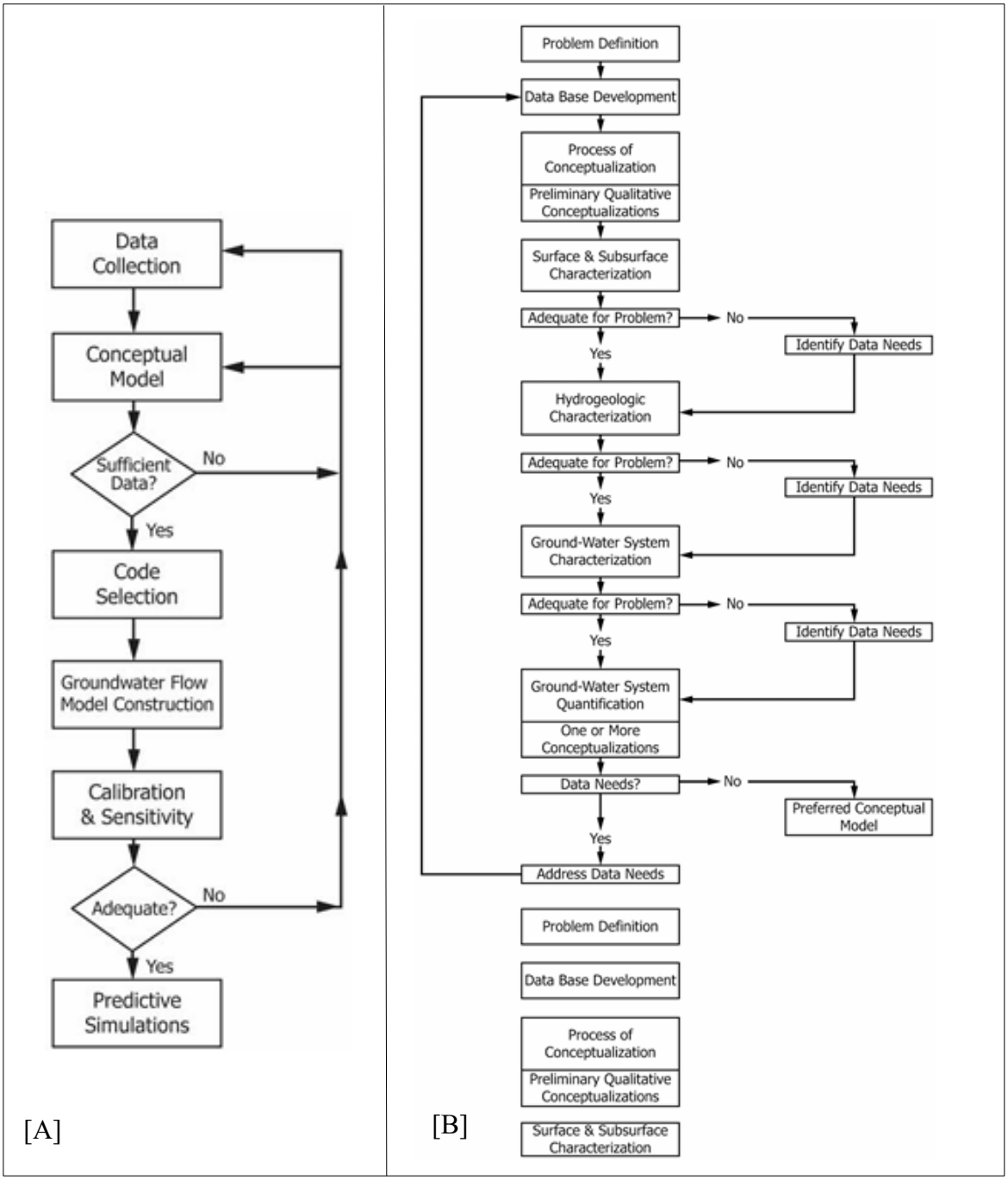

Figure 12. [A] Flow chart of the modelling process (D5447 – 17, [104]); [B] Procedure for conceptualization and characterization of groundwater flow systems (D5979 -96, [105]).

2.3.1 Geothermal Aquifer Potential (GAP)

The novel methodology introduced in this section, termed the Geothermal Aquifer Potential (GAP) method, represents a purpose-built approach to quantitatively assessing the geothermal potential of groundwater.

The GAP method is based on the following assumptions:

- Shallow and unconfined aquifers are exploited using a well doublet configuration, a typical setup for geothermal system.
- The amount of heat that can be potentially exploited from the groundwater is evaluated using Equation 1, considering legal constraints on the maximum allowable temperature difference. At this stage, the model assumes a constant groundwater temperature, but it can be enhanced with urban-scale heat maps, if available, for a more refined potential estimation. The allowable water discharge is estimated using Equation 2 in Table 1, introducing thresholds for the forecasted drawdowns at the abstraction well, as well as the minimum groundwater depth. No universally accepted value for permissible drawdown exists. Some studies propose thresholds ranging from 10% to 75% of the aquifer thickness, while others define maximum exploitable discharge limits without a consistent aquifer yield criterion. In this study, the defined threshold value of 10% of the aquifer thickness was derived from in situ observations and studies performed on existing geothermal plants [71]. Moreover, to prevent a rise in groundwater level to the surface, a technical safety margin must be imposed to avoid any potential interference with existing structures (such as basements or underground parking typical in urban areas).
- The critical distance between wells in a doublet is considered to assess the maximum exploitable discharge, incorporating technical considerations of geothermal plant design and enforcing non-interference criteria for both hydraulic and thermal feedback between wells. The Clyde and Madabhushi equation [112] for determining the minimum interference distance between wells in a doublet was adopted. The latter is expressed as:

Equation 3

$$L < \frac{2 \cdot Q}{T \cdot \pi \cdot i} \quad (7)$$

where L is the minimum distance, Q is the flow rate, T denotes transmissivity, and i is the hydraulic gradient.

The main assumptions behind this methodology are: i) a homogeneous and semi-infinite aquifer medium, ii) well screens intercept the full thickness of the aquifer, iii) no interference from other wells or heat exchangers in the surroundings, iv) constant pumping rate and v) vertical hydraulic gradient are neglected.

Moreover, additional physical constraints were defined (**Table 5**):

- The final minimum acceptable groundwater depth at the reinjection well was set to 3 m in order to avoid any interference of the potential groundwater rise with existing underground floors.
- The well radius was set at 0.25 m, a typical value for geothermal wells used in open-loop configurations [113,114].
- An additional drawdown constraint of 0.1 m was introduced to limit hydraulic interference at the boundary of the defined elementary cell of the discretisation.
- The spacing between the wells was set at 50 m, which is a common distance in urban open-loop geothermal plants [115,116].

Table 5. List of the main constraints used in the GAP model

Parameter	Value
well radius	0.25 m
drawdown in well	10% of aquifer thickness
drawdown monitoring point	0.1 m
monitoring point distance	50 m
doublet distance	50 m

It should be noted that the above-described parameters can be adjusted to better reflect the specific conditions of the considered study area. It is clear that the methodology resolution, and consequently the drawdown monitoring point distance and well-doublet distance, depend on the density of available data measurements. The outcome of these calculations is a map of the estimated flow rate (in m^3/s) across the entire study area.

This integrated approach enables a precise evaluation of both hydrodynamic and thermal characteristics of the aquifer, ultimately yielding a quantitative measure of its geothermal potential in terms of kilowatts per unit area.

Figure 13 reports the schematic workflow for the evaluation of groundwater geothermal potential with the GAP method. Further details for each step of the GAP methodology, from data acquisition and pre-processing to the numerical evaluation of thermal and hydraulic parameters, will be provided in the following subsections.

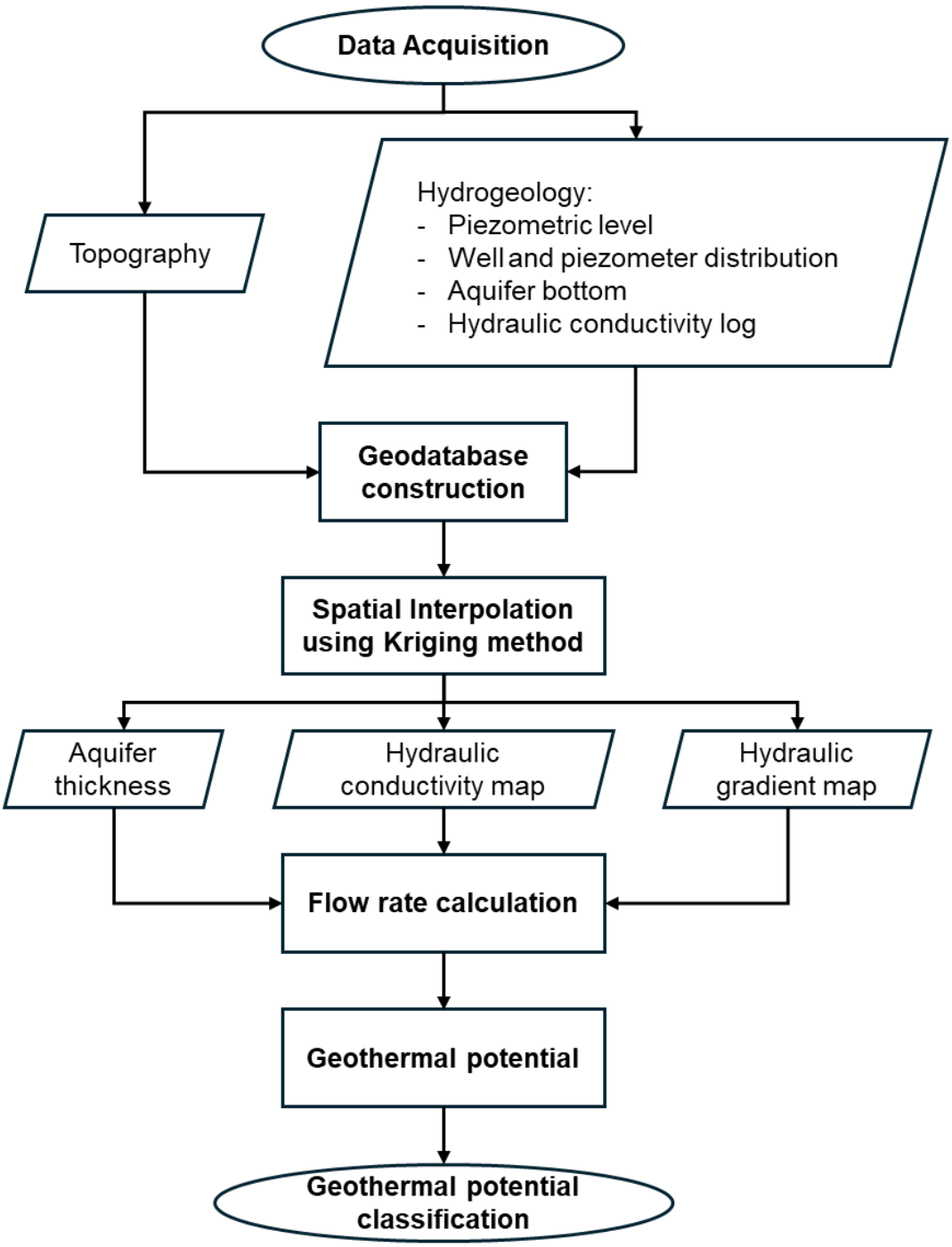

Figure 13. Workflow of the GAP methodology.

The final geothermal potential map is made more interpretable and informative by discretising the continuous thermal power distribution into discrete classes. The heating (and cooling) demand of buildings varies widely depending on size, use and insulation [117,118]. For instance, typical single-family homes require approximately 7–11 kW of heating capacity (e.g. ~7 kW for a 100 m² dwelling at medium insulation, ~11.2 kW for a 90 m² house in a colder climate zone). In contrast, larger multi-family buildings or public facilities require tens to hundreds of kilowatts. For example, a multi-class school have a heating system rated between 300 and 600 kW. These values suggest a natural stratification into demand classes,

allowing the geothermal potential to be categorised into six main classes, as outlined in **Table 6**.

This classification is based on the estimated thermal power output and the corresponding building typologies and it aligns with guidelines such as UNI/TS 11300-1:2014 [119], EPBD [120] and DIRECTIVE (EU) 2024/1275 [121].

Class 1 includes small, well-insulated homes or single unit dwellings. In new or renovated buildings, design loads typically range from 20 to 70 W/m². Thus, a compact dwelling (<100 m²) generally requires less than 10 kW, consistent with the previously noted 7–11 kW range. This category also includes individual offices or retail shops with low heating/cooling loads.

At the other end of the scale, Class 6 includes entire urban neighbourhoods or campus-scale groups of buildings, such as cluster of dozens of houses or city blocks. At this level, peak demands frequently reach the hundreds of kW or even low MW. Geothermal systems designed for Class 6 resemble district heating and cooling networks, extending beyond individual building and playing a key role in strategic, city-wide energy planning.

Table 6. Class distribution used in the GAP model.

Class	Lower Power (kW)	Higher Power (kW)	Thermal Demand	Building Type	Housing Units
1	5	20	Very Low	Single-Family House	1
2	20	50	Low	Small Condominium	4-8
3	50	100	Moderate	Medium Condominium	8-15
4	100	200	High	Large Condominium	15-30
5	200	500	Very High	Residential Block	30-40
6	>500	-	District	Multi Residential Block	>40

2.3.2 MODFLOW

This chapter presents a unified, replicable methodology for three-dimensional numerical simulation of open-loop (extraction/injection) geothermal systems using the USGS MODFLOW 6 (version 6.6.1) code through the ModelMuse (version 5.4) graphical interface, together with geospatial preprocessing in QGIS (version 3.40.4), parameter estimation with Pilot Points and PEST, and heat-transport coupling. The aim is to document the governing equations, discretization strategy, boundary-condition representation, parameterization and calibration workflow, and quality-assurance procedures required to produce robust predictions of hydraulic and thermal impacts of open-loop geothermal installations in shallow alluvial aquifer environments. The model comprises two layers representing the different aquifer systems, two General Head Boundaries (GHB) corresponding to the upstream and downstream boundary conditions of the model, and the simulation of the watercourses using the River package.

The simulation of open-loop geothermal systems hinges on accurately representing groundwater flow and heat transport within heterogeneous aquifers. This methodology integrates the three-dimensional finite-difference groundwater code MODFLOW with the ModelMuse graphical interface to construct, execute, and analyse numerical models of open-loop geothermal plants. Groundwater flow is governed by the continuity equation in porous media. In three dimensions, the partial differential form is

Equation 4

$$\frac{\partial}{\partial x}\left[K_{xx}\frac{\partial h}{\partial x}\right]+\frac{\partial}{\partial y}\left[K_{yy}\frac{\partial h}{\partial y}\right]+\frac{\partial}{\partial z}\left[K_{zz}\frac{\partial h}{\partial z}\right]+W=S_s\frac{\partial h}{\partial t}$$

where K_{xx}, K_{yy}, and K_{zz} are directional hydraulic conductivities, h is hydraulic head, W denotes sources and sinks per unit volume, S_s is specific storage, and t is time.

The numerical implementation in MODFLOW 6 is based on a control-volume finite-difference (CVFD) formulation whereby the integral form of the flow equation is applied to each discrete control volume V:

Equation 5

$$\int_S (K\nabla h)\cdot n dS=\int_V S_s\frac{\partial h}{\partial t}\,dV+\int_V q\,dV$$

where S represents the control volume surface, n is an outward-pointing unit normal perpendicular to the volume surface, K is the hydraulic conductivity tensor, h is the hydraulic head, S_s is the specific storage, q is the volumetric source/sink term per unit volume, and V is the control volume. This formulation ensures mass

conservation within each control volume while allowing flexible grid geometries and connections between cells.

The discretization process transforms the continuous partial differential equation into a system of algebraic equations that can be solved numerically. For each model cell, the discrete form of the flow equation becomes:

Equation 6

$$\sum_m T_{n,m}\,(h_m - h_n) + W_n = S_{s,n} V_n \frac{\partial h_n}{\partial t}$$

where $T_{n,m}$ represents the conductance between cells n and m, h_n and h_m are the hydraulic heads at cells n and m respectively, W_n is the volumetric flux rate for cell n, and $S_{s,n}$ is the specific storage for cell n. The conductance terms are assembled from cell transmissivities, interface area, and link distances according to MODFLOW 6 conventions. The numerical solver and linear algebra options available in MODFLOW 6 (e.g., direct vs iterative solvers, preconditioners) should be selected and reported based on model size and conditioning; default solver settings are acceptable for small models but large, highly heterogeneous domains typically require iterative solvers and tailored preconditioning to ensure efficient and stable convergence.

Heat transport in saturated porous media is modelled using the conservative energy balance for the coupled fluid/solid system. Using standard SI notation, fluid density ρ_f [kg·m^{-3}], solid density ρ_s [kg·m^{-3}], fluid specific heat $c_{p,f}$ [J·kg^{-1}·K^{-1}], solid specific heat $c_{p,s}$ [J·kg^{-1}·K^{-1}], porosity θ [–], and effective thermal conductivity λ_{eff} [W·m^{-1}·K^{-1}], the conservative form of the heat transport equation is:

Equation 7

$$(\rho c)_b \frac{\partial T}{\partial t} + \nabla \cdot (\rho_f c_{p,f}\, q\, T) = \nabla \cdot (\lambda_{eff} \nabla T) + Q_T$$

Equation 8

$$(\rho c)_b = \theta \rho_f c_{p,f} + (1-\theta)\rho_s c_{p,s}$$

where $(\rho c)_b$ is the bulk volumetric heat capacity [J·m^{-3}·K^{-1}], q is specific discharge [m·s^{-1}], T [K or °C] is temperature, and Q_T [W·m^{-3}] denotes internal thermal sources or sinks (injection/extraction thermal power per unit volume).

The heat transport simulation incorporates both conductive and advective heat transfer mechanisms. The conductive component follows Fourier's law, while the advective component depends on groundwater velocity and thermal properties. The effective thermal parameters must account for the composite nature of the saturated porous medium, typically employing volume-weighted averages of fluid and solid thermal properties.

Thermal conductivity of the saturated porous medium is represented as an effective parameter λ_{eff} obtained by volume weighting or more advanced mixing laws depending on the degree of saturation and the heterogeneity of the matrix. Typical parameter ranges used are: volumetric heat capacity of water ≈ 4.18×10^6 $J\cdot m^{-3}\cdot K^{-1}$, solid matrix volumetric heat capacity in the order $1.3–2.5\times10^6$ $J\cdot m^{-3}\cdot K^{-1}$, and thermal conductivities of order 0.6–3.0 $W\cdot m^{-1}\cdot K^{-1}$ depending on lithology and porosity.

The numerical mesh, spatial discretization and temporal scheme are central to simulation fidelity for open-loop geothermal systems. For sites where, small scale thermal plumes and well interactions are important, quadtree (2-D) refinement provide an efficient approach to concentrate resolution in the vicinity of wells and monitoring points while coarsening away from the area of interest to reduce computational cost. The horizontal discretisation ranges from 1 m (well vicinity) to 10 m (periphery) in the case studies. Vertical layering represents primary hydrostratigraphic units with at least one cell across each significant lithologic interface. Vertical discretisation must respect expected thermal and hydraulic gradients. MODFLOW 6's CVFD framework and flexible grid connections make quadtree refinement straightforward to implement, but careful attention should be paid to interface transmissivity calculations between dissimilar cell sizes to avoid artificial resistance or excessive numerical dispersion. Temporal discretization consists of a calibration steady-state phase (representing pre-operational or long-term averages) followed by transient operational scenarios: time steps must resolve daily to seasonal load cycles and abrupt operational changes (start/stop cycles). Adaptive time stepping available in MODFLOW 6 should be used conservatively; document the minimum and maximum time-step lengths and the convergence tolerances used in each transient run.

Boundary conditions must represent regional flow drivers, surface water bodies, and anthropogenic stressors in a physically consistent manner. General Head Boundaries (GHB) are appropriate to represent far-field hydraulic gradients or external reservoirs where head is specified and flux is linearly proportional to the head difference:

Equation 9

$$Q_{GHB} = C_{GHB}(h_{ext} - h_{cell})$$

Where Q_{GHB} is the boundary flux, C_{GHB} is the boundary conductance, h_{ext} is the specified boundary head, and h_{cell} is the calculated cell head. Rivers are represented with the River package (RIV[3]), which simulates head-dependent exchange between surface water and groundwater.

[3] RIV: River Package Pane

The river conductance is calculated using the geometric relationship:

Equation 10

$$C_{riv} = \frac{K_z L\, W}{M}$$

Where K_z is the vertical hydraulic conductivity of riverbed sediments, L is the river reach length in the cell, W is the river width and M is the riverbed thickness. When river stage exceeds cell head or vice versa, the head-dependent flux is computed as the conductance times the head difference, with proper sign convention; in thermal simulations, river boundary temperatures may be prescribed or coupled as a time-dependent forcing term depending on available monitoring data.

Open-loop geothermal wells are modelled explicitly using Multi-Aquifer Well package (MAW[4]) available in MODFLOW 6 and ModelMuse. Well representations must capture multi-layer completions and the distribution of screened intervals; when wellbore thermal and mixing effects are significant, include wellbore mixing or cell-by-cell thermal injection specifications that preserve energy conservation (specify temperatures for injected water or specify thermal power). Operational schedules (time-varying extraction/injection rates and temperatures) are input as stress packages; for long operational scenarios, represent weekly schedules (weekday operation, weekend shutdowns) and monthly variability where monitoring data are available. When coupling flow and thermal models, ensure synchronized time stepping and consistent mass/energy balance reporting to avoid artificial error accumulation.

The calibration of a numerical hydrogeological model can be conducted under various conditions, including steady-state, transient, or a combination of both. In the cases under consideration, the calibration was executed using the Pilot Points (PP) technique in a steady-state regime, utilising average piezometric level data collected from wells and piezometers. The entire procedure was managed via the PESTHP inverse modelling code, a tool designed for the estimation of parameters and the analysis of uncertainties in complex numerical environmental models. The method employed involves an iterative procedure to optimize the parameters. This allows for the reiteration of the process steps, which include the resolution of the flow equation, the verification of the correlation between calculated and observed piezometry, and the modification of the parameters to enhance the correlation. This process is repeated until the difference between the calculated and measured loads reaches a minimum that is deemed acceptable. In this case, a minimum acceptable error of 0.01 m was set.

[4] MAW: Multi-Aquifer Well Package Pane

The optimization of the parameters results in the minimisation of the objective function Φ, defined as the weighted sum of the squares of the differences between the experimental observations h' and the simulated loads h:

Equation 11

$$\Phi = \sum_{i=1}^{m} [w_i (h'_i - h_i)]^2$$

The weight attributed to an observation, denoted by the symbol (w_i), is inversely proportional to its variability or uncertainty. This ensures that more emphasis is placed on the most reliable observations.

The parameters involved in the calibration process can be assigned not only according to the classic uniform value zones, but also through spatial distributions (interpolations) defined at PP [21]. This method applies the principles of geostatistics to transition from the points where the parameter value is associated to the spatial distribution over the entire considered area (model domain). The surfaces are generated from the PP through the process of Kriging, which estimates the unknown values through a weighted average of the measured points, with the relative weights depending on the size of the search radius. In this case, the unknown parameter (hydraulic conductivity) varies spatially in a gradual manner based on geostatistical schemes (variograms) that consider the heterogeneity of the model. Pilot Points play a pivotal role in the calibration process, enabling a more realistic representation of the spatial variability of parameters within the model. Rather than assigning a uniform value to a large area, the parameter values can gradually vary across the model domain based on the values assigned. Consequently, during the iterative calibration process, the values at the PP are adjusted to minimise the difference between the simulated and observed data. This implies that the PP directly influences the optimisation of the model parameters. By capturing the spatial variability of parameters and allowing for their optimisation, this technique can significantly improve the accuracy of the model predictions. This leads to a more reliable and robust hydrogeological model. The weights assigned to the observations at each PP are inversely proportional to their variability or uncertainty. This means that more reliable observations have a greater influence on the calibration process, thereby reducing the overall uncertainty of the model.

2.3.3 FEFLOW

The numerical simulation of open-loop geothermal systems represents one of the most challenging applications in hydrogeological modelling, requiring the solution of coupled groundwater flow and heat transport equations in complex three-dimensional domains with significant spatial and temporal heterogeneity [122]. This methodology presents a comprehensive framework for developing, calibrating, and validating transient numerical models using the finite element software FEFLOW, integrated with advanced parameter estimation techniques for robust uncertainty quantification [123].

A deep and comprehensive understanding of the mathematical formulation and the implementation details is imperative for the configuration, resolution, and critical evaluation of the reliability of models designed for the prediction of coupled groundwater flow and heat transport. Contemporary energy engineering research increasingly demands accurate and efficient modelling frameworks, capable of handling the spatial complexity and physical heterogeneity inherent in real-world geothermal energy systems. A thorough presentation of FEFLOW's governing equations is therefore essential for both reliable simulation and defensible engineering decisions. This presentation includes steady-state, transient, and heat transport scenarios, alongside modern calibration workflows carried out using PEST++. In particular it focuses on the GLM algorithm and ensemble-based IES methodology.

FEFLOW (standing for Finite Element subsurface FLOW simulation system) is a comprehensive numerical environment for the simulation of flow, heat, and mass transport in porous and fractured media. The software has been developed over the course of several decades, and it is capable of supporting multi-physics modelling. This includes variable-density flow, full or partial saturation, and the distinctly coupled processes that are inherent to geothermal applications. The governing partial differential equations that describe transient or steady groundwater flow, as well as conductive, convective, and dispersive heat transport, are central to the modelling framework. The standard mathematical model for saturated groundwater flow in a porous medium, as implemented in FEFLOW, is derived from the combination of Darcy's Law and the continuity equation (modified from Table 3.6 of Ref. [122]) assumed that the liquid phase moves slowly in the porous medium. The general three-dimensional, density-dependent groundwater flow equation is as follows:

Equation 12

$$\nabla \cdot (\rho f q f) = \rho f Q$$

with,

Equation 13

$$qf = -\frac{k}{\mu}\nabla(p + \rho f g z)$$

where,

- ρf denotes the fluid density [kg/m³]
- qf is the Darcy velocity vector [m/s]
- Q represents sources or sinks of mass per unit volume [1/s]
- k is the intrinsic permeability [m²]
- μ is the dynamic viscosity of the fluid [kg/(m·s)]
- p is the fluid pressure [Pa]
- g is the gravitational acceleration [m/s²]
- z is the elevation [m]

The movement of water beneath the earth's surface, within saturated and unsaturated porous media, can be modelled using Richards' equation [124]. This equation is derived from the mass conservation equation and Darcy-Buckingham's law. Consequently, the following pressure head form can be postulated:

Equation 14

$$\big(c(h) + S_s S_W(h)\big)\frac{\theta h}{\theta t} + \nabla \cdot (-K(h)\nabla \mathrm{H}) = \mathrm{r}$$

where $c(h)$ is the specific moisture capacity ($c = d\theta(h)/dh$), H and h are respectively the hydraulic piezometric and pressure head such as $H = h + z$, z is the depth taken positive upward, S_s is the specific storage, S_W is the relative saturation of the aqueous phase ($S_W(h) = \theta(h)/\theta_s$), $\theta(h)$ and θ_s are the actual and saturated water contents respectively and r is the source-sink term [125].

In the event of unsaturated conditions, which are frequently applicable in the context of shallow geothermal and vadose zone studies, FEFLOW utilises an extension of the classical Richards' equation. This extension acknowledges the functional dependency between water content, pressure head and unsaturated hydraulic conductivity [126]. In the case of transient groundwater flow, the temporal derivative of storage, when combined with flux divergence and sources/sinks, yields the following equation:

Equation 15

$$\frac{\partial(\rho f \theta)}{\partial t} + \nabla \cdot (\rho f q f) = \rho f Q$$

with θ being volumetric water content, and other terms as previously defined.

This general formulation accommodates confined, unconfined, and variably-saturated media by appropriate parameterization and boundary condition assignments.

A distinguishing feature of geothermal simulation is the need for accurate heat transport prediction. FEFLOW's capacity for heat transport is governed by an energy balance equation, which is capable of representing advective, conductive, and dispersive regimes. The general equation for heat transport in saturated porous media, as solved by FEFLOW, is as follows:

Equation 16

$$\frac{\partial(c\rho T)}{\partial t} + \nabla \cdot (\rho_f c_f q_f T - \lambda \nabla T) = QT$$

where c represents specific heat capacity [J/kg·K], ρ represents density (with cρ denoting bulk volumetric heat capacity), T is temperature [K], λ is the effective thermal conductivity [W/m·K], and QT denotes sources/sinks of thermal energy [W/m³]. The initial term delineates transient storage of internal energy, the advective term signifies heat conveyed by the moving groundwater, and the conductive term modells molecular conduction according to Fourier's law. The sink/source term facilitates the incorporation of external heat adders, such as injection wells.

When considering both the contributions of a porous matrix and groundwater, the total volumetric heat capacity is a weighted sum:

Equation 17

$$c\rho = (1 - n)\rho_s c_s + n\rho_f c_f$$

Where n is the porosity, ρ_s and c_s are the density and specific heat of the solid matrix, respectively, and ρ_f and c_f are the fluid equivalents. The energy equation thus explicitly accounts for the storage and transfer of heat within both the solid and liquid phases. This is a critical factor in simulating subsurface thermal plumes, particularly when exploring the feasibility, sustainability, and environmental impacts of open-loop geothermal exploitation. The assumption underlying steady-state modelling is that the hydraulic head and temperature remain constant over time, thus resulting in the exclusion of temporal derivative terms. The resulting equations have the capacity to simplify model initialisation, provide a baseline for system equilibrium assessments, and often serve as a pragmatic foundation for subsequent transient analyses. However, in order to capture the natural and operational dynamics associated with geothermal energy use, such as seasonal load variation, thermal front migration, or system startup/failure events, it is necessary to implement transient models. These require appropriate time-stepping schemes and increased attention to initial condition specification.

FEFLOW is a numerical implementation of the finite element method (FEM). It enables the subdivision of the model domain into arbitrarily shaped elements (e.g.

triangles in 2D, prisms or tetrahedra in 3D). This facilitates mesh refinement around wells, geological heterogeneities, or critical interfaces (**Figure 14**).

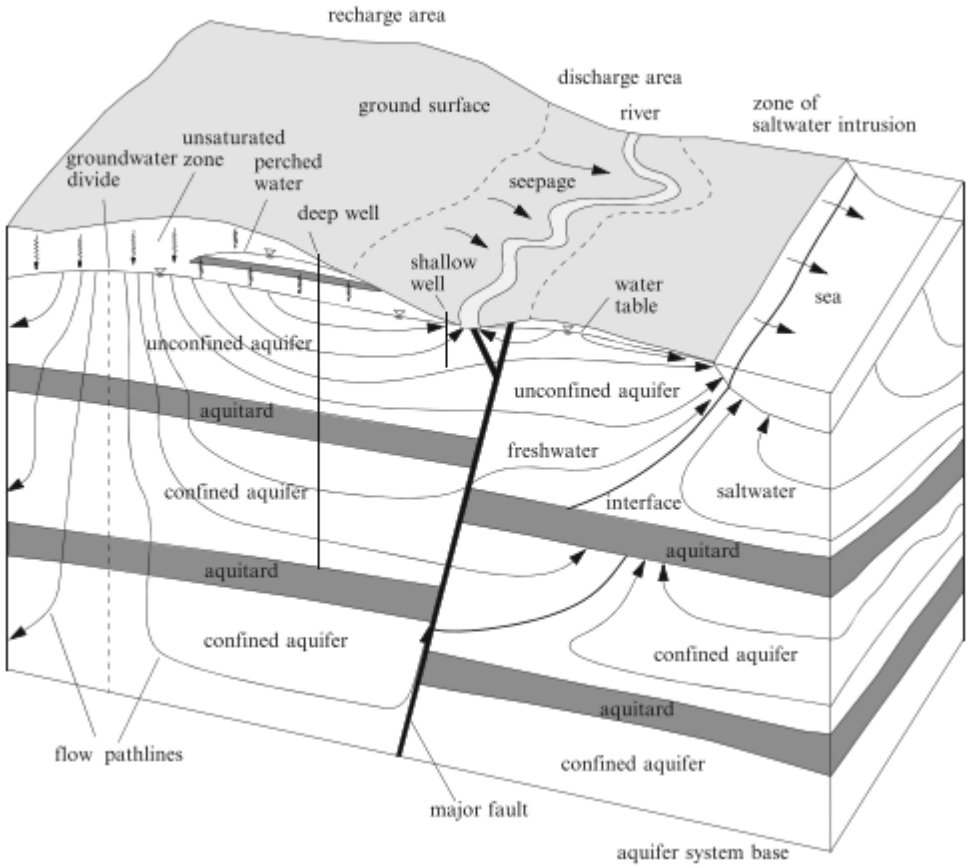

Figure 14. Illustration of typical flow regimes in a multilayered aquifer system [122]

The mesh is constructed such that material properties, sources, and boundary conditions may be assigned with spatial fidelity. In the context of complex regional models, hydrological features such as rivers or variable aquifer stratigraphy are incorporated through boundary conditions encompassing Dirichlet (fixed head/temperature), Neumann (fixed flux/energy), or Cauchy (generalised transfer) forms. FEFLOW facilitates both structured and unstructured meshing, thereby ensuring optimal computational efficiency and geometric flexibility. The simulation of dynamic boundaries, such as those encountered in open-pit mining and dewatering in construction, is further enabled by the concurrent deactivation of elements and the utilisation of time-varying mesh geometries.

Temporal discretization is achieved through the implementation of schemes such as the fully implicit, unconditionally stable, backward Euler method or the second-order accurate, conditionally stable, Crank-Nicolson method. These methods permit the determination of time steps that are adaptively determined based on solution change criteria. For steady-state models, single-time-step solutions are sufficient, given the absence of dependence on system history. For transient simulations, especially those involving nonlinearities stemming from

flow-heat-density couplings or multiphase effects (e.g., freezing/thawing), robust time-stepping control is essential to avoid instabilities or excessive computational cost.

Discretisation of the core equation systems results in the generation of substantial, sparse algebraic systems. FEFLOW is equipped with a suite of direct and iterative solvers, encompassing preconditioned conjugate gradient (PCG), biconjugate gradient stabilized (BiCGSTAB), and sophisticated algebraic multigrid solvers such as SAMG, PETSc AMG and PARDISO parallel direct solver. The selection of solver is contingent upon problem size, the level of precision required, the treatment of boundaries, and hardware capabilities, including GPU support in PETSc for larger models. The solver's robustness and efficiency are critical to runtime and convergence, particularly in inverse modelling workflows where models may be executed thousands of times during calibration or uncertainty analysis. FEFLOW's sophisticated solver control schemes possess the capability to automatically alternate between divergent solving strategies on the basis of matrix properties, thereby optimising computational efficiency on a case-by-case basis.

Open-loop geothermal systems require the simulation of fluid extraction (production) and subsequent reinjection, usually via paired wells. FEFLOW's model structure enables the explicit representation of these wells, capturing the induced flow field and the spatially complex thermal plume resulting from heat exchange. The interaction between thermal processes and groundwater flow can particularly be dominated by advection. This requires precise calibration of hydraulic conductivity, porosity and related properties. However, in settings characterised by low permeability or the use of closed-loop exchangers, conduction may become the predominant phenomenon. The software facilitates the setup of models for both cases and can represent complex well geometries, combinations of open- and closed-loop systems, and heterogeneous backgrounds.

The credibility of geothermal simulations depends on calibrating model parameters against observed field data (e.g. hydraulic heads, temperatures and flow rates). FEPEST is a sophisticated graphical user interface that facilitates the management of PEST-based calibration and uncertainty tasks within the FEFLOW simulation environment. Beyond providing a convenient way to set up parameter estimation and parallelised computation, FEPEST supports methodologies such as pre-calibration Monte Carlo analysis, which are critical for assessing parameter sensitivity and uncertainty prior to formal calibration, especially when dealing with high-dimensional and spatially heterogeneous systems. These interfaces empower users to harness the full theoretical sophistication of the PEST suite without being burdened by the intricacies of low-level file and batch scripting. However, it is essential to have a robust understanding of the underlying mathematical and algorithmic principles to ensure the interpretation of results is meaningful, to facilitate robust decision-making, and to enable advanced customisation. PEST++ is a modern advancement in PEST parameter estimation [123]. It has been developed to manage large-scale, highly parameterised models in a computationally efficient and user-friendly manner, whilst also facilitating parallelisation. The

integration of PEST++ with FEFLOW is now widely regarded as the optimal approach for high-stakes environmental and energy simulations (**Figure 15**).

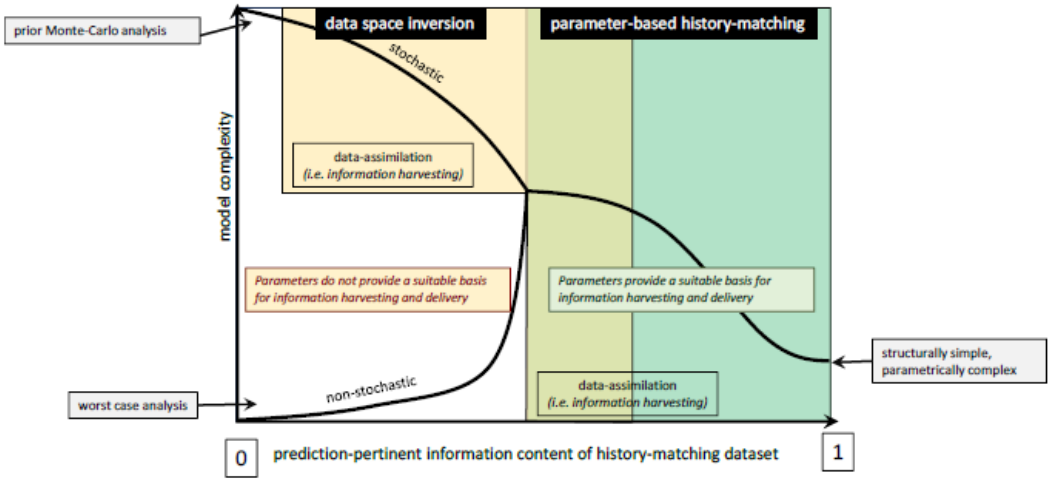

Figure 15. Map of decision-support modelling appropriateness [127].

The theoretical foundation of PEST++ rests on the formulation of parameter estimation as a nonlinear inverse problem, where the objective is to identify parameter vectors that minimize the discrepancy between observed system states and those simulated by the numerical model. The classical parameter estimation problem seeks the parameter vector d which minimizes the weighted sum of squared residuals between observed (d_{obs}) and simulated (d_{sim}) system states, commonly referred to as the measurement objective function Φ:

Equation 18

$$\Phi = (d_{obs} - d_{sim})^T W (d_{obs} - d_{sim})$$

Where Φ is the scalar objective function value that quantifies the mismatch between observed data and model simulations (the calibration process seeks to minimize Φ), d_{obs} is the vector of observed data from field measurements or monitoring (these are target values for calibration), d_{sim} is the vector of simulated data produced by the numerical model given the current set of parameter values, $(d_{obs} - d_{sim})^T$ is the weighted sum of squared residuals, between observed and simulated values for each measurement, calculated as the inner product of the residual vector weighted by W that represents the weighting matrix that accounts for measurement uncertainties and the relative importance of different observations. This formulation is predicated on the maximum likelihood estimation principle, operating under the assumption of Gaussian measurement errors, thus establishing a rigorous statistical interpretation of calibration results.

In order to address the inherent ill-posedness and prevent overfitting that commonly afflict hydrogeological inversion problems due to characteristically low data-to-parameter ratios, regularization terms are systematically incorporated following Tikhonov regularization principles. The total objective function is augmented as follows:

Equation 19

$$\Phi_{total} = \Phi_{measurement} + \lambda\Phi_{regularization}$$

where the regularization component typically assumes the form:

Equation 20

$$\Phi_{regularization} = (p - p_{prior})^T W_p (p - p_{prior})$$

In this expression, p_{prior} represents prior parameter estimates informed by expert knowledge and field observations, W_p constitutes the parameter weighting matrix that encodes spatial correlation and relative confidence in different parameter values, and λ serves as the regularization weight factor that controls the relative emphasis placed on data fitting versus adherence to prior information. This regularization framework enables systematic incorporation of expert knowledge, spatial correlation information, and geostatistical constraints to produce physically plausible and hydrogeologically realistic parameter distributions while maintaining mathematical rigor in the optimization process.

PEST++ implements two primary calibration algorithms, each of which has been designed to address specific problem characteristics and computational requirements inherent in different modelling contexts. The PESTPP-GLM (Gauss-Levenberg-Marquardt) algorithm is an example of a gradient-based optimisation methodology that operates iteratively. In this methodology, the Jacobian matrix J is constructed, which contains sensitivities of simulated outputs to each parameter. The parameter vector is then updated according to the following equation (pag 108 eq. 7.4.1 Ref.[127]):

Equation 21

$$p - p_0 = (J^t Q J)^{-1} J^t Q r$$

Where p_0 designates parameter values at the start of the iteration while r designates model-to-measurement residuals calculated using the p_0 parameter set. J is the Jacobian matrix calculated using the p_0 parameter set, Q is the observation weigth matrix (W in Equation 19).

Use of Equation 21 directly to estimate parameters for a nonlinear model can be numerically inefficient. In practice, the diagonal terms of the $J^t Q J$ matrix should be enhanced through use of the following equation to calculate parameter improvements:

Equation 22

$$p - p_0 = (J^t Q J + \lambda I)^{-1} J^t Q r$$

λ is the so-called “Marquardt parameter”, or simply “Marquardt lambda”, named after Marquardt who employed this strategy [128].

The Marquardt parameter fulfils several critical functions: it ensures numerical stability during the initial iterations when the objective function surface may exhibit strong nonlinearity, it prevents numerical singularity of the normal equations matrix, and it provides adaptive regularisation based on local problem conditioning characteristics. In cases of highly parameterised problems where the normal matrix becomes singular or ill-conditioned, the truncated Singular Value Decomposition (SVD) provides numerical stability through the effective computation of the Moore-Penrose pseudo-inverse (Section 8.2.5 Ref. [127]). This process automatically identifies and handles parameter combinations that are poorly constrained by available data.

Advanced regularization within PESTPP-GLM can incorporate comprehensive prior covariance information through the formulation:

Equation 23

$$\Delta p = -\left(J^t \sum\nolimits_{\epsilon}^{-1} J + \lambda \sum\nolimits_{\theta}^{-1} J\right)^{-1} J^t \sum\nolimits_{\epsilon}^{-1} (d_{obs} - d_{sim})$$

where $\sum_{\epsilon}^{-1} J$ represents the observation error covariance matrix, $\sum_{\theta}^{-1} J$ represents the parameter prior covariance matrix that encodes spatial correlation structure and parameter uncertainty characteristics, and λ the Marquardt damping factor. This "regularized GLM" approach ensures solution stability even when observational information is insufficient relative to parameter space dimensionality, while maintaining the ability to honor complex geostatistical relationships between parameters (chapter 8 Ref. [127]).

The alternative calibration paradigm enabled by PESTPP-IES (Iterative Ensemble Smoother) represents a fundamental shift toward ensemble-based parameter estimation, particularly suited for high-dimensional problems and models with pronounced nonlinearities in parameter-to-output mapping relationships. Rather than computing local derivatives explicitly through finite difference calculations, the IES approach propagates an ensemble of parameter realizations through the forward model, using empirical covariances to update parameter distributions based on observed data. The IES algorithm is fundamentally grounded in Bayes' theorem for parameter estimation (chapter 12.3 Ref. [127]).

Many environmental models necessitate spatially varying parameters; a prime example of this would be hydraulic conductivity. However, it is important to note that assigning a parameter to every cell inevitably results in an overwhelming number of parameters, which far exceeds the information content of the available data. The pilot point method is a powerful solution that blends parsimony and flexibility.

Pilot points are spatially distributed locations at which parameter values are defined explicitly. It is acknowledged that pilot points can be useful for any model parameter or boundary condition. However, it is important to note that they are most commonly applied to aquifer hydraulic conductivity. The earliest applications of this concept can be traced back to the works of de Marsily and subsequent

contributions by Certes and de Marsily [129] and LaVenue and Pickens [130]. These initial studies were further expanded upon by RamaRao et al. [131], and LaVenue and de Marsily [132]. The latter authors combined the use of pilot points with a methodology for optimal selection of pilot-point locations. Furthermore, a methodology was developed for the utilisation of pilot points in conjunction with stochastic fields to derive multiple hydraulic-property distributions. The purpose of this methodology is twofold: firstly, to calibrate a model, and secondly, to respect the geostatistical characterisation of a study area. The employment of multiple field realizations in the context of model predictions enables the exploration of estimates of the uncertainty associated with these predictions.

A fundamental component of effective PEST++ implementation lies in pilot point parameterization, which enables flexible spatial representation of hydraulic and thermal properties without imposing overly restrictive assumptions about parameter homogeneity [133,134]. Rather than assuming piecewise constant or uniform properties throughout the model domain, pilot points allow specification of properties at strategically chosen locations, with intermediate values interpolated geostatistically using proven techniques such as kriging or inverse-distance weighting:

Equation 24

$$p_{cell} = \sum_{i} w_i(X_{cell}, X_i)\, p_i$$

where p is the pilot point value (ex. hydraulic conductivity), and X the positions, p_{cell} is the interpolated value, p_i the initial one, and w_i is the weight defined by the chosen interpolation function and the spatial variogram. This approach enables direct exploitation of heterogeneity inferred from field measurements, yielding realistic spatial parameter fields that honor both data constraints and geological understanding while maintaining computational tractability.

2.4 Case Studies

This chapter presents a comprehensive investigation of geothermal energy systems in the Turin metropolitan area through multiple case studies that span different scales of analysis, from regional to site-specific. The study area represents a distinctive hydrogeological setting within the Po Plain, offering exceptional opportunities for the development of open-loop GWHPs. The case studies examine the geological and hydrogeological framework at progressively detailed scales, culminating in numerical modelling analyses (chapter 2.5 Results) that demonstrate the feasibility and environmental impact of geothermal energy systems in urban environments.

The investigation adopts a hierarchical approach, encompassing a broad geological characterisation of northern Italy, followed by a focus on the Piedmont regional scale, and subsequently examining the specific hydrogeological conditions of Turin at the municipal level. Three distinct numerical modelling case studies are presented: firstly, an urban-scale simulation of all existing geothermal systems in Turin was conducted using MODFLOW software; secondly, a detailed validation modelling of the Politecnico di Torino geothermal installations was performed with monitoring data integration; and thirdly, a prospective analysis of three potential new geothermal sites was conducted using FEFLOW software.

This multi-scalar approach provides a comprehensive framework for understanding the complex interactions between geological structures, hydrogeological processes, and anthropogenic influences that control the development and sustainability of shallow geothermal resources in densely urbanized areas. The case studies demonstrate how advanced numerical modelling techniques can support evidence-based decision-making for renewable energy planning and environmental protection in urban contexts.

The Northern Italy regions encompasses one of Europe's most significant hydrogeological systems, extending from the Alpine chain to the Apennine foothills. The Po Plain represents the largest alluvial basin in Italy and constitutes the most productive and prosperous region of the country, with per-capita income levels comparable to those of central and northern European countries. This densely populated area hosts approximately 28% of Italy's population and includes numerous UNESCO World Heritage sites [135].

The Po Plain is formed as a foreland basin during the complex tectonic evolution involving the collision between the Eurasian and African plates[136]. This geological setting has created optimal conditions for groundwater accumulation and shallow geothermal energy exploitation across vast urbanized areas [137]. The area lies on the buried sector of the Adria microplate, a promontory of the African plate or independent microplate, positioned between the NE-verging northern Apennines and the S-verging southern Alps [138]. The development of these two facing fold-and-thrust belts, connected with the broad collision of the

Eurasian and African plates, led to the formation of the Po Plain basin representing the foreland basin of both orogens [139,140].

From the Tertiary period onwards, the Po Plain has evolved as a complex sedimentary basin influenced by both Alpine and Apennine orogenesis. The structural and sedimentary framework has been extensively constrained using numerous seismic reflection profiles and deep-well logs from decades of hydrocarbon exploration [141]. The basin architecture consists of superimposed sedimentary cycles that record the progressive filling of the foreland depression, with the external fronts of both chains mostly buried under a thick siliciclastic sequence (late Eocene–present) consisting of syntectonic sediments and recent alluvial deposits [142,143].

The siliciclastic sequence can be subdivided into two major depositional cycles [135–137,139–146]:

- *Lower Cycle* (Late Eocene–Early Messinian): The formation is primarily fed by the Alpine chain, and the cycle consists of silty and shaly deposits (Gallare Marls; late Eocene to Miocene) intercalated with sandy and conglomeratic formations (Gonfolite Formation; Oligocene), passing upward to sandy marls (Marnoso-arenacea Formation; Langhian to Messinian), clays (Colombacci Formation; Messinian), and evaporitic deposits (Gessoso Solfifera Formation; Messinian).
- *Upper Cycle* (Late Messinian–Present): Fed by both the northern Apennines and the southern Alps, this cycle consists primarily of marine sandy and conglomeratic formations (Sergnano Gravel, Porto Corsini, Porto Garibaldi, Santerno, and Asti sandstones; Pliocene to middle–late Pleistocene) that transition into extensive alluvial deposits (middle–late Pleistocene to present). It is notable that the continental deposits south of the Po River consist of alluvial fan and plain deposits embedded in clays with elongated shapes, whereas the sedimentary bodies north of the Po River are wider, generally tabular, and contain minor amounts of fine-grained sediments.

These clastic sequences are superimposed on a carbonate and marly substratum (Triassic–middle Eocene), which overlies platform and continental Permian–Triassic formations, lying in turn on the Variscan crystalline basement. The Triassic deposits are occasionally intruded by intra-sedimentary volcanic bodies, thereby introducing a complex subsurface architecture [147].

The Quaternary evolution of the Po Plain has been characterized by multiple glacial-interglacial cycles that have profoundly influenced the sedimentary architecture and hydrogeological properties of the basin. During glacial periods, extensive alluvial fan systems developed at the outlets of major Alpine valleys, creating highly permeable coarse-grained sedimentary bodies. These formations constitute the primary aquifer systems exploited for water supply and geothermal energy applications throughout Northern Italy.

The hydrogeological framework is dominated by extensive multi-layered aquifer systems hosted within Quaternary alluvial deposits. The shallow unconfined aquifers, typically found at depths of 10-50 meters below ground surface, exhibit excellent hydraulic properties with permeability values ranging from 10^{-3} to 10^{-2} m/s. These aquifers maintain direct hydraulic connection with major river systems including the Po, Adda, Ticino, and their tributaries, creating complex surface water-groundwater interactions that sustain both water supply and renewable energy applications [148].

The thermal characteristics of shallow groundwater in Northern Italy are particularly favourable for geothermal energy exploitation. Natural groundwater temperatures typically range from 12-16°C, reflecting the temperate continental climate and geothermal gradient of approximately 30°C per kilometer. Regional studies have documented systematic spatial variations in groundwater temperature, with progressive warming from Alpine foothills toward the central Po Plain driven by longer residence times and geothermal flux from depth [149].

The Piedmont region represents a distinctive sector of the Po Plain, characterized by unique geological and hydrogeological conditions that make it particularly suitable for shallow geothermal energy development. Located in the northwestern part of Italy (Figure 16), the region extends from the Western Alps to the Po River, encompassing diverse morphological features including mountain chains, morainic amphitheatres, fluvioglacial terraces, and alluvial plains [150].

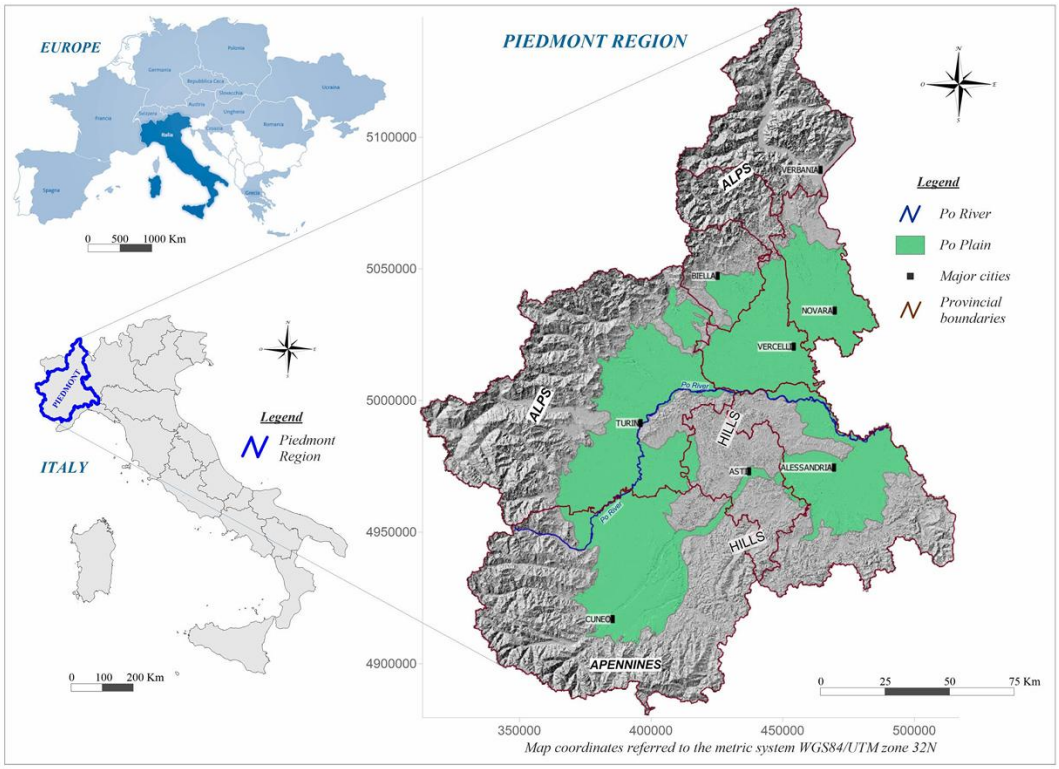

Figure 16. Piedmont region location map [150].

The Piedmont region is underlain by the Cenozoic Tertiary Piedmont Basin (BTP), a syn-orogenic foredeep that experienced Alpine–Apennine collision from

the Oligocene through the Messinian [151]. The BTP succession is comprised of seven synthems, namely: a) two Late Eocene–Early Miocene terrigenous units (conglomerates, sandstones, marls), b) a Burdigalian carbonate, c) two Langhian–Tortonian terrigenous synthems and d) Messinian evaporites [152]. Each synthem is separated by regionally traceable unconformities linked to major compressional phases [153–155]. These deposits rested atop Paleozoic–Mesozoic metamorphic complexes of the Alps and were later draped by Pliocene marine and deltaic strata: the Argille Azzurre Formation (upper epibathyal–circalittoral clays), the Sabbie di Asti (circalittoral–littoral sands), and the Villafranchian succession, which recorded a transition from deltaic to continental environments [156].

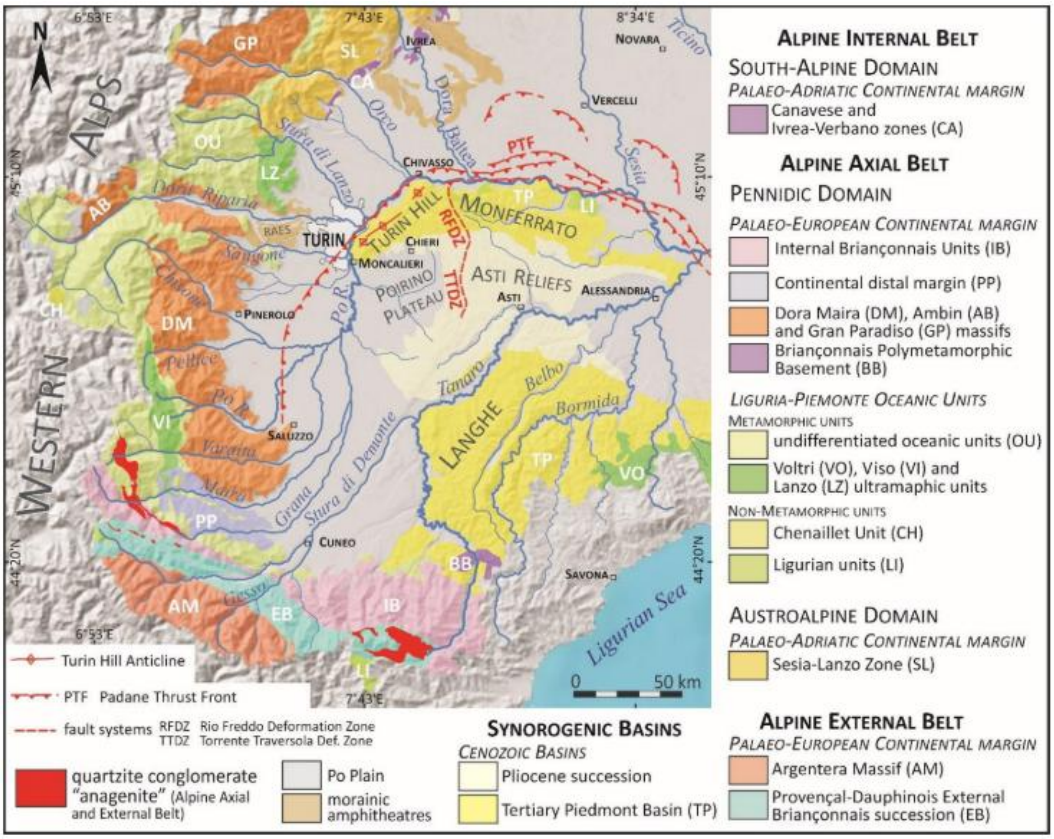

Figure 17. Geological map of Western Alps and Tertiary Piedmont Basin [152].

The hydrogeological conceptual model of the Piedmont plain represents a complex multi-layered aquifer system that has developed through extensive Quaternary sedimentation and tectonic processes. This system consists of three superimposed hydrogeological complexes, arranged from top to bottom: the Alluvial deposits complex (lower Pleistocene-Holocene), the 'Villafranchiano' transitional complex (late Pliocene–early Pleistocene), and the Marine complex (Pliocene) [157–162].

The subsoil's hydrogeological structure is significantly influenced by two major structural elements: the Rivoli-Avigliana Morainic Amphitheatre (RAMA) to the west and the Turin Hill Miocene anticline to the east. The Piedmont Region exhibits a complex morphological and structural framework defined by the Alpine and Apennine mountain chains, the Monferrato and Langhe hills, endorheic and fluvio-

glacial systems, and extensive alluvial deposits at the outlets of major Alpine and Apennine valleys [150]. To the north, large glacial lakes transition into the extensive alluvial plains of the Po River, while to the west lies the RAMA, a significant glacial landform that fundamentally controls regional groundwater flow patterns. The piezometric surface gradually flows towards the nearby base level, following the path of the Po River, with average runoff direction fluctuating between NW-SE and WNW-ESE and an average hydraulic gradient of 0.35% [73].

The shallow unconfined aquifer is hosted within the Alluvial deposits complex, consisting of coarse gravel and sand of fluvial or fluvioglacial origin, with subordinate silty-clayey intercalations. This complex demonstrates favourable characteristics for geothermal energy exploitation, with thickness generally ranging between 20 and 50 meters and high hydraulic conductivity values ($k = 5\times10^{-3} \div 5\times10^{-4}$ m/s) [150]. The high permeability of these deposits facilitates efficient groundwater flow and heat exchange processes essential for open-loop geothermal systems. Deeper aquifer systems are present in the underlying fluvial-lacustrine 'Villafranchiano' complex and the Pliocene marine sediments. These aquifer systems serve as key sources of drinking water throughout the Piedmont plain due to their high productivity and superior groundwater quality compared to the shallow aquifer [163].

The regional geological framework includes highly consolidated sediments, predominantly marls, clays, silts, clayey limestone, conglomerates, sandstone, and gypsum, which represent the Tertiary Piedmont Basin deposits of Eocene-Miocene age. These sedimentary formations are characterized by low permeability and permit only limited groundwater circulation along fractured zones, resulting in the development of springs with low to very low discharge rates (typically less than 1 l/s or a few l/s). While these formations do not constitute viable targets for geothermal exploitation, they play important roles as confining layers and contribute to the overall hydrogeological structure of the region [150].

The crystalline rocks of the Alps border the plain on the northern and western sides, forming the structural foundation of the regional hydrogeological system. These formations are predominantly impermeable or exhibit slight permeability through fracture networks. In mountainous areas, water resources are primarily located in valley-floor aquifers developed within sedimentary non-cohesive deposits such as debris, landslide bodies, and glacial deposits, or within intensely fractured bedrock systems. Springs with low discharge rates are generally associated with thin and discontinuous Quaternary deposits, while springs with higher discharge are linked to significant aquifer systems corresponding to large and thick landslide bodies or highly fractured bedrocks affected by deep-seated gravitational slope deformations (DSGSDs) [164,165]. Additionally, localized karstic circulation systems may develop within calcareous rock formations in alpine environments.

Glacial deposits are present in the major morainic amphitheatres of Rivoli-Avigliana, Serra d'Ivrea, and Upper Novarese. These formations consist of glacigenic successions with interglacial paleosols and deposits, ranging in age from terminal Early Pleistocene to Late Pleistocene [166]. The hydraulic properties of

these deposits vary significantly depending on grain size, weathering processes, and argillization of sediments. Glacial and fluvioglacial deposits may host shallow aquifer systems and locally developed perched aquifers, contributing to the overall complexity of the regional groundwater system. The low plain sectors function as regional discharge areas, with the Po River serving as the main regional discharge axis for groundwater flow [167]. This flow pattern creates a systematic hydraulic gradient from the Alpine foothills toward the Po River, providing optimal conditions for sustainable groundwater extraction and geothermal energy applications. The Figure 18 shows the hydrogeological complex of Piedmont Region (data derived from Arpa Piemonte geoportal [168]).

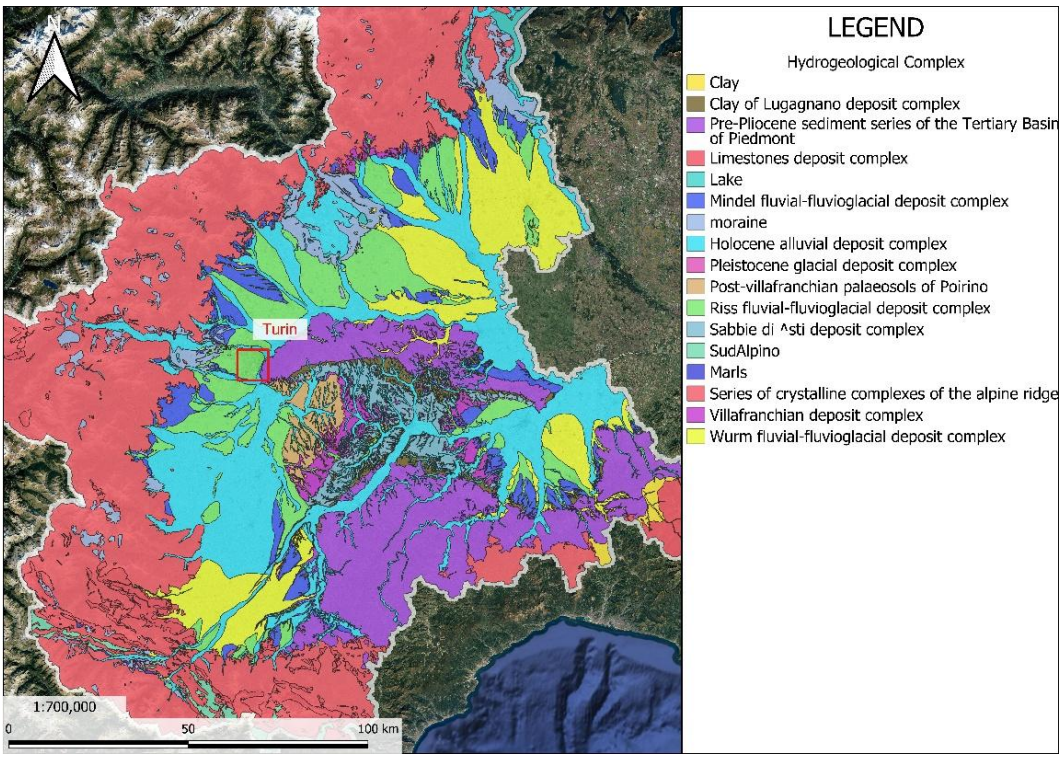

Figure 18. Hydrogeological map of Piedmont (data from [168]).

The city of Turin (Torino) is an exceptional case study for the development of shallow geothermal energy, combining favourable geological conditions and significant urban energy demand. Situated in northwestern Italy on the Piedmont plain (Figure 19), Turin lies at the intersection of intricate morphological, climatic, geological and hydrogeological systems, providing ideal conditions for the sustainable use of groundwater heat pumps.

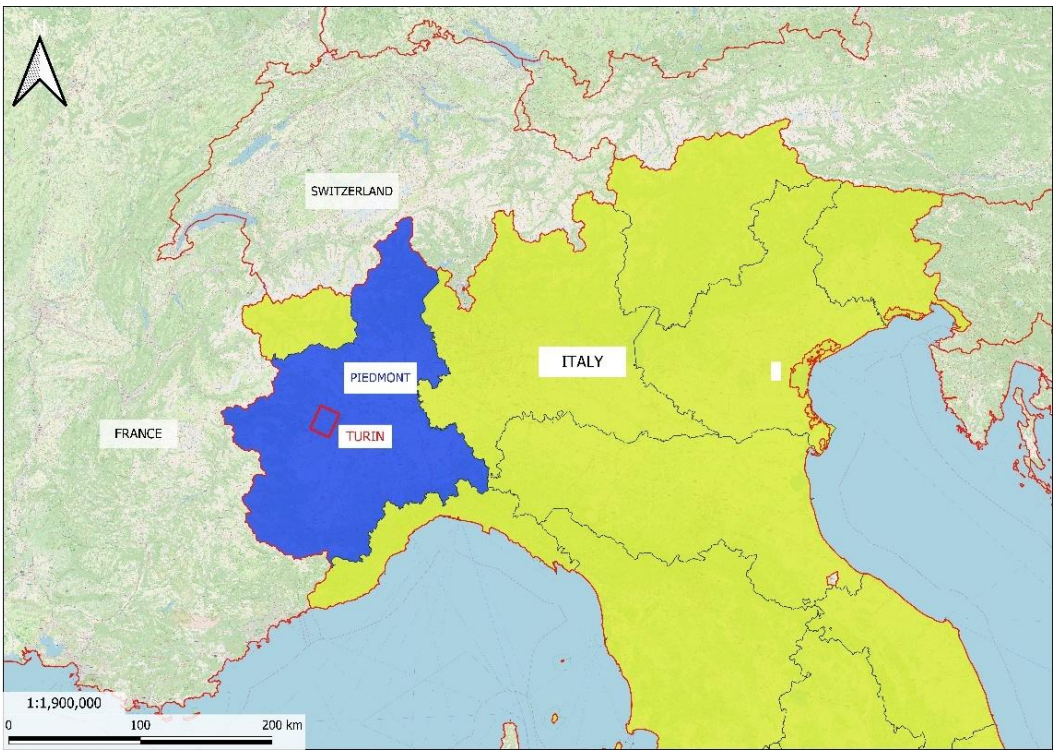

Figure 19. Map showing the geographical location of Turin area.

Turin is located on the Po Plain, south of the Western Alps, and covers an area of 130 km² with a population of 857,910 inhabitants (Figure 20 A) as of 2019, making it the fourth-largest Italian city with a population density of less than 6,600 inhabitants per square kilometre. The Metropolitan City of Turin, in its broader sense, encompasses 315 municipalities and a total area of 6,821 km², with a population of approximately 2,208,370 inhabitants (Figure 20 B). This constitutes a substantial urban agglomeration, which consequently exhibits significant energy requirements for heating and cooling applications. The city has been selected as one of ten Italian cities participating in the EU's "100 Climate-Neutral and Smart Cities by 2030" mission, committing to achieve net-zero CO_2 emissions by 2030, twenty years ahead of the European target, necessitating rapid deployment of renewable energy technologies including geothermal systems.

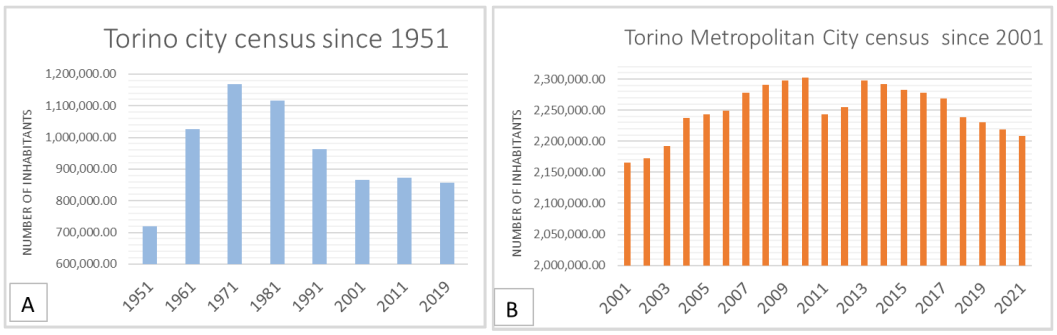

Figure 20. (A) Number of inhabitants in Torino city since 1951, data from ISTAT; (B) Number of inhabitants in Torino Metropolitan City since 2001 [73].

The urban morphological setting of Turin is fundamentally controlled by its position within a complex geological framework extending from the Rivoli-Avigliana Morainic Amphitheatre (RAMA) in the west to Turin Hill in the east. The topography of the area is defined by the presence of major river systems, with the Stura di Lanzo River to the north, the Dora Riparia River flowing through the central urban area, and the Sangone River to the south, all of which ultimately discharge into the Po River that flows northeastward along the western boundary of Turin Hill. The topographical features of the city have been shaped by the eastward-sloping Susa Valley, which is supplied by an extensive outwash fan and drained by the Dora Riparia River.

The climatic conditions of Turin are indicative of its continental temperate setting within the Po Plain, characterised by warm summers and cold winters that create significant seasonal heating and cooling demands. During the winter months (December-February), Turin experiences cold and damp conditions with average temperatures ranging from 2.2°C in January to 4.2°C in February, with minimum temperatures frequently dropping below freezing to -1.5°C in January and -0.3°C in February. The winter season is characterised by the lowest annual precipitation levels, averaging 28.6 mm in January, though the relative humidity remains high at approximately 69-80% (data from [169]). Snowfall is a common occurrence during the winter months, with an average annual accumulation of 25 centimetres. However, significant snowfall events, reaching heights of 40-55 centimetres, have been documented in historical records [170]. The summer months (June-August) are characterised by warmer and more humid conditions, with average temperatures reaching 24°C in July, the warmest month, and maximum temperatures averaging 29°C. The range of minimum summer temperatures is from 15.5°C in June to 17.4°C in July, indicating significant diurnal temperature variations. The summer period is characterised by moderate to high humidity levels (72-74%) and increased thunderstorm activity, particularly during the afternoon and evening hours (data from [169]). These meteorological phenomena contribute to the seasonal precipitation maximum in May (average of 127 mm) and significant rainfall in June (average of 104 mm).

Temperatures are subject to the effects of global climate change, as evidenced by historical climate series analysis which shows an increase of 0.8°C per century in the plain areas of the Piedmont region [170]. The average annual temperature has increased from 12.5 to 13.7°C between the periods 1870-2010 and 1971-2010, reflecting significant warming trends that have implications for energy demand patterns and geothermal system performance [171]. Throughout the twentieth century, the urban areas of Turin experienced significantly elevated temperatures in comparison to the rural areas that surrounded them. This phenomenon is known as the urban heat island effect [172,173]. Research has documented that Turin's urban groundwater temperatures are 0.6-1.6°C above rural sectors, with urban aquifer temperatures averaging 14-16°C compared to 12-14°C in rural areas [174]. This temperature rise over the last 150 years is attributed to vigorous urban expansion, with the increase in the number of inhabitants and vehicles in Turin city being among the largest contributors to urban air warming [171]. The substantial

artificial land cover, incorporating roads and buildings, absorbs and retains solar radiation, consequently transferring heat to the underlying aquifer system.

From a geological perspective, Turin is positioned within a structurally complex setting controlled by the interaction between Alpine and Apennine orogenic processes. The city is underlain by the western termination of the Turin Hill anticline, a NE-SW fold cored by Tertiary Piedmont Basin units that form the structural backbone of the Turin metropolitan area (Figure 21). This uplifted anticline has been reactivated during the Quaternary period, resulting in the formation of a sequence of five to fifteen terraced fluvial gravel and sand bodies along its flanks, positioned at elevations up to 480 metres above sea level on the western slopes. The anticline axis plunges southwest beneath the modern Turin Plain and is offset eastward by the Rio Freddo Deformation Zone, creating complex subsurface structural controls that influence groundwater flow patterns and aquifer geometry [175].

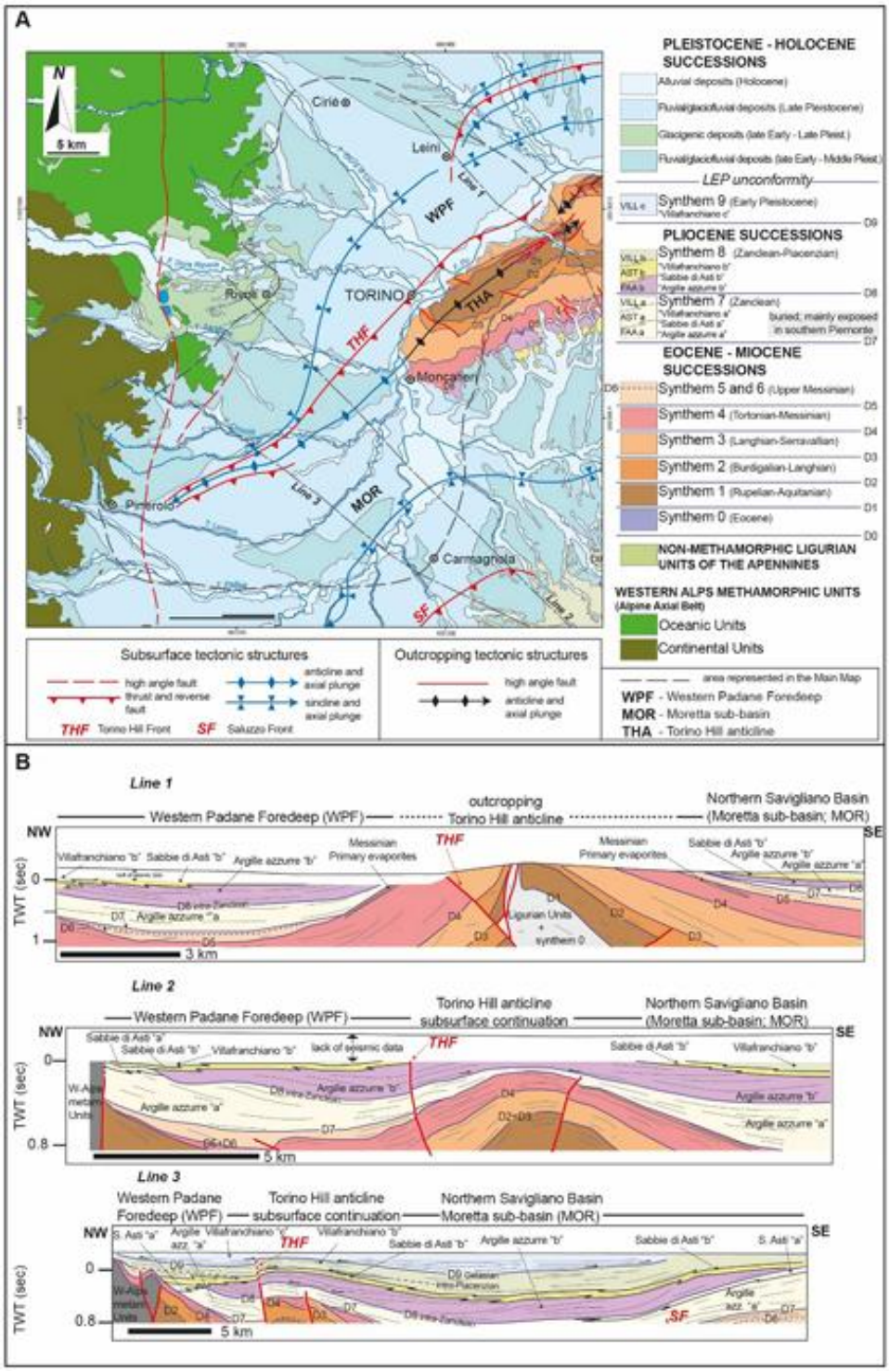

Figure 21. [A] Geological sketch map of Western Piedmont; [B] Line drawings of seismic lines across the Turin Hill Front (THF) and thrust-related folds [175].

This study is primarily concerned with Quaternary formations (Figure 22 and Figure 23), which are described briefly from the most recent terms:

- Recent and current river floods are relatively weak and are confined to the active river beds, consisting of clean gravels and sands with occasional finer lenses. They are situated on less permeable interglacial conglomerate beds;
- Medium to recent river floods are mostly scarce on current riverbeds and occur along the Po and other primary watercourses. They predominantly consist of sandy-gravel deposits and are limited to a few metres thick;

- Ancient river floods appear as discontinuous patches slightly terraced relative to the present riverbed and often fill in the “fossilized meanders” of the paleo-river. These outcrops gradually yield to the recent and ongoing river floods;
- Gravelly sandy-clay fluvioglacial deposits, a terrace system with reddish-yellow palaeosols, is located approximately ten metres above the Middle-Recent Alluvium of the Po River. It presents itself as a strong alternating sequence of partially altered gravels and sands, reaching tens of metres in depth, intermixed with finer sandy and silty layers that are generally less cohesive.

The morphology of the terraces’ boundaries is marked by deep incisions, particularly along the Dora Riparia River’s riverbed. The sample appears as a dense, well-cemented gravel. The matrix consists of a limited amount of silt and clay, with abundant pebbles that are more than a tenth of a metre in size. The proportion of sand is minor, while gravel is dominating.

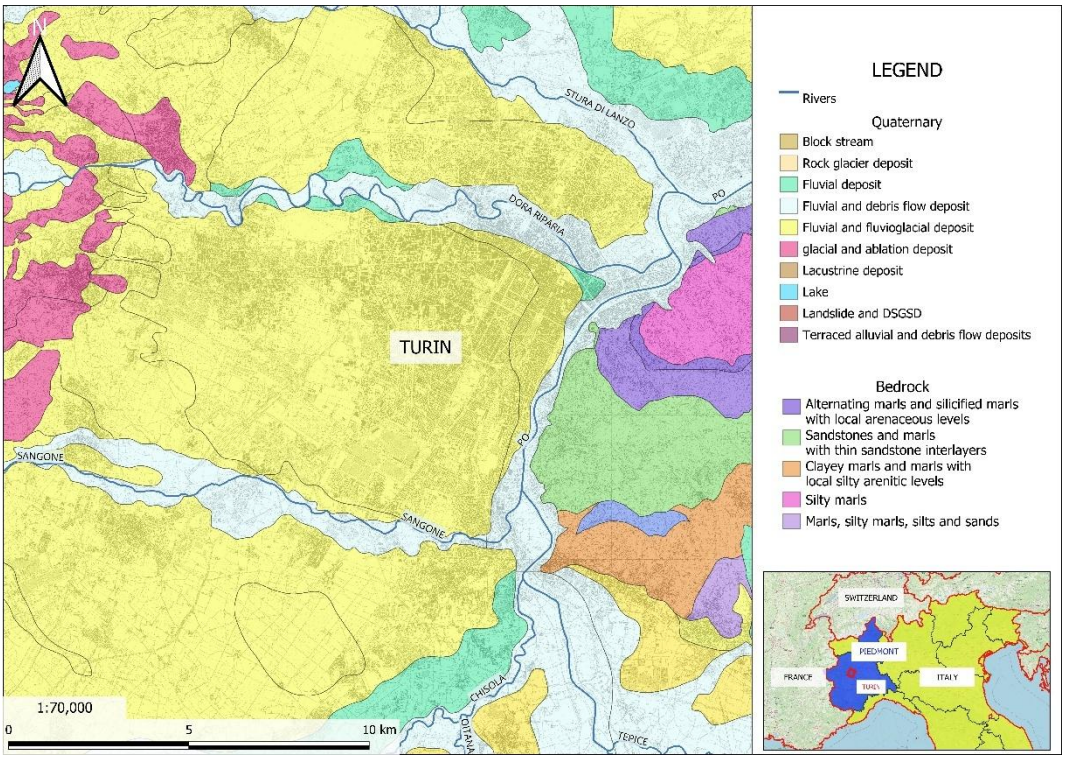

Figure 22. Geological map of Turin area (modified from [73]).

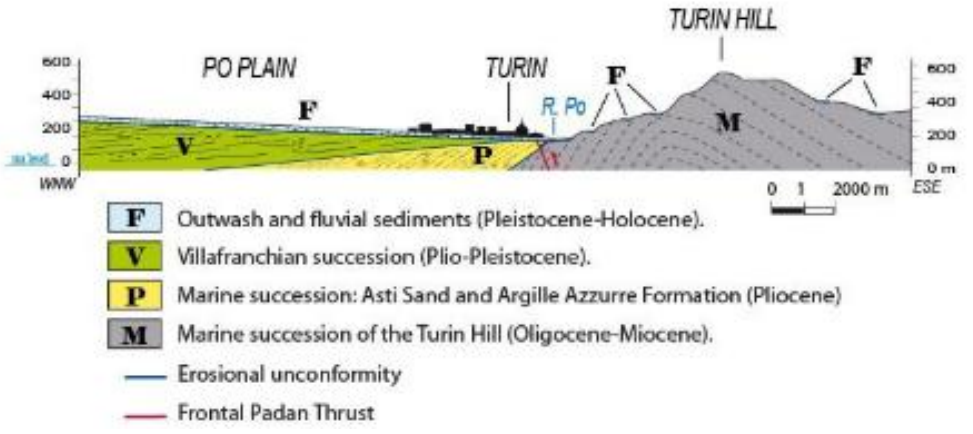

Figure 23. Cross section of shallow Quaternary deposit of the Turin area [162].

The subsurface geology beneath Turin is characterised by a well-defined stratigraphic succession, comprising three distinct hydrogeological units (**Figure 24** and Figure 25). The Turin unit, designated as Unit 1 in this study, is a glaciofluvial formation comprising sandy gravels and overbank silts. This unit, measuring between 9 and 57 metres in thickness, was deposited by the Dora Riparia and paleo-Stura systems. The Turin unit is characterised by its presence in a blanket, and its deposition occurred on an erosional surface that was incised into the underlying Villafranchian succession. It is evident that the uppermost unit represents the primary target for geothermal energy applications, due to its high permeability (hydraulic conductivity values ranging from 10^{-3} to 10^{-4} m/s) and substantial thickness, which enables efficient heat exchange processes represented by Layer A (Figure 26) of the numerical model presented in Section 2.5 Results.

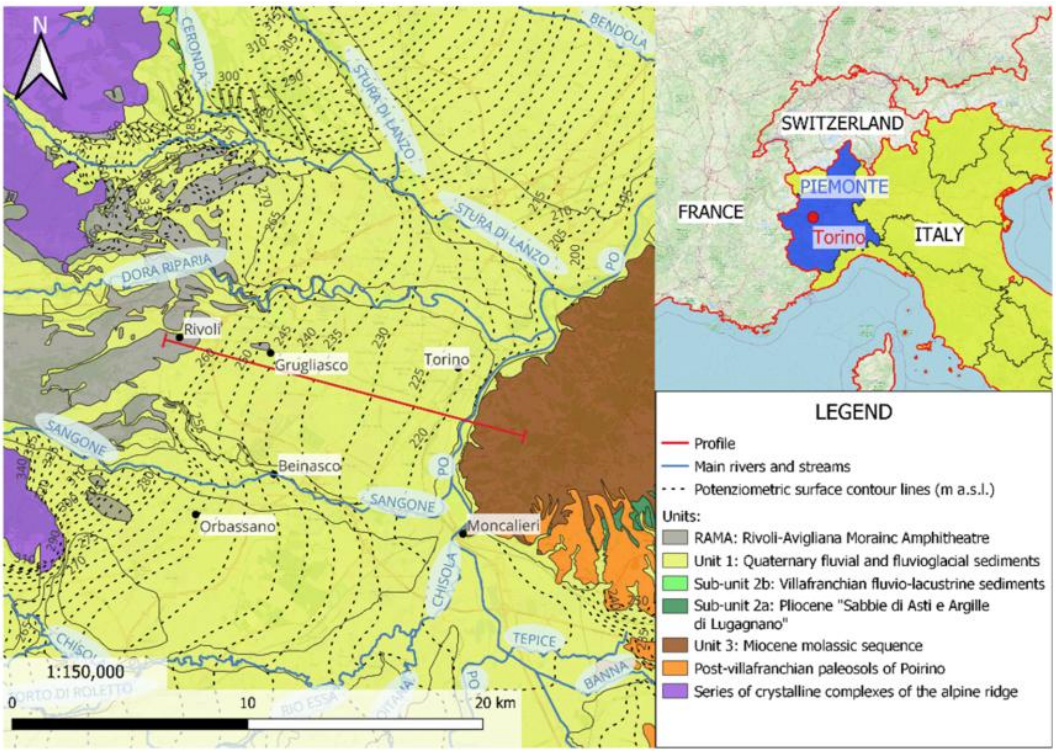

Figure 24. Hydrogeological map of Turin (Torino) municipality area showing the distribution of major lithostratigraphic units and the potentiometric surface of the shallow aquifer system. Contour lines represent groundwater levels in meters above sea level, illustrating regional flow directions and recharge gradients. The red line indicates the location of the hydrogeological profile shown in Figure 25 **[70].**

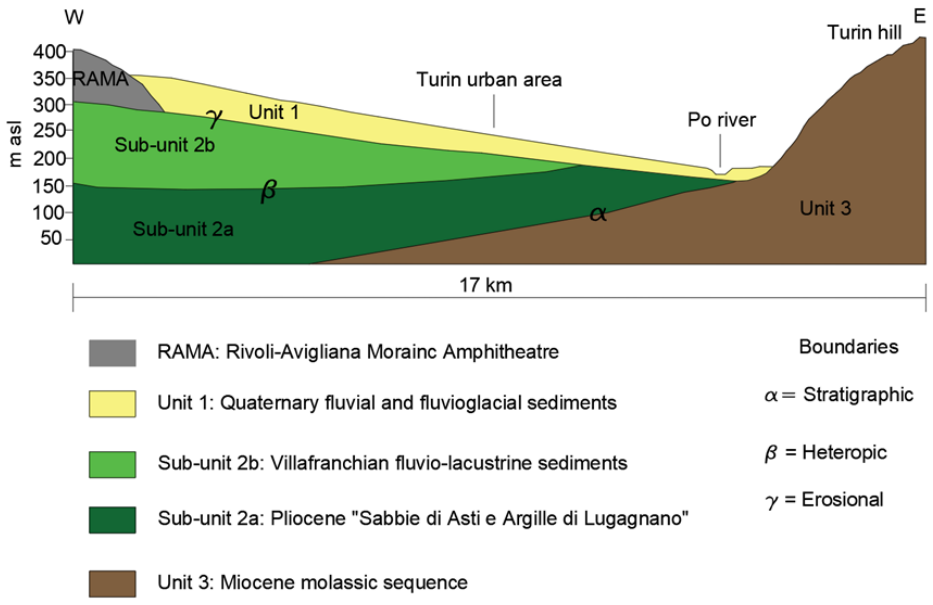

Figure 25. Geological cross-section across the Turin area (W–E), illustrating the vertical and lateral distribution of key lithostratigraphic units relevant to groundwater flow and geothermal potential. The section spans from the Rivoli–Avigliana Morainic Amphitheatre (RAMA) to the Turin Hill, crossing the Po River and urban area. Stratigraphic, heteropic, and erosional boundaries are marked (α, β, γ), highlighting the complex sedimentary architecture that governs aquifer geometry and hydraulic connectivity [70].

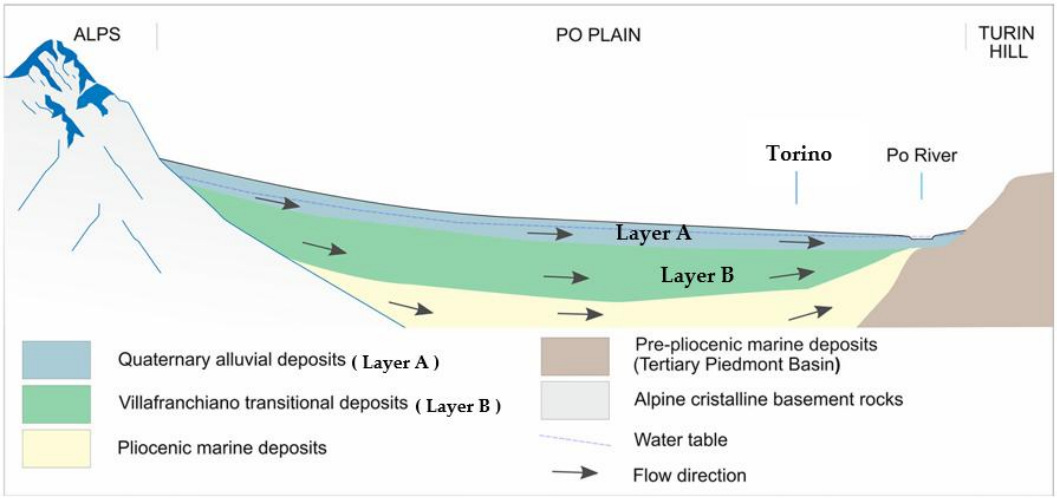

Figure 26. Cross section (W-E orientation), [73].

Unit 2b: The underlying Villafranchian succession (Piacenzian-Calabrian) is characterised by alternating silt and fine gravel of the Lower Complex (of deltaic origin) and locally preserved fluvial gravels of the Upper Complex, much of which was removed by Pleistocene alpine stream erosion. The unit 2b supports a multi-layered aquifer system that is extensively exploited for drinking water supply, a practice facilitated by the aquifer's excellent productivity and superior water quality compared to that of the shallow aquifer. However, regulatory constraints exist that preclude the utilisation of these deeper aquifers for geothermal applications. This is in order to preserve their strategic importance for municipal water supply, as represented by Layer B in the numerical model (Figure 26).

Unit 2a comprises Pliocene marine sediments, including the Argille di Lugagnano Formation and the Sabbie di Asti, which are located at depths of 3-20 metres beneath the eastern Holocene terraces of the Po river. The marine sediments under consideration have been confirmed through geophysical surveys and borehole logs, and it is asserted that they provide important hydrogeological controls and contribute to the confined nature of the intermediate aquifer systems [162].

The third unit, which is the deepest, is composed of a Miocene molassic sequence. Unit 3 contains confined aquifers with low yield, which are primarily exploited in hilly areas for domestic use.

The shallow aquifer maintains direct hydraulic connection with the main surface water drainage network, creating complex surface water-groundwater interactions that provide natural recharge mechanisms and help maintain thermal equilibrium. The groundwater flow is predominantly west-to-east, exhibiting a mean piezometric gradient of approximately 0.35% (range 0.6-1.2%), a phenomenon that is governed by the overarching topographic and structural framework extending from the RAMA to the Po River. The piezometric surface exhibits a gradual convergence towards the Po River, which functions as the regional base level and primary discharge axis for the groundwater flow system (**Figure 27**). The mean runoff direction exhibits fluctuations between the northerly-southerly (NW-SE) and westerly-easterly (WNW-ESE) orientations, indicative of the impact of the RAMA structural controls situated to the west and the Turin Hill Miocene anticline positioned to the east.

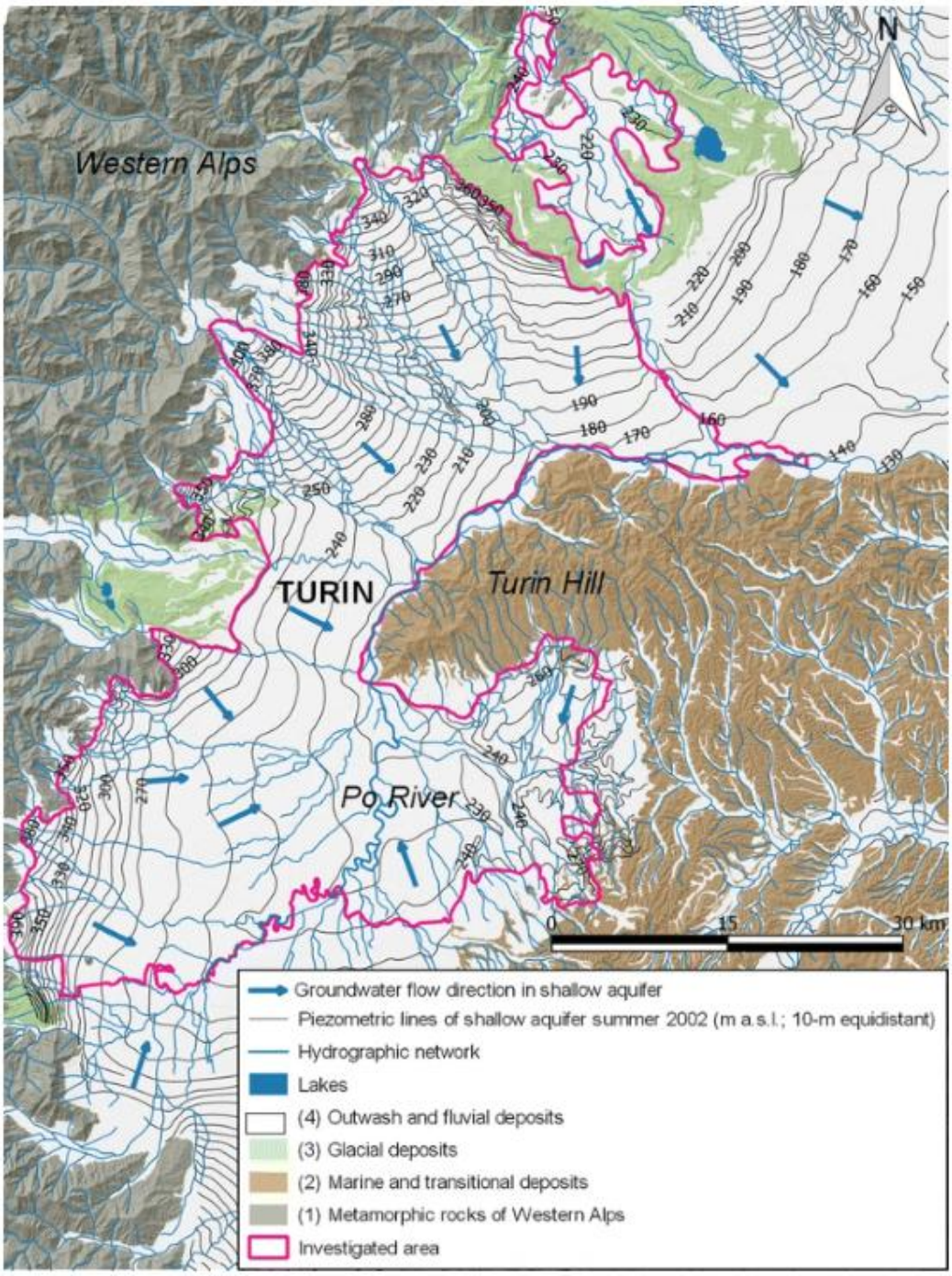

Figure 27. Geo-hydrological map of the Turin Area and groundwater flow direction [174].

The thermal characteristics of Turin's shallow groundwater system are particularly favourable for geothermal applications, with natural temperatures averaging 15°C throughout the shallow aquifer and reflecting stable conditions in the saturated zone. Current geothermal development in Turin includes 44 operational open-loop groundwater heat pump systems as of 2023, representing significant progress towards sustainable urban energy supply while demonstrating the practical feasibility of large-scale geothermal deployment in dense urban environments (Figure 28). The existing installations vary in scale, ranging from

small residential systems with flow rates of 1-2 l/s to large commercial systems exceeding 100 l/s.

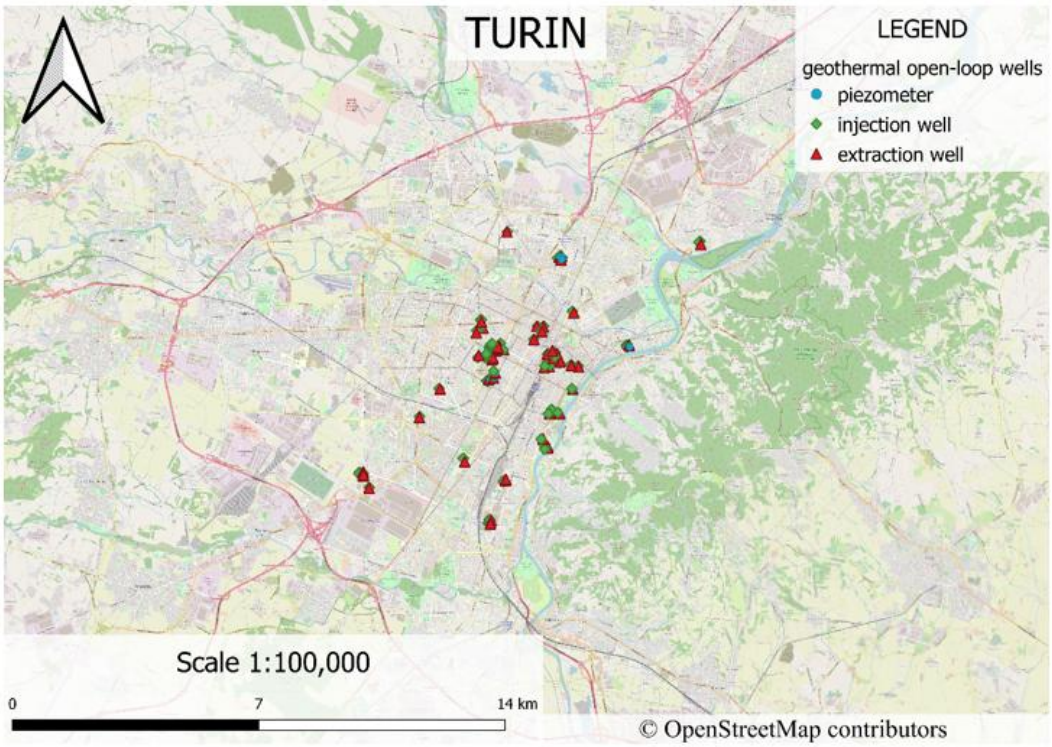

Figure 28. Geothermal open-loop wells location in Turin municipality.

The multidisciplinary understanding of the geological and hydrogeological setting provides the foundation for detailed numerical modelling studies and site-specific feasibility assessments. These assessments can guide future geothermal system deployment while ensuring long-term environmental protection and resource sustainability in this strategically important urban area.

These geological and hydrogeological characteristics are critical for assessing shallow aquifer geothermal potential using the GAP methodology.

The collection of groundwater data was obtained from freely available geodatabases provided by the Piedmont Region, with the aim of determining the hydrogeological setting of the Turin urban area.

For the reconstruction of the hydrogeological parameter maps (groudwater level, aquifer thickness and hydraulic conductivity distribution), the data were obtained from the following platforms:

- Geoportale Piemonte [176]
- Geoportale Arpa Piemonte [168]
- aperTO [177].

The map domain spans approximately 170 km², as depicted in Figure 29. In the selected CRS (WGS 84 / UTM zone 32N, EPSG: 32632), the domain is delineated by the following vertices:

- A: X= 385000.31160; Y= 4987311.36700
- B: X= 391177.27430; Y= 4999604.59400
- C: X= 402194.34640; Y= 4994154.15100
- D X= 396017.37050; Y= 4981860.92000

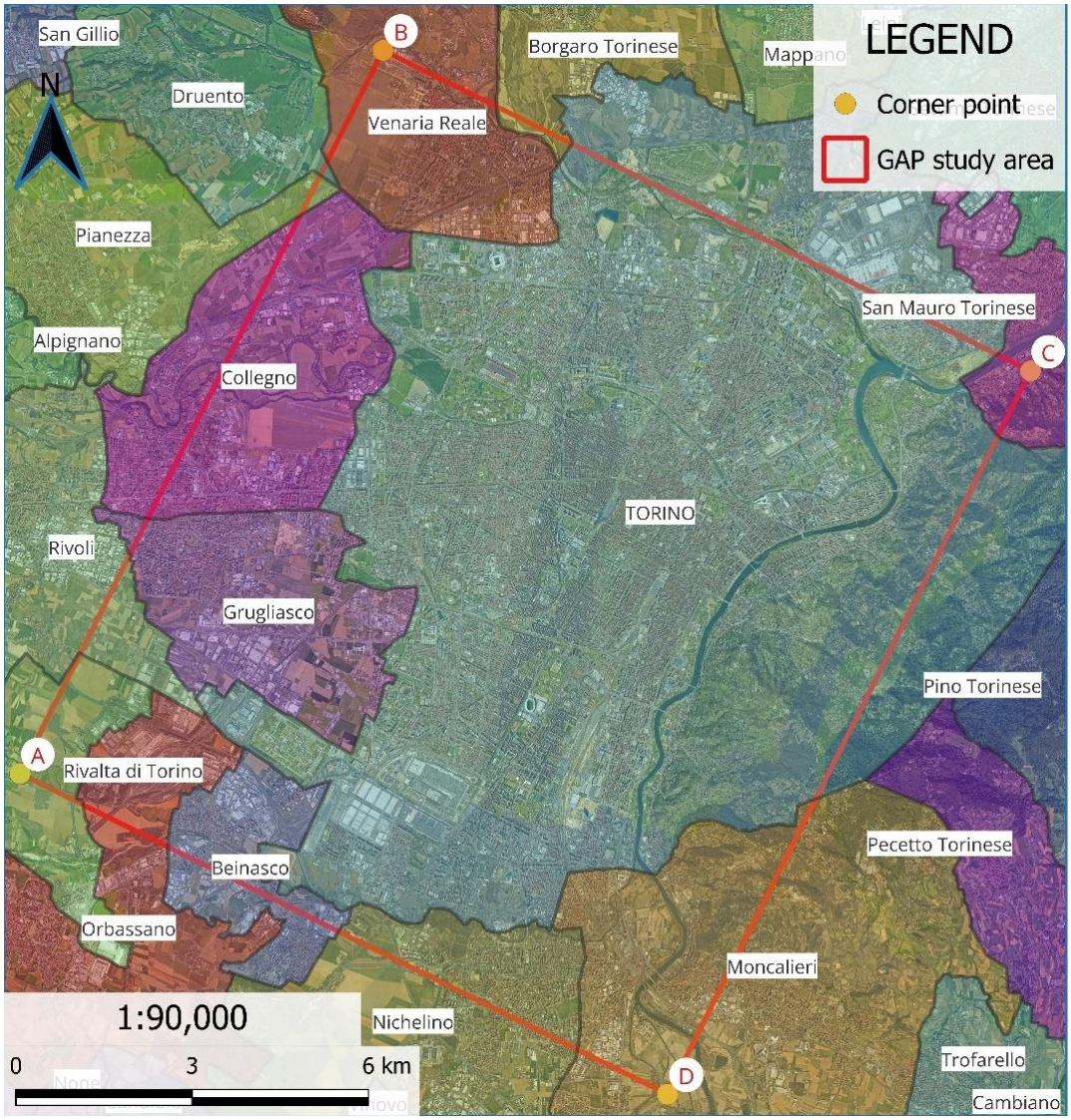

Figure 29. GAP study area map and corner points.

The GAP method case study includes several municipalities (Figure 29), including: Turin, Grugliasco, Collegno, Venaria Reale, San Mauro Torinese, Moncalieri, Nichelino, Beinasco, Orbassano, Rivalta di Torino and Rivoli.

Geographic data, necessary for the GAP methodology, were obtained from the following sources:

- Annual Reference Cartographic Base 2024 a black and white raster map at a scale of 1:10,000 (2024).
- Digital Terrain Model (DTM 5) ICE 2009-2011 derived from aerial imagery, this raster dataset features an accuracy of 0.30 m and a resolution of 5 m.
- Surface aquifer piezometry, a shapefile dataset representing the piezometric surface at a scale of 1:100,000, corresponding to the June–July 2002 period.
- Surface aquifer base a dataset at a scale of 1:50,000, with data updated as of 5 April 2022.

Two distinct model area were developed using FEFLOW finite element software to assess the feasibility and long-term thermal behaviour of prospective open-loop geothermal systems in the Turin metropolitan area. The selected sites, designated as Turin North and Turin South, represent contrasting hydrogeological conditions and operational scales, providing a comprehensive evaluation framework for shallow geothermal resource exploitation in heterogeneous urban aquifer systems. The spatial distribution of these model domains within the broader Turin context is presented in Figure 30, which displays the geological map of the metropolitan area at 1:70,000 scale, clearly delineating the model area north and model area south against the backdrop of Quaternary geological units. The geological characterization reveals the predominance of fluvial, fluvioglacial, and glacial deposits, with the Turin Hill marking the eastern boundary of the alluvial plain.

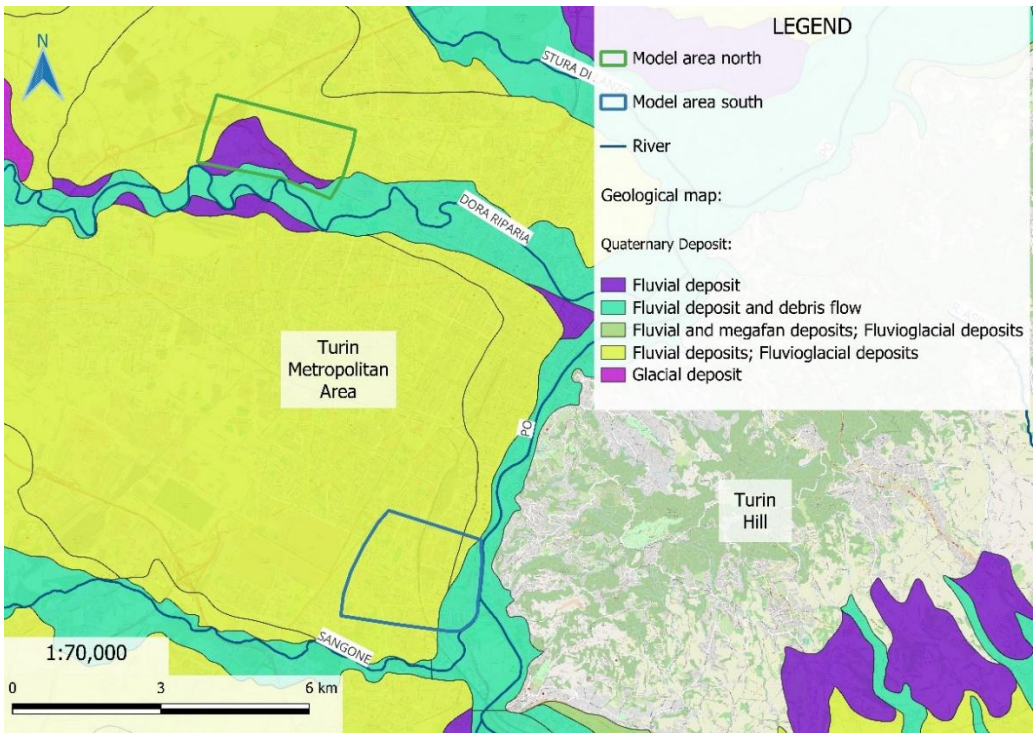

Figure 30. Simplified geological map of Turin metropolitan area.

Figure 31 presents the regional piezometric surface configuration derived from ARPA monitoring data, displayed at 1:70,000 scale with contour lines ranging from 240 to 285m a.s.l.. This regional-scale piezometric characterization provides essential boundary conditions for the subsequent detailed numerical models and confirms the general flow direction that governs thermal plume propagation in open-loop systems.

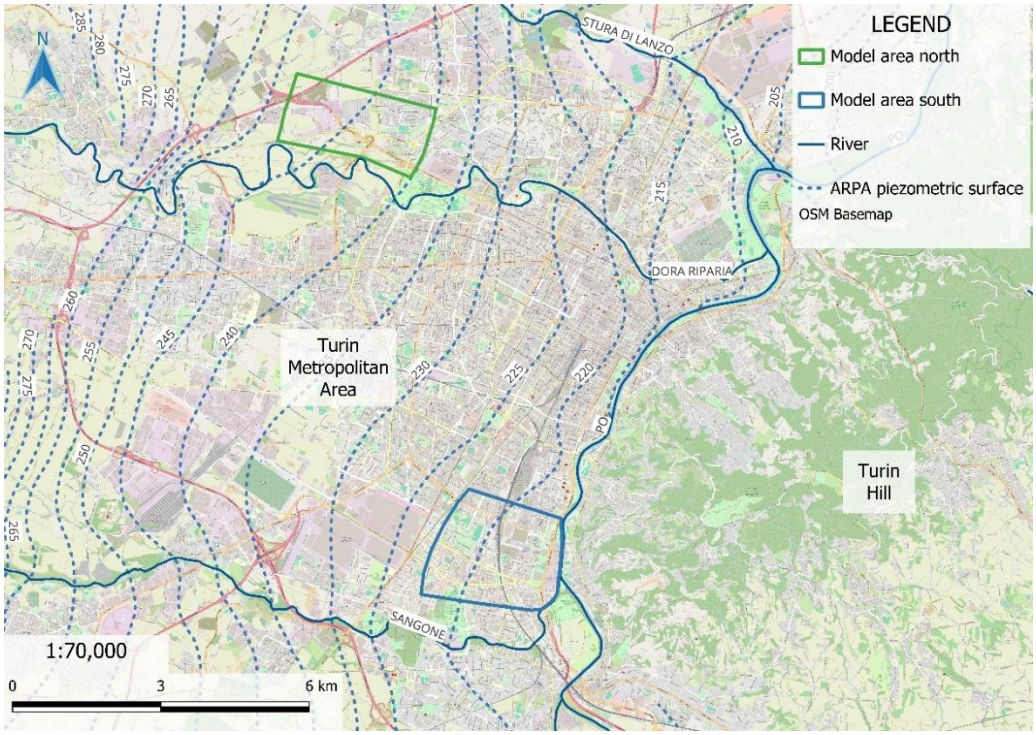

Figure 31. Piezometric surface map of Turin metropolitan area.

Figure 32 provides a detailed zoom view of the southern study area and the proposed geothermal well locations distinguished as intake (extraction) and discharge (reinjection) wells.

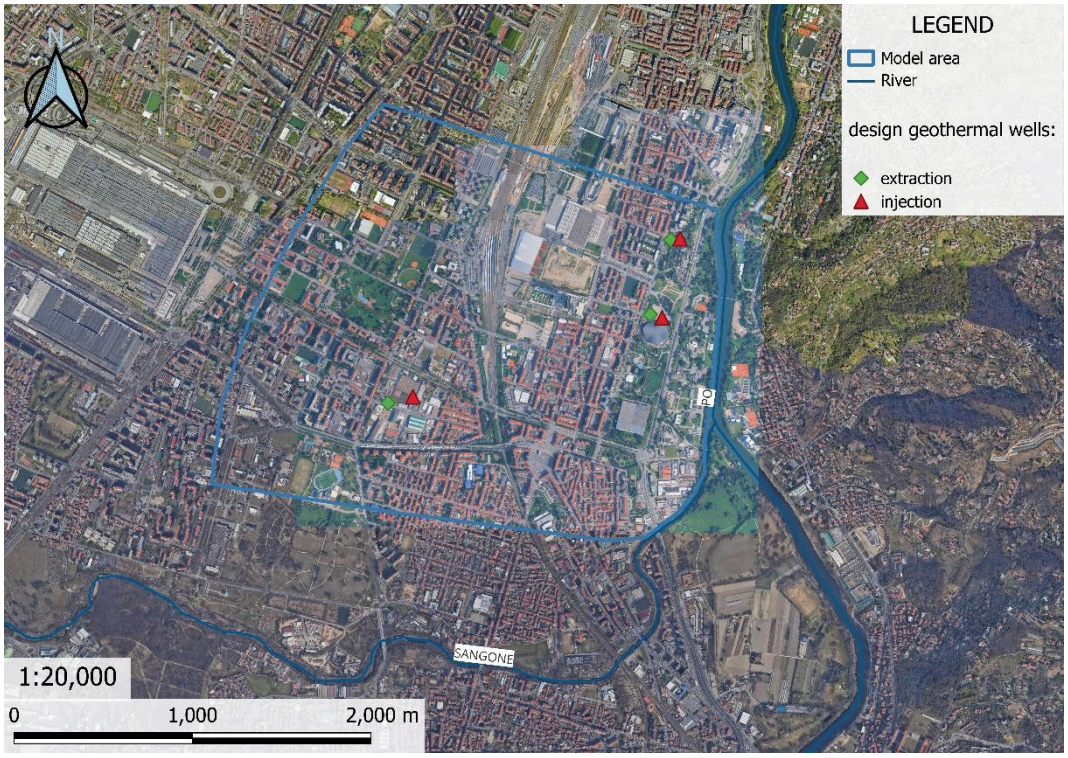

Figure 32. Zoom view of south model area and design open-loop wells location.

2.5 Results

This chapter presents the primary outcomes of the analyses conducted for open-loop geothermal systems in the case study of Turin. The investigation employs a comprehensive multi-scale analytical framework that progresses from regional to site-specific assessment, following a top-down approach that enables systematic evaluation of shallow geothermal potential across different spatial resolutions (Figure 33). The results are organized according to three hierarchical approaches (case study), each operating at a distinct spatial scale and employing specific methodological tools.

The first approach operates at the city scale, utilizing the GAP methodology (2.5.1 GAP Case Study) to assess the overall geothermal potential of Turin's urban area. This regional-scale assessment provides a comprehensive overview through potential mapping, which serves as a foundational tool for identifying suitable areas for geothermal exploitation based on hydrogeological and thermal properties of the shallow aquifer system. Notably, the extensive data preparation phase required for the GAP methodology, including the spatialization of piezometric information, hydraulic conductivity distributions, and aquifer thermal properties, established a comprehensive georeferenced database that was subsequently utilised across all subsequent modelling phases.

The second approach employs MODFLOW-based numerical modelling at two different scales. The primary model consists of a city-scale groundwater flow and heat transport model, the purpose of which is to simulate the cumulative effects of all existing open-loop geothermal installations throughout Turin's urban area. This model facilitates the assessment of potential hydraulic and thermal interference between multiple systems operating within the same aquifer. The spatialised hydrogeological parameters that were derived from the GAP assessment were incorporated directly into the MODFLOW model grid. This process resulted in a substantial reduction in model setup time and an enhancement of the reliability of boundary conditions. Subsequently, a district-scale calibrated model focuses specifically on the Politecnico di Torino campus, providing detailed analysis of the existing geothermal plants and their interactions with local hydrogeological conditions.

The third approach involves the implementation of FEFLOW software for site-scale simulations, with case studies divided between the northern and southern zones of Turin to account for spatial variations in geological and hydrogeological settings. FEFLOW's advanced capabilities in simulating coupled groundwater flow and heat transport processes enable precise evaluation of open-loop system performance, including the assessment of extraction-injection well configurations and their influence on aquifer thermal dynamics. The spatially distributed hydraulic conductivity fields and piezometric surfaces, which had been developed for the GAP and MODFLOW analyses, were refined and adapted for the higher resolution FEFLOW meshes. This ensured continuity in the parameterization framework

across all modelling scales. This fine-scale analysis is critical for optimising designs and for evaluating potential environmental impacts on adjacent installations.

This hierarchical methodology ensures comprehensive characterization of Turin's shallow geothermal resource, progressing from broad potential assessment to detailed performance simulation, thereby providing robust scientific support for sustainable exploitation of the urban aquifer thermal capacity. The methodological synergy achieved through shared spatial datasets across different analytical tools represents a significant advancement in computational efficiency and model consistency for multi-scale geothermal resource assessment.

Figure 33. Flow chart representation of the main results using the top-down scale approach.

2.5.1 GAP Case Study

In this study, a grid composed of 50×50 m square cells was used. This resolution facilitates the integration of the geothermal potential map with other geospatial layers, providing enhanced topological and spatial context. The combination of class discretisation and the use of polygon shapefiles enables a more effective and user-friendly visualisation of geothermal potential. The dual approach adopted in this study enhances interpretability by highlighting key variations in thermal power distribution and providing precise spatial delineation, which are both essential for scientific analysis and practical applications in geothermal resource management.

Following data import into QGIS, spatial interpolation was performed using the Kriging method through the SmartMap Plugin [178].

To evaluate the hydraulic conductivity (k) across the Turin metropolitan area, data were initially retrieved from the Piedmont Geoportal and supplemented with additional stratigraphic sections from the ARPA Piemonte database. These sections, which include lithological descriptions from borehole investigations, enabled the categorization of hydraulic conductivity into three classes, following the approach of Gizzi et al. [74]: (i) gravel with pebbles ($3.1 \cdot 10^{-3}$ m/s), (ii) gravel with sand ($2.6 \cdot 10^{-3}$ m/s), and (iii) sand with gravel embedded in a silty matrix ($1.5 \cdot 10^{-3}$ m/s). The integration of these datasets yielded approximately 300 measurement points representative of the shallow aquifer (Figure 34).

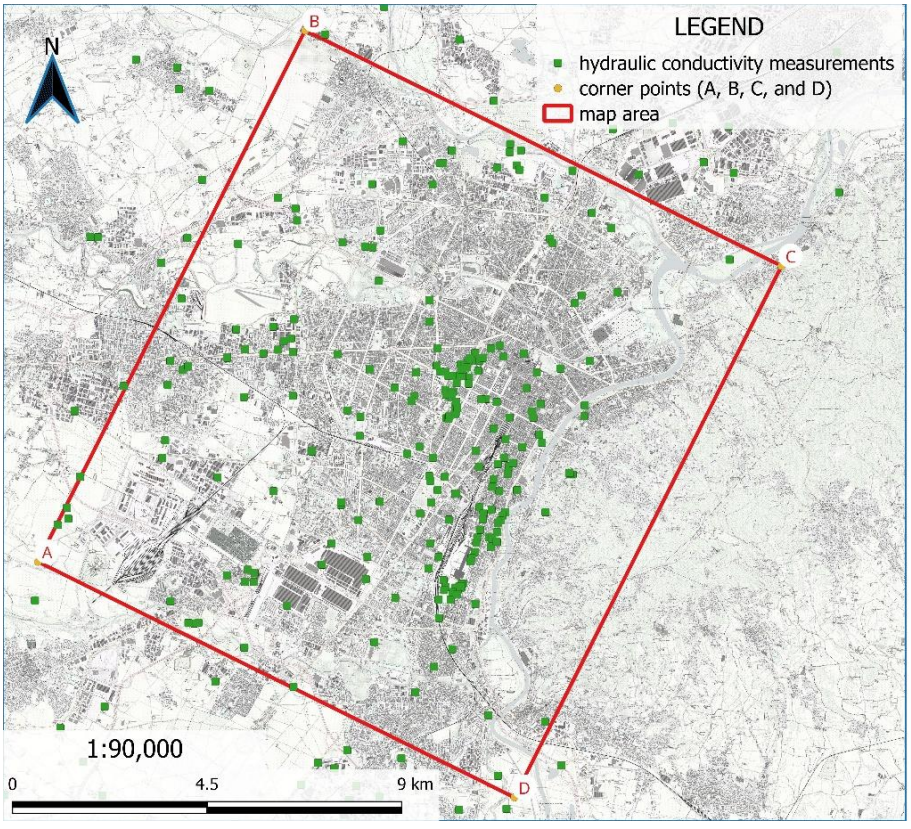

Figure 34. Example of hydraulic conductivity data set used on QGIS.

Subsequently, the hydraulic conductivity values were transformed to their logarithmic scale to better conform to the assumptions of spatial stationarity and normality inherent in geostatistical methods. The Kriging interpolation was then performed using the SmartMap Plugin in QGIS, which offers an integrated framework for geostatistical analysis. In this process, the plugin automatically identifies and excludes outlier data, ensuring that anomalous values do not skew the interpolation results (Figure 35).

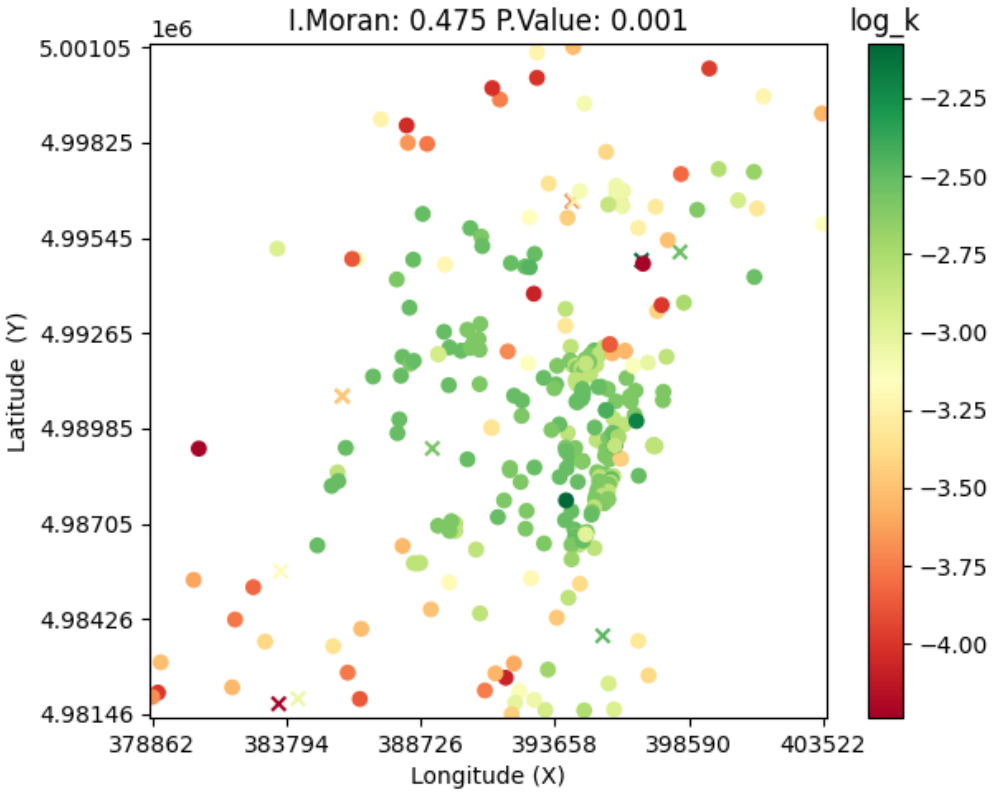

Figure 35. Distribution of data visualised on SmartMap Plugin, the colour shows the logarithmic value of the hydraulic conductivity in the area.

The spherical variogram model was selected as the best fit for this dataset, based on its ability to capture the spatial autocorrelation characteristics shown in the variogram graph (Figure 36).

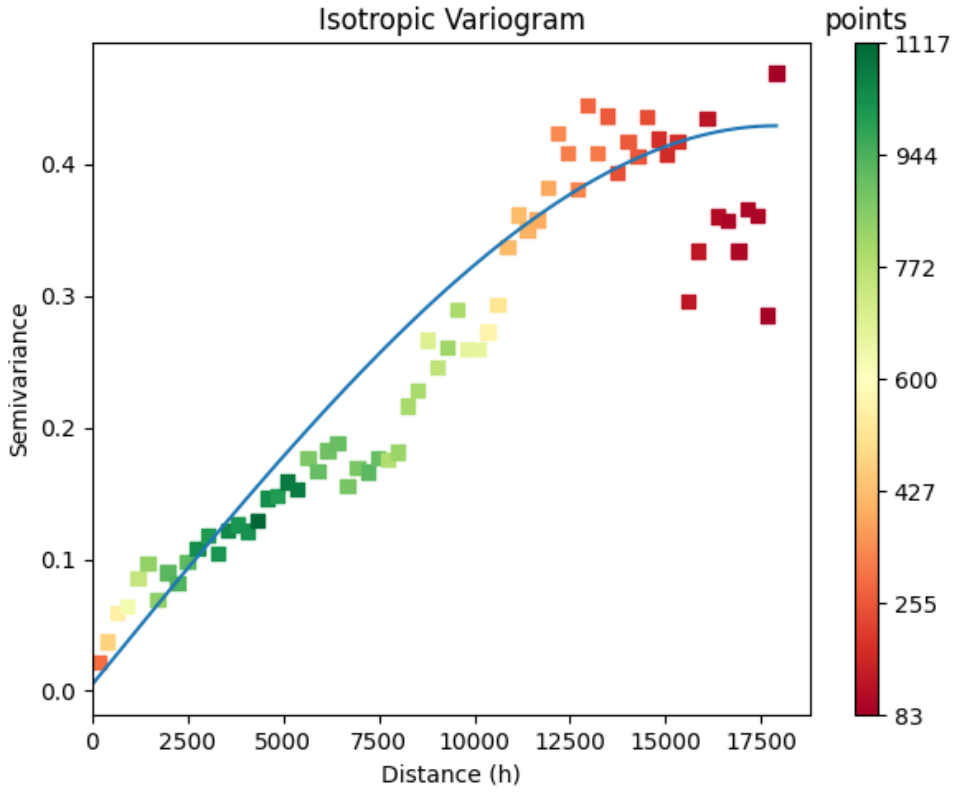

Figure 36. The Variogram show the distribution and trend of the value, the blu line is the best fit used for interpolation.

The Kriging process, therefore, involved estimating the logarithmic hydraulic conductivity at unsampled locations, generating a continuous raster file representing the spatial variability of k across the study area. Finally, using the QGIS Raster Calculator, the logarithmic values were back-transformed to yield the actual hydraulic conductivity values in m/s. The resulting map, which delineates the spatial distribution of hydraulic conductivity, forms a critical component of the overall hydrogeological model.

The hydraulic conductivity map was subsequently generated using the Kriging interpolation method, with the spherical variogram model selected as the best fit for the dataset. This map, which delineates the spatial distribution of hydraulic conductivity, constitutes a critical component of the overall hydrogeological model (Figure 37).

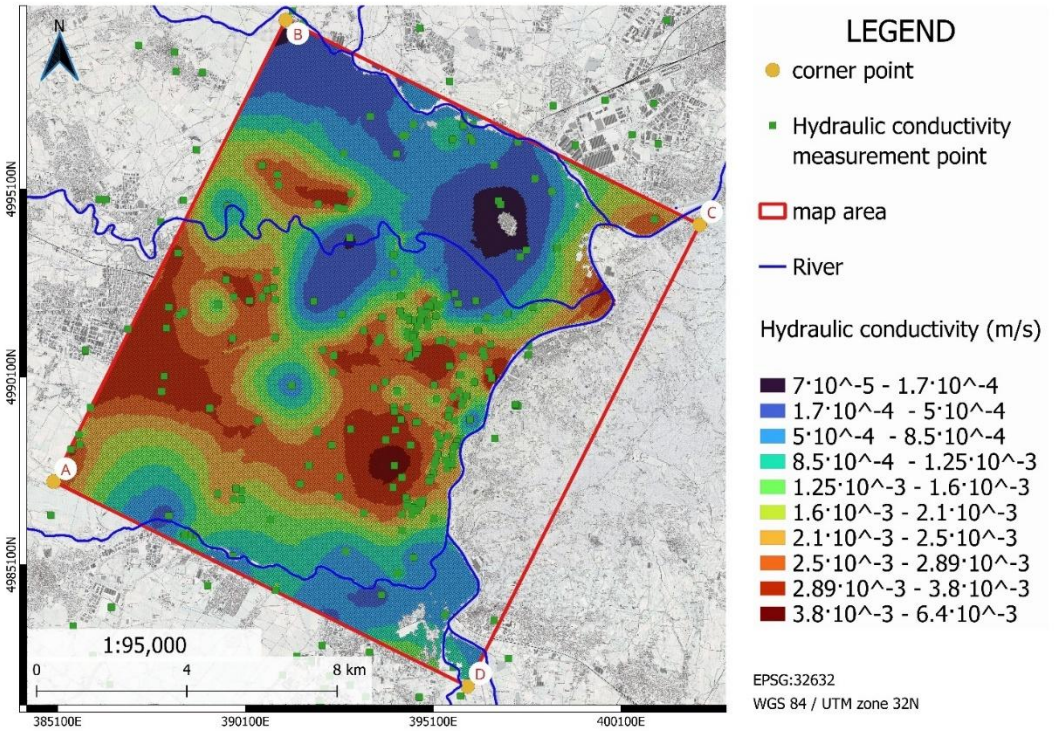

Figure 37. Spatial distribution of hydraulic conductivity (m/s) within the study area. Measurement locations are shown as green squares, and conductivity values are classified into ten intervals ranging from 7·10-5 to 6.4·10-3 m/s. The map reveals significant heterogeneity in aquifer permeability. This variability directly influences groundwater flow dynamics and the feasibility of open-loop geothermal exploitation.

To accurately characterize the geometry and capacity of a shallow unconfined aquifer system, determining aquifer thickness is a fundamental step. This parameter, representing the vertical extent of the saturated zone, directly influences groundwater availability and the feasibility of open-loop geothermal systems.

Aquifer thickness was estimated by combining the interpolated piezometric surface, derived from the regional monitoring network of ARPA Piemonte, with the updated geospatial dataset of the aquifer base elevation provided by the Piano di Tutela delle Acque (PTA) as of 2021 (Figure 38). The piezometric surface, which reflects the elevation of the water table in metres above sea level (m a.s.l.), was generated using Kriging interpolation techniques within the QGIS environment, as previously described for hydraulic conductivity. A similar interpolation was applied to the aquifer base elevation dataset.

The final aquifer thickness raster was then computed using the "Field Calculator" tool in QGIS, by performing a cell-by-cell subtraction between the piezometric surface and the aquifer base elevation.

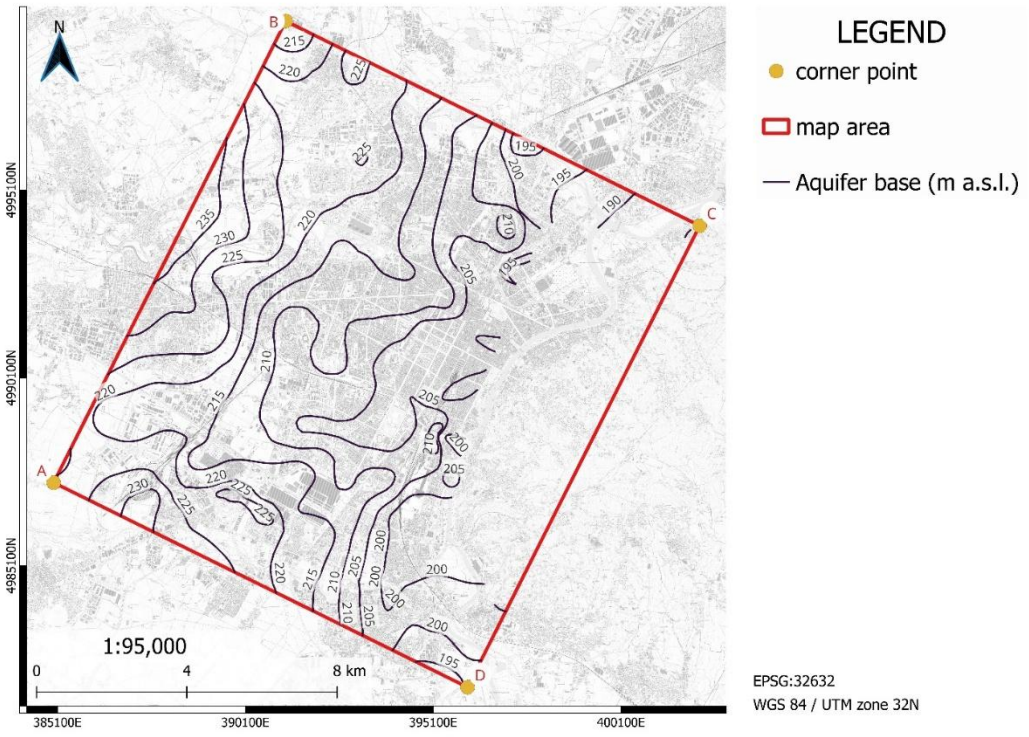

Figure 38. Map of aquifer base elevation (m a.s.l.) within the study area. Black contour lines indicate the depth of the aquifer base, ranging from 190 to 235 m a.s.l., revealing the structural geometry of the subsurface and its influence on groundwater flow.

The result is a two-dimensional shapefile that quantifies the thickness of the aquifer throughout the study area, expressed in meters (Figure 39). The highest thickness values (31.5–34.5 m) are located in the northwestern corner near point B and in the central sector of the map, reflecting depositional zones characterised by deep gravelly sequences. Conversely, the thinnest zones (4.5–7.5 m), identified by dark purple areas, are primarily located in the southern portion of the map, near point D, and along major river corridors. These spatial variations in aquifer thickness are consistent with the regional hydrogeological setting, where increased sediment compaction or erosional processes near active riverbeds lead to reduced saturated zone thickness.

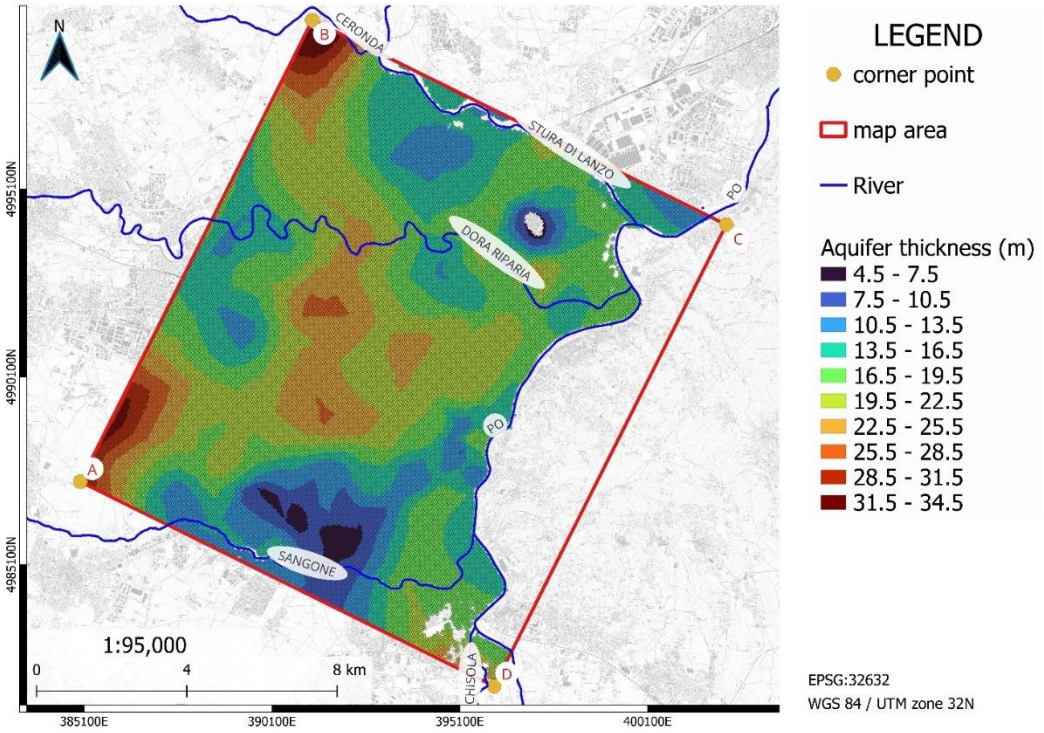

Figure 39. Spatial distribution of aquifer thickness (m) within the study area. Thickness values range from 4.5 m to 34.5 m. This map supports the hydrogeological characterization of the urban subsurface and informs resource potential assessments.

Figure 40 shows the spatial distribution of the maximum extractable groundwater discharge in the urban area of Turin, as estimated using the GAP methodology. The map displays the predicted discharge from the shallow alluvial aquifer in classes ranging from 1 to 200 l/s, represented by a continuous colour scale from dark blue (lowest values) to dark red (highest values). This pattern highlights a marked spatial heterogeneity, reflecting variations in hydrogeological properties such as hydraulic conductivity, aquifer thickness, and hydraulic gradients across the study area.

Higher discharge values are predominantly located along the main fluvial corridors and in sectors where the aquifer is thicker and more transmissive, whereas lower values occur in areas with less favourable hydrogeological conditions. The resulting map provides a spatially explicit representation of the groundwater abstraction potential derived from the GAP workflow and can be interpreted as a first-order estimate of the maximum sustainable discharge at the urban scale. These results offer a quantitative framework to support preliminary planning of open-loop geothermal systems and to identify priority zones for more detailed site-specific investigations.

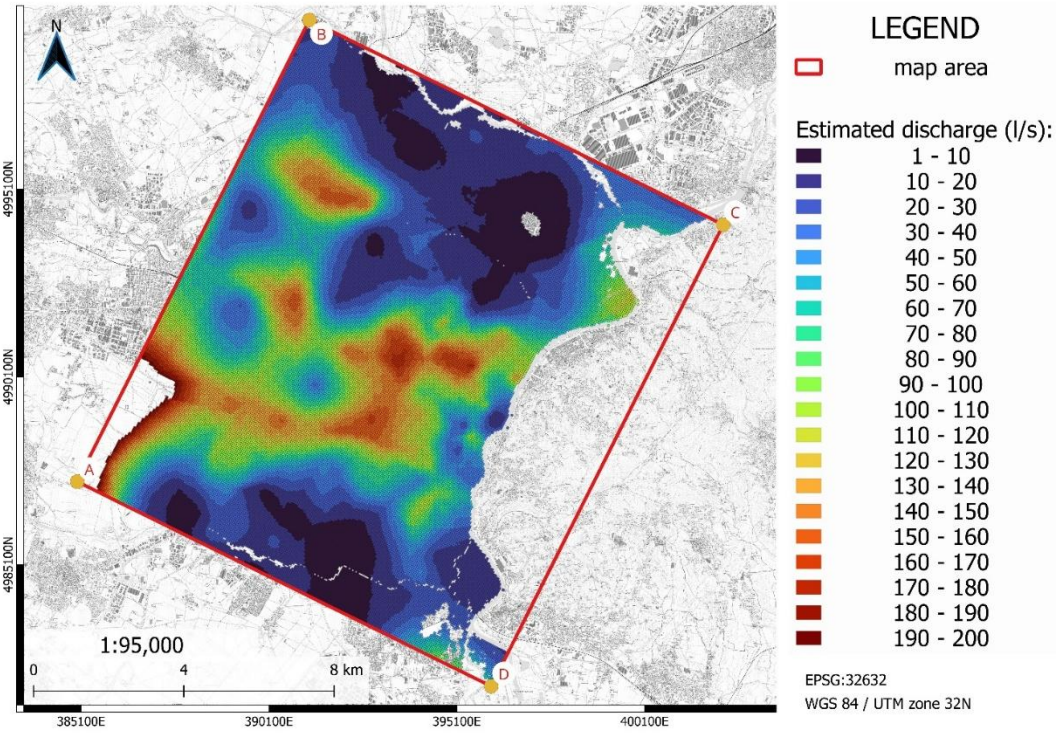

Figure 40. Estimated groundwater discharge rates (l/s) across the study area following application of the GAP method. Values range from 1 to 200 l/s. The map provides a spatially explicit output of the GAP model, supporting preliminary assessments of geothermal abstraction potential.

The final geothermal potential map is shown in Figure 41, illustrating the distribution of geothermal potential across the study area based on the GAP classification method. The map is divided into six main classes, ranging from low potential (Class 1: 5-10 kW, in dark blue) to high potential (Class 6: >500 kW, in dark red). The map highlights a quite homogeneous distribution of geothermal potential, with the central and western sectors of the city largely falling within the highest class (Class 6), mirroring a high suitability for the development of open-loop systems.

Similarly to the discharge distribution (Figure 40), lower geothermal potential values are observed in proximity to main river systems, where areas are classified down to Class 2. This pattern is mainly attributed to the reduced aquifer thickness in these zones, as river valleys often correspond to areas with limited sediment accumulation and higher groundwater flow velocities, resulting in a lower storage capacity.

In contrast, the central and southern parts of the study area show extensive zones classified as Class 5 and Class 6 (orange and dark red), corresponding to thermal power values in excess of 200 kW. These high-potential areas are likely associated with thicker aquifer deposits, composed of coarse-grained materials such as gravel and sand with higher hydraulic conductivity. The increased thickness of the saturated zone enhances the efficiency of heat extraction, making these locations more favourable for geothermal applications.

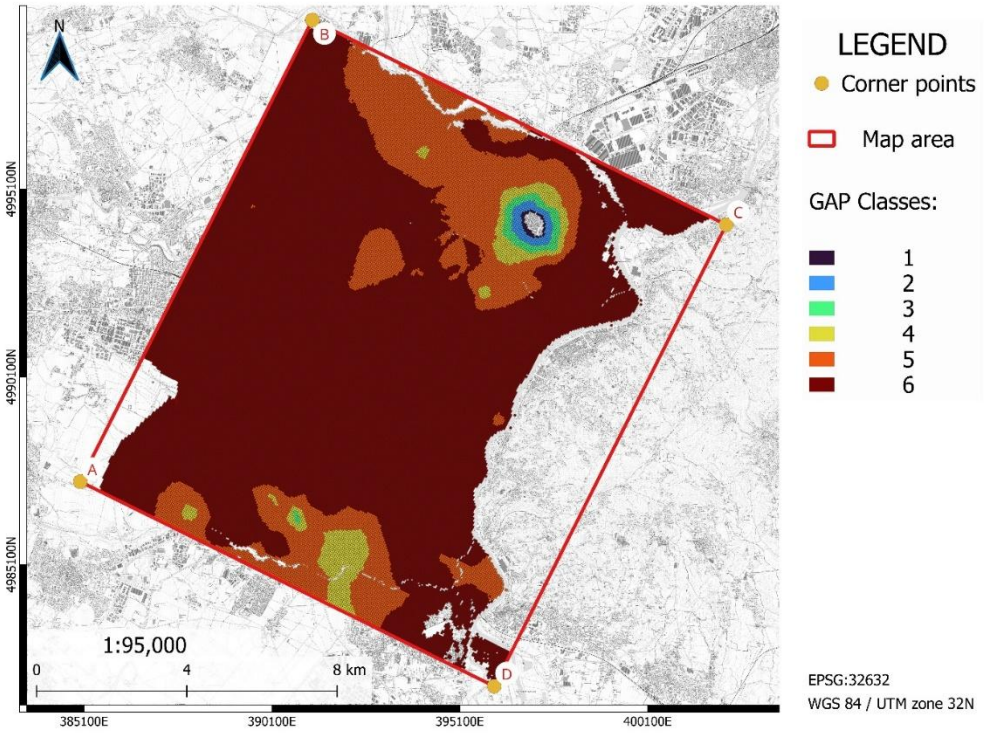

Figure 41. Spatial distribution of GAP potential classes across the study area. Most of the area is dominated by Class 6 (dark red), indicating zones with favorable aquifer properties and high predicted discharge rates.

The histogram in Figure 10 illustrates the distribution of groundwater thermal power (kW) in the study area, derived using the GAP method. The bars report, for each power class, the fraction of 50 × 50 m cells belonging to that interval. The distribution is markedly right-skewed and can be interpreted in terms of three main clusters of groundwater thermal potential.

The first cluster, which includes powers between roughly 200 and 600 kW, represents the dominant portion of the aquifer and accounts for about 40–45% of all cells. Within this interval, the most populated classes are 300–400 kW and 400–500 kW, each contributing approximately 6–7% of the cells, while the adjacent 200–300 kW and 500–600 kW classes reach values of the order of 4–5%. Cells in this cluster generally correspond to the central sectors of the alluvial plain, where the aquifer thickness and hydraulic conductivity are moderate, and they are suitable for supplying the heating and cooling demands of typical multi-family residential buildings and small office or school complexes.

A second cluster can be recognised between about 600 and 1500 kW, comprising nearly 30–35% of the total cells. In this range, the relative frequencies gradually decrease from around 3–4% per class at 600–800 kW to about 2% per class close to 1200–1500 kW. These cells are mainly located in zones where the aquifer is thicker and the flow conditions are favourable, and they can sustain medium-scale geothermal systems serving building aggregates, mixed-use blocks or campus-type facilities with relatively high thermal loads.

The third cluster, corresponding to powers exceeding approximately 1500–2000 kW, represents about 10–15% of the mapped cells and includes the tail of the

distribution up to powers above 4000–4500 kW. Although less frequent, these high-potential cells often coincide with coarse, highly permeable gravel bodies, where the combination of large saturated thickness and high transmissivity produces substantial extractable thermal power. These areas are especially appropriate for large groundwater heat pump installations, decentralised energy hubs or small district heating and cooling networks, where a limited number of wells can serve multiple end-users.

Finally, the remaining 10–15% of cells exhibit powers below 200 kW and are mostly confined to marginal sectors of the aquifer, affected by reduced saturated thickness, lower hydraulic conductivity or locally unfavourable boundary conditions. While less attractive for high-capacity systems, these low-potential zones can still host small-scale installations for individual buildings, provided that the design properly accounts for the limited available groundwater flow and the need to control thermal interference with neighbouring systems.

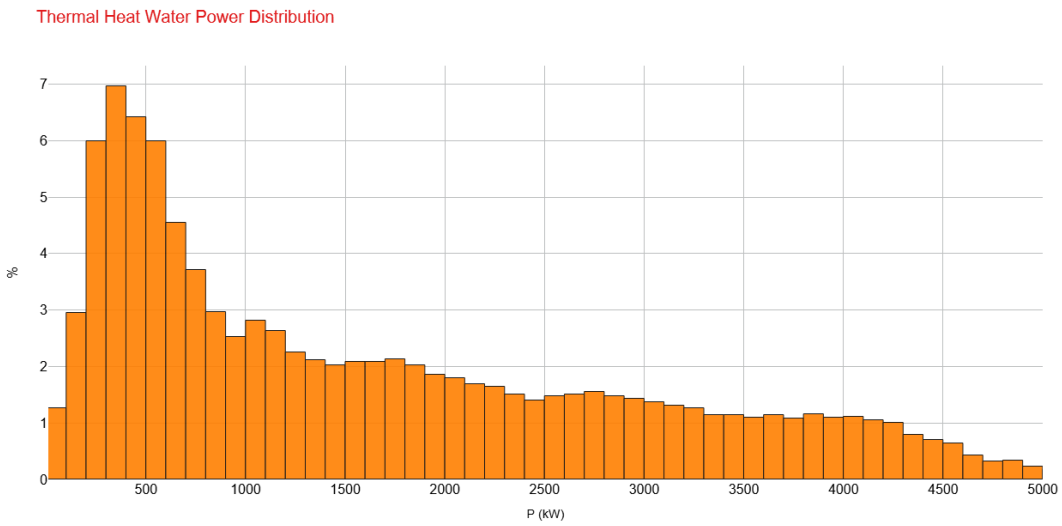

Figure 42. Histogram chart of the thermal water power distribution expressed in kW.

The classification into discrete classes (**Table 6**) is instrumental for several important purposes. First, it enhances the visualisation of the geothermal potential by clearly delineating areas of varying thermal power, thus facilitating the identification of zones of low, moderate, and high potential. This categorisation is of particular importance in a planning context, as it facilitates decision-making processes related to site selection, resource allocation, and potential economic feasibility. Furthermore, the classification helps to simplify complex data, improving the clarity and readability of the resulting map and enabling stakeholders to quickly assess the spatial distribution of geothermal resources.

The GAP analysis presented above identifies spatial distribution of geothermal potential across the Turin metropolitan area, providing essential guidance for strategic planning and site selection. However, to validate the technical feasibility of specific installations and assess long-term sustainability under realistic

operational conditions, detailed numerical modelling is required. The following sections present two complementary numerical case studies: Section 2.5.2 MODFLOW employs numerical modelling to simulate cumulative impacts from all existing geothermal installations across urban Turin, while Section 2.5.3 utilises FEFLOW to analyse prospective large-scale installations in northern and southern sectors with rigorous parameter calibration and extended temporal projections.

2.5.2 MODFLOW Case Studies

The initial case study encompasses the numerical simulation of all geothermal wells currently present in the city of Turin. In the absence of a system for registering wells, the location and number of said wells were determined by means of an analysis of all discharge authorisation applications (identified as industrial discharges) for the city of Turin, conducted on a case-by-case basis. As illustrated in Figure 43, the geothermal wells are categorised into two distinct types: intake wells (green diamond) and discharge wells (red triangle). The creation of a geodatabase containing key information in QGIS software was then undertaken. This geodatabase included the total number of wells (154 as of 2024), geographical coordinates for each well, and the maximum authorised flow rate.

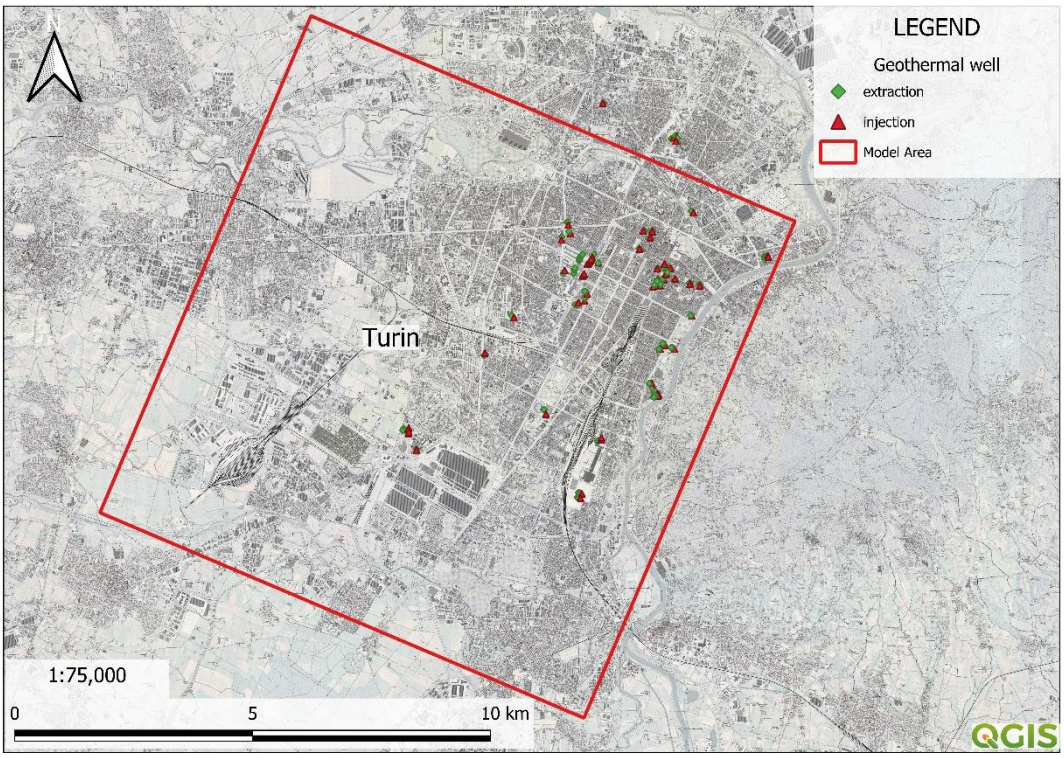

Figure 43. Map of the model area and location of simulated wells.

Fluid flow and heat transport mechanisms in the unconfined aquifer were modelled by using the modular finite-difference groundwater flow model (MODFLOW 6) developed by the U.S. Geological Survey (as explained in chapter 2.3.2 MODFLOW). The groundwater flow equation is solved using the finite-difference approximation. The flow region is subdivided into blocks in which the medium properties are assumed to be uniform. Flowrate and cumulative-volume balances from each type of inflow and outflow are computed for each time step. The multi-species transport model MT3DMS is applied to simulate heat transport in shallow confined aquifers [179]. ModelMuse (version 5.4.0.0) was used as a graphical user interface and modelling environment [180].

Starting from the assigned hydrodynamic and thermal parameters for Unit 1 and Unit 2, a two-unit conceptual model simulation was performed, wherein hydro-stratigraphic Unit 1 contains the exploited unconfined alluvial aquifer. The plan-view grid dimensions in the model were set at 11x11 km (121 km^2). The model area was intentionally designed to be larger than the Turin city urban area under investigation to minimize the impact of assumed boundary conditions on model outcomes. Boundary conditions were fixed as follows: the recharge area limits of the deep aquifer at the western border, Dora Riparia, Sangone and Po River at the North, South and East border, respectively. General Heads Boundary (GHB) were set on the western and eastern boundaries following available onsite potentiometric surface measurements (Figure 44).

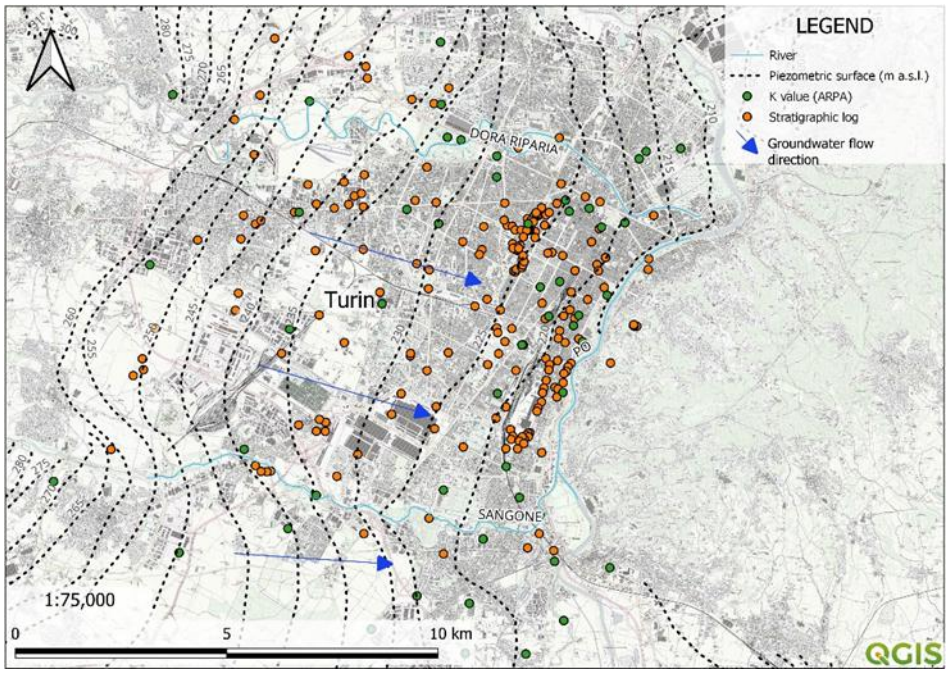

Figure 44. Available geological and hydrogeological information and data for the Turin plain area [74].

As shown in Figure 45, the graphical interface of Model Muse presents the base map of Turin and the delineation of the model area. The green line in the north-west is indicative of the upstream GHB, representing the model inflow, whilst the red line in the south-east corresponds to the downstream GHB, signifying the model outflow. The blue lines represent the boundary conditions of the rivers, whilst the green squares indicate the geothermal intake wells and the red squares denote the discharge wells.

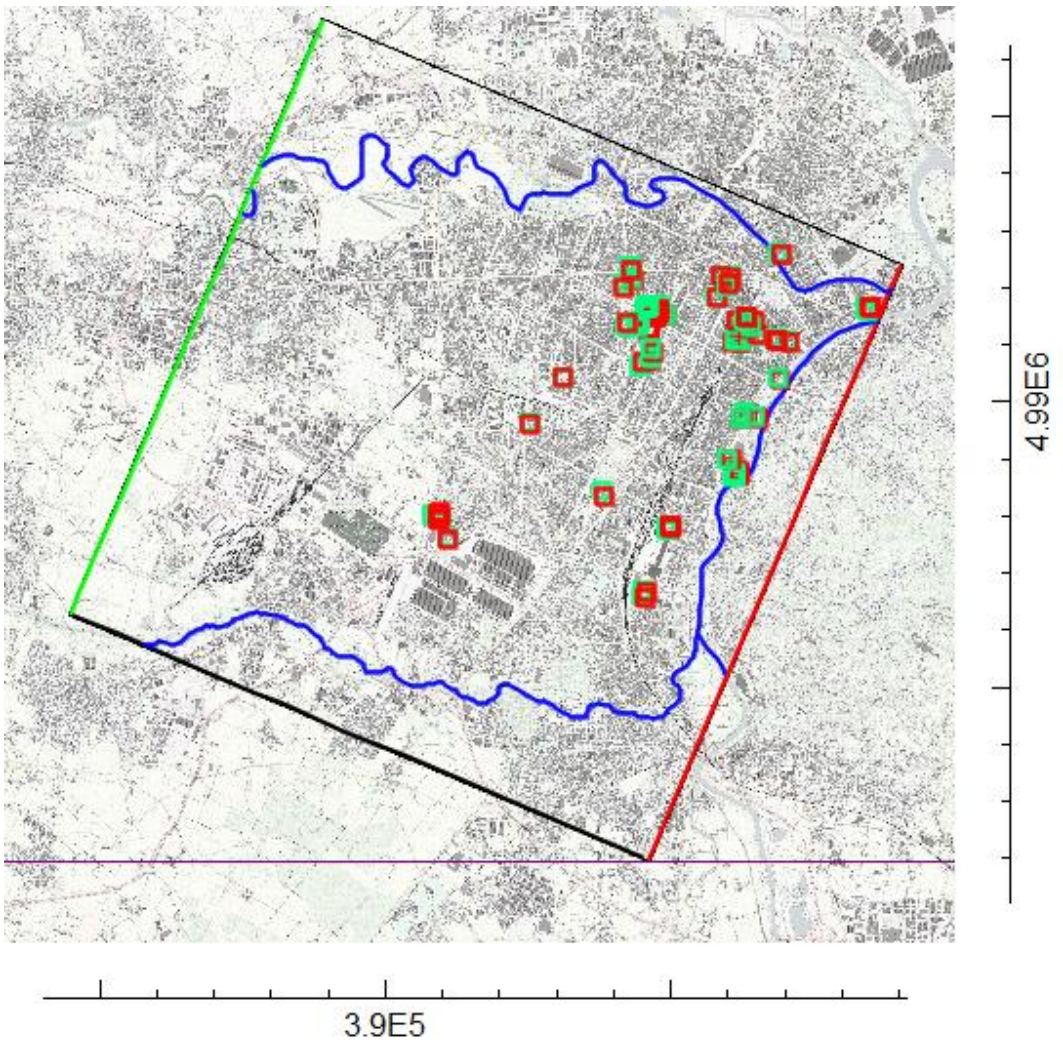

Figure 45. Model area, GHB (green line inflow, red line outflow), rivers blue lines, and Multilayer well (green squares are intake wells, and red squares are discharge wells) visualised in Model Muse interface.

An average natural groundwater temperature of 15.0 °C was set throughout the shallow aquifer, reflecting the undisturbed average groundwater temperature of the saturated zone [78]. The river package is used to simulate the interference with rivers, while the well package is used for existing geothermal wells. The154 wells were modelled through the following three-years scenarios: 1) maximum flow rate (Qmax) scenario with cooling/heating operating seasons mode for 6 months/year; 2) average monthly flow rate (Qmean) scenario with cooling/heating operating seasons mode for 6 months/year. The Qmax value for each plant was determined based on the information provided in the single environmental authorization (AUA [177]) documents. It depends on the size of the plant, with the value ranging between 1 l/s flow rate for very small plants and 100 l/s flow rate for large plants. Conversely, the Qmean value considered was set at one-fourth of the Qmax. Reinjection temperatures of 8°C and 21°C were considered for the winter (6 months) and summer (6 months) plant-functioning seasons, respectively, due to the regulation limits. Moreover, abstracted and reinjected discharges were considered to be equal over the plant operational period.

Because the model domain corresponds to a densely built-up urban area characterized by extensive soil sealing (buildings, roads) and a stormwater drainage system that rapidly exports rainfall, diffuse areal recharge from direct precipitation infiltration was set to 0 in the simulations. This choice does not imply that the urban aquifer is unrecharged: the urban hydrogeology literature shows that recharge pathways in cities are more complex than in rural environments and often include significant "secondary recharge" from leakage of water-supply mains, sewer networks, and stormwater systems, as well as irrigation return flow. For example, Lerner [181] highlights that part of the direct recharge is lost due to imperviousness and drainage, but additional recharge can occur through stormwater drainage systems and pipe-network leakage. In Nottingham (UK), Yang et al. [182] estimated a total urban recharge of ~211 mm/yr, largely dominated by water-mains leakage (~138 mm/yr) and sewer leakage (~10 mm/yr). In Barcelona, Vázquez-Suñé et al. [183] used hydrochemical/isotopic mixing to show that the main contributors to total recharge were water-supply network losses (22%) and sewage network losses (30%), while rainfall recharge was mostly concentrated in non-urbanized areas (17%) and runoff infiltration contributed 20%. More recent evidence also indicates that anthropogenic contributions can compensate for reduced diffuse infiltration: in the highly urbanized Upper Tietê watershed (São Paulo metropolitan region, Brazil), recharge in urban areas served by water and sewer mains was reported as 437 mm/yr, comparable to or higher than recharge in surrounding rural areas (106–407 mm/yr) [184].

In the present study, no spatially distributed information on water/sanitation network leakage (rates and spatial patterns), irrigation return flow, or stormwater infiltration facilities was available; therefore, secondary recharge was not explicitly parameterized to avoid introducing poorly constrained fluxes. As discussed by Sanford [185], recharge in groundwater models is commonly either specified from measurements or inferred during calibration, and the appropriate representation depends on study objectives and boundary controls. For Turin, however, spatially distributed leakage/recharge data were not available at the resolution required by the city-scale model; therefore, secondary recharge was not parameterized to avoid introducing poorly constrained, spatially heterogeneous fluxes. The shallow aquifer in Turin shows a predominant west–east groundwater flow toward the Po River, and long-term monitoring over 2010–2022 indicates an average water-table decline of ~1 m, suggesting that any anthropogenic recharge is likely balanced (or exceeded) by discharge to rivers and/or pumping at the metropolitan scale [186].

To quantify the potential error introduced by neglecting a background areal recharge, we consider an upper-bound range of 50–200 mm/yr (typical of urban settings where infrastructure leakage substantially contributes to recharge). Over the ~130 km² municipal area of Turin, this corresponds to a net inflow of approximately 0.21–0.82 m³/s (210–820 l/s). In an alluvial aquifer hydraulically controlled by nearby rivers, a first-order Dupuit estimate indicates that neglecting such distributed recharge would translate into a maximum head bias on the order of a few centimeters to a few decimeters (≈ 0.05–0.4 m, depending on characteristic distance to discharge boundaries and transmissivity), i.e., comparable to or smaller

than typical urban piezometric variability at seasonal/interannual scales. Therefore, while the omission of urban recharge may affect regional water-balance partitioning, its expected impact on the 3-year thermal-interference assessment (dominated by boundary-conditioned flow and by balanced abstraction–reinjection of the geothermal systems) is considered limited.

Model Muse supports the DISV (Discretisation by Vertices) grid, namely the quadtree refined grid. The city-scale model comprises 216,229 cells (Figure 46). A quadtree refined grid, starts with a structured grid and then subdivides cells into four equal parts. Those cells may be further subdivided (Figure 47).

Figure 46. Model grid.

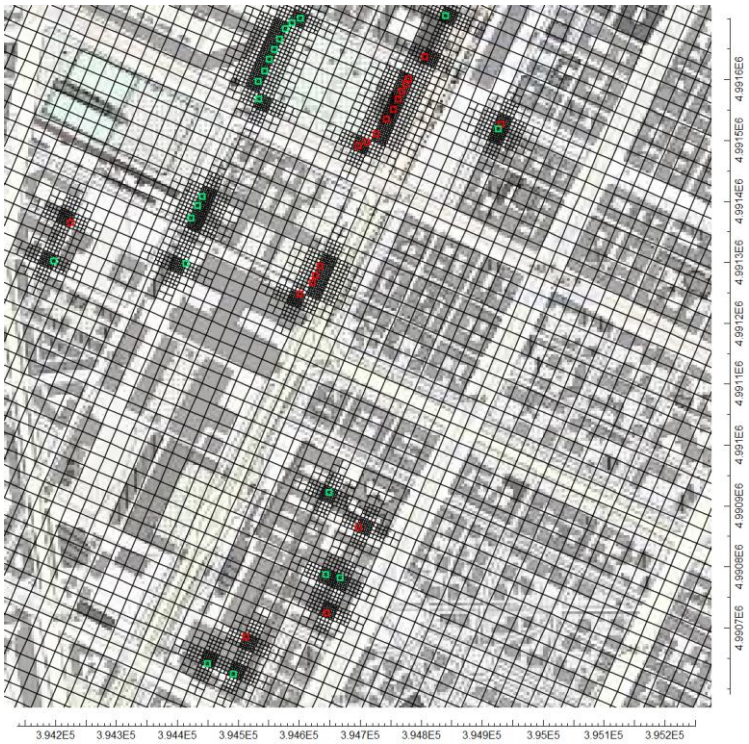

Figure 47. Zoom on Politecnico di Torino and IntesaSanPaolo open-loop plants.

The results from the two simulation scenarios, involving different pumping capacities (average monthly flow rate in Figure 48 and maximum in Figure 49) can be individually analysed for each geothermal plant, adopting a case-by-case approach for identifying preliminary strategies related to water withdrawal and urban landscape planning. In these simulations, only authorized open-loop geothermal wells were included. Other groundwater abstractions in the urban area of Turin (e.g., industrial, construction dewatering, private wells) were not explicitly modelled because an updated and reliable census is not available and existing records are often incomplete, lacking key inputs such as exact location, screened depth, pumping rates and operating schedules. Without these data, estimating a realistic cumulative discharge would be highly uncertain, so non-geothermal pumping was omitted to avoid introducing poorly constrained stresses.

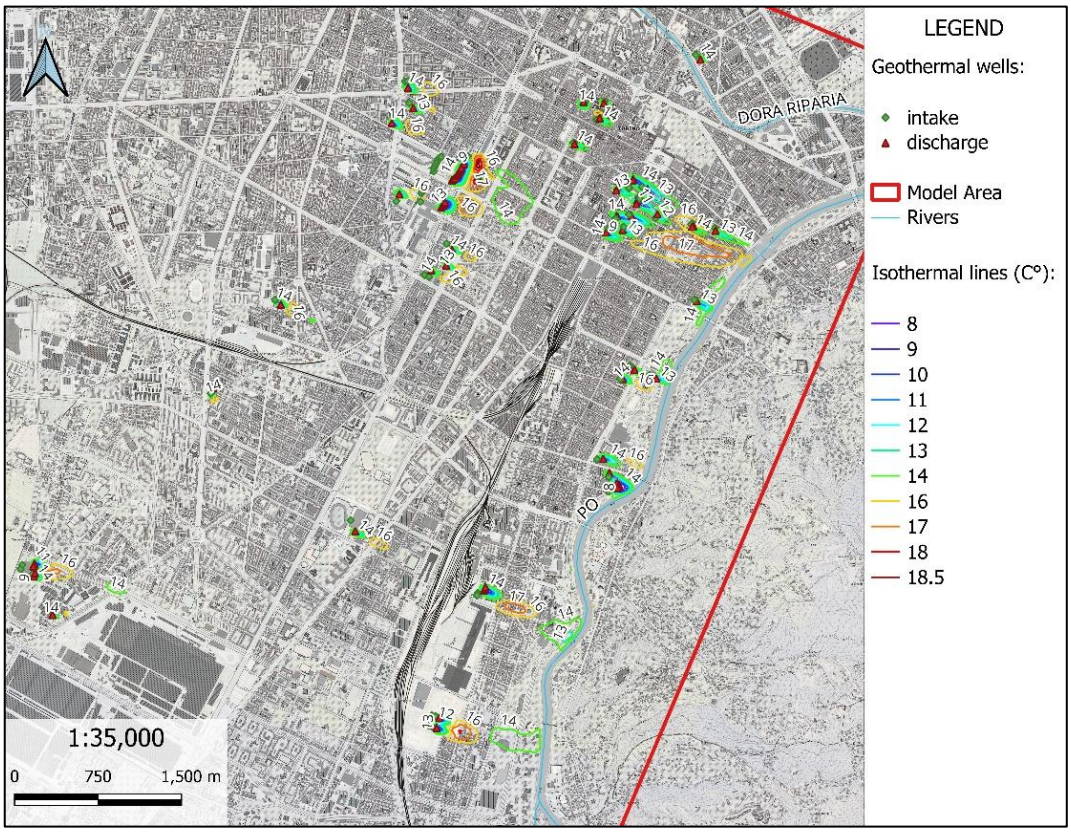

Figure 48. Mean flow rate (Qmean) scenario's results with cooling/heating operating seasons mode for 6 months/year at the end of the 3rd year simulation.

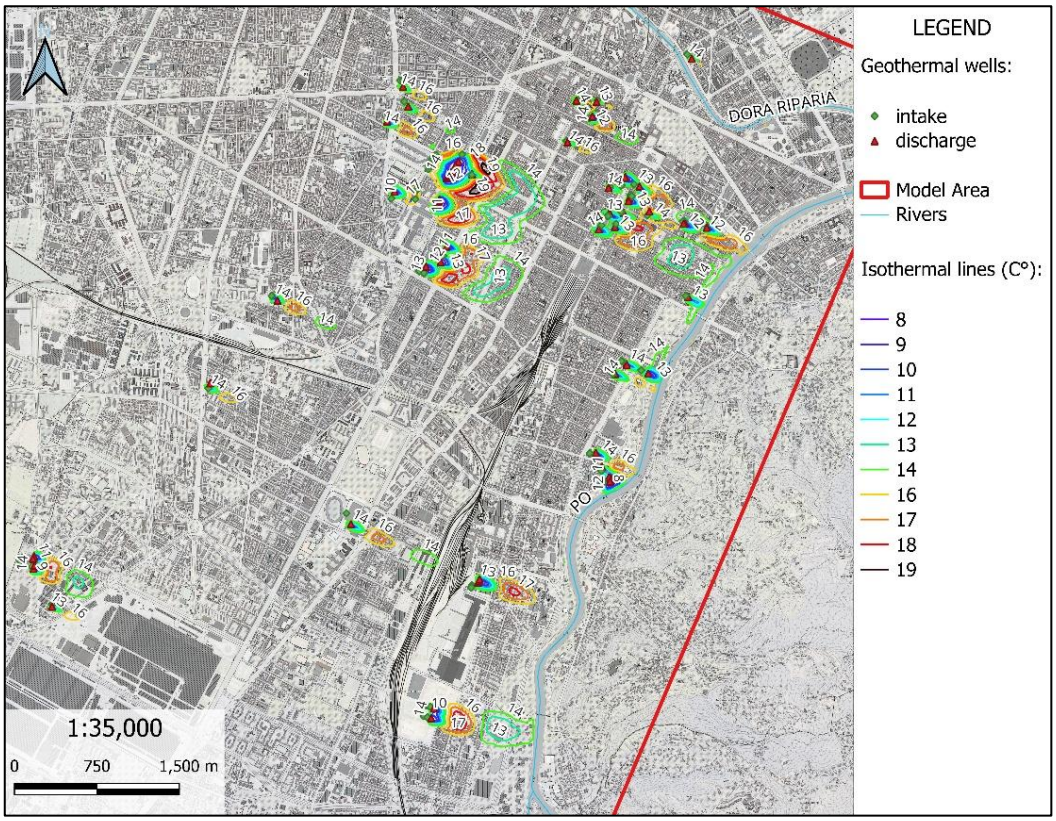

Figure 49. Maximum flow rate (Qmax) scenario's results with cooling/heating operating seasons mode for 6 months/year at the end of the 3rd year simulation.

Below, a description of the impacts recorded around the university complex of the Politecnico di Torino is provided.

The buildings connected to the existing Politecnico di Torino GWHP plants host university offices and laboratories. The open-loop geothermal plants at Politecnico di Torino include three 35-m deep control piezometers downstream of the injection wells (S2, S3, S4), as well as five abstraction and three injection wells with similar technical characteristics. All components of these geothermal systems affect the Turin shallow unconfined aquifer. Both scenarios showed changes in the piezometric levels and the extent of the thermally affected zone at the end of the three-year operation period. The findings from Qmean scenario reveal that the aquifer exhibits a positive response to both hydraulic and thermal disruptions during a three-year analysis period (Figure 50) since there are no significant alterations in the groundwater flow field detected around the Politecnico di Torino complex. However, noticeable thermal variations are linked to the modelled operational season the Politecnico di Torino plants, specifically during the last winter and summer of the third year of plant operation. Upon examining the generated scenario, the thermal plume resulting from the third summer plant operation season is characterised by a one-degree temperature change compared to the average undisturbed groundwater temperature (15°C). The highest recorded thermal alteration associated with winter plant operation season is represented by the 8°C isotherm. The described Qmean scenario turns out to realistically define the existing conditions: taking into account the temporal aspect, particularly during a specific season of synchronized operation, newly constructed plants located in the

Politecnico di Torino downstream direction can be favourably impacted by this disturbance. This setup can capitalize on the undisturbed temperature of the aquifer, which remains at 16 ºC.

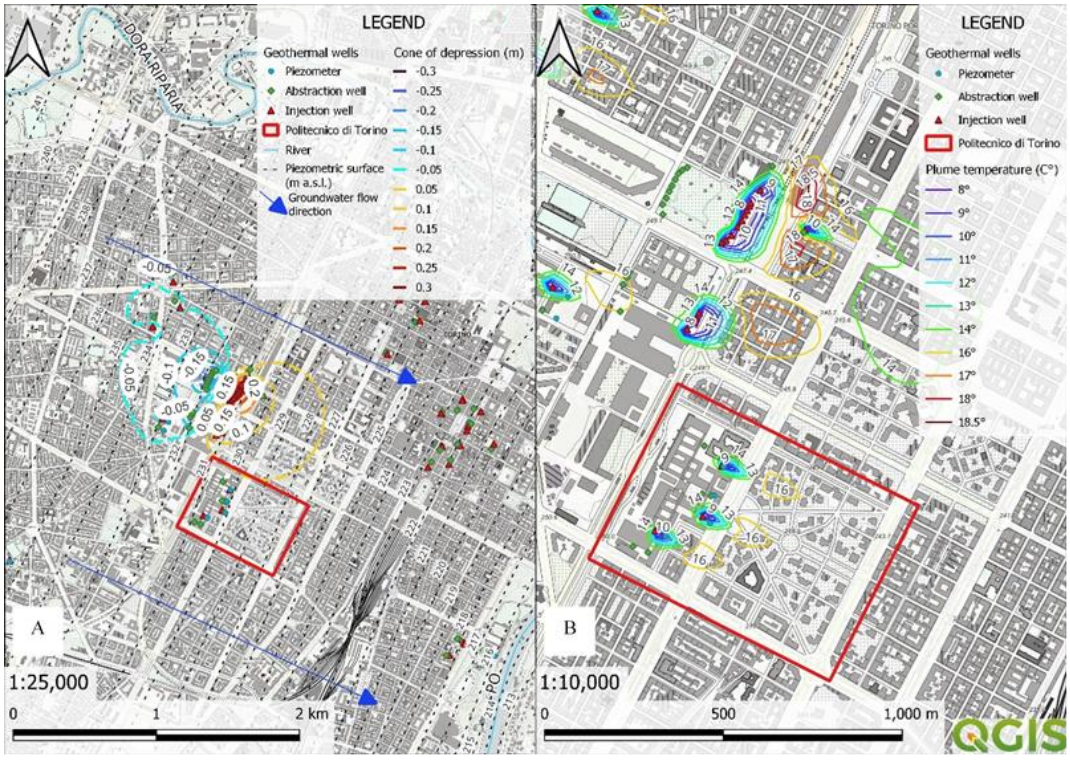

Figure 50. Average flow rate (Qmean) scenario's results with cooling/heating operating seasons mode for 6 months/year: A) groundwater flow field disturbances B) temperature field disturbances (Ref. [74]).

The same positive response was observed for the Qmax scenario (Figure 51). The maximum alteration in the groundwater flow level detected around the Politecnico di Torino University complex is 0.2 m. Visible changes in the undisturbed groundwater temperature (15 °C) are connected to the operational seasons modelled in the last two years. Upon analysing the generated scenario, the thermal plume arising from the third summer plant operation season is defined by a three-degree temperature variation isotherm (18 °C).

The highest recorded temperature alterations associated with the last two winter plant operation seasons are represented by the 13 °C and 9 °C isotherms, respectively. Although this scenario exaggerates the influence on the undisturbed state of the aquifer, a downstream geothermal system will experience adverse effects due to thermal interference from the upstream one. Properly designing the construction of a new plant is crucial, and this involves accurately characterizing the hydrogeological system at the neighbourhood scale (i.e., water drainage network, groundwater flow direction, groundwater hydrogeological gradient, aquifer hydraulic conductivity value). Therefore, determining the appropriate distance between plants becomes essential.

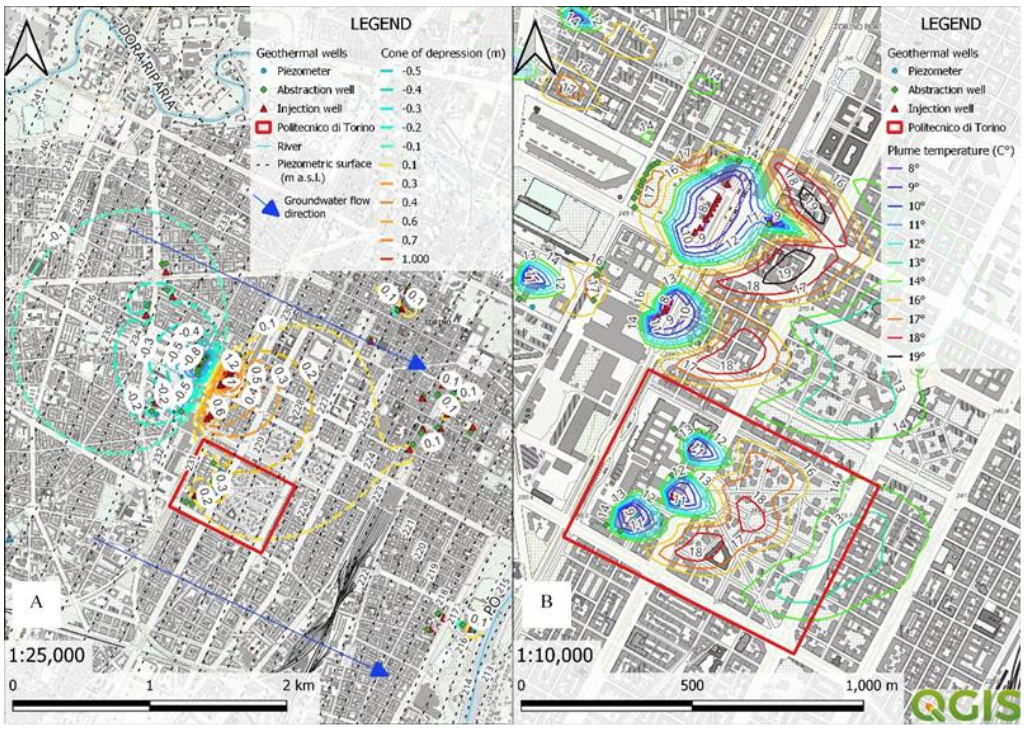

Figure 51. Maximum flow rate (Qmax) scenario's results with cooling/heating operating seasons mode for 6 months/year: A) groundwater flow field disturbances B) temperature field disturbances [74].

The reported and described results appear to be valid: this is confirmed by the findings from the validation process conducted on Qmean scenario results. Hourly recorded data from Politecnico di Torino plants' control piezometers S2, S3, S4 were considered for this purpose. To test the performance of the urban-scale model, a comparative analysis was conducted between the observed and recorded groundwater temperature data and the model-simulated one. Daily averages were calculated from hourly measurement data from S2, S3, S4; these values were thus compared with the daily average values for selected plant operation days. Root Mean Square Error (RMSE) turned out to be less than 1 °C, as shown in Figure 5. June had the highest error rate due to the intermittent operational status of Politecnico di Torino's facilities caused by ambient temperature fluctuations. Therefore, the modelling framework that relies on average flow rates and temperatures is insufficient in capturing these variations. During July and August, when there are continuous operational activities, the average error rate decreases to less than 0.5 degrees Celsius. This validates the model's ability to capture spatiotemporal thermal dynamics within the Politecnico di Torino.

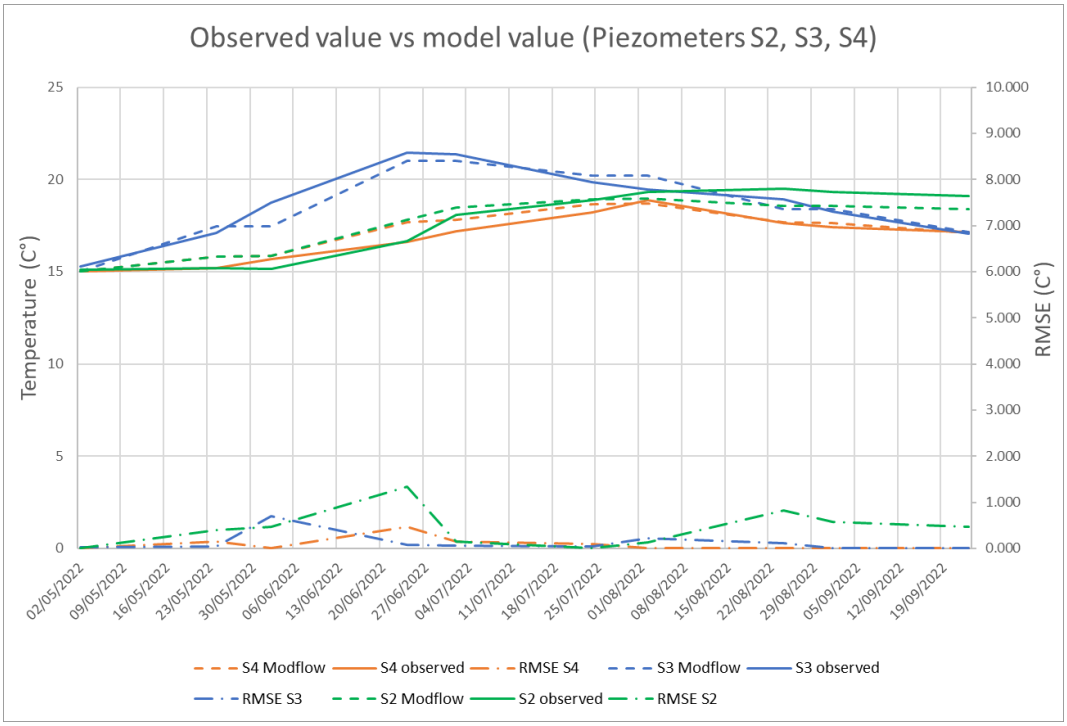

Figure 52. Comparison between Observed and Simulated values and RMSE calculated values for the three piezometers considered, located downstream the geothermal plants at Politecnico di Torino [74].

In the second case study, the focus was exclusively on the geothermal installations of Politecnico di Torino, with simulations, calibrations and presentations conducted exclusively on these installations. The Politecnico di Torino is home to five distinct power plants, which are located across multiple campus sites in the city of Turin (Figure 53). These installations represent a significant example of shallow geothermal energy exploitation in a dense urban context, enabling sustainable cooling for university buildings while maintaining minimal environmental impact on the aquifer. The geographical distribution of these plants encompasses three primary operational areas: the Main Campus, the Energy Center, and Valentino Castle (Figure 53). Each site operates as an independent building. This configuration necessitates careful monitoring to assess potential hydraulic and thermal interference between systems, as well as cumulative impacts on groundwater resources.

Figure 53 presents a comprehensive map of the model area and geothermal well distribution across the Politecnico di Torino campus sites. The legend distinguishes between three types of monitoring and operational points: piezometers (blue circles), intake wells (green diamonds), and discharge wells (red triangles). The spatial arrangement shows wells P5, P6, P3, P4, P2, P7 at the main campus, wells P1E, P2E at the Energy Center, and wells P1V, P2V at Valentino Castle. This map serves as the fundamental reference for all subsequent hydraulic and thermal analyses presented in this work.

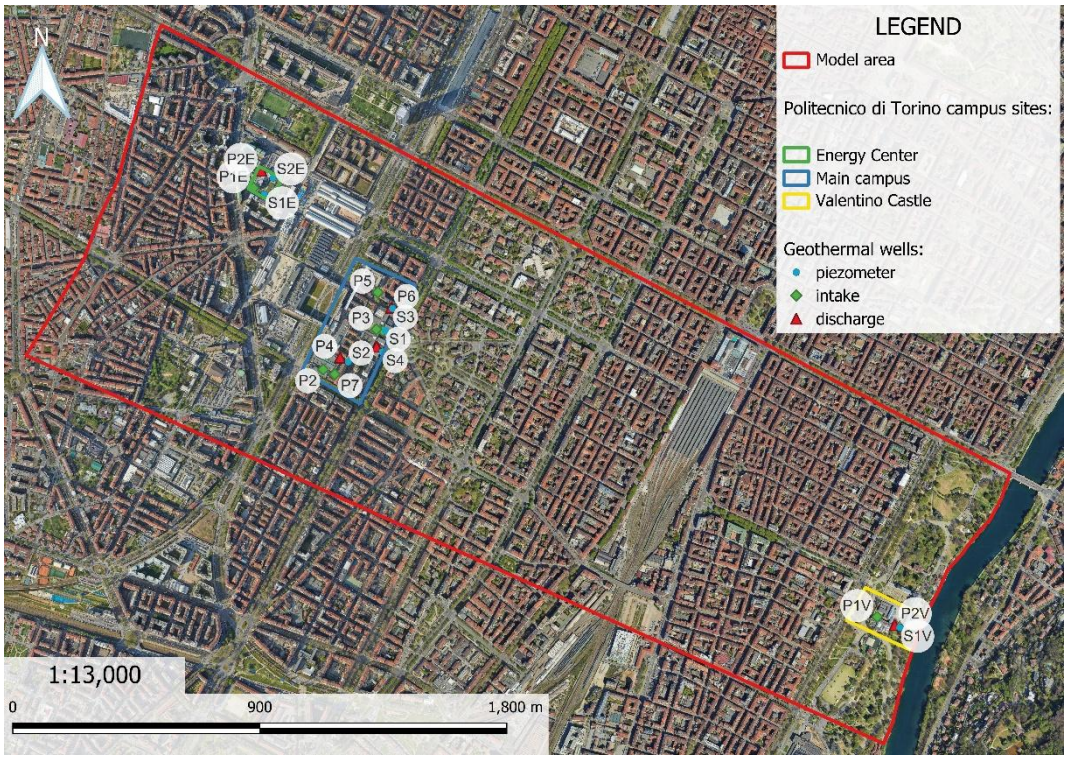

Figure 53. Map of model area and geothermal well distribution.

All installations employ OTT ecoLog800 multiparametric probes (Figure 54) positioned approximately 2 m below piezometric levels, recording electrical conductivity, temperature, and pressure at 15-minute intervals with real-time GSM/GPRS transmission capabilities. The probe's robust design allows for long-term deployment in groundwater environments, while its telemetric capabilities ensure continuous data availability for system management and regulatory compliance verification. The positioning of these probes approximately 2 meters below the piezometric surface ensures measurements are taken within the saturated zone while avoiding potential surface water influences or seasonal water table fluctuations. The utilisation of multiparametric probes facilitated the analysis of the thermal plume pattern and the subsequent response of the aquifer, which was associated with the injection of hot water into the discharge wells. This high-frequency monitoring approach represents a significant advancement over traditional monthly or quarterly sampling protocols, enabling detection of short-term operational impacts and rapid validation of numerical model predictions.

Figure 54. Multiparametric probes that measure the electrical conductivity, temperature and pressure parameters of the shallow aquifer.

Water quality monitoring through accredited EUROLAB S.r.l. analysis confirms consistent compliance with regulatory standards, with electrical conductivity variations following temperature-dependent patterns but remaining within acceptable ranges throughout operational cycles.

An analysis of the geothermal plants of the Politecnico di Torino was conducted, with the consideration of an average summer operating cycle from June to October. This analysis incorporated the assumption of continuous daily operation for five days per week, with no operation occurring on weekends. A comprehensive simulation was developed for the year 2024, and detailed forecasts of the evolution over time of the thermal plume diffusion in the aquifer were produced.

This was achieved by utilising daily volume data obtained from the operating machines and monthly temperature data obtained from continuous monitoring.

The model domain (Figure 55) covers an area of approximately 4.1 km² as shown in Figure 55. In the WGS 84 / UTM zone 32N (EPSG: 32632) reference system, the coordinates of the vertices are precisely defined to ensure reproducibility:

- **A**: X= 393368.334 ; Y= 4990692.247
- **B**: X= 393860.461 ; Y= 4991894.779
- **C**: X= 396952.114 ; Y= 4990263.623
- **D** X= 396491.739 ; Y= 4989279.372

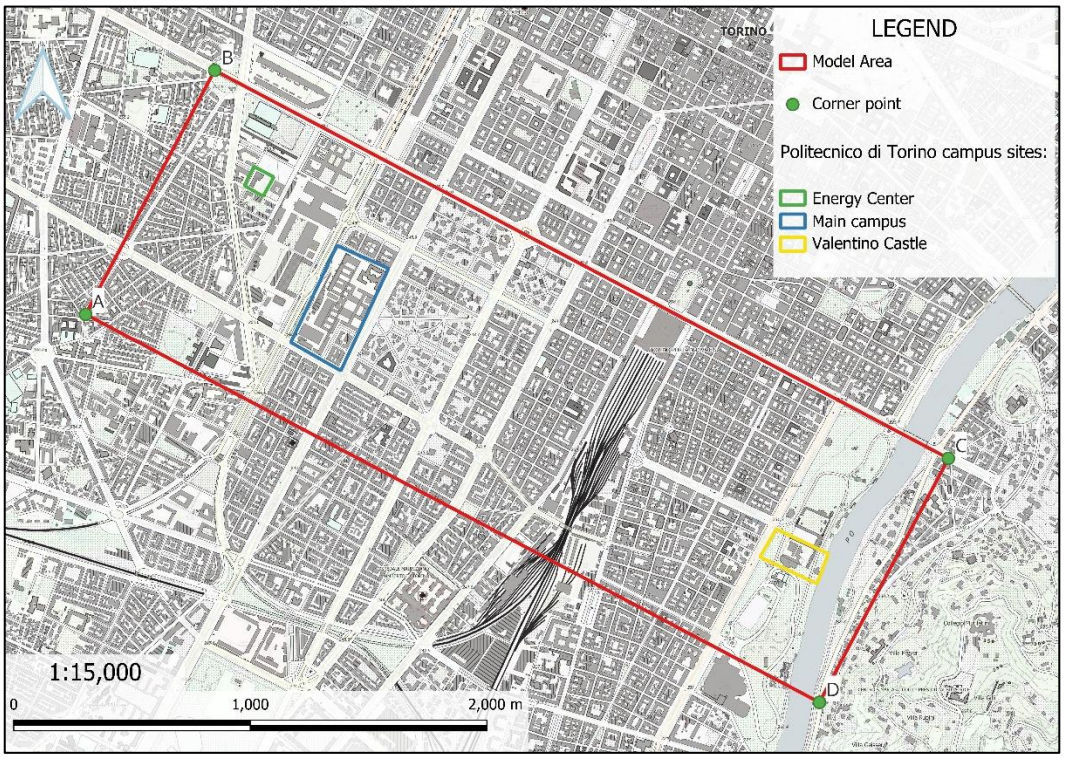

Figure 55. Coordinate points and model area.

In order to better define the specific hydrogeological properties for the area with the highest data density, the initial uniform grid with 10 m cell size was densified using quadtree refinement at the geothermal wells and piezometers. This adaptive meshing technique allows computational resources to be concentrated where spatial resolution is most critical, near the wells where hydraulic gradients and thermal anomalies are steepest, while maintaining computational efficiency in peripheral areas. The area discretisation previously referenced resulted in the establishment of a grid comprising 43,593 cells for the model. The width of this grid ranged from a maximum of 10 metres in the peripheral regions of the model to a minimum of 1 metre at the geothermal plants, providing a dynamic range of spatial resolution that spans one order of magnitude. The Figure 56 provides an example of the refinement of the geothermal wells in the main building on the Politecnico di Torino campus. This figure visually demonstrates how the quadtree algorithm progressively subdivides cells approaching the wells, creating a nested structure that transitions smoothly from coarse to fine discretization.

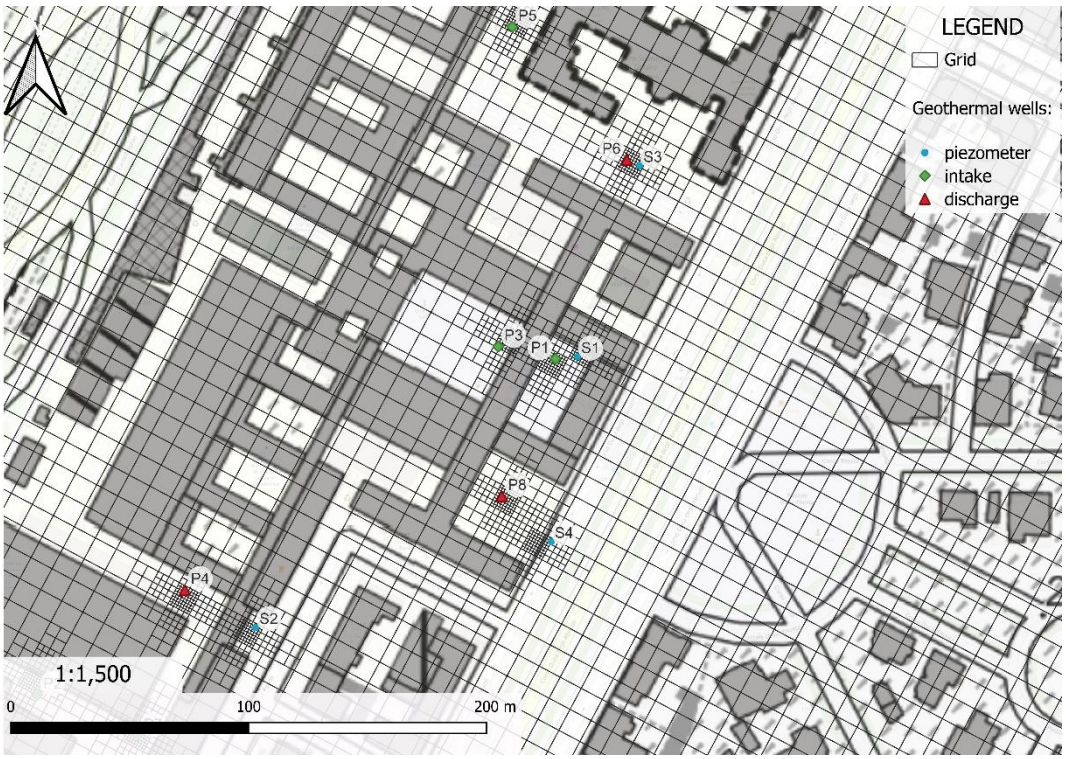

Figure 56. Example of the refinement of the geothermal wells in the main building on the Politecnico di Torino campus.

The analysis of the available stratigraphic data enabled the definition and adoption of an appropriate vertical discretisation within the computational domain. This discretisation encompasses two layers (Layer A and Layer B), which, although distinguishable in terms of lithological and hydrogeological characteristics, are not hydraulically independent. Thus, collectively, they represent the first two aquifer units of the study area, corresponding to the Quaternary alluvial deposits that characterize the Turin subsurface. Layer A represents the uppermost, more permeable sandy-gravel aquifer, while Layer B corresponds to an underlying sandy unit with moderate permeability, both of which are interconnected and contribute to regional groundwater flow.

The surface delineating the upper boundary of the modelled volume (top of layer A) was determined by assigning the elevation values extracted from the 5×5 m resolution DTM of the Piedmont Region to each cell of the initial layer. This DTM was derived from the ICE aerial survey conducted between 2009 and 2010, representing the most accurate topographic data available for the study area at the time of model development. The base of the shallow aquifer, i.e. the bottom of layer A, was reconstructed using elevation data obtained from the Piedmont Region Geoportal (released in April 2022 [168]), ensuring consistency with the most recent geological interpretations and borehole data compilations.

Temporal discretisation was accomplished through the development of a preliminary model consisting of a single stress period (SP) under steady-state conditions. This period represented the hydraulic regime when the plant was non-operational. The configuration was utilised to assess the numerical robustness and structural stability of the model prior to the transient simulations, verifying that the

model could achieve convergence and produce physically reasonable piezometric surfaces under equilibrium conditions.

The selection of the datasets employed for the delineation of the boundary conditions (BCs) was driven not only by the necessity of model conservatism but also by several critical considerations. Firstly, the spatial coverage of the model domain was maximised by incorporating the most extensive set of validated data available. Secondly, temporal consistency among datasets describing different BCs was deemed essential to ensure the reliability and comparability of simulation results.

In order to effectively reproduce the regional groundwater flow pattern, GHB conditions were assigned to layers A and B along the model perimeter. The GHB values were computed by extrapolating the hydraulic head variations both upstream and downstream of the calculation domain, based on observed gradients measured at monitoring piezometers managed by ARPA Piemonte and data retrieved from the Geoportale Piemonte [168]. This approach allows groundwater to flow into or out of the model domain in response to simulated pumping stresses, while maintaining consistency with regional hydrogeological conditions. As a precautionary measure and to maintain the simplicity of the model, surface recharge resulting from average annual precipitation was not simulated. This conservative assumption is justified because such recharge could potentially influence and attenuate the thermal plume generated by the plants. By excluding recharge, the model produces conservative (worst-case) estimates of thermal plume extent and persistence, providing a safety margin for regulatory assessment and system design.

The calibration of the hydrogeological model was conducted under transient, steady-state, and combined flow conditions in this study, employing the Pilot Points (PPs) technique. The calibration was based on average piezometric level data collected from wells and piezometers overseen by the Politecnico di Torino university, covering the period from January to May during which the plants were inactive, ensuring that observed heads reflected natural conditions unaffected by pumping. During the calibration and validation phases, model management, parameter optimisation, and uncertainty evaluation were performed using the PEST HP inverse modelling software, a well-established tool for parameter estimation and sensitivity analysis in complex environmental systems (as explained in chapter 2.3.2 MODFLOW).

In the present case study, all observation points, whether wells or piezometers, are assigned equal weighting, as each measurement has been verified and validated prior to its utilisation in the modelling process. This uniform weighting approach is appropriate when all observations are of comparable accuracy and reliability, as is the case with the high-quality monitoring network at Politecnico di Torino. The parameters employed in the calibration are defined not only through conventional zonation methods, assigning uniform values to each zone, but also through spatially distributed representations based on interpolation at specific reference points. This approach applies fundamental principles of geostatistics to derive the spatial distribution of each parameter across the model domain, starting from the discrete locations where parameter values are associated with the PPs. From these PPs,

continuous parameter fields are generated through Kriging, a geostatistical interpolation technique that estimates unknown values by computing a weighted average of neighbouring measured points, where the weighting factors depend on the search radius and the spatial correlation structure defined by the variogram.

In this study, the parameter subject to calibration, namely the hydraulic conductivity, exhibits a gradual spatial variability consistent with the observed heterogeneity of the subsurface. The calibration setup comprises 500 PPs (Figure 57), corresponding to the distribution of the horizontal hydraulic conductivity values (Kx) within layer A. The allocation of PPs is concentrated in areas where higher spatial resolution and greater accuracy are required, particularly near the geothermal installations where accurate parameter estimation is critical for reliable impact prediction. Figure 57 presents the map of the geographical distribution of Pilot Points and observation points throughout the model domain. The dense distribution of PPs (shown as blue cross) enables the geostatistical interpolation algorithm to capture fine-scale spatial variability in hydraulic conductivity. Observation points (wells and piezometers where hydraulic heads are measured, yellow dots) are also shown, providing the calibration targets that guide the parameter optimization process. The spatial relationship between PPs and observation points is fundamental to the calibration strategy, as PPs located near observation points exert stronger influence on the goodness-of-fit at those locations.

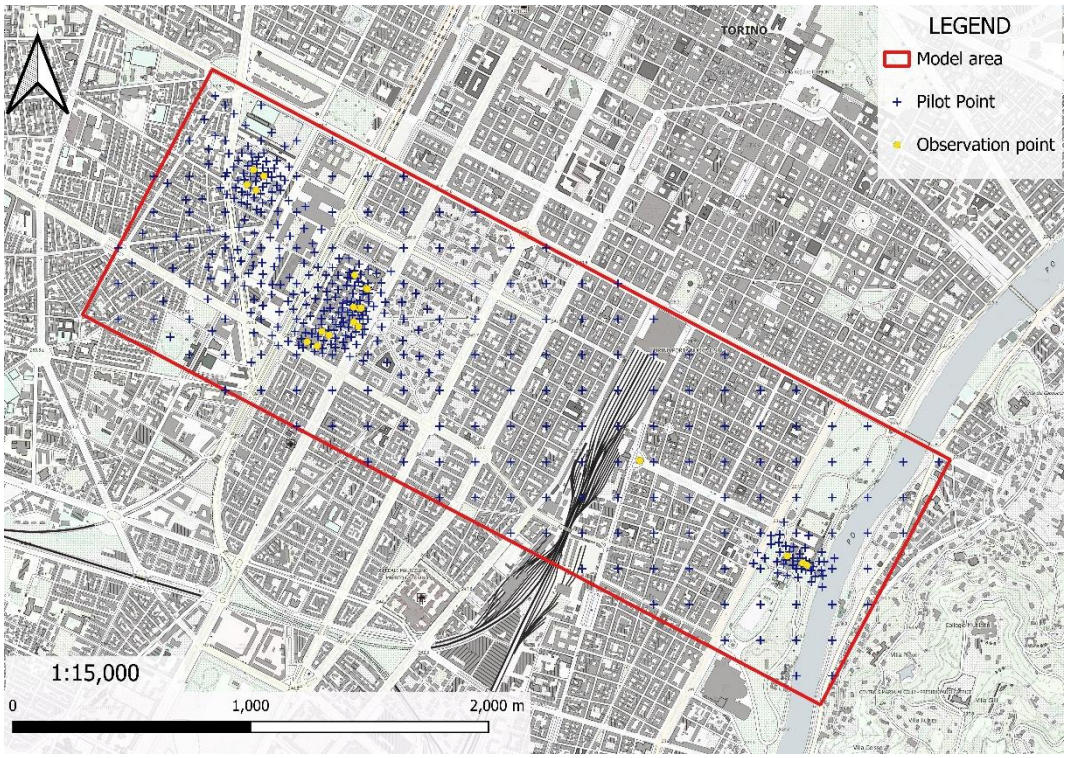

Figure 57. Map of the geographical distribution of PPs and observation points.

The initial (prior) hydraulic conductivity values, ranging from a minimum of 6.9×10^{-5} m/s to a maximum of 6.3×10^{-3} m/s, were derived from the analysis of ARPA Piemonte well test data and the stratigraphic profiles available from the Piedmont Region Geoportal. Based on these data, an initial hydraulic conductivity

map was generated through Kriging interpolation (**Figure 58**). This prior distribution represents the best estimate of aquifer properties based on available field data, providing a physically realistic starting point for the optimization process. The legend clearly indicates the color gradient representing hydraulic conductivity magnitude, with warmer colors corresponding to higher permeability zones typically associated with coarse gravel deposits, and cooler colors indicating lower permeability zones with higher silt or sand content.

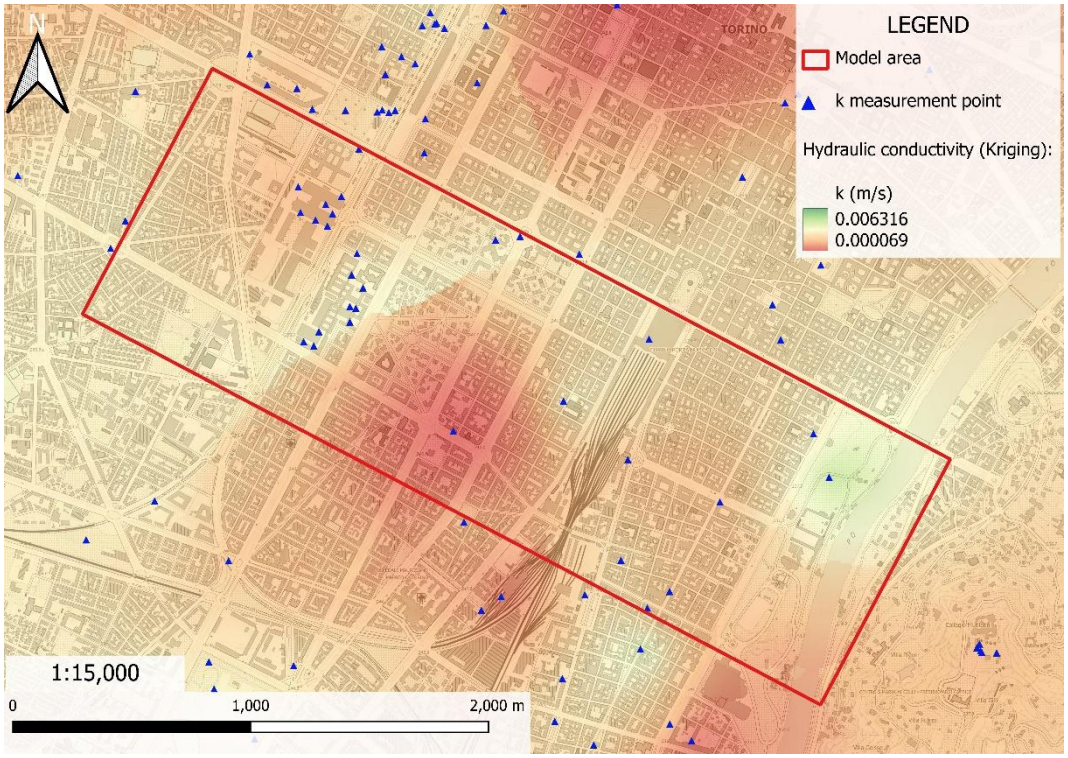

Figure 58. Hydraulic conductivity k distribution map, using kriging, before the calibration process.

Although this prior information represents an essential starting condition, it is not restrictive within the calibration process. The PEST algorithm is allowed to adjust PP values within reasonable bounds to achieve optimal fit with observed data. Following calibration, the resulting hydraulic conductivity distribution (Figure 59) exhibits values varying from approximately 2.6×10^{-4} m/s (in blue) to about 1×10^{-2} m/s (in red). Figure 59 displays the distribution map of hydraulic conductivity after the calibration process. Compared to **Figure 58**, this calibrated distribution shows more pronounced spatial variability and heterogeneity, particularly in the vicinity of geothermal installations where the dense monitoring network provides strong constraints on parameter estimation.

The upper-end value ($K \approx 1\times10^{-2}$ m/s) is the outcome of the calibration and is confined to very limited patches of the model domain. Such high conductivities are compatible with highly permeable coarse alluvial gravel bodies that characterize the shallow subsurface of Turin and its surroundings (Quaternary gravelly outwash and fluvial deposits). However, these localized “bubble-like” anomalies may also reflect unmodelled stresses, such as unknown/uncertain pumping wells (e.g., areas close to major infrastructures such as the Intesa Sanpaolo skyscraper), which the

calibration may compensate for by locally increasing K. Since these anomalous zones are sufficiently far from the geothermal plants analysed, they are not expected to significantly affect the simulated thermal-interference outcomes, but they should be considered priority areas for further site investigations and/or verification of additional pumping wells to be explicitly incorporated in future model updates.

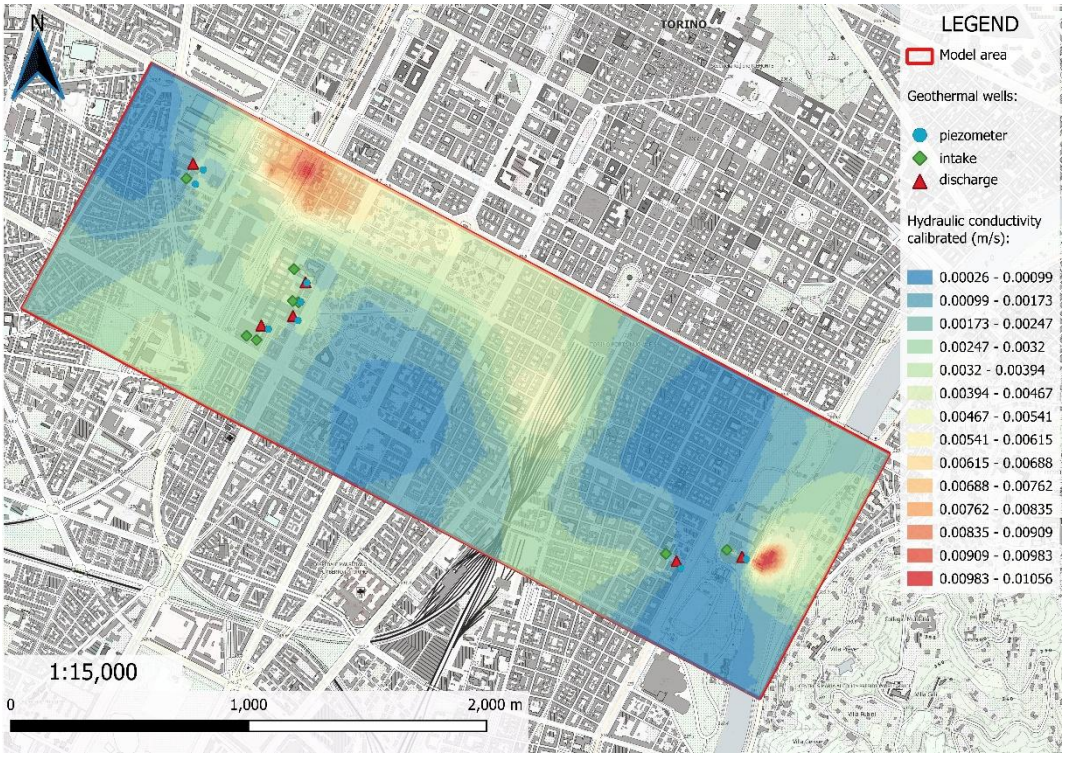

Figure 59. Distribution map of hydraulic conductivity after the calibration process.

As illustrated in Figure 60, the comparison between simulated and observed piezometric heads after calibration yields a Root Mean Square Weighted Residual (RMSWR) of less than 0.035 m, confirming a satisfactory correspondence between model outputs and field observations. The tight distribution around the diagonal confirms minimal systematic bias and random scatter, indicating that the model performs consistently well across the full range of hydraulic heads present in the study area. This exceptionally low residual, representing an average error of only 3.5 cm across the entire domain, demonstrates that the calibrated model accurately reproduces the observed hydraulic conditions and can be confidently applied for predictive simulations of geothermal system impacts.

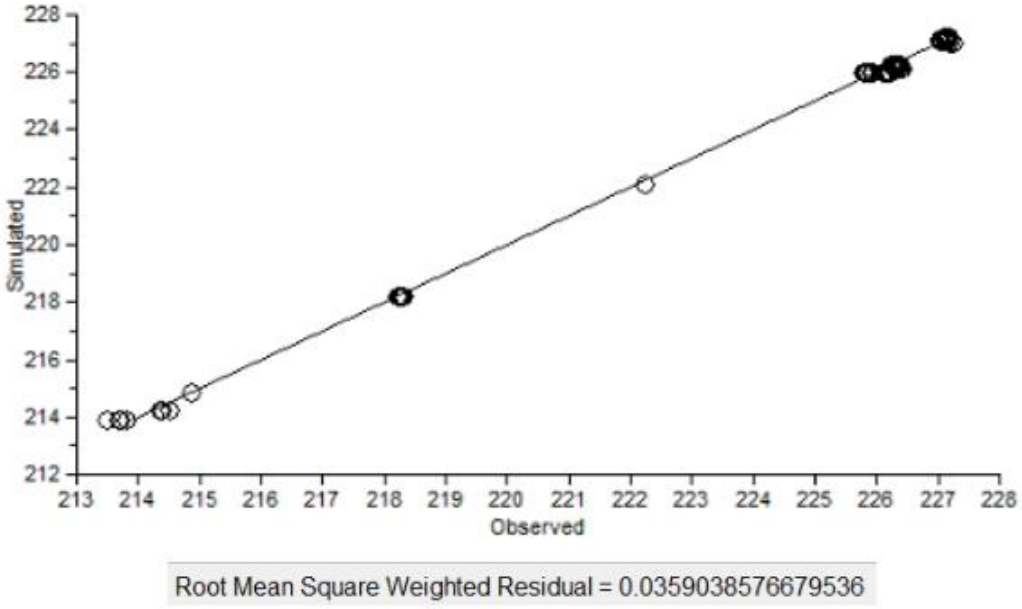

Figure 60. Observed vs Simulated value graph after calibration.

Figure 61 presents a comparison between the piezometric surface simulated by MODFLOW 6, following the calibration, and the piezometry surface published by ARPA in 2002. The observed discrepancies are primarily attributable to the interpolation methodology and the density and temporal distribution of the available field data. The general agreement in hydraulic gradient direction and magnitude confirms that the calibrated model successfully reproduces regional groundwater flow patterns. Minor local discrepancies are visible, particularly in areas with sparse observation coverage, but the overall consistency validates the model's ability to represent the hydrogeological system at the regional scale.

Furthermore, the ARPA piezometric map was generated using traditional simplified interpolation methods applied to a sparser network of observation points, whereas the MODFLOW 6 simulation produces a fully physics-based piezometric surface that satisfies Darcy's law at every grid cell. Moreover, temporal differences between the 2002 ARPA survey and the calibration period (January-May of the simulation year) may contribute to observed differences, particularly if regional groundwater levels have changed due to variations in precipitation, river stage, or anthropogenic extraction.

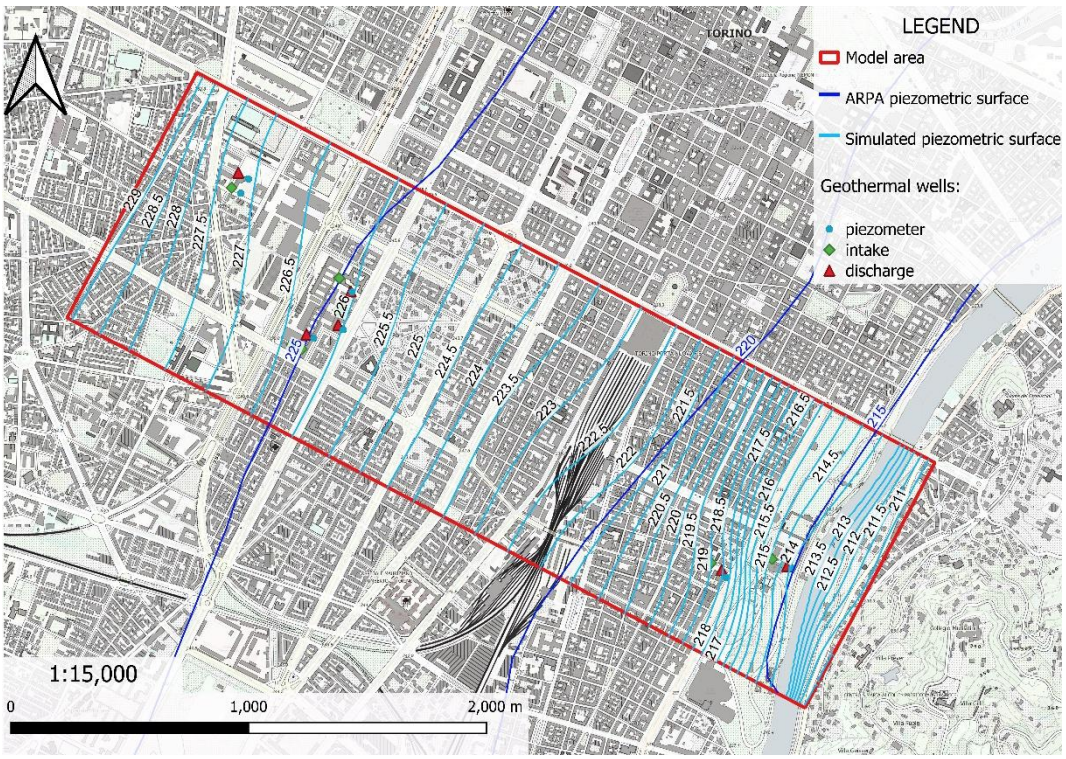

Figure 61. Piezometric surface map of the study area,

The fundamental purpose of the calibration process is to assess and constrain the uncertainties arising from the pronounced spatial variability of geomaterials. The resulting calibrated model demonstrates a significantly enhanced ability to represent the hydrogeological reality in contrast to simplified numerical models that assume a single, homogeneous hydraulic conductivity value across the domain.

The analysis of the stabilised hydraulic heads obtained from the calibrated semi-analytical model allows for the estimation of both the magnitude and the spatial extent of the piezometric disturbance generated by the operation of the geothermal plants under maximum extraction conditions, corresponding to the summer period (end of July). The transient simulation was conducted assuming a continuous operational period of 31 days, thereby conservatively representing the month of July with uninterrupted operation at the maximum flow rate (24 hours per day, 7 days per week). This scenario represents a stress test that exceeds actual operating conditions, providing a conservative upper bound for hydraulic impacts. The hydrodynamic parameters adopted for this simulation are reported in **Table 7**. It is noteworthy that, within this modelling framework, hydraulic conductivity constitutes the only variable parameter, and its spatial distribution is defined according to the calibrated model results. All other parameters (storativities, porosities, thermal properties, and dispersivities) are assigned uniform values based on literature and site-specific measurements and ensure that the thermal transport simulation produces realistic plume geometries.

Table 7. Hydrodynamic parameters used in the model [187].

PARAMETERS	VALUE layer A	VALUE layer B
Conductivity Kxx [m/s]	Variable	$2.7*10^{-4}$
Conductivity Kyy [m/s]	Variable	$2.7*10^{-4}$
Conductivity Kzz [m/s]	Variable	$0.5*10^{-4}$
Storativity	0.106	0.106
Porosity	0.2	0.2
Volumetric heat capacity of the fluid [106J/m³K]	4.18	4.2
Volumetric heat capacity of the solid [106J/m³K]	1.3	2.52
Heat conductivity of the fluid [J/msK]	0.65	0.65
Heat conductivity of the solid [J/msK]	3	3
Longitudinal dispersivity [m]	5	5
Transverse dispersivity [m]	0.5	0.5

The results of the initial transient simulation conducted under maximum flow rate conditions for all wells located within the Politecnico di Torino University campus indicate the absence of hydraulic interference among the different operational areas (Figure 62). The spatial pattern reveals three distinct, impact zones corresponding to the Main Campus, Energy Center, and Valentino Castle installations. Even under these conservative stress conditions, the piezometric disturbance remains limited and localized to individual operational zones, confirming that the spatial separation between installations is sufficient to prevent cumulative impacts. The map uses a color gradient to represent piezometric changes (drawdown and mounding), with negative values (blue tones) indicating water level decreases at extraction zones and positive values (red-yellow tones) indicating water level increases at reinjection zones. The magnitude of piezometric disturbance remains modest (± 0.01 to ± 0.1 m), and the lateral extent of disturbance is limited to several hundred meters from each well field. This spatial confinement demonstrates that even under worst-case operational assumptions, regional groundwater resources remain unaffected and no significant drawdown propagates to neighboring properties or sensitive environmental receptors.

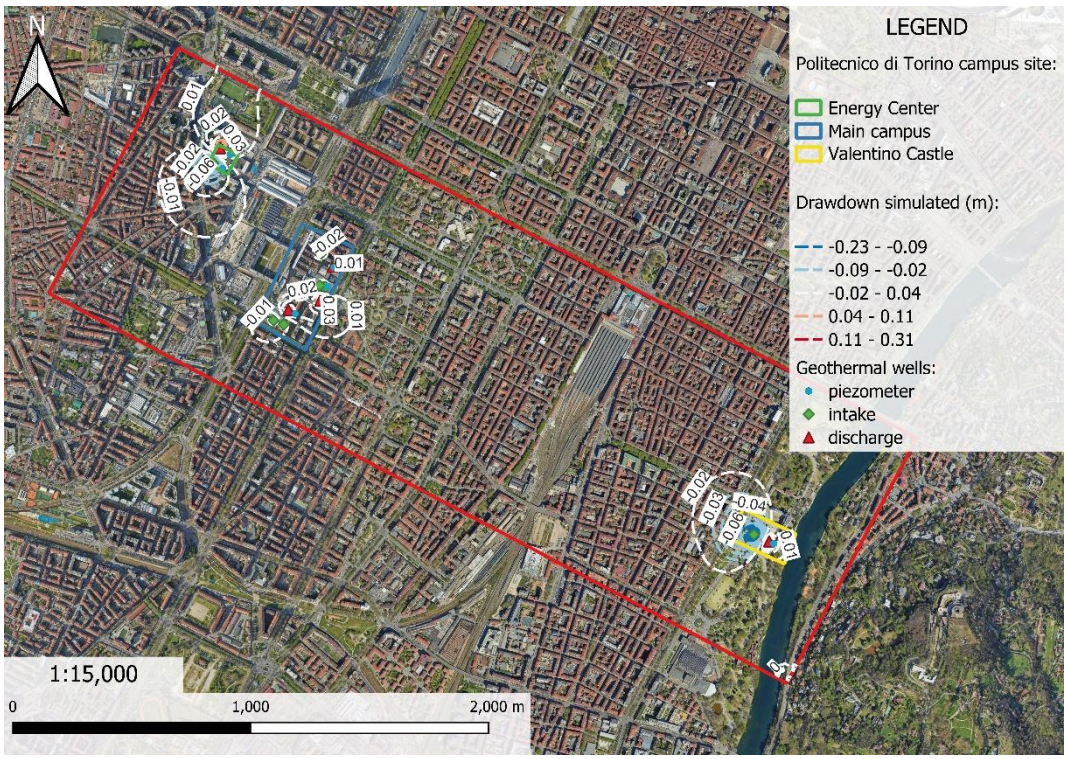

Figure 62. Drawdown map of the model area.

As illustrated in Figure 63, the piezometric response within the Main Campus area reveals the interaction between two discharge wells, giving rise to a single cone of elevation with a peak amplitude of approximately 0.01 m and an areal extension of about 250 m in the groundwater flow direction. The elongation of disturbance zones in the direction of regional groundwater flow (approximately northeast-southwest based on the contour orientation) reflects the advective displacement of the pressure perturbation by ambient hydraulic gradients. This mounding effect results from the injection of water into the aquifer, creating a localized zone of elevated hydraulic heads that dissipates with distance. The rapid attenuation of effects beyond 250 m downstream demonstrates the buffering capacity of the aquifer and the minimal risk of far-field impacts. A similar interaction is observed for the two intake wells, which generate a single but shallower depression cone, extending over approximately 150 m.

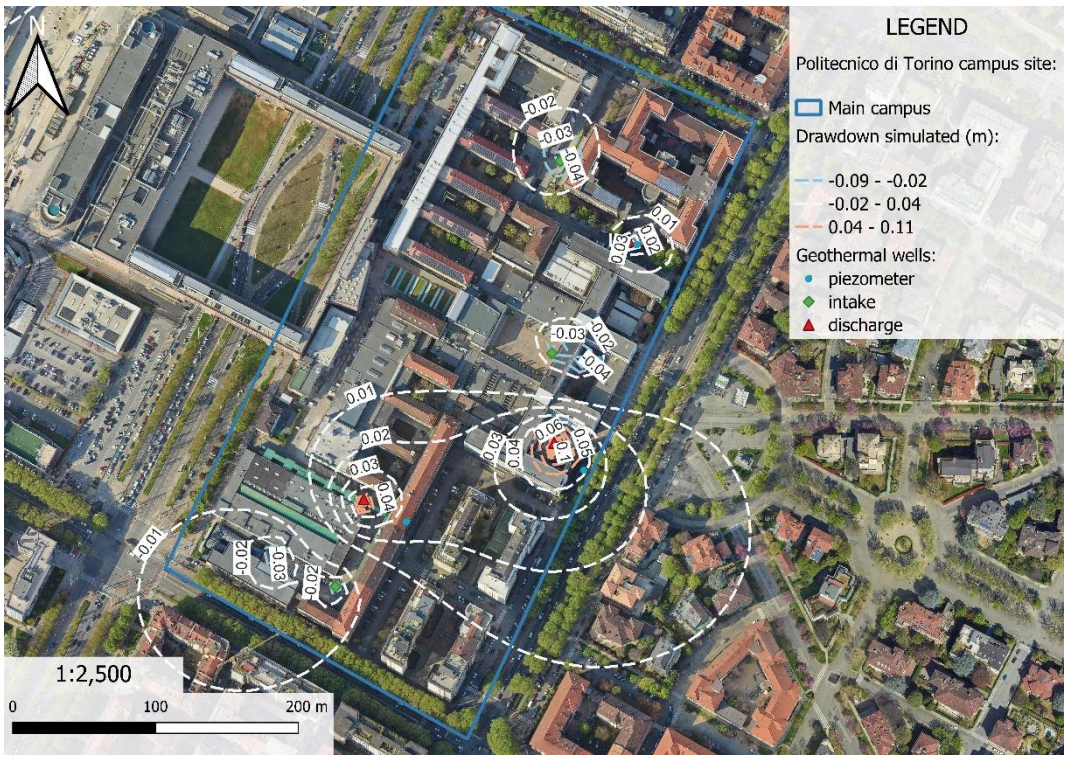

Figure 63. Drawdown map of the main campus.

The simulation results for the Energy Centre (Figure 64), where a well doublet configuration is present, highlight the development of two zones of piezometric interference. These zones extend radially to a distance of roughly 300 m from the wells, exhibiting a drawdown or rising effect of about 0.01 m. The doublet configuration, consisting of one extraction well and one injection well, creates a dipole pattern in the piezometric field, with a depression cone around the intake well and an elevation cone around the discharge well.

Figure 64. Drawdown map of the Energy Center.

The last case analysed concerns the Valentino Castle campus, where the system configuration also consists of a geothermal doublet (Figure 65). In this instance, a marked asymmetry is observed between the spatial extent of the depression cone and that of the piezometric rise. Specifically, the drawdown area extends up to approximately 280 m upstream of the extraction (intake) well, with a maximum head decrease of about 0.02 m, while the recharge area around the injection (discharge) well remains comparatively confined, with an extent of only about 80 m. This asymmetry is primarily attributed to the proximity of the injection well to the River Po corridor, which in the numerical model is represented as a fixed-head boundary condition (i.e., a strong hydraulic control). With this representation, the boundary may act as either a source or a sink depending on the local gradient; in the Valentino area, the simulated piezometric pattern indicates a predominantly draining behaviour toward the river, which effectively dissipates part of the injection-induced mounding. Consequently, the head build-up around the discharge well is limited and does not propagate far upstream. This configuration highlights the strong control exerted by boundary conditions on the hydraulic response to pumping and reinjection, especially when wells are located close to major surface-water bodies.

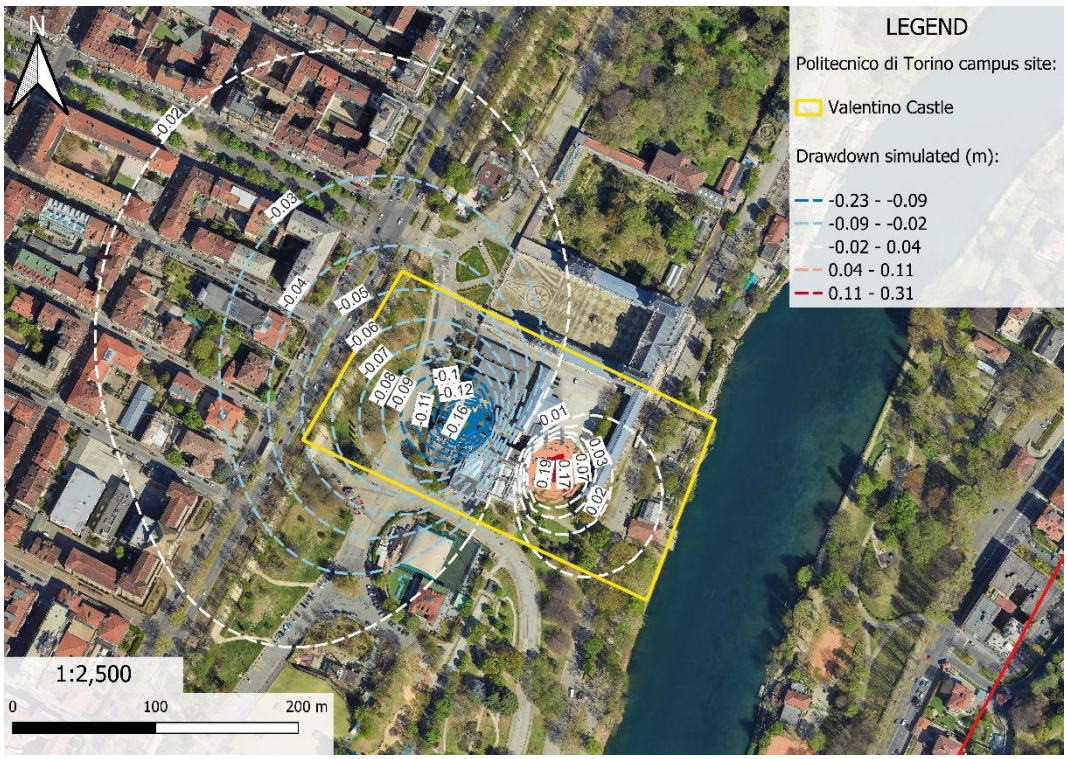

Figure 65. Drawdown map of the Valentino Castle.

A transient simulation scenario was defined and implemented following an initial steady-state stress period, with a total duration of one year. This scenario was discretised on a weekly basis, assigning to each week an average extraction flow rate uniformly distributed over 24 hours. The applied values correspond to the monthly mean flow rates recorded during the 2024 operational period of the geothermal plants. The wells were simulated under a continuous operational regime for five consecutive days, followed by a two-day shutdown, in order to more accurately reproduce the actual operating conditions of the geothermal systems installed at the Politecnico di Torino University. This operational pattern reflects typical university building usage, with reduced heating/cooling demand on weekends.

The longitudinal dispersivity (αL) was set to 5 m, in accordance with the empirical relationship proposed by Gelhar [188], which assumes a value equal to one-tenth of the injection–target distance (i.e., the distance to the potentially impacted downstream well). This scaling relationship is widely accepted in groundwater transport modelling and ensures that dispersion parameters are consistent with the spatial scale of the problem. The transverse dispersivity was defined as 10% of the longitudinal value, consistent with typical anisotropy ratios observed in alluvial aquifers where longitudinal mixing (along flow paths) exceeds transverse mixing (perpendicular to flow). The monthly average temperatures used as thermal input data were derived from continuous monitoring of the wells and subsequently implemented within the ModelMuse interface. This approach ensures that simulated injection temperatures reflect actual operational conditions, including seasonal variations and system efficiency changes over the annual cycle.

By using measured rather than design temperatures, the model produces realistic thermal plume predictions that can be directly validated against field observations.

The transport simulation was performed based on the previously calibrated flow model and was divided into 49 transient stress periods. The primary objective of this model was to assess the long-term evolution of the thermally induced disturbance under realistic operating conditions with conservative assumptions. The temporal evolution of the temperature field is captured through weekly time steps, allowing resolution of both short-term operational fluctuations and long-term cumulative trends. As illustrated in Figure 66, a comparison is presented in the form of line graphs between the observed and simulated temperature values in a geothermal well on the Main Campus. This analysis was conducted over the period from June 1 to September 29, 2024, coinciding with the operational phase of the geothermal plants. The figure displays the monitoring well (P4), with the observed and simulated temperatures represented by different colours. The close agreement between observed and simulated temperatures throughout the monitoring period validates the thermal transport model and demonstrates its capability to reproduce both the timing and magnitude of thermal plume arrival at different monitoring locations. Minor discrepancies are visible during peak temperature periods, potentially reflecting small-scale heterogeneities or transient operational adjustments not captured in the weekly-averaged input data. The temporal validation demonstrated in Figure 66 is critical because it confirms that the model correctly represents the key controlling processes for thermal plume evolution: advection by groundwater flow, mechanical dispersion, and heat exchange with the solid aquifer matrix. The ability to match observed temperatures at multiple monitoring locations simultaneously indicates that the calibrated hydraulic conductivity distribution, assigned thermal parameters, and boundary conditions are all consistent with field conditions.

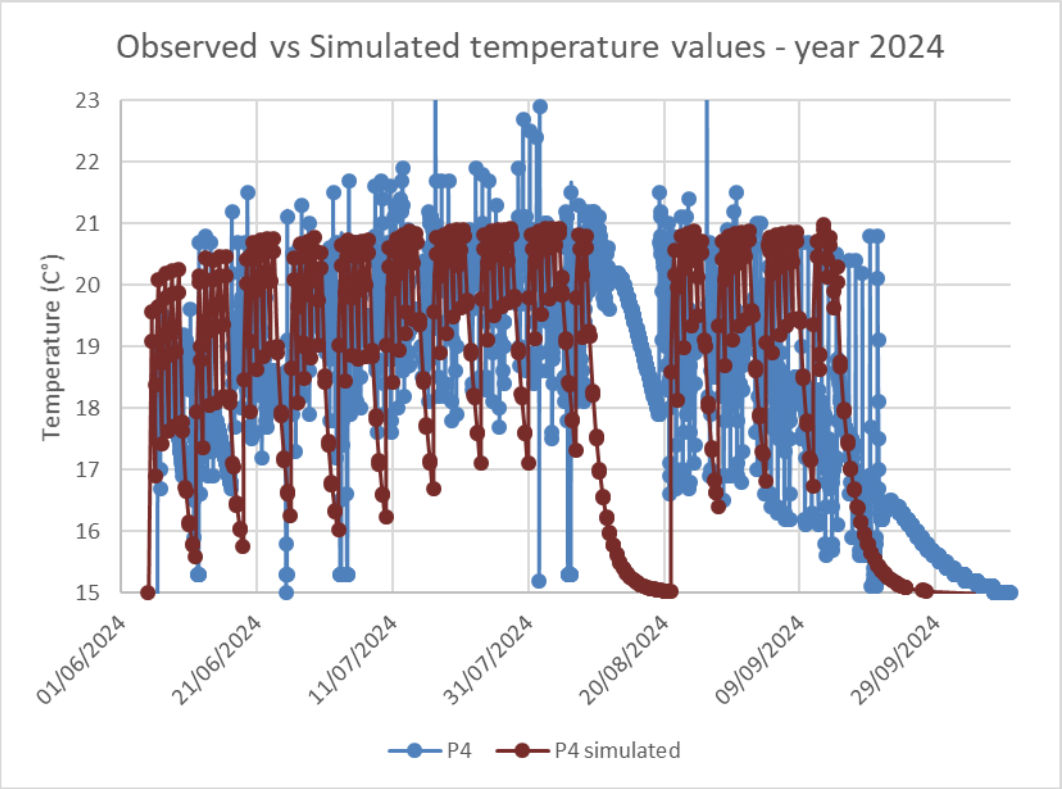

Figure 66. Line graph of the observed vs simulated values of the temperature in the discharge geothermal well P4 of Politecnico di Torino.

As illustrated in Figure 67, the thermal plume map of the entire study area is presented, and this map represents the geothermal plant simulation at the end of August 2024. The neighbourhood-scale map provides a comprehensive overview of all thermal disturbances across the Politecnico di Torino installations. Isothermal contour lines at 16°C, 17°C, 18°C, and 19°C have been superimposed on the model domain. The background natural aquifer temperature (in undisturbed conditions) is approximately 15°C; therefore, the 16°C isotherm represents the outer boundary of measurable thermal impact. The map reveals the presence of elongated thermal plumes extending downstream from discharge wells at all three operational sites (Main Campus, Energy Center, Valentino Castle), with the plumes oriented parallel to the regional groundwater flow direction. The maximum temperature anomalies (19°C isotherm) persist in a localised surroundings of the injection points, while the 16°C and 17°C isotherms extend several hundred metres downstream. It is important to note that the thermal plumes resulting from different installations remain spatially separated. This confirms the absence of thermal interference between sites, even after continuous summer operation.

Figure 67. Thermal plume map of the study area representing the geothermal plants simulation at the end of August 2024.

As illustrated in Figure 68, the thermal plume simulation of the Main Campus at the end of August 2024 is displayed at a detailed scale of 1:2,500. The map illustrates the intricate thermal configuration that emerges from the concurrent operation of multiple discharge wells. The geometry of the plume is elongated and oriented northeast-southwest, a configuration that is consistent with the regional groundwater flow direction as inferred from the calibrated piezometric surface. Individual plumes from separate discharge wells have been observed to merge and form a compound thermal anomaly in downstream areas, though it should be noted that the temperatures remain below regulatory thresholds for thermal pollution (22°C maximum).

The position of the intake wells is indicated in order to demonstrate the absence of thermal interaction between the intake wells and the discharge wells; the positions of the piezometers are also indicated, demonstrating the correct interception of the thermal plume for monitoring purposes.

Figure 68. Thermal plume simulation of the main campus at the end of August 2024.

As illustrated in Figure 69 and Figure 70, the thermal plume simulation of the Energy Center and Valentino Castle was conducted at the end of August 2024. It has been demonstrated that the Energy Center's doublet configuration gives rise to a plume structure that is less complex than that observed at the Main Campus. This is characterised by a single elongated thermal anomaly that originates from the discharge well (P2E). As demonstrated by the isothermal contours, there is a progressive decrease in downstream temperature, with a 16°C isotherm observed within 200 metres. The thermal plume behaviour exhibited by the Valentino Castle is particularly distinctive, a consequence of its proximity to the River Po boundary. The thermal plume is characterised by a distinct downstream truncation, which is attributable to the model area's limitation.

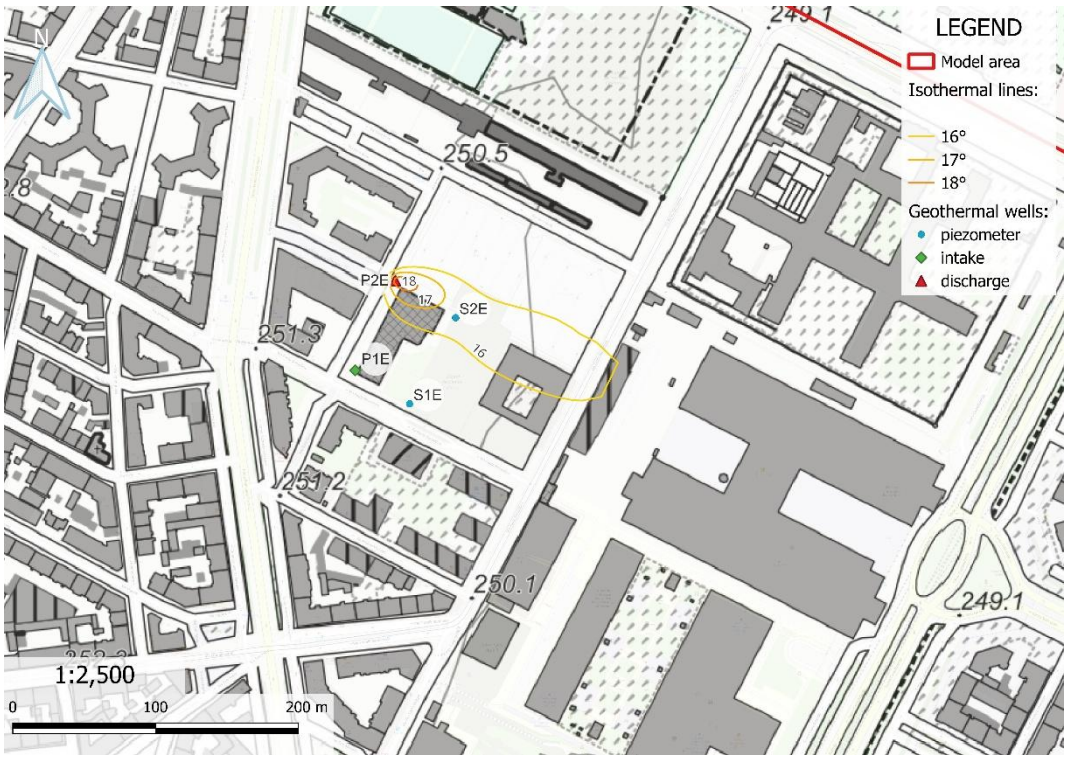

Figure 69. Thermal plume simulation of the Energy Center at the end of August 2024.

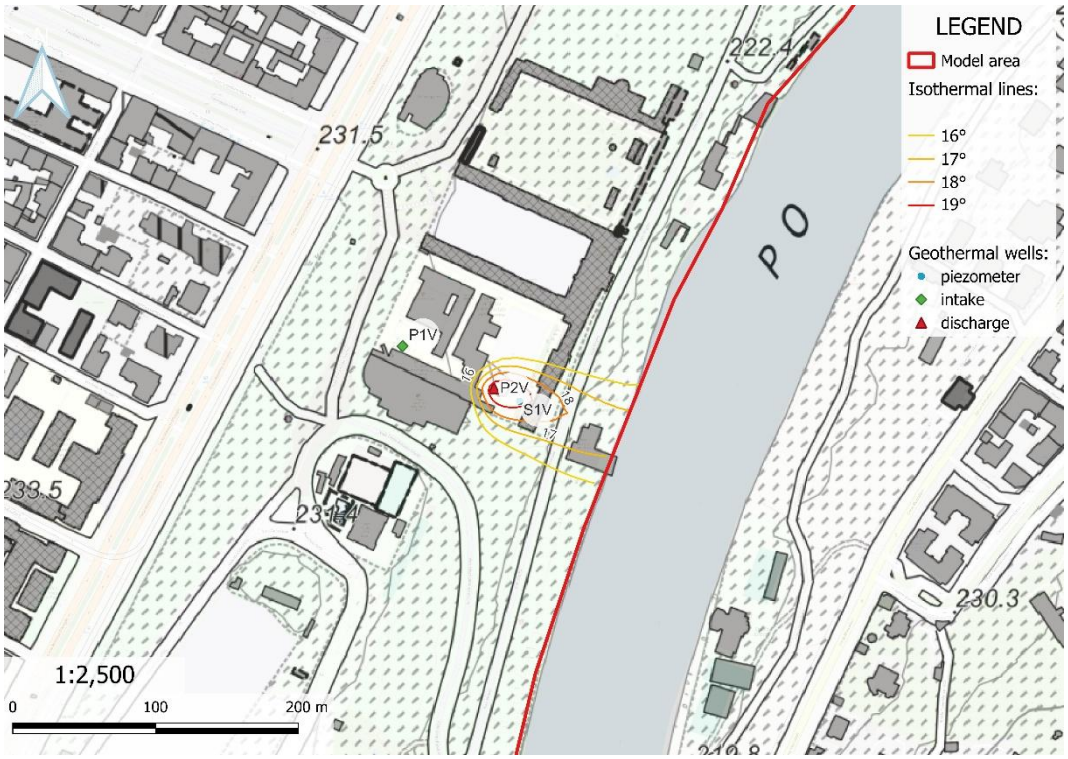

Figure 70. Thermal plume simulation of the Valentino Castle at the end of August 2024.

2.5.3 FEFLOW Case Studies

The Turin North model (Figure 30) was subjected to rigorous calibration using the PESTPP-GLM (Parameter ESTimation using Gauss-Levenberg-Marquardt algorithm) module integrated within FEPEST, the parameter estimation interface for FEFLOW. The calibration process employed 1,137 pilot points distributed throughout the model domain to optimize the spatial distribution of hydraulic conductivity, enabling representation of aquifer heterogeneity at an appropriate scale while maintaining computational efficiency. Figure 71 illustrates the spatial distribution of these pilot points across the northern model domain, demonstrating the high-density parameterization strategy adopted to capture spatial variability in hydraulic properties. Each pilot point represents a location where hydraulic conductivity can be independently adjusted during the automated calibration process, with values at intervening locations determined through kriging interpolation. The pilot points are distributed throughout the entire model area, with enhanced density close to the geothermal wells. The figure also shows the distribution of observation points (monitoring wells with measured hydraulic head data) used as calibration targets. The calibration process minimized the discrepancy between simulated and observed hydraulic heads at monitoring well locations by iteratively adjusting pilot point conductivity values according to the Gauss-Levenberg-Marquardt optimization algorithm.

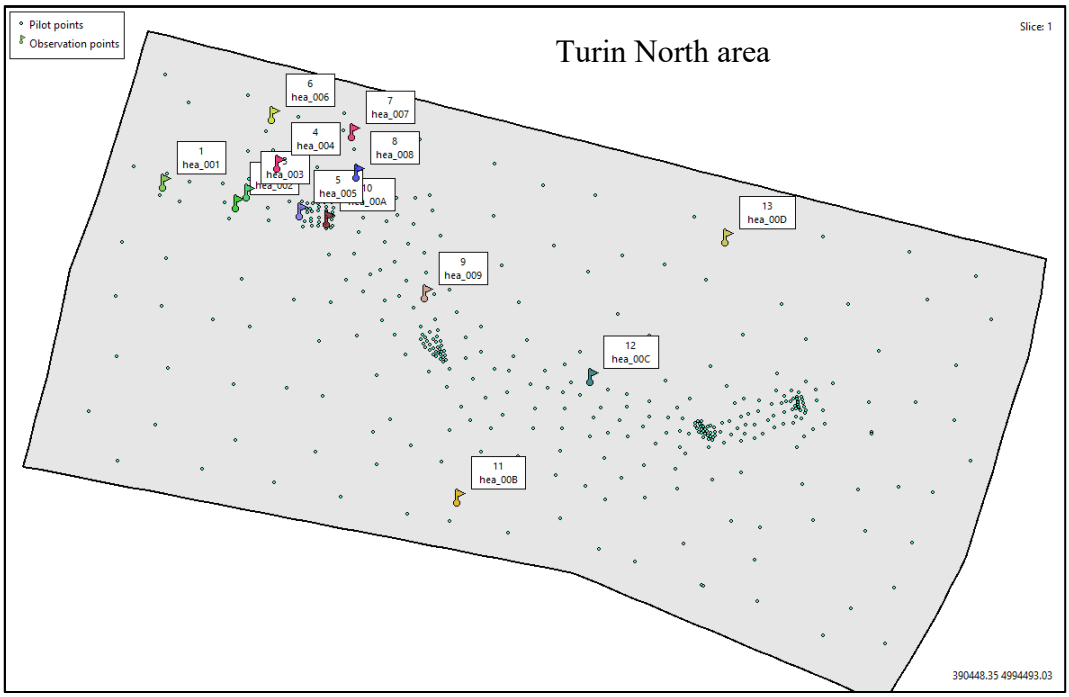

Figure 71. Turin North model area and distribution of Pilot Points and Observation points.

Figure 72 displays the scatter plot of observed versus simulated hydraulic heads, with observed values (x-axis) ranging from approximately 246.5 to 250.0 m a.s.l. and simulated values (y-axis) spanning a comparable range. The data points

cluster closely along the 1:1 line, indicating excellent correspondence between model predictions and field observations. This tight clustering, demonstrates that the calibrated model accurately reproduces the observed piezometric configuration across the entire range of hydraulic head values present in the study area.

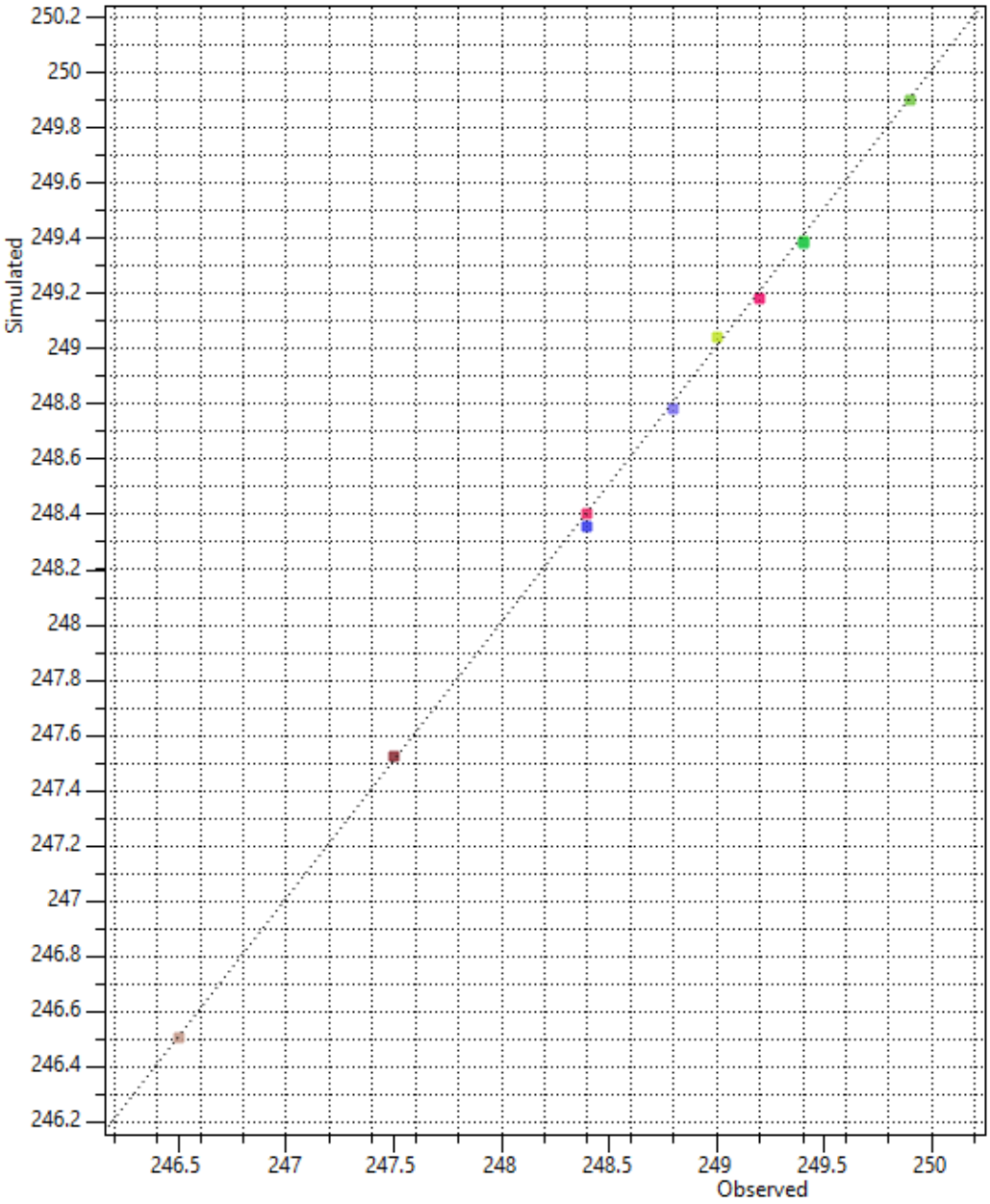

Figure 72. Observed vs Simulated plot, after calibration process.

Figure 73 presents the evolution of the objective function (Phi) through the iterative calibration process, displayed on a logarithmic scale. The initial Phi value of 48.5067 (iteration 0) represents the sum of squared weighted residuals prior to optimization, reflecting the substantial misfit between initial parameter estimates and observations. Through ten successive iterations, the optimization algorithm progressively reduces Phi to a final value of 0.0554351, representing a reduction of more than two orders of magnitude and confirming convergence to an optimal parameter set. The rapid decrease in Phi during the first three iterations indicates

that major adjustments to hydraulic conductivity distribution were necessary. While the gradual asymptotic approach to the final value in subsequent iterations reflects fine-tuning of parameter values to achieve optimal fit. The stabilization of Phi after iteration 7-8 confirms that the calibration has converged and that further iterations would yield negligible improvements.

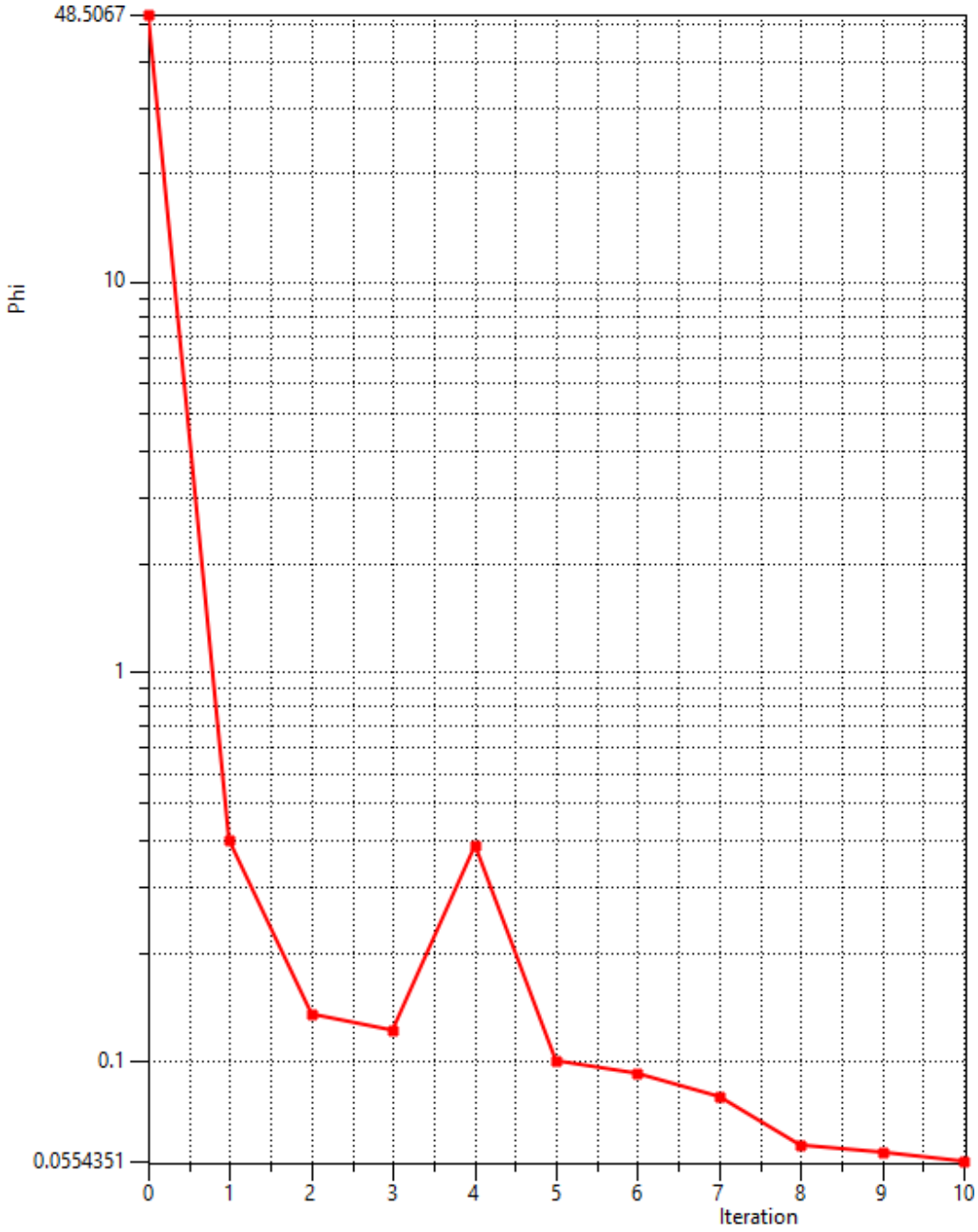

Figure 73. Objective function (Phi) plot after 10 iterations.

The calibrated hydraulic conductivity field for the Turin North model is presented in Figure 74, displaying the spatial distribution of horizontal hydraulic conductivity (K_{xx}).

The conductivity values, represented using a color-coded classification scheme, range from approximately 6.30×10^{-4} m/s (darkest colors) to 1.16×10^{-2} m/s (lightest

colors), spanning nearly two orders of magnitude. This substantial spatial variability reflects the heterogeneous nature of fluvial and fluvioglacial deposits, with higher conductivity values (approaching 10^{-2} m/s) corresponding to coarse gravel-dominated facies and lower values (in the 10^{-3} m/s range) associated with finer-grained sandy intervals or mixed gravel-sand sequences. The spatial pattern reveals preferential high-conductivity pathways that generally align with paleochannel directions, controlling both groundwater flow velocities and thermal plume propagation trajectories. This calibrated conductivity distribution provides the essential hydraulic framework for subsequent thermal transport simulations and enables realistic prediction of thermal plume extent and migration rates.

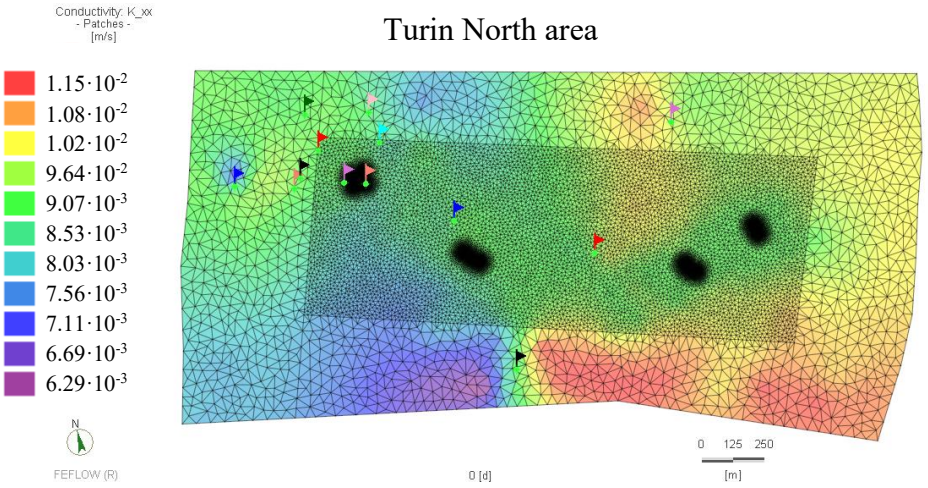

Figure 74. Calibrated hydraulic conductivity map in [m/s].

The Turin North case study simulates two large-scale open-loop geothermal installation. Figure 75 presents a three-dimensional representation of the numerical model, illustrating the vertical discretization strategy employed to represent the complex hydrostratigraphic framework. The red layers correspond to the shallow unconfined aquifer, which constitutes the primary target for geothermal exploitation due to its high transmissivity and favorable thermal characteristics. The blue layers represent the deeper confined aquifer system within the Pliocene formations, which exhibits lower hydraulic conductivity and is not suitable for geothermal purposes due to regulatory prohibitions. The three-dimensional representation clearly demonstrates the aquifer geometry, including lateral extent, thickness variations, and hydrostratigraphic boundaries.

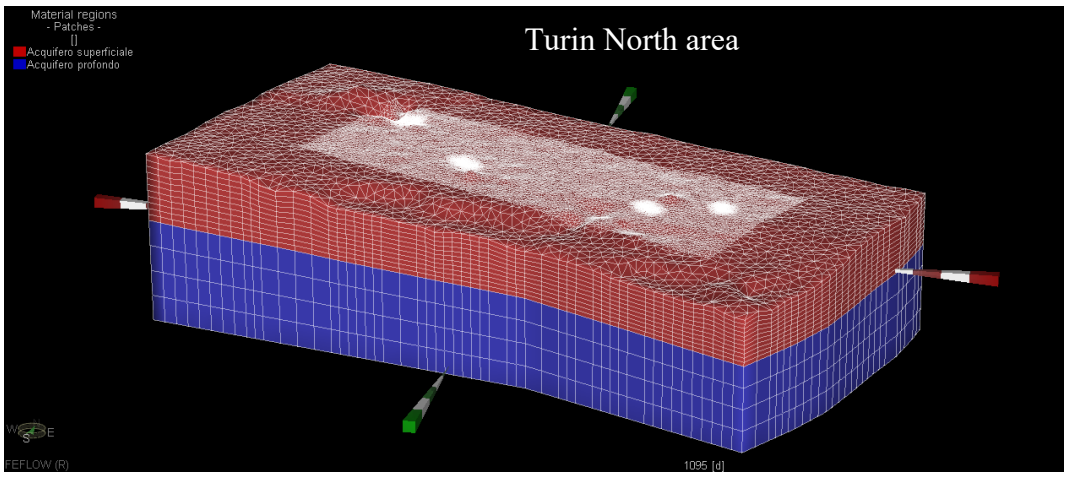

Figure 75. 3D model representation, the red layers correspond to shallow aquifer, the blue ones represent the deeper aquifer.

Figure 76 displays the horizontal mesh discretization and well positions for the upstream plant configuration (4 intake and 4 discharge wells). The finite element mesh employs unstructured triangular elements with local refinement in the vicinity of wells to accurately capture steep hydraulic and thermal gradients. The mesh resolution ranges from approximately 5 meters near wells to 50-80 meters in areas distant from pumping influences. The well locations are strategically positioned to maximize thermal extraction while maintaining adequate separation between extraction (intake) and reinjection (discharge) wells to prevent thermal recycling. The upstream plant is designed to provide substantial heating capacity (8,860 kW water thermal power) through extraction of 300 l/s from the shallow aquifer, where natural groundwater temperature is approximately 15.5°C. The simulation extends over three years (1,095 days) of seasonal operation, encompassing multiple heating-cooling cycles to assess both short-term performance and medium-term sustainability.

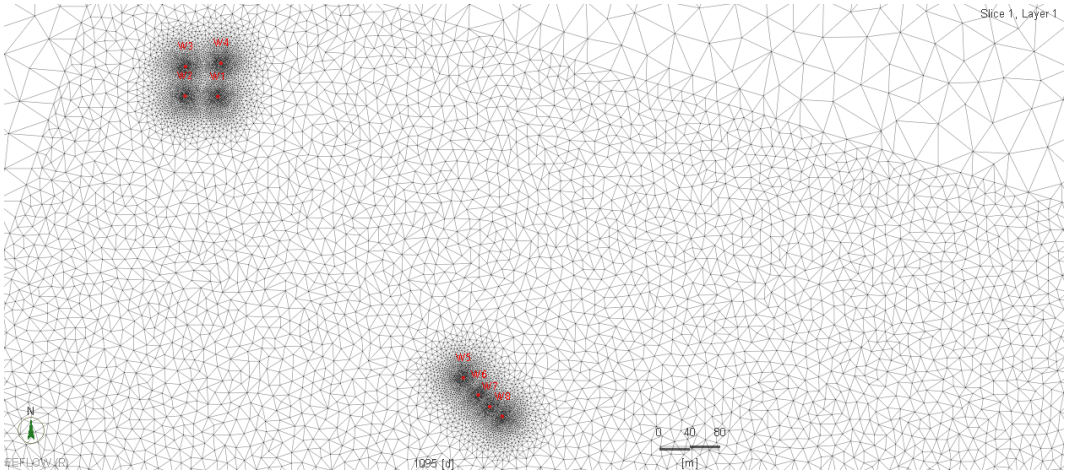

Figure 76. Wells position and mesh discretisation.

Figure 77 displays the thermal interference pattern in horizontal section after 916 days of simulation, corresponding to the end of the last winter (heating) period before the final summer. The temperature distribution reveals several critical

features: higher temperature zones (warm colors ranging from 16-22°C) represent the thermal plume from the previous summer cooling operation, wherein warmer water was reinjected into the aquifer. The front of this warm plume (16°C isotherm) has migrated approximately 1,200 meters downgradient from the discharge well over a six-month period, demonstrating the strong advective transport capacity of the high-conductivity aquifer. The persistence of elevated temperatures several months after cessation of summer cooling operations confirms that thermal plumes exhibit substantial residence time in the aquifer and that natural thermal dissipation processes (conduction, dispersion) are relatively slow compared to advective transport rates.

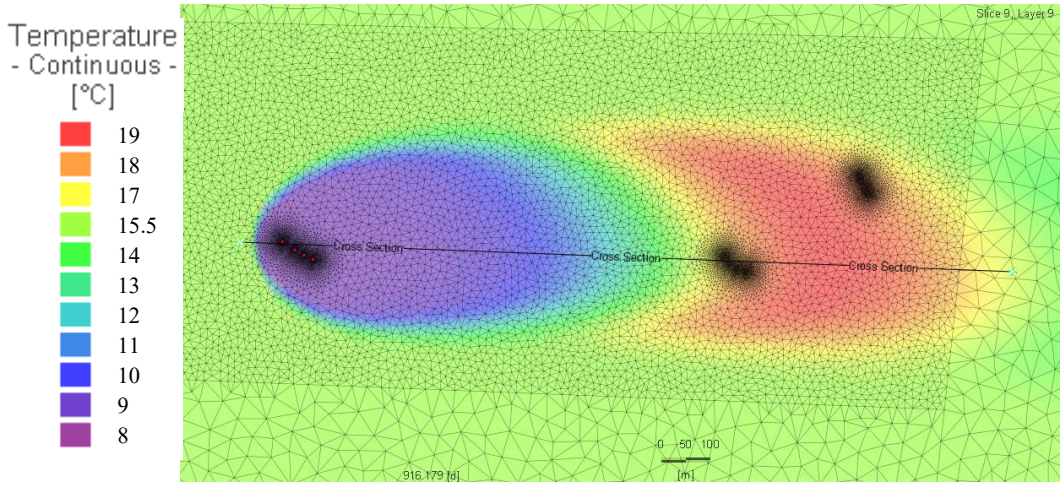

Figure 77. Thermal interference of the Turin North open-loop upstream plant in horizontal section after 916 days of simulation.

Figure 78 presents the corresponding vertical cross-section through the upstream plant after 916 days, providing insights into the three-dimensional structure of the thermal plume. The cross-section extends from ground surface (approximately 270 m elevation) to the base of the model domain (approximately 150 m elevation), encompassing both the shallow aquifer and upper portions of the Pliocene deeper aquifer. The thermal impacts are predominantly concentrated within the shallow aquifer (upper 40-50 meters of saturated thickness), with minimal thermal penetration into the underlying lower-permeability Pliocene formations. The vertical distribution exhibits thermal stratification, with the coldest temperatures (8-10°C) concentrated in the lower and middle portions of the aquifer. The cross-section also reveals that thermal plumes maintain coherent structure over distances of several hundred meters, indicating that dispersive mixing, while present, does not rapidly dissipate thermal plume.

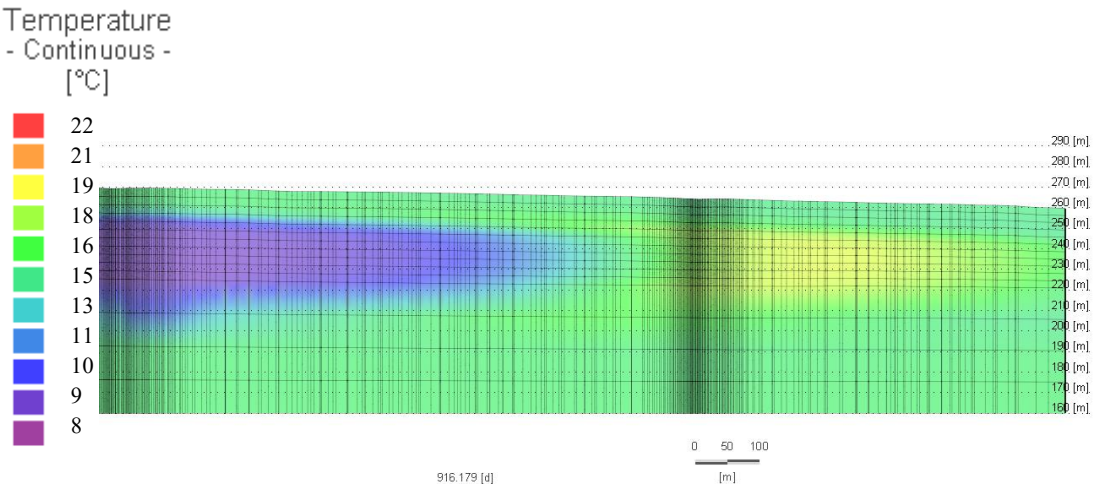

Figure 78. Cross section of the thermal interference of the Turin North open-loop upstream plant after 916 days of simulation.

Figure 79 displays the thermal interference pattern in horizontal section after 1,095 days (three years), representing the final simulation time step. Comparison with Figure 77 (916 days) reveals continued evolution of the thermal field. The alternating pattern of warm and cool plumes, corresponding to seasonal operational cycles, demonstrates the dynamic nature of thermal impacts in seasonally operated systems. Importantly, the extraction (intake) wells, positioned upgradient from the reinjection zone, continue to draw water at near-ambient aquifer temperatures (15-16°C), confirming the absence of thermal recycling throughout the three-year simulation period.

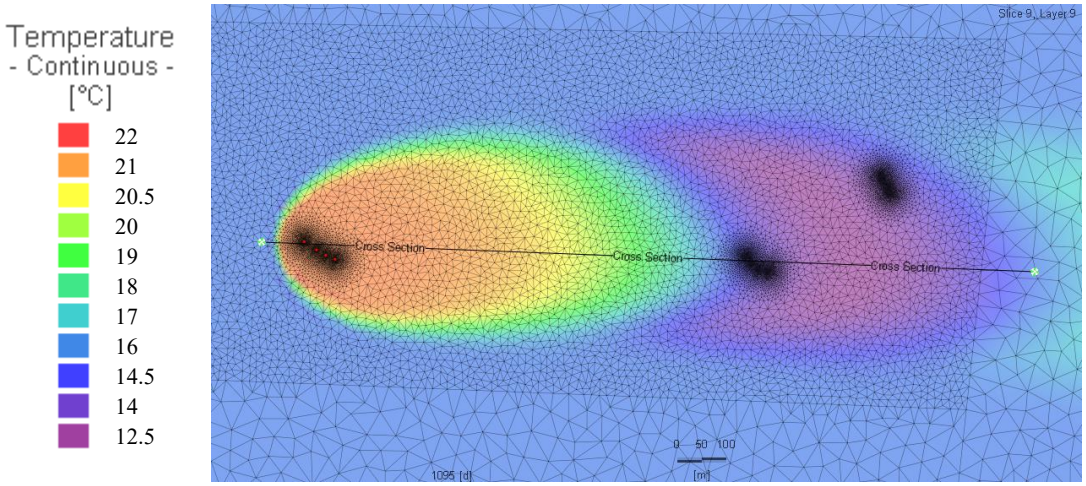

Figure 79. Thermal interference of the Turin North open-loop upstream plant in horizontal section after 1095 days of simulation.

Figure 80 presents the vertical cross-section after 1,095 days, complementing the plan view perspective. The cross-section reveals that thermal impacts remain predominantly confined to the shallow aquifer, with minimal downward migration into the Pliocene unit. The persistence of vertically stratified thermal structure, even after three years of operation, indicates that vertical mixing processes are relatively

slow and that the aquifer system exhibits pronounced anisotropy with horizontal transport dominating over vertical components.

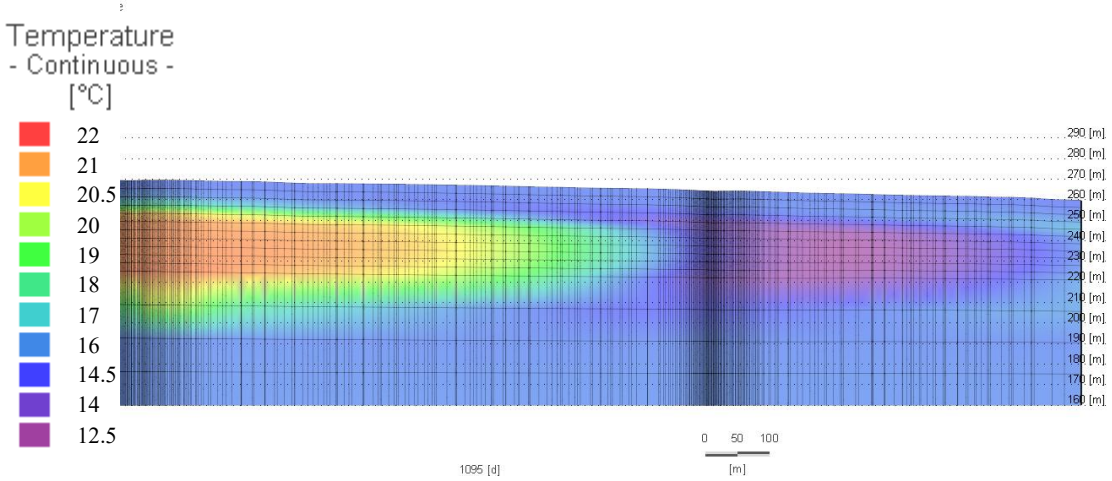

Figure 80. Cross section of the thermal interference of the Turin North open-loop upstream plant after 1095 days of simulation.

Figure 81 presents a critical metric for assessing long-term system sustainability: the temporal evolution of groundwater temperature at each simulated well throughout the 1,095-day simulation period. The graph displays multiple temperature traces, with blue lines corresponding to discharge (reinjection) wells and black lines representing intake (extraction) wells. The discharge well temperatures exhibit substantial seasonal oscillations, reflecting the alternating heating and cooling operational modes. In contrast, the intake well temperatures (black lines) exhibit remarkable stability throughout the entire simulation period. This stability is the most critical indicator of system sustainability, demonstrating that thermal recycling does not occur under the simulated well configuration and operational regime. The absence of any long-term declining trend in intake temperatures confirms that the aquifer system possesses sufficient thermal capacity and advective flushing to sustain the proposed extraction rates without progressive thermal depletion.

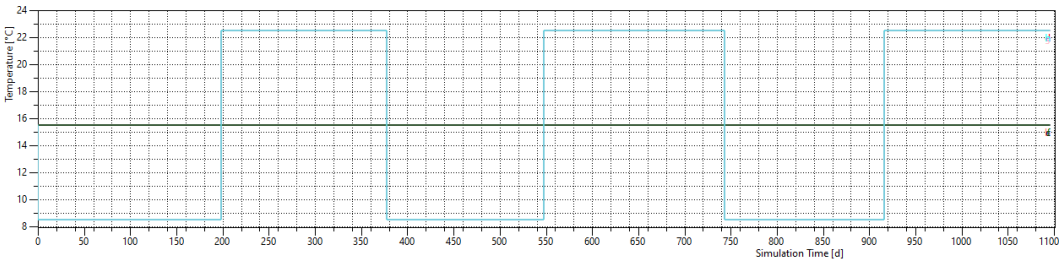

Figure 81. Graph showing temperature trends for each simulated well in the Turin North open-loop upstream plant throughout the simulation period. The blue lines correspond to the discharge wells and the black one to the intake wells.

Figure 82 quantifies the cumulative thermal energy exchange through presentation of the annual energy budget expressed in megawatt-hours (MWh). The graph displays seasonal cycles with negative values representing net heat extraction during winter heating periods and positive values representing net heat rejection during summer cooling periods. Each winter and summer season results in cumulative thermal extraction of approximately 45 GWh per season, approximately 90 GWh per year, considering both heating and cooling.

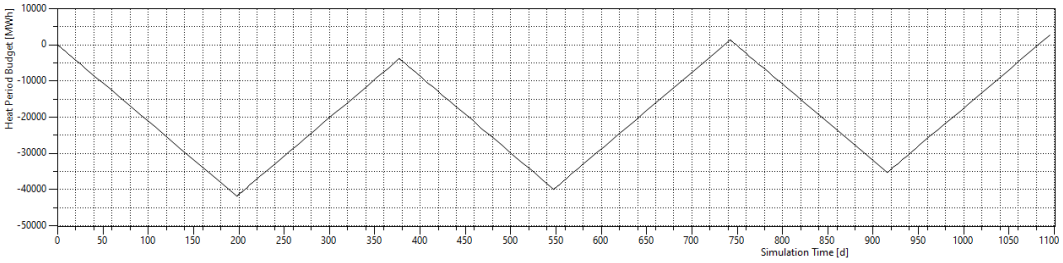

Figure 82. Annual energy budget of the open-loop plant (MWh), negative value represent heating period, positive value cooling period.

The downstream plant, positioned several hundred meters downgradient from the upstream installation, operates at similar scale (300 l/s) and is simulated without the influence of thermal plume generated by upstream plant. The simulation of both plants is presented in the chapter ATES 4.3.3 Case Study 3. The simulation for the downstream plant extends to 1,800 days (approximately five years) to evaluate longer-term thermal evolution and cumulative impacts.

The horizontal and vertical thermal interference patterns (Figure 83, Figure 84, Figure 85, and Figure 86) and the temporal temperature plot (Figure 87) demonstrate a high similarity to the upstream plant. The most significant challenge will therefore be to operate the plants simultaneously while limiting the thermal interference that two plants of this size can generate in a relatively small area.

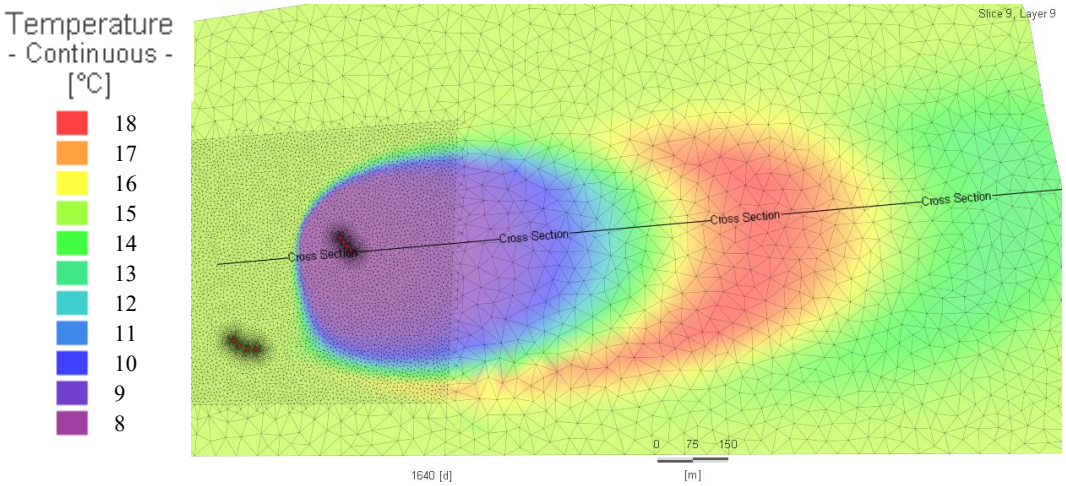

Figure 83. Thermal interference of the Turin North open-loop downstream plant in horizontal section after 1640 days of simulation.

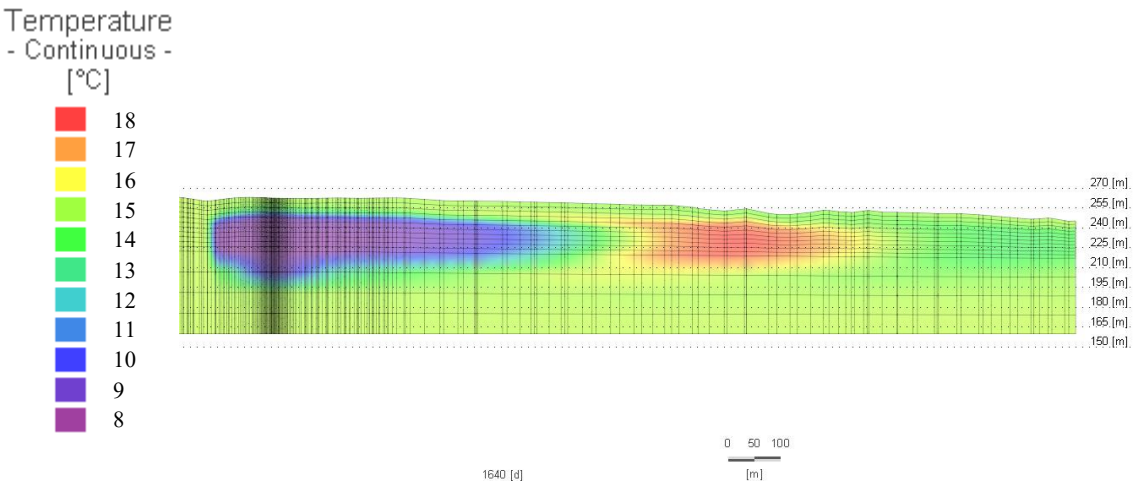

Figure 84. Cross section of the thermal interference of the Turin North open-loop downstream plant after 1640 days of simulation.

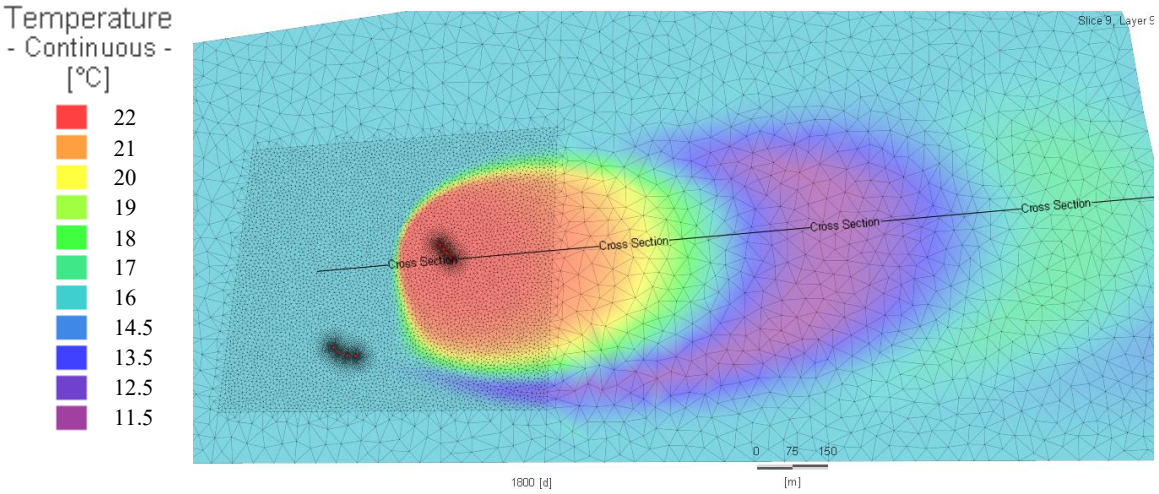

Figure 85. Thermal interference of the Turin North open-loop downstream plant in horizontal section after 1800 days of simulation.

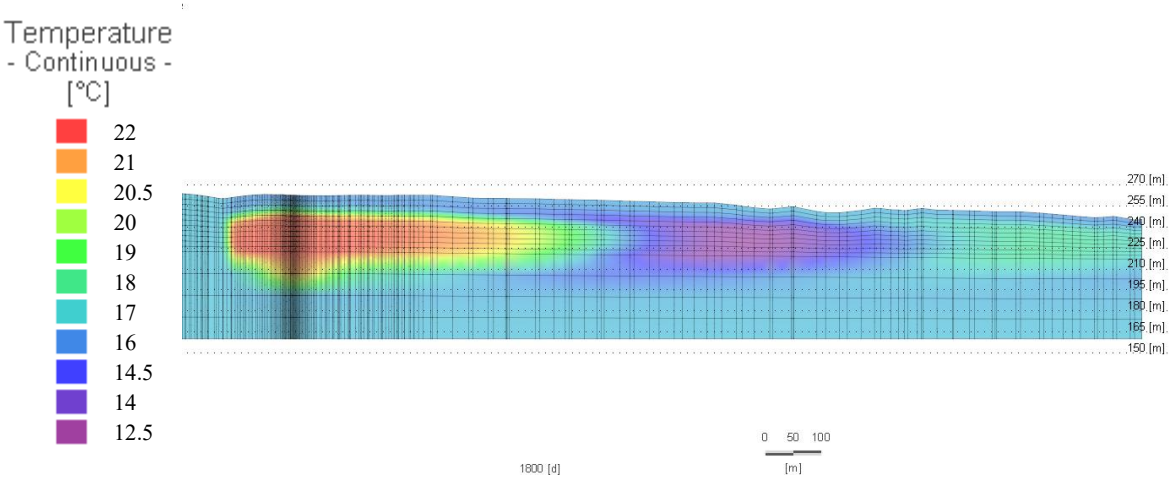

Figure 86. Cross section of the thermal interference of the Turin North open-loop downstream plant after 1800 days of simulation.

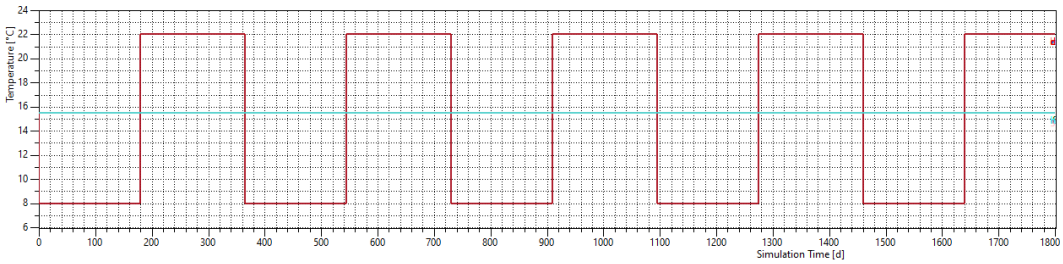

Figure 87. Graph showing temperature trends for each simulated well in the Turin North open-loop downstream plant throughout the simulation period. The red lines correspond to the discharge wells and the blue one to the intake wells.

The Turin South case study simulates three different geothermal plants to evaluate possible thermal interference and assess different spatial configurations in a more hydrogeologically constrained setting. Two of the installations are located close to the boundary outflow represented by the Po River, which serves as a major hydraulic control on groundwater flow patterns and potentially provides enhanced thermal flushing compared to interior locations distant from surface water interactions. The western plant has a flow rate of 40 l/s, while the two plants near the River Po have a flow rate of 25 l/s. The total thermal power of the water in all three plants is approximately 2,750 kW.

The Turin South model employs an interpolated but uncalibrated hydraulic conductivity field due to the paucity of observation points in this area necessary to support a robust calibration procedure. The absence of sufficient monitoring wells with reliable head data precludes the application of automated parameter estimation techniques, necessitating reliance on spatial interpolation of hydraulic conductivity values derived from limited pumping test data, grain size analyses, and regional geological correlations. This methodological limitation introduces greater uncertainty in model predictions for the southern site compared to the rigorously calibrated northern model. Figure 88 presents the hydraulic conductivity distribution map for the Turin South case study following the kriging interpolation process (see chapter 2.5.2 MODFLOW and Figure 58). The conductivity values range from approximately 6.74×10^{-4} m/s (darkest blue colors) to 4.91×10^{-3} m/s (lightest yellow colors), representing approximately one order of magnitude variation. The spatial distribution exhibits gradational patterns with higher conductivity zones (approaching 5×10^{-3}m/s) concentrated in the central and western portions of the model domain, while lower conductivity areas (below 1×10^{-3} m/s) dominate the eastern and peripheral zones.

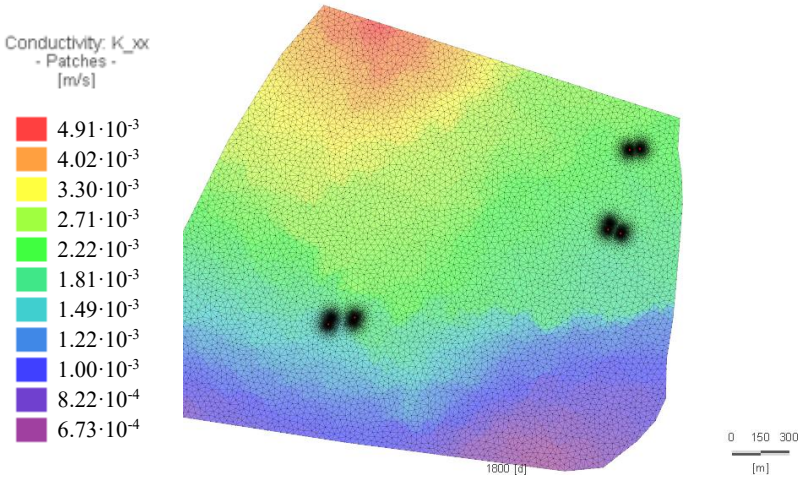

Figure 88. Hydraulic conductivity distribution map of the Turin South case study, after interpolation process.

Figure 89 displays the thermal interference pattern for all three Turin South plants in horizontal section after 1,640 days of simulation (winter period). The temperature distribution reveals distinct thermal plumes emanating from each installation, with spatial extent and intensity varying according to individual plant operational parameters and local hydrogeological conditions. The temperature scale ranges from 8°C to 17°C, indicating substantial thermal perturbation relative to the ambient aquifer temperature (approximately 14.5°C at this location). Cold plumes (temperatures below 14°C) associated with winter heating operations are clearly visible as blue zones extending 200-400 meters downgradient from reinjection wells. The relatively limited spatial extent of thermal plumes compared to the Turin North sites reflects the combined influences of lower extraction rates, and reduced hydraulic conductivity.

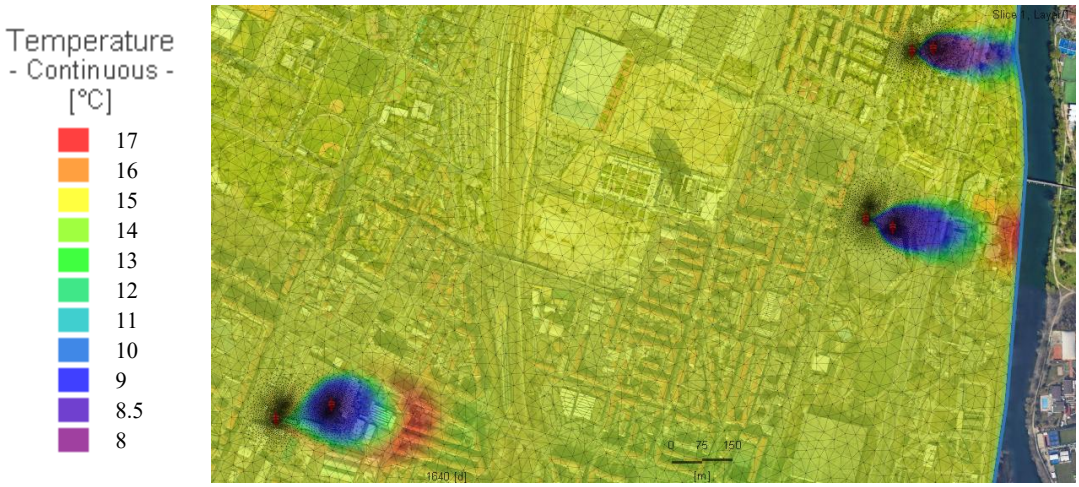

Figure 89. Thermal interference of the Turin South open-loop plants in horizontal section after 1640 days of simulation.

Figure 90 displays the thermal distribution after 1,800 days (summer period), representing the final simulation time. There is no thermal interference between the various geothermal plants.

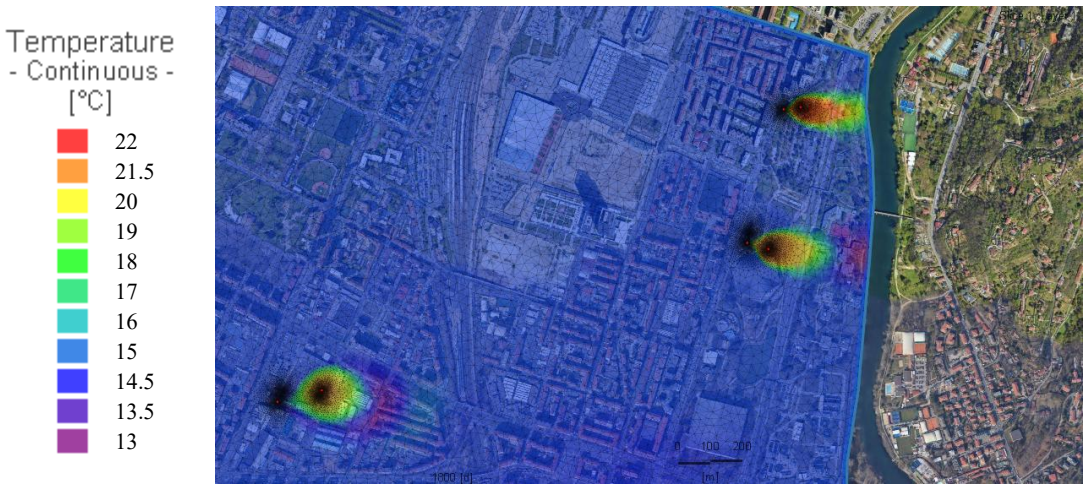

Figure 90. Thermal interference of the Turin South open-loop plants in horizontal section after 1800 days of simulation.

Figure 91 presents the temporal temperature evolution for all simulated wells in the Turin South installations throughout the simulation period. Colored lines correspond to intake (extraction) wells from the three different plants, while blue lines represent discharge (reinjection) wells. The intake well temperatures show critical behaviour for assessing system sustainability. The graph reveals that intake wells exhibit slight fluctuations during seasonal periods, demonstrating minor thermal interference due to the limited spacing between intake and discharge wells. However, the magnitude of this thermal recycling effect is less than 1°C and does not compromise the water heat pump plant operation. Most intake wells maintain temperatures within the range of 13.5-15.5°C throughout the simulation period, indicating that despite the spatial constraints and closer well spacing compared to the Turin North sites, thermal recycling remains within acceptable limits. The relatively stable long-term baseline temperatures, with seasonal fluctuations but no systematic declining trend over five years, suggest that the system configuration achieves a sustainable balance between thermal extraction and natural replenishment at the simulated operational rates.

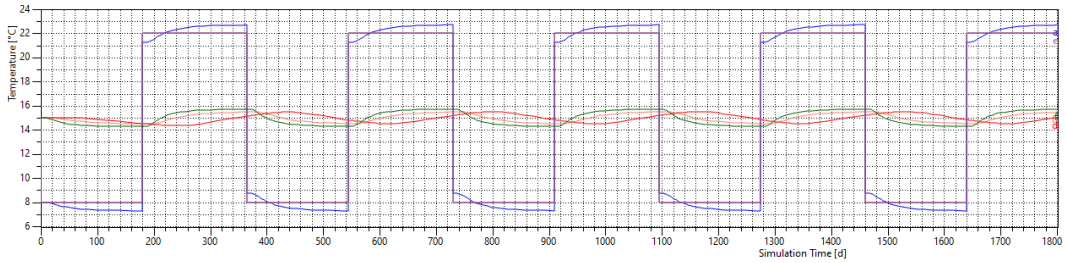

Figure 91. Graph showing temperature trends for each simulated well in the Turin South open-loop plants throughout the simulation period. The coloured lines correspond to the intake wells and the blue one to the discharge wells.

Figure 22 quantifies the cumulative energy budget for the combined Turin South installations, expressed in MWh with negative values representing heating periods and positive values representing cooling periods. The saw-tooth pattern

characteristic of seasonal operation is evident, with each winter heating season resulting in cumulative thermal extraction of approximately 11 GWh for the three plants combined seasonally. This substantially smaller energy delivery compared to the Turin North installations (45 GWh per plant per season) reflects the reduced scale of operation.

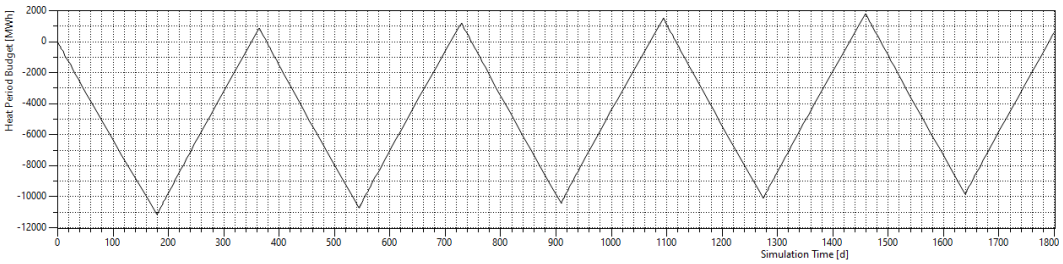

Figure 92. Annual energy budget of the total Turin South open-loop plants (MWh), negative value represents heating period, positive value cooling period.

2.6 Discussion

The three-tier methodology, GAP for strategic screening, MODFLOW for urban cumulative assessment, and FEFLOW for site-specific validation, enables an efficient allocation of modelling effort while maintaining scientific rigor and consistency across scales. The use of two numerical models is motivated by the fact that the two questions addressed in this work are inherently different in terms of spatial scale, required conceptual detail, and computational burden. At the city scale, the objective is to quantify cumulative hydraulic and thermal interference generated by many open-loop systems operating simultaneously. This requires a model that is robust, computationally efficient, and able to handle very large grids and numerous stressors (wells, rivers/boundaries, long transient periods) while supporting scenario runs. In this context, MODFLOW6–based workflows are advantageous because they are widely validated for regional groundwater simulations, offer stable solvers and standardized packages for wells and boundary conditions, and allow fast scenario-based assessment on refined grids at metropolitan extent (e.g., DISV/quadtree), which is essential to explore multiple operational hypotheses and to map cumulative impacts consistently.

Conversely, at the site-specific scale, the goal shifts from screening to design support and permitting-oriented verification, where local heterogeneity, boundary representation near structures, and the detailed geometry of the well doublet become more influential. Here, FEFLOW provides advantages due to its finite-element formulation, which allows more flexible representation of complex local stratigraphy, anisotropy, and irregular boundaries, as well as more detailed coupling of flow and heat transport around the installation and in the near-field. This level of detail is typically unnecessary at city scale, but becomes crucial when optimizing well spacing, predicting local thermal plumes, and supporting project-specific authorizations. Using a single model for both purposes would either (i) force a city-scale model to include local complexities that are not supported by data everywhere and would dramatically increase run time, or (ii) reduce the site-specific analysis to a coarse regional representation, losing the resolution and geometric flexibility required for design and validation. Therefore, the two-model framework is not a redundancy but a scale-appropriate strategy: MODFLOW provides a consistent and efficient platform to evaluate urban cumulative impacts, while FEFLOW focuses resources where they are most needed to deliver high-confidence, site-level predictions. Sites identified as high-potential through GAP and demonstrating acceptable cumulative impacts in MODFLOW can then proceed to detailed FEFLOW analyses for final design optimization and permitting support. This hierarchical approach has been applied to prospective installations in Turin, demonstrating practical utility for guiding sustainable urban geothermal development.

The findings of the study demonstrate that the GAP method offers a robust, spatially explicit framework for evaluating shallow geothermal potential in urban environments. By integrating hydrogeological parameters with legal and technical constraints, it enables the generation of high-resolution potential maps that can

effectively support strategic energy planning and decision-making processes. In particular, the marked decrease in potential near river systems highlights the necessity of accounting for hydrogeological limitations when planning geothermal well doublets. Conversely, the identification of high-potential zones in the central and southern sectors provides strategic guidance for the optimal placement of geothermal wells, thereby maximising energy extraction efficiency.

The proposed methodology relies on the assessment of a set of reference parameters (Table 5). In particular, two groups of parameters contribute to the evaluation of the flow rate:

- Well-related parameters, which are associated with the design choices of the doublet system, including well radius, monitoring point distance, and the percentage of drawdown in the well.
- Aquifer-related parameters, which depend on the spatial distribution and availability of hydrogeological data and, therefore, on the level of detail adopted to represent aquifer properties.

In this context, a two-step sensitivity analysis was performed to evaluate the influence of a priori assumptions.

First, the influence of well-related parameters on the geothermal potential classification was assessed by varying one reference parameter at a time. During this first step, aquifer characteristics were fixed to the values listed in Table 8. These parameters are representative of an average shallow aquifer in urban areas; moreover, although they can be modified, they are typically derived either from detailed hydrogeological characterization or from existing legislative frameworks.

Table 8. Reference parameter for the aquifer characteristics

Aquifer parameters	**Value**
b [m]	20
K [m/s]	0.0001
i [-]	0.003
ΔT [°C]	7
S_{VCwat} [MJ/Km^3]	4.18

Figure 93 shows the variation of flow discharge Q, calculated using the Dupuit approach, assuming a drawdown in the pumping well equal to 10% of the aquifer thickness and a drawdown at the reference point of 0.1 m, as a function of the distance r_2 from the pumping well and for different well radii (r_1 = 0.15, 0.25, and 0.40 m). The selected well radii are representative of common geothermal wells used in open-loop systems. For all well diameters, the discharge decreases with increasing r_2, reflecting the reduction of the hydraulic gradient with distance from

the well. Larger well radii systematically result in higher discharge values, highlighting the influence of well geometry on the achievable flow rate. However, for increasing r_2, the influence of well radius on discharge becomes negligible.

The dotted curve represents the discharge calculated from the critical length by inverting Equation (7), which in this case is assumed to correspond to the distance r_2. This curve shows an opposite trend, with discharge increasing with r_2, and intersects the Dupuit-based curves at distances where the two limiting conditions become comparable. In general, the discharge obtained from Equation (7) is highly conservative when the distance between hypothetical wells is moderate.

At first glance, the discharge does not appear to be strongly influenced by r_2, especially for larger values of this parameter. Moreover, in terms of geothermal potential classes, neither the well radius nor the reference distance significantly affects class attribution. Specifically, the system transitions from class 5 at very low r_2 values to class 3 at higher r_2 values.

This aspect is further investigated in Figure 93c, which shows the normalized difference Δ [%] between the thermal power G calculated under reference conditions ($r_1 = 0.25$ m and $r_2 = 50$ m) and the values obtained by varying r_1 and r_2, normalized by the reference value ($\Delta = \frac{G(r_1 = 0.25\ \mathrm{m}; r^2 = 50\ \mathrm{m}) - G}{G(r_1 = 0.25\ \mathrm{m}; r^2 = 50\ \mathrm{m})} \cdot 100$). The results highlight a strong sensitivity to r_2 at short distances, where deviations are large and negative, followed by a progressive stabilization for increasing r_2. Variations in r_1 mainly affect the magnitude of the normalized difference, confirming that well radius plays a secondary, though non-negligible, role compared to the distance between wells.

The green rectangle in Figure 93c highlights a variation range within ±15%. Within this interval, r_2 spans from a few meters up to approximately 200 m, indicating that, at the urban scale, a reference distance of $r_2 = 50$ m represents a reasonable compromise. For this range of distances, the associated variability in thermal power remains within the same order of magnitude as typical engineering uncertainties, supporting the robustness of the adopted reference value for practical applications.

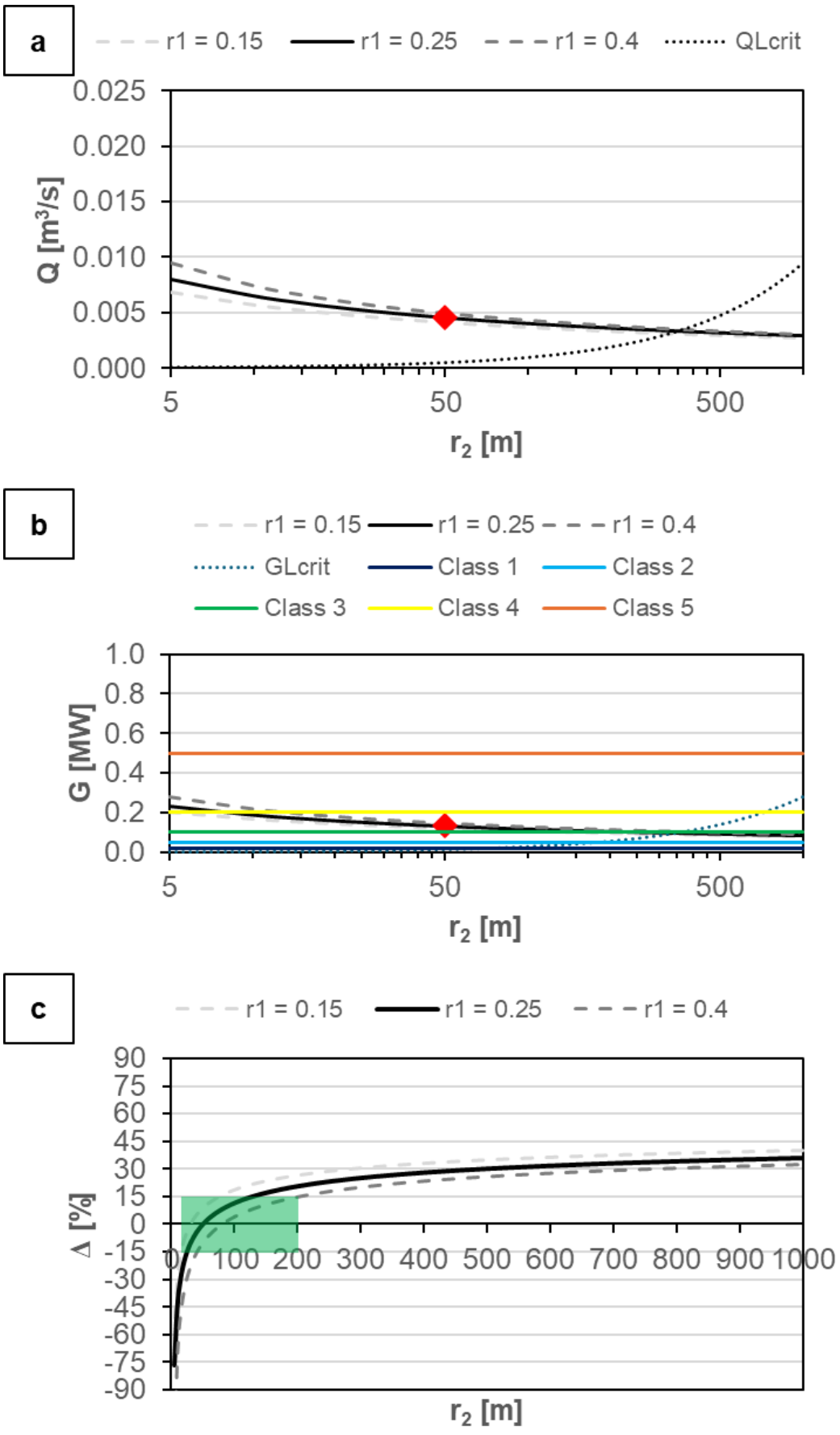

Figure 93. Trend of (a) flow discharge, (b) thermal power, and (c) normalized differences as a function of the distance from well r_2, as reported in Equation (3), for different well radii.

Analogously to what was done for the well radii, a sensitivity analysis was carried out to investigate the effect of drawdown on the hydraulic and thermal behaviour of the system.

Figure 94 shows the trends of flow discharge (a–b), thermal power (c–d), and normalized differences (e–f) as functions of the distance from well r_2. The drawdown at the pumping well was varied between 5% and 25%, while the drawdown at distance r_2 ranged from 0.05 m to 0.5 m. When the drawdown is imposed at the pumping well (Figure 94a, c, e), the flow discharge exhibits a marked decrease with increasing r_2, particularly for higher drawdown values. This behaviour reflects the reduced hydraulic influence of the pumping well as the distance increases, with the largest sensitivity occurring at short distances ($r_2 < 50$ m).

When the drawdown is applied at distance r_2 (Figure 94b, d, f), both flow discharge and thermal power display a more limited sensitivity to distance. The curves are flatter compared to the previous case, indicating that variations in drawdown away from the well mainly induce local effects and have a reduced impact on the overall system performance.

The normalized differences (Figure 94e–f) further emphasize these trends. In the case of drawdown at the pumping well, normalized differences increase rapidly at short distances and then tend to stabilize, highlighting a strong sensitivity of the system close to the well and considering high values for r2. Conversely, when drawdown is imposed at r_2, the normalized differences show a smoother and more gradual increase with distance, confirming a weaker and more distributed influence. Overall, Figure 94 demonstrates that drawdown at the pumping well plays a dominant role in controlling both hydraulic and thermal responses, especially at short distances from r_2. In contrast, drawdown variations occurring away from the well have a secondary effect, mainly affecting local conditions without significantly altering the overall system behaviour.

Among the well-related parameters, drawdown at the pumping well emerges as the most sensitive. In this context, the adopted value of 10% of the aquifer thickness can be considered a reasonable compromise between system productivity and the long-term resilience of the aquifer.

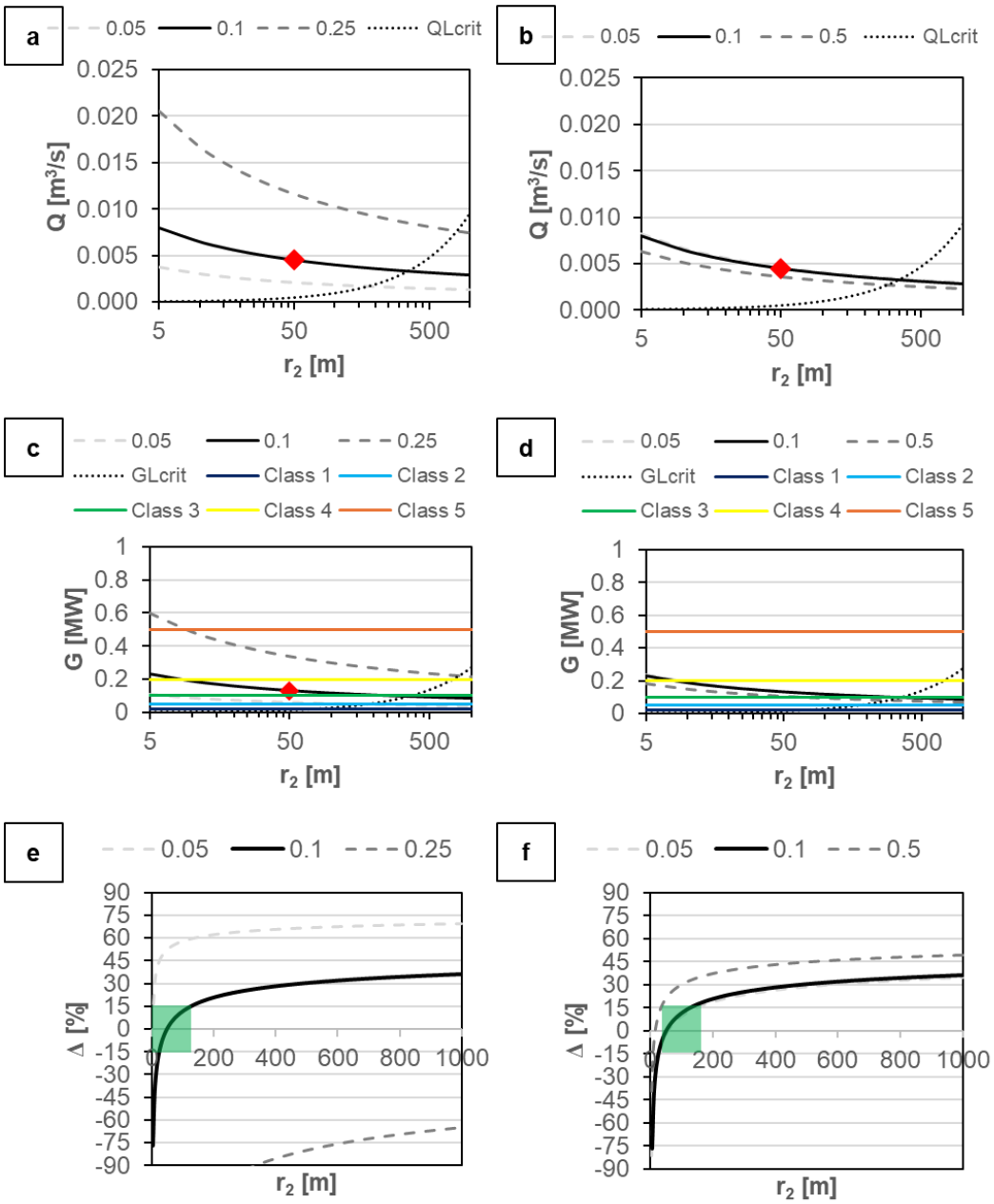

Figure 94. Trend of (a-b) flow discharge, (c-d) thermal power, and (e-f) normalized differences as a function of the distance from well r_2, as reported in Equation (3), for different drawdown values at the pumping well (a, c and e) and at a distance r2 (b, d and f).

With regard to the aquifer-related parameters, the sensitivity analysis was conducted by considering a reasonable range of variation for each parameter and by evaluating both the least and the most severe configurations for discharge assessment. The term "reasonable" refers to parameter values representative of the hydrogeological context of Turin, which, for an alluvial aquifer in an urban setting, can also be considered representative of many other geological contexts.

Figure 95 illustrates the envelope of discharge and the corresponding thermal power as functions of the distance to the controlling well, which in the model represents the cell size. The maximum and minimum curves, derived from all combinations of the hydrogeological parameters (Table 9), delineate the range of variability of system performance.

Table 9. Range of variability of the aquifer-related parameters.

Aquifer parameters	Value	
	min	max
b [m]	5	35
K [m/s]	0.0001	0.010
i [-]	0.001	0.01

Regardless of the distance r_2, both discharge and geothermal power may differ by up to three orders of magnitude, highlighting the strong influence of hydraulic parameters on their estimation and, consequently, on the resulting model classification.

It should be noted, however, that this variability represents a spatial variability driven by the heterogeneous hydrogeological properties of the aquifer. At the local scale, such variability does not occur to the same extent, as each model cell is characterized by a single representative set of parameters. Apart from a limited uncertainty related to the availability and density of hydrogeological information, this approach significantly reduces the effective sensitivity of the model at the cell scale.

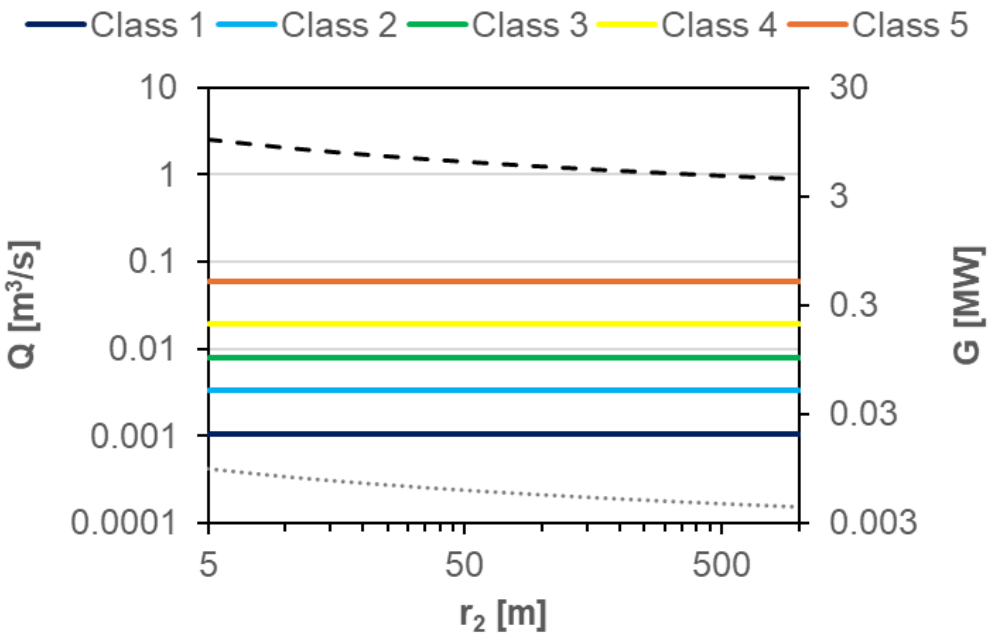

Figure 95. Range of variation of discharge and thermal power (secondary axis) as functions of the distance to the controlling well (i.e., the model cell size), bounded by the maximum (black dashed line) and minimum (black dotted line) values obtained from all combinations of the hydrogeological parameters.

The reliability of the proposed method is further supported by comparison with some existing open-loop geothermal plants across the city. The validation of the GAP method was carried out using a dedicated dataset collected in 2025 by the Politecnico di Torino, consisting of five geothermal abstraction wells located on the university campus (named P1, P2, P5, P1E and P1C shown in Figure 96). These wells represent the only monitoring points within the urban area of Turin for which

simultaneous measurements of extracted flowrate and associated drawdown are available. Although the GAP method is intended for application across the entire city, no comparable datasets exist for private or municipal open-loop geothermal installations. Consequently, the validation relies exclusively on these five university wells. This constraint introduces a fundamental limitation: the dataset is spatially restricted, and not fully representative of the variability expected across the broader urban aquifer. The results presented here should therefore be interpreted as an initial, partial validation rather than a definitive assessment of the method's performance at the city scale.

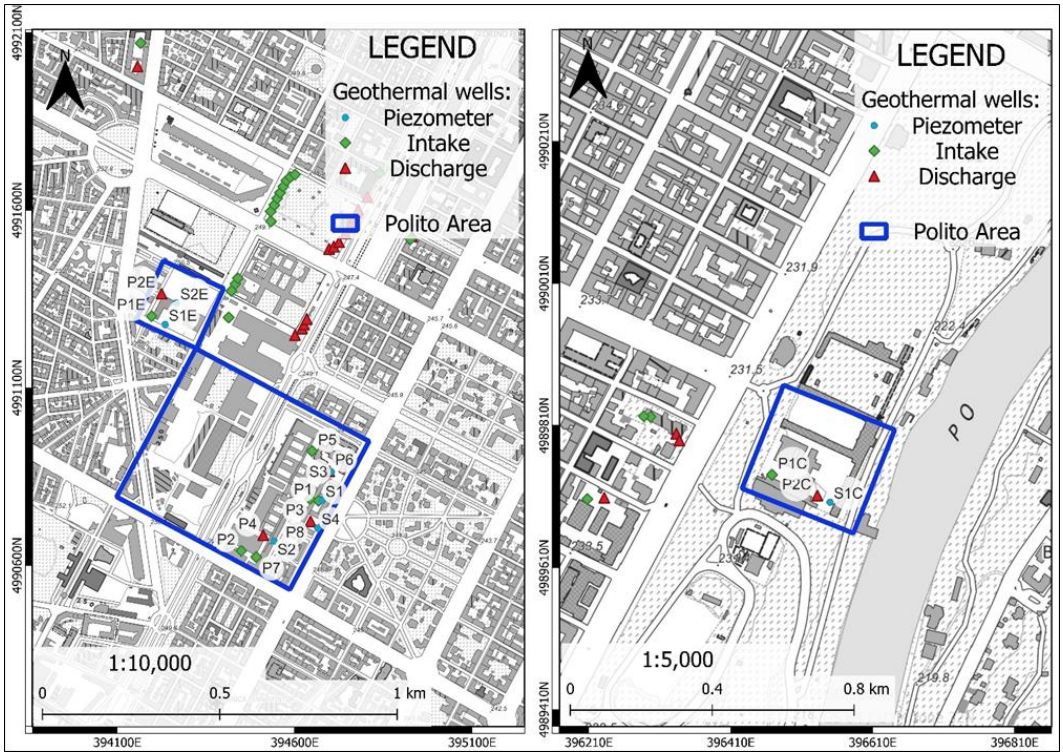

Figure 96. Politecnico di Torino (Polito) geothermal wells location.

The intake geothermal wells and the main hydraulic properties used for validation are summarised in Table 10. Two operational scenarios were considered to test the robustness of the GAP method under different hydraulic conditions. The first scenario corresponds to the maximum abstraction flowrate recorded for each well, representing the upper operational limit of the geothermal systems. The second scenario reflects a standard operating flowrate, representative of typical open-loop system functioning during regular thermal demand.

Table 10. Main properties of the Polito geothermal wells used for validation.

Name	*Hydraulic conductivity [m/s]*	*Aquifer thickness [m]*	*Max flowrate [l/s]*	*Max drawdown [m]*	*Standard flowrate [l/s]*	*Standard drawdown [m]*
P1	0.0031	21.6	47.21	0.7	18.33	0.38
P1C	0.0022	15.7	40.82	1.1	20.99	0.6
P1E	0.0035	22.16	11.11	0.21	5.05	0.15
P2	0.0031	21.5	62.69	1	24.99	0.44
P5	0.0033	21.85	27.77	0.38	13.89	0.21

Figure 97 presents the scatter plot comparing predicted and observed maximum flowrates. The GAP method shows strong agreement with field measurements, with a global coefficient of determination of $R^2 = 0.996$. The mean absolute error (MAE) for the maximum-flow scenario is 1.92 l/s, while the root-mean-square error (RMSE) is 2.21 l/s. The 95% confidence band around the regression line is narrow, confirming the stability of the relationship and the low dispersion of residuals under maximum-flow conditions.

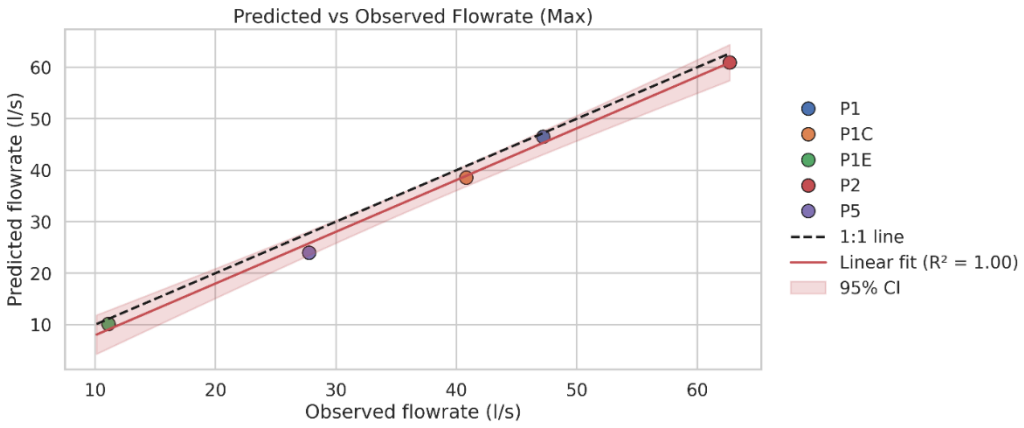

Figure 97. Predicted vs observed maximum flowrates scatter plot for the five monitored geothermal wells (P1, P1C, P1E, P2, P5). The 1:1 reference line represents perfect agreement, while the regression line and its 95% confidence band quantify the predictive performance of the GAP method. The strong correlation ($R^2 = 0.996$) and narrow confidence interval indicate high accuracy under maximum-flow conditions, with a systematic but limited underestimation of the extracted flowrate.

Figure 98 repeats the analysis for standard operating flowrates. The correlation remains positive, with $R^2 = 0.963$, but the predictive performance is weaker than in the maximum-flow scenario. The MAE increases to 2.05 l/s, and the RMSE rises to 2.44 l/s. Deviations from the 1:1 line are particularly evident for well P5, which exhibits the highest relative error. The wider 95% confidence band suggests increased variability and reduced predictive accuracy when wells operate at lower flowrates.

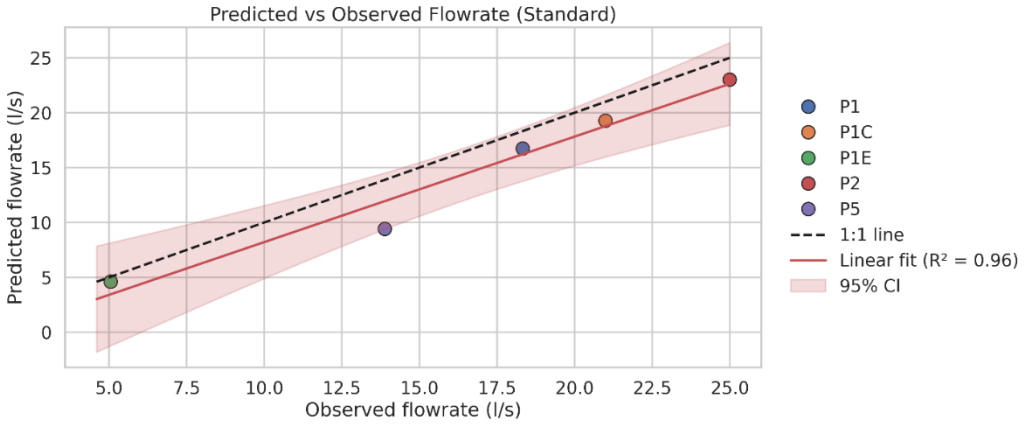

Figure 98. Predicted vs observed standard operating flowrates scatter plot. Although the correlation remains positive ($R^2 = 0.963$), deviations from the 1:1 line increase compared to the maximum-flow scenario, particularly for well P5. The wider 95% confidence band reflects greater variability and reduced predictive accuracy at lower pumping rates.

To complement the correlation analysis, Figure 99 and Figure 100 provide Bland–Altman plots for maximum and standard flowrates. For maximum flowrates (Figure 99), the mean difference between predicted and observed values is –1.92 l/s, with limits of agreement spanning approximately ±3.9 l/s around the bias. These relatively narrow limits indicate that prediction errors remain well-bounded across the full range of maximum flowrates. In contrast, the standard-flow Bland–Altman plot (Figure 100) shows a more pronounced negative bias (–2.05 l/s) and wider limits of agreement (approximately ±4.8 l/s), confirming that the method tends to underpredict more substantially under standard operating conditions. The increased dispersion at lower mean flowrates highlights the sensitivity of the method to local aquifer variability when pumping rates are reduced.

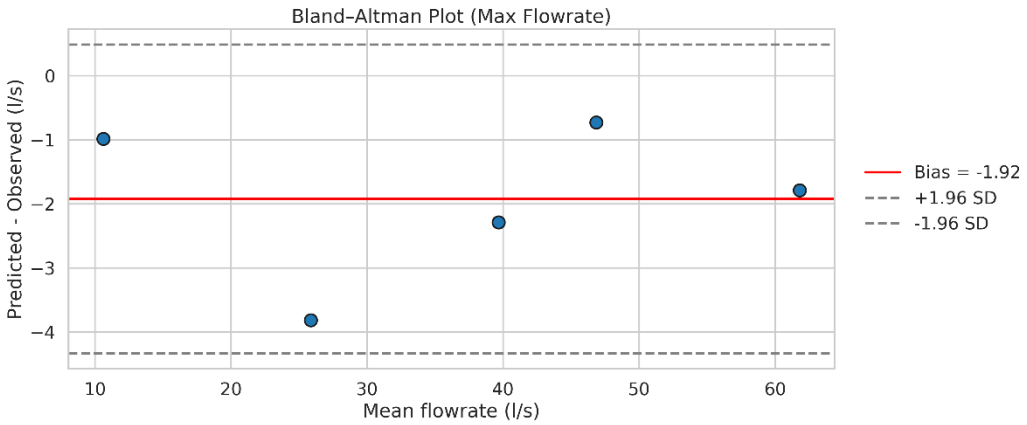

Figure 99. Bland–Altman plot for maximum flowrates showing the difference between predicted and observed values as a function of their mean. The mean bias (–1.92 l/s) indicates a slight systematic underestimation by the GAP method, while the relatively narrow limits of agreement (±1.96 SD) demonstrate that prediction errors remain well-bounded across the full range of maximum pumping conditions.

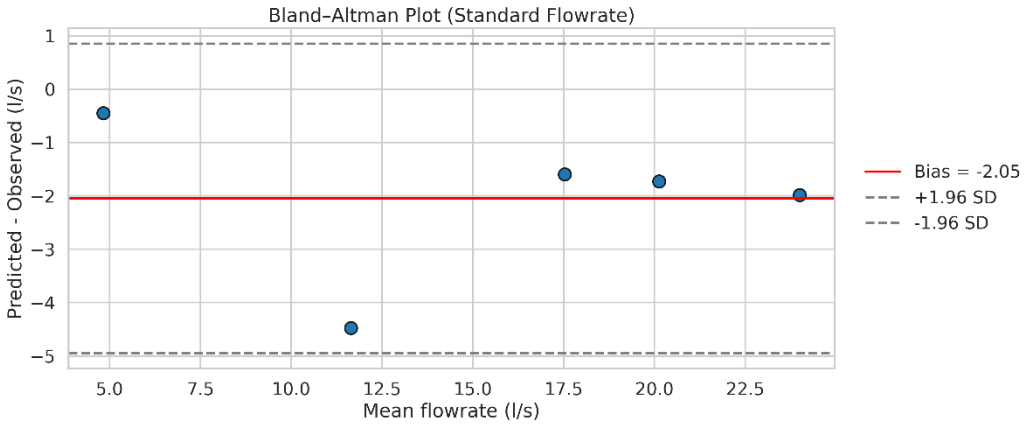

Figure 100. Bland–Altman plot for standard operating flowrates. The more pronounced negative bias (–2.05 l/s) and wider limits of agreement reveal increased dispersion and stronger underestimation under standard-flow conditions.

Figure 101 summarizes the RMSE values for each well under both scenarios. RMSE values for the maximum-flow scenario range from 0.73 l/s (P1) to 3.82 l/s (P5), while for the standard-flow scenario they range from 0.45 l/s (P1E) to 4.48 l/s (P5). In this representation, RMSE values are plotted as negative bars to visually emphasize the conservative nature of the GAP method, which systematically underestimates the extracted flowrate. This graphical choice highlights a key property of the method: it does not overestimate the available groundwater resource. From a resource-management perspective, such conservative behaviour is advantageous, as it reduces the risk of over-allocating groundwater volumes in urban geothermal planning.

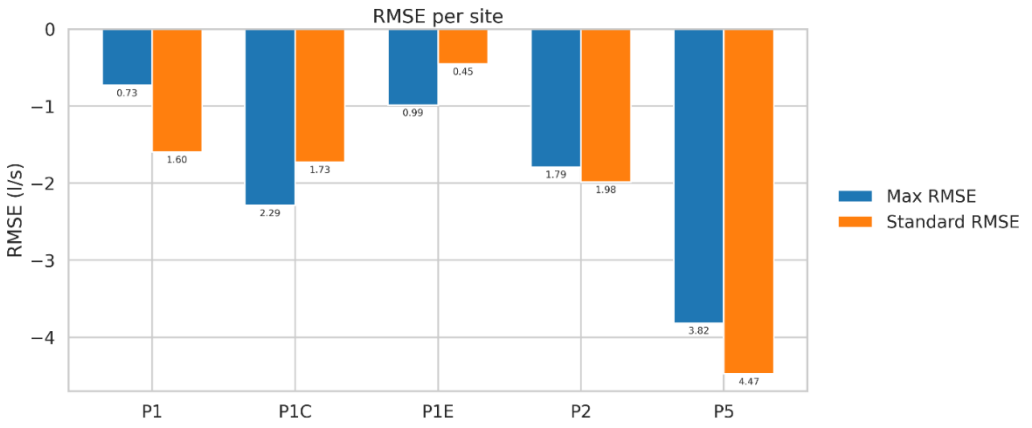

Figure 101. RMSE bar chart per site for maximum and standard flow scenarios. RMSE values are plotted as negative bars to visually emphasize the conservative nature of the GAP method, which systematically underestimates the extracted flowrate across all wells and scenarios.

The GAP method offers a rapid and accessible approach for preliminary assessment of open-loop geothermal potential over extensive urban areas. It leverages open-access data and QGIS platform, using techniques such as interpolation of hydrogeological parameters and simple analytical calculations to generate maps. Its modular design allows users to adjust key parameters (e.g. well separation distance, acceptable drawdown percentage, cell size) according to specific project requirements, facilitating sensitivity analyses without requiring advanced numerical modelling expertise. Furthermore, the workflow produces a structured geodatabase that can serve as input for detailed groundwater simulations (e.g., MODFLOW, FEFLOW), ensuring the time invested in data preparation also benefits more advance modelling efforts.

Notwithstanding the aforementioned advantages, the method introduces uncertainties at each interpolation stage, from kriging of hydraulic conductivity and piezometric surface to the estimation of aquifer thickness and hydraulic gradient. These cumulative errors are inherent to geospatial modelling and cannot be reduced within GAP itself, unlike in calibrated numerical models. Furthermore, the method treats each 50×50 m grid cell as hydraulically independent, using a simplified analytical solution (Thiem–Dupuit, Equation 3) that does not account for well interference or local heterogeneities. This assumption limits the method's accuracy, especially in densely developed or geologically complex areas. The use of fixed cell dimension also constrains spatial resolution: finer heterogeneities remain unresolved, while larger cells may obscure critical variations. Furthermore, the method assumes a standardised geothermal plant configuration, such as a fixed distance between the intake and discharge wells (50 m). Modifying this parameter would alter the calculated potential. However, such discretisation facilitates visual interpretation, enabling clear identification of zoned with low, moderate, or high potential. This categorisation supports planning decisions by simplifying complex data and enhancing the readability of maps stakeholders.

The primary strength of GAP lies in its operational efficiency and user-friendliness (Table 11). Professional with basic hydrogeological and GIS knowledge can produce high-resolution geothermal potential maps much faster than would be possible with full 3D numerical simulations. The capacity to quickly test variations in input parameters, such as drawdown limits or well spacing, empowers decision-makers to prioritise the most promising areas before undertaking expensive studies. Furthermore, GAP's use of open-source software and publicly available data fosters comprehensive transparency, reproducibility and accessibility for public agencies, consultants and academic institutions. In dense urban contexts, where space is limited and planning decisions are complex, GAP provides an effective screening tool to optimise the siting of open-loop systems, support retrofit strategies, and contributing to the broader transition toward renewable heating and cooling solutions.

Table 11. Strengths and limitations of GAP method.

Strengths	Limitations
Rapid Results: Simple analytical calculations via QGIS Field Calculator allow generation of high-resolution maps in minimal time.	**Uncertainty Propagation:** Errors from multiple interpolation steps (K, thickness, gradient) accumulate and cannot be reduced via calibration within GAP.
Parameter Flexibility: Key variables (well spacing, drawdown percentage, cell size) can be adjusted easily for sensitivity analyses.	**Cell Independence:** Each 50×50 m cell is treated as hydraulically isolated, so interference between adjacent cells or existing wells is not modeled.
Single-Platform Workflow: All data processing—from geodatabase creation to statistical interpolation and cartography—is performed in open-source QGIS.	**Simplified Analytics:** Relies on Thiem–Dupuit assumptions and uniform cell values, limiting accuracy in heterogeneous or densely exploited settings.
Geodatabase Ready for Numerical Models; Data preparation steps align with requirements of MODFLOW/FEFLOW, enabling seamless transition to detailed simulations if needed.	**Resolution Constraints:** Fixed grid size resolves only features ≥ cell dimension; finer heterogeneities remain unrepresented.
Broad Accessibility: Requires only hydrogeological and GIS skills—no advanced numerical modelling expertise—expanding potential user base.	
Preliminary Screening Tool: Ideal for rapid, large-area assessments to identify promising zones for geothermal open-loop installations before committing to resource-intensive numerical modelling.	

The results obtained from the MODFLOW modelling case studies align closely with published literature findings on open-loop GWHP aquifer behaviour, plume evolution, and system interaction. The thermal plume's length and width respond predictably to operational parameters (injection temperature and flow rate), groundwater velocity, aquifer geometry, dispersivity, and porosity, as highlighted in recent sensitivity analyses and numerical studies [76,189]. The observed longitudinal extension (up to 300 m) and rapid dissipation between operational cycles are typical of well-managed systems in transmissive urban aquifers [190]. The calibration approach employing Pilot Points and advanced inversion modelling ensures that local heterogeneity and hydrodynamic factors are captured, producing more accurate drawdown and thermal plume predictions than conventional zonation methods. The spatially distributed hydraulic conductivity field obtained through PEST-driven optimization reflects the complex depositional history of the Turin alluvial plain and enables the model to reproduce observed piezometric and temperature responses.

Real-time monitoring via multiparametric probes, validated through comparison with simulation results, demonstrates minimal risk of system interference or aquifer destabilization. The thermal anomalies traced by temperature time series (Figure 66) and mapped thermal plumes (Figure 67, Figure 68, and Figure 69) respect both regulatory limits and aquifer health thresholds. Maximum temperature increases of 3-4°C above background remain localized within 50-100 m of injection points, and the 16-17°C isotherms (representing 1-2°C increases) define the practical extent of measurable thermal impact at 200-300 m downstream. The absence of thermal interference between installations, even under conservative continuous operation assumptions, demonstrates that current system spacing is adequate for independent operation. This finding is significant for urban groundwater resource management, as it suggests that multiple geothermal systems can coexist within a shared aquifer if appropriate spacing is maintained and operational monitoring is implemented. Hydraulic interference was similarly absent, with localized drawdown and mounding effects (±0.01 to 0.1 m) attenuating rapidly with distance and showing no overlap between operational zones. This confirms that extraction and reinjection are hydraulically balanced at each site, minimizing net aquifer depletion and maintaining regional water budgets. The rapid hydraulic recovery observed during weekend shutdowns indicates high aquifer transmissivity and good connectivity, favorable characteristics for sustainable geothermal exploitation.

Future system expansions or operational adjustments should incorporate several critical considerations. First, ongoing multiparametric monitoring should be maintained and potentially expanded to capture vertical temperature stratification and long-term trends [191]. Second, numerical model refinement should be conducted periodically as additional data become available, particularly regarding cumulative and long-term impacts if operational intensity increases. Third, regulatory compliance with maximum permissible temperature changes (typically ±7°C from background) should be verified continuously through comparison of monitoring data with model predictions.

Finally, in the FEFLOW case studies, fundamental methodological distinction between the Turin North and South case studies, rigorous PESTPP-GLM calibration versus interpolation without calibration, has profound implications for model reliability and predictive confidence. The high-density pilot point parameterization strategy (1,137 pilot points) enabled flexible representation of aquifer heterogeneity while maintaining computational tractability through kriging interpolation between pilot point locations. This approach represents a significant advancement over traditional zonation methods, wherein hydraulic conductivity is assumed uniform within predefined geological units, and zone boundaries are often subjectively determined. The pilot point method allows hydraulic conductivity to vary continuously throughout the model domain according to patterns that emerge from the calibration process itself, rather than being constrained by prior geological interpretations that may not fully capture the complexity of fluvial depositional systems. However, several sources of uncertainty remain even in the rigorously calibrated Turin North model. First, the calibration targets only hydraulic head data; thermal parameters (volumetric heat capacity, thermal conductivity, thermal dispersivity) were specified based on literature values and limited site-specific measurements rather than being calibrated through comparison with observed temperature data. The absence of comprehensive thermal monitoring during the calibration period precludes rigorous validation of thermal transport predictions, introducing uncertainty regarding thermal plume extent, temperature distributions, and heat budget quantification. Second, the calibration represents a non-unique inverse problem: multiple different hydraulic conductivity distributions may yield comparable agreement with observed head data, particularly in areas distant from observation wells where parameter sensitivity is low. The calibrated parameter set should be interpreted as one realization that provides good agreement with observations, rather than a unique determination of true aquifer properties.

For the Turin South model, the absence of calibration introduces substantially greater uncertainty in all model predictions. The interpolated hydraulic conductivity field, derived from limited pumping test data and geological correlations, represents a reasonable first-order approximation but lacks the rigorous validation provided by systematic comparison with observed head data. Consequently, predictions of thermal plume extent, temperature distributions, and thermal recycling onset should be interpreted with appropriate caution, and comprehensive monitoring during initial operational phases is essential to validate model assumptions and implement adaptive management strategies if actual system behaviour diverges from predictions.

The contrasting results between the large-scale Turin North installations (300 l/s per plant, 8,860 kW thermal power) and the smaller Turin South systems (25-40 l/s per plant, 2,750 kW combined) highlight fundamental relationships between operational scale, well spacing, and system sustainability. The Turin North upstream plant, despite extracting more than three times the flow rate of all Turin South plants combined, exhibits no evidence of thermal recycling over the three-year simulation period, with intake well temperatures remaining stable at 15°C. In contrast, the Turin South installations, though operating at much smaller individual

scales, exhibit measurable thermal interference (less than 1°C temperature depression) within the five-year simulation period. This apparent paradox, wherein larger systems demonstrate greater sustainability than smaller systems, is resolved by recognizing the critical importance of wells spacing and aquifer characteristic. This depends not only on saturated thickness and porosity but also on hydraulic conductivity and associated groundwater velocity. These findings have critical implications for sustainable geothermal development strategies. High-transmissivity aquifer systems can support large-scale installations with substantial thermal extraction rates, provided that adequate well spacing is maintained to prevent thermal recycling. Lower-transmissivity systems require more conservative approaches, including reduced extraction rates, increased well spacing (which may be spatially constrained in urban settings), or hybrid operational strategies such as seasonal aquifer thermal energy storage (chapter 4 ATES) that balance heating and cooling loads to minimize net thermal deficit.

The methodological framework presented for open-loop systems in the Turin alluvial aquifer demonstrates particular strengths under conditions of moderate to high hydraulic conductivity, unconfined aquifer geometry, and stable regional hydraulic gradients. However, the sustainability and operational viability of open-loop systems are critically dependent on site-specific hydrogeological characteristics, necessitating careful evaluation when considering deployment in alternative geological contexts. A substantial body of literature documents the challenges associated with open-loop GWHP deployment in fractured rock systems, particularly granite, gneiss, and metamorphic formations prevalent in Alpine and pre-Alpine regions. In these environments, groundwater occurrence is controlled by fracture aperture, fracture density, and orientation rather than matrix porosity. Consequently, aquifer yield estimation becomes significantly more uncertain, and groundwater flow paths are inherently anisotropic and often poorly characterized. The thermal plume behaviour in fractured media differs fundamentally from porous media: thermal breakthrough may occur more rapidly due to preferential flow along fracture networks, and thermal recovery may be substantially reduced due to the limited contact area between circulating water and rock matrix. Carbonate formations including limestone and dolomite present distinct challenges and opportunities for open-loop systems. These aquifers typically exhibit high transmissivity due to secondary porosity created by dissolution, enabling substantial water extraction. However, the high hydraulic conductivity (often $>1.0\times10^{-3}$ m/s) combined with conduit-dominated flow patterns creates conditions conducive to rapid thermal plume migration and potential upstream thermal recycling. Additionally, karst phenomena including sinkholes, losing streams, and preferential recharge zones introduce complexity in groundwater tracing and thermal plume prediction. In such environments, numerical modelling incorporating fracture networks and preferential flow paths becomes essential; analytical methods assuming homogeneous porous media flow grossly underestimate thermal plume extent. The Turin case study focuses on unconfined aquifer conditions where recharge is direct and water table fluctuations influence seasonal thermal response. In contrast, confined aquifers protected by

thick clay aquitards present fundamentally different scenarios. These systems typically exhibit slower thermal plume migration due to reduced advective transport, enabling longer operational life before thermal breakthrough. However, they also present regulatory and practical challenges: drilling costs increase substantially with depth, water quality may be more variable, and regulatory restrictions typically protect deeper aquifers to preserve water supplies. The GAP methodology developed in this thesis, based on shallow unconfined aquifer assumptions, would require modification for confined aquifer applications. Semi-confined situations, where multiple aquifer layers are present with moderate vertical conductivity (as in the Turin subsurface), require multi-layer numerical models like those demonstrated in Chapter 2.5.2, with careful attention to cross-formational flow and potential thermal migration between aquifer units. The three-tier analytical framework (GAP, MODFLOW, FEFLOW) developed for Turin demonstrates robust transferability to alternative hydrogeological contexts.

2.7 Conclusion & Further Investigation

The comprehensive analysis presented in this chapter, integrating regulatory frameworks, methodological innovations, and detailed numerical case studies, establishes that open-loop groundwater heat pump systems represent a technically viable, environmentally sustainable, and strategically important renewable energy resource for urban decarbonization, provided that deployment occurs within carefully designed governance, technical, and monitoring frameworks that ensure long-term groundwater resource protection.

The European-national-regional regulatory cascade, from Water Framework Directive 2000/60/EC through Italian Legislative Decree 152/2006 to Piedmont Regional implementation instruments, establishes a comprehensive but complex governance framework that simultaneously promotes renewable energy deployment (RED II/III directives) while maintaining rigorous groundwater protection standards. The AUA, introduced through Presidential Decree 59/2013, attempts to streamline permitting but continues to require substantial technical documentation, particularly for large installations (exceeding 10 l/s discharge), including three-year thermal plume modelling, demonstration of absence of feasible discharge alternatives, downstream piezometer installation, and annual monitoring reporting.

The GAP methodology, demonstrates that shallow unconfined aquifers in alluvial urban settings possess substantial geothermal potential capable of supporting district-scale heating and cooling applications. The validation demonstrates that the GAP method provides robust and conservative estimates of abstraction flowrates under maximum pumping conditions and reasonably accurate predictions under standard operating conditions. The systematic underestimation observed across all wells and scenarios, bias values of –1.92 l/s (max) and –2.05 l/s (standard), is a desirable feature for preliminary assessments, as it ensures that the method does not overpredict the exploitable resource. However, the limited number of monitoring points and their concentration within a single university campus represent a significant constraint. A more comprehensive validation across the wider urban area of Turin would require additional datasets, including measurements from private and municipal geothermal installations. Until such data become available, the results presented here should be interpreted as an initial but incomplete assessment of the method's performance, highlighting both its potential and the need for further data collection to support city-wide application.

The Turin metropolitan area exhibits thermal power potential ranging from 5-20 kW per well doublet in zones with thin aquifers (Class 1, suitable for single-family homes) to exceeding 500 kW in high-transmissivity zones (Class 6, suitable for multi-building districts or neighborhood-scale networks). This spatial heterogeneity, characteristic of fluvial-glacial depositional environments, necessitates site-specific hydrogeological characterization rather than relying on regional average parameters for system design.

The MODFLOW urban-scale cumulative impact assessment, simulating 154 existing installations across Turin, confirms that properly designed and spatially distributed open-loop systems can operate without creating significant hydraulic or thermal interference over multi-year operational periods. However, scenarios with high extraction rates and extended operational seasons demonstrate potential for cumulative thermal impacts that could affect downstream installations, emphasizing the critical importance of strategic spatial planning and cumulative thermal budgeting at the aquifer sector scale.

The FEFLOW site-specific case studies reveal fundamental scale-dependent relationships between aquifer properties, well spacing, and system sustainability. The Turin North installations, exploiting high-transmissivity aquifers (hydraulic conductivity up to 1.16×10^{-2} m/s) and hundreds of metres of spacing, successfully sustain large-scale extraction (300 l/s per plant, 8,860 kW thermal power) without thermal recycling over three-year operational periods. In contrast, the Turin South installations, constrained by lower transmissivity (maximum 4.91×10^{-3} m/s), and tens of metres of spacing, exhibit incipient thermal recycling (less than 1°C temperature depression) after five years despite substantially smaller operational scales (25-40 l/s per plant, 2,750 kW combined). This apparent paradox underscores that system sustainability depends primarily on aquifer advective thermal capacity (product of transmissivity, hydraulic gradient, and saturated thickness) and well spacing rather than absolute extraction magnitude.

The integration of MODFLOW and FEFLOW modelling platforms provides complementary capabilities: MODFLOW's computational efficiency enables urban-scale cumulative assessment of dozens to hundreds of installations, while FEFLOW's advanced finite element discretization enable representation of complex aquifer heterogeneity and rigorous parameter uncertainty quantification.

Open-loop geothermal systems offer multiple strategic advantages for urban decarbonization that extend beyond simple thermal energy delivery and barriers summarise in **Table 12**. The table organizes factors across five dimensions: technical performance, spatial planning, economic considerations, social impacts, and regulatory frameworks. Advantages (left column) highlight the strategic value proposition, while barriers (right column) identify systematic challenges requiring policy interventions and technical solutions for widespread deployment.

Table 12. Comparative assessment of advantages and barriers for open-loop geothermal systems in urban decarbonization contexts.

Dimension	✓ ADVANTAGES	✗ BARRIERS
TECHNICAL AND PERFORMANCE	**Superior system efficiency**: COP 4-6 vs. air-source heat pumps COP 2.5-4	**Insufficient hydrogeological data:** Comprehensive aquifer characterization requires substantial public investment in monitoring networks
	Reliable year-round performance: Stable groundwater temperature (14-16°C) eliminates degradation during extreme weather	-
	Dual heating-cooling capability: Bidirectional operation addresses both winter heating and increasing summer cooling demands	-
	District heating compatibility: Integration with fourth-generation networks (50-70°C supply temperature) reduces distribution losses	-
SPATIAL AND URBAN PLANNING	**Minimal surface footprint**: Subsurface infrastructure avoids conflicts with limited urban surface area	**Spatial constraints**: Adequate well spacing may be difficult to achieve in dense urban areas
	Retrofit compatibility: Integration with existing buildings through basement or green areas	**Subsurface conflicts**: Potential interference with metro tunnels, utility networks, and other underground infrastructure
	Distributed generation: Reduces transmission infrastructure needs compared to centralized systems	**Cumulative impact management**: Multiple installations in same aquifer require coordinated spatial planning
ECONOMIC AND FINANCIAL	**Lower operational costs**: Reduced expenses vs. fossil fuels with 8-15 year payback periods	**High upfront capital costs**: drilling and installation expenses create financing barriers

Dimension	✓ ADVANTAGES	✗ BARRIERS
ECONOMIC AND FINANCIAL	**Favorable lifecycle economics**: Long operational lifetime (20-30 years) with minimal maintenance	**Insufficient financial incentives**: Lack of feed-in tariffs and tax credits comparable to solar and wind systems
SOCIAL AND ENERGY SECURITY	**Enhanced energy security**: Indigenous renewable resource reduces import dependence	**Social acceptance challenges**: Concerns about groundwater impacts and environmental risks
	Climate resilience: Load-independent performance during heat waves and cold snaps when grid stress is maximum	-
REGULATORY AND GOVERNANCE	**Renewable energy alignment**: Supports RED II/III directives and national decarbonization targets	**Complex authorization procedures**: Multi-agency approvals extend permitting to 12-24 months
	Environmental compatibility: Proper design enables operation within groundwater protection standards	**Risk-averse regulatory interpretation**: Absence of precedents encourages overly conservative restrictions
	Cumulative monitoring potential: Operational data can improve regional hydrogeological knowledge	**Fragmented governance**: Overlapping municipal, provincial, regional, and basin authorities create coordination difficulties

Open-loop groundwater heat pump systems represent a mature, technically proven, and strategically critical renewable energy technology capable of delivering substantial contributions to urban heating and cooling decarbonization targets established under the European Green Deal and national climate commitments. The shallow alluvial aquifers characteristic of many European urban areas, including Turin and comparable Po Valley cities, possess exceptional thermal capacity (Class 4-6 potential supporting 100-500+ kW installations) when exploited through properly designed systems incorporating adequate well spacing (500-1,000 meters), rigorous hydrogeological characterization, and adaptive monitoring.

The methodological framework established in this chapter, progressing from rapid GAP screening through urban-scale MODFLOW cumulative assessment to detailed FEFLOW site-specific validation with rigorous pilot point calibration, provides a replicable, scientifically defensible decision support system applicable to urban geothermal development globally. The open-access implementation using QGIS and public-domain modelling codes (MODFLOW 6, PEST++) democratizes

access to sophisticated assessment tools, enabling municipalities and regional authorities to conduct strategic planning without prohibitive consulting costs.

Realizing the full potential of urban open-loop geothermal systems requires integrated governance reforms addressing current fragmentation: streamlined permitting through designated "geothermal acceleration zones" (as envisioned in RED III), establishment of clear quantitative cumulative impact thresholds, development of public hydrogeological databases enabling informed cumulative assessment, and financial incentive alignment with other renewable technologies. The Council Conclusions on Geothermal Energy Promotion (December 2024) provide political momentum for these reforms, calling for a European Geothermal Action Plan and harmonization of regulatory procedures across Member States.

The question is not whether open-loop systems can sustainably contribute to urban energy transitions, but rather how to optimize deployment patterns, governance frameworks, and monitoring infrastructures to maximize renewable energy delivery while maintaining rigorous groundwater resource protection. The Turin case study demonstrates that with appropriate technical design, regulatory oversight, and adaptive management, urban aquifers can support large-scale geothermal exploitation over multi-decadal timeframes without compromising either groundwater resource sustainability or system thermal performance. This achievement positions open-loop geothermal systems as an indispensable component of the diversified renewable energy portfolio required to achieve climate neutrality by 2050 while respecting the essential character of groundwater as a common heritage resource requiring careful stewardship for present and future generations.

Chapter 3

Closed-loop

"[…] This theory of the phenomena
we had witnessed seemed satisfactory to me;
for however great and stupendous the phenomena of nature,
fixed physical laws will or may always explain them."

Jules Verne (1864)[5]

Closed-loop geothermal systems utilise sealed underground heat exchanger networks to exploit subsurface thermal stability for building heating and cooling without direct groundwater contact. The treatment establishes fundamental operating principles, heat transfer mechanisms across multiple temporal scales, and thermal interference phenomena constraining multi-borehole installations. Ground thermal properties, thermal conductivity, diffusivity, and volumetric heat capacity, fundamentally determine system performance and long-term sustainability. Two analytical methodologies are presented: the simplified VDI 4640 approach, discussed for contextual understanding of small-scale installations using tabulated heat extraction rates, and the comprehensive ASHRAE methodology, which is employed for all system sizing calculations. The ASHRAE framework, based on cylindrical source theory, incorporates temporal load variations through superposition of thermal resistance components across daily, monthly, and annual time scales, explicitly accounts for thermal interference through temperature penalty calculations weighted by borefield geometry, and establishes hydraulic design criteria through Reynolds number analysis. Two case studies in the Turin metropolitan area demonstrate practical application. A commercial building with mixed heating and cooling reveals that cooling mode typically governs sizing despite balanced annual energy consumption due to fundamental thermodynamic asymmetries in heat pump operation. A large-scale industrial heating application with continuous operation explores multiple borefield configurations ranging from deep borehole strategies minimizing land requirements to shallow multiple borehole approaches optimizing hydraulic performance, revealing fundamental trade-offs between capital costs, operational efficiency, land area constraints, and thermal interference penalties.

[5] *Journey to the Center of the Earth, Chapter XXXVII 'The Liedenbrock Museum', Jules Verne, (1864).*

3.1 Overview

Closed-loop geothermal systems, also referred to as ground-coupled heat pump (GCHP) systems or borehole heat exchanger (BHE) systems, represent a highly efficient and sustainable renewable energy technology that exploits the thermal stability of the subsurface for building heating and cooling applications [192,193]. These systems consist of a sealed circulation network buried underground, facilitating heat exchange with the surrounding ground through a continuously circulating heat transfer fluid, without direct contact with groundwater resources [194]. This fundamental characteristic distinguishes closed-loop systems from open-loop alternatives, precluding the necessity for groundwater extraction or reinjection, thereby making such systems less invasive from a regulatory and environmental perspective [195,196].

The fundamental components of a closed-loop geothermal system comprise several integrated subsystems that function synergistically to enable efficient thermal energy exchange with the subsurface. The primary heat exchange mechanism consists of high-density polyethylene (HDPE) pipes arranged in various configurations, most commonly the double-U configuration for vertical borehole installations. The double-U configuration (**Figure 102** B) employs four individual pipes connected to form two parallel flow paths within a single borehole, maximizing heat transfer surface area while maintaining structural integrity and installation feasibility [197,198]. This configuration has been demonstrated to provide 26-29% higher thermal efficiency compared to single U-tube (**Figure 102** A) arrangements due to the increased contact area between the heat transfer fluid and the surrounding ground. Alternative configurations include single U-tubes, coaxial heat exchangers (**Figure 102** C, and **Figure 102** D), and spiral configurations, each offering distinct advantages depending on geological conditions, borehole depth, and thermal performance requirements [199–202].

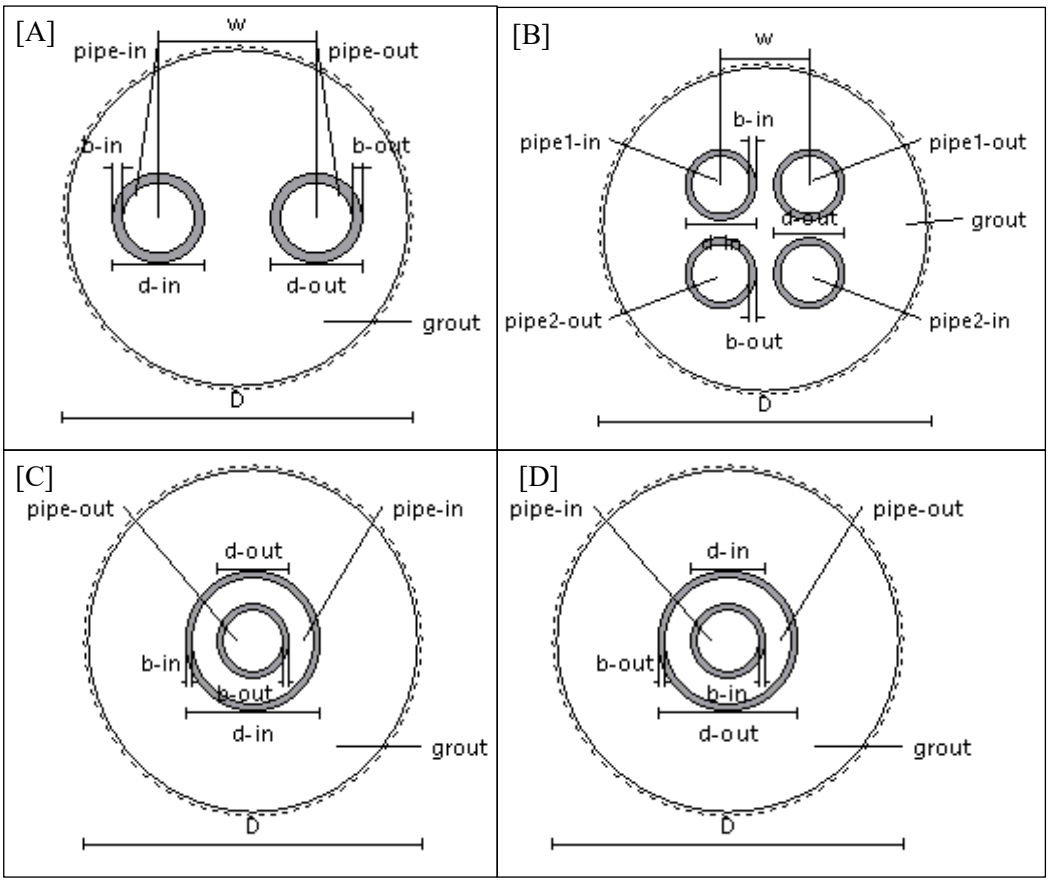

Figure 102. BHE configuration available in FEFLOW: [A] Single U-shape; [B] Double U-shape; [C] Coaxial (anular intlet); [D] Coaxial (centered inlet).

The pipe material selection is critical for long-term system performance and durability. HDPE pipes with typical outer diameters ranging from 25 to 40 mm (DN20 to DN32) exhibit excellent chemical resistance, mechanical strength, and thermal stability over the operational lifetime of the system, typically 25-50 years [203,204]. The thermal conductivity of HDPE, approximately 0.40-0.50 W/(m·K), represents a thermal resistance component that must be carefully considered in system design calculations [205,206]. The thermal interface between the heat exchanger pipes and the surrounding ground is established through careful borehole construction and grouting procedures. The borehole diameter, typically ranging from 100 to 150 mm depending on pipe configuration and geological conditions, must accommodate the pipe assembly while minimizing material usage and drilling costs [207]. The annular space between the pipe configuration and the borehole wall, typically 20-40 mm in radial thickness, is filled with specialized grout material that serves multiple critical functions [208]. The grout material must provide structural support to maintain proper pipe positioning, prevent vertical groundwater migration along the borehole annulus, protect groundwater resources from surface contamination, and establish efficient thermal coupling between the pipes and the surrounding ground formation. Traditional cement-based grouts exhibit thermal conductivities in the range of 0.7-1.2 W/(m·K), while thermally enhanced grouts incorporating additives such as silica sand, graphite, or specialized minerals can

achieve thermal conductivities of 2.0-3.0 W/(m·K) or higher [207]. The selection of grout thermal conductivity represents a critical design parameter, as increasing grout thermal conductivity from 1.0 to 2.5 W/(m·K) can reduce required borehole length by 15-25% for equivalent thermal performance. Recent research has demonstrated that grout thermal conductivity improvements beyond 4-5 W/(m·K) provide diminishing returns, as the soil thermal resistance becomes the limiting factor in overall system performance. Furthermore, thermally enhanced grouts incorporating high specific heat capacity in addition to high thermal conductivity provide superior performance under intermittent operation modes, which better represent actual building heating and cooling load profiles [208].

In multi-borehole installations, thermal interference between adjacent heat exchangers represents a critical design consideration that significantly influences long-term system performance and sustainability [209,210]. The degree of thermal interference depends on multiple factors: borehole spacing (typical practical recommendations report minimum spacings on the order of 5–8 m in compact fields, with larger spacings advised for high-load or long-duration operations), operational patterns (continuous vs. intermittent operation, heating-dominated vs. cooling-dominated or thermally balanced regimes), ground thermal properties (in particular thermal diffusivity, which controls the radial thermal penetration and temporal evolution of the thermal plume), and system configuration (hydraulic circuit arrangement, i.e. series versus parallel connections, which alters per-borehole flow rate, inlet/outlet temperatures and thus local thermal gradients) [211–213].

The economic viability of closed-loop geothermal systems depends on the balance between higher initial capital costs (primarily borehole drilling and installation) and reduced operational costs through improved energy efficiency [214,215]. Recent technological developments in drilling technology, improved design methodologies, policy incentives, and increasing conventional energy costs have progressively improved the economic competitiveness of geothermal heat pump systems across diverse applications and geographic contexts [216].

3.2 Regulatory Framework

The regulatory framework governing closed-loop geothermal systems has evolved significantly across European, national and regional levels, reflecting the growing recognition of shallow geothermal energy as a sustainable solution for building heating and cooling. At the European level, harmonisation initiatives aim to establish common technical standards, environmental protection requirements, and administrative procedures to facilitate cross-border technology transfer and market development [217]. These efforts concentrate on establishing uniformity across member states whilst respecting national sovereignty and local conditions, acknowledging that excessive regulatory intricacy has the potential to hinder the adoption of renewable energy sources and that inadequate oversight may compromise environmental protection or system performance [218].

In Italy, the regulatory evolution has undergone significant development through the implementation of Legislative Decree No. 22 of February 11, 2010, which established a national reorganization of the regulatory framework concerning the exploration and exploitation of geothermal resources [92]. The decree defines small local geothermal heat utilisations as those that simultaneously satisfy specific conditions. These conditions include the construction of plants with thermal power below 2 MW, obtained from geothermal fluid at a conventional effluent temperature of 15 degrees Celsius, and obtained through the drilling of wells up to 400 metres for exploration, extraction, and utilisation of geothermal fluids or hot water for a total thermal power not exceeding 2,000 kW. The decree explicitly includes closed-loop systems among small local uses of geothermal heat and establishes that closed-loop geothermal probe plants are not subject to mining regulations pursuant to Royal Decree No. 1443 of 1927 and Article 826 of the Civil Code, thereby recognising the fundamental difference between closed-loop systems and traditional geothermal extraction.

The most significant regulatory advancement occurred with the Legislative Decree enacted on 30 September 2022, known as the Geothermal Probes Decree, which represents the first effective instrument to formalise and regulate the implementation of closed-loop geothermal plants [93]. This decree applies to small local utilisations and establishes requirements for the installation of plants for heating and air conditioning of buildings, identifying cases where the implementation of such plants, up to a thermal power of 100 kW, falls under either the free construction regime or the simplified authorization procedure pursuant to Article 6 of Legislative Decree No. 28 of 2011 [219]. Prior to this decree, geothermal probes were subject to Decree January 22, 2008, No. 37, which generally addressed the installation of systems within buildings. However, this decree was not specific to geothermal installations, necessitating regional adaptation with local regulations. The 2022 decree establishes a two-tier regulatory system based on system characteristics and installation parameters. In the context of the free construction regime, installations are required to adhere to stringent technical specifications with the objective of minimising environmental impact and ensuring system reliability. Geothermal probes may be extended horizontally to a

depth of 2 metres from ground level or vertically to a depth of 80 metres from ground level, with a thermal power limitation of 50 kW. The installations in question are required to serve existing buildings without altering volumes or surfaces, without modifications to usage designations, without interventions on structural elements, and without increasing the number of housing units or urban planning parameters.

The Simplified Authorisation Procedure (PAS) extends the regulatory framework to accommodate larger installations, allowing horizontal geothermal probes to extend to depths not exceeding 3 metres from ground level and vertical probes to reach depths up to 170 metres. Thermal power thresholds are increased to 100 kW in order to accommodate larger residential complexes, commercial buildings, and small industrial applications. The regulatory framework incorporates specific technical requirements for system design and installation procedures, with a particular emphasis on environmental protection through groundwater protection requirements, thermal impact limitations, and geological stability considerations. For plants equipped with closed-circuit geothermal probes and thermal power ranging from 50 kW to 100 kW, design procedures may employ Thermal Response Tests (TRT) to assess subsurface thermal parameters or conduct comprehensive survey campaigns. Conversely, installations with thermal power below 50 kW may resort to previously conducted studies as alternatives to new investigations, provided such studies adhere to prevailing technical standards. The national regulatory framework allocates specific implementation responsibilities to regional and autonomous provincial authorities. These authorities are responsible for the electronic registration of interventions within their respective territories, as well as the establishment of verification procedures to ensure the congruence between submitted data and actual installations.

At the regional level, the Piedmont region has a regulatory framework that is aligned with national objectives, but which also includes specific provisions aimed at the valorisation of local resources. The regulatory foundation for energy resource management is provided by Regional Law 23/2002. The promotion of the use of renewable sources and energy efficiency is a key element of this law, as is the definition of regional energy planning as an instrument to favour the transition towards a sustainable energy system. In this context, geothermal systems are to be fully utilised. The Region has implemented measures to encourage the adoption of low-emission technologies through the Regional Air Quality Plan (PRQA), which is currently undergoing an update that commenced on 12 September 2024. The PRQA offers incentives for the utilisation of geothermal systems as a substitute for fossil fuels for heating purposes, thereby contributing to the enhancement of air quality. Specific financing schemes, co-financed by the Regional Operational Program of the European Regional Development Fund (POR FESR), have been implemented to support the adoption of these innovative technologies, with particular reference to their integration in urban and industrial energy efficiency projects. Notwithstanding the advantageous regulatory framework, the implementation of geothermal projects in Piedmont may be impeded by intricate authorisation procedures and the paucity of detailed hydrogeological and geological

data. However, the Region is adopting targeted strategies to streamline regulatory processes and promote the establishment of geological data sharing platforms to facilitate the planning and development of new projects. The regulatory experience of Italy with closed-loop geothermal systems provides valuable insights for European harmonisation efforts. The Italian experience demonstrates effective approaches to balancing environmental protection, administrative efficiency, and technology promotion through a tiered regulatory system that accommodates diverse system scales while maintaining appropriate oversight and environmental safeguards. This comprehensive regulatory framework ensures that closed-loop geothermal installations maintain compatibility with existing environmental conditions while promoting the sustainable development of shallow geothermal energy systems across multiple administrative levels.

3.3 Methodology

This chapter provides a comprehensive analysis and detailed design of a closed-loop geothermal system. The analysis and design are carried out utilizing a rigorous analytical approach with the ASHRAE methodology as presented in Appendix A of UNI 11466:2012, the national reference standard for the sizing of vertical borehole heat exchanger (BHE) systems. The simplified procedure, based on the VDI 4640 guidelines, is also presented as a suitable methodology. Nevertheless, it was not utilised in the case studies presented, as these exceed the minimum power requirements. However, it is a valid method employed for small-scale systems and is therefore mentioned and presented as a possibility in the dimensioning of BHE.

The system design is centred on the optimisation of the number and depth of geothermal boreholes, in accordance with spatial constraints and the requisite thermal performance. The core dimensioning equations from VDI 4640 and UNI 11466 are applied systematically, with all calculations executed in Microsoft Excel. These analyses yield preliminary results for the closed-loop system's sizing. Nevertheless, in order to enhance the fidelity of system modelling, especially with regard to the impact of local groundwater flow, numerical modelling will be necessary, as water movement has been shown to considerably affect the efficiency of closed-loop systems where aquifers with moderate velocities are present.

3.3.1 VDI

VDI 4640 is a widely adopted methodology for preliminary sizing of borehole heat exchangers (BHEs) in shallow geothermal systems [220]. The VDI 4640 standard provides a systematic approach for the design and dimensioning of closed-loop geothermal systems, offering both simplified methods for small installations and more sophisticated approaches for larger systems. The VDI 4640 guideline establishes distinct design approaches based on the scale and complexity of the geothermal installation. The methodology delineates between small systems with heating capacities up to 30 kW and larger installations exceeding this threshold. The guideline provides tabulated values for specific heat extraction rates and nomographic tools for preliminary sizing of small systems (**Table 13**). These tools enable rapid sizing without the need for complex computational analyses.

The simplified approach is applicable to installations that meet specific technical constraints, such as borehole lengths ranging from 40 to 100 metres, minimum inter-borehole distances of 5 metres for depths of 40-50 metres and 6 metres for depths exceeding 50 metres, exclusive heat extraction operation (no cooling), and utilisation of double U-pipes with diameters DN20, DN25, or DN32, or coaxial heat exchangers with diameters exceeding 60 mm [221]. The validity of the tabulated extraction rates is ensured by these parameters, which also prevent thermal interference between adjacent boreholes. For systems with a heating capacity in excess of 30 kW or an annual operating duration exceeding 2400 full-load hours, the VDI 4640 necessitates the implementation of more advanced analytical or numerical calculation methodologies [222]. This requirement acknowledges the increased complexity and thermal interactions present in larger installations, where simplified tabulated values may lead to inadequate system performance or oversizing.

Table 13. Different values of underground (W/m) from [220].

underground	spec. extraction rate	
	for 1800 h	for 2400 h
general figures:		
bad underground (λ <1,5 W/m/K)	25W/m	20 W/m
regular rock and water saturated sediments (λ =1,5 - 3,0 W/m/K)	65 W/m	50 W/m
rock λ > 3,0 W/m/K	84 W/m	70 W/m
different underground:		
gravel, sand dry	<25 W/m	<20 W/m
gravel, sand water-saturated	65 – 80 W/m	55 – 65 W/m
clay, loam humid	35 – 50 W/m	30 – 40 W/m
limestone (massive)	55 – 70 W/m	45 – 60 W/m
sandstone	65 – 80 W/m	55 – 65 W/m
acid magmatites (e.g. granite)	65 – 85 W/m	55 – 70 W/m
basic magmatites (e.g. basalt)	40 – 65 W/m	35 – 55 W/m
gneiss	70 – 85 W/m	60 – 70 W/m
high groundwater-flow in gravel/sand for single systems		80 – 100 W/m

The methodology's core component involves the extraction rates of specific heat, expressed in watts per metre of borehole length (W/m), which correlate directly with the geological and hydrogeological characteristics of the installation site. The VDI 4640 acknowledges the significant influence of groundwater presence on thermal performance. The standard differentiates between dry and water-saturated conditions for unconsolidated sediments, acknowledging that water saturation substantially increases thermal conductivity and heat extraction potential. For instance, dry gravel and sand formations typically yield extraction rates below 25 W/m for 1800 operating hours, while water-saturated equivalents can achieve 65-80 W/m under similar conditions. This differentiation is indicative of the enhanced heat transfer mechanisms present in saturated formations, where groundwater movement can contribute significantly to convective heat transport in addition to pure conduction [223]. The methodology incorporates two operational scenarios based on annual full-load hours: 1800 hours and 2400 hours represent divergent heating demand profiles and system utilisation patterns. An increase in the operational hours of the system has been shown to result in a reduction in specific extraction rates due to the increased thermal depletion of the surrounding ground. This temporal consideration ensures sustainable long-term operation while preventing excessive ground temperature depression that could compromise system efficiency.

The total required borehole length for simplified VDI approach is calculated using:

Equation 25

$$L_{total} = \frac{Q_h}{q_s}$$

Where L_{total} is the total required borehole length [m], Q_h is the peak heating capacity of heat pump [W], q_s is the specific heat extraction rate [W/m] selected from tabulated values based on geological conditions and operating hours.

3.3.2 ASHRAE

The ASHRAE methodology, as implemented in standards including UNI 11466:2012 and documented in ASHRAE design guides, provides a rigorous analytical framework based on cylindrical source theory for precise borehole heat exchanger sizing [224]. This approach accounts for temporal variations in building loads across multiple time scales and provides high accuracy for complex installations including both heating and cooling applications [225].

The fundamental formula for total BHE length is:

Equation 26

$$L_h = \frac{\left\{\dot{Q}_a \cdot R_{ga} + \dot{Q}_{g,h_D} \cdot \left[R_b + (PLF_{m,h_D} \cdot R_{gm}) + (R_{gd} \cdot F_{sc})\right]\right\}}{\left[\theta_g - \left(\frac{\theta_{wi} + \theta_{wo}}{2}\right)_{h_D} - \theta_p\right]}$$

$$L_c = \frac{\left\{\dot{Q}_a \cdot R_{ga} + \dot{Q}_{g,c_D} \cdot \left[R_b + (PLF_{m,c_D} \cdot R_{gm}) + (R_{gd} \cdot F_{sc})\right]\right\}}{\left[\theta_g - \left(\frac{\theta_{wi} + \theta_{wo}}{2}\right)_{c_D} - \theta_p\right]}$$

where:

- $\mathbf{L_h}$ **:** is the BHE total length calculated for heating mode [m]
- $\mathbf{L_c}$ **:** is the BHE total length calculated for cooling mode [m]
- $\dot{\mathbf{Q}}_a$ **:** is the average heat flow exchanged with the ground over the year [W]
- $\dot{\mathbf{Q}}_{g,h_D}$**:** is the design heat output on the ground side during the heating season [W]
- $\dot{\mathbf{Q}}_{g,c_D}$**:** is the design heat output on the ground side during the cooling season [W]
- $\mathbf{PLF}_{m,h_D}$**:** is the partial load factor in the design heating month
- $\mathbf{PLF}_{m,c_D}$**:** is the partial load factor in the design cooling month
- $\mathbf{F}_{sc}$**:** is the loss factor for possible thermal short-circuiting in the ground heat exchanger between the flow pipe and the return pipe
- $\mathbf{R}_b$**:** is the equivalent thermal resistance per unit length of the heat exchanger corresponding to the heat exchange between the heat transfer fluid and the borehole surface (interface surface between the borehole fill and the ground) $\left[m\ \frac{K}{W}\right]$
- $\boldsymbol{R_{ga}}$**:** is the effective thermal resistance of the ground, per unit length, referred to the annual impulse $\left[m\ \frac{K}{W}\right]$
- $\mathbf{R}_{gm}$**:** is the effective thermal resistance of the ground, per unit length, referred to the monthly impulse $\left[m\ \frac{K}{W}\right]$
- $\mathbf{R}_{gd}$**:** is the effective thermal resistance of the ground, per unit length, referred to the daily impulse $\left[m\ \frac{K}{W}\right]$
- $\boldsymbol{\theta_g}$**:** is the temperature of the undisturbed ground (not affected by heat exchange) [C°]

- $\boldsymbol{\theta_{wi}}$**:** is the temperature of the heat transfer fluid entering the ground heat exchanger (temperature at the heat pump outlet) under design conditions [C°]
- $\boldsymbol{\theta_{wo}}$**:** is the temperature of the heat transfer fluid leaving the ground heat exchanger (temperature entering the heat pump) under design conditions [C°]
- $\boldsymbol{\theta_{p}}$**:** is the penalty temperature (parameter indicating the temperature variation of the ground) [C°]

Each term has a specific physical meaning and will be analysed in detail individually.

Following Eq. A.9 of UNI 11466 [224], the mean annual ground heat exchange is:

Equation 27

$$\dot{Q}_a = \frac{\left[Q_{h,hp,out_D} \cdot \left(1 - \frac{1}{COP_{ms}}\right) \cdot \tau_h + Q_{c,hp,out\ D} \cdot \left(1 - \frac{1}{EER_{ms}}\right) \cdot \tau_c\right]}{8760}$$

where the terms τ_h and τ_c represent, respectively, the number of equivalent full-load hours per year of the heating and cooling system, calculated using the following equations:

Equation 28

$$\tau_h = \frac{\sum_{i=1}^{12} Q_{h,hp,out_i}}{\dot{Q}_{h,hp,out_D}}$$

where $Q_{h,hp,out}$ is the monthly thermal energy demand supplied by the heat pump [Wh].

The monthly partial load factor PLF_{m,h_D} indicates the percentage of operating time of the system during the design month:

Equation 29

$$PLF_{m,h_D} = \frac{Q_{h,hp,out_D}}{24 \cdot \dot{Q}_{h,hp,out_D} \cdot N_{days\ project\ month}}$$

where:

- $\boldsymbol{Q_{h,hp,out_D}}$**:** is the energy requirement in the design month for heating [Wh]
- $\boldsymbol{\dot{Q}_{h,hp,out_D}}$**:** is the design thermal power of the heat pump [W]
- $\boldsymbol{N_{days\ project\ month}}$**:** is the number of days in the project month

The equivalent thermal resistance of the exchanger R_b is the sum of three components according to the equation:

Equation 30

$$R_b = R_{pp} + R_{gr} + R_t$$

where R_{pp} is the thermal resistance of the pipe through which the fluid flows, R_{gr} is the thermal resistance of the filling material (pipe/soil interface) and R_t is the thermal resistance of any external pipe (normally removed at the end of drilling and therefore zero for calculation purposes).

Equation 31 allows the resistance of the pipe in which the heat transfer fluid flows to be calculated:

Equation 31

$$R_{pp} = \frac{\left[\frac{1}{2 \cdot \pi \cdot \lambda_{pp}} \cdot ln\left(\frac{d_e}{d_i}\right) + \frac{1}{\pi \cdot d_i \cdot h_i}\right]}{N_{pipes}}$$

where:

- d_e: is the external diameter of the pipe [m]
- d_i: is the internal diameter of the pipe [m]
- λ_{pp}: is the thermal conductivity of the pipe material equal to 0.3 $\left[\frac{W}{(mK)}\right]$
- h_i: is the heat transfer coefficient for convection inside the pipe $\left[\frac{W}{(m^2K)}\right]$
- N_{pipes}: is the number of pipes that make up the heat exchanger for the double U, equal to 4

The coefficient h_i is calculated as follows:

Equation 32

$$h_i = \frac{(2\lambda_{pp})}{d_i \ln\left(\frac{d_e}{d_i}\right)}$$

For double-U type borehole heat exchangers, the thermal resistance of the filling can be calculated using the following formula:

Equation 33

$$R_{gr} = \frac{1}{2\pi\lambda_{gr}} \cdot \left[ln\left(\frac{D_b}{d_e}\right) - \frac{3}{4} + \left(\frac{D}{D_b}\right)^2 - \frac{1}{4} \cdot ln\left(1 - \left(\frac{D}{D_b}\right)^8\right) - \frac{1}{2} \cdot ln\left(\frac{\sqrt{2} \cdot D}{d_e}\right) - \frac{1}{4} \cdot ln\left(\frac{2 \cdot D}{d_e}\right)\right]$$

where:

- λ_{gr}: is the thermal conductivity of the filling material $\left[\frac{W}{(mK)}\right]$
- D_b: is the perforation diameter [m]
- d_e: is the pipe external diameter [m]
- D: is the spacing between the legs of the double U = 0,0452[m]

The thermal resistances of the soil surrounding the borehole in which the heat exchanger is inserted are of the impulse type and are divided according to the duration of the impulse itself. The thermal resistance R_{ga} is defined as the annual impulse, i.e. the time it takes for the soil to reach a new level of stability in heat exchange, which can take one or more years. The thermal resistance R_{gm} is defined as the monthly impulse corresponding to the average heat exchange in the design month. The thermal resistance R_{gd} is defined as the daily impulse corresponding to the peak heat exchange in the design hours.

In order to establish a correlation between the temporal parameters that define the exchange impulse and the geometric characteristics of the heat exchanger, as well as the properties of the soil, the following relationship is employed, wherein the Fourier number is defined as follows:

Equation 34

$$F_o = \frac{4 \cdot \alpha_g \cdot \tau}{D_b^2}$$

where:

- α_g: is the diffusivity of the soil = $\frac{\lambda_e}{S_{vc}} \left[\frac{m^2}{s}\right]$
- τ: is the duration of the impulse considered [s]
- D_b: is the diameter of the borehole [m]

The impulse considered for calculating the annual equivalent thermal resistance has a duration of 3650 days (10 years), as it is assumed that this period of time is sufficient for the thermal flow exchanged with the ground to stabilise. The impulse considered for calculating the monthly equivalent thermal resistance has a duration of 30 days. The impulse considered for calculating the daily equivalent thermal resistance has a duration of 0.25 days (6 hours).

It is necessary to define three Fourier numbers in consideration of the following pulse durations:

- τ_1= 3650 days (315.360.000 s)
- τ_2= 3650 + 30= 3680 days (317.952.000 s)
- τ_f= 3650 + 30 + 0,25= 3680,25 days (317.973.600 s)

In conjunction with Equation 34, which is employed to calculate the Fourier numbers necessary for defining the equivalent thermal resistances of the soil, the following relationships are utilised:

Equation 35

$$F_{o1} = \frac{4 \cdot \alpha_g \cdot (\tau_f - \tau_1)}{D_b^2}$$

Equation 36

$$F_{o2} = \frac{4 \cdot \alpha_g \cdot (\tau_f - \tau_2)}{D_b^2}$$

Equation 37

$$F_{of} = \frac{4 \cdot \alpha_g \cdot \tau_f}{D_b^2}$$

For each Fourier number obtained using the above equations, the corresponding G-Factor is calculated using the following relationship:

Equation 38

$$G = 0{,}0758 \cdot \ln(F_o) + 0{,}1009$$

The three equivalent thermal resistances of the soil are therefore calculated using the following equations:

Equation 39

$$R_{ga} = \frac{G_f - G_1}{\lambda_g}$$

Equation 40

$$R_{gm} = \frac{G_1 - G_2}{\lambda_g}$$

Equation 41

$$R_{gd} = \frac{G_2}{\lambda_g}$$

where:

- G_f: is the G-Factor relative to the Fourier number F_{of}
- G_1: is the G-Factor relative to the Fourier number F_{o1}
- G_2: is the G-Factor relative to the Fourier number F_{o1}
- λ_g: is the equivalent thermal conductivity of the soil $\left[\frac{W}{(mK)}\right]$

Equation 26 in the denominator contains the relationship from Equation 42, which defines the temperature difference in the geothermal heat exchanger, designated as $\Delta\vartheta_{sgv}$:

Equation 42

$$\Delta\vartheta_{sgv} = \vartheta_g - \left(\frac{\vartheta_{wi} + \vartheta_{wo}}{2}\right)_D - \vartheta_p$$

The measurement of the undisturbed ground temperature ϑ_g can be accomplished through various investigative methodologies. A common technique involves the profiling of the vertical temperature distribution within the borehole exchanger by means of the immersion of a data acquisition and transmission probe. This enables the calculation of the geothermal gradient at discrete depths. An alternative and widely adopted approach is the Thermal Response Test (TRT), which evaluates the ground's thermophysical properties by inducing a controlled, forced circulation of the heat transfer fluid within the borehole heat exchanger in the absence of other thermal sources. In a standard TRT procedure, a constant heat load is applied to the circulating fluid, and the consequent temporal evolution of the fluid's inlet and outlet temperatures is carefully monitored. The temperature data thus acquired facilitates the determination of key thermal parameters, namely the effective thermal conductivity of the ground and the borehole thermal resistance, both of which are critical for the accurate design and sizing of ground heat exchanger systems. The significance of TRT in geothermal system design is well-established and has been extensively reviewed in recent scientific literature [226]. This is particularly true in regard to its integration with geotechnical site characterisation, which promotes widespread and cost-effective application of shallow geothermal technologies.

Recent technological advancements have introduced enhanced thermal response test (ETRT) methodologies that significantly expand the capabilities of conventional TRT procedures through the integration of distributed temperature sensing (DTS) systems with optical fibre technology [227,228]. These innovative approaches utilise fibre optic cables equipped with actively heated elements, thereby enabling continuous temperature measurements with high spatial resolution (typically 0.25-1 m) along the entire borehole depth during both the heating and recovery phases. The DTS technology utilises the principles of Raman or Brillouin scattering, whereby laser pulses are transmitted through the optical fibre and the backscattered signals are analysed to determine temperature profiles based on the time-of-flight principle and amplitude ratios of Stokes and anti-Stokes signals [229]. Enhanced TRT systems have been demonstrated to exhibit superior performance in identifying thermal heterogeneities and groundwater flow effects within geological strata [227]. These systems provide depth-dependent thermal conductivity measurements and enable the detection of localized convective heat transfer that may not be captured by conventional averaging methods. The enhanced methodology typically requires lower heating power (<20 W/m) compared to standard TRT while maintaining measurement accuracy, and the permanent installation of hybrid cables allows for repeated testing throughout the system's operational lifetime, facilitating long-term monitoring of ground thermal behaviour and borehole performance assessment [230].

For the results chapter, an undisturbed temperature of 18 °C was assumed, which is presumably the temperature of the ground at a depth of 100 m (average geothermal gradient in Turin 2-3 °C per 100 m). The depth of 100 m was determined

by the necessity to incorporate a solitary undisturbed ground temperature value that could approximate both the lower surface values and the higher deep values.

The temperature of the heat transfer fluid at the inlet ϑ_{wi} and outlet ϑ_{wo} is a critical parameter in the design of closed-loop heat exchangers. It is notable that a substantial disparity exists between the mean temperature of the fluid within the exchanger and the temperature of the undisturbed ground. This disparity facilitates a reduction in the size of the heat exchange system, thereby rendering the construction process more economical. However, this approach has a greater impact on the thermal state of the surrounding ground and generally leads to lower heat pump performance, increasing the system's energy consumption. The presence of a low discrepancy between the mean temperature of the fluid within the exchanger and the ambient temperature of the undisturbed ground facilitates enhanced performance of the heat pump and reduced energy consumption of the system. However, this approach gives rise to a substantial heat exchange system with the subsoil, which results in the construction of the system becoming excessively costly.

Achieving the correct balance between the various factors influencing the choice (system size and heat pump performance) necessitates consideration of the range within which the difference between the temperature of the fluid leaving the heat exchanger ϑ_{wo} and the ground temperature ϑ_g in heating mode varies: namely, 6 to 11 °C. It is imperative to investigate the temperature disparity of the incoming heat transfer fluid, ensuring that the fluid flow rate through the pipes is sufficient to maintain a non-laminar flow regime inside the pipes (Reynolds number > 2300) and that the fluid's velocity does not result in excessive pressure drops, thereby necessitating the utilisation of an excessively energy-intensive pumping system. It is generally accepted that, for the purpose of calculating ϑ_{wi}, a temperature difference of 3 to 5 °C is sufficient to balance the aforementioned system parameters.

The penalty temperature facilitates the execution of analytical adjustments to the average temperature difference between the ground and the heat transfer fluid, thereby ensuring the consideration of mutual interference from the thermal fields induced by the heat exchangers active in the ground.

Subsequent to the determination of the quantity and geometric configuration of the heat exchangers to be installed, the following relationship can be utilised:

Equation 43

$$\theta_p = \frac{1 \cdot N_4 + 0{,}5 \cdot N_3 + 0{,}25 \cdot N_2 + 0{,}1 \cdot N_1}{N_{tot}} \cdot \theta_{p1}$$

where:

- N_4 : is the number of exchangers surrounded on all four sides by other exchangers;
- N_3 : is the number of exchangers surrounded on three sides by other exchangers;

- N_2: is the number of exchangers surrounded on two sides by other exchangers;
- N_1: is the number of exchangers surrounded on one side by other exchangers;
- θ_{p1}: is the penalty temperature for a ground heat exchanger surrounded on all four sides by other similar exchangers.

Equation 43 relates to a specific grid arrangement of ground heat exchangers.

The penalty temperature, designated as θ_{p1}, is determined through a comprehensive consideration of the thermal storage capacity exhibited by the parallelepiped of soil, which is influenced by the operational dynamics of the heat exchanger. This determination is achieved by employing the following relationship:

Equation 44

$$\theta_{p1} = \frac{Q_{stored}}{\rho \cdot c_p \cdot d_s^2 \cdot L}$$

where:

- Q_{stored}: is the heat accumulated in the ground by the geothermal heat pump system after 10 years of operation [J];
- ρ: is the equivalent volumetric mass of the ground $\left[\frac{Kg}{m^3}\right]$;
- c_p: is the equivalent specific heat of the ground $\left[\frac{J}{(Kg \cdot K)}\right]$;
- d_s: is the distance between the ground heat exchangers [m];
- L: is the total length of the ground heat exchangers [m].

The heat accumulated in the ground after 10 years Q_{stored} is obtained using the linear source solution and considering a cylinder with a radius of 8 to 10 m, as these are the average distances of interest for heat transmission over this period of time [231]. Given that the temperature gradient is not constant along the radius of the cylinder under investigation, the average temperature variation between concentric circular rings (Figure 103) is considered. The calculation of Q_{stored} is obtained from:

Equation 45

$$Q_{stored} = \sum_{i=1}^{n} \rho \cdot c_p \cdot \pi \cdot L \cdot ((R_i + \Delta R)^2 - R_i^2) \cdot \Delta\theta_{gi}$$

where:

- R_i: is defined as the inner radius of the circle (equal to 0.5 d_s) [m];
- ΔR: is defined as the increase in radius [m];
- $\Delta\theta_{gi}$: is the temperature variation of the i-th surface compare the undisturbed ground temperature ϑ_g [C°].

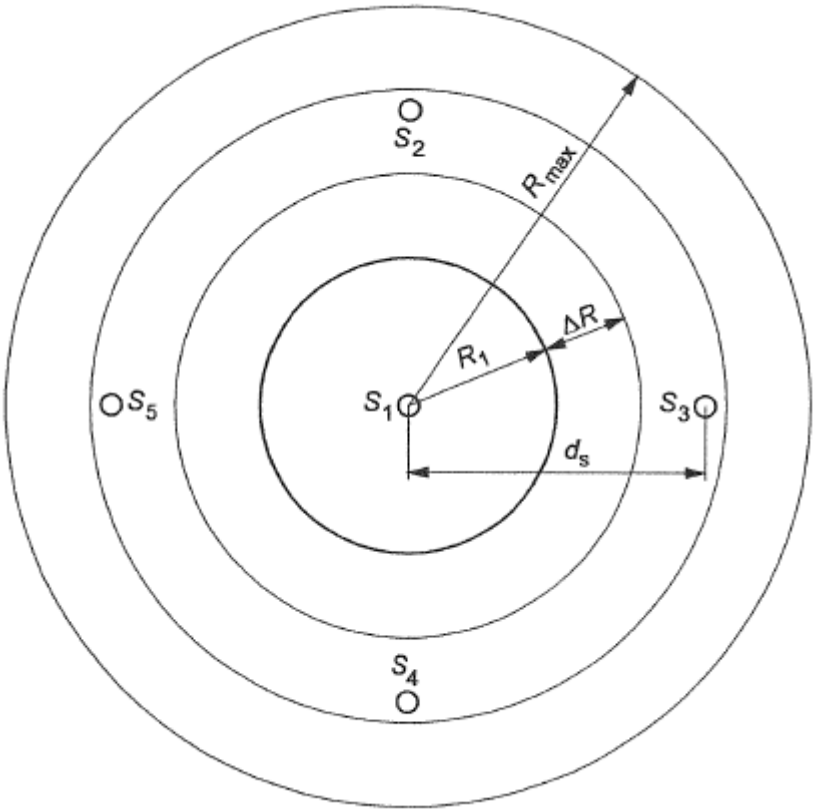

Figure 103. Schematic representation of heat accumulation in the ground.

The temperature difference $\Delta\theta_{gi}$ is calculated using the following formula:

Equation 46

$$\Delta\theta_{gi} = \frac{\dot{Q}_a \cdot I(X)}{2 \cdot \pi \cdot \lambda_g \cdot L}$$

where:

- $\dot{Q}_a$: is net annual average heat transfer to the ground [W]
- λ_g: is the equivalent thermal conductivity of the ground $\left[\frac{W}{(m \cdot K)}\right]$;
- $I(X)$: is the coefficient calculated from the term X.

Equation 47

$$X = \frac{R}{2 \cdot \sqrt{\alpha_g \cdot \tau}}$$

Equation 48

$$\mathrm{I}(X) = -0{,}57707078 \cdot \ln(X) + 0{,}1 \quad per\ 0{,}5 \leq X \geq 1$$

Equation 49

$$\mathrm{I}(X) = -0{,}932002 \cdot \ln(X) - 0{,}14601 \quad per\ 0{,}01 \leq X \geq 0{,}5$$

where:

- R: is the average radius considered ($R_i + 0{,}5 \cdot \Delta R$) [m];
- τ: time (3650 days).
- α_g: is the diffusivity $\alpha_g = \frac{\lambda_g}{\rho \cdot c_p}$

The final step is to calculate the total water flow rate in the circuit using:

Equation 50

$$\dot{m}_t = \frac{Q_{h,hp,out_D} \cdot \left(1 - \frac{1}{COP_D}\right)}{c_p \cdot \Delta\theta_{hD}}$$

In the case of the ground heat exchangers being connected in parallel, carrier fluid discharge in the single BHE is $\dot{m}_s = \frac{\dot{m}_t}{n_{bhe}}$ [kg/s]. It depends by the total number of boreholes in the closed-loop plant and their disposition. However, since they are double U probes, it can be shown that each individual pipe has a flow rate equal to $\frac{\dot{m}_s}{2}$. It is recommended that the flow regime within the pipes be examined. The thermophysical properties of water that are of interest at a temperature of 10°C are as follows:

- Density ρ= 999,7 $\left[\frac{Kg}{m^3}\right]$;
- Dynamic viscosity μ= 1,31 · 10^{-3} $\left[\frac{kg}{(m \cdot s)}\right]$.

The Reynolds number is a dimensionless parameter that quantifies the ratio between inertial forces and viscous forces in a flow. It is utilised to predict the flow regime (laminar, transitional, turbulent) as a function of flow rate/velocity, geometry and fluid properties. The calculation is derived from the following formula:

Equation 51

$$Re = \frac{4 \cdot \dot{m}_s}{\pi \cdot d_i \cdot \mu}$$

Values below 2000 correspond to laminar flow, characterised by parallel flow lines and losses that are proportional to velocity. In the range between 2000 and 4000, the flow transitions to a state of transitional flow, which is sensitive to disturbances and boundary conditions. Finally, values above 4000 indicate a turbulent flow state, marked by the presence of mixing and vortices. The recommended Reynolds number, Re ≥ 2500, is indicative of non-laminar flow, and should be used as a minimum design value to avoid excessively high values that unnecessarily increase pumping power. ASHRAE guidelines recommend maintaining Re within the range of 2500–4000 as a typical design range. Indeed, at flow rates below 2300, the flow becomes laminar, thereby exacerbating internal convective exchange. Conversely, at flow rates much higher than this, pumping energy increases significantly, although with marginal thermal benefits.

Finally, it is also useful to check the value of the water velocity inside the exchanger to ensure compatibility with pressure drops using the following relationship:

Equation 52

$$v = \frac{4 \cdot \dot{m}_s}{\pi \cdot {d_i}^2 \cdot \rho}$$

Typical design velocities range from 0.3 to 0.6 m/s for double U-tube configurations, balancing heat transfer performance against pressure drop and pumping power requirements.

3.4 Case Study

Two representative case studies are presented to demonstrate the application of the ASHRAE comprehensive methodology to practical installations with distinct thermal characteristics and operational requirements.

Two case studies were hypothesised: the first system was used to heat and cool an office building (30,000 m^3) with a thermal power of 300 kW for heating and 280 kW for cooling. The second was purely industrial purpose, with a design thermal power of 2500 kW exclusively for heating, with a constant monthly thermal consumption of 1,041,667 kWh distributed evenly over the twelve months of the year, corresponding to a total useful annual energy of 12.5 GWh.

3.4.1 First Case Study

The monthly thermal energy consumption demonstrates the seasonal variation characteristic of mixed heating-cooling applications in temperate continental climates (Table 14).

Table 14. Monthly thermal consumption for heating and cooling an office building in Turin.

Month	Thermal Consumption (kWh)	Load Type
January	82,800	Heating
February	72,000	Heating
March	69,000	Heating
April	66,000	Heating
May	-64,860	Cooling
June	-73,920	Cooling
July	-77,280	Cooling
August	-77,280	Cooling
September	-62,040	Cooling
October	-40,020	Cooling
November	66,000	Heating
December	69,000	Heating

The key heat pump performance indices are:

- $\boldsymbol{COP_D}$ = 3.8: Design coefficient of performance for heating
- $\mathbf{COP_{ms}}$ = 4.7: Seasonal average coefficient of performance
- $\boldsymbol{EER_D}$ = 3.3: Design energy efficiency ratio for cooling
- $\mathbf{EER_{ms}}$ = 4.1: Seasonal average energy efficiency ratio

Operating fluid temperatures are specified as:

- θw_i = 6°C (inlet to heat pump in heating mode)
- θw_o= 2°C (outlet from heat pump in heating mode)
- θc_i = 28°C (inlet to heat pump in cooling mode)
- θc_o= 32°C (outlet from heat pump in cooling mode)

The chosen solution incorporates double-U tube BHEs with the following specifications:

- Outer pipe diameter (d_e): 32 mm
- Inner pipe diameter (d_i): 26.2 mm
- Pipe spacing (D): 45.2 mm
- Thermal conductivity of pipe (λ_{pp}): 0.3 W/mK
- Borehole diameter (D_b): 150 mm
- Minimum distance between BHEs (d_s): 7 m (to minimize thermal interference)

The installation site exhibits geological characteristics typical of the Turin metropolitan area, consisting of quaternary alluvial deposits with moderate water saturation:

- Undisturbed ground temperature (θ_g): 15.7°C
- Thermal conductivity (λ): 1.7 W/mK
- Density (ρ): 2200 kg/m³
- Specific heat (c_p): 1091 J/kgK
- Volumetric heat capacity (S_{vc}): 2.4 MJ/m³K

3.4.2 Second Case Study

This case study examines a large-scale closed-loop geothermal system serving an industrial facility requiring continuous process heating throughout the annual cycle. The constant thermal load profile represents a distinctly different operational scenario compared to the previous commercial building case study.

Thermal Load Profile:

- Design heating capacity: Q_{h,hp,out_D}= 2,500 kW
- Annual energy consumption: 12,500,000 kWh (12.5 GWh)
- Monthly energy consumption: 1,041,667 kWh (constant year-round)
- Load profile: Constant 24/7 operation with minimal seasonal variation
- No cooling requirement (heating only)

The key heat pump performance indices are:

- $\boldsymbol{COP_D}$ = 3.8: Design coefficient of performance for heating
- $\mathbf{COP_{ms}}$ = 4.7: Seasonal average coefficient of performance

Operating fluid temperatures are specified as:

- $\boldsymbol{\theta w_i}$ = 12°C (inlet to heat pump)
- $\boldsymbol{\theta w_o}$= 7°C (outlet from heat pump)

The chosen solution incorporates double-U tube BHEs with the following specifications:

- Outer pipe diameter ($\mathbf{d_e}$): 32 mm
- Inner pipe diameter ($\mathbf{d_i}$): 26.2 mm
- Pipe spacing (**D**): 45.2 mm
- Thermal conductivity of pipe ($\boldsymbol{\lambda_{pp}}$): 0.3 W/mK
- Borehole diameter ($\mathbf{D_b}$): 100 mm
- Minimum distance between BHEs ($\mathbf{d_s}$): 8 m (to minimize thermal interference)

The ground properties utilised for system sizing are:

- Undisturbed ground temperature ($\boldsymbol{\theta_g}$): 18°C
- Thermal conductivity ($\boldsymbol{\lambda}$): 1.7 W/mK
- Density ($\boldsymbol{\rho}$): 2200 kg/m³
- Specific heat ($\mathbf{c_p}$): 950 J/kgK
- Volumetric heat capacity ($\mathbf{S_{vc}}$): 2.09 MJ/m³K

3.5 Results

Two distinct closed-loop geothermal configurations were designed to serve different thermal demand profiles using the ASHRAE comprehensive methodology. The first case study addresses a commercial office building with mixed heating and cooling requirements, while the second examines a large-scale industrial heating application with constant thermal load. The following sections present the quantitative results obtained through systematic application of the sizing equations presented in Section 3.3.2 ASHRAE.

3.5.1 First case study

The sizing procedure began by calculating the equivalent full-load hours for both heating and cooling using Equation 28. The annual heating energy of 424,800 kWh divided by the design heating capacity of 300 kW yielded 1,416 equivalent hours per year for heating, while the 395,400 kWh cooling energy divided by 280 kW design cooling capacity produced 1,412 equivalent hours for cooling. These values indicate moderate operational intensity compared to continuously operating industrial applications. The annual average ground heat exchange was determined using Equation 27, which accounts for the heat pump efficiency factors and equivalent operating hours for both heating and cooling modes. The calculation yielded $\dot{Q}_a$ = -17,971 W, with the negative value indicating net heat rejection to the ground. This result demonstrates that despite higher heating energy consumption, the cooling operation generates greater ground-side thermal loads.

The borehole thermal resistance and the ground thermal resistance components were calculated using the methodology described in Equation 28 through Equation 41. The temperature penalty calculation, which accounts for thermal interference between multiple boreholes using Equation 43 and Equation 44, was performed iteratively. For the preliminary sizing, a rectangular borehole array with 7-meter spacing was assumed, and the accumulated heat in the ground after 10 years of operation was calculated considering the net annual thermal imbalance. The iterative process converged to a temperature penalty of θ_p= -1.2 °C. The negative value indicates that the net cooling operation produces ground warming rather than cooling, which actually benefits heating mode operation by increasing the effective temperature difference while reducing the driving force for cooling mode.

The fundamental ASHRAE sizing equation (Equation 26) was applied separately for heating and cooling design conditions. For heating mode, the numerator combined the annual average thermal load of -17,971 W multiplied by the annual ground resistance of 0.2071 (m·K)/W with the design thermal load of 221,053 W multiplied by the sum of borehole resistance (0.0793 (m·K)/W), monthly ground resistance weighted by the part-load factor (0.371 × 0.2068 = 0.0767 (m·K)/W), and daily ground resistance weighted by the short-circuit loss factor (0.1020 × 1.05 = 0.1071 (m·K)/W). The denominator represented the effective temperature difference between the undisturbed ground temperature of 15.7°C and the mean fluid temperature of 4°C during heating operation, adjusted by the temperature penalty of -1.2°C, yielding an effective difference of 12.9°C. The calculation produced a required length of 4,220 meters for heating operation.

For cooling mode, the same equation structure was applied with cooling-specific parameters. The design ground heat rejection during peak cooling was calculated as $\dot{Q}_{g,c_D}$= 280,000 × (1 + 1/3.3) = 364,848 W. With the mean fluid temperature of 30°C during cooling, the effective temperature difference between ground and fluid was 15.7 - 30.0 - (-1.2) = -13.1°C. The negative sign indicates heat rejection to ground, and the calculation yielded a required length of 7,612 meters for cooling mode.

The design requirement is determined by the larger of the two calculated lengths, establishing the cooling mode as the dimensioning condition with 7,612 meters total borehole heat exchanger length required. This result reflects the fundamental asymmetry in ground-source heat pump systems, where cooling operation typically imposes greater demands on the ground heat exchanger due to the combined rejection of building cooling load plus compressor work, even when annual energy consumption is nearly balanced.

The total length of 7,612 meters was distributed among 80 individual boreholes arranged in a rectangular borefield geometry optimized for the available site configuration. The borefield was designed with 8 rows and 10 columns, maintaining the 7-meter inter-borehole spacing established during the thermal interference analysis. This configuration yields a total land area of approximately 49 meters × 63 meters, or roughly 3,087 m², providing a compact footprint suitable for many different commercial building complexes. Each individual borehole was designed to a depth of 95 meters, representing a practical drilling depth that balances construction feasibility, equipment accessibility, and cost-effectiveness while remaining well within the capabilities of standard drilling equipment. The 95-meter depth provides access to the thermally stable ground zone below the influence of seasonal surface temperature variations, ensuring consistent system performance throughout the annual cycle.

The hydraulic analysis using Equation 50 through Equation 52 determined the circulation system requirements for the final borefield configuration. The total system flow rate of approximately 12.8 kg/s was distributed equally among the 80 boreholes, yielding an individual borehole flow rate of 0.16 kg/s. For the double U-tube configuration, this flow divides equally between the two parallel U-tube legs, resulting in 0.08 kg/s per individual pipe. The Reynolds number calculation yielded Re = 8,427, indicating fully developed turbulent flow well above the transition regime threshold of 2,300. While this Reynolds number exceeds the optimal design range of 2,500-4,000 recommended in ASHRAE guidelines, it remains acceptable for commercial applications where the enhanced convective heat transfer coefficients associated with higher Reynolds numbers can improve thermal performance during peak load conditions. The corresponding flow velocity of 0.25 m/s represents a moderate value that ensures adequate heat transfer while maintaining reasonable pressure drops throughout the circulation system.

3.5.2 Second case study

The second case study examines a large-scale industrial heating application requiring continuous process heating with constant thermal load throughout the annual cycle. The sizing procedure commenced with calculation of equivalent full-load hours using Equation 28, which yielded 12,500,000 kWh / 2,500 kW = 5,000 hours per year, substantially exceeding the commercial building application and approaching continuous operation. The annual average ground heat exchange was determined using Equation 27, producing $\dot{Q}_a$ = 1,123,336 W, a substantial positive value confirming sustained net heat extraction from the ground characteristic of heating-dominated industrial applications. The part-load factor for the design month was calculated using Equation 29 as 1,041,667 kWh / (24 hours × 30 days × 2,500 kW) = 0.560. This significantly higher value compared to the commercial building reflects the constant operational pattern with 56% continuous utilisation throughout each month. The design ground heat output was calculated as 2,500,000 × (1 - 1/3.8) = 1,842,105 W. The borehole thermal resistance and the ground thermal resistance components were calculated using the methodology described in Equation 28 through Equation 41.

Given the substantially larger scale of this installation, multiple borehole configurations were analysed to explore trade-offs between individual borehole depth, total number of boreholes, and available site constraints. Four distinct configurations were evaluated through iterative application of the temperature penalty calculation using Equation 43 and Equation 44 and the fundamental sizing equation.

Configuration 1: (Deep Borehole Strategy) employs deep individual boreholes to minimize land area requirements. The temperature penalty calculation converged to θ_p = 2.9°C for a rectangular array of 46 rows by 4 columns with 8-meter spacing. Application of Equation 1 with the effective temperature difference of (18.0 - 9.5 - 2.9) = 5.6°C yielded a total required length of 146,109 meters. This was distributed among 184 boreholes with individual depths of 397 meters, occupying approximately 8,640 m² total area. The hydraulic analysis produced total system flow of 87.78 kg/s, individual borehole flow of 0.239 kg/s, Reynolds number of 8,847, and flow velocity of 0.44 m/s. The substantially elevated Reynolds number indicates fully turbulent flow with enhanced heat transfer coefficients but substantially increased pumping power requirements due to quadratic pressure drop dependencies.

Configuration 2: (Shallow Multiple Borehole Approach) explores optimized hydraulic conditions through reduced individual drilling depths. The significantly higher borehole density resulted in increased thermal interference, with the temperature penalty calculation converging to θ_p= 3.3°C. The reduced effective temperature difference of (18.0 - 9.5 - 3.3) = 5.2°C necessitated increased total length of 157,348 meters. This was distributed among 572 boreholes with 138-meter depth arranged in a 44 × 13 rectangular array, occupying 33,024 m² area. The substantially larger number of boreholes reduced individual flow rates to 0.077

kg/s, yielding Reynolds number of 2,846 and velocity of 0.14 m/s. These hydraulic parameters reside within the optimal design range of 2,500-4,000, ensuring efficient operation with minimized pumping power while maintaining adequate turbulent mixing for effective convective heat transfer.

Configuration 3: (Intermediate Balance Solution) represents a balanced intermediate approach with 323 boreholes at 243-meter depth arranged in a 17 × 19 array occupying 18,432 m². The temperature penalty of 3.29°C produced total length requirement of 157,046 meters. The hydraulic conditions yielded flow rate of 0.136 kg/s per borehole, Reynolds number of 5,040, and velocity of 0.25 m/s. While the Reynolds number exceeds the optimal upper limit of 4,000, it remains within acceptable operational range.

Configuration 4: (Minimized Footprint with Reduced Spacing) explores maximizing spatial utilisation through reduced inter-borehole spacing of 5 meters rather than 8 meters. The decreased spacing significantly enhances thermal interference effects, with temperature penalty reaching θ_p = 4.94°C. The substantially reduced effective temperature difference necessitated total length of 229,835 meters distributed among 420 boreholes with 274-meter individual depth. The Reynolds number of 3,876 and velocity of 0.19 m/s remain within acceptable ranges, though the enhanced thermal interference substantially increases total drilling requirements.

The selection of these configurations is contingent on a number of site-specific constraints (**Table 15**). These include the available land area, the drilling cost structures (which typically exhibit exponential increases beyond 250-300 metre depths), the costs of land acquisition or leasing, regulatory constraints on borehole density or individual depths, and the relative economic importance of minimising capital investment versus operational pumping energy consumption over the 25-50 year system design lifetime.

Table 15. Comparison of Borefield Configuration Parameters for Industrial Heating Case Study.

Configuration	*Length (m)*	*Width (m)*	*Number of BHEs*	*Depth (m)*	*Total Pipe Length (km)*	*Reynolds Number*	*Flow Rate per Pipe (kg/s)*	*Water Velocity (m/s)*
1	382	32	184	397	146	8,847	0.23	0.44
2	382	110	572	138	157	2,846	0.076	0.14
3	158	200	323	243	230	5,040	0.135	0.25
4	382	32	420	274	230	3,876	0.10	0.19

3.6 Discussion

The comprehensive analysis of closed-loop geothermal systems through two distinct case studies reveals fundamental insights into the design methodology, operational characteristics, and critical trade-offs that govern system performance and economic viability. The ASHRAE methodology, as implemented in international standards including UNI 11466:2012, provides a rigorous analytical framework capable of accurately sizing borehole heat exchanger installations across diverse thermal demand profiles and operational patterns.

The first case study, addressing a commercial office building with mixed heating and cooling requirements, demonstrates the importance of comprehensive thermal load characterization throughout the entire annual cycle. The calculation of annual average ground heat exchange yielded -17,971 W, indicating net heat rejection to the ground despite nearly balanced annual heating and cooling energy consumption. This counterintuitive result emerges from the fundamental thermodynamic asymmetry in ground-source heat pump operation, where cooling mode rejects the sum of building cooling load plus compressor work to the ground, while heating mode extracts only the difference between building heating load and compressor work. This asymmetry produces cooling-dominated ground thermal loads even in apparently balanced applications, with profound implications for long-term thermal sustainability and system sizing requirements. The design analysis revealed that cooling mode governs the dimensioning condition, requiring 7,612 meters total borehole length compared to only 4,220 meters for heating operation. This 80% difference underscores the necessity of analyzing both heating and cooling conditions rather than relying exclusively on peak capacity or annual energy consumption metrics. The temperature penalty of -1.2°C calculated for this application warrants careful interpretation. The negative value indicates that sustained net heat rejection to the ground produces progressive ground warming rather than cooling, effectively increasing the temperature difference driving force during heating mode while reducing it during cooling operation. This phenomenon suggests that over multi-decade operational periods, the system performance may actually improve for heating while gradually degrading for cooling as ground temperatures drift upward. Long-term monitoring strategies incorporating distributed temperature sensing capabilities would enable quantification of these thermal evolution effects and potentially inform adaptive operational strategies to maintain thermal balance.

The final borefield configuration of 80 boreholes at 95-meter depth arranged in an 8 × 10 rectangular array occupying approximately 3,087 m² represents a practical solution compatible with standard drilling equipment and conventional installation practices. The Reynolds number of 8,427, while exceeding the optimal design range of 2,500-4,000, reflects a conscious design decision prioritizing adequate thermal performance during peak cooling loads over minimized pumping power. For this moderately sized commercial application, the incremental pumping energy penalty

remains proportionally small compared to total system energy consumption, and the enhanced convective heat transfer associated with fully turbulent flow provides operational benefits during design conditions. Alternative design iterations reducing the Reynolds number through increased temperature difference (5-6°C rather than 4°C) or modified borefield geometry would reduce pumping requirements but potentially compromise thermal performance margins.

The second case study, examining large-scale industrial continuous heating applications, reveals fundamentally different design considerations emerging from sustained thermal extraction at 2.5 MW annual average over multi-decade operational periods. The equivalent full-load hours of 5,000 hours per year approach continuous operation, producing substantially higher part-load factors (0.560) compared to the commercial building (0.371) and imposing correspondingly greater demands on ground thermal capacity. The exploration of four alternative borefield configurations demonstrates the complex optimization space governing large-scale installations, where competing objectives including minimized land area, optimal hydraulic performance, drilling cost structures, and long-term thermal sustainability must be simultaneously addressed. The temperature penalty analysis reveals systematic increases with borefield density, from 2.9°C for Configuration 1 to 3.3°C for Configuration 2, and reaching 4.94°C for the densely spaced Configuration 4. These values quantify the progressive thermal interference effects as borehole spacing decreases and thermal extraction density increases. The 70% increase in temperature penalty from Configuration 1 to Configuration 4 directly translates to proportionally reduced effective temperature difference driving heat transfer, necessitating substantially increased total borehole length to maintain equivalent thermal performance. This relationship underscores the critical importance of adequate borehole spacing in large installations, where the impulse to maximize spatial utilisation must be balanced against fundamental thermal physics governing ground heat transfer.

The comparative methodology analysis demonstrates that the ASHRAE approach provides substantially improved accuracy compared to simplified VDI 4640 methods for complex applications. For the commercial building case study, the VDI simplified approach would estimate approximately 5,200 meters total length using tabulated extraction rates of 65 W/m for water-saturated sand and gravel formations, representing 32% underestimation compared to the ASHRAE cooling-mode requirement of 7,612 meters.

3.7 Conclusion & Further Investigation

The comprehensive analysis of closed-loop geothermal systems presented in this research demonstrates the maturity and practical reliability of consolidated analytical design methodologies, while simultaneously highlighting clear opportunities for continued advancement aimed at improving system optimization, monitoring strategies, and long-term thermal management. The ASHRAE comprehensive methodology provides a rigorous framework for accurate system sizing across diverse applications, explicitly accounting for temporal load variations, thermal interference effects, and ground thermal property influences that fundamentally govern performance and long-term sustainability.

The case study analyses confirm that optimising the design of closed-loop geothermal systems requires the simultaneous consideration of multiple objectives, which are often competing. It is important to note that no single configuration can be assumed to universally optimise all design targets. This highlights the importance of conducting site-specific analyses, which necessitate the evaluation of local constraints, cost structures, hydraulic performance and operational priorities as a unified entity. In the context of commercial applications characterised by a combination of heating and cooling demands, the selection of cooling mode frequently dictates the sizing requirements. This is primarily due to the thermodynamic asymmetries inherent in the operation of ground-source heat pumps. Consequently, there is a compelling need for a more comprehensive annual load characterisation rather than a simplistic approach that relies on peak-condition sizing. In the context of large-scale industrial heating applications, the configuration of borefields is predominantly influenced by considerations pertaining to land availability and the cost structures associated with drilling. The implementation of deeper borehole solutions is known to minimise the footprint of the project; however, this is often accompanied by increased drilling costs and the potential for sub-optimal hydraulics. Conversely, the employment of multiple shallower borehole configurations has been shown to enhance operational efficiency. Nevertheless, this approach necessitates a substantially larger land area. These findings serve to confirm the robustness of the ASHRAE framework for design decision-making, while concomitantly clarifying the physical mechanisms that should be better represented when moving towards higher-fidelity performance prediction.

Future research directions that would substantially advance closed-loop geothermal technology implementation, and specifically those that would allow the ASHRAE method to evolve towards results more directly comparable with advanced numerical simulation tools (e.g. FEFLOW), include several key areas. Enhanced ground thermal characterisation is a primary priority. The integration of distributed temperature sensing and depth-resolved measurements within thermal response testing would enable the identification of vertical variations in thermal properties, the detection of groundwater-driven anomalies, and the derivation of more representative parameters for analytical sizing. In particular, the assumption

of homogeneous ground properties over the full borehole depth can be considered as a common simplification. A more nuanced approach, one which acknowledges the potential variability of ground properties with depth, could lead to a more precise definition of effective stratified properties or depth-dependent parameter sets that better reflect real geological conditions.

A secondary critical development pertains to the explicit representation of geological heterogeneity within the analytical procedure. Whilst the ASHRAE approach relies on effective parameters, future work could investigate systematic strategies to incorporate layered stratigraphy and laterally variable formations through equivalent-medium formulations, interval-based property weighting, or hybrid correction factors calibrated against site data. This would enhance the analytical method's capacity to capture non-uniform heat transfer domains, thereby reducing the discrepancy between simplified analytical predictions and high-resolution numerical outputs.

The effects of groundwater flow represent a significant area for methodological enhancement. In circumstances where advection is a pertinent factor, analytical assumptions that are exclusively conductive in nature have the potential to generate estimates of long-term temperature evolution and thermal interference that are subject to bias. It is recommended that subsequent studies investigate the potential for groundwater influence to be screened, parameterised, and integrated into the ASHRAE methodology through the utilisation of practical correction terms, effective transport parameters, or simplified advection–conduction modules. Such developments would enable the analytical framework to reproduce, at least in an approximate but defensible way, the additional heat transport mechanisms that are naturally resolved in advanced numerical simulators such as FEFLOW. Three-dimensional simulations incorporating realistic geological heterogeneity, groundwater flow, and spatially variable thermal properties can be used to quantify when and why analytical assumptions break down. They can also be used to derive calibration relationships that translate numerical insight into improved analytical formulations. Whilst the computational requirements may limit the routine use of fully three-dimensional models in everyday design, continued progress in computing power and model reduction techniques may progressively enable a broader application of such models. In the near term, a pragmatic pathway is the development of hybrid workflows in which numerical simulations are applied selectively, for example, to complex sites or large installations, in order to validate analytical sizing, calibrate correction factors and define more reliable long-term sustainability envelopes.

Despite the fact that double U-tube configurations are a mature and well-researched solution, alternative coaxial or enhanced geometries may offer performance improvements or cost reductions that become increasingly significant as design evolves towards more compact footprints and higher extraction/rejection densities. In addition, the ongoing evolution of policy and regulatory frameworks continues to exert a significant influence on the potential deployment of these technologies. The hypothesis that the streamlining of permitting processes for low-risk closed-loop installations could result in a reduction of non-technical barriers

and an acceleration in the rate of adoption is one that merits investigation. This is provided that there is assurance in the continued robustness and alignment of technical standards with improved characterisation and monitoring practices, thus ensuring environmental protection, long-term performance, and public safety. This chapter corroborates the robustness of the ASHRAE analytical framework for closed-loop geothermal design, while delineating a clear trajectory for future research. The overarching objective of these efforts is to facilitate more reliable, site-specific, and sustainable system design.

Chapter 4

"[…] Anything one man can imagine, other men can make real."

Jules Verne (1873)[6]

ATES

Aquifer Thermal Energy Storage (ATES) systems represent an advanced technological solution for seasonal thermal energy management in urban environments, offering significant potential for reducing energy consumption and greenhouse gas emissions through the strategic storage and recovery of thermal energy in subsurface aquifer formations. This chapter presents a comprehensive analysis of three innovative ATES system configurations implemented in an urban area in northern Italy, specifically examining their integration with heat pump systems for building thermal management. The investigation addresses the unique challenges posed by high groundwater flow velocities and develops novel operational strategies that enable effective thermal energy storage under conditions typically considered unfavorable for conventional ATES applications.

[6] *Around the World in Eighty Days, Jules Verne, (1873).*

4.1 Overview

ATES systems utilise naturally occurring aquifer formations as seasonal thermal energy storage reservoirs, exploiting the substantial thermal capacity of groundwater-saturated geological formations to store and subsequently recover thermal energy across seasonal cycles. Unlike conventional thermal storage systems that rely on purpose-built tanks or engineered structures, ATES technology leverages existing hydrogeological resources, offering significant economic and spatial advantages for large-scale thermal energy management applications.

The fundamental operational principle involves the bidirectional exchange of groundwater between extraction and injection wells configured as doublets or multiplets, with well functions alternating according to seasonal thermal demands (**Figure 104** A). During cooling-dominated periods (summer), relatively cool groundwater is extracted from designated cold wells, circulated through building systems or heat exchangers to provide cooling services, and subsequently reinjected at elevated temperatures into warm wells where the thermal energy is stored within the aquifer formation. During heating-dominated periods (winter), this operational cycle reverses: warmed groundwater is extracted from warm wells, thermal energy is recovered through heat pump systems, and the cooled water is reinjected into cold wells, completing the seasonal storage cycle (**Figure 104** B).

Due to its sustainable nature and wide applicability, interest in investing in ATES technology is experiencing significant growth worldwide. In Flanders (northern Belgium), the number of operational systems has steadily increased from 30 to 368 over the past5 years, demonstrating rapid market adoption driven by favorable regulatory frameworks and growing recognition of ATES benefits [232]. In Wallonia (southern Belgium) and Brussels (central Belgium), this growth manifests differently, with more complex aquifers, respectively a shallow alluvial aquifer and a fractured bedrock aquifer, being targeted for ATES development despite higher technical uncertainty [233]. Meanwhile, the Netherlands continues to lead global ATES deployment with thousands of operational systems, benefiting from decades of experience, comprehensive regulatory frameworks, and extensive hydrogeological characterization [234]. This growing international interest has stimulated substantial research investment in this field to improve understanding of the coupled groundwater flow and heat transport processes occurring within aquifer systems.

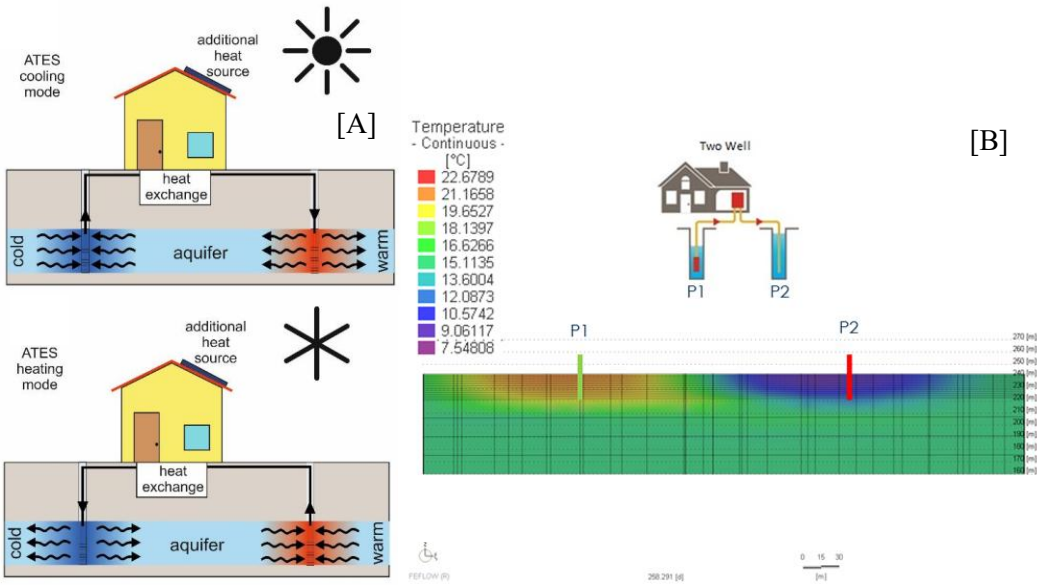

Figure 104. [A] operating principles of ATES plant (modified from [235]); [B] cross section of conventional ATES using FEFLOW.

The successful implementation of ATES technology is fundamentally dependent on specific hydrogeological characteristics that determine aquifer suitability for thermal energy storage applications. The primary hydrogeological parameters include [236–240]:

- *Hydraulic Conductivity*: the aquifer must possess sufficient hydraulic conductivity (typically exceeding 10^{-4} m/s) to enable adequate well yields without excessive hydraulic drawdown that could cause operational problems or environmental impacts. Higher hydraulic conductivity enables operation at higher flow rates, increasing thermal capacity and improving economic viability;
- *Saturated Thickness*: adequate aquifer thickness (generally > 10 meters) ensures sufficient three-dimensional storage volume and reduces the influence of thermal exchange with confining layers, which represent major pathways for conductive heat loss. Thicker aquifers provide larger thermal storage capacity and improve efficiency by reducing the relative importance of boundary heat losses;
- *Effective Porosity*: aquifer effective porosity (typically 20-30% for unconsolidated sediments) determines the volume of water available for thermal storage and influences the rate of thermal plume migration under natural groundwater flow. Higher porosity increases thermal storage capacity but may also increase thermal dispersion, requiring careful optimization in system design;
- *Natural Groundwater Flow Velocity*: this parameter represents perhaps the most critical constraint for conventional ATES design. Natural groundwater flow velocities below 25 m/year are specified in conventional design guidelines to ensure thermal plume stability and high recovery efficiency. This threshold exists because excessive groundwater flow causes advective transport of stored thermal plumes away from injection wells, reducing recovery efficiency and potentially

causing thermal interference with neighboring systems or sensitive environmental receptors;

- Thermal Conductivity: the thermal conductivity of aquifer materials and surrounding confining layers influences conductive heat losses during thermal storage periods;
- Confinement Conditions: the aquifer must be confined or semi-confined by low-permeability geological layers (aquitards) to minimize vertical thermal losses and ensure thermal plume containment within the storage formation. Complete confinement is ideal, but semi-confined conditions can still support effective ATES operation if vertical hydraulic conductivity is sufficiently low (**Figure 105**).
-

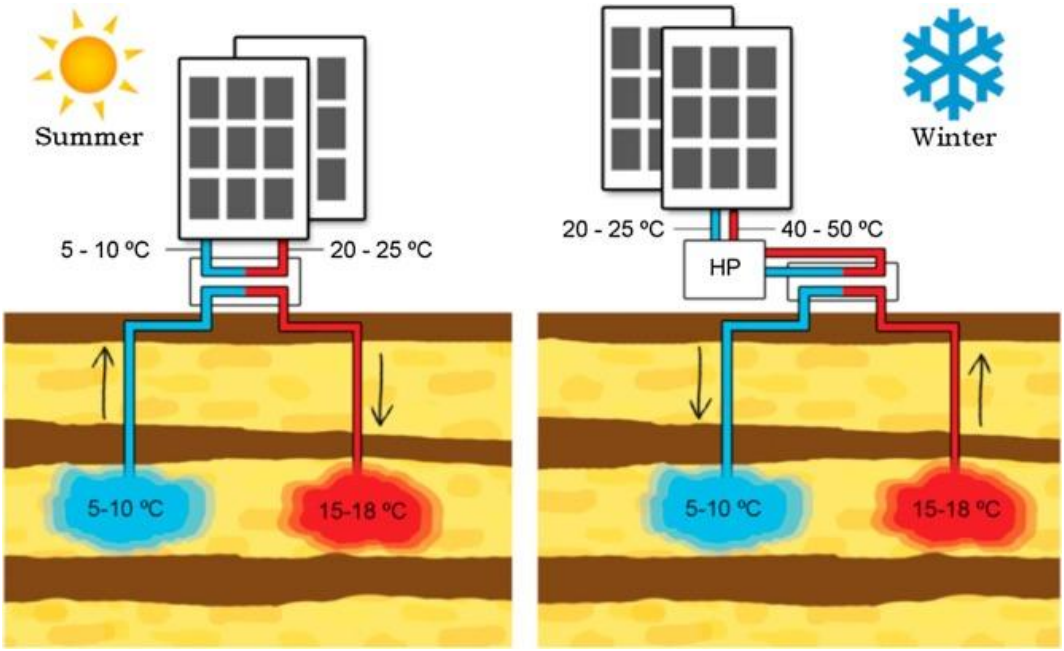

Figure 105. ATES double working principle [240].

Traditional ATES system design assumes minimal ambient groundwater flow, enabling thermal plumes to remain relatively stationary near injection wells throughout storage periods, facilitating efficient recovery during subsequent extraction cycles. Under these idealized conditions, well doublets are typically spaced 50-150 meters apart, with specific spacing determined by aquifer transmissivity, operational flow rates, and thermal storage requirements. However, many urban aquifer systems exhibit groundwater flow velocities substantially exceeding conventional ATES design thresholds, particularly in alluvial basin settings characterized by coarse-grained sediments and appreciable hydraulic gradients. The Po River plain in northern Italy, including the Turin metropolitan area, represents an example of this hydrogeological setting, with Quaternary alluvial deposits (coarse gravel and sand) exhibiting high hydraulic conductivity and groundwater flow velocities frequently exceeding 1000-1500m/year.

Under such conditions, traditional ATES configurations experience significantly degraded thermal recovery efficiency due to advective displacement of stored thermal plumes with injected thermal energy migrating substantial

distances downgradient before it can be recovered. This chapter addresses this fundamental limitation through three innovative system configurations that explicitly account for advective thermal transport and strategically position wells to intercept migrating thermal plumes. These modified approaches transform the typically detrimental effect of groundwater flow into an asset, enabling thermal energy storage and recovery in hydrogeological settings previously considered unsuitable for ATES applications.

The key conceptual innovation involves abandoning the conventional paradigm of attempting to minimize thermal plume migration through close well spacing and low flow rates. Instead, these designs embrace thermal advection as an inherent characteristic of the hydrogeological system and position extraction wells downstream to intercept migrating thermal plumes. This strategic approach enables successful ATES operation even when groundwater flow velocities exceed conventional design limits by one to two orders of magnitude.

The three case studies examined in this research demonstrate progressively increasing sophistication in exploiting advective thermal transport:

- Case Study 1 implements a hybrid sequential activation strategy where a conventional open-loop system is operated initially to establish thermal plume behaviour, followed by activation of a downstream extraction well positioned to intercept the migrating thermal plume;

- Case Study 2 employs a seasonal reversible four-well configuration with asymmetric flow rates optimized to match regional heating and cooling demands while maintaining thermal balance within the aquifer system;

- Case Study 3 demonstrates a cascaded thermal plume recovery concept where two separate open-loop installations operate synergistically, with the downstream system intercepting and recovering thermal plumes generated by the upstream system, enabling unprecedented scale and efficiency.

4.2 Case Studies

Figure 106 presents a location map showing the model areas for the three ATES case studies, all situated in the northern metropolitan area of Turin. The study area selection was based on available green area and favourable and detailed hydrogeological characterization data from regional monitoring networks.

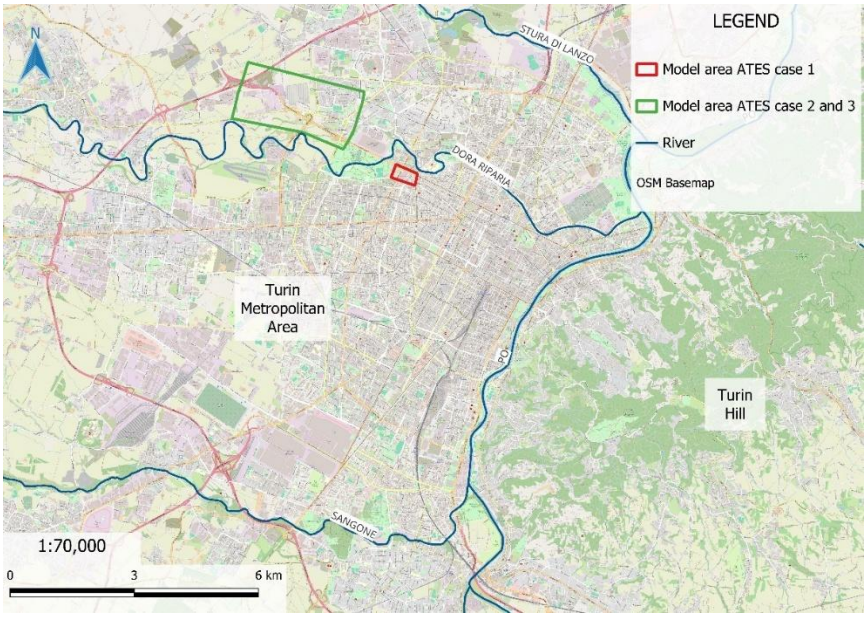

Figure 106. Case studies location map.

Figure 107 displays a simplified geological map of the Turin metropolitan area, illustrating the distribution of Quaternary deposits that host the shallow aquifer. The geological setting is dominated by fluvial and fluvioglacial deposits of Pleistocene to Holocene.

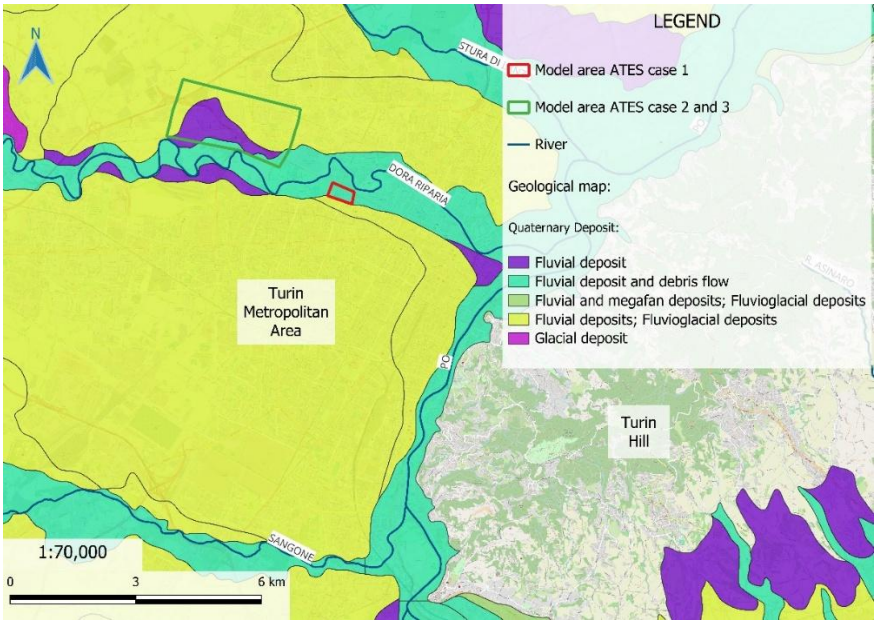

Figure 107. Simplified geological map of Turin area.

4.2.1 Case Study 1

The first case study analysed a pioneering approach to ATES system design under challenging hydrogeological conditions, demonstrating how conventional open-loop geothermal installations can be strategically enhanced through sequential well activation to achieve seasonal thermal storage capabilities. The system confronts the fundamental challenge of operating in an aquifer characterized by natural groundwater flow velocity of approximately 378 m/year (1.04 m/day), more than ten times the conventional ATES design threshold of 25 m/year. The innovative aspect of this design lies in its phased implementation strategy, which manages technical risk while enabling validation of numerical model predictions before committing to full ATES configuration. This approach offers significant practical advantages for real-world implementation, particularly in aquifer systems where thermal plume behaviour may be uncertain due to geological heterogeneity or limited prior characterization.

The model area contains various stratigraphic profiles available from the regional environmental agency (ARPA Piemonte) geoportal database[168]. **Figure 108** and **Figure 109** present two representative simplified stratigraphic cross-sections (designated S1 and S3) from boreholes in the study area, used to construct the numerical model geometry and assign appropriate hydrogeological parameters. The water table occurs at approximately 15-15.5 meters depth across the study area.

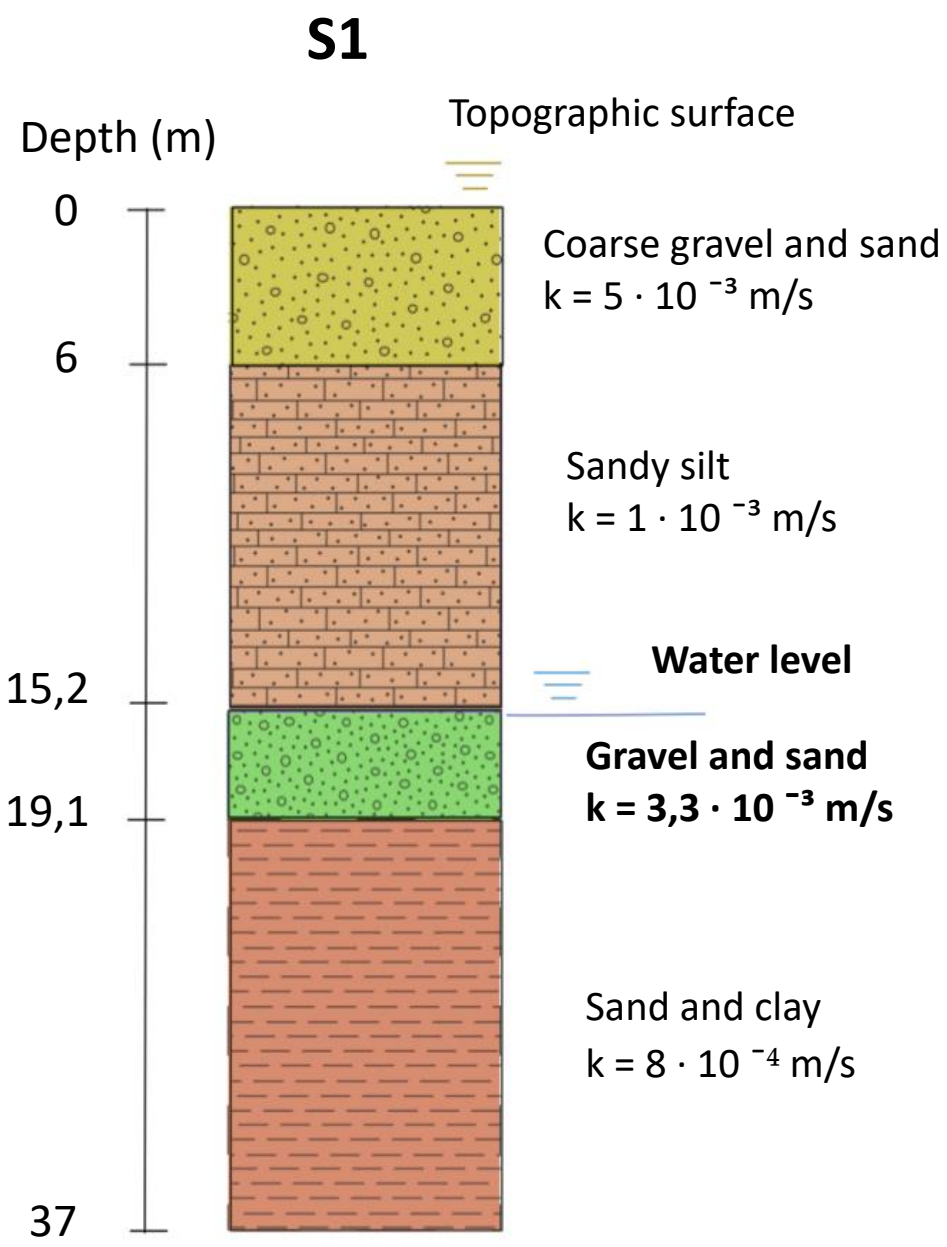

Figure 108. Simplified stratigraphic cross section number 102046, named S1 (data from [168]).

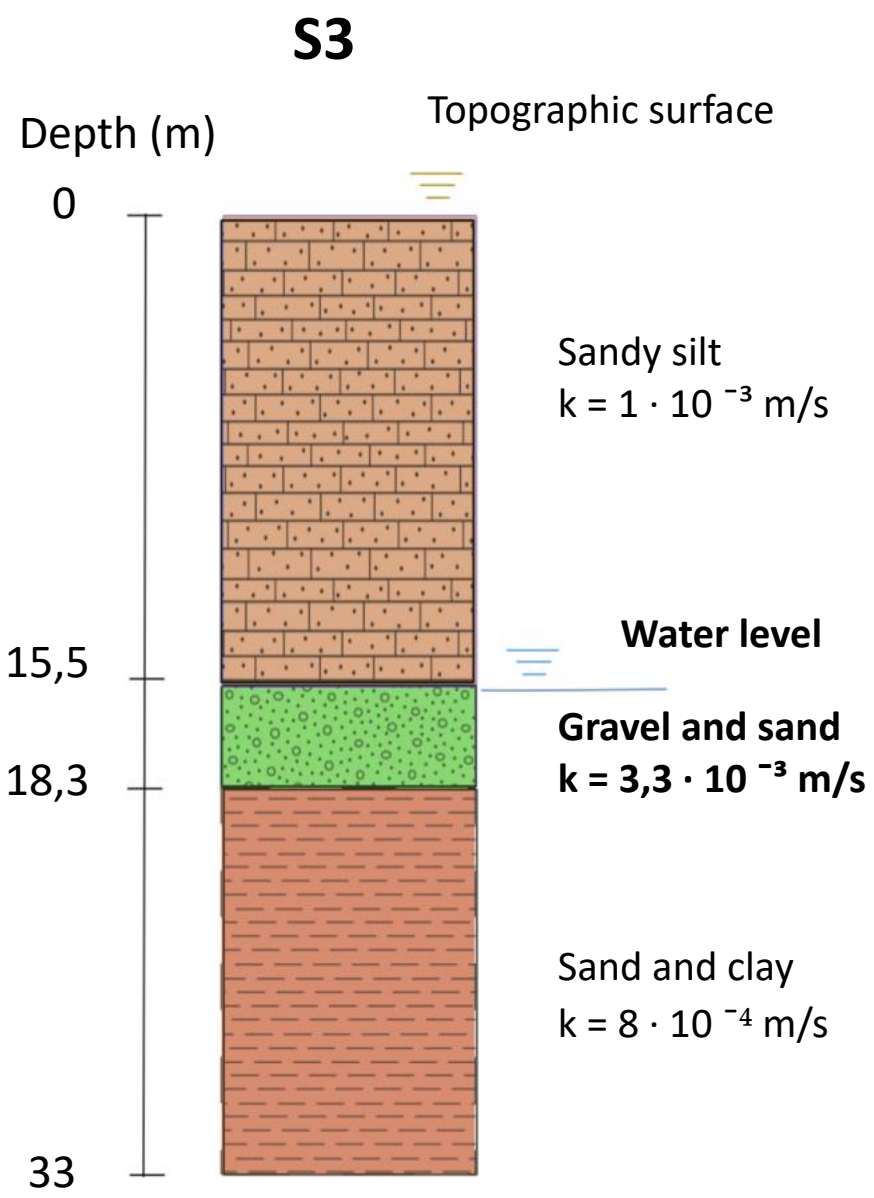

Figure 109. Simplified stratigraphic cross section number 102048, named S3 (data from [168]).

Figure 110 illustrates the three-dimensional model domain and layer discretization developed in FEFLOW to represent these hydrogeological conditions. Three main layers were simulated to adequately represent the geological formations:

- **Layer 1** (topographic surface to 18 m depth): Gravel and sand with hydraulic conductivity of 3.3×10^{-3} m/s;
- **Layer 2** (18-40 m depth): Sand and clay with hydraulic conductivity of 8×10^{-4} m/s;
- **Layer 3** (below 40 m depth): Confined deeper aquifer of sandy gravel and silt and clay interval with low hydraulic conductivity of 1×10^{-5} m/s.

Layer 3 is designated as a strategic aquifer reserve for potable water supply and therefore cannot be exploited for geothermal applications under regulatory constraints. Nevertheless, its explicit inclusion in the numerical model enhances

both physical and numerical stability of ATES simulations. The low permeability of Layer 3 is precisely the property that creates confinement of overlying layers, thus defining the confining units as observed in standard hydrogeological terminology. Although not directly utilised for ATES operations, Layer 3 serves critical functions in model accuracy: it provides a realistic lower boundary condition representing the transition to aquitard material, thereby eliminating arbitrary boundary assumptions at 40 m depth that could introduce spurious vertical transport effects. Furthermore, the low thermal conductivity and water flux in Layer 3 establish thermally stable lower boundary conditions, permitting accurate specification of geothermal gradients without artificial heat effects. In transient coupled thermal-hydraulic simulations, the low-permeability layer enhances numerical stability by preventing unrealistic pressure and temperature fluctuations at depth-discretised boundaries, a factor which is of particular importance for long-term ATES cycles. This three-layer discretisation provides a scientifically justified balance between model complexity and computational efficiency, while capturing the essential hydrogeological features controlling thermal plume behaviour in the shallow aquifer. This is consistent with standard numerical modelling practice for shallow geothermal systems [241–243].

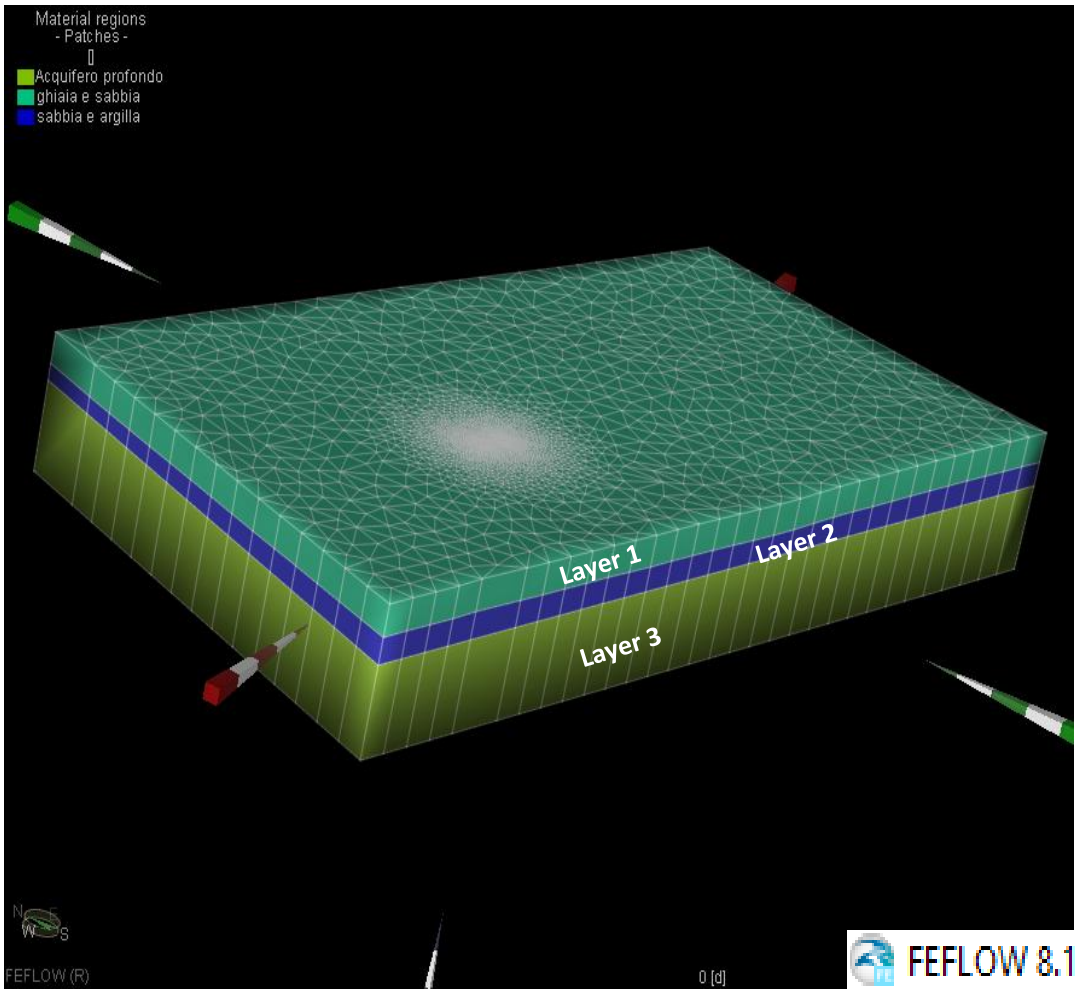

Figure 110. 3D model domain and layer discretisation.

Figure 111 displays the well positions and finite element mesh for Case Study 1, showing the strategic spatial arrangement of the three-well system. The figure illustrates the high-resolution triangular mesh refinement near well locations to accurately represent steep thermal and hydraulic gradients, with coarser discretization in far-field areas

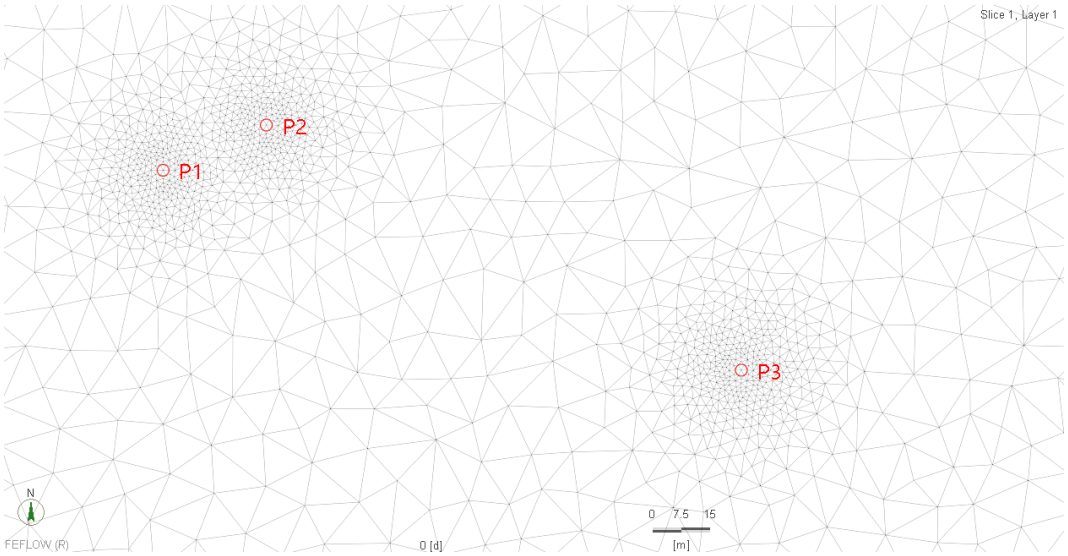

Figure 111. Wells position and FEFLOW triangular mesh (ATES Case 1).

During the initial two years, the system functions as a conventional open-loop geothermal installation with well P1 serving as the extraction point and well P2 as the injection point, separated by approximately 30 meters. This configuration operates continuously at a flow rate of 5 l/s, intentionally limited to prevent thermal interference between intake and discharge wells in the closely-spaced doublet configuration. The system provides thermal energy for heat pump operation while simultaneously establishing a thermal plume that migrates downgradient with the natural groundwater flow. The relatively low flow rate (5 l/s) corresponds to a theoretical thermal power capacity of approximately 150 kW. The theoretical power calculations are calculated from the Equation 2 assuming a temperature delta of 7 and using the volumetric heat capacity of water (4.18 MJ/Km^3). The selection of a 7 ΔT is driven by compliance with the environmental regulatory framework of the Piedmont Region, which establishes absolute thermal thresholds for reinjected groundwater, specifically prohibiting discharge temperatures above 22°C or below 8°C. Given an average undisturbed aquifer temperature of 15°C, a thermal alteration of 7°C represents the maximum permissible deviation. Consequently, this value was adopted to model the system under conditions of maximum thermodynamic performance while ensuring strict adherence to environmental constraints.

During this phase, several monitoring piezometers were positioned downgradient of well P2 to track thermal plume evolution and validate numerical model predictions of plume trajectory, migration velocity, and temperature

distribution. These monitoring data provide critical information for confirming that the thermal plume develops as predicted and reaches the intended location for well P3, validating the fundamental concept before significant additional investment.

The critical innovation occurs during Phase 2, implemented after two years of open-loop operation when sufficient observational data confirms thermal plume behaviour and optimal positioning for the downstream extraction well (P3). well P1 is converted from extraction to injection well as well P2, then well P3 is now operating as extraction well. positioned strategically downstream to intercept the thermal plume generated during the previous operational phase. This configuration inverts the conventional well arrangement, with injection occurring upstream and extraction downstream, explicitly designed to capture advectively transported thermal energy. The increased separation between injection wells (P1, P2) and extraction well (P3) enables a substantial flow rate increase to 20 l/s total (10 l/s each for P1 and P2, 20 l/s for P3), corresponding to a theoretical thermal power capacity of 574 kW, nearly four times the Phase 1 capacity.

4.2.2 Case Study 2

The second ATES case study area is the same of the open-loop plant case 2 (chapter 2.4 Case Studies). This installation demonstrates a more sophisticated approach to seasonal thermal energy storage, implementing a four-well configuration with bidirectional seasonal operation designed to serve substantial heating and cooling demands while achieving enhanced thermal recovery efficiency through optimized operational strategies. This system represents a significant scale increase compared to the first case study installation, with substantially higher flow rates and thermal capacities suitable for district-scale applications serving multiple buildings or large institutional facilities. This design plant employs four wells arranged in two doublets, with well functions alternating seasonally according to thermal demand characteristics (**Figure 112**). During summer cooling operations, Wells P1-P2 function as injection points receiving heated water from building cooling systems, while Wells P3-P4 serve as extraction points providing cool groundwater for cooling services. During winter heating operations, this configuration reverses completely: Wells P1-P2 become extraction points providing warmed groundwater for heat pump systems, while Wells P3-P4 serve as injection points receiving cooled water returned from heat pump evaporators. The distance between P2 and P4 is 190 m. This bidirectional operational strategy creates distinct warm and cold thermal zones within the aquifer formation, with each zone serving alternately as thermal source and thermal sink across seasonal cycles. The spatial separation between doublets enables development of substantial thermal storage capacity while maintaining sufficient distance to prevent short-term thermal interference between simultaneous injection and extraction operations.

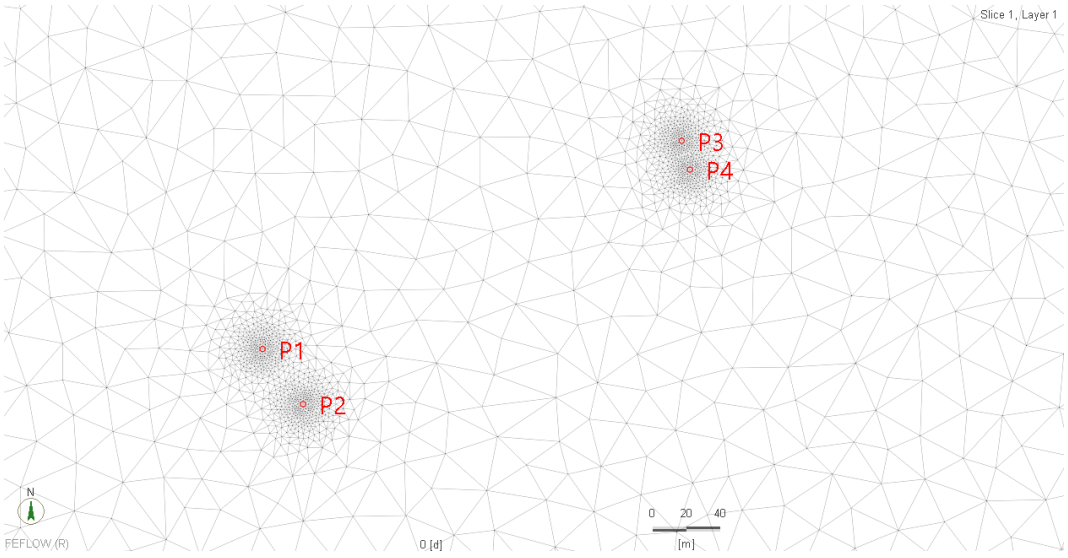

Figure 112. Wells position and FEFLOW triangular mesh (ATES Case 2).

A critical innovation implemented involves asymmetric flow rates optimized to match seasonal thermal demand profiles characteristic of the installation location. Summer cooling operations utilise a flow rate of 80 l/s, while winter heating operations employ an increased flow rate of 125 l/s, reflecting the higher thermal power requirements for space heating compared to space cooling in the regional

climate. This asymmetric flow strategy directly addresses the common challenge in ATES systems of matching seasonal energy input and extraction to maintain long-term thermal balance within the aquifer. By adjusting flow rates according to actual thermal demands, the system achieves more effective utilisation of stored thermal energy while avoiding excessive thermal drift that could compromise long-term performance. Five-years of operating system are simulated and presented in the chapter 4.3 Results.

4.2.3 Case Study 3

The third ATES case study is the most ambitious and innovative configuration examined involves the coordinated operation of two geographically separated open-loop plant (open-loop case study 1 and 2 chapter 2.4 Case Studies) positioned strategically to exploit natural groundwater flow for cascaded thermal plume recovery (**Figure 113**). This integrated approach demonstrates how multiple open-loop systems can be designed to operate synergistically, with downstream installations operating as ATES plant intercepting and utilizing thermal plumes generated by upstream systems. The case study integrated system comprises sixteen wells total distributed across two distinct installation sites separated by approximately 826 meters in the direction of natural groundwater flow. The upstream open-loop plant, employs eight wells configured as case 1 in chapter 2.4 Case Studies and work as standalone open-loop plant. The downstream plant, similarly employs eight wells with operational parameters adapted to optimize thermal plume recovery from the upstream installation. The 826-meter separation distance represents a carefully optimized value that balances competing design objectives. Sufficient separation enables thermal plumes generated at upstream plant to develop fully and migrate to the downstream location under the influence of natural groundwater flow (~ 2 km/year), providing opportunities for thermal recovery. Simultaneously, the separation must not be excessive, as greater distances increase thermal losses through conductive heat exchange with surrounding geological formations and reduce the magnitude and quality of thermal energy available for recovery. Both installations operate with combined flow rates of 300 l/s, representing a substantial increase in system scale compared to the previously described configurations. This high flow rate enables significant thermal power output suitable for large urban district applications while creating substantial thermal plumes with sufficient thermal content to remain viable across the inter-site separation distance.

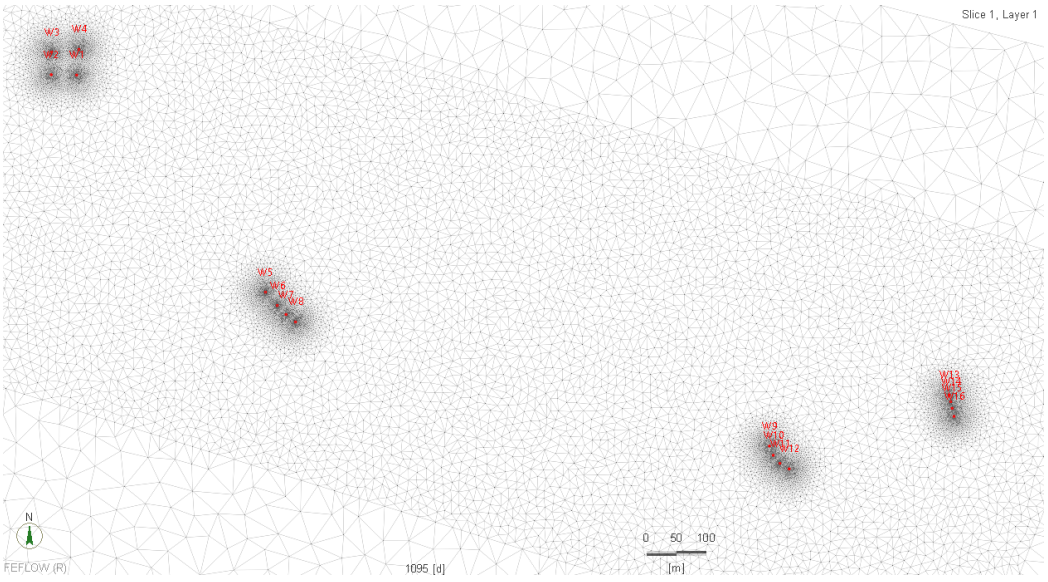

Figure 113. Wells position and FEFLOW triangular mesh (ATES Case 3).

The conceptual innovation of cascaded recovery transforms what would conventionally be considered thermal pollution or environmental impact from the upstream plant into a valuable thermal resource for the downstream plant, exemplifying circular economy principles applied to urban thermal energy management. To identify optimal operational strategies and quantify performance under various operating conditions, five distinct operational scenarios were evaluated through comprehensive numerical modelling. These scenarios explore different combinations of heating and cooling operation at each site, representing various potential end-use requirements and system integration possibilities (Table 16).

Table 16. Plant configuration for different scenarios, indicating the months of operation for heating and cooling.

	Upstream plant			**Downstream plant**		
Scenario	*Flowrate (l/s)*	*Heating (month)*	*Cooling (month)*	*Flowrate (l/s)*	*Heating (month)*	*Cooling (month)*
1	300	6	6	300	6	6
2	300	12	0	300	6	6
3	300	6	6	300	12	0
4	300	12	0	300	12	0
5	300	0	12	300	12	0

- **Scenario 1 -** *Balanced Bidirectional Operation*: Both plants operate with 6 months heating and 6 months cooling, representing buildings with balanced thermal loads such as modern office buildings with high internal gains year-round;
- **Scenario 2 -** *Upstream Heating Only, Downstream Balanced*: Upstream plant operates year-round heating (e.g., residential buildings without air conditioning), while downstream maintains balanced operation;
- **Scenario 3 -** *Upstream Balanced, Downstream Heating Only*: Upstream maintains balanced operation while downstream focuses on heating;
- **Scenario 4 -** *Both Plants Heating Only*: Both installations operate exclusively in heating mode, representing a heating-dominated district without cooling services;
- **Scenario 5 -** *Complementary Operation*: Upstream operates year-round cooling while downstream operates year-round heating, creating ideal conditions for cascaded thermal energy recovery. This represents specialized facilities such as data centres (upstream) paired with residential districts (downstream).

4.3 Results

4.3.1 Case Study 1

Figure 114 presents the thermal interference pattern in horizontal section after 360 days of simulation, representing conditions at the end of the first winter season in open-loop configuration. The figure clearly demonstrates that the thermal plume generated by injection at Well P2 has successfully migrated to reach the intended location for Well P3, validating the fundamental design concept. The thermal plume exhibits an elongated morphology aligned with the groundwater flow direction (west-southwest),with temperatures elevated 2-4°C above ambient aquifer conditions. **Figure 115** displays a cross-sectional view of thermal interference after 360 days, revealing the vertical distribution of the thermal plume within the aquifer system. This visualization demonstrates that thermal effects are largely confined to Layer 1 and 2 (the shallow aquifer), with minimal vertical migration into underlying Layer 3. These Phase 1 results provide confidence to proceed with Phase 2 ATES configuration, confirming that thermal plumes develop as predicted and will be accessible for recovery at the P3 location.

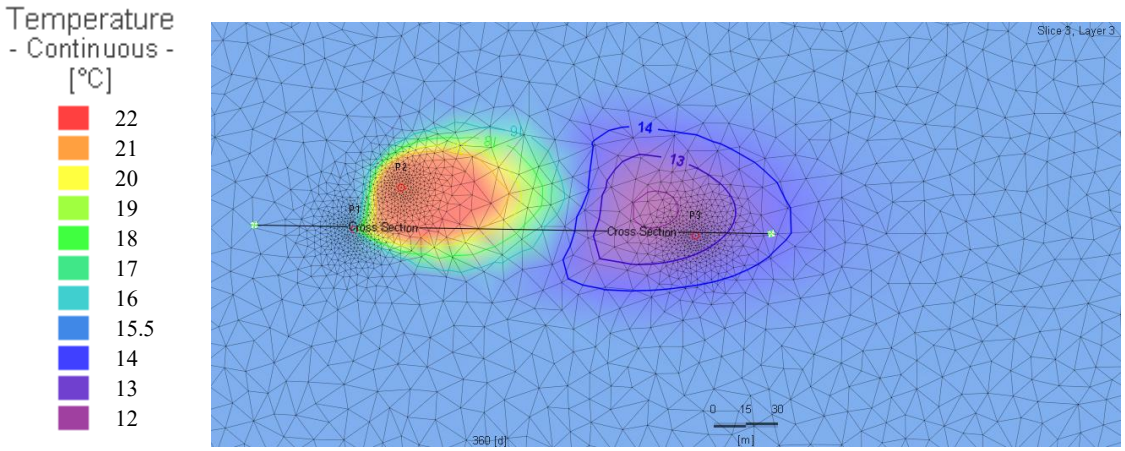

Figure 114. Thermal interference of the ATES case study 1 in horizontal section after 360 days of simulation.

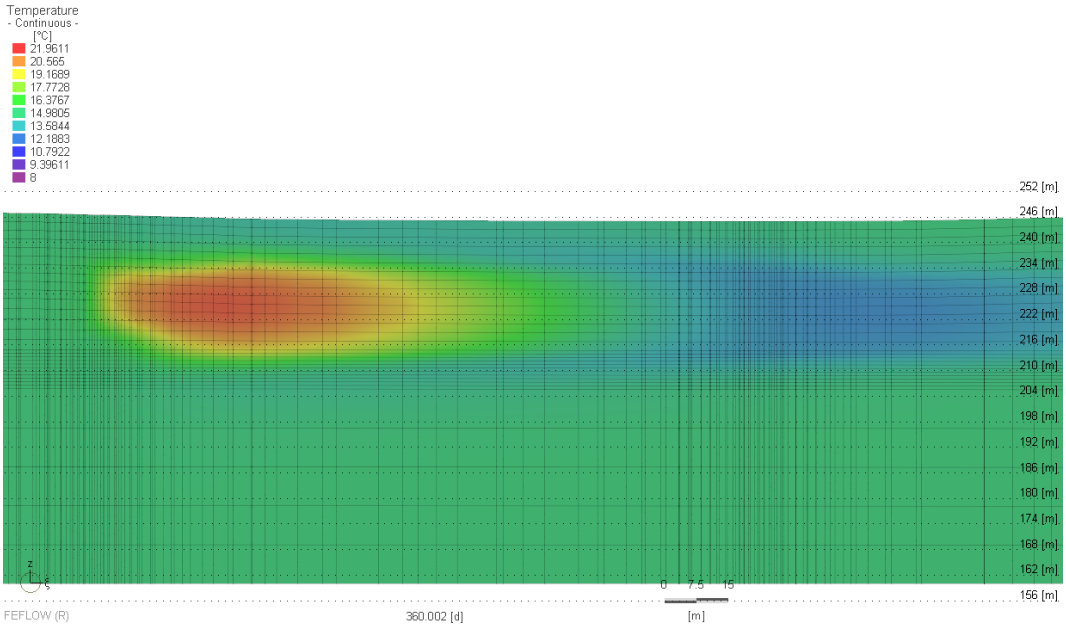

Figure 115. Cross section of the thermal interference of the ATES case study 1 after 360 days of simulation.

From the third year the new P3 well is operating as the intake well and wells P1 and P2 as discharge. Thanks to this new configuration the flowrate is augmented to 20 l/s for intake P3 and 10 l/s for discharge P1 and P2 each.

The results at the end of the winter of the fifth year of simulation (after 1620 days and 1800 days) are shown in **Figure 116** and **Figure 118**. These figures demonstrate a fundamentally different thermal pattern compared to Phase 1, with the active ATES configuration creating distinct seasonal thermal zones. The cold/hot plume generated during the previous summer has been effectively absorbed by extraction at Well P3, while thermal effects are limited to the area between injection wells and extraction well, with minimal thermal pollution extending beyond P3. The extraction temperature at Well P3 reaches approximately 2 °C differences relative to ambient conditions of 15°C baseline (**Figure 120**).

Figure 117 and **Figure 119** present the corresponding cross-sectional view after 1620 and 1800 days, confirming that vertical thermal containment remains

effective throughout ATES operation, with all significant thermal effects occurring within the shallow aquifer layer.

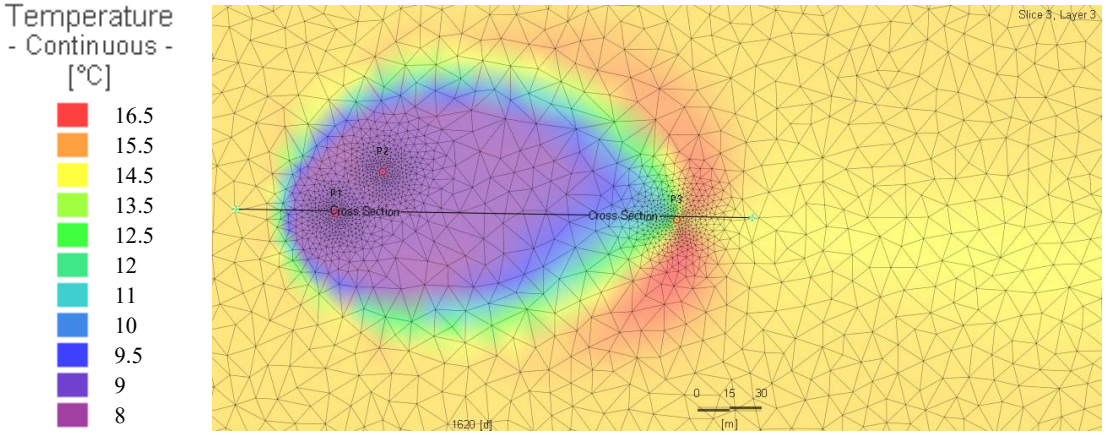

Figure 116. Thermal interference of the ATES case study 1 in horizontal section after 1620 days of simulation.

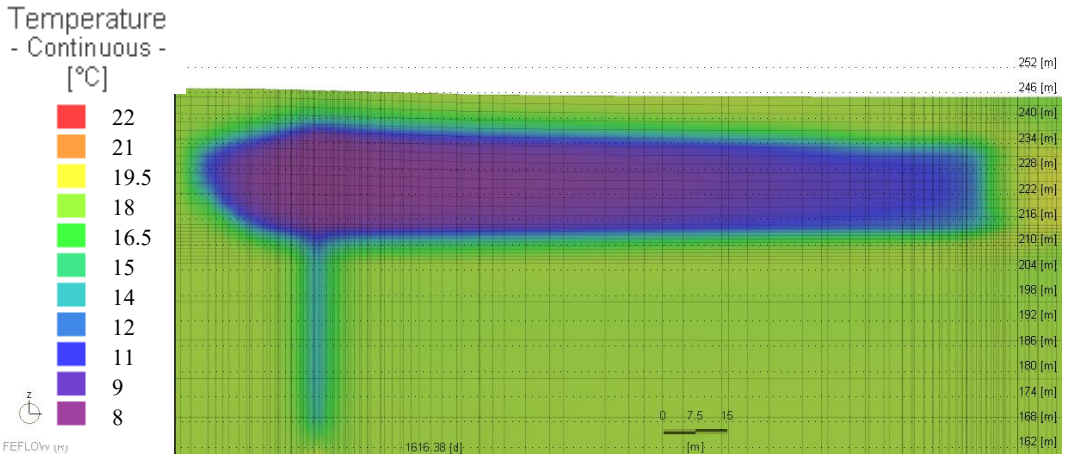

Figure 117. Cross section of the thermal interference of the ATES case study 1 after 1620 days of simulation.

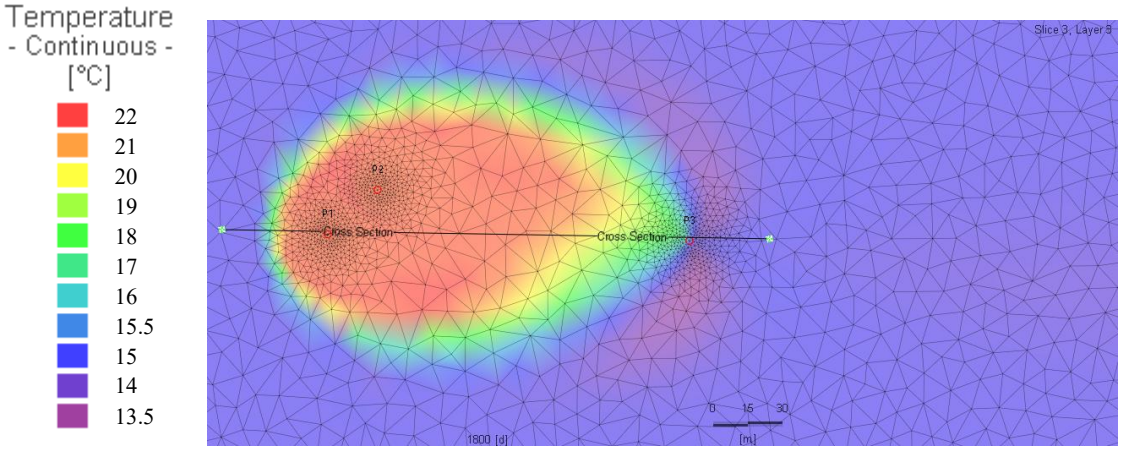

Figure 118. Thermal interference of the ATES case study 1 in horizontal section after 1800 days of simulation.

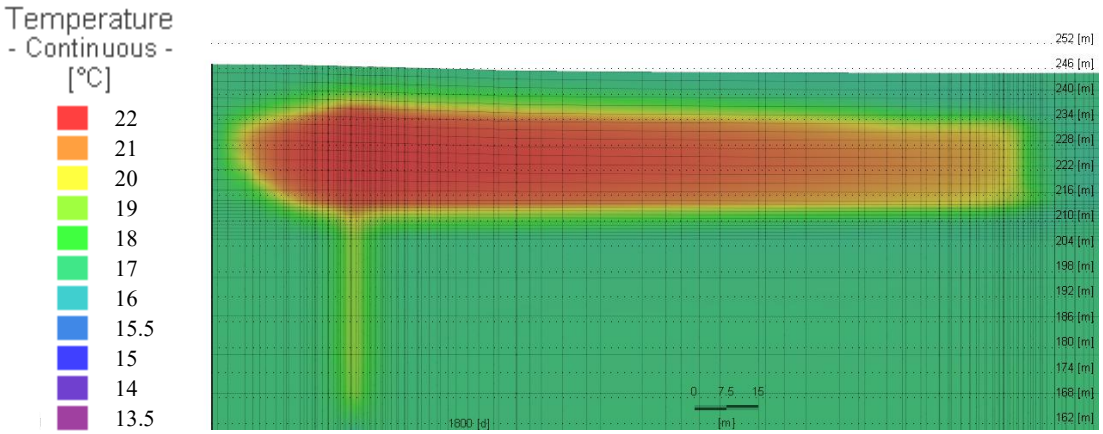

Figure 119. Cross section of the thermal interference of the ATES case study 1 after 1800 days of simulation.

The three-dimensional visualizations presented in Appendix A, ranging from Figure 170 (day 1495) to Figure 173 (day 1800). These visualizations depict isosurfaces corresponding to two distinct thermal thresholds: the 20°C isotherm (orange) and the 12°C isotherm (blue). This representation facilitates a comprehensive assessment of the complex three-dimensional thermal dynamics inherent to the aquifer system. Analysis of the thermal distribution reveals that volumes exceeding 20°C are spatially confined to limited zones and exhibit rapid thermal dissipation. Similarly, the cold plume, defined by temperatures below 12°C, remains localized within the near-field region of the reinjection wells. These specific reference temperatures were selected as indicators to quantify the spatial extent of thermal anomalies and to evaluate the potential thermal interference within the aquifer.

Figure 120 displays the temperature evolution at all three wells throughout the five-year simulation period, providing comprehensive insight into system thermal dynamics. Well P1 functions as an extraction well during Years 0 to 2 in the open-loop phase, maintaining near-ambient temperature of approximately 15°C, then converts to an injection well during Years 2 to 5 in the ATES phase, exhibiting strong seasonal variation between 8°C for winter injection and 22°C for summer injection. Well P2 functions as an injection well throughout the simulation showing seasonal temperature variation, while Well P3 remains inactive during monitoring phase then functions as extraction well during ATES phase, exhibiting characteristic sinusoidal variation with approximately 2°C amplitude centered on 15°C ambient temperature. The P3 temperature profile demonstrates winter thermal recovery with extraction temperatures reaching approximately 17°C, representing successful recovery of summer-stored heat at 2°C above ambient, and summer thermal recovery with temperatures declining to approximately 13°C, representing recovery of winter-stored cooling at 2°C below ambient. This approximately 2°C temperature recovery, while modest compared to ideal ATES systems, represents significant improvement over conventional open-loop systems operating at constant ambient temperature. The recovered temperature differential translates directly to improved heat pump coefficient of performance. The cyclical fluctuation of well P3 confirms successful thermal energy storage and recovery across multiple

operational seasons. The system maintains full compliance with applicable regulatory temperature limits for groundwater reinjection wells P1 and P2, specifically 8°C minimum during winter operations and 22°C maximum during summer operations. These constraints, established to protect groundwater quality and aquifer ecosystem integrity, represent fundamental design constraints that limit achievable temperature differentials and consequently system thermal capacity.

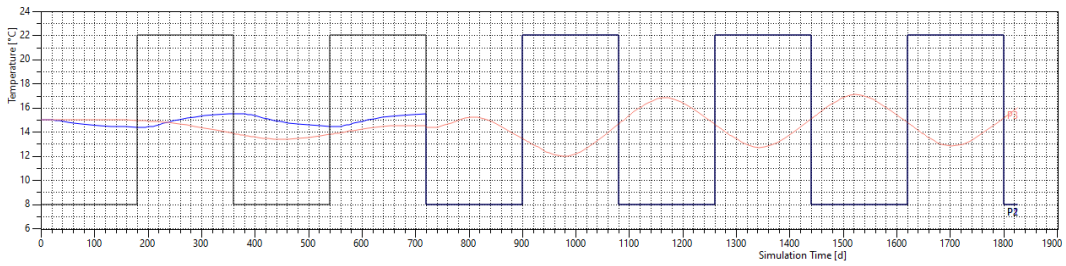

Figure 120. Aquifer temperature plot in the different geothermal wells location during 5 years of simulation, the blue line is P1, the black one is P2 and the red one is P3.

Figure 121 presents the heat rate budget throughout the five-year simulation, expressed in kilowatts of thermal power, with negative values corresponding to winter heating and positive values corresponding to summer cooling. During Phase 1 spanning Years 0 to 2, relatively stable power output around 150 to 200 kilowatts is observed. During Phase 2 spanning Years 2 to 5, substantially increased power output with pronounced seasonal variation is evident, with winter heating power ranging from negative 500 to negative 650 kilowatts and summer cooling power ranging from positive 600 to positive 785 kilowatts. **Figure 122** provides a detailed view of the final summer period, revealing that maximum power output approaches 785 kilowatts during optimal conditions in the fifth year. The achieved maximum thermal power of 785 kilowatts represents approximately 37% improvement over standard open-loop performance at equivalent flow rates where 20 liters per second with fixed 7°C temperature differential yields 574 kilowatts.

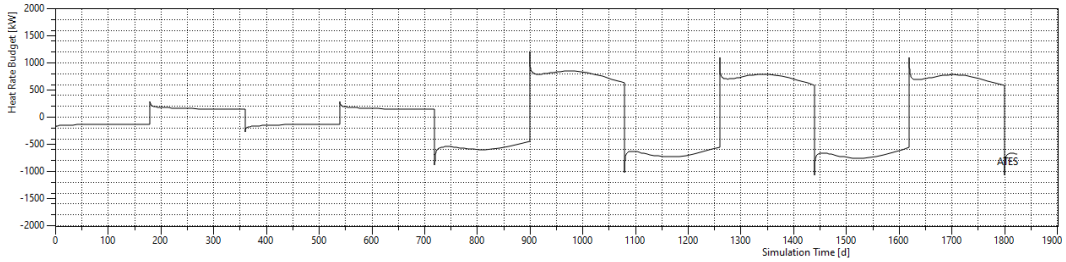

Figure 121. Water thermal power plot: negative value corresponds to winter period (heating), positive value corresponds to summer period (cooling).

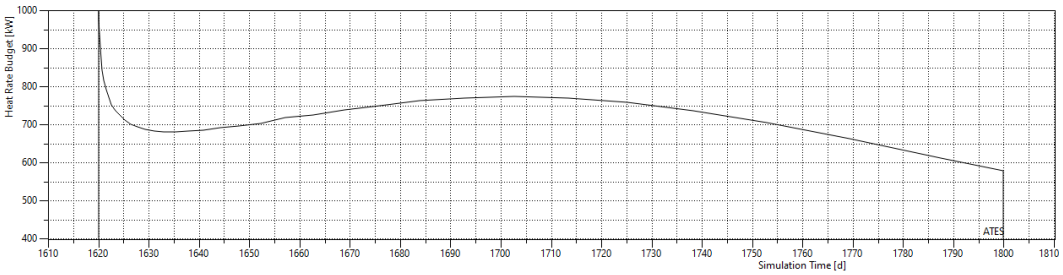

Figure 122. Water thermal power plot zoom, last summer simulation period (from 1620 day to 1800 day).

4.3.2 Case Study 2

The results show the creation of two distinct thermal plumes (hot and cold) that are partially reabsorbed by the system. The water flow in this area is very fast and the system is only able to recover part of the generated thermal plume. Nevertheless, it achieves a general improvement in extractable power. **Figure 123** and **Figure 126** present the thermal interference pattern in horizontal section after 1620 and 1800 days of simulation corresponding to the end of the fifth year for the four-well seasonal reversible system. The figure demonstrates partial thermal plume recovery rather than complete reabsorption, which is a consequence of the high groundwater flow velocity estimated at 2000 meters per year causing substantial advective transport and different flowrate. The cold thermal zone in the north area consists of residual effects from previous winter injection. **Figure 124** and **Figure 125** display cross-sectional views along two transects at day 1620, revealing vertical thermal distribution patterns. Both cross-sections demonstrate primary thermal activity confined to shallow layers corresponding to the upper 15 to 20 meters of the first aquifer. Vertical thermal gradient exhibits warm water slight upward migration due to buoyancy while cool water shows modest downward tendency.

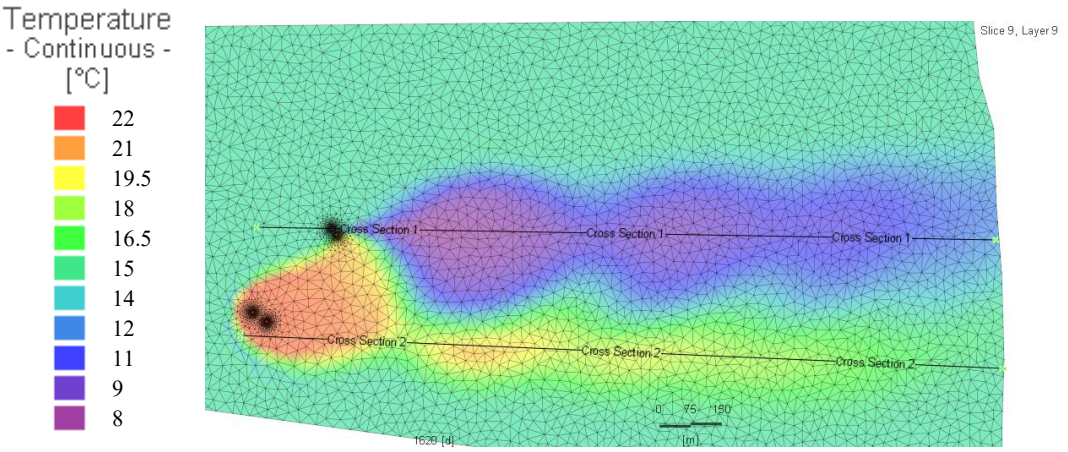

Figure 123. Thermal interference of the ATES case study 2 in horizontal section after 1620 days of simulation.

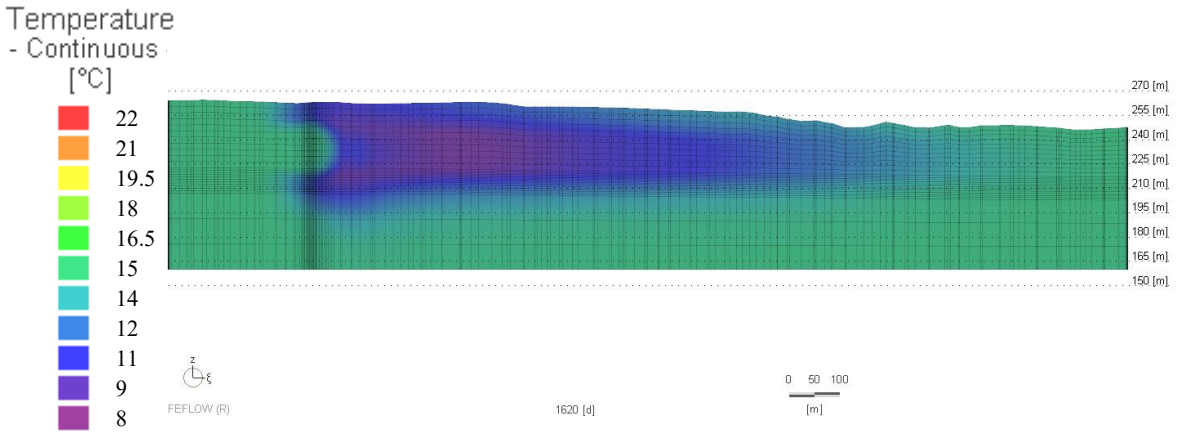

Figure 124. Cross section 1 of the thermal interference of the ATES case study 2 after 1620 days of simulation.

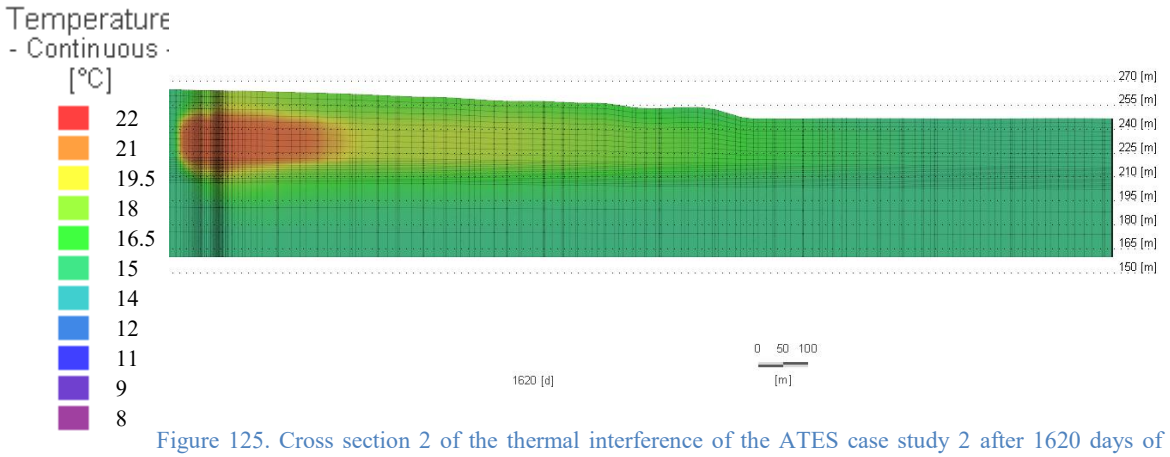

Figure 125. Cross section 2 of the thermal interference of the ATES case study 2 after 1620 days of simulation.

Figure 127 and **Figure 128** present corresponding visualizations for the end of winter at day 1800, showing the seasonal reversal of thermal patterns.

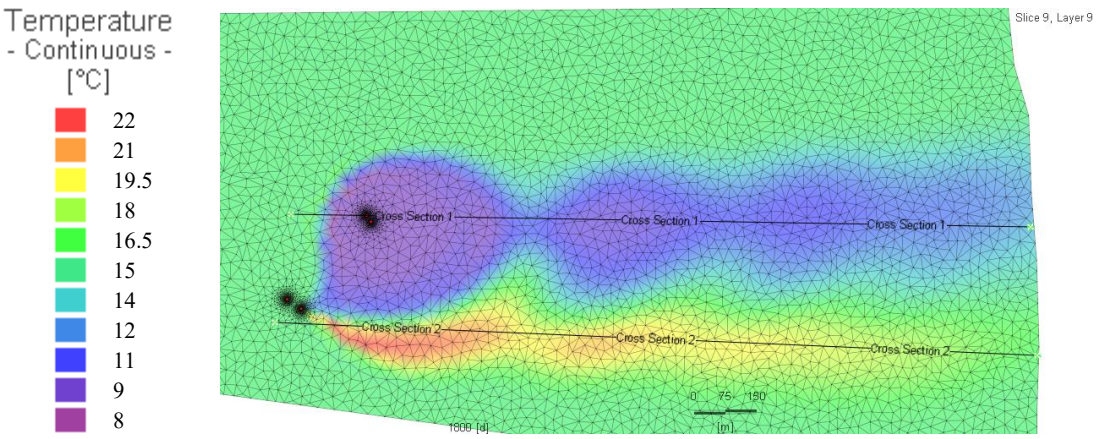

Figure 126. Thermal interference of the ATES case study 2 in horizontal section after 1800 days of simulation.

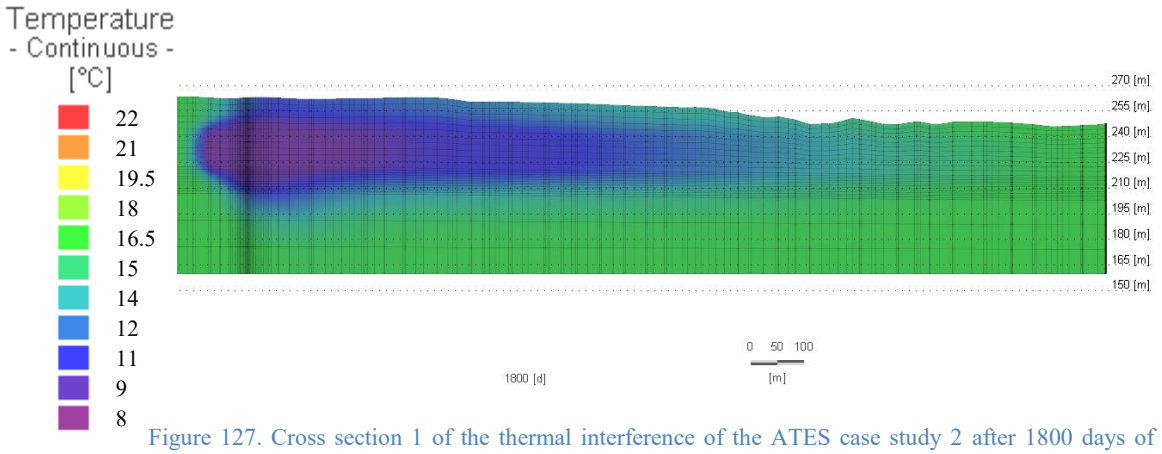

Figure 127. Cross section 1 of the thermal interference of the ATES case study 2 after 1800 days of simulation.

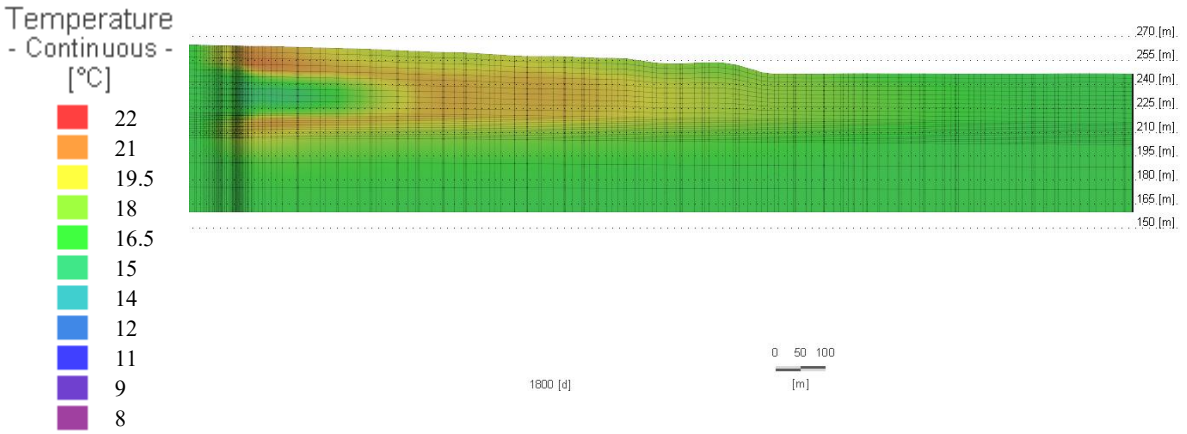

Figure 128. Cross section 2 of the thermal interference of the ATES case study 2 after 1800 days of simulation.

The three-dimensional visualizations in Appendix A (**Figure 174** and **Figure 175**) employ 20°C yellow-orange and 12°C blue isosurfaces to delineate thermal zones. These figures reveal asymmetric plume geometries where the blue plume at 12°C extends more than 2 kilometers downstream during winter reflecting higher winter flow rates of 125 liters per second, while the yellow plume at 20°C is limited to approximately 800 meters during summer corresponding to lower flow rates of 80 liters per second. This asymmetry is intentional and beneficial, serving heating optimization as larger cold plume volume provides greater thermal storage capacity, cooling constraint as smaller warm plume reduces potential urban heat island and climate change contributions.

Figure 129 displays water thermal power during the final summer period from days 1440 to 1620, comparing ATES performance against theoretical open-loop baseline. The ATES performance demonstrates maximum power of approximately 4500 kW during early summer, declining to approximately 2000 kW by end of summer, with average performance around 3000 kW. The open-loop baseline maintains constant power of 2300 kW throughout summer. Performance analysis reveals peak improvement of 74% enhancement during early summer, end-of-season performance approaching baseline as stored thermal resource depletes, and seasonal average showing approximately 30% improvement over open-loop operation. The declining summer performance reflects progressive depletion of the

cold thermal plume stored during the previous winter and the assimilation of the same seasonal plume, resulting in reduction of power.

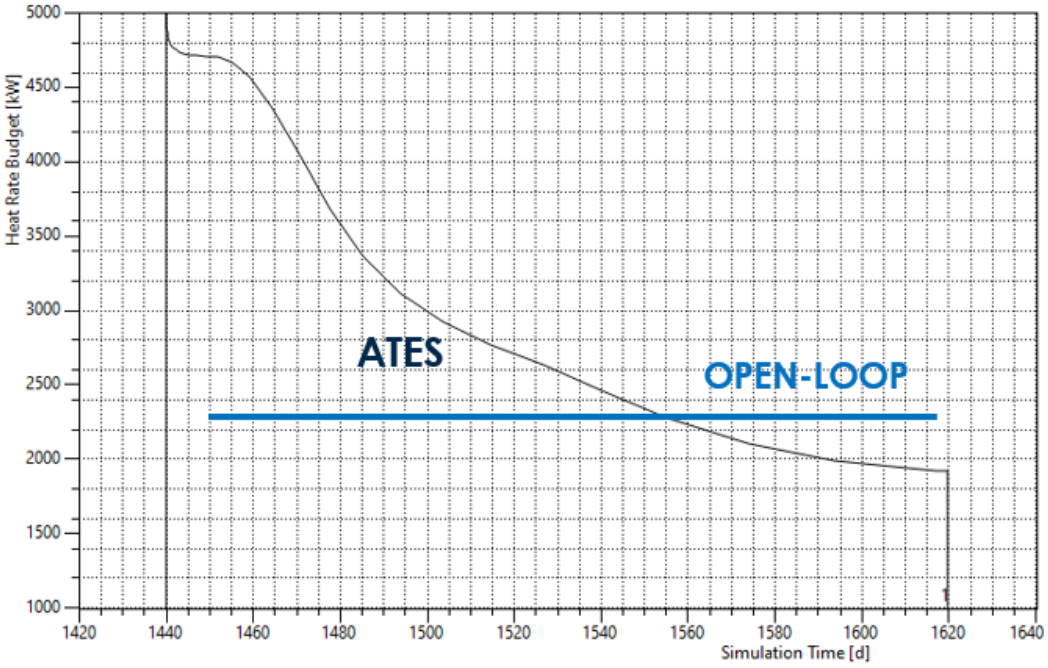

Figure 129. Water thermal power plot: negative value (black line) corresponds to winter period (heating), positive value corresponds to summer period (cooling). This represents the last summer period (cooling mode from day 1440 to day 1620), blue line represents a theoretical open-loop plant operate with a fixed ΔT.

Figure 130 presents the analysis for the final winter period from days 1620 to 1800, comparing ATES performance against open-loop baseline. The ATES performance demonstrates maximum power of approximately 7000 kilowatts during early winter, moderate decline with power stabilizing around 3700 to 4000 kilowatts through winter, and average performance around 5000 kilowatts. The open-loop baseline maintains constant power of 3650 kilowatts. Performance analysis reveals peak improvement of 92% enhancement during early winter, end-of-season performance maintaining 10 to 15% improvement even after partial thermal depletion, and seasonal average showing approximately 37% improvement over open-loop operation. The winter performance characteristics differ from summer exhibiting higher absolute performance, better sustained performance, and greater thermal recovery, reflecting the system's optimization for heating-dominated operation consistent with regional climate characteristics.

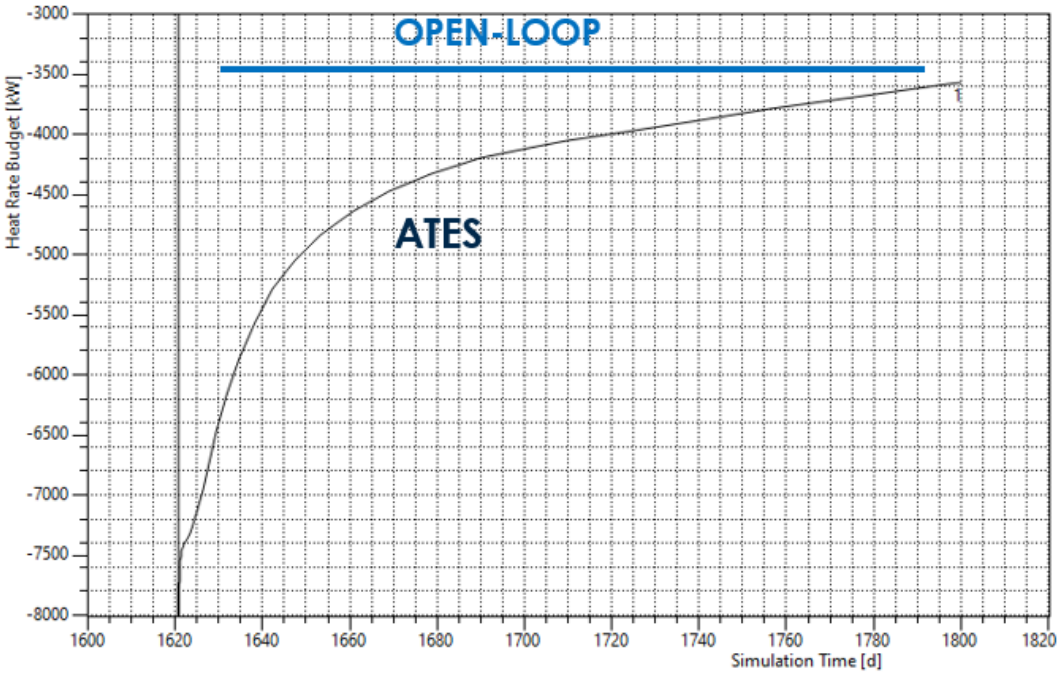

Figure 130. Water thermal power plot: negative value (black line) corresponds to winter period (heating), positive value corresponds to summer period (cooling). This represents the last winter period (heating mode from day 1620 to day 1800), blue line represents a theoretical open-loop plant operate with a fixed ΔT.

4.3.3 Case Study 3

Figure 131 displays thermal interference in horizontal section after 910 days for Scenario 1, where both upstream and downstream plants operate with balanced 6-month heating and 6-month cooling periods. The figure reveals the upstream plant thermal pattern exhibiting distinct cold and warm zones alternating seasonally with thermal plumes migrating eastward with groundwater flow. The downstream plant thermal pattern successfully intercepts upstream thermal plumes while creating its own seasonal thermal zones and demonstrating partial thermal recovery from upstream operations. The interaction zone between plants shows complex thermal mixing with temperature gradients indicating thermal energy transfer between systems. **Figure 132** presents a cross-sectional view after 910 days, confirming vertical thermal containment throughout the 826-meter separation distance.

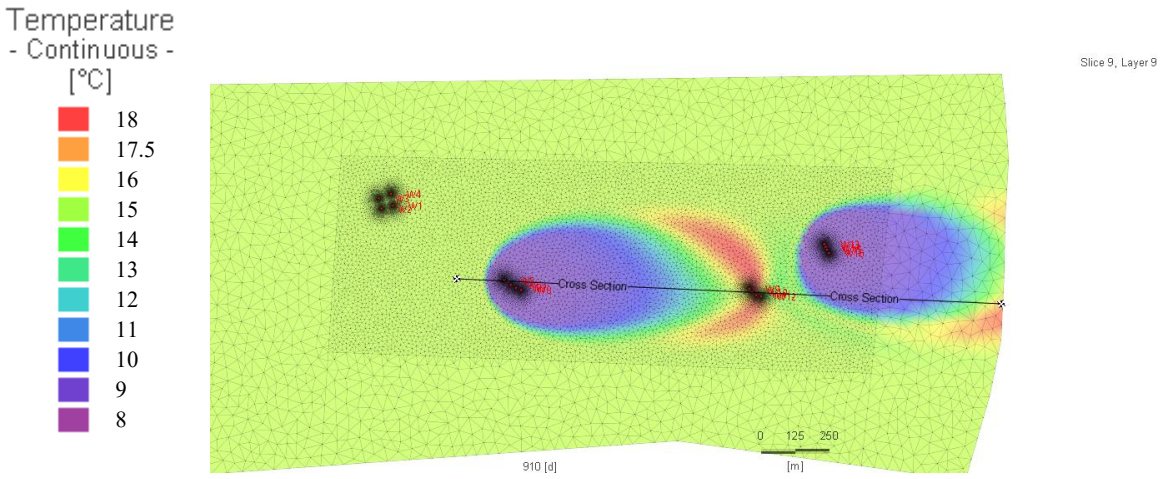

Figure 131. Thermal interference of the ATES case study 3 in horizontal section after 910 days of simulation (Scenario 1).

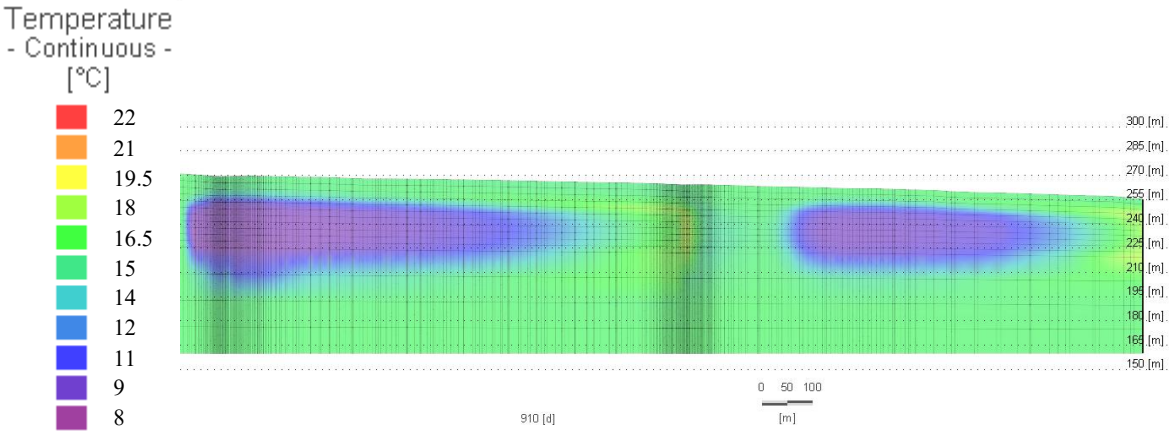

Figure 132. Cross section of the thermal interference of the ATES case study 3 after 910 days of simulation (Scenario 1).

Figure 133 and Figure 134 show corresponding conditions after 1095 days at the end of summer, illustrating seasonal reversal with warm thermal plumes dominating the upstream area and the downstream plant successfully accessing warmed groundwater.

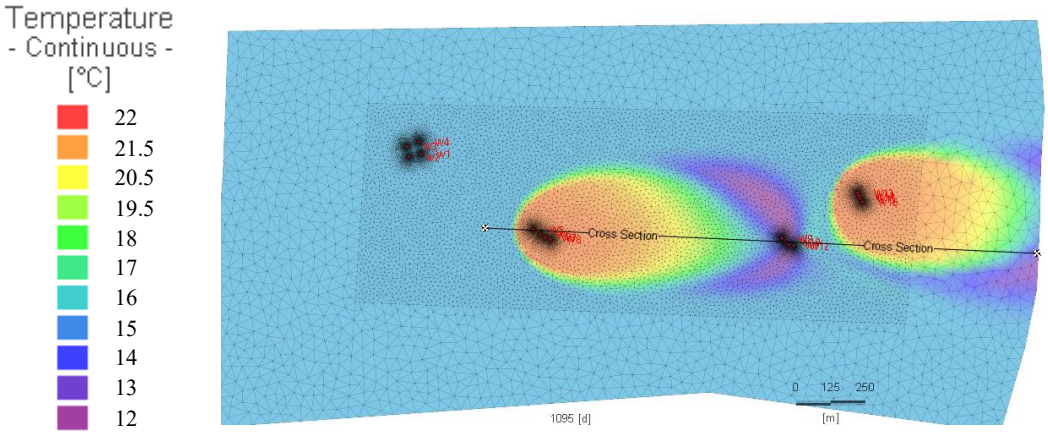

Figure 133. Thermal interference of the ATES case study 3 in horizontal section after 1095 days of simulation (Scenario 1).

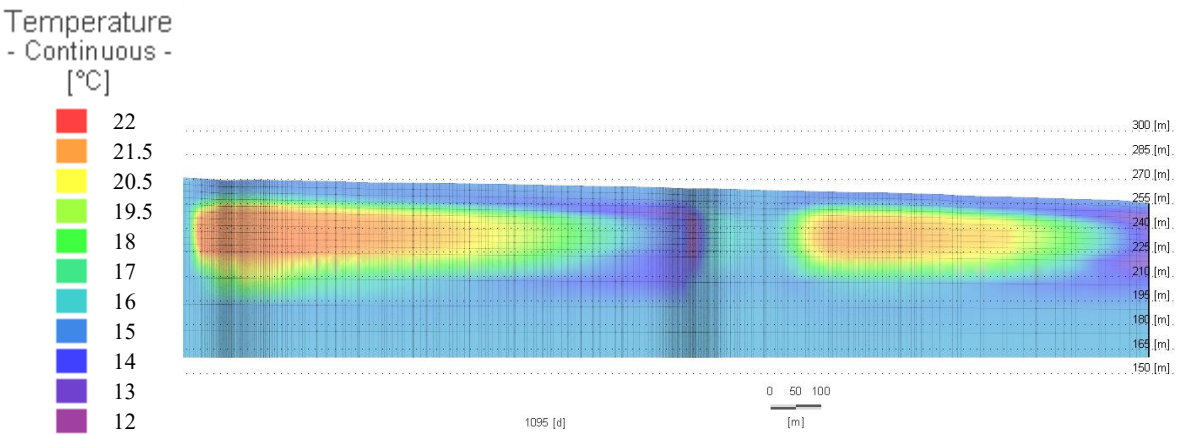

Figure 134. Cross section of the thermal interference of the ATES case study 3 after 1095 days of simulation (Scenario 1).

The sequential three-dimensional visualizations in Appendix A from **Figure 176** (day 744) to **Figure 180** (day 1095) track thermal plume evolution in Scenario 1. At day 744 representing early winter, developing cold thermal plumes from winter injection are evident with residual warm plumes from previous summer migrating downgradient. By day 784 mid-winter, expansion of cold thermal zones occurs with progressive advection of warm plumes toward downstream and establishment of continuous thermal connection between installations. At day 910 end of winter demonstrates maximum extent of cold plumes with downstream positioned to intercept upstream warm water from previous summer. At day 1095 end of summer shows maximum extent of warm plumes with cold plumes reaching downstream and full thermal connectivity established. The 3D vertical cross-section (**Figure 180**) confirms all thermal effects remain confined to the shallow aquifer.

Figure 135 presents temperature trends for all wells in Scenario 1, with upstream plant wells exhibiting strong seasonal variation between 8°C and 22°C, while downstream extraction wells display moderate variations from 11°C to 19°C reflecting thermal benefit from upstream operations. **Figure 136** detailed view shows sinusoidal temperature variation at downstream wells with winter extraction temperatures elevated 2 to 4°C above ambient and summer extraction temperatures reduced 2 to 4°C below ambient, confirming successful thermal energy transfer via groundwater advection.

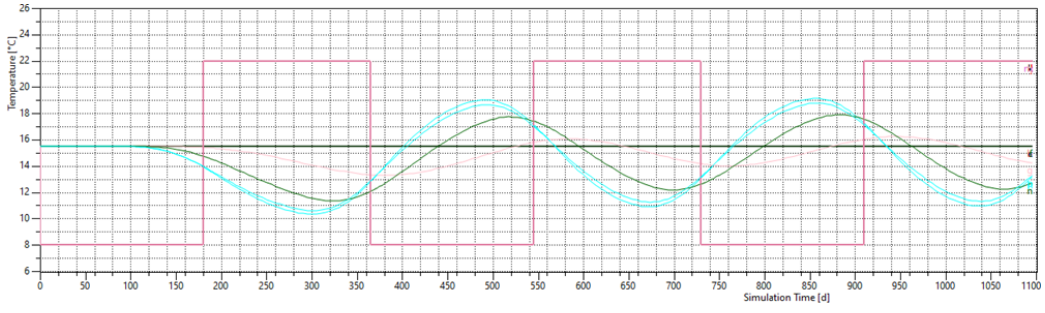

Figure 135. Graph showing temperature trends for each simulated well in Scenario 1 throughout the simulation period. The blue, green and pink lines correspond to the intake wells in the downstream plant.

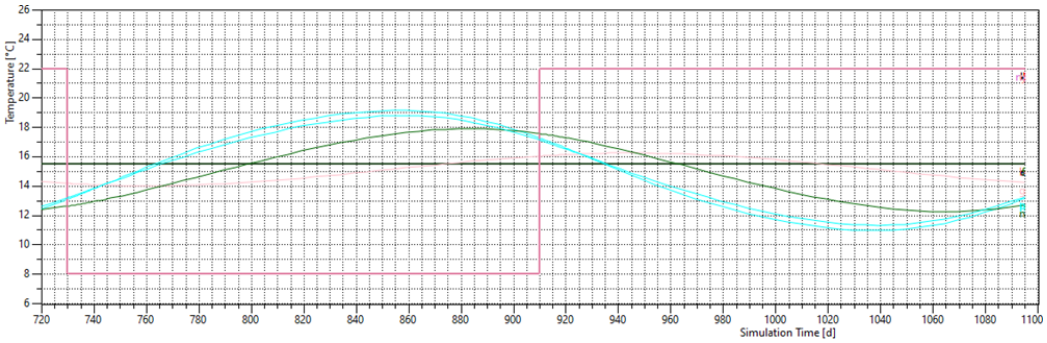

Figure 136. Graph showing temperature trends for each simulated well in Scenario 1 in the last year of simulation. The blue, green and pink lines correspond to the intake wells in the downstream plant.

In Appendix A all the related figure to the different Scenarios are presented.

Figure 181 displays thermal interference for Scenario 2 with upstream heating only and downstream balanced operation. This configuration creates continuous cold plume generation at upstream causing interference with downstream operations and reduced downstream heating performance. **Figure 182** and **Figure 183** confirm that continuous upstream cooling creates persistent cold thermal zones impacting downstream warm water extraction. **Figure 184** and **Figure 185** temperature time-series reveal downstream extraction wells show depressed winter temperatures negatively impacting heating though enhanced cooling performance in summer, demonstrating suboptimal performance due to thermal demand mismatch and the importance of operational coordination.

Figure 186 through **Figure 193** document Scenario 3 with upstream balanced and downstream heating only. The thermal patterns reveal upstream creates balanced seasonal zones while downstream generates continuous cold plumes, resulting in moderate thermal recovery. The 3D visualizations show extensive cold plume generation from downstream continuous heating with partial interception of upstream warm plumes and asymmetric thermal distribution. Temperature time-series indicate downstream maintains elevated winter temperatures but with limited summer recovery representing unused capacity and moderate overall efficiency. This scenario shows better performance than Scenario 2 but remains suboptimal.

Figure 194 through **Figure 198** examine Scenario 4 with both plants continuously heating, representing worst-case interference. Thermal patterns show continuous cold generation at both locations with severe thermal depletion in interaction zone. The 3D visualization reveals extensive interconnected cold zones with limited recovery potential. Temperature time-series demonstrate severely depressed downstream temperatures from 11°C to 13°C with minimal benefit from upstream and poor performance. This scenario confirms necessity of complementary or balanced operations for effective cascaded recovery.

Figure 199 through **Figure 203** document Scenario 5 representing complementary configuration with upstream cooling only and downstream heating only. The thermal patterns reveal upstream generates continuous warm plume from year-round cooling, this warm plume migrates efficiently to downstream location, downstream successfully extracts warmed water for heating, and minimal thermal

waste occurs. The 3D visualization in **Figure 201** shows clear thermal connectivity with continuous warm plume from upstream to downstream, efficient thermal transport across 826-meter separation, and compact thermal footprint indicating effective recovery. Temperature time-series in **Figure 202** and **Figure 203** demonstrate downstream extraction wells maintain consistently elevated temperatures from 17°C to 20°C, exceptional thermal recovery of 5 to 7°C above ambient during heating operations, and stable performance throughout operational period.

The quantitative performance comparison presented in **Table 17** shows maximum extractable water power for all five scenarios. Scenario 1 demonstrates balanced performance with highest combined capacity of 21.08 megawatts heating and 19.97 megawatts cooling, providing operational flexibility for mixed demands with moderate efficiency. Scenario 2 exhibits upstream heating penalty with severely reduced downstream heating of only 1.50 megawatts though enhanced downstream cooling of 16.35 megawatts, yielding overall poor performance and demonstrating destructive interference. Scenario 3 shows moderate performance maintaining good heating capacity of 21.08 megawatts total but reduced cooling of only 8.18 megawatts, underutilizing potential cooling capacity. Scenario 4 represents worst case with catastrophic downstream heating of only 1.50 megawatts, no cooling capacity, and total heating of 10.95 megawatts less than half of Scenario 1, confirming severe negative consequences of misalignment. Scenario 5 demonstrates optimal operation with downstream heating of 16.52 megawatts, modest cooling of 8.18 megawatts, and optimal suitability for complementary demand profiles.

Table 17. Results of the different simulated Scenarios (maximum extractable water power).

	Upstream plant					**Downstream plant**				**Total water power heating**	**Total water power cooling**
Scenario	Flowrate (l/s)	Heating (month)	Water power heating (MW)	Cooling (month)	Water power cooling (MW)	Heating (month)	Water power heating (MW)	Cooling (month)	Water power cooling (MW)	(MW)	(MW)
1	300	6	9.45	6	8.18	6	11.63	6	11.79	21.08	19.97
2	300	12	9.45	0	0	6	1.50	6	16.35	10.95	16.35
3	300	6	9.45	6	8.18	12	11.63	0	0.00	21.08	8.18
4	300	12	9.45	0	0	12	1.50	0	0.00	10.95	0.00
5	300	0	0	12	8.18	12	16.52	0	0.00	16.52	8.18

4.4 Discussion

The three case studies presented demonstrate conclusively that innovative ATES system design can successfully overcome the fundamental limitations typically associated with high groundwater flow velocities, substantially expanding the potential application domain for ATES technology. Conventional ATES design guidelines specify maximum acceptable groundwater flow velocity of approximately 25 meters per year based on requirements for thermal plume stability and recovery efficiency in bidirectional doublet configurations. The study sites exhibit groundwater flow velocities ranging from 378 meters per year in Case Study 1 to approximately 2000 meters per year in Case Studies 2 and 3, exceeding conventional limits by factors of 15 to 80 times. These conditions would typically preclude ATES consideration under conventional design paradigms, relegating such sites to simple open-loop geothermal systems with no thermal storage capability. The fundamental innovation implemented across all three case studies involves strategic well positioning that explicitly accounts for advective thermal transport, transforming groundwater flow from a detrimental factor causing thermal loss into an operational asset enabling thermal energy transport and recovery. Rather than attempting to minimize thermal plume migration through close well spacing and low flow rates, these designs embrace thermal advection as an inherent characteristic of the hydrogeological system and position extraction wells downstream to intercept migrating thermal plumes. This conceptual shift from preventing thermal migration to strategically exploiting it represents a paradigm change in ATES technology with broad implications for expanding applicability to alluvial aquifer systems worldwide that exhibit high transmissivity and appreciable hydraulic gradients.

The cascaded thermal plume recovery concept demonstrated in Case Study 3, particularly in Scenario 5, represents a particularly innovative approach with potential for widespread application in urban energy systems. Urban areas frequently contain multiple buildings or facility clusters with differing and often complementary thermal demand profiles, creating natural opportunities for integrated ATES system design. Examples include data centers generating continuous cooling loads paired with residential buildings in temperate climates that are heating-dominated, hospitals requiring year-round heating paired with office buildings having significant cooling loads, industrial facilities rejecting low-grade heat paired with district heating networks, and food storage facilities requiring continuous cooling paired with agricultural greenhouses requiring heating. This approach achieves improved individual system efficiency, enhanced urban energy integration where waste heat becomes resource, reduced environmental impact through conversion of thermal pollution to useful resource, implementation of circular economy principles, and economic optimization through shared infrastructure. The 826-meter separation distance suggests cascaded ATES

systems can integrate buildings or facilities several city blocks apart, providing substantial flexibility for urban energy planning.

The relationship between groundwater flow velocity and optimal well spacing represents a critical design parameter requiring site-specific optimization. The case studies demonstrate that higher groundwater flow velocities necessitate greater well separation to enable thermal plume migration to downstream extraction points, careful alignment with groundwater flow direction, and provide potential for larger system capacity due to continuous thermal transport. However, excessive separation causes increased conductive losses proportional to transport time, reduced thermal plume temperature due to dispersion, greater uncertainty in timing and characteristics, and higher risk of external interference. The optimal separation distances ranging from 137 to 200 meters for small systems up to 826 meters for large integrated systems provide initial guidance, though site-specific optimization through numerical modelling remains essential.

While detailed economic analysis extends beyond the scope of this thesis, several important economic and practical factors merit discussion regarding ATES implementation feasibility and deployment potential. ATES systems involve substantial initial capital investment for well drilling, installation, equipment, and control systems, but offer significant operational cost savings through reduced energy consumption compared to conventional heating and cooling systems. Capital cost analysis indicates that well drilling and installation typically represents 40-60% of total ATES project costs, with specific values depending on well depth, geological conditions, and required number of wells [244]. The expected payback time is less than 10 years in the worst case. The multi-well configurations required for the modified ATES designs presented here involve higher drilling costs than conventional two-well doublet systems, potentially affecting project economics. However, the improved performance and efficiency achieved through these configurations may justify the additional capital investment through enhanced operational savings. The sequential activation approach implemented in the first case study offers particular economic advantages by enabling phased system development with reduced initial investment risk. Initial implementation as a conventional open-loop system requires only two-well installation, with the third well added subsequently after confirming system performance and thermal plume behaviour. This phased approach reduces initial capital requirements and enables validation of numerical model predictions before committing to full ATES configuration.

Regulatory requirements represent critical considerations affecting ATES deployment. Groundwater use requires permits for water extraction, injection authorization, environmental assessment, and building system permits. The Netherlands provides premier example with dedicated ATES regulations establishing clear technical requirements, monitoring obligations, thermal radius zones preventing interference, coordinated permitting, and balance between environmental protection and technology facilitation [245]. The Dutch approach has enabled thousands of systems with minimal environmental incidents.

ATES systems contribute significantly to environmental sustainability through greenhouse gas emission reductions of 40 to 60% in primary energy consumption, with Case Study 2 scale avoiding 500 to 1000 tons CO_2 per year and Case Study 3 scale avoiding 1500 to 3000 tons per year. ATES enhances renewable energy integration where thermal storage decouples generation from consumption timing, enables excess renewable electricity utilisation, provides grid balancing services, and facilitates higher renewable penetration. ATES cooling applications combat urban heat island effects through active aquifer cooling reversing warming trends, reducing surface temperatures, and creating extensive cold zones with Case Study 2 plumes extending over 2 km.

4.5 Conclusion & Further Investigation

This research has demonstrated that innovative ATES system design can successfully enable seasonal thermal energy storage in aquifer systems characterized by groundwater flow velocities exceeding conventional design thresholds by one to two orders of magnitude. The hybrid sequential ATES in Case Study 1 achieved 37% performance improvement over conventional open-loop systems through phased implementation with downstream thermal plume interception, validating the fundamental concept of exploiting rather than preventing thermal advection. The seasonal reversible ATES in Case Study 2 demonstrated 30 to 37% seasonal performance improvements through asymmetric flow rate optimization and four-well bidirectional configuration, proving suitable for district-scale applications with balanced or heating-dominated thermal demands. The cascaded recovery ATES in Case Study 3 achieved exceptional performance through synergistic operation of upstream and downstream installations, with optimal complementary operation in Scenario 5 delivering 16.52 megawatts downstream heating capacity representing state-of-the-art performance for open-loop derived systems. The fundamental design innovation involves strategic well positioning that explicitly accounts for advective thermal transport by natural groundwater flow, positioning extraction wells downstream to intercept migrating thermal plumes rather than attempting to minimize migration through close spacing. This conceptual transformation expands ATES technology applicability substantially with significant implications for urban areas worldwide situated on alluvial aquifer systems with high transmissivity and appreciable hydraulic gradients.

While numerical modelling results provide substantial insights, several important limitations merit acknowledgment. The models employ simplified representations of heterogeneous aquifer systems with assumed homogeneous properties that may not fully represent actual conditions. Field-scale heterogeneity could influence thermal plume migration patterns and recovery efficiency. The models assume transient-state groundwater flow with constant direction and velocity, whereas actual systems may exhibit temporal variations related to seasonal recharge, nearby pumping, boundary condition changes, and climate cycles affecting flow patterns. Geochemical reactions and temperature-induced effects on mineral precipitation, gas solubility, microbiological activity, and well performance receive limited treatment and could influence long-term operation. The five-year simulation provides insights into performance after initial transients but may not represent very long-term behaviour over decades-long operational lifetimes. Progressive thermal accumulation or depletion over multi-decadal periods could affect sustainability. The models lack long-term field validation of thermal plume predictions, with direct observation over multiple seasonal cycles strengthening confidence and enabling refinement. Long-term field monitoring programs at operating ATES sites under high groundwater flow conditions are critically needed

to validate numerical predictions, quantify actual thermal recovery efficiency, assess long-term sustainability, document thermal and hydraulic evolution, and identify operational issues and maintenance requirements. Monitoring should include temperature at multiple depths and distances, hydraulic head measurements, water quality sampling, well performance testing, and energy metering for accurate quantification.

Economic analysis and life cycle assessment providing comprehensive evaluation of costs, benefits, and environmental impacts across full system lifecycles would support decision-making regarding ATES deployment and inform policy development. Comparative analysis with alternative heating/cooling technologies under various economic and regulatory scenarios would clarify conditions favoring ATES implementation. Investigation of ATES integration with fourth and fifth generation district networks, renewable energy systems, multi-energy optimization frameworks, thermal grids, and seasonal solar thermal storage would enhance renewable integration. Development of ATES-specific regulatory frameworks informed by performance data, monitoring results, international best practices, and stakeholder input could accelerate adoption. Technology transfer through training programs, knowledge sharing, demonstration projects, and public outreach would facilitate broader implementation. With continued research, development, and field experience, ATES technology can play substantial role in advancing sustainable energy futures based on efficient renewable resource utilisation and optimal urban energy system integration.

Chapter 5

"[…] Because the sea, my boy, may be considered as an immense reservoir, in which is stored the heat of the summer. When winter comes, it restores this heat, which insures for the regions near the ocean a medium temperature, less high in summer, but less low in winter."

Jules Verne (1874)[7]

BTES

Borehole Thermal Energy Storage systems represent an innovative technology enabling seasonal thermal energy accumulation within subsurface geological formations through networks of closely-spaced vertical boreholes equipped with heat exchangers. Unlike open-loop systems requiring adequate aquifer properties or closed-loop installations serving instantaneous building demands, BTES technology leverages the inherent thermal inertia of soil and rock formations to store substantial thermal energy quantities over extended operational horizons, subsequently recovering that energy during periods of peak heating or cooling demand. The fundamental operating principle involves circulating thermal fluids through borehole heat exchangers to transfer energy conductively into surrounding geological media during charging phases, with subsequent reverse circulation enabling thermal recovery during discharging phases, effectively transforming subsurface formations into long-term thermal batteries suitable for seasonal load shifting and renewable energy integration. The technology encompasses distinct temperature classifications spanning low-temperature building applications operating below 40°C through high-temperature systems exceeding 80°C suitable for seasonal solar thermal storage, industrial waste heat recovery, and absorption cooling applications. Global deployment demonstrates geographical concentration within Scandinavia and Central Europe where mature design practices and supportive regulatory frameworks have established operational experience informing technology adaptation to diverse geological contexts worldwide. The investigation synthesizes worldwide BTES distribution patterns, characterizes key design parameters and their performance influences, develops rigorous coupled numerical modelling methodologies, and examines case studies validating technical feasibility for district-scale renewable thermal applications.

[7] *The Mysterious Island, Chapter 20, Jules Verne, (1874).*

5.1 Overview

Declaration: The topic described in this chapter was previously published in the following publication:

- Berta A., Tiwari A. K., Singh R.M., Taddia G.: Optimizing High-Temperature Borehole Thermal Energy Storage (HT-BTES) Systems, a case study from Trondheim, Norway. European Geothermal Congress (EGC25), 2025.

BTES does not necessitate the utilisation of particular aquifers, thereby conferring greater versatility and enabling its implementation in a more expansive array of geological settings. Furthermore, BTES systems can markedly diminish energy consumption and GHGs emissions in buildings by employing borehole heat exchangers (BHEs) to facilitate heat transfer between the ground and building systems, resulting in reduced energy costs and a smaller environmental footprint [246]. Despite the higher initial costs associated with drilling, BTES remains a cost-effective solution over time, particularly in comparison to battery storage systems [247]. While batteries are constrained by the degradation of chemical reactions over time, BTES offers increasing energy returns, thereby further substantiating its role as a promising option for long-term energy storage [44]. Furthermore, the emphasis on energy efficiency in buildings, particularly in public structures that constitute a substantial proportion of national energy expenditure, has prompted European governments to prioritise solutions such as BTES in their energy efficiency strategies [248].

BTES operates by harnessing the thermal capacity of subsurface materials, such as soil or rock, for the storage and retrieval of thermal energy. The energy is exchanged with the surrounding medium predominantly through conduction, utilising multiple closely spaced boreholes equipped with BHEs, which circulate a fluid, typically water or brine, that acts as a heat exchanger [249]. This approach allows BTES systems to store significant quantities of heat, thereby compensating for the reduced specific heat capacity of the storage medium by increasing the storage volume and reducing the necessity for the transportation of energy over long distances by storing it at local BTES fields [250].

The inherent characteristics of subsurface heat storage frequently impede the recovery of more than 60% of the stored heat, owing to the occurrence of thermal losses to surrounding areas [251]. Conventional BTES systems operated on annual cycles rarely achieve cyclic energy recovery factors of 45%-56% after multiple years of operation [252]. However, recent research has demonstrated that by reducing the charge–discharge cycle to a timescale of days, a concept termed "short-cycle" BTES, thermal recovery can be significantly enhanced [253]. Analytical and numerical models indicate that shorter cycle durations enhance the ratio of charge rate to loss rate, reducing the absolute amount of heat lost per cycle and thereby

boosting recovery efficiency. In particular, the utilisation of BTES arrays on daily to weekly cycles has been demonstrated to facilitate the recovery of factors that exceed 85%. The operation of such short cycles has been demonstrated to increase the fraction of heat retrieved each cycle. Furthermore, it has been shown to allow higher cumulative thermal throughput per year without raising overall losses [253].

When adequately designed, BTES systems have the capacity to achieve high coefficients of performance (COP), frequently exceeding those of conventional air and ground-source heat pumps [254]. This enhancement is attributable not only to the relatively elevated and stable subsurface temperatures, but also to the integration of a "free-heating" mode, in which heat is extracted directly from the borehole field whenever the average borehole-surface temperature exceeds the building's required supply temperature, with a minor adjustment for approach differences. In this mode, the energy consumption is limited to circulation pumps alone. Consequently, operational energy use, cost and emissions are all reduced to almost zero.

A compelling demonstration of free-heating design is provided by the very-high-temperature BTES (VHT-BTES) case study in Uppsala, Sweden, which targets a mid-scale residential field of 25 houses [255]. The numerical modelling simulation in this study utilises concentrated solar collectors (CSC) to charge a concentric, double-ring array of ten 80-m boreholes, with the objective of achieving an average surface temperature of 140°C during the four-month summer period. Optimisation of the borehole spacing and CSC capacity yielded seasonal COP (SCOP) values rising from 8 to 23 over the initial four years, with both heat-pump and free-heating modes active. It is important to note that, from the fifth year onwards, the borehole field attains a minimum discharge temperature above the free-heating threshold. At this point, the system meets 100% of its heating demand via free heating alone. This effectively provides cost-free, emission-free space heating for the entire winter season, with the exception of the minimal power needed by circulation pumps. The findings emphasise the significance of site-specific optimisation, encompassing factors such as solar collector sizing, borehole layout, and cycle scheduling. The results demonstrate that free-heating BTES designs have the potential to achieve remarkably high COPs and near-zero operational costs, even in cold climates [255].

Several review papers have been published on TES systems, each of which has contributed to a greater understanding of these technologies [256–260]. Moreover, several comprehensive reviews of the state of the art of BTES have been published, offering deeper insights into its potential, advancements, and challenges [44,250,252,261–273], but none of them analyses the actual distribution and main characteristics of the plants. BTES represents a well-established form of seasonal thermal energy storage, recognised for its economic efficiency and broad applicability across various sectors [249,274]. The utilisation of BHEs installed in the subsurface enables the storage and retrieval of substantial quantities of heat, thus facilitating thermal management over varying timescales [275].

The comprehensive investigation of BTES systems presented herein builds upon a systematic analysis of 75 operational BTES installations distributed globally

to establish classification frameworks, characterize critical design parameters, document numerical modelling methodologies, and validate long-term system performance through rigorous case studies (chapter 5.2).

Given the lack of a universally accepted classification framework in the literature, BTES systems can be systematically organised along two principal axes: operating temperature and thermal energy source. The temperature-based classification (**Table 18**) distinguishes high-temperature (HT) from low-temperature (LT) configurations. HT-BTES systems operate with storage temperatures typically above 40 °C and frequently within the 60–90 °C range during both charging and discharging phases [262]. Such systems are predominantly supplied by industrial or municipal waste heat, high-temperature district heating return lines, and solar thermal plants [44] [276]. HT-BTES systems are highly effective in stabilising district heating networks, particularly those reliant on seasonal or intermittent sources such as solar thermal energy [274]. Case studies demonstrate the efficacy of HT-BTES in stabilising high-temperature district heating networks, even in cold climates. For instance, a power-constrained, HT-BTES integrated with curtailed wind power at the University of Edinburgh's King's Buildings campus utilised a maximum storage temperature of 95°C. The system delivered return-line preheating, which boosted overall system COPs to over 200% [276]. The medium to deep HT-BTES configurations extend the potential for storage by utilising deeper borehole arrays, thereby offering increased thermal capacity and improved insulation from ambient ground temperatures [275,277]. Their main functional objective is to buffer substantial surpluses of high-grade heat during periods of low demand (often in summer) and to make this heat available during the heating season. A characteristic feature of HT-BTES is a multi-year start-up or “conditioning” phase, generally lasting three to six years, during which the subsurface is gradually heated until a quasi-steady operational temperature is reached. In this regime, annual heat losses stabilise and the system approaches an approximate balance between yearly injection and extraction. Heat losses in HT systems are comparatively higher than in LT systems because they scale with the temperature gradient between the storage core and the surrounding undisturbed ground, and they are also controlled by the surface-to-volume ratio of the array and the effectiveness of any insulation applied [252].

In contrast, LT-BTES systems operate at temperatures typically only 10–20 °C above undisturbed ground temperature. These installations are commonly integrated with heat pumps in configurations where heat extracted from buildings in summer is injected into the ground, and later retrieved in winter to cover heating demand. The closer proximity of storage temperature to ambient ground temperature implies lower thermal losses and reduced thermal stresses on both the ground and engineered components, making LT systems particularly suitable for widespread deployment in diverse geological and climatic contexts. At large scales and with appropriately optimised layouts, storage efficiencies of 80–90% are reported, as a consequence of the reduced loss term and the more uniform temperature field [254]. LT-BTES is therefore a strong candidate for mainstream adoption in both individual buildings with balanced heating–cooling needs and in

multi-building complexes, where it can support low-temperature district loops and contribute to the decarbonisation of heating and cooling [278].

Table 18. Temperature BTES classification.

Aspect	HT-BTES	LT-BTES
Typical T° range	> 40 °C, often 60–90 °C	~10–40 °C, typically 10–20 °C above ambient
Main sources	Solar thermal, waste heat, DH surplus	Heat pumps, ambient and internal gains
Main applications	District heating, industrial processes	Building heating and cooling, DHC support
Start-up behaviour	Multi-year conditioning to quasi-steady	Rapid equilibrium on seasonal timescales
Heat loss drivers	High ΔT to surroundings; shape factor	Low ΔT; mainly geometry-controlled
Scale	Medium to large (district/campus)	From single building to district

The second classification axis is based on the type of thermal resource supplying the BTES field. Four primary source categories can be identified: solar energy, district heating, waste heat, and heat pumps (**Table 19**). An analysis of the 75 case studies indicates that approximately half of the installations are powered primarily by heat pumps, more than 40% by solar energy, while the remainder utilise hybrid or other thermal sources (**Figure 137**).

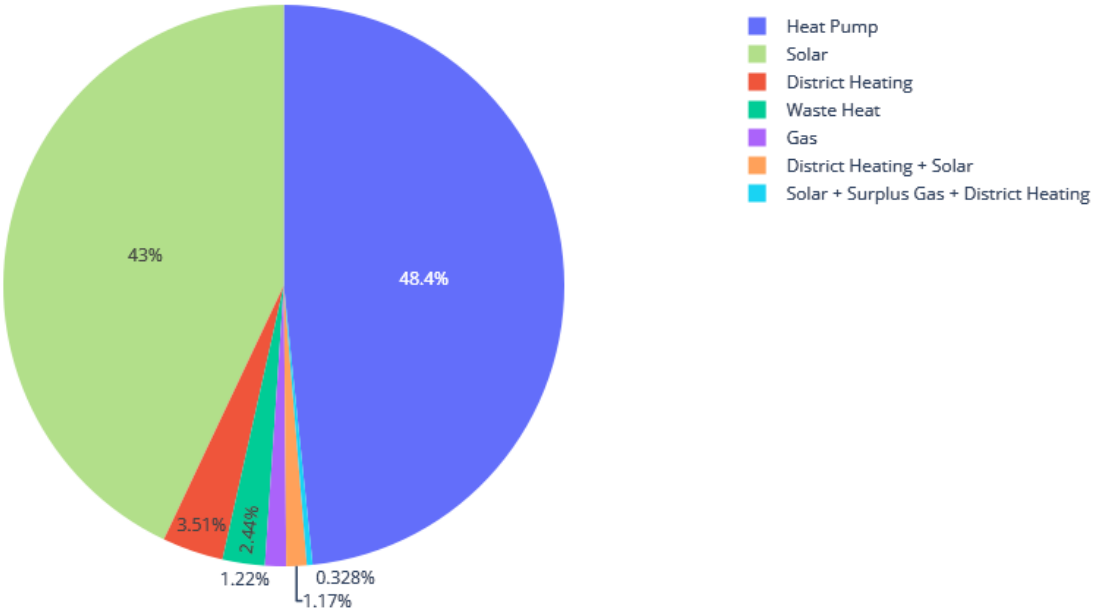

Figure 137. Pie chart representing the percentage of the different BTES source from the 75 case studies.

Solar-driven BTES systems combine solar thermal collectors with the storage field to capture summertime surpluses and release them during winter. Solar fluid, heated in the collectors, circulates through the boreholes and raises the temperature of the storage volume, creating a high-temperature zone that acts as a seasonal reservoir [279]. In winter, a colder fluid is passed through the same boreholes to recover the stored heat for space heating [248,261,280,281]. Such systems have been shown to substantially reduce the mismatch between solar availability and heating demand at both building and district scale. Numerical simulations and field data demonstrate that, when adequately dimensioned, solar-BTES can cover a large fraction of winter heating loads in cold climates and significantly lower greenhouse gas emissions compared with fossil-based reference systems, with reported reductions in global warming potential of the order of several tens of percent relative to conventional boilers [248,264,270,274,281–302].

BTES coupled to district heating (DH) plays a crucial role in the evolution towards fourth-generation district heating (4GDH) systems, which operate at supply temperatures of 50–70 °C rather than the approximately 100 °C typical of third-generation networks [73,303–305]. The transition to lower temperatures is motivated by the need to integrate low-temperature renewable and waste heat sources, reduce distribution losses, and improve overall exergy efficiency. BTES provides the seasonal storage function needed to balance variable renewable inputs and heating demand on annual timescales. In DH contexts, surplus heat from waste incineration plants or industrial processes, often around 85 °C, can be stored in the BTES field at intermediate temperatures (for example 45–60 °C) and later upgraded with heat pumps to deliver supply temperatures exceeding 70 °C where required [306] [307]. Solar district heating configurations with BTES frequently employ a hierarchy of short-term (tank) and long-term (BTES) storage, with control systems diverting heat to the borehole field when short-term capacity is saturated. Distributed placement of BTES fields within the DH network helps reduce average network temperatures, decrease line losses, and enhance the COP of any integrated heat pumps [282] [308]. Further details on DH-BTES can be found in the following papers [249,265,287,290,308–314].

Waste-heat-driven BTES constitutes a particularly effective strategy for industrial and urban systems characterised by relatively constant waste heat production and strongly seasonal heat demand [252]. Continuous heat outputs from combined heat and power plants, metallurgical processes, and waste incineration facilities often exceed local demand in summer [249]. Since waste streams cannot usually be stored, the associated heat is frequently rejected. The integration of BTES allows this surplus to be accumulated underground and utilised later, increasing the overall utilisation factor of the primary energy input and improving plant economics. In urban settings, such configurations can feed into district heating and cooling networks, contributing to shorter payback times for the infrastructure and enabling a higher share of renewable and recovered heat in the energy mix [315] [250].

Heat pump-driven BTES systems constitute the most widespread configuration, particularly at building and campus scale. In these installations, the BTES field operates close to undisturbed ground temperature, and the thermal level required by the buildings is reached or supplied by a heat pump. In summer, the heat pump (operating in cooling mode or via a dedicated chiller) rejects heat from the building to the borehole field, typically raising the fluid temperature to approximately 20–25 °C [252]. In winter, the heat pump extracts heat from the BTES field via fluid typically maintained just above freezing, thereby exploiting the stored energy and benefiting from a seasonally elevated ground temperature due to prior charging [289]. This approach serves to minimise thermal losses and preserve storage efficiency. This renders LT-BTES systems particularly efficacious for space heating and cooling in buildings, as they can support balanced thermal loads throughout the year [273]. By stabilizing the BTES temperature close to natural ground levels, these systems reduce thermal fluctuations and enable heat pumps to operate within their optimal temperature ranges, thereby improving overall system efficiency. Achieving optimal performance necessitates meticulous system design, ensuring a balance between storage efficiency and the integration of renewable energy sources [278]. Similar configurations are increasingly adopted in non-residential buildings (offices, hospitals, greenhouses) where simultaneous or overlapping heating and cooling loads can be balanced via the BTES storage.

Table 19. Comparison of BTES source types.

Source type	Temperature range	Role of BTES	Main benefits
Solar thermal	Medium to high (40–90 °C)	Seasonal storage of summer surplus	High RES share, strong emission reduction
District heating	Medium (50–70 °C, 4GDH)	Seasonal buffer, load shifting, peak shaving	Higher flexibility, reduced fossil backup
Waste heat	Medium to high (≈80–90 °C)	Storage of continuous surplus for winter use	Valorisation of waste energy, economic gain
Heat pump	Low to medium (~10–25 °C)	Seasonal balancing of building loads	High COP, widespread applicability
Hybrid	Combinations of above	Optimised multi-source integration	Increased resilience and operational flexibility

From a performance standpoint, the storage efficiency of BTES is often evaluated by the recovery factor, which serves as a major indicator of the system's overall performance. The recovery factor (Equation 53) is defined as the ratio of extracted energy to charged energy, representing the proportion of energy recovered from the total energy initially charged. In order to obtain a more accurate representation, the storage efficiency (η) can be defined as follows:

Equation 53

$$\eta = \frac{E_{out}}{E_{in}}$$

When inlet and outlet mass flow rates and heat capacities are constant, this reduces to the simple ratio of temperature differences:

Equation 54

$$\eta = \frac{\Delta T_{extraction}}{\Delta T_{charge}}$$

where $\Delta T_{extraction} = T_{out,ex} - T_{in,ex}$ and $\Delta T_{charge} = T_{in,char} - T_{out,char}$. This straightforward metric provides a clear, directly measurable indicator of system performance and facilitates comparison across different BTES designs and operating conditions. An effective BTES configuration aims to minimise thermal losses and optimise the actual storage efficiency, which is crucial for evaluating the practical viability of BTES systems as sustainable energy solutions [316]. A number of studies on sensitivity analysis have been conducted to refine these factors [193,199,252,281,317–324], enabling BTES systems to achieve higher storage efficiencies and contributing to the broader adoption of renewable thermal energy solutions.

The most influential design and operating parameters include array geometry, borehole spacing, grout and soil/rock thermal conductivity, charging and discharging rates, inlet and outlet temperatures, groundwater flow conditions, and the specific BHE configuration. Array geometry has a strong impact on the surface-to-volume ratio (the so-called shape factor) of the storage [262]. Cylindrical or compact circular arrays are generally preferred over elongated or sparse layouts because they minimise the contact surface between the hot storage zone and the colder surrounding ground for a given stored volume, thereby reducing radial thermal losses and promoting a more uniform internal temperature field [246]. Circular arrays also facilitate the implementation of controlled charging and discharging strategies, for instance by charging preferentially from the core outwards and discharging from the periphery inwards, often coupled with reversible flow paths [278]. In situations where groundwater flow is significant, elliptical or otherwise deformed geometries aligned with the flow direction can reduce advective heat losses by minimising the path length along which the hottest regions are exposed to moving water [316].

Borehole spacing is a significant determinant of the system's thermal performance and overall efficiency. Proper borehole spacing serves to minimise

thermal interference between adjacent boreholes, optimise land use and balance the costs associated with installation and operation [317]. If the spacing between boreholes is insufficient, thermal interference may occur. However, excessive spacing between boreholes can also diminish system efficiency by necessitating a larger land area and augmented pumping energy to transport the heat transfer fluid across greater distances [319]. This configuration not only results in increased costs but also introduces complexity to the circulation requirements within the BTES system [316]. In BTES systems, the spacing is typically closer than in conventional GSHP systems, where the objective is to prevent thermal interaction. In the context of BTES applications, the optimal borehole spacing is typically within the range of 1.5 to 3 metres. This range has been demonstrated to provide an equilibrium between the competing demands of maximising thermal interaction and minimising land area usage and operational costs. Research by Woloszyn [320] and others has identified that this distance allows for optimal thermal performance, enabling the heat transfer fluid to interact effectively with the surrounding thermal zones without causing excessive thermal overlap that could reduce the gradient necessary for efficient heat transfer [261,316].

The thermal conductivity of the grout filling the annulus between the BHE pipes and the borehole wall is a key engineered parameter, as it directly influences the radial heat transfer capacity of the system. High-conductivity grouts (for example, those enhanced with silica sand or graphite) significantly reduce the thermal resistance between the fluid and the surrounding formation, thereby improving both charging and discharging performance [317,291]. Likewise, the thermal conductivity of the soil or rock controls the spread of the thermal plume and the rate at which the storage exchanges heat with the far field. Materials with higher conductivity facilitate faster charging and more uniform temperature distributions but also increase the rate of heat loss to the surroundings at high operating temperatures [289]. Groundwater flow can further complicate the dynamics of heat transfer [74]. The occurrence of high groundwater flow can result in a notable decline in the efficiency of BTES systems. This is due to the rapid transportation of thermal energy away from the boreholes, which disperses heat from the storage area and impedes the effective recovery of energy during the discharging phase [261]. In an optimal BTES setting, soils with stable characteristics, such as low porosity and minimal groundwater flow, are preferable. Low permeability and reduced hydraulic gradients facilitate more uniform temperature distributions within the BTES volume, thereby minimizing heat loss and enhancing retrieval efficiency. Furthermore, soils with low thermal conductivity and limited saturation levels reduce radial heat dissipation, thus maintaining the temperature gradients essential for efficient energy storage and recovery [261].

Charging and discharging rates, together with inlet and outlet temperatures, define the temporal structure of the thermal loading of the BTES. Higher charge rates and larger temperature differences allow more rapid accumulation of energy but can create stronger temperature gradients and higher losses [280] [319]. Some academic papers address the design of BTES systems at elevated temperatures,

although such high-temperature applications present a number of unique challenges [249,252,254,265,266,281,288,307,308,313,325,326]. The shift from traditional yearly cycles to short-cycle operation, with repeated charge–discharge events on the scale of days or weeks, has been shown to increase the ratio of useful recovered energy to losses by decreasing the time window available for diffusion-driven dissipation in each cycle. Finally, the choice of BHE configuration (single U-tube, double U-tube, coaxial, etc.) affects the borehole thermal resistance and hence the required borehole length and number for a given load (detail in chapter 5.2.2).

Table 20. Key parameters characteristics.

Parameter	Physical role	Main design objective	Typical design tendency
Array geometry	Controls shape factor and heat loss area	Minimise surface-to-volume ratio	Compact circular/cylindrical arrays
Borehole spacing	Governs thermal interference and volume use	Balance interference vs. drilling cost	Moderate spacing (few metres), optimised
Grout conductivity	Sets radial heat transfer capacity	Reduce borehole thermal resistance	Use grouts conductivity similar to ground
Soil/rock conductivity	Controls plume spread and loss rate	Ensure adequate charging, acceptable losses	Leverage high-k for LT; mitigate for HT
Charge/discharge rate	Defines cycle duration and ΔT	Maximise recovery factor, limit peak losses	Move from annual to shorter cycles where feasible
Inlet/outlet temperature	Determines usable ΔT and free-heating potential	Match source/sink levels and system COP	Optimise within source and demand limits
Groundwater flow	Introduces advective transport	Minimise advective loss or exploit beneficially	Align geometry to flow direction
BHE type	Determines borehole resistance and hydraulics	Optimise heat transfer vs. complexity	Select configuration per scale and budget

5.2 BTES Worldwide Distribution

This chapter presents the first comprehensive review of BTES installations worldwide, providing a geospatial analysis and database to map their current distribution and characteristics design parameters. While previous studies have analysed international research activity, collaboration networks, and technological trends in the BTES field, these have not provided specific insights into the geographical distribution, technical specifications, and operational characteristics of actual installed systems. To address this gap, this review identifies 75 BTES case studies globally through meticulous bibliographic research, focusing exclusively on data traceable to peer-reviewed scientific literature, and conference proceedings with verifiable source documentation. This approach ensures the reliability, transparency, and reproducibility of the data compilation process, enabling future researchers to validate and extend the database.

Nevertheless, it is evident that the actual number of BTES installations worldwide is considerably higher than the number of cases identified in this study (**Table 21**). For example, a comprehensive census conducted in Sweden in 2020 reported approximately 76 operational installations, which is significantly higher than the 19 installations documented through literature sources and included in this chapter [327]. This substantial discrepancy underscores the limitation of relying exclusively on published academic sources and highlights the need for more systematic reporting mechanisms, national registry databases, and standardized documentation protocols for BTES systems on a global scale.

In order to enhance transparency and reproducibility, a structured literature search and selection protocol was implemented. Peer-reviewed publications were identified through comprehensive searches of Web of Science, Scopus, and Google Scholar, covering the period from 1980 to 2025. The search strategy encompassed the utilisation of keywords such as "UTES," "BTES," "case study," "numerical modelling," and "technical report" to identify site-specific reports of real-world installations. Inclusion criteria for the study comprised data sets that yielded spatially referenced information (e.g., coordinates or detailed location) and documented at least one key system parameter. From an initial yield of approximately 500 potentially relevant records identified through database searches, abstract and conclusion screening reduced the pool to approximately 150 full-text articles warranting detailed review, of which 75 case studies meeting all inclusion criteria were incorporated into the final geodatabase. For each selected case study, the following data fields were systematically extracted when available: country of installation, precise geographic coordinates or location description, borehole heat exchanger (BHE) configuration type (single U-tube, double U-tube, or coaxial), borehole depth range, total number of boreholes in the field, thermal storage capacity (MWh), operational temperature range, and year of commissioning. It was ensured that every database entry remains fully traceable to

its original published source, with complete bibliographic references provided to facilitate verification and future database expansion.

Table 21 provides a comprehensive listing of identified BTES plants organized by country, indicating the total number of documented installations in each nation and the associated paper references that constitute the evidence base for each entry. The table reveals substantial geographic concentration in certain regions, with Sweden leading with 19 documented installations, followed by China (11 installations) and Norway (9 installations). Other countries with notable BTES deployment include Germany (7 installations), Finland (6 installations), and Canada (3 installations).

Table 21. List of BTES plants by country

Country	Number of BTES plants	Paper Reference
Canada	3	[247,278,282,286,292,297,302,325,328,329]
China	11	[246,265,274,280,291,299,300,330–337]
Denmark	1	[309,314,338]
Finland	6	[311,339–343]
France	1	[344,345]
Germany	7	[275,277,298,338,346–352]
Italy	3	[189,248,283,290,353,354]
Netherland	1	[294]
Norway	9	[249,273,288,301,308,355–358]
Poland	1	[273]
Romania	2	[359]
South Corea	1	[284]
Sweden	19	[254,266,295,296,307,313,327,360–370]
Switzerland	3	[310,371,372]
United Kingdom	2	[199,263,373–375]
United States	4	[264,293,376]
Czech Republic	1	[377]

To illustrate this distribution, a geodatabase was created using QGIS, version 3.34.13-Prizren, resulting in detailed maps and graphs that depict the geographic and statistical spread of BTES installations. This geodatabase provides a foundation for the future tracking and updating of global BTES developments. By offering a clear, structured, and spatially explicit repository of data on BTES systems, this geodatabase aims to provide a foundational resource for researchers, practitioners,

policymakers, and technology developers seeking to understand current deployment patterns, identify best practices, and expand the strategic deployment of BTES technologies worldwide.

A geopackage file containing the complete geodatabase, attribute tables, and metadata documentation is available for download free of access from the Mendeley Data repository, facilitating data sharing, collaborative analysis, and continuous database refinement by the international research community [378].

Borehole Thermal Energy Storage (BTES) systems are classified based on depth into two main categories: low-depth BTES (LD-BTES, up to 250 meters) and high-depth BTES (HD-BTES, 250 to 1000+ meters), with borehole depth fundamentally influencing thermal efficiency, storage capacity, drilling costs, and geological risk. Low-depth BTES systems, typically extending to 150 meters, currently dominate global installations due to lower drilling costs and proven performance in residential heating, small-scale commercial buildings, and district heating networks with moderate thermal demands. However, these systems face inherent limitations including restricted thermal storage capacity, increased thermal losses in shallow subsurface environments, and potential impacts on nearby aquifers. Despite these constraints, LD-BTES remains the predominant approach for moderate-climate applications where seasonal storage complements but does not dominate the overall heating system.

High-depth BTES systems represent a technological advancement, accessing depths from 250 to 1000+ meters with significantly larger formation volumes per borehole, making them ideal for space-constrained urban and industrial settings. These systems accommodate higher temperature inputs (60-90°C or higher) suitable for integration with concentrating solar thermal systems, industrial waste heat recovery, and combined heat and power systems, while substantially improving heat pump performance. However, only limited HD-BTES installations currently exist worldwide, with the majority of performance data derived from numerical simulations rather than long-term field monitoring, highlighting the critical need for comprehensive field demonstration projects to validate predictions and build technological confidence [262,273,275,312,346,379].

The 75 documented BTES installations (**Figure 138**) reveals that the majority of operational systems worldwide are situated at relatively shallow depths, with median depths in the range of 100-150 meters and a strong concentration below 200 meters. To date, only a limited number of installations have been developed to greater depths (>250 m), with documented examples primarily located in Canada, Norway, Finland, and Germany, countries with either strong policy drivers for renewable heating, favorable deep geology, or active research programs exploring advanced BTES concepts. It is therefore evident that while HD-BTES demonstrates considerable technical promise and potential advantages for specific applications, the majority of existing operational insights, performance data, and lessons learned are derived from numerical simulations and modelling studies rather than long-term monitoring of actual installations [199,275,277,322,346,351,352,379–383].

This observation highlights a critical knowledge gap and research need: field demonstration projects with comprehensive monitoring programs are essential to

validate simulation predictions, characterize actual long-term thermal behaviour, assess geological and mechanical impacts, and build confidence in HD-BTES technology among developers, financiers, and regulatory authorities.

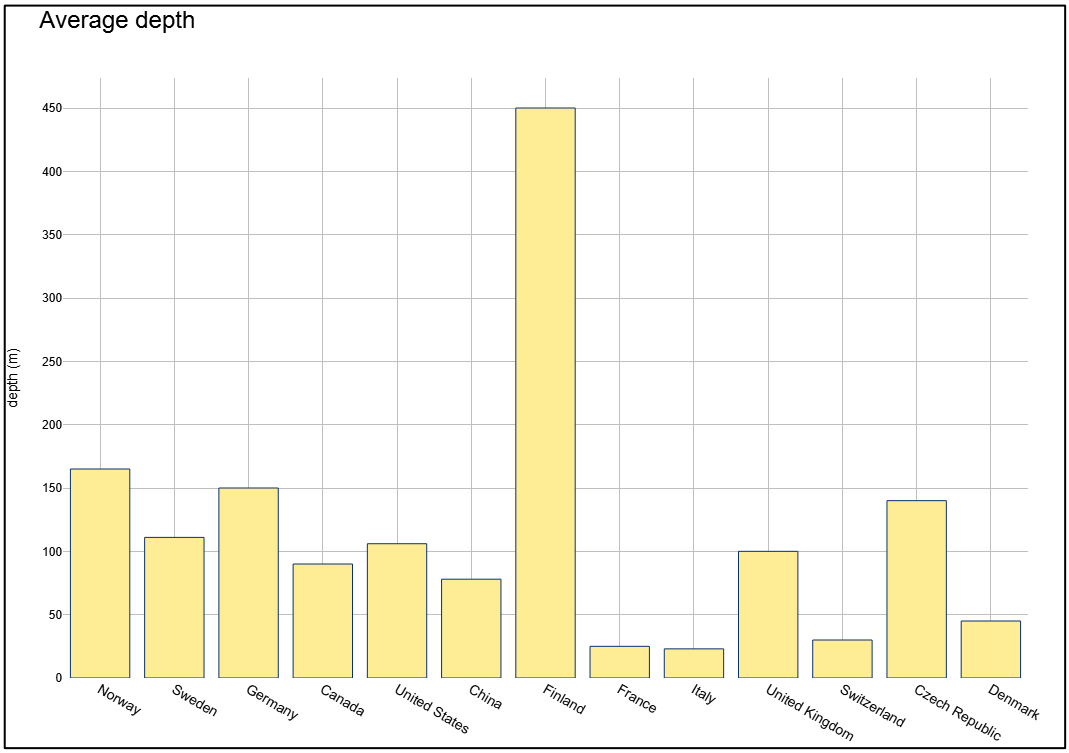

Figure 138. Barchart of the average depth in different countries.

The geographical distribution of BTES capacity, measured in megawatt-hours (MWh) across countries, provides essential insights into the global adoption intensity and aggregate thermal storage infrastructure deployment, revealing significant regional variations in technology diffusion and renewable heating integration. The worldwide analysis of 75 documented BTES installations demonstrates substantial geographical disparities in thermal energy storage capacity deployment (**Figure 139**). Sweden emerges as the global leader with capacity in the tens of thousands of MWh annually, reflecting its pioneering BTES development since the 1980s, supportive national energy policies including carbon taxation and renewable heating mandates, extensive district heating networks, and favorable crystalline bedrock geology. Similarly, China and Canada exhibit considerable BTES deployment driven by distinct motivations: China pursues urban air quality improvement and rapid district heating network expansion supported by carbon reduction policies, while Canada's heating-dominated climate creates significant seasonal energy imbalances coupled with strong renewable energy policies and historical research leadership in thermal storage technologies. However, the analysis reveals critical documentation deficiencies: approximately 28% of the 75 installations lack available thermal storage capacity data, with several countries including Romania and France exhibiting completely undocumented BTES systems regarding thermal energy capacity and operational performance. These gaps highlight the urgent necessity for improved international data sharing

mechanisms, standardized BTES registries with uniform reporting templates, and enhanced emphasis on comprehensive performance documentation in both academic and industry technical reports to facilitate evidence-based assessment of global thermal storage infrastructure development and technology diffusion patterns.

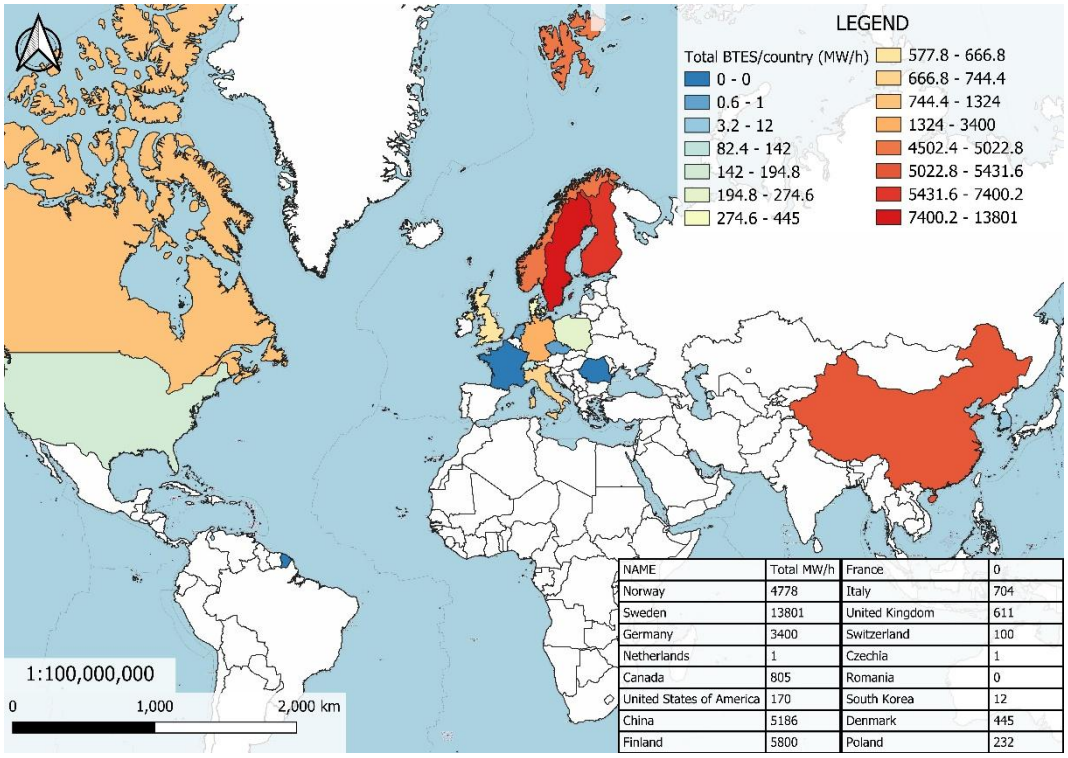

NAME	Total MW/h	France	0
Norway	4778	Italy	704
Sweden	13801	United Kingdom	611
Germany	3400	Switzerland	100
Netherlands	1	Czechia	1
Canada	805	Romania	0
United States of America	170	South Korea	12
China	5186	Denmark	445
Finland	5800	Poland	232

Figure 139. Worldwide map representing the total power in MWh of the 75 BTES by country.

5.2.1 Country and Temporal Distribution

This chapter presents a comprehensive analysis of the geographical and temporal distribution of BTES installations identified in the systematic literature review, with a particular focus on the examination of observed spatial clustering patterns, and temporal deployment trends.

Figure 140 provides a visual representation of the geographic distribution of the 75 identified BTES installations worldwide. The map employs green triangles to indicate individual installation locations with their respective geographic coordinates, providing precise spatial reference for each documented system. Countries are color-coded using a graduated color scheme to represent the total number of BTES plants in each nation, with darker shades indicating higher concentrations of installations. This visualization technique facilitates immediate identification of geographic clusters and regional adoption patterns. The map demonstrates that BTES plants are predominantly concentrated in Northern Europe, particularly Scandinavia, with substantial clustering observed in Sweden, Norway, and Finland. These regions are characterized by their strong renewable energy policies, ambitious carbon neutrality targets, well-established district heating infrastructure, technological leadership in sustainable heating and cooling systems, and favorable geological conditions (crystalline bedrock with good thermal properties). The prevalence of BTES in Scandinavian countries also reflects supportive regulatory frameworks, including streamlined permitting processes, and financial incentives for renewable heating technologies.

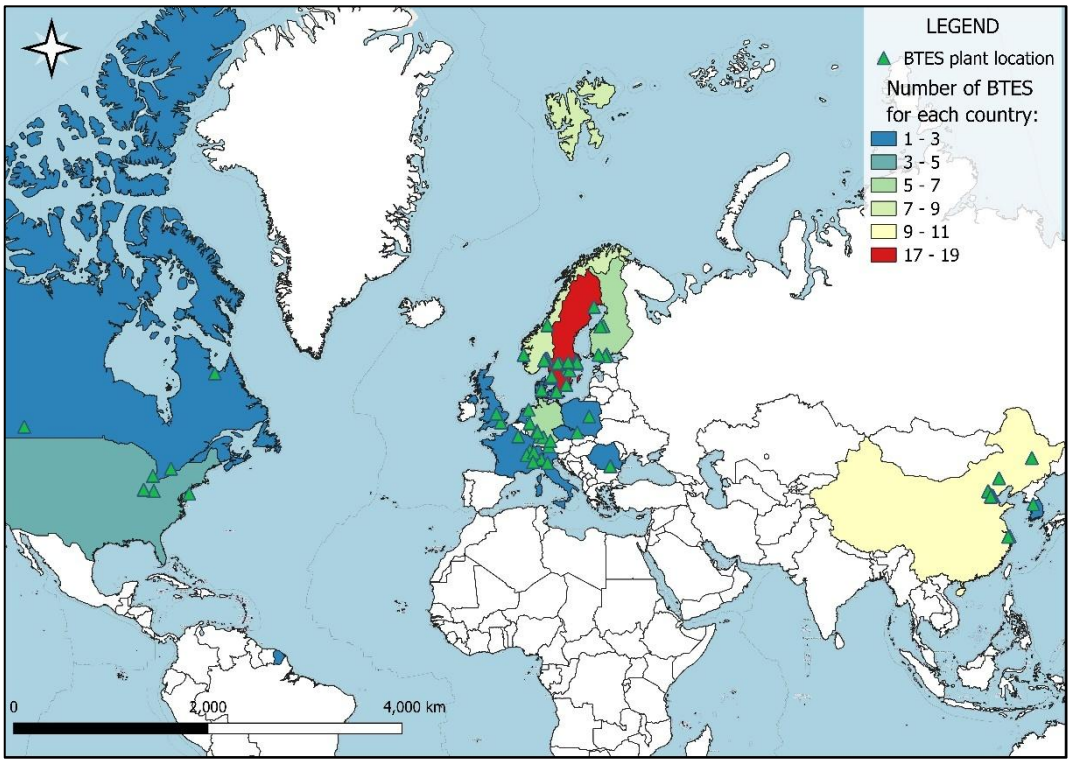

Figure 140. BTES Country distribution: the green triangles indicate the 75 BTES plants and their respective locations. The varying colours in the map indicate the total amount of BTES plants in each country.

Secondary clusters are evident in Central Europe (Germany, Switzerland) and Asia (China), reflecting growing interest and deployment in regions with different climatic conditions and energy system configurations. The relative scarcity of documented installations in Southern Europe, Africa, South America, and large portions of Asia suggests either limited adoption of BTES technology in these regions, application of alternative thermal storage technologies more suited to local conditions, or insufficient documentation and reporting of existing systems in the scientific literature.

Figure 141 presents a bar chart quantifying the number of BTES plants in each country, providing a clear comparative visualization of installation frequencies across nations. The chart illustrates that Sweden is the nation with the highest concentration, with 19 identified BTES plants included in this literature-based review. However, as previously indicated, a comprehensive national census conducted in Sweden in 2020 reveals that the actual number of installations in the country is considerably higher, with a minimum of 76 recorded operational plants.

Following Sweden, China and Norway occupy the second and third positions respectively in terms of documented installations, with 11 and 9 systems identified through literature sources. This ranking reflects the growing prominence and accelerating deployment of BTES technology in both Scandinavian countries (where heating demand, renewable energy targets, and district heating networks drive adoption) and in Asia (where rapid urbanization, air quality concerns, and diversification of heating sources motivate interest in seasonal thermal storage). This clustering reflects the advanced integration of BTES technologies in regions with supportive frameworks, while also indicating potential areas for further adoption in other parts of the world.

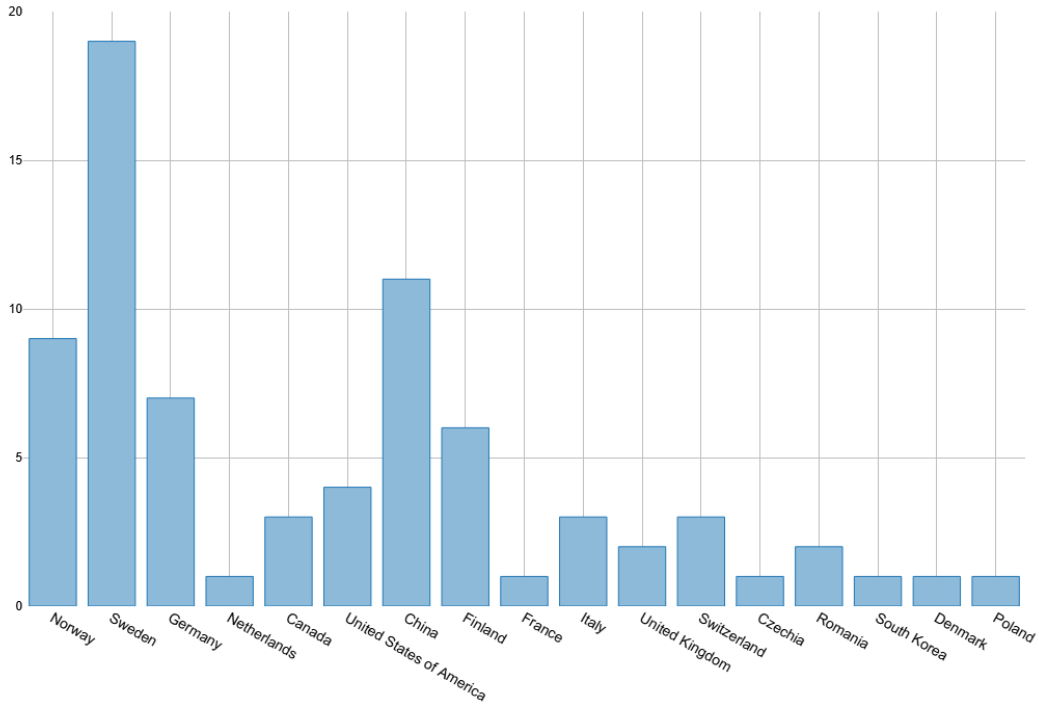

Figure 141. Bar chart of the sum of BTES plants for each country.

From a temporal perspective, **Figure 142** illustrates the evolution of BTES deployment over time, revealing important trends in technology adoption rates and maturation. **Figure 142** presents a dual-axis temporal distribution graph with an orange line representing the cumulative sum of BTES plants year by year (total installed capacity over time) and a blue line showing the number of new BTES plants commissioned each year (annual installation rate). The graph demonstrates a gradual increase in BTES installations since the early 1980s, when pioneering demonstration projects first validated the technical feasibility of large-scale seasonal thermal storage in boreholes. A notable acceleration in deployment rate is observed after 2008, coinciding with several catalyzing factors: the global financial crisis and subsequent green stimulus investments, growing awareness of climate change and associated policy responses, rising fossil fuel prices increasing the economic competitiveness of renewable heating, and maturation of BTES design methodologies and modelling tools. The post-2008 acceleration suggests that BTES technology has transitioned from an experimental demonstration phase to an established commercial technology with growing market adoption, though deployment rates remain concentrated in specific geographic regions with favorable conditions.

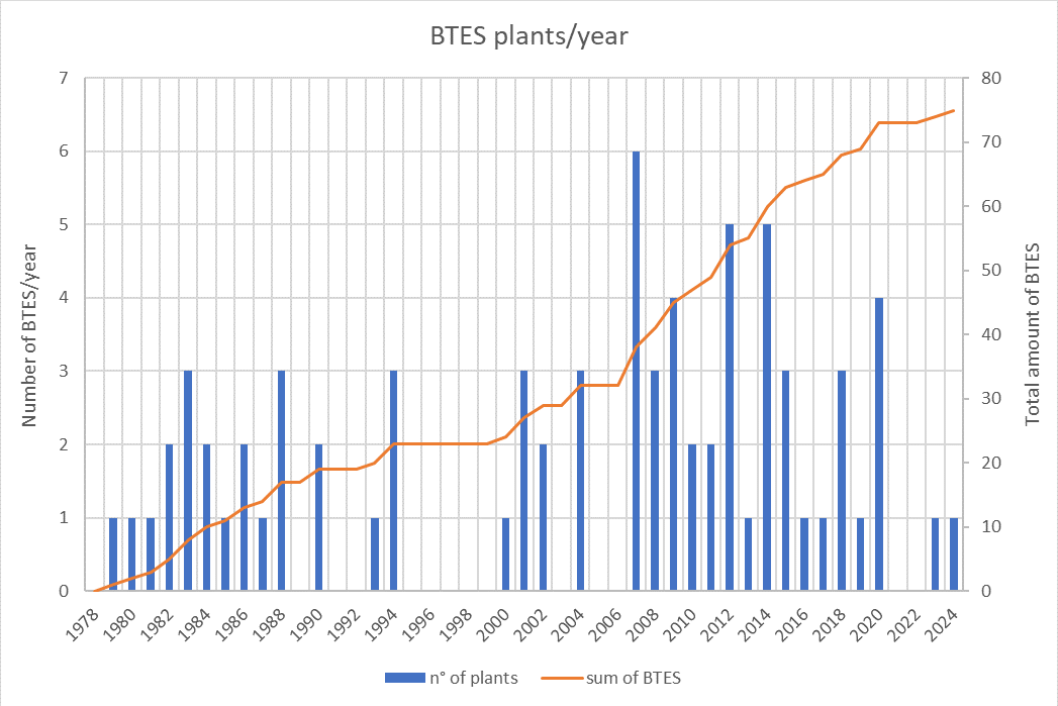

Figure 142. Temporal distribution of BTES plants: the orange line represents the sum of BTES plants year by year, while the blue line shows the number of BTES plants built each year.

5.2.2 Type of Borehole Distribution

The selection of the BHE type represents a crucial design choice in BTES systems, exerting a direct influence on the system's thermal performance, material requirements, and operational efficiency. This chapter presents an analysis of the distribution of three main BHE configurations (single U-tube, double U-tube, and coaxial designs) across 75 case studies. The analysis aims to highlight the prevalence, regional adoption, and functional attributes of these configurations. Information on the specific type of BHE employed is available for 59 of the 75 case studies analysed (approximately 79% data completeness), thus providing a detailed and statistically meaningful perspective on global trends in BHE configuration selection.

Single U-tube BHEs represent the most prevalent configuration, comprising approximately 65% of the installations examined (**Figure 143**). These systems typically comprise a single loop of high-density polyethylene (HDPE) or cross-linked polyethylene (PEX) pipes inserted into the borehole, with fluid circulating down one leg and returning through the other. Standard pipe dimensions include an outside diameter of 40 mm, though 32 mm pipes are also occasionally employed, particularly in shallower boreholes or installations with spatial constraints [317]. The widespread adoption of single U-tube configurations can be attributed to several advantageous characteristics: uncomplicated design facilitating straightforward installation procedures, cost-effectiveness with lower material requirements compared to double U-tube systems, simplicity of installation reducing labour time and specialized equipment needs, well-established installation practices and widespread contractor familiarity, and proven long-term reliability across diverse geological conditions. These factors have rendered single U-tube BHEs a standard selection for a multitude of applications, particularly in smaller-scale BTES systems, residential heating projects, and installations where moderate thermal performance is sufficient to meet demand requirements.

Double U-tube BHEs represent approximately 28% of documented installations, constituting the second most common configuration globally. These systems are characterized by two independent U-shaped pipe loops installed within a single borehole, with heat transfer fluid typically flowing in opposite directions through each loop (parallel or series configuration depending on hydraulic circuit design). This configuration substantially increases the contact surface area between the circulating fluid and the surrounding subsurface formation, thereby enhancing the efficiency of heat transfer per unit borehole length and improving the thermal performance per borehole [317]. Double U-tube systems exhibit several performance advantages: higher thermal capacity per borehole enabling more compact borehole field layouts, improved thermal contact with formation reducing borehole thermal resistance, enhanced system flexibility through independent loop operation or zoning possibilities, and better performance in formations with lower thermal conductivity where increased heat transfer area compensates for reduced

formation properties. These characteristics make double U-tube BHEs particularly advantageous in projects that require higher thermal capacity to meet substantial heating or cooling loads, installations constrained by limited surface area for borehole placement (urban sites, building footprints), or geological settings with moderate thermal properties where enhanced heat exchange efficiency justifies the additional cost.

Coaxial BHEs, representing less than 10% of total documented installations, constitute a specialized and less commonly adopted configuration. These systems comprise a central flow pipe (typically the supply line) surrounded by an outer concentric return pipe, or alternatively an outer annular supply with central return pipe, creating a coaxial geometry along the full borehole length. This configuration is specifically designed to minimize hydraulic flow resistance through larger flow cross-sections, maximize heat exchange efficiency through optimized thermal contact geometry, reduce thermal short-circuiting between inlet and outlet flows compared to U-tube designs, and provide superior performance in deep boreholes where pressure losses in U-tubes become prohibitive. However, the specialized design, higher manufacturing costs, more complex installation procedures requiring specialized equipment, limited contractor familiarity and installation experience, and higher material costs represent significant barriers to widespread adoption of coaxial systems. Despite these limitations, coaxial BHEs are particularly suitable for specific applications including very deep boreholes (>200 m) where pressure drop considerations favor the configuration, high-temperature applications requiring optimized thermal performance, and research or demonstration projects exploring advanced BHE technologies.

Figure 143 presents a pie chart visualizing the percentage distribution of the three different types of BHE configurations employed in the 75 documented BTES installations worldwide. The chart clearly illustrates the dominance of single U-tube systems (approximately 65%), followed by double U-tube configurations (approximately 28%), with coaxial designs representing a small fraction (less than 10%) of the total. This distribution pattern reflects the pragmatic balance between thermal performance requirements, economic constraints, and installation complexity considerations that govern BHE selection in real-world projects.

Figure 144 presents a polar plot of the global distribution of these BHE types, with single U-tube systems situated at the centre, coaxial designs in the mid-range, and double U-tube configurations occupying the outer edges. The plot reveals that only a few countries, such as Sweden, Switzerland, and Germany, employ all three BHE types, which demonstrates a flexible and diversified approach to system design. In contrast, other nations, including the United States, the United Kingdom, Norway, Canada, and Finland, demonstrate exclusive reliance on single U-tube systems, which suggests a preference for simpler and more standardised solutions. These findings demonstrate the considerable impact of regional and project-specific factors on BHE selection, including geological conditions, technological expertise, and economic considerations.

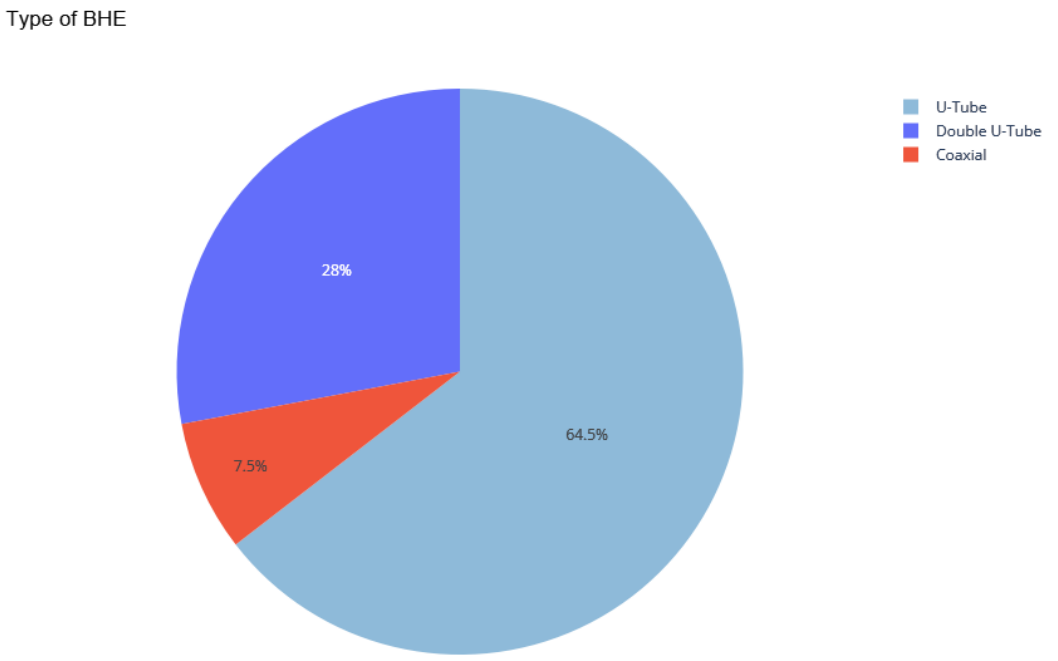

Figure 143. Pie chart representing the percentage of the three different type of BHE in the 75 BTES.

Figure 144 presents a polar plot visualization of the global distribution of BHE types across different countries, providing insight into regional preferences and technology adoption patterns. In this polar representation, single U-tube systems are positioned toward the centre of the plot, coaxial designs occupy the mid-range radial positions, and double U-tube configurations are located at the outer edges. The plot reveals that only a few countries, notably Sweden, Switzerland, and Germany, employ all three BHE types in their documented installations, which demonstrates a flexible, diversified, and technologically mature approach to system design. This diversity suggests well-developed technical expertise, willingness to optimize BHE selection based on site-specific conditions, and active research and development activities exploring advanced configurations. In contrast, other nations, including the United States, the United Kingdom, Norway, Canada, and Finland, demonstrate exclusive reliance on single U-tube systems, which suggests a preference for simpler and more standardised solutions. Understanding these regional patterns provides valuable insights for technology transfer initiatives, identification of markets ready for advanced BHE configurations, and strategic planning for BTES deployment in emerging markets.

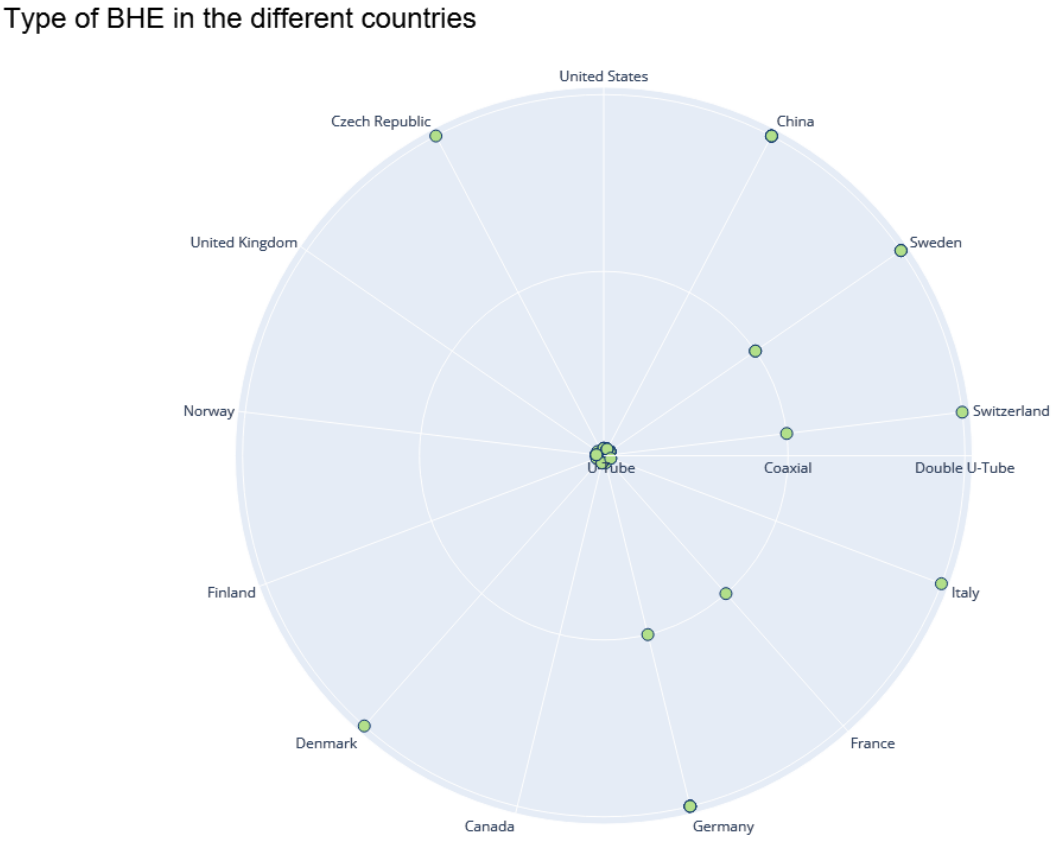

Figure 144. Polar Plot of type of tubes utilised in BTES in the different countries.

5.3 Case Studies

Two main case studies were analysed for the BTES systems analysis, in completely different geological and hydrogeological contexts: the first in Trondheim, Norway; and the second in Turin, Italy. These contrasting environments provide valuable comparative insights into BTES performance under diverse subsurface conditions, enabling evaluation of technology adaptability across climatic zones, geological formations, and thermal storage requirements. This case study originates from the collaboration between NTNU University and the Applied Geology group of the DIATI Department at Politecnico di Torino, which promotes a six-month Erasmus period at NTNU Trondheim University (NO), contributing to joint research activities and technical exchange within the BTES system investigations.

5.3.1 Case Study 1

In the context of Norway, where approximately nine BTES installations have been documented in the southern regions (**Figure 145** A), there is a growing interest in expanding BTES projects into the northern areas [281,384]. This study focuses on a high-temperature BTES project in Norway, located in the Nyhavna area of Trondheim (**Figure 146**). As part of a broader urban redevelopment initiative transforming an industrial harbour into a Zero Emission Neighbourhood (ZEN), the project exemplifies the integration of sustainable energy solutions into urban planning strategies (**Figure 145** B). The surplus thermal energy generated by an adjacent waste incineration plant is planned to be stored in the subsurface via a network of borehole heat exchangers (BHEs) and subsequently extracted during the colder months to meet local heating demands. This waste heat integration strategy represents a critical component of circular economy principles in urban energy systems, converting otherwise-discarded industrial process heat into valuable seasonal thermal storage, reducing primary energy consumption and associated greenhouse gas emissions.

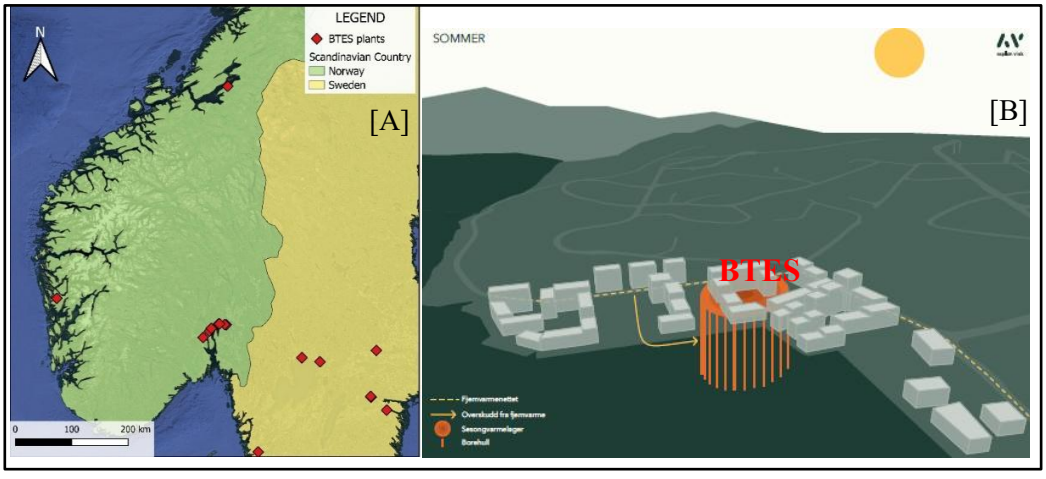

Figure 145. [A] BTES distribution maps in Scandinavian area; [B] Design representation of Nyhavna BTES project (modified from [385]).

Figure 146 displays the study area framework, providing geographic context for the Nyhavna district within the broader Trondheim metropolitan area. The figure shows the coastal location of the site, proximity to Trondheim Fjord, topographic features, and spatial relationships with surrounding infrastructure and natural resources.

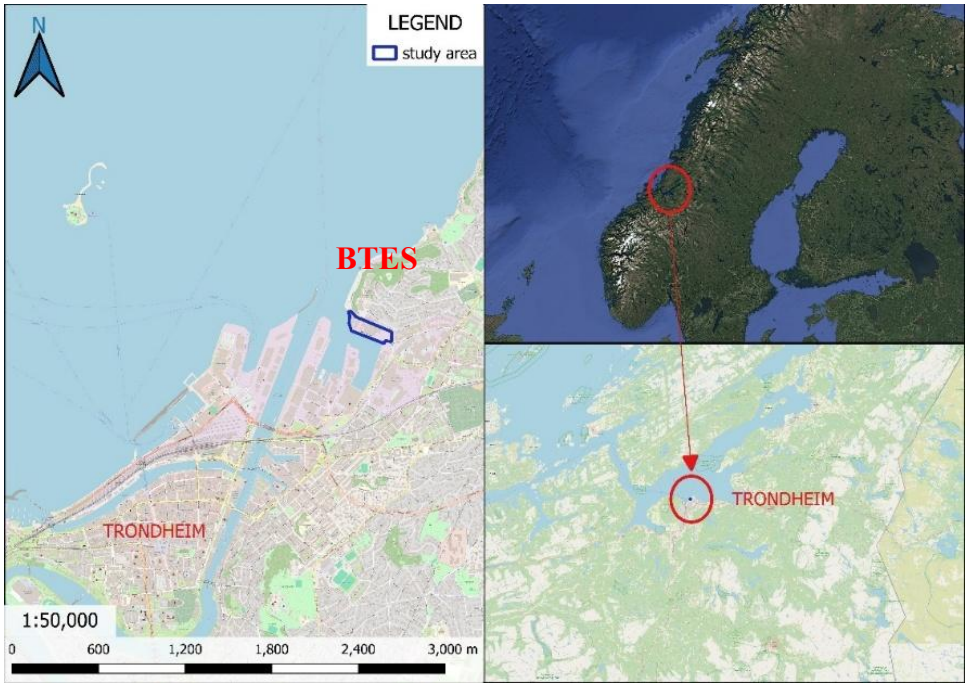

Figure 146. Study area framework.

The performance and efficiency of BTES systems are strongly dependent on the geological properties of the host formation, including thermal conductivity, volumetric heat capacity, hydraulic properties, and mechanical stability under cyclic thermal loading [352]. In this section, the Nyhavna BTES project is underpinned by a comprehensive geotechnical investigation that includes drilling of seven test boreholes, and detailed geomechanical analyses involving laboratory point load tests on greenstone core samples subjected to cyclic thermal loading [386,387]. An average effective thermal conductivity of approximately 3.86 W/m·K (excluding anomalous results due to localized water-bearing conditions) indicates favourable conditions for heat storage. This thermal conductivity value substantially exceeds typical values for sedimentary formations (1.5-2.5 W/(m·K)) and confirms that the crystalline metamorphic bedrock at Nyhavna provides excellent thermal transport properties that facilitate efficient heat injection and extraction while maintaining thermal plume confinement.

Moreover, laboratory testing reveals that cyclic thermal exposure may enhance the mechanical strength of the bedrock, a critical factor for the long-term stability of the storage system [386]. This phenomenon contrasts with thermal degradation observed in some sedimentary rocks and confirms the suitability of the Trondheim greenstone for high-temperature thermal cycling over decades of operation.

Complementing the laboratory and field measurements, a detailed 3D geological model of the area was developed using FEFLOW software. This model integrates lithological data from boreholes and cone penetration tests with digital elevation models and orthophotos, enabling refined subsurface visualization and interdisciplinary collaboration for infrastructure planning.

The BTES design that has been proposed for Nyhavna is one that entails the installation of a network of 65 boreholes , each drilled to 100 meters depth. The system has been designed to operate at a maximum temperature of 80°C. This ensures that any surplus thermal energy collected during the summer months is effectively stored for subsequent use in the winter. This design is notable for its integration of waste heat from proximate facilities, a feature that is both a component of the local renewable energy strategy and a significant contributor to the reduction of greenhouse gas emissions.

Nyhavna is a coastal neighbourhood in Trondheim, Norway. This area, formerly characterised by industrial harbour facilities, is currently undergoing a transition into a sustainable, zero-emission district. Nyhavna's topography is distinguished by its low-lying nature, characterised by gentle slopes that seamlessly blend urban development with the natural coastal landscapes of the region.

The underlying geology, characterised by unconsolidated Quaternary deposits superimposed on a resilient Precambrian bedrock, further delineates the physical environment, combining varied sedimentary characteristics with a stable geological foundation. This influence both hydrological and thermal dynamics.

The bedrock in the Trondheim area is predominantly composed of metamorphic volcanic and sedimentary rocks formed within a Precambrian depression. The geological framework is dominated by greenstone, tuff, and putelava formations, with an estimated age of approximately 500 million years [388,389]. The region was significantly affected by the Caledonian orogeny around 400 million years ago, an event that not only deformed the pre-existing volcanic rocks but also thrust sedimentary layers, such as shale and sandstone, originally deposited on the seabed, up onto the continent [390]. Due to the intricate tectonic evolution of the region, the stratigraphy does not invariably exhibit a straightforward vertical age progression; in certain instances, younger rock formations have been observed to occur beneath older formations. The bedrock at the Nyhavna area is overlaid by a variable cover of Quaternary deposits (gray color in **Figure 147**), which are primarily the result of deglaciation and subsequent human-induced fill activities. The uppermost layer, as documented by Norwegian geological surveys, consists of fill material that largely originates from historical dumping practices between 1885 and 1937, as well as later urban development processes [391].

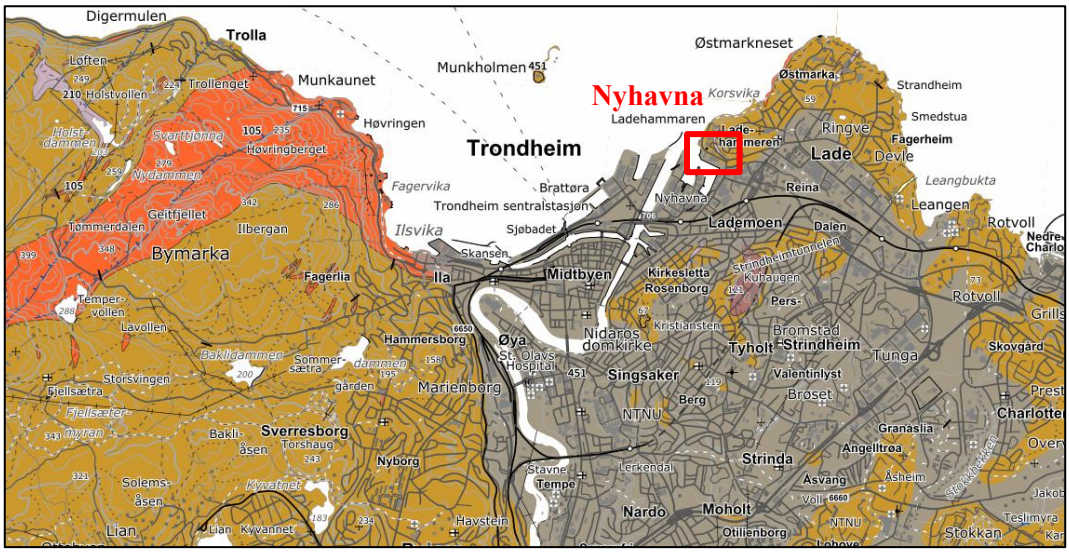

Figure 147. Geological map of Trondheim city (modified from [392]).

The hydrogeological data indicate that groundwater conditions are largely dictated by the fracture systems within the bedrock and the characteristics of the overlying sediments. In addition, tidal fluctuations have been recorded at some locations, suggesting that the groundwater level may be partly modulated by the sea level, as well as by the local drainage basin dynamics [386].

From a geotechnical perspective, the complexity of the stratigraphy at Nyhavna area presents several challenges for engineering and construction. The interface between the competent bedrock and the overlying loose sediments is well defined, with the latter consisting predominantly of fill deposits, sand, and clay. The mechanical properties of the loose overburden, including the compressibility and potential for settlement, are of particular importance given the planned installation of up to 65 energy boreholes [393]. These geotechnical parameters, when incorporated into numerical stability and settlement models, provide the basis for assessing the initial stability and deformation behaviour of the area during and after drilling.

5.3.2 Case Study 2

The second case study presents the design and numerical simulation of a shallow BTES system for a site located in the northern sector of Turin, Italy. The system is conceived to provide seasonal thermal energy storage for heating applications, utilizing excess heat available during warmer months to meet heating demands during the cold season. The site represents a typical urban setting where space constraints, hydrogeological conditions, and the presence of shallow aquifers impose significant design considerations that influence borehole depth, configuration geometry, and operational parameters. The subsurface model domain comprises two distinct hydrostratigraphic layers representing the shallow and deep aquifer systems characteristic of the Turin alluvial plain. The thermophysical properties of these two aquifers exhibit significant differences related to

mineralogical composition, grain size distribution, and degree of sediment compaction (**Table 22**).

Table 22. Thermophysical characteristics of the two layers simulated using FEFLOW.

Parameters	Unit measurement	Shallow aquifer (0-50 m)	Deep aquifer (>50 m)
Hydraulic Conductivity	m/s	$9 \cdot 10^{-3}$	$1 \cdot 10^{-5}$
Porosity	-	0,20	0,20
Thermal Conductivity	W/(m·K)	1,7	2,5
Volumetric Heat Capacity	MJ/(m³·K)	2,09	1,5
Depth	m	0-50	>50
Lithology	-	Gravel and sand	Sand and silt

The first shallow aquifer (0 to 50 m depth) consists predominantly of gravels and sands with a thermal conductivity of 1.7 W/(m·K), a value that is moderate yet adequate for low-to-medium enthalpy geothermal applications. The volumetric heat capacity of the solid matrix reaches 2.09 MJ/(m³·K), indicating favorable thermal storage capacity per unit volume and suggesting effective retention of injected thermal energy. These properties are consistent with coarse-grained fluvial deposits typical of Quaternary alluvial sequences in the Po Plain. The second deeper aquifer (>50 m depth) exhibits a thermal conductivity of 2.5 W/(m·K), reflecting the increased presence of high-conductivity mineralogical components (quartz, feldspars) and higher degree of compaction and diagenetic alteration with depth. The volumetric heat capacity is reduced to 1.5 MJ/(m³·K) due to different mineralogical composition, finer grain size (sands and silts), and reduced porosity associated with deeper burial and compaction. The determination of optimal borehole depth for this BTES installation was governed not primarily by soil physical properties, but rather by the presence and characteristics of the shallow groundwater table.

In the northern Turin study area, the shallow aquifer exhibits elevated groundwater flow velocities, which would substantially reduce the effectiveness of seasonal thermal storage in saturated zones through advective heat dissipation. Under conditions of significant groundwater flow, stored thermal energy is transported downstream by the moving groundwater, substantially reducing storage efficiency and causing thermal plumes to extend far beyond the borehole field. The average depth to the water table in the study area is approximately 22 meters below ground surface. To avoid thermal interference with the mobile groundwater and minimize advective heat losses, the BTES system was designed as a shallow installation with 20-meter deep boreholes, entirely situated within the unsaturated zone above the water table. This design strategy ensures that thermal storage occurs

in porous media where heat transport is dominated by conduction rather than advection, substantially improving storage efficiency and thermal plume confinement. The 20-meter installation depth represents an optimized compromise between multiple competing factors: maximizing storage efficiency by remaining above the aquifer, minimizing drilling complexity and associated costs compared to deeper installations, providing adequate storage volume for the target heating application, and limiting thermal losses to the atmosphere from excessive shallow placement. The BTES installation occupies a total surface area of approximately 490 m² with a field radius of 12.4 meters, employing a circular borehole arrangement designed to maximize thermal storage efficiency by creating a thermally concentrated central core zone that better retains heat over extended storage periods (**Figure 148**). Circular configurations have been demonstrated to provide superior thermal performance compared to linear or rectangular arrays by minimizing the surface-to-volume ratio of the heated storage volume, thereby reducing conductive losses to surrounding cooler formations (Section 5.1).

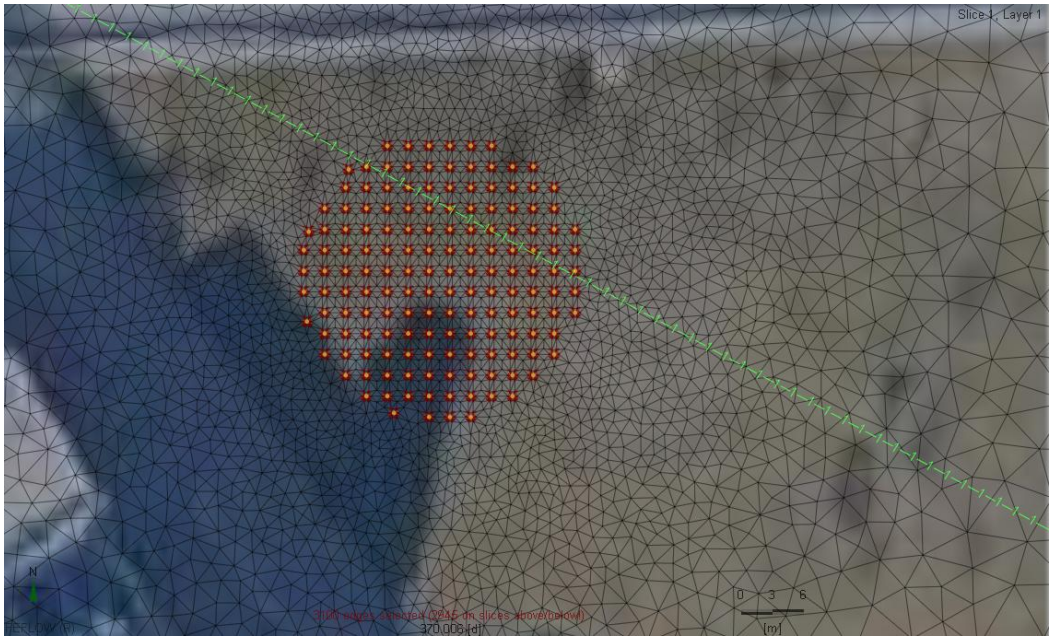

Figure 148. BTES array and mesh discretisation.

The principal technical parameters common to all simulated scenarios are summarized in **Table 23**. The system comprises 155 boreholes, each 20 meters deep, configured with single U-tube borehole heat exchangers. Single U-tube configurations represent the most widely adopted BHE design globally, accounting for approximately 65% of BTES installations due to their design simplicity, installation ease, cost-effectiveness, and proven long-term reliability. Each U-tube consists of high-density polyethylene (HDPE) pipes with an outer diameter of 26 mm and wall thickness of 2.9 mm, dimensions commonly employed in shallow geothermal systems and providing adequate mechanical strength while maintaining low thermal resistance. The hydraulic system is configured with parallel connection of all 155 boreholes, ensuring uniform fluid distribution across the borehole field and enabling consistent thermal loading and extraction across all heat exchangers.

The heat transfer fluid is demineralized water with anti-corrosion and anti-freeze additives, necessary to guarantee system longevity, prevent pipe degradation, and maintain optimal performance across all operational temperature ranges. The discharge phase inlet temperature is fixed at 10°C across all scenarios, representing a typical return temperature from a heat pump evaporator in winter heating mode.

Table 23. Main technical parameters used in the model that were common to all scenarios.

Parameters	Unit Measurement	Value
Number of BHEs	n°	155
Depth	m	20
Array geometry	-	Circular
BHE spacing	m	2
Area	m²	490
Radius	m	12,4
BHE type	-	Single-U
Pipe diameter	mm	26 (esterno)
Pipe thickness	mm	2,9
Pipe material	-	HDPE
BHE connection	-	Parallel
Intlet temperature	°C	10

Figure 149 presents a schematic diagram of a single U-tube geothermal probe, illustrating the fundamental operational principle. The diagram shows fluid circulation down one leg of the U-tube and return through the other leg, with arrows indicating flow direction. Key input parameters for numerical simulations include individual borehole flow rate and inlet fluid temperature, while model outputs provide outlet fluid temperature that feeds the heat pump system.

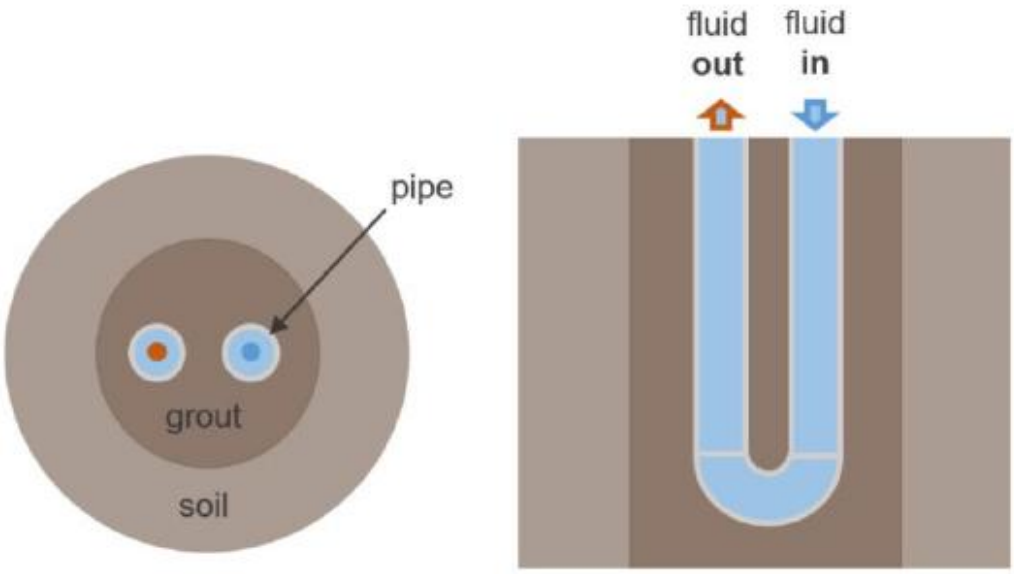

Figure 149. Single-U BHE configuration.

The finite element mesh was adaptively refined in proximity to the borehole locations and throughout the surrounding thermal storage zone to accurately capture steep thermal gradients and thermal interference patterns generated by the closely-spaced borehole array. **Figure 150** illustrates the 3D mesh refinement, revealing both horizontal densification around boreholes and vertical discretization refinement in the upper 20 meters. Vertical layering was increased in the zone penetrated by boreholes, with layer thickness of 1 meter throughout the 20-meter borehole depth, ensuring adequate vertical resolution to capture axial temperature variations and heat exchange with surrounding strata.

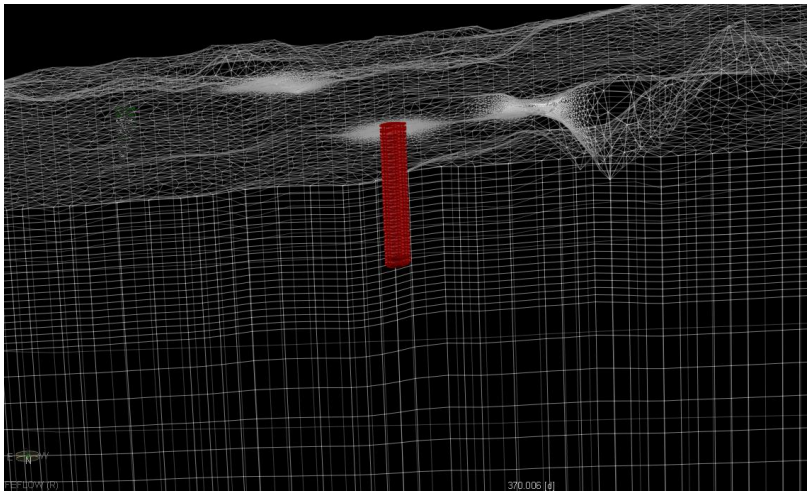

Figure 150. Cross section of the 3D mesh refinement.

Five distinct operational scenarios were simulated to comprehensively evaluate BTES performance under varying charging temperatures, flow rates, and seasonal cycle durations (Table 3). These scenarios were designed to explore the parameter space relevant to integration with different heat sources (low-temperature waste heat vs. high-temperature solar thermal or industrial processes) and different heat extraction strategies (continuous moderate extraction vs. intensive peak demand extraction). The variation in flow rates between charging and discharging phases in some scenarios reflects operational strategies aimed at optimizing thermal balance, where lower discharge flow rates increase residence time in boreholes and enhance heat extraction efficiency.

Table 24. Main operating characteristics in the various analysed scenarios.

Scenarios	**Charging time**	**Charging flow rate**	**Discharging flow rate**	**Charging temperature**
	month	**(l/s)**	**(l/s)**	**(C°)**
1	6	*0,6*	*0,4*	*35*
2	6	*0,6*	*0,4*	*80*
3	12	*0,6*	*1*	*35*
4	12	*0,6*	*1*	*80*
5	6	*1*	*1*	*35*

5.4 Results

The successful design and optimisation of BTES systems require a careful evaluation of several interrelated parameters that govern thermal exchange, storage efficiency, and operational viability. The results presented here provide quantitative performance benchmarks and design insights to support strategic deployment of shallow BTES technology as a component of sustainable urban energy systems.

5.4.1 Case Study 1

In the first case study, a comprehensive parametric investigation was performed, testing multiple configurations to ensure that the final design met the technical criteria for the Nyhavna project. The final configuration that was selected for the initial numerical analysis consists of a circular array comprising 65 borehole heat exchangers (BHEs), with a spacing of 2 metres and a drilling depth of 100 metres below the surface.

The geometry of the array has been demonstrated to exert a direct influence on the thermal performance and land use efficiency of BTES installations. A range of geometrical configurations were evaluated, incorporating linear, rectangular, and circular arrangements. The final configuration implemented in this study adopts a circular (cylindrical) array. This geometry has been shown to minimise the surface-area-to-volume ratio, thereby reducing thermal losses from the periphery and enhancing overall heat retention [255]. Furthermore, the symmetry provided by the circular arrangement optimises the distribution of temperature gradients, which is crucial during both the charging and discharging phases [364]. The configuration of 65 BHEs that has been selected ensures that the cumulative thermal capacity meets the project's heating requirements while maintaining a compact installation footprint.

Borehole spacing has been identified as a critical factor in the analysis of thermal interaction between adjacent BHEs. Insufficient spacing can lead to excessive thermal interference, thereby reducing the temperature gradient necessary for efficient heat exchange. Conversely, excessive spacing may result in underutilisation of the available subsurface space and increased pumping costs [246]. It was determined through the implementation of various parametric modelling tests that a spacing of 2 metres was the adequate distance for this specific case study. This space is sufficient to minimise thermal overlap, thereby ensuring that each borehole operates under near-ideal conditions while maintaining compact array geometry [320,394].

The depth at which the BHEs are installed is pivotal in achieving effective thermal storage without adversely affecting the surrounding geotechnical conditions [352]. In the Nyhavna project, BHEs are drilled to a depth of 100 metres, with the thermal exchange starting below the clay layer (from a depth of 30 metres). It is critical to thermally insulate the clay layer to prevent a decrease in storage performance and to ensure the integrity of the soil's mechanical properties.

The thermal performance of a BTES system is not solely a function of its physical configuration; operational conditions play a significant role as well. In this study, two fundamental operational phases were identified as the primary focus:

a) Charging Phase (Summer period): During the charging phase, a high inlet temperature is essential to store an adequate amount of thermal energy. The system was designed to operate with an inlet fluid temperature (T_{in}) of 80°C, the outlet temperature (T_{out}) varying from 45 to 60°C.
b) Discharging Phase (Winter period): For efficient energy recovery, the system is configured to operate with a lower discharge temperature. The T_{in} during the discharging phase is maintained at 10°C, maximizing the temperature difference between the stored heat and the T_{out} during extraction.

In addition to temperature control, the flow rate of the heat-transfer fluid is a critical parameter that must be taken into consideration. A single flow rate of 1 l/s (both charging and discharging phase) was selected for each borehole, thus balancing the need for rapid heat transfer with the minimisation of hydraulic energy losses. It is posited that this flow rate is sufficient to maintain a stable thermal profile in the boreholes, whilst ensuring that the pumping energy remains within economically feasible limits. The total water flow of BTES is 65 l/s.

The selection of the BHE type represents a crucial design choice in BTES systems, exerting a direct influence on the system's thermal performance, material requirements, and operational efficiency. In this study, the Single U-Tube is evaluated (**Figure 151**).

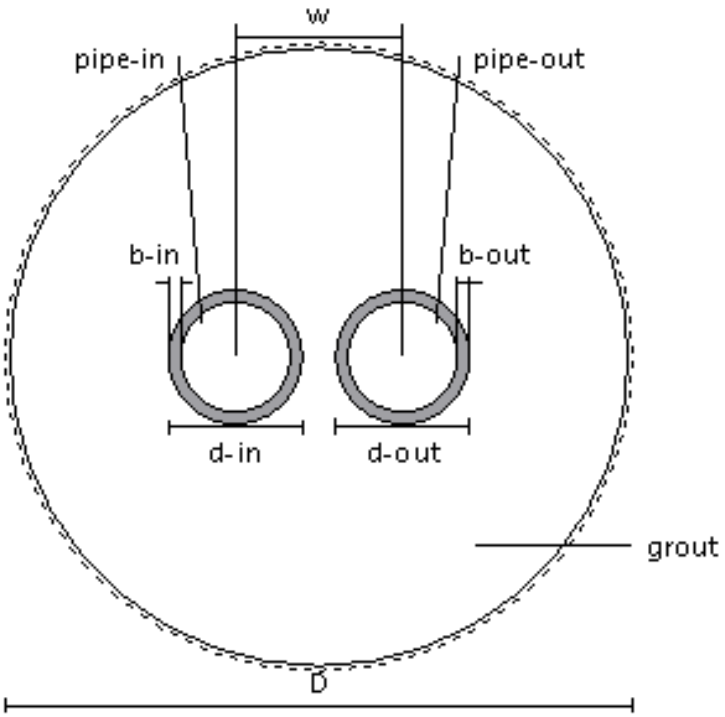

Figure 151. Single U-Tube setting on FEFLOW BHE.

The Single U-Tube design is one of the most prevalent configurations used in BTES systems [255]. This design consists of a single continuous U-shaped pipe, typically fabricated from high-density polyethylene (HDPE), which is inserted into the borehole. The fluid circulates downward through one leg and returns upward via the opposing leg, thereby establishing a temperature gradient along the borehole wall. The Single U-Tube system offers simplicity and cost efficiency, making it a popular choice in many applications. Its design (**Table 25**) is well documented and characterized by predictable thermal behaviour in moderate-depth installations [280].

Table 25. BHE value used in FEFLOW.

BHE geometry	Value (m)
Borehole Diameter (D)	0.15
Pipe Distance (w)	0.04
Inlet Pipe Diameter (d-in)	0.032
Inlet Pipe Wall Thickness (b-in)	0.0029
Outlet Pipe Diameter (d-out)	0.032
Outlet Pipe Wall Thickness (b-out)	0.0029

The numerical model incorporates site-specific thermal properties such as the thermal conductivity, volumetric heat capacity, and hydraulic conductivity of the different layers. In **Table 26** the geotechnical and thermal properties are summarised. By integrating these geotechnical parameters into the FEFLOW-based numerical model, the simulation accurately reproduces the transient heat transfer processes and the effect of groundwater flow on heat distribution. This integration is critical for predicting long-term performance, assessing thermal recovery factors, and optimizing the overall design of the BTES system.

Table 26. Main parameters used in FEFLOW.

Layer	Depth Range	Temperature (°C)	Hydraulic Conductivity (m/s)	Porosity	Specific Heat Capacity (J/kg·K)	Density (kg/m³)	Volumetric Heat Capacity (J/m³·K)	Thermal Conductivity (W/m·K)
Sand Layer	0 – 5 m	8	1×10^{-3}	0.3	830–1000	1800	1.8×10^{6}	2.5
Clay	5 – 25 m	8	~1×10^{-9}	0.44	1537	1951	3.0×10^{6}	1.32
Bedrock (Greenstone/ Greenschist)	25 m – up to 100 m (and deeper)	8 at upper bedrock, increasing to 10 at 100 m	~1×10^{-8} (for fractured crystalline rock)	0.015	850	2900	2.465×10^{6}	3.2

Particularly, FEFLOW provides specialised modules for simulating Borehole Heat Exchangers representing BHEs as one-dimensional elements embedded within the 3D finite-element mesh. The software integrates preprocessing, simulation, and postprocessing workflows, including specific tools for configuring BHEs and visualizing energy performance metrics.

The simulation domain is divided into three stratigraphic layers:

- Sand Layer (upper unconsolidated deposits): Characterized by relatively high hydraulic conductivity and thermal conductivity.
- Clay Layer: Exhibiting low hydraulic conductivity, high porosity, and lower thermal diffusivity.
- Fractured Rock Layer (bedrock): Featuring low porosity but relatively high thermal conductivity.

Each layer is assigned constant properties based on field characterization. The 3D mesh is generated by extruding a 2D mesh into vertical layers (**Figure 152** A); additional horizontal slices are inserted every 2 meters to capture vertical temperature gradients accurately. To capture the detailed thermal plume generated by the BTES operation, the mesh is locally refined around each BHE (**Figure 152** B).

An initial steady-state groundwater flow simulation was performed to establish the hydraulic field. This steady-state solution provided the initial conditions for the subsequent transient thermal simulation.

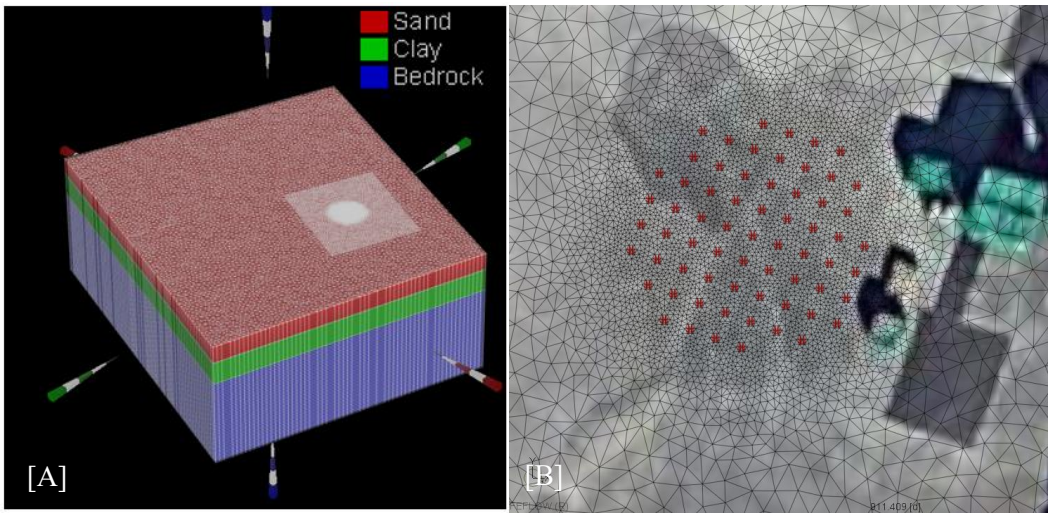

Figure 152. [A] 3D model setup and layer discretization; [B] Refinement around BHEs.

The model is constrained by two distinct types of boundary conditions (flow and thermal conditions). In the context of flow analysis, the implementation of fixed-head (Dirichlet) boundaries at the inflow and outflow zones is a fundamental approach. In contrast, other boundaries are designated as no-flow boundaries. With regard to the thermal boundary condition, a variable inlet temperature flux is set from the surface (8°C) to the bottom (10°C), in order to simulate the natural geothermal gradient of the area. In the case of BHE, the operational cycles are simulated by a prescribed inlet temperature condition. This condition involves an inlet temperature of 80°C during the one-and-a-half-year charging phase, and 10°C during the six-month discharging phase.

The BHE array is modeled using FEFLOW's BHE module. The 65 BHEs are connected in a circular configuration, and each borehole is assigned properties, including geometry (Single U-Tube), grout characteristics, and fluid parameters,

using the dataset editor. The integrated BHE interconnection establishes a continuous circuit, which allows the simulation of a unified BTES plant. This approach simplifies the network by assigning a common inlet and outlet condition across the array and allows the simulation of simultaneous heat injection or extraction for the entire system. The transient simulation is conducted over a three-year period, applying different flow rate depending on the cycle, thereby capturing the dynamic thermal response during both the charging and discharging phases (six months each).

The initial charging phase is comprised of a 1.5-year period of charging, succeeded by a 6-month discharging phase. The third year is characterised by a 6-month cycle of charging and discharging. During the charging process, thermal energy is injected at a temperature of 80°C, while the discharging process is conducted with a reinjection temperature of 10°C. The flow rate of both phases is 1 l/s each BHEs. The horizontal temperature distribution at a depth of 37 m after 545 days of charging is illustrated in **Figure 153** A. The circular thermal plume is centred around the borehole array and exhibits a radially symmetric structure, with maximum temperatures in the core exceeding 67°C above ambient (9°C). The isotherms extend laterally from this central zone, indicating a gradual decrease in temperature with increasing radial distance. The dense triangular mesh and refined nodes surrounding the boreholes ensure an accurate representation of the steep thermal gradient near the heat sources. This distribution serves to emphasise the efficacy of the system in establishing a well-confined thermal storage zone, characterised by minimal lateral losses. This accomplishment is attributable to two primary factors: geological confinement and optimised spatial design.

As illustrated in **Figure 153** B, the vertical temperature cross-section of the subsurface following the initial charging phase is represented. The thermal anomaly is distinctly confined below 25 metres, corresponding to the clay-bedrock interface, with the plume penetrating deep into the fractured bedrock. The maximum subsurface temperatures are close to 68°C, and the geometry is principally cylindrical, extending vertically to depths in excess of 80 m. This stratigraphic control enhances the vertical propagation of the plume while preventing upward heat migration, thus reducing the risk of thermal interference with sensitive shallow layers. The symmetrical configuration of the thermal plume is indicative of the homogeneous thermal loading conditions and the high degree of mesh refinement implemented around the boreholes, ensuring a seamless depiction of radial temperature gradients. The vertical slices, inserted at 2-metre intervals, serve to enhance the resolution, thereby facilitating the precise observation of vertical thermal stratification.

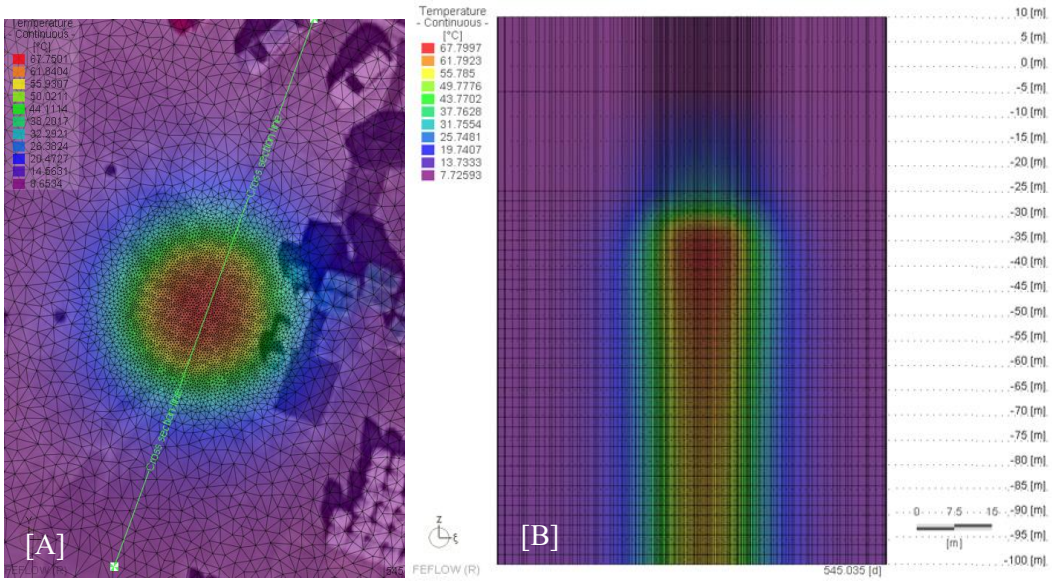

Figure 153. [A] Areal map of temperature after first charging phase, the green line indicates the vertical cross section trace; [B] Cross section of vertical temperature distribution after charging phase (1.5 years).

As illustrated in **Figure 154** A and **Figure 154** B, the horizontal and vertical profiles are shown at the conclusion of the two-year simulation and the end of the discharging phase. The thermal plume displays a significant decrease in temperature, with maximum temperatures falling below 23°C. The central zone exhibits a slight elevation, indicative of residual thermal energy stored within the bedrock matrix. The symmetry and shape of the plume are largely preserved, but with reduced intensity due to the processes of heat extraction and conductive dissipation. This demonstrates that the BTES system can effectively discharge stored energy over the winter period, with predictable and localized cooling behaviour.

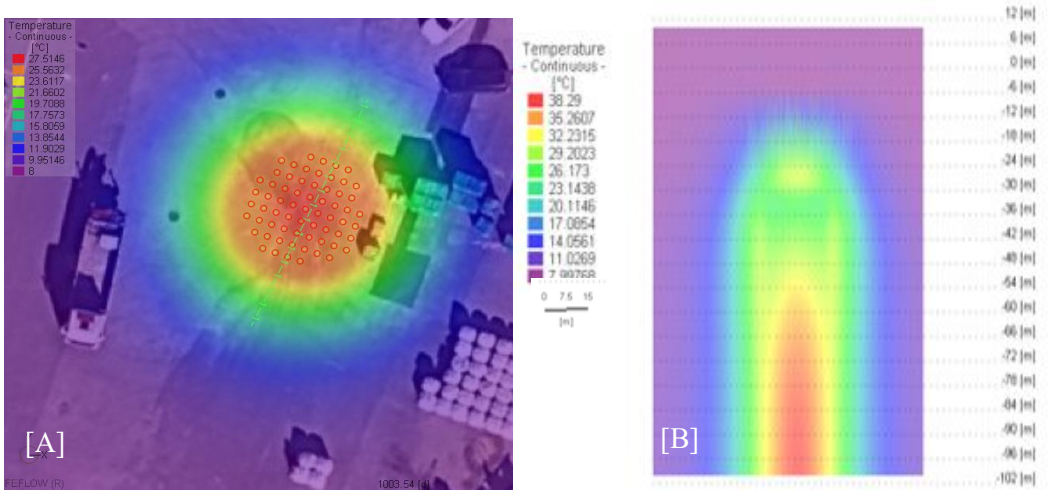

Figure 154. [A] Areal map of temperature after discharging phase, the green line indicates the vertical cross section trace; [B] Cross section of vertical temperature distribution after discharging phase.

As demonstrated in **Figure 155**, the graph presents the development of the inlet and outlet temperatures of the BTES system. The coloured lines represent the temperature of the individual BHEs, with those in the core exhibiting higher temperatures and gradually decreasing in the discharging phase until after four

months. Subsequently, these values are aligned with the temperatures of the outermost layers.

It appears that the efficiency of the system is subject to a decline over time, attributable to the rapid dissipation of heat approximately halfway through the discharge period (3 months). Subsequent to this juncture, the outlet temperatures on average fall below 25°C, which, while still providing some useful heating capacity, represents diminished thermal quality and reduced system efficiency as the temperature difference between supply and return narrows. Flow rates are maintained at steady state (1.0 l/s per borehole) throughout each phase, ensuring consistent hydraulic conditions.

The operational performance of the Nyhavna BTES system has been evaluated through FEFLOW Heat Rate Budget and simulation, revealing both the thermal behaviour of the subsurface and the energy balance of the system. As is the case with the majority of HT-BTES installations worldwide, the initial years of operation are dominated by a thermal charging phase, during which a significant quantity of heat is injected into the ground to establish a suitable thermal regime. This start-up period typically spans one to six years depending on system size, operating temperature, geological conditions, and target storage volume, and is essential for elevating the temperature of the storage medium and its surrounding geological volume to a functional level that enables efficient seasonal cycling.

During this phase, thermal energy is dissipated radially and vertically from the borehole array into the fractured bedrock, gradually reducing the temperature gradient between the heated core and the surrounding subsurface. As the system progresses toward a quasi-steady state, heat losses stabilise and annual energy balances improve. Although it may take decades to reach full thermodynamic equilibrium, a stable operating condition, where heat injection and extraction become more efficient and predictable, is generally reached after the initial few years of operation.

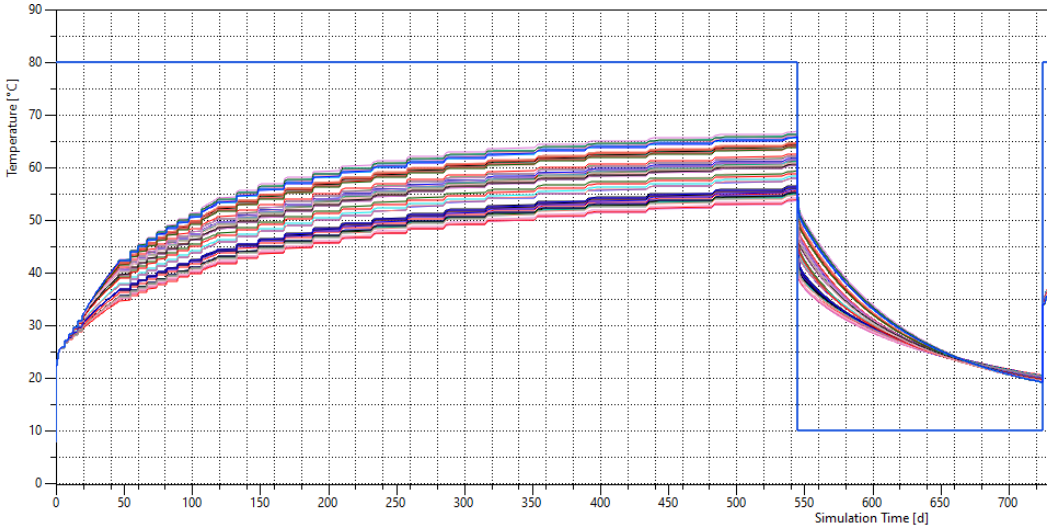

Figure 155. Inlet/outlet temperature graph: the blue stable line is the inlet temperature, the different colored lines represent the 65 different BHEs outlet temperature.

In the case of the Nyhavna installation, the results (**Figure 156** A) demonstrate that after 550 days of operation, a total of 1400.87 MWh of thermal energy was injected during the charging phases, while only 315.23 MWh was recovered during the discharging periods (day 730). This corresponds to an early-cycle efficiency of approximately 22.5% (calculated as extracted energy / injected energy × 100), reflecting the substantial energy investment required to establish the thermal reservoir and overcome natural thermal losses during the system maturation phase. The maximum subsurface temperature was recorded at 66.8°C at the conclusion of the second-year charging period, subsequently decreasing to 20.5°C upon discharging. This observation signifies the system's capacity for heat accumulation and the substantial energy reserves remaining in the storage zone following extraction.

In the third year (days 730-1095), representing the first full seasonal cycle with 6-month charging and 6-month discharging phases, thermal input decreased markedly to 500.03 MWh during the charging phase. Furthermore, thermal recovery exhibited a substantial increase, reaching 272.15 MWh during the discharge phase. This development led to an enhancement in the energy recovery ratio to 54.4% (272.15 / 500.03 × 100%), signifying a dramatic improvement in the efficiency of energy utilisation as the thermal regime matured and the system transitioned toward quasi-steady operation. The peak temperature recorded at the conclusion of the third charging phase was marginally lower, at 64.13°C, and the post-discharging temperature stabilised at approximately 20.46°C (**Figure 156** B). This finding indicates the occurrence of a thermal plateau phase, during which the storage zone begins to stabilize its thermal conditions between consistent upper and lower temperature bounds, a hallmark of the transition to quasi-steady operational phase where annual temperature oscillations become repeatable and system performance becomes predictable.

A

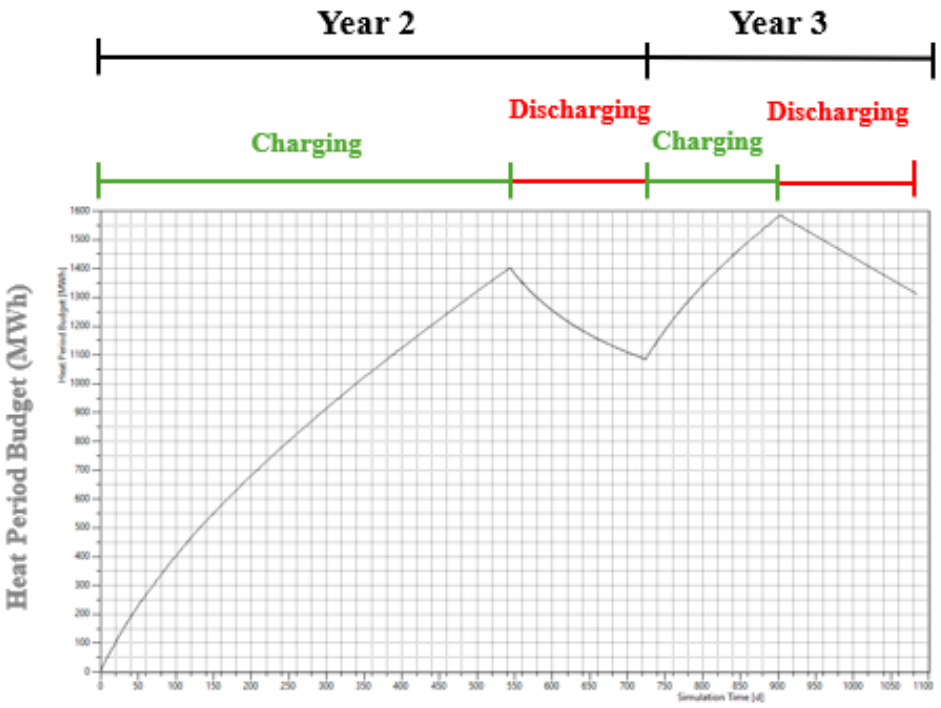

B

Time	Charging (MWh)	Discharging (MWh)	Performance (%)	Max Temperature (C°) after charging period	Max Temperature (C°) after discharging period
After 2 years (730 d)	1400.87	315.23	22.50	66.80	20.5
After 3 years (1085 d)	500.03	272.15	54.43	64.13	20.46

Figure 156. [A] Rate Budget chart of BTES plant; [B] summary of the main results.

5.4.2 Case Study 2

The second case study presents comprehensive numerical simulation results for the five BTES operational scenarios over a five-year simulation period, focusing on thermal performance metrics including outlet temperatures, thermal plume spatial extent, energy balance, and storage efficiency. Each scenario is analysed individually to elucidate the influence of operational parameters on system performance, followed by comparative analysis highlighting key design insights.

Scenario 1 simulates five years of BTES operation with 6-month charging and discharging cycles, employing a charging flow rate of 0.6 l/s per borehole at 35°C inlet temperature, followed by discharge at 0.4 l/s per borehole with 10°C inlet temperature. The asymmetry in flow rates (higher during charging, lower during discharging) was implemented to maximize thermal energy accumulation during the summer charging phase while slowing heat extraction during winter to increase mean system temperature and improve heat pump source conditions. Total system flow rates reach 93 l/s during charging and 62 l/s during discharging.

Results demonstrate that during the charging phase, the maximum mean outlet temperature from boreholes reaches 26°C by the end of the fifth-year summer period (**Figure 157**). The plot reveals cyclical temperature oscillations corresponding to alternating charging (higher outlet temperatures) and discharging (lower outlet temperatures) phases. Temperature variations between individual boreholes are visible, reflecting their positions within the circular array, central boreholes experience stronger thermal interaction and higher sustained temperatures, while peripheral boreholes show greater temperature fluctuations and faster thermal recovery between cycles.

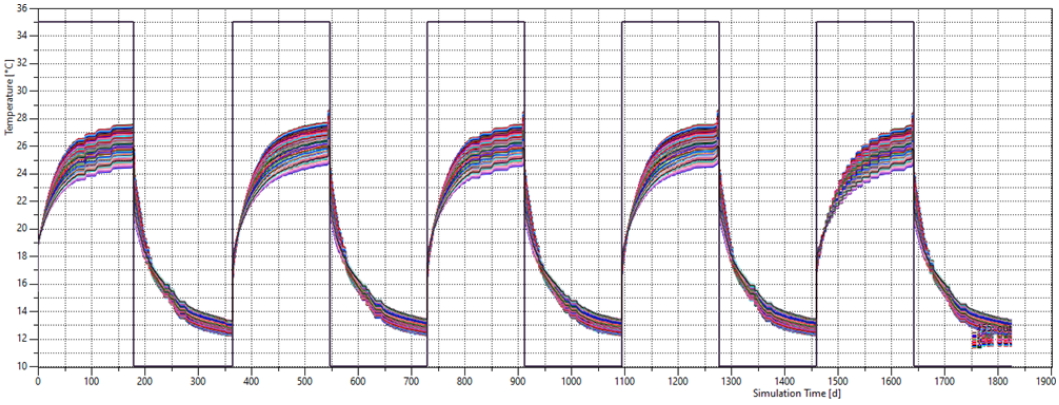

Figure 157. Graph showing the outlet temperatures from each BHEs throughout the entire simulation period.

During the discharge phase, the initial mean outlet temperature at the beginning of winter heating season reaches approximately 20°C, declining to a minimum of 12.5°C by the end of the 6-month extraction period (**Figure 158**). The gradual decline to 12.5°C over the discharge period indicates progressive depletion of the stored thermal energy as heat is extracted from the subsurface storage volume.

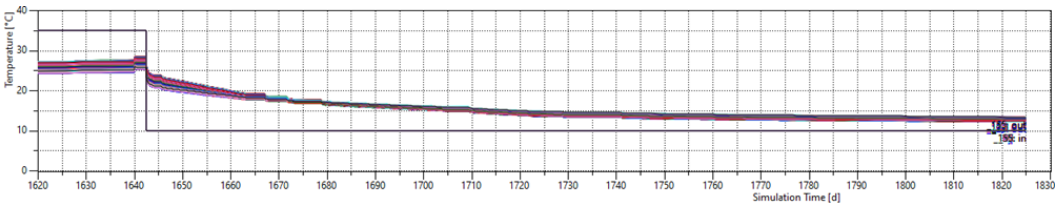

Figure 158. Graph showing the outlet temperatures from each BHEs at the end of the fifth year.

The spatial extent of thermal impact is quantified through horizontal and vertical cross-sections of subsurface temperature at peak charging conditions. Figure 8 shows the horizontal thermal interference pattern at the end of the fifth charging period, revealing a thermally anomalous zone extending approximately 30 meters radially from the borehole field centre (**Figure 159**). The thermal plume exhibits roughly circular geometry consistent with the circular borehole arrangement, with peak temperatures exceeding 25°C in the central core and gradual attenuation to background temperatures (~15-16°C) at 30-meter radius.

Figure 159. Thermal interference of the BTES system in horizontal section at the end of the fifth charging period.

Figure 160 illustrates the vertical thermal interference pattern in cross-section at the end of the fifth charging period. The thermal anomaly penetrates to approximately 21 meters depth, extending slightly below the 20-meter borehole depth.

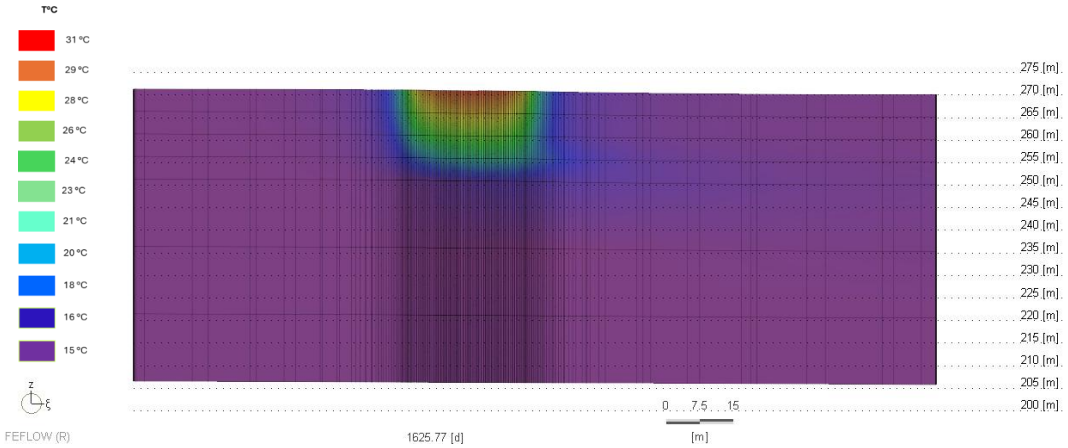

Figure 160. Thermal interference of the BTES system in vertical section at the end of the fifth charging period.

Figure 161 presents the horizontal thermal plume at the end of the fifth discharge period, showing substantially reduced thermal anomaly extent and **Figure 162** displays the vertical thermal cross-section at the end of the fifth discharge period, revealing that thermal effects remain concentrated in the upper 15-18 meters.

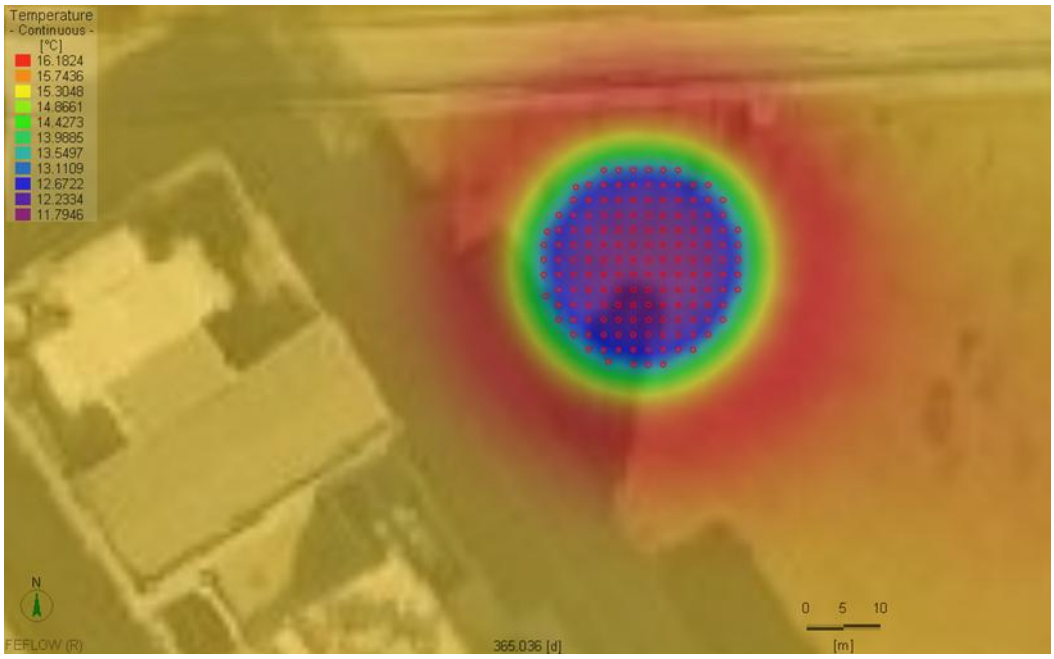

Figure 161. Thermal interference of the BTES system in horizontal section at the end of the fifth discharging period.

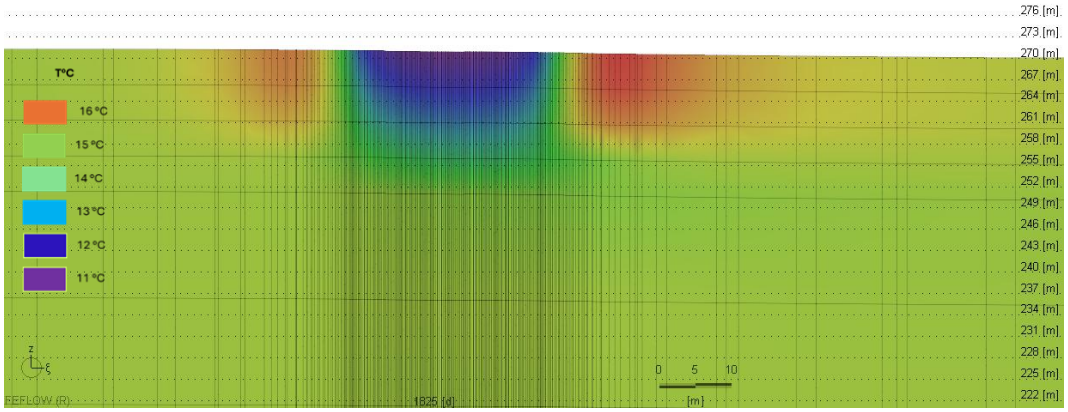

Figure 162. Thermal interference of the BTES system in vertical section at the end of the fifth discharging period.

The energy balance for the first Scenario, averaged over the five-year simulation period, reveals that an average of 110 MWh of thermal energy were injected into the subsurface per charging season, while 37 MWh were extracted per discharge season, yielding a mean storage efficiency of 33.5%. **Figure 163** presents the annual energy budget and efficiency evolution, showing relatively stable performance across the five-year period. The moderate efficiency reflects substantial thermal losses through conduction to surrounding cooler formations, losses to the atmosphere through the shallow overburden, and incomplete thermal recovery during the 6-month discharge period. However, the extracted 37 MWh per year provides significant heating energy equivalent to approximately 3,700 m³ of natural gas combustion, representing substantial fossil fuel displacement and carbon emission reduction.

Figure 163. BTES energy budget and efficiency chart.

The second Scenario employs identical operational duration and flow rates as first Scenario but increases the charging temperature to 80°C, representing high-temperature thermal storage. This substantial temperature increase dramatically alters system thermal behaviour, energy capacity, and efficiency. During the charging phase, the maximum mean outlet temperature reaches 52°C at the end of the fifth summer (**Figure 164**).

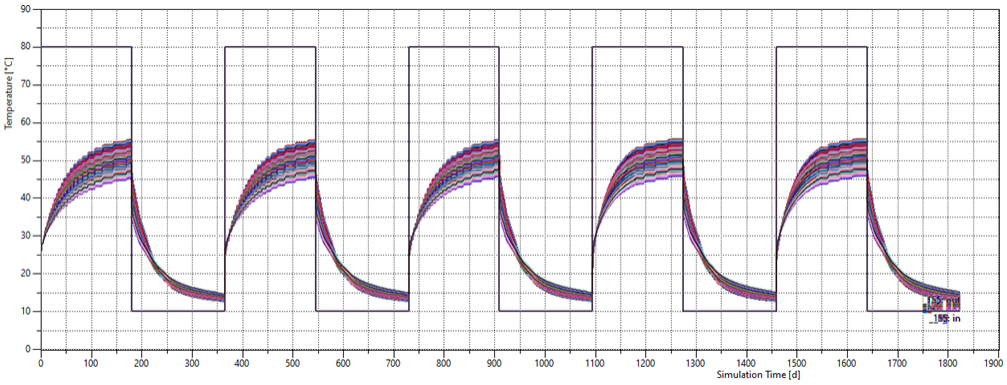

Figure 164. Graph showing the outlet temperatures from each BHEs throughout the entire simulation period.

During the discharge phase, the initial maximum outlet temperature reaches 28°C after one month of operation, declining to a minimum of 14°C by the end of the discharge period (**Figure 165**).

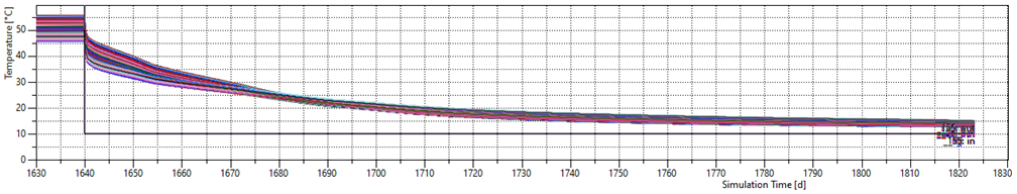

Figure 165. Graph showing the outlet temperatures from each BHEs at the end of the fifth year.

The total energy balance over five years reveals that 1,792 MWh were injected during charging periods, while 370 MWh were recovered during discharge, yielding a mean efficiency of 20.6%. Thermal plume figures for the second Scenario (placed in Appendix B, **Figure 204**, **Figure 205**, **Figure 206**, and **Figure 207**) demonstrate substantially larger thermal impact zones compared to the first Scenario, with thermal anomalies extending beyond 50 meters from the borehole field.

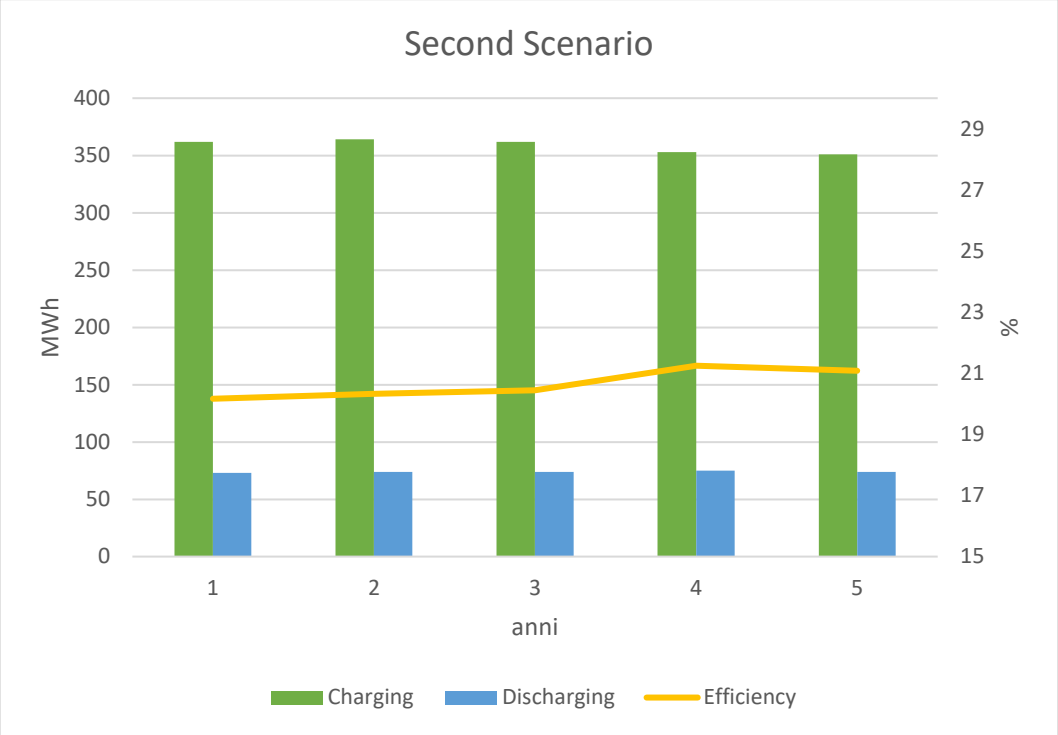

Figure 166. BTES energy budget and efficiency chart.

The third Scenario introduces a fundamentally different operational strategy: the first year is dedicated exclusively to thermal activation, with continuous heat injection at 35°C throughout the entire first year to pre-heat the subsurface storage volume from natural ground temperature to operational temperatures.

From the second year forward, the system operates with standard 6-month charging and discharging cycles, but with different flowrate (0.6 l/s during charging and 1 l/s during discharging). This difference is due to enhance the discharge rate. Results demonstrate that during the charging phase, the maximum mean outlet temperature reaches 27°C, similar to first Scenario despite higher flow rates, indicating that the extended first-year activation successfully elevated baseline subsurface temperatures. During discharge, the initial maximum temperature reaches 20°C, declining to 13°C by the end of the discharge period (Appendix B, **Figure 208** , and **Figure 209**). With regard to energy, 703 MWh were fed into the ground system during the charging period, over a period of five years, while 342 MWh were extracted during the discharging period. The total average system efficiency was found to be 49%. However, system efficiency increases substantially over time, exceeding 60% from the second year onward after the thermal regime stabilizes. The figures relating to the thermal impact are shown in the Appendix B (**Figure 211**, **Figure 212**, **Figure 212**, and **Figure 213**).

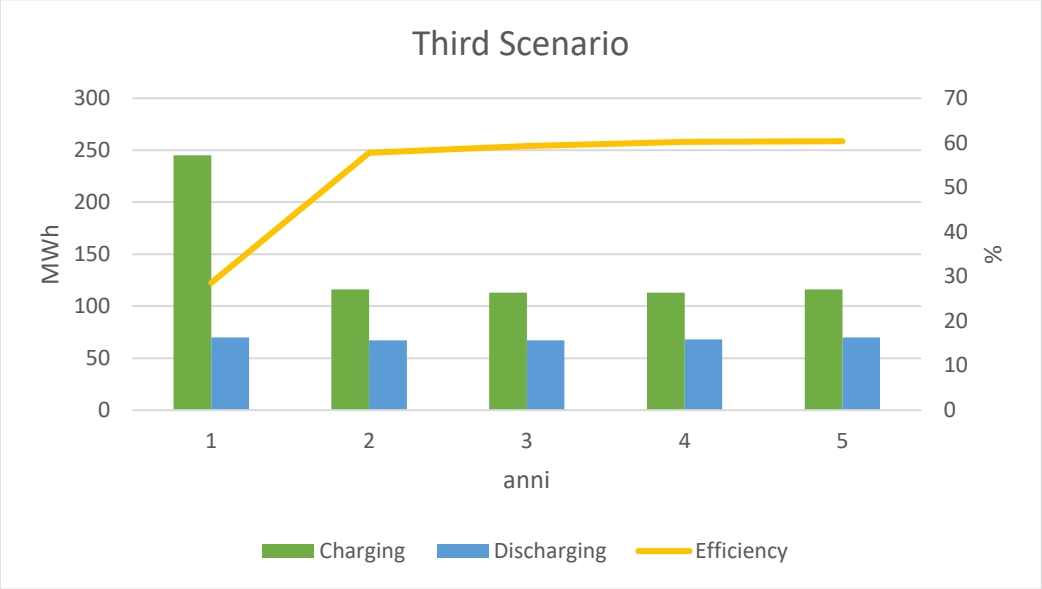

Figure 167. BTES energy budget and efficiency chart.

The fourth Scenario combines high-temperature storage (80°C) with the extended first-year activation strategy employed in the third Scenario. Results show that during charging, the maximum mean outlet temperature reaches 53°C. During discharge, the initial maximum temperature reaches 35°C, declining to 13°C by period end (Appendix B, **Figure 214**, and **Figure 215**). The total energy balance indicates 2,247 MWh injected and 630 MWh recovered, yielding a mean efficiency of 28%. However, like the third Scenario, efficiency increases from 34% in year 2 to over 36% in year 5 as the thermal regime stabilizes. **Figure 168** illustrates this efficiency evolution and energy budget. The figures relating to the thermal impact are shown in the Appendix B (**Figure 216**, **Figure 217**, **Figure 218**, and **Figure 219**).

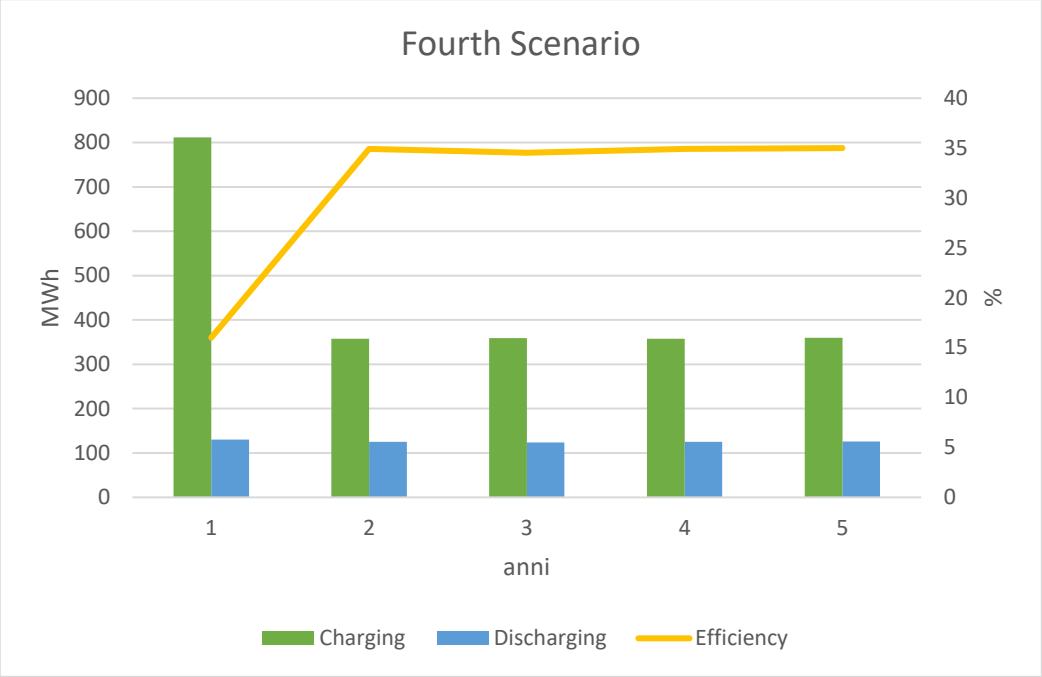

Figure 168. BTES energy budget and efficiency chart.

The fifth Scenario represents a simplified operational approach with balanced 1.0 L/s flow rates during both charging and discharging, 6-month cycles, and 35°C charging temperature, without the first-year activation employed in the third and fourth Scenario. Total system flow reaches 155 l/s during both phases. This scenario explores whether high balanced flow rates alone, without extended activation, can achieve favorable efficiency by accelerating thermal regime development. Results show that during charging, the maximum mean outlet temperature reaches 26°C, similar to the first and third Scenario. During discharge, the initial temperature reaches 20°C, declining to 13°C by period end (Appendix B, **Figure 220**, and **Figure 221**). The energy balance indicates 804 MWh injected and 354 MWh recovered over five years, yielding a mean efficiency of 44% (**Figure 169**). Thermal impact figures are shown in Appendix B (**Figure 222**, **Figure 223**, **Figure 224**, and **Figure 225**).

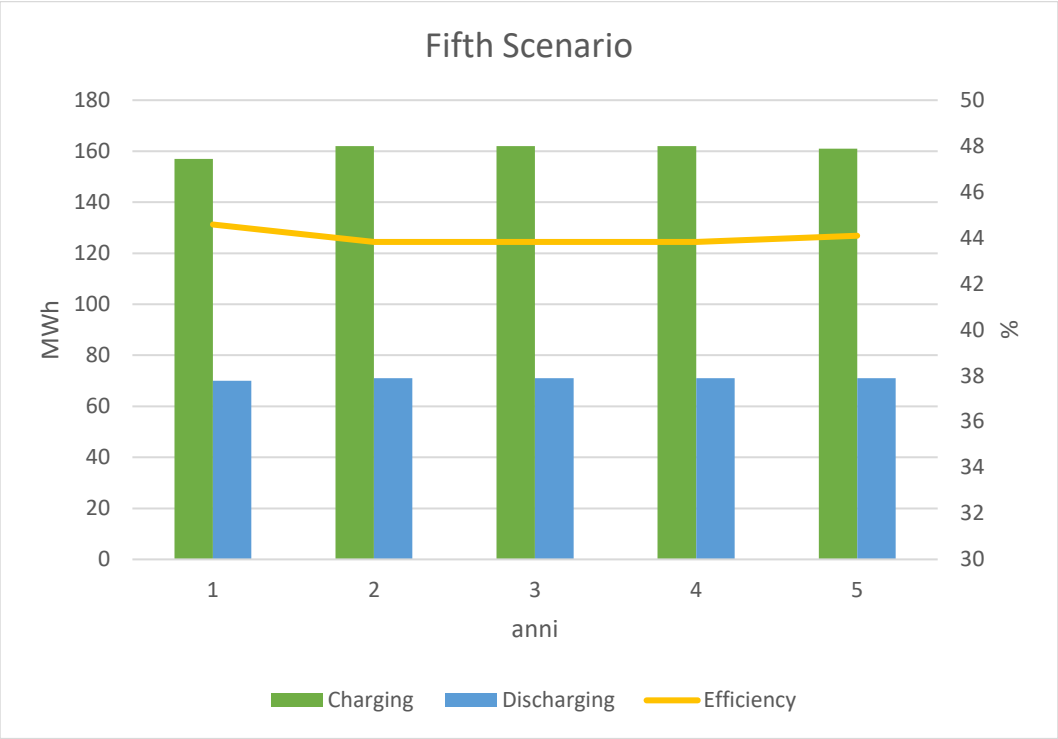

Figure 169. BTES energy budget and efficiency chart.

5.5 Discussion

The numerical simulation results for both case studies provide valuable insights into the complex interplay between operational parameters, geological conditions, and thermal storage performance in BTES systems across diverse settings, high-temperature bedrock storage in Norway and shallow unsaturated-zone storage in Italy.

The operational performance observed in the Nyhavna BTES system aligns well with established trends in high-temperature BTES technology worldwide, confirming that the simulation results are physically realistic and representative of actual system behaviour. These trends are consistent with the performance trajectories observed in other high-temperature BTES systems. For instance, the Emmaboda BTES plant in Sweden, operational for over 15 years with similar operating temperatures (70-85°C), has achieved a long-term recovery efficiency stabilized at approximately 69% after the initial 5-7 year maturation period. The Emmaboda system employs 140 boreholes drilled to 150 m depth in crystalline bedrock (granite-gneiss) with thermal conductivity 3.0-3.5 W/(m·K), and stores industrial waste heat from a wood processing facility [395]. In comparison, the Luleå BTES in northern Sweden, which utilises industrial waste heat as thermal input from a steel manufacturing facility, has reported recovery efficiencies ranging from 30% to 55% during the first 5 years of operation, progressively increasing to 60-65% efficiency after 10 years of continuous operation. The Luleå system comprises 144 boreholes to 150 m depth, operates at 55-70°C charging temperature, and is situated in glacial till overlying crystalline bedrock [395]. The Neckarsulm BTES in Germany, integrated with a large-scale solar thermal collector field (7,300 m² collector area), employs 528 boreholes to 30 m depth in saturated sand-gravel aquifer and achieves 40-50% seasonal efficiency at operating temperatures 30-80°C. The SKEWS BTES in Berlin, Germany, uses 80 boreholes to 70 m depth with 60-75°C operating temperatures, achieving 45-55% efficiency [396,397].

When evaluated within this comparative framework, the Nyhavna system performance, 22.5% efficiency in the initial operational phase (first 2 years) increasing to 54.4% efficiency in year 3, is worthy of note and highly consistent with international experience. While other full-scale HT-BTES systems, including those located in Sweden (Emmaboda, Luleå), Germany (Neckarsulm, SKEWS), and Belgium (Mol), have reported seasonal recovery rates ranging from 10% to 70%, the majority of these systems required 3-7 years of continuous operation in order to approach the higher efficiency levels (>60%). The Nyhavna trajectory, reaching 54% efficiency in year 3, suggests that the system will likely achieve higher efficiency within 5-7 years, matching or exceeding the performance of established international installations.

The numerical simulation results for the northern Turin BTES system provide valuable insights into the complex interplay between operational parameters, geological conditions, and thermal storage performance in shallow unsaturated

zone applications. The observed storage efficiencies ranging from 21% to 49% across the five scenarios reflect multiple concurrent heat loss mechanisms inherent to shallow BTES systems operating in unsaturated porous media. Conductive losses to surrounding formations represent the dominant loss pathway, with heat propagating radially and vertically from the heated storage volume toward cooler undisturbed ground at natural temperature (~15.5°C). The findings indicate insufficient thermal performance of the systems across all Scenarios. In fact, after approximately 1-2 months, the temperature during the discharge phase falls below the average undisturbed soil temperature. The BTES system functions effectively for a period of approximately two months during the discharge phase, that is to say, until the BTES temperature remains higher than or equal to that of the ground. This limitation is primarily attributable to the geology of the area, and its mitigation can be achieved through the optimisation of the system design. However, it should be noted that this limitation cannot be fully eliminated. In the event that the primary objective of the system is to achieve and maintain elevated temperatures, this principle applies to both HT and LT Scenarios. It is possible, albeit at the expense of the overall efficiency of the system, to construct three distinct BTES systems that possess identical characteristics and utilise them in the discharge phase for a period of only two months. This approach encompasses the six winter months and optimises temperature. It is evident that the efficiency of the systems will undergo a decline as a consequence of the annual cycle of charging and discharging, which will be distributed over a period of 10 months and 2 months, respectively. However, it should be noted that the temperature will be maintained at a higher level. This rotational approach would mitigate thermal drawdown, and support sustained high-temperature output, but at the expense of performance. This strategy raises questions about optimal zone sizing, discharge sequencing and year-round thermal management tailored to specific project objectives.

5.6 Conclusion & Further Investigation

This chapter has presented a comprehensive investigation of Borehole Thermal Energy Storage technology through systematic literature review, global deployment analysis, and detailed numerical simulations of two contrasting case studies in Trondheim (Norway) and northern Turin (Italy). The research advances understanding of BTES performance determinants, design optimization strategies, and technology deployment potential in diverse geological and climatic contexts, providing critical insights for broader adoption of seasonal thermal energy storage in decarbonized urban energy systems.

Comparative analysis illuminates critical geological controls: deep bedrock BTES (100 m, Nyhavna) substantially outperformed shallow unsaturated-zone BTES (20 m, Turin) across efficiency metrics (54% vs. 21-49%), but performance advantages must be weighed against 3-5× higher drilling costs per meter, site-specific geological constraints, and regulatory complexity. Both systems demonstrated spatial thermal impacts compatible with urban deployment (25-70 m plume extent depending on temperature), while unsaturated-zone placement eliminates groundwater thermal contamination concerns complicating saturated-zone permitting. The research confirms BTES technology has achieved sufficient maturity for confident deployment in appropriate settings with proper design optimization, supported by validated numerical tools (FEFLOW), established performance benchmarks (20-30% activation-phase efficiency, 40-70% steady-state), and identified critical success factors (rigorous site characterization, optimized operational strategies, comprehensive monitoring).

While this research advances BTES understanding, several critical priorities warrant focused investigation. The most urgent priority is comprehensive instrumented monitoring of operational shallow unsaturated-zone BTES systems with multi-depth temperature sensors, high-frequency thermal and hydraulic measurements, long-term performance tracking (5-10 years), and validation of predicted efficiencies, thermal geometries, and operational constraints. The scarcity of published operational data from shallow systems represents a fundamental knowledge gap limiting technology confidence. The planned Nyhavna construction offers exceptional validation opportunities through dense subsurface monitoring networks including fiber-optic distributed temperature sensing, thermal response testing across the array, continuous inlet/outlet monitoring for all 65 boreholes, and long-term groundwater thermal impact assessment. The novel multi-zone rotational concept warrants detailed investigation including optimal zone sizing, discharge sequencing strategies, integrated control algorithms, and techno-economic assessment. Hybrid BTES-ATES configurations combining unsaturated-zone storage with underlying aquifer thermal storage could exploit advantages of both technologies through optimal vertical distribution, hydraulic isolation, and integrated control. Temperature-cascading strategies where high-temperature BTES serves direct loads initially, intermediate-temperature storage supplies heat

pumps mid-winter, and residual low-temperature storage provides preheating late-winter could maximize utilisation across full temperature degradation curves.

Development of integrated frameworks coupling detailed BTES models with whole-building energy simulation platforms would enable holistic optimization considering building thermal mass, occupancy variability, heat pump performance curves, and coordinated control strategies. Comprehensive techno-economic studies incorporating life-cycle cost analysis across regional cost variations, sensitivity to uncertain parameters, comparison to alternative technologies, and identification of optimal application niches are essential. Development of internationally harmonized standards for BTES design, installation, operation, and monitoring including minimum characterization requirements, thermal impact assessment methodologies, quality assurance protocols, and standardized performance metrics would support technology deployment. Systematic assessment of regulatory barriers across jurisdictions identifying best-practice approaches balancing environmental protection with renewable heating promotion would inform policy development in emerging BTES markets.

The research confirms BTES represents a viable and increasingly mature solution for seasonal thermal storage in urban heating applications, waste heat valorization, and renewable integration. Realizing full potential requires sustained research investment, comprehensive field demonstration, interdisciplinary collaboration, and supportive policy frameworks recognizing strategic value of thermal storage in decarbonized energy systems. As nations pursue carbon neutrality targets and renewable heating mandates, BTES will play increasingly critical roles providing seasonal storage capacity necessary to balance intermittent renewable supply with winter-peaked heating demands, ultimately contributing to resilient, sustainable, and economically viable urban energy infrastructure.

Chapter 6

Concluding Remarks

This doctoral work has developed and applied a comprehensive methodological framework for assessing and deploying low-enthalpy geothermal solutions in complex urban environments, with a particular focus on the Metropolitan City of Turin. In doing so, it has progressively addressed the set of questions articulated in **Figure 10** and introduced in Chapter 1. After an initial phase devoted to exploring the current definition of energy transition, the role of geothermal energy in supporting renewable energy systems, and the main challenges in integrating thermal energy sources, the core of the thesis has concentrated on three further groups of questions. The first group (Q1) concerns the definition and assessment of technologies: which geothermal solutions are the most effective, how geological and hydrogeological conditions influence technology selection, and which methodological steps are essential for a comprehensive evaluation. The second group (Q2) relates to the application of numerical tools: which simulation methods maximise result accuracy and how model prediction can be improved using model calibration. The third group (Q3) is explicitly associated with this concluding chapter: what the key outcomes of the research are, what implications arise for geothermal system deployment, and which future research directions are recommended. The central thread of the thesis has been to determine under which conditions shallow geothermal energy can become a technically robust, environmentally sustainable and operationally reliable component of the urban energy transition, and how these questions can be answered in an integrated manner.

With respect to the Q1 and Q2 question groups, a key contribution is the design and implementation of an integrated assessment framework that links regional-scale screening to site-specific thermo-hydraulic simulation, using only widely accessible data and standard numerical tools. At the regional scale, the Geothermal Aquifer Potential (GAP) methodology has been formalised and implemented to identify zones of higher and lower suitability for open-loop systems by combining distributed hydrogeological information, regulatory thresholds and thermo-hydraulic constraints. At finer scales, three-dimensional groundwater and heat transport models have been developed using MODFLOW, FEFLOW and PEST to represent existing and prospective installations in the alluvial aquifer of Turin. These models are constrained by stratigraphic and piezometric data from regional geoportals and monitoring networks and are refined through automated calibration where data permit. Together, the GAP mapping, the conceptual models and the calibrated simulations demonstrate that open-data-based workflows can

support spatially explicit decision tools for technology selection, design and cumulative impact assessment in metropolitan contexts.

The analysis of open-loop systems has directly addressed the questions concerning which geothermal solutions are most effective and how geological and hydrogeological conditions influence technology selection (Q1), while also contributing to the evaluation of methodological steps for comprehensive assessment (Q1) and the role of calibration in improving predictive accuracy (Q2). By quantifying the cumulative thermo-hydraulic effects of multiple groundwater heat pump installations in a densely exploited aquifer, the thesis shows how the specific characteristics of Turin's alluvial system condition the suitability and performance of open-loop schemes. The GAP map developed for Turin delineates areas of high, moderate and low potential under regulatory and thermo-hydraulic constraints, thus providing an initial filter for planning. In the most critical zones, calibrated three-dimensional models have been used to evaluate hydraulic drawdown, thermal plume evolution and interactions between neighbouring systems under current and stress-test operating scenarios. Results show that, in the high-transmissivity alluvial aquifer underlying Turin, and for the range of loads considered, the simulated hydraulic and thermal impacts remain spatially confined and compatible with regulatory constraints, provided that well spacing, reinjection temperatures and cumulative loads are respected.

For closed-loop systems, the thesis has contributed further to the evaluation of which technologies are most effective under given conditions (Q1) and which simulation and design methods are most appropriate (Q2). Existing analytical design methodologies (in particular VDI and ASHRAE) have been critically examined and tested against more detailed three-dimensional simulations. The case studies show that closed-loop systems are technically robust and broadly applicable, especially in areas where groundwater abstraction is constrained by regulation or hydrogeological conditions. However, the work also demonstrates that analytical methods have intrinsic limitations when applied to heterogeneous ground conditions, complex borefield geometries and long-term operation. The thesis therefore positions analytical approaches as useful first-order design tools, which should, however, be complemented by numerical modelling for larger or more complex projects if accurate, long-term predictions are required.

The ATES investigations provide a more exploratory but novel contribution to the questions on technology effectiveness and simulation methods (Q1 and Q2). By testing the feasibility of thermal storage systems in a high-velocity alluvial aquifer, where such applications are not conventionally considered optimal, the thesis shows that the design space for ATES is broader than often assumed. Through a series of three-dimensional simulations under different well configurations and operating regimes, the work demonstrates that it is possible to design ATES schemes that recover a significant fraction of stored heat, even under strong regional groundwater flow, provided that the orientation and spacing of warm and cold wells are carefully aligned with the natural flow field. The comparison with a theoretical open-loop baseline shows that such storage-enhanced configurations can improve overall energy utilisation and reduce thermal discharge to the wider aquifer. These results

extend the perceived applicability domain of ATES and illustrate the importance of explicitly exploiting, rather than neglecting, advective transport processes in design, thereby speaking directly to the question of which simulation methods and design strategies maximise result accuracy.

The BTES work addresses the same set of questions - on technology effectiveness, the role of geological and hydrogeological conditions, and the methodological steps required for comprehensive evaluation (Q1 and Q2) – at two distinct levels. First, a global survey of 75 BTES installations has been compiled, covering geographical distribution, borehole configurations, depth ranges, temperature levels and system typologies. This meta-analysis reveals common design patterns and performance envelopes, which can serve as benchmarks for future projects and provides a broader context within which to interpret the local case studies. Second, detailed three-dimensional simulations have been conducted for BTES systems in deep crystalline bedrock (Nyhavna, Trondheim) and in the shallow unsaturated deposits of the Turin area. The results confirm the high storage efficiencies achievable in deep bedrock fields, and show that shallow unsaturated BTES configurations can still deliver acceptable efficiencies and spatially limited thermal impacts, with the additional advantage of decoupling from groundwater and thus potentially facing fewer regulatory constraints. Together, these findings support the role of BTES as a mature option for seasonal storage in both saturated and unsaturated contexts within urban environments and demonstrate the value of combining statistical evidence from the literature with site-specific numerical analysis.

Taken as a whole, the analyses carried out in Chapters 2–5 allow a comparative qualitative assessment of the main shallow geothermal options for the Metropolitan City of Turin, thereby providing an integrated answer to the concluding questions concerning the key outcomes of the research and the implications for geothermal system deployment (Q3). Open-loop groundwater heat pumps emerge as particularly attractive in areas where the alluvial aquifer exhibits high transmissivity and where regulatory conditions permit abstraction and reinjection with limited ΔT. In these zones, high coefficients of performance and high specific thermal yields can be achieved, subject to explicit management of cumulative loads and careful siting to avoid interference with potable water wells and sensitive receptors. Closed-loop borehole systems, by contrast, are especially suitable in areas of low transmissivity, in multi-layered hydrostratigraphic settings or where groundwater protection priorities restrict direct use of the aquifer. Their long-term performance is stable when borefield design accounts for realistic ground properties and potential advective effects, and they present a lower regulatory burden where interaction with groundwater is negligible. ATES, in the configurations explored here, is best suited to clusters of buildings with pronounced seasonal imbalances between heating and cooling demands, in parts of the aquifer where thickness and confinement permit repeated storage and recovery cycles; under high groundwater velocities, its feasibility depends critically on the alignment of well layouts with the natural flow field. Finally, BTES appears particularly promising for campus- or district-scale seasonal storage, either in bedrock or in unsaturated deposits, where

long-term thermal accumulation can be managed and where decoupling from groundwater offers both environmental and regulatory advantages.

These comparative insights have direct implications for the stakeholders concerned with the governance and implementation pathways highlighted in **Figure 10** and encapsulated in Q3. For municipal and regional planners in the Metropolitan City of Turin, the work suggests that subsurface information and geothermal suitability should be more explicitly integrated into spatial planning and energy strategy documents. GAP maps, calibrated models and thermal impact assessments provide a basis for delineating geothermal management zones, where cumulative thermal budgets, allowable well densities and maximum ΔT thresholds are explicitly defined rather than inferred case by case. Such zoning would support the coordinated development of open-loop, closed-loop, ATES and BTES systems while reducing the risk of undesirable interference and preserving flexibility for future subsurface uses.

For utilities and project developers, including major actors such as IREN S.p.A., the thesis illustrates the value of adopting model-based design workflows grounded in open and standardised tools, directly responding to the questions on how simulation and calibration can improve predictive accuracy (Q2) and to the broader deployment implications (Q3). Feasibility studies that incorporate regional screening, local calibration and scenario simulations can more accurately predict system performance, assess risks and identify optimal combinations of technologies in different parts of the metropolitan area. The results also point to the benefits of diversifying portfolios installations rather than relying on a single technology class. Utilities are in a strong position to coordinate long-term monitoring of groundwater levels, temperatures and system performance, and to share anonymised data with public authorities and researchers. This is a key aspect of reinforcing the open-data ethical principles that underpin the methodological framework proposed in this thesis.

For regulators and permitting authorities, the analyses provide an evidence base for moving towards a more risk-proportionate and model-informed regulatory approach, in line with the concluding questions on implications for geothermal system deployment (Q3). GAP maps and numerical models can be formally recognised as decision-support tools within the authorisation process, with applications required to demonstrate consistency with these tools commensurate with system size and risk level. Streamlined procedures could be envisaged for low-risk closed-loop and unsaturated-zone BTES systems, while more demanding modelling and monitoring obligations would be reserved for large open-loop and ATES installations in sensitive zones. The thesis also offers guidance on standardising monitoring requirements, for example in terms of the number and placement of observation wells, and the temporal resolution of data collection, tailored to the thermo-hydraulic risks posed by each technology and configuration.

Despite its breadth, the work is not exempt from limitations, which must be acknowledged when interpreting the results and when considering extensions of the framework in relation to Q1–Q3. The quality and density of available data, especially regarding long-term groundwater temperature series and fine-scale

stratigraphy, remain imperfect, and in some case studies parameter fields have been constrained more by literature and analogue information than by local measurements. Modelling assumptions, such as the representation of heterogeneous formations by a limited number of homogeneous or weakly heterogeneous layers, the simplification of boundary conditions and the partial treatment of unsaturated processes, introduce uncertainties in simulated plume extents and performance metrics. The thesis has also focused primarily on physical and regulatory feasibility; while qualitative considerations of costs and non-technical barriers are provided, comprehensive techno-economic optimisation and socio-technical analysis – including user behaviour, social acceptance and institutional capacity – lie largely outside the present scope. Furthermore, while many methodological elements are transferable, the quantitative findings are specific to the hydrogeological and regulatory context of Turin and to the particular case studies examined, and should therefore be adapted before being applied elsewhere.

These limitations naturally point to several directions for future research that directly address the final question group (Q3) on recommended future research directions and also deepen and broaden the answers to Q1 and Q2. There is a clear need for enhanced field validation, through denser and more systematic monitoring of hydraulic heads, temperatures and, where relevant, water quality in the vicinity of operating geothermal systems. Such data would enable more advanced joint calibration of hydraulic and thermal parameters and more rigorous quantification of predictive uncertainty. The development of integrated three-dimensional digital twins of the urban subsurface, combining geology, groundwater, infrastructure and contamination, would allow interactions between geothermal schemes and other underground uses to be assessed more holistically. Future studies should also incorporate climate change scenarios explicitly, exploring how shifts in recharge, groundwater levels, urban heat islands and seasonal load profiles may affect long-term system performance and design criteria. Coupling thermo-hydraulic models with detailed cost and revenue models would open the way to techno-economic optimisation of system sizing, technology mixes and operating strategies, and to rigorous identification of the most favourable niche applications for each technology. Finally, there is scope for more extensive comparative analysis of national and regional regulatory frameworks, with the aim of identifying best practices for reconciling groundwater protection with the promotion of shallow geothermal energy in urban areas.

The thesis has shown that shallow geothermal energy can play a central role in the decarbonisation of urban thermal systems when its deployment is supported by rigorous hydrogeological characterisation, advanced numerical modelling and coherent regulatory frameworks. The methodological framework and case studies developed for the Metropolitan City of Turin provide a coherent and replicable example of how open-data-based tools can be used to guide technology selection, design and governance of shallow geothermal systems. In this way, the work contributes to the broader effort to build sustainable, resilient and low-carbon urban energy systems in Europe and beyond.

References

1. Singh HV, Bocca R, Gomez P, et al. (2019) The energy transitions index: An analytic framework for understanding the evolving global energy system. *Energy Strategy Reviews* 26: 100382.
2. United NAtion Sustainable Development Goals. Available from: https://sdgs.un.org/.
3. Díaz A, Marrero GA, Puch LA, et al. (2019) Economic growth, energy intensity and the energy mix. *Energy Econ* 81: 1056–1077.
4. Chen B, Xiong R, Li H, et al. (2019) Pathways for sustainable energy transition. *J Clean Prod* 228: 1564–1571.
5. Emeka O, Evelyn O, Felix N, et al. (2024) Carbon Farming, Carbon Market, Climate Justice and Just Energy Transition in Reducing Carbon Emission in Nigeria (A Review). *THE PROGRESS: A Journal of Multidisciplinary Studies* 5: 10–23.
6. Krause J (2024) Financial Instruments of the Green Energy Transition: Research Landscape Analysis. *Financial Markets, Institutions and Risks* 8: 2024.
7. Zhang E, Pasternak S, Brown A (2024) Considerations for Embedding Equity in the Energy Transition. *Climate and Energy* 41: 1–10.
8. World Energy Council (2024) World Energy Trilemma Report 2024 Evolving with resilence and justice.
9. Khan I, Zakari A, Dagar V, et al. (2022) World energy trilemma and transformative energy developments as determinants of economic growth amid environmental sustainability. *Energy Econ* 108: 105884.
10. Šprajc P, Bjegović M, Vasić B (2019) Energy security in decision making and governance - Methodological analysis of energy trilemma index. *Renewable and Sustainable Energy Reviews* 114.
11. Feng C, Yang J, Kang H (2022) An Analysis of the Relationship between Energy Trilemma and Economic Growth. *Sustainability 2022, Vol 14, Page 3863* 14: 3863.
12. Elkhatat A, Al-Muhtaseb S (2024) Climate Change and Energy Security: A Comparative Analysis of the Role of Energy Policies in Advancing Environmental Sustainability. *Energies* 17.
13. Wyman O, World Energy Council (2022) World Energy trilemma Index 2022.
14. Fernandez MI, Go YI, Wong DML, et al. (2024) Review of challenges and key enablers in energy systems towards net zero target: Renewables, storage, buildings, & grid technologies. *Heliyon* 10: e40691.
15. Xu J, Liu Q, Wider W, et al. (2024) Research landscape of energy transition and green finance: A bibliometric analysis. *Heliyon* 10: e24783.

16. International Energy Agency, International Renewable Energy Agency, United Nations, et al. (2024) TRACKING SDG 7.
17. Igliński B, Kiełkowska U, Mazurek K, et al. (2024) Renewable energy transition in Europe in the context of renewable energy transition processes in the world. A review. *Heliyon* 10: e40997.
18. Sinha A, Venkatesh A, Jordan K, et al. (2024) Diverse decarbonization pathways under near cost-optimal futures. *Nature Communications 2024 15:1* 15: 1–15.
19. JRC (2025) Heat Pumps in the European Union Status Report on Technology Development, Trends, Value Chains and Markets.
20. European Union (2023) Directive - EU - 2023/2413 - of the European Parliament and of the Council of 18 October 2023 amending Directive (EU) 2018/2001, Regulation (EU) 2018/1999 and Directive 98/70/EC as regards the promotion of energy from renewable sources, and repealing Council Directive (EU) 2015/652.
21. IEA (2022) Renewable electricity .
22. Institute for Advanced Sustainability Studies (IASS) (2019) Strengthening International Cooperation for a Global Energy Transition.
23. IPCC (2023) Chapter 14: International Cooperation, Cambridge University Press.
24. United Nations (2015) Paris Agreement.
25. den Elzen MGJ, Dafnomilis I, Forsell N, et al. (2022) Updated nationally determined contributions collectively raise ambition levels but need strengthening further to keep Paris goals within reach. *Mitig Adapt Strateg Glob Chang* 27: 33.
26. International energy Agency (IEA) (2023) Renewables 2023 Analysis and forecast to 2028.
27. Energy Agency I (2019) Renewables 2020 - Analysis and forecast to 2025.
28. Oh H, Beckers K (2023) Cost and Performance Analysis for Five Existing Geothermal Heat Pump-Based District Energy Systems in the United States.
29. Salhein K, Salheen SA, Annekaa AM, et al. (2025) A Comprehensive Review of Geothermal Heat Pump Systems. *Processes 2025, Vol 13, Page 2142* 13: 2142.
30. Ołtarzewska A, Krawczyk DA (2022) Analysis of Heat Pumps Efficiency in Selected Locations - A Case Study. *Environmental and Climate Technologies* 26: 648–657.
31. - International Energy Agency I (2025) World Energy Outlook Special Report The Future of Heat Pumps.
32. EHPA (2025) Market data - European Heat Pump Association, 2025. Available from: https://ehpa.org/market-data/.
33. Żelazna A, Pawłowski A (2025) Review of the Role of Heat Pumps in Decarbonization of the Building Sector. *Energies 2025, Vol 18, Page 3255* 18: 3255.
34. - International Energy Agency I (2022) Renewables 2022.
35. EurObservER (2024) Heat-Pumps Barometer.

36. Weiss W, Spörk-Dür M (2024) Solar Heat Worldwide Global Market Development and Trends 2023 Detailed Market Figures 2022 SOLAR HEAT WORLD WIDE.
37. PlanEnergi (2024) IEA-ES Task 39: Large Thermal En-ergy Storages for District Heating Final report.
38. Johansen K, Werner S (2022) Something is sustainable in the state of Denmark: A review of the Danish district heating sector. *Renewable and Sustainable Energy Reviews* 158: 112117.
39. Winskel M, Heptonstall P, Gross R (1240) Reducing heat pump installed costs: Reviewing historic trends and assessing future prospects. *Appl Energy* 375: 1–16.
40. Fambri G, Mazza A, Guelpa E, et al. (2023) Power-to-heat plants in district heating and electricity distribution systems: A techno-economic analysis. *Energy Convers Manag* 276.
41. Roth A, Gaete-Morales C, Kirchem D, et al. (2024) Power sector benefits of flexible heat pumps in 2030 scenarios. *Commun Earth Environ* 5: 1–12.
42. Yang T, Liu W, Kramer GJ, et al. (2021) Seasonal thermal energy storage: A techno-economic literature review. *Renewable and Sustainable Energy Reviews* 139.
43. Borko K, Brenčič M, Savšek Z, et al. (2025) Insights into Aquifer and Borehole Thermal Energy Storage Systems for Slovenia's Energy Transition. *Energies 2025, Vol 18, Page 1019* 18: 1019.
44. Lanahan M, Tabares-Velasco PC (2017) Seasonal Thermal-Energy Storage: A Critical Review on BTES Systems, Modeling, and System Design for Higher System Efficiency. *Energies 2017, Vol 10, Page 743* 10: 743.
45. Huang Y, Hamzat A, Abdullah M, et al. (2025) Comprehensive review of emerging trends in thermal energy storage mechanisms, materials and applications. *Front Energy Res* 13: 1651471.
46. Rezaie M, Aghajani H (2013) A New Combinational Terminology for Geothermal Systems. *International Journal of Geosciences* 2013: 43–48.
47. Muffler P, Cataldi R (1978) Methods for regional assessment of geothermal resources. *Geothermics* 7: 53–89.
48. Lee KC (1996) Classification of geothermal resources-an engineering approach, *Twenty-First Workshop on Geothermal Reservoir Engineering*.
49. Babaei M, Nick HM (2019) Performance of low-enthalpy geothermal systems: Interplay of spatially correlated heterogeneity and well-doublet spacings. *Appl Energy* 253: 113569.
50. Adebayo P, Beragama Jathunge C, Darbandi A, et al. (2024) Development, modeling, and optimization of ground source heat pump systems for cold climates: A comprehensive review. *Energy Build* 320: 114646.
51. Sarbu I, Sebarchievici C (2014) General review of ground-source heat pump systems for heating and cooling of buildings. *Energy Build* 70: 441–454.
52. Le AT, Wang L, Wang Y, et al. (2021) Measurement investigation on the feasibility of shallow geothermal energy for heating and cooling applied in

agricultural greenhouses of Shouguang City: Ground temperature profiles and geothermal potential. *Information Processing in Agriculture* 8: 251–269.
53. Gehlin S, Spitler JD (2022) Subtask 1-Annotated Bibliography IEA HPT Annex 52-Long-term performance monitoring of GSHP systems for commercial, institutional and multi-family buildings Subtask 1 report Annotated Bibliography.
54. Menegazzo D, Lombardo G, Bobbo S, et al. (2022) State of the Art, Perspective and Obstacles of Ground-Source Heat Pump Technology in the European Building Sector: A Review. *Energies (Basel)* 15.
55. Liu H, Zhang H (2020) Performance Evaluation of Ground Heating and Cooling Systems: Long-term performance measurements of two case buildings.
56. Rybach L (2022) Shallow Systems—Geothermal Heat Pumps. *Comprehensive Renewable Energy, Second Edition: Volume 1-9* 1–7: 197–219.
57. Toffanin R, Caputo P, Belliardi M, et al. (2022) Low and Ultra-Low Temperature District Heating Equipped by Heat Pumps—An Analysis of the Best Operative Conditions for a Swiss Case Study. *Energies 2022, Vol 15, Page 3344* 15: 3344.
58. Bruno Della Vedova, Bottio I, Cei M, et al. (2023) Geothermal Energy Use, Country Update for Italy. *European Geothermal Congress 2022* 1–7.
59. Previati A, Crosta GB (2021) Regional-scale assessment of the thermal potential in a shallow alluvial aquifer system in the Po plain (northern Italy). *Geothermics* 90: 101999.
60. Elshehabi T, Alfehaid M (2025) Sustainable Geothermal Energy: A Review of Challenges and Opportunities in Deep Wells and Shallow Heat Pumps for Transitioning Professionals. *Energies 2025, Vol 18, Page 811* 18: 811.
61. Nkinyam CM, Ujah CO, Asadu CO, et al. (2025) Exploring geothermal energy as a sustainable source of energy: A systemic review. *Unconventional Resources* 6: 100149.
62. Ricks W, Norbeck J, Jenkins J (2022) The value of in-reservoir energy storage for flexible dispatch of geothermal power. *Appl Energy* 313: 118807.
63. Witter E, Dobson P, Akindipe D, et al. (2025) A review of Geological Thermal Energy Storage for seasonal, grid-scale dispatching. *Renewable and Sustainable Energy Reviews* 218: 115761.
64. Jackson MD, Regnier G, Staffell I (2024) Aquifer Thermal Energy Storage for low carbon heating and cooling in the United Kingdom: Current status and future prospects. *Appl Energy* 376: 124096.
65. Kurek KA, van Ophem J, Strojny J (2024) Arguments for a Community-Based Approach to Geothermal Energy Development. *Energies 2024, Vol 17, Page 2299* 17: 2299.
66. Pellizzone A, Allansdottir A, De Franco R, et al. (2017) Geothermal energy and the public: A case study on deliberative citizens' engagement in central Italy. *Energy Policy* 101: 561–570.

67. Ouerghi FH, Omri M, Nisar KS, et al. (2024) Investigating the potential of geothermal energy as a sustainable replacement for fossil fuels in commercial buildings. *Alexandria Engineering Journal* 97: 215–229.
68. Li J, Tarpani RRZ, Stamford L, et al. (2023) Life cycle sustainability assessment and circularity of geothermal power plants. *Sustain Prod Consum* 35: 141–156.
69. Kassem MA, Moscariello A (2024) Advancing sustainable energy: a systematic review of geothermal-powered district heating and cooling networks. *International Journal of Sustainable Energy* 43.
70. Berta A, Gizzi M, Taddia G, et al. (2024) The role of standards and regulations in the open-loop GWHPs development in Italy: The case study of the Lombardy and Piedmont regions. *Renew Energy* 223: 120016.
71. Gizzi M, Taddia G, Abdin EC, et al. (2020) Thermally Affected Zone (TAZ) Assessment in Open-Loop Low-Enthalpy Groundwater Heat Pump Systems (GWHPs): Potential of Analytical Solutions. *Geofluids* 2020: 2640917.
72. Kim H, Nam Y, Bae S mu, et al. (2018) Development of a multi-well pairing system for groundwater heat pump systems. *Energies (Basel)* 11.
73. Berta A, Taddia G (2024) Exploring Urban Sustainability: The Role of Geology and Hydrogeology in Numerical Aquifer Modelling for Open-Loop Geothermal Energy Development, the Case of Torino (Italy). *Geosciences 2024, Vol 14, Page 180* 14: 180.
74. Gizzi M, Berta A, Vagnon F, et al. (2024) Groundwater heat pumps diffusion in the Turin City urban area: modelling for the thermally affected zone analysis of an open-loop geothermal system. *Italian journal of engineering geology and environment* 165–173.
75. Taddia G (2016) Low Enthalpy Geothermal Open Loop Heat Pumps: a suitable tool for thermal energy supply in urban areas.
76. Piga B, Casasso A, Pace F, et al. (2017) Thermal Impact Assessment of Groundwater Heat Pumps (GWHPs): Rigorous vs. Simplified Models. *Energies 2017, Vol 10, Page 1385* 10: 1385.
77. Cappellari D, Piccinini L, Pontin A, et al. (2022) Sustainability of an Open-Loop GWHP System in an Italian Alpine Valley. *Sustainability 2023, Vol 15, Page 270* 15: 270.
78. Gizzi M, Berta A, Vagnon F, et al. (2024) Geothermal Technologies: Progress Through Examples of Sustainable Applications in an Urban Context. *Geoingegneria Ambientale e Mineraria* 51–57.
79. Davis K, Leiteritz R, Pflüger D, et al. (2023) Deep learning based surrogate modeling for thermal plume prediction of groundwater heat pumps.
80. Park D, Lee E, Kaown D, et al. (2021) Determination of optimal well locations and pumping/injection rates for groundwater heat pump system. *Geothermics* 92.
81. European Commision (2023) Communication from the commission to the european parliament, the european council, the council, the european economic and social committee and the committee of the regions.
82. REN21 (2021) Renewables in Cities Global Status Report .

83. Italian Republic (2019) Law No. 160 of 27 December 2019 ‘ State budget estimate for the 2020 financial year and multi-year budget for the three-year period 2020-2022.’, Italy, https://www.gazzettaufficiale.it/atto/stampa/serie_generale/originario.
84. Italian Republic (2019) Law No 141 of 12 December 2019, “Conversion into law, with amendments, of Decree-Law No 111 of 14 October 2019, setting out urgent measures for compliance with the obligations laid down in Directive 2008/50/EC on air quality and extension of the deadline referred to in Article 48, paragraphs 11 and 13, of Decree-Law No 189 of 17 October 2016, converted, with amendments, by Law No 229 of 15 December 2016”.
85. Ministero dell’Ambiente e della Sicurezza Energetica (2024) Piano nazionale integrato per l’energia e il clima, Italy.
86. European Community (2018) Directive (EU) 2018/2001 of the European Parliament and of the Council of 11 December 2018 on the promotion of the use of energy from renewable sources.
87. European Community (2023) Directive - EU - 2023/2413 - EN - Renewable Energy Directive - EUR-Lex.
88. European Community (2023) Directive - 2023/1791 - EN - EUR-Lex.
89. European Community (2000) Directive 2000/60/EC of the European Parliament and of the Council of 23 October 2000 establishing a framework for Community action in the field of water policy.
90. European Union (2024) Geothermal energy: Council calls for faster deployment - Consilium, 2024. Available from: https://www.consilium.europa.eu/en/press/press-releases/2024/12/16/geothermal-energy-council-calls-for-faster-deployment/.
91. European Commision (2021) InvestEU - European Commission, 2021. Available from: https://commission.europa.eu/funding-tenders/find-funding/eu-funding-programmes/investeu_en.
92. Italian Republic (2010) Legislative Decree No 22 of 11 February 2010, “Revisions to the regulations concerning the exploration and exploitation of geothermal resources, in accordance with Article 27, paragraph 28, of Law 23 July 2009, no. 99”.
93. Italian Republic (2022) Decree 30 September 2022, “Requirements for installing systems that generate heat from geothermal resources, designed for the heating and air-conditioning of buildings, and simplification measures for the installation of these systems”.
94. Italian Republic (2013) Presidential Decree No. 59 of 13 March 2013, “Regulation regulating the single environmental authorisation and the simplification of administrative requirements in environmental matters for small and medium-sized enterprises and plants not subject to integrated environmental authorisation, pursuant to Article 23 of Decree-Law No. 5 of 9 February 2012, converted, with amendments, by Law No. 35 of 4 April 2012”, Italy.

95. Italian Republic (2006) Legislative Decree No 152 of 3 April 2006, “Environmental regulations”. , Italy, https://www.gazzettaufficiale.it/atto/serie_generale/caricaDettaglioAtto/originario?atto.dataPubblicazioneGazzetta=2006-04-14&atto.codiceRedazionale=006G0171.
96. PTA (2021) Update of the 2007 Plan (D.C.R. of 13 March 2007, no. 117-10731) by D.C.R. no. 179 - 18293, following D.G.R. no. 8-3089 of 16 April 2021, Italy.
97. Regione Piemonte (1996) Legge regionale 30 aprile 1996, n. 22.
98. Regione Piemonte (2009) D.G.R. 34-11524 del 3/06/2009 - Base dell’acquifero superficiale .
99. Regione Piemonte (2022) D.G.R. n. 34-11524 del 3/06/2009 - Aggiornamento della cartografia della base dell’acquifero superficiale alla scala 1:50.000.
100. PTC2 (2011) Publication in the B.U.R. no. 32 of 11 August 2011 of d.C.r. no. 121-29759 of 21 July 2011 “Provincial Territorial Coordination Plan”, Italy.
101. PTGM (2022) Documents referred to in Article 6(4) of Regional Law 56/1977 “Metropolitan General Territorial Plan”, Italy.
102. Italian Republic (2007) Regional Presidential Decree N0 7/R of 25 June 2007, “First definition of obligations concerning the measurement of public water withdrawals and returns (Regional Law no. 61 of 29 December 2000)”, Italy.
103. Mishra PK, Kuhlman KL (2013) Unconfined Aquifer Flow Theory-from Dupuit to present.
104. ASTM International (2017) D5447 − 17 Standard Guide for Application of a Numerical Groundwater Flow Model to a Site-Specific Problem .
105. ASTM International (2019) D5979 − 96 - Standard Guide for Conceptualization and Characterization of Groundwater Systems 1.
106. ASTM International (2016) D5609 − 16 - Standard Guide for Defining Boundary Conditions in Groundwater Flow Modeling .
107. ASTM International (2014) D5610 − 94 - Standard Guide for Defining Initial Conditions in Groundwater Flow Modeling .
108. ASTM International (2018) D5981/D5981M − 18 - Standard Guide for Calibrating a Groundwater Flow M0del Application .
109. ASTM International (2014) D5490 - Standard Guide for Comparing Groundwater Flow Model Simulations to Site-Specific Information.
110. ASTM International (2016) D5611 − 94 Standard Guide for Conducting a Sensitivity Analysis for a Groundwater Flow Model Application.
111. ASTM International (2016) D5718 − 13 - Standard Guide for Documenting a Groundwater Flow Model Application .
112. Clyde CG, Asce F, Madabhushi G V, et al. (1983) Spacing of Wells for Heat Pumps. *J Water Resour Plan Manag* 109: 203–212.

113. García-Gil A, Vázquez-Suñe E, Alcaraz MM, et al. (2015) GIS-supported mapping of low-temperature geothermal potential taking groundwater flow into account. *Renew Energy* 77: 268–278.
114. Taddia G (2018) Underground exploitation in urban areas by geothermal heat pump systems: the example of turin politecnico test site (nw italy). *Alpine and Mediterranean Quaternary* 31: 235–244.
115. Lo Russo S, Taddia G (2010) Advective Heat Transport in an Unconfined Aquifer Induced by the Field Injection of an Open-Loop Groundwater Heat Pump.
116. Gizzi M, Taddia G, Abdin EC, et al. (2020) Thermally Affected Zone (TAZ) Assessment in Open-Loop Low-Enthalpy Groundwater Heat Pump Systems (GWHPs): Potential of Analytical Solutions. *Geofluids* 2020.
117. Staffell I, Pfenninger S, Johnson N (2023) A global model of hourly space heating and cooling demand at multiple spatial scales. *Nature Energy 2023 8:12* 8: 1328–1344.
118. Schüler N, Mastrucci A, Bertrand A, et al. (2015) Heat Demand Estimation for Different Building Types at Regional Scale Considering Building Parameters and Urban Topography. *Energy Procedia* 78: 3403–3409.
119. UNI (2014) UNI/TS 11300-1, Italy.
120. European Commission (2024) Energy Performance of Buildings Directive.
121. European Union (2024) Directive 2024/1275 - Energy performance of buildings (recast).
122. Diersch HJG (2014) FEFLOW: Finite element modeling of flow, mass and heat transport in porous and fractured media. *FEFLOW: Finite Element Modeling of Flow, Mass and Heat Transport in Porous and Fractured Media* 9783642387395: 1–996.
123. White JT, Hunt RJ, Fienen MN, et al. (2020) Approaches to highly parameterized inversion: PEST++ Version 5, a software suite for parameter estimation, uncertainty analysis, management optimization and sensitivity analysis. *Techniques and Methods*.
124. Zhang Z, Xu D, Gong C, et al. (2025) Finite analytic method for simulating water flow using water content-based Richards' equation. *Journal of Groundwater Science and Engineering* 13: 147–155.
125. Younes A, Fahs M, Belfort B (2013) Monotonicity of the cell-centred triangular MPFA method for saturated and unsaturated flow in heterogeneous porous media. *J Hydrol (Amst)* 504: 132–141.
126. Islam MS, Master Thesis, Techniques for improving Richards' equation solvers.
127. Doherty J (2025) Calibration and Uncertainty Analysis for Complex Environmental Models Second Edition PEST: complete theory and what it means for modelling the real world.
128. Marquardt DW (1963) An Algorithm for Least-Squares Estimation of Nonlinear Parameters. *Journal of the Society for Industrial and Applied Mathematics* 11: 431–441.

129. Certes C, de Marsily G (1991) Application of the pilot point method to the identification of aquifer transmissivities. *Adv Water Resour* 14: 284–300.
130. LaVenue AM, Pickens JF (1992) Application of a coupled adjoint sensitivity and kriging approach to calibrate a groundwater flow model. *Water Resour Res* 28: 1543–1569.
131. RamaRao BS, LaVenue AM, De Marsily G, et al. (1995) Pilot Point Methodology for Automated Calibration of an Ensemble of conditionally Simulated Transmissivity Fields: 1. Theory and Computational Experiments. *Water Resour Res* 31: 475–493.
132. Lavenue M, De Marsily G (2001) Three-dimensional interference test interpretation in a fractured aquifer using the Pilot Point Inverse Method. *Water Resour Res* 37: 2659–2675.
133. Doherty J, Moore C (2021) Decision-Support Modelling viewed through the lens of Model Complexity.
134. Doherty JE, Fienen MN, Hunt RJ (2010) Approaches to Highly Parameterized Inversion: Pilot-Point Theory, Guidelines, and Research Directions Scientific Investigations Report 2010-5168.
135. Livani M, Petracchini L, Benetatos C, et al. (2023) Subsurface geological and geophysical data from the Po Plain and the northern Adriatic Sea (north Italy). *Earth Syst Sci Data* 15: 4261–4293.
136. Dercourt J, Zonenshain LP, Ricou LE, et al. (1986) Geological evolution of the tethys belt from the atlantic to the pamirs since the LIAS. *Tectonophysics* 123: IN1-315.
137. Doglioni C (1993) Some remarks on the origin of foredeeps. *Tectonophysics* 228: 1–20.
138. Pieri M, Groppi G (1981) Subsurface Geological Structure of the Po Plain. Consiglio Naxionale delle Ricerche-Progetto Finalizzato Geodinamica. 414.
139. Carminati E, Doglioni C, Scrocca D (2003) Apennines subduction-related subsidence of Venice (Italy). *Geophys Res Lett* 30: 1717.
140. Castellarin A, Vai GB (1986) Southalpine Versus Po Plain Apenninic Arcs. *Developments in Geotectonics* 21: 253–280.
141. Turrini C, Lacombe O, Roure F (2014) Present-day 3D structural model of the Po Valley basin, Northern Italy. *Mar Pet Geol* 56: 266–289.
142. Turrini C, Toscani G, Lacombe O, et al. (2016) Influence of structural inheritance on foreland-foredeep system evolution: An example from the Po valley region (northern Italy). *Mar Pet Geol* 77: 376–398.
143. Turrini C, Angeloni P, Lacombe O, et al. (2015) Three-dimensional seismo-tectonics in the Po Valley basin, Northern Italy. *Tectonophysics* 661: 156–179.
144. Viti M, Mantovani E, Babbucci D, et al. (2016) Seismotectonics of the Padanian Region and Surrounding Belts: Which Driving Mechanism? *International Journal of Geosciences* 7: 1412–1451.
145. Fantoni R, Franciosi R (2008) Geological Framework of PO Plain and Adriatic Foreland System. *70th European Association of Geoscientists and*

Engineers Conference and Exhibition 2008: Leveraging Technology Incorporating SPE EUROPEC 2008 5: 3133–3137.
146. Pezzo G, Petracchini L, Devoti R, et al. (2020) Active Fold-Thrust Belt to Foreland Transition in Northern Adria, Italy, Tracked by Seismic Reflection Profiles and GPS Offshore Data. *Tectonics* 39: e2020TC006425.
147. Amadori C, Toscani G, Giulio A Di, et al. (2019) From cylindrical to non-cylindrical foreland basin: Pliocene-Pleistocene evolution of the Po Plain-Northern Adriatic basin (Italy). *Basin Research*.
148. Stevenazzi S, Zuffetti C, Camera CAS, et al. (2023) Hydrogeological characteristics and water availability in the mountainous aquifer systems of Italian Central Alps: A regional scale approach. *J Environ Manage* 340: 1–17.
149. Egidio E, Mancini S, De Luca DA, et al. (2022) The Impact of Climate Change on Groundwater Temperature of the Piedmont Po Plain (NW Italy). *Water 2022, Vol 14, Page 2797* 14: 2797.
150. Antonio De Luca D, Lasagna M, Debernardi L (2020) Hydrogeology of the western Po plain (Piedmont, NW Italy). *J Maps* 16: 265–273.
151. Amadori C, Langone A, Marini M, et al. (2020) Unexpected thermal history of a syn-collisional basin revealed by geo-and thermochronology: the case of the Tertiary Piedmont Basin (Western Alps, Italy), *EGU 2020*.
152. Forno MG, Gianotti F, Storti U (2022) Geomorphology of the Po Fluvial Terraces in Turin Deduced by New Subsoil Data (NW Italy). *Water (Switzerland)* 14.
153. Dela Pierre F, Piana F, Boano P, et al. (2003) Foglio 157 "Trino" della Carta Geologica d'Italia alla scala 1:50.000, Roma, ITA.
154. Festa A, Dela Pierre F, I. R. A. C. E. A., et al. (2009) Note Illustrative della Carta Geologica d'Italia alla scala 1:50.000 foglio 156 Torino Est, Roma, ITA.
155. Piana F, Polino R (1995) Tertiary structural relationships between Alps and Apennines: the critical Torino Hill and Monferrato area. Northwestern Italy. *Terra Nova* 7: 138–143.
156. Ghielmi, Rogledi, VIgna, et al. (2019) POLITECNICO DI TORINO Repository ISTITUZIONALE La successione messiniana e plio-pleistocenica del Bacino di Savigliano (settore occidentale del Bacino Terziario Piemontese-Italia. 3–141.
157. Bove A, Casaccio D, Destefanis E, et al. (2005) Idrogeologia della pianura piemontese. *Environmental Science*.
158. Civita M, Lo Russo S, Vigna B (2005) Carta idrogeologica schematica del piemonte (nw italia) 1:250.000., ITA.
159. Debernardi L, De Luca DA, Lasagna M (2008) Correlation between nitrate concentration in groundwater and parameters affecting aquifer intrinsic vulnerability. *Environmental Geology* 55: 539–558.
160. Lucchesi S (2001) Sintesi preliminare dei dati di sottosuolo della pianura piemontese centrale . *GEAM*.

161. Piedmont Basin T, Vigna I/, Fiorucci B;, et al. (2010) Relations between stratigraphy, groundwater flow and hydrogeochemistry in Poirino Plateau and Roero areas of the Tertiary Piedmont Basin, Italy. *Memorie descrittive della carta geologica d'italia* XC: 267–292.
162. Forno MG, De Luca DA, Bonasera M, et al. (2018) Synthesis on the turin subsoil stratigraphy and hydrogeology (NW Italy). *Alpine and Mediterranean Quaternary* 31: 147–170.
163. De Luca D, Lasagna M, Mancicni S (2019) Strategies for deep aquifers protection at local and regional scale: the Piedmont region example. *GEAM*.
164. De Luca DA, Abdin EC, Forno MG, et al. (2019) The Montellina Spring as an Example of Water Circulation in an Alpine DSGSD Context (NW Italy). *Water 2019, Vol 11, Page 700* 11: 700.
165. De Luca DA, Masciocco L, Caviglia C, et al. (2014) Distribution, Discharge, Geological and Physical–Chemical Features of the Springs in the Turin Province (Piedmont, NW Italy). *Engineering Geology for Society and Territory - Volume 3: River Basins, Reservoir Sedimentation and Water Resources* 253–256.
166. Gianotti F, Forno G, Ivy-Ochs S, et al. (2015) Stratigraphy of the ivrea morainic amphitheatre (nw italy): an updated synthesis. *AMQ*.
167. Lasagna M, De Luca DA (2016) The use of multilevel sampling techniques for determining shallow aquifer nitrate profiles. *Environmental Science and Pollution Research* 23: 20431–20448.
168. ARPA Piedmont (2025) Geoportale Arpa Piemonte, 2025. Available from: https://geoportale.arpa.piemonte.it/app/public/.
169. Arpa Piemonte (2025) Home page | Arpa Piemonte Meteorological data, 2025. Available from: https://www.arpa.piemonte.it/rischi_naturali/snippets_arpa_graphs/map_meteoweb/?rete=stazione_meteorologica.
170. Cortemiglia GC, Biancotti A, Cagnazzi B, et al. (1999) Serie climatiche ultracentenarie - Climatic sequence of over one hundered years. 3: 1–91.
171. Garzena D, Fratianni S, Acquaotta F (2014) Considerazioni sull'isola di calore urbana di Torino attraverso l'analisi dei dati climatici. *GEOLOGIA DELL'AMBIENTE* 90–97.
172. Oke TR (1995) The Heat Island of the Urban Boundary Layer: Characteristics, Causes and Effects. *Wind Climate in Cities* 81–107.
173. Voogt J (2014) Encyclopedia of Natural Resources | Urban Heat Islands , CRC Press.
174. Bucci A, Barbero D, Lasagna M, et al. (2017) Shallow groundwater temperature in the Turin area (NW Italy): vertical distribution and anthropogenic effects. *Environ Earth Sci* 76.
175. Irace A, Marcelli I, Fioraso G, et al. (2024) Subsurface geology of the Torino metropolitan area (Westernmost Po Plain, NW Italy). *J Maps* 20.
176. Piedmont Region (2023) Piedmont Region Geoportal, 2023. Available from: https://www.geoportale.piemonte.it/cms/.

177. Metropolitan City of Turin (2025) Benvenuti - aperTO, 2025. Available from: http://aperto.comune.torino.it/.
178. Pereira GW, Valente DSM, de Queiroz DM, et al. (2022) Smart-Map: An Open-Source QGIS Plugin for Digital Mapping Using Machine Learning Techniques and Ordinary Kriging. *Agronomy 2022, Vol 12, Page 1350* 12: 1350.
179. Bedekar V, Morway ED, Langevin CD, et al. (2016) MT3D-USGS version 1: A U.S. Geological Survey release of MT3DMS updated with new and expanded transport capabilities for use with MODFLOW. *Techniques and Methods*.
180. Winston RB (2019) ModelMuse Version 4: A graphical user interface for MODFLOW 6. *Scientific Investigations Report*.
181. Lerner DN (2002) Identifying and quantifying urban recharge: A review. *Hydrogeol J* 10: 143–152.
182. Yang Y, Lerner DN, Barrett MH, et al. (1999) Quantification of groundwater recharge in the city of Nottingham, UK. *Environmental Geology* 38: 183–198.
183. Vázquez-Suñé E, Carrera J, Tubau I, et al. (2010) An approach to identify urban groundwater recharge. *Hydrol Earth Syst Sci* 14: 2085–2097.
184. Conicelli B, Hirata R, Galvão P, et al. (2021) Determining groundwater availability and aquifer recharge using GIS in a highly urbanized watershed. *J South Am Earth Sci* 106: 103093.
185. Sanford W (2002) Recharge and groundwater models: An overview. *Hydrogeol J* 10: 110–120.
186. Zaniboni L, De Luca DA, Egidio E, et al. (2025) Understanding groundwater behaviour in urban environments: thermal and piezometric analysis in the Turin city area (NW Italy). *Groundw Sustain Dev* 30: 101472.
187. Lo Russo S, Taddia G, Verda V (2012) Development of the thermally affected zone (TAZ) around a groundwater heat pump (GWHP) system: A sensitivity analysis. *Geothermics* 43: 66–74.
188. Gelhar LW (1986) Stochastic subsurface hydrology from theory to applications. *Water Resour Res* 22: 135S-145S.
189. Gizzi M, Vagnon F, Taddia G, et al. (2023) A Review of Groundwater Heat Pump Systems in the Italian Framework: Technological Potential and Environmental Limits. *Energies 2023, Vol 16, Page 4813* 16: 4813.
190. La Vigna F (2022) Review: Urban groundwater issues and resource management, and their roles in the resilience of cities. *Hydrogeol J* 30: 1657–1683.
191. Gizzi M, Taddia G, Russo S Lo (2021) Use of a temperature-measuring chain for the reconstruction of the vertical thermal disturbance induced by an open-loop groundwater heat pump system. *Italian Journal of Engineering Geology and Environment* 97–105.
192. Khaleghi K, Livescu S (2023) A review of vertical closed-loop geothermal heating and cooling systems with an Emphasis on the importance of the subsurface. *J Pet Sci Eng* 220: 111137.

193. Dehkordi SE, Schincariol RA (2014) Effect of thermal-hydrogeological and borehole heat exchanger properties on performance and impact of vertical closed-loop geothermal heat pump systems. *Hydrogeol J* 22: 189–203.
194. Casasso A, Sethi R (2014) Efficiency of closed loop geothermal heat pumps: A sensitivity analysis. *Renew Energy* 62: 737–746.
195. Saulsbury JW (2020) A Comparison of the Environmental Effects of Open-Loop and Closed-Loop Pumped Storage Hydropower, Richland, WA (United States).
196. Gizzi M (2021) Closed-Loop Systems for Geothermal Energy Exploitation from Hydrocarbon Wells: An Italian Case Study. *Applied Sciences 2021, Vol 11, Page 10551* 11: 10551.
197. Kerme ED, Fung AS (2021) Heat transfer analysis of single and double U-tube borehole heat exchanger with two independent circuits. *J Energy Storage* 43: 103141.
198. Li L, Zhang W, Xu S, et al. (2023) Experimental study on heat transfer performance of double U-shaped buried tube heat exchanger. *Coal Geology & Exploration* 51: 14.
199. Brown CS, Kolo I, Banks D, et al. (2024) Comparison of the thermal and hydraulic performance of single U-tube, double U-tube and coaxial medium-to-deep borehole heat exchangers. *Geothermics* 117: 102888.
200. Malhotra T, Davis D, Adams D, et al. (2023) Design of an Improved Vertical Spiral Closed Loop Geothermal Heat Exchanger, *ASME International Mechanical Engineering Congress and Exposition, Proceedings (IMECE)*, American Society of Mechanical Engineers Digital Collection.
201. Zhou A, Huang X, Wang W, et al. (2021) Thermo-Hydraulic Performance of U-Tube Borehole Heat Exchanger with Different Cross-Sections. *Sustainability 2021, Vol 13, Page 3255* 13: 3255.
202. Wang G, Zhou F, Jia H, et al. (2025) Heat extraction performance of multi-level, multi-branch, closed loop coaxial horizontal borehole heat exchanger geothermal system. *Appl Therm Eng* 269: 126045.
203. Badenes B, Sanner B, Mateo Pla MÁ, et al. (2020) Development of advanced materials guided by numerical simulations to improve performance and cost-efficiency of borehole heat exchangers (BHEs). *Energy* 201: 117628.
204. Sagia Z, Stegou A, Rakopoulos C (2012) Borehole Resistance and Heat Conduction Around Vertical Ground Heat Exchangers. *The Open Chemical Engineering Journal* 6: 32–40.
205. Travaš L, Rujnić Havstad M, Pilipović A (2023) Optimization of Thermal Conductivity and Tensile Properties of High-Density Polyethylene by Addition of Expanded Graphite and Boron Nitride. *Polymers (Basel)* 15: 3645.
206. Chong Q, Wang J, Gates ID (2022) Evaluation of closed-loop U-Tube deep borehole heat exchanger in the Basal Cambrian Sandstone formation, Alberta, Canada. *Geothermal Energy* 10: 1–20.
207. Khattak S, Badenes B, Urchueguia J, et al. (2023) Thermodynamic Performance Analysis of High Thermal Conductivity Materials in Borehole

Heat Exchangers in the European Climate. *Buildings 2023, Vol 13, Page 2276* 13: 2276.
208. Sipio E Di, Garbin E, Fedele L, et al. (2021) New borehole heat exchanger thermal enhanced grout formulations, *EGU21*, Copernicus Meetings.
209. FascÌ ML, Lazzarotto A, Acuna J, et al. (2019) Analysis of the thermal interference between ground source heat pump systems in dense neighborhoods. *Sci Technol Built Environ* 25: 1069–1080.
210. Sáez Blázquez C, Farfán Martín A, Martín Nieto I, et al. (2017) Efficiency analysis of the main components of a vertical closed-loop system in a borehole heat exchanger. *Energies (Basel)* 10.
211. Wallin A, Thomasson T, Abdurafikov R (2023) Urban low-to-medium deep borehole field regeneration with waste heat from energy efficient buildings: A techno-economic study in Nordic climate. *Energy Build* 300: 113628.
212. Koohi-Fayegh S, Rosen MA (2012) On Thermally Interacting Multiple Boreholes with Variable Heating Strength: Comparison between Analytical and Numerical Approaches. *Sustainability 2012, Vol 4, Pages 1848-1866* 4: 1848–1866.
213. Jahanbin A, Semprini G, Impiombato AN, et al. (2020) Effects of the Circuit Arrangement on the Thermal Performance of Double U-Tube Ground Heat Exchangers. *Energies 2020, Vol 13, Page 3275* 13: 3275.
214. IEA (2023) Energy Efficiency 2023.
215. Kwon Y, Bae S, Chae H, et al. (2023) Economic and performance analysis of ground source heat pump system for high-rise residential buildings considering practical applications. *Energy Reports* 10: 4359–4373.
216. Eze VHU, Eze EC, Alaneme GU, et al. (2025) Recent progress and emerging technologies in geothermal energy utilization for sustainable building heating and cooling: a focus on smart system integration and enhanced efficiency solutions. *Front Built Environ* 11: 1594355.
217. Garabetian T, Dumas P (2020) Recommendations for European harmonisation: Towards a common geothermal environmental framework across Europe.
218. Angelino L (2017) Policy and regulation for geothermal energy in the EU. *Perspectives For Geothermal Energy In Europe* 255–287.
219. Italian Republic (2011) Legislative Decree No 28 of 3 March 2011, “Implementation of Directive 2009/28/EC on the promotion of the use of energy from renewable sources and amending and subsequently repealing Directives 2001/77/EC and 2003/30/EC”, Italy.
220. Wärmepumpenanlagen E, Energietechnik F (2019) VDI 4640 Thermal use of the underground Ground source heat pump systems .
221. Phys Manfred Reuß D, Sanner B Chapter 2.5 DESIGN OF CLOSED LOOP HEAT EXCHANGERS.
222. Hess S, Vollmer R, Wapler J, et al. (2018) Ambient Heat Source Availability for Low-Ex Heating of Multi-Family Buildings 1. Heat Pumps for Multi-Family Houses. 17.

223. Dalla Santa G, Galgaro A, Sassi R, et al. (2019) An updated ground thermal properties database for GSHP applications.
224. Ente Italiano di Normazione (2012) UNI 11466: Sistemi geotermici a pompa di calore - Requisiti per il dimensionamento e la progettazione.
225. Fossa M, Morchio S, Priarone A, et al. (2024) Accurate design of BHE fields for geothermal heat pump systems: The ASHRAE-Tp8 method compared to non aggregated schemes applied to different European test cases. *Energy Build* 303: 113814.
226. Franco A, Conti P (2020) Clearing a Path for Ground Heat Exchange Systems: A Review on Thermal Response Test (TRT) Methods and a Geotechnical Routine Test for Estimating Soil Thermal Properties. *Energies 2020, Vol 13, Page 2965* 13: 2965.
227. Kyrkou K, Booth A, Loveridge F, et al. (2025) Distributed thermal response testing in a fractured chalk aquifer with high groundwater flow. *EGU25*.
228. Liu H, Stumpf AJ, Lin YFF, et al. (2023) Distributed Thermal Response Multi-Source Modeling to Evaluate Heterogeneous Subsurface Properties. *Groundwater* 61: 224–236.
229. Mazzotti Pallard W, Lazzarotto A, Acuña J, et al. (2023) Calibration and Uncertainty Quantification for Single-Ended Raman-Based Distributed Temperature Sensing: Case Study in a 800 m Deep Coaxial Borehole Heat Exchanger. *Sensors 2023, Vol 23, Page 5498* 23: 5498.
230. Cao D, Shi B, Zhu HH, et al. (2019) A field study on the application of distributed temperature sensing technology in thermal response tests for borehole heat exchangers. *Bulletin of Engineering Geology and the Environment* 78: 3901–3915.
231. Carslaw HS, Jaeger JC (1959) Conduction of heat in solids. *chs*.
232. Tas L, Hartog N, Bloemendal M, et al. (2025) Efficiency and heat transport processes of low-temperature aquifer thermal energy storage systems: new insights from global sensitivity analyses. *Geothermal Energy* 13: 1–27.
233. De Paoli C, Duren T, Petitclerc E, et al. (2023) Modelling Interactions between Three Aquifer Thermal Energy Storage (ATES) Systems in Brussels (Belgium). *Applied Sciences 2023, Vol 13, Page 2934* 13: 2934.
234. Jackson MD, Regnier G, Staffell I (2024) Aquifer Thermal Energy Storage for low carbon heating and cooling in the United Kingdom: Current status and future prospects. *Appl Energy* 376: 124096.
235. Casasso A, Giordano N, Bianco C, et al. (2022) UTES - Underground Thermal Energy Storage. *Encyclopedia of Energy Storage: Volume 1-4* 1–4: 382–393.
236. Schepper G De, Bolly P-Y, Vizzotto P, et al. (2020) Investigations into the First Operational Aquifer Thermal Energy Storage System in Wallonia (Belgium): What Can Potentially Be Expected? *Geosciences 2020, Vol 10, Page 33* 10: 33.
237. Geerts D, Daniilidis A, Kramer GJ, et al. (2025) Analytically estimating the efficiency of high temperature aquifer thermal energy storage. *Geothermal Energy* 13: 1–21.

238. Li S, Wang G, Zhou M, et al. (2024) Thermal performance of an aquifer thermal energy storage system: Insights from novel multilateral wells. *Energy* 294: 130915.
239. Stemmle R, Lee H, Blum P, et al. (2024) City-scale heating and cooling with aquifer thermal energy storage (ATES). *Geothermal Energy* 12: 1–26.
240. Bloemendal M, Jaxa-Rozen M, Olsthoorn T (2018) Methods for planning of ATES systems. *Appl Energy* 216: 534–557.
241. Knight Merz S (2012) Australian groundwater modelling guidelines, National Water Commission.
242. Macdonald D (2012) The use of Geological and Hydrogeological Models in Environmental Studies.
243. Sinclair KM (2013) Australian groundwater modelling guidelines Companion to the guidelines, National Water Commission.
244. Schüppler S, Fleuchaus P, Blum P Techno-economic and environmental analysis of an Aquifer Thermal Energy Storage (ATES) in Germany.
245. Bonte EU, Stuijfzand M;, Huismann PJ;, et al. (2011) VU Research Portal Underground thermal energy storage: environmental risks and policy developments in the Netherlands.
246. Shen H, Cao Z, Klemeš JJ, et al. (2023) Numerical Study on Heat Transfer and Performance of Seasonal Borehole Thermal Energy Storage. *Heat Transfer Engineering* 44: 2027–2039.
247. Sojoudi M, Li B, Norouzi E (2024) Thermal-hydro-mechanical modeling of short-term ground responses due to the borehole thermal energy storage operations in a Canadian subarctic region. *Renew Energy* 229: 120753.
248. Buscemi A, Chiaruzzi C, Ciulla G, et al. (2019) A solar assisted seasonal borehole thermal energy storage system for a non-residential building in the Mediterranean area. *SolarEnergy* 192: 120–132.
249. Georges L, Haase M, Novakovic V, et al. (2020) Integration of a high-temperature borehole thermal energy storage in a local heating grid for a neighborhood. *31-38* 13–14.
250. Sadeghi H, Jalali R, Singh RM (2024) A review of borehole thermal energy storage and its integration into district heating systems. *Renewable and Sustainable Energy Reviews* 192: 114236.
251. Kallesøe AJ, Vangkilde-Pedersen T, Guglielmetti L, et al. (2019) HEATSTORE Underground Thermal Energy Storage (UTES) – state-of-the-art, example cases and lessons learned.
252. Skarphagen H, Banks D, Frengstad BS, et al. (2019) Design considerations for borehole thermal energy storage (BTES): A review with emphasis on convective heat transfer. *1-26* 2019.
253. Desguers T, Brown CS, Kolo I, et al. (2025) Short-cycle borehole thermal energy storage: Impact of thermal cycle duration on overall performance. *Appl Therm Eng* 258: 124610.
254. Ekmekci E, Aydin M, Ozturk ZF, et al. (2024) Very high temperature BTES: A potential for operationally cost-free and emission-free heating. *Appl Energy* 360: 122859.

255. Ekmekci E, Aydin M, Ozturk ZF, et al. (2024) Very high temperature BTES: A potential for operationally cost-free and emission-free heating. *Appl Energy* 360: 122859.
256. Sharma A, Tyagi V V., Chen CR, et al. (2009) Review on thermal energy storage with phase change materials and applications. *Renewable and Sustainable Energy Reviews* 13: 318–345.
257. Deng J, Qiang W, Peng C, et al. (2022) Can deep borehole heat exchangers operate stably in long-term operation? Simulation analysis and design method. *Journal of Building Engineering* 62: 105358.
258. Sarbu I, Sebarchievici C (2018) A Comprehensive Review of Thermal Energy Storage. *Sustainability 2018, Vol 10, Page 191* 10: 191.
259. Raut D, Tiwari AK, Kalamkar VR (2022) A comprehensive review of latent heat energy storage for various applications: an alternate to store solar thermal energy. *Journal of the Brazilian Society of Mechanical Sciences and Engineering 2022 44:10* 44: 1–38.
260. Mahon H, O'Connor D, Friedrich D, et al. (2022) A review of thermal energy storage technologies for seasonal loops. *Energy* 239: 122207.
261. Zeng S, Cheng X, Yang J (2024) Review of borehole thermal energy storage systems in unsaturated soils: Materials, mechanism, and future development. *Energy Storage* 6: e612.
262. Kolo I, Brown CS, Nibbs W, et al. (2024) A comprehensive review of deep borehole heat exchangers (DBHEs): subsurface modelling studies and applications. *Geothermal Energy 2024 12:1* 12: 1–49.
263. Brown CS, Kolo I, Lyden A, et al. (2024) Assessing the technical potential for underground thermal energy storage in the UK. *Renewable and Sustainable Energy Reviews* 199: 114545.
264. Elhashmi R, Hallinan KP, Chiasson AD (2020) Low-energy opportunity for multi-family residences: A review and simulation-based study of a solar borehole thermal energy storage system. *Energy* 204: 117870.
265. Guo F, Zhu X, Zhang J, et al. (2020) Large-scale living laboratory of seasonal borehole thermal energy storage system for urban district heating. *Appl Energy* 264.
266. Nilsson E, Rohdin P (2019) Performance evaluation of an industrial borehole thermal energy storage (BTES) project – Experiences from the first seven years of operation. *Renew Energy* 143: 1022–1034.
267. Liu M, Steven Tay NH, Bell S, et al. (2016) Review on concentrating solar power plants and new developments in high temperature thermal energy storage technologies. *Renewable and Sustainable Energy Reviews* 53: 1411–1432.
268. Paksoy H, Beyhan B (2015) Thermal energy storage (TES) systems for greenhouse technology. *Advances in Thermal Energy Storage Systems: Methods and Applications* 533–548.
269. Mier González R (2023) Energy storage systems: a state-of-the-art study.

270. Rad FM, Fung AS (2016) Solar community heating and cooling system with borehole thermal energy storage - Review of systems. *Renewable and Sustainable Energy Reviews* 60: 1550–1561.
271. Alva G, Lin Y, Fang G (2018) An overview of thermal energy storage systems. *Energy* 144: 341–378.
272. Gao L, Zhao J, Tang Z (2015) A Review on Borehole Seasonal Solar Thermal Energy Storage. *Energy Procedia* 70: 209–218.
273. Gehlin S (2016) Borehole thermal energy storage. *Advances in Ground-Source Heat Pump Systems* 295–327.
274. Guo F, Li P, An L, et al. (2024) Analysis on the Long-term Performance of a Large-scale Seasonal Borehole Thermal Energy Storage System.
275. Sass I, Krusemark M, Seib L, et al. (2024) Medium-Deep Borehole Thermal Energy Storage (MD-BTES): from Exploration to District-Heating Grid Connection, Insights from SKEWS and PUSH-IT Projects.
276. Desguers T, Friedrich D (2024) Design of a high-temperature, power-constrained electrified district heating network with thermal storage and curtailed wind integration. *Sustainable Energy Technologies and Assessments* 67: 103815.
277. Schulte DO, Rühaak W, Oladyshkin S, et al. (2015) Optimization of Medium-Deep Borehole Thermal Energy Storage Systems.
278. Ahmadfard M, Bernier M, Paleshi A, et al. (2020) Modeling and simulation of a dual temperature BTES system, In: Adam R, Ralph E (Eds.), IBPSA-Canada.
279. Bauer D, Marx R, Nußbicker-Lux J, et al. (2010) German central solar heating plants with seasonal heat storage. *Solar Energy* 84: 612–623.
280. Wang Y, Liu Y (2024) Research on Thermal Characterization of Soil Heat Transfer in Cross-Seasonal Borehole Thermal Storage Systems. *Environmental Science and Engineering* 321–338.
281. Ahmed AA, Assadi M, Gholami R, et al. (2023) Numerical modelling of a high temperature borehole thermal energy storage system: Norway case study. *IOP Conf Ser Mater Sci Eng* 1294: 012059.
282. Wu X, Sameti M, Nasiri F, et al. (2024) An off-grid solar district energy system with borehole thermal energy storage: Life cycle assessment in a subarctic region. *Journal of Building Engineering* 91: 109576.
283. Murali D, Acosta-Pazmiño IP, Loris A, et al. (2024) Experimental assessment of a solar photovoltaic-thermal system in a livestock farm in Italy. *Solar Energy Advances* 4: 100051.
284. Adesanya MA, Yakub AO, Rabiu A, et al. (2024) Dynamic modeling and techno-economic assessment of hybrid renewable energy and thermal storage systems for a net-zero energy greenhouse in South Korea. *Clean Technol Environ Policy* 26: 551–576.
285. Maragna C, Rey C, Perreaux M (2023) A novel and versatile solar Borehole Thermal Energy Storage assisted by a Heat Pump. Part 1: System description. *Renew Energy* 208: 709–725.

286. Rad FM, Fung AS, Rosen MA (2017) An integrated model for designing a solar community heating system with borehole thermal storage. *Energy for Sustainable Development* 36: 6–15.
287. Flynn C, Sirén K (2015) Influence of location and design on the performance of a solar district heating system equipped with borehole seasonal storage. *Renew Energy* 81: 377–388.
288. Alonso MJ, Ramstad RK, Holmberg H, et al. (2021) Fjell 2020 High Temperature Borehole Energy Storage-System Control for Various Operation Modes.
289. Kurevija T, Macenić M, Galović V (2023) Regeneration of the rock temperature using solar thermal energy storage in a ground source heat pump systems-is it worth it for northern Croatia?
290. Ciampi G, Rosato A, Sibilio S (2018) Thermo-economic sensitivity analysis by dynamic simulations of a small Italian solar district heating system with a seasonal borehole thermal energy storage. *Energy* 143: 757–771.
291. Guo F, Yang X (2021) Long-term performance simulation and sensitivity analysis of a large-scale seasonal borehole thermal energy storage system for industrial waste heat and solar energy. *Energy Build* 236: 110768.
292. Lim HS, Ok JS, Park JS, et al. (2020) Efficiency improvement of energy storage and release by the inlet position control for seasonal thermal energy storage. *Int J Heat Mass Transf* 151: 119435.
293. Aldubyan M, Chiasson A (2017) Thermal Study of Hybrid Photovoltaic-Thermal (PVT) Solar Collectors Combined with Borehole Thermal Energy Storage Systems. *Energy Procedia* 141: 102–108.
294. Wijsman AJThM, van Meurs GAM (1984) The Seasonal Heat Store in Groningen. *First EC Conference on Solar Heating* 886–893.
295. Platell O, Widstroem H (1981) Sunstore project: 1977 - 1980. A low temperature solar heating system and seasonal storage for heating buildings. Sunstore - projektet 1977 - 1980. Solvaermesystem med laag temperatur och saesongslagring foer uppvaermning av lokaler.
296. Platell O, Wikstroem H (1983) Sunstore experimental house in Sigtuna. Performance measurement and assessment 1981-1982.
297. Sibbitt B, McClenahan D, Djebbar R, et al. (2012) The Performance of a High Solar Fraction Seasonal Storage District Heating System – Five Years of Operation. *Energy Procedia* 30: 856–865.
298. Reuss M, Beuth W, Schmidt M, et al. (2006) Solar district heating with seasonal storage in Attenkirchen.
299. Xu J, Li Y, Wang RZ, et al. (2014) Performance investigation of a solar heating system with underground seasonal energy storage for greenhouse application. *Energy* 67: 63–73.
300. Wang X, Zheng M, Zhang W, et al. (2010) Experimental study of a solar-assisted ground-coupled heat pump system with solar seasonal thermal storage in severe cold areas. *Energy Build* 42: 2104–2110.

301. Alonso MJ, Ramstad RK, Holmberg H, et al. (2021) Fjell 2020 High Temperature Borehole Energy Storage-System Control for Various Operation Modes.
302. Gunawan E, Giordano N, Jensson P, et al. (2020) Alternative heating systems for northern remote communities: Techno-economic analysis of ground-coupled heat pumps in Kuujjuaq, Nunavik, Canada. *Renew Energy* 147: 1540–1553.
303. Lund H, Werner S, Wiltshire R, et al. (2014) 4th Generation District Heating (4GDH). Integrating smart thermal grids into future sustainable energy systems. *Energy* 68: 1–11.
304. Buffa S, Cozzini M, D'Antoni M, et al. (2019) 5th generation district heating and cooling systems: A review of existing cases in Europe. *Renewable and Sustainable Energy Reviews* 104: 504–522.
305. Zeh R, Ohlsen B, Philipp D, et al. (2021) Large-scale geothermal collector systems for 5th generation district heating and cooling networks. *Sustainability (Switzerland)* 13.
306. Brange L, Englund J, Sernhed K, et al. (2017) Bottlenecks in district heating systems and how to address them. *Energy Procedia* 116: 249–259.
307. Ramstad RK, Justo Alonso M, Acuña J, et al. (2023) The borehole thermal energy storage at Emmaboda, Sweden: First distributed temperature measurements. *Sci Technol Built Environ* 29: 146–162.
308. Kauko H, Pinel D, Graabak I, et al. (2022) Assessing the potential of seasonal thermal storage for local energy systems: Case study for a neighborhood in Norway. *Smart Energy* 6: 100075.
309. Hansen KES, Xydis G (2023) Long-term heat storage opportunities of renewable energy for district heating networks. *Proceedings of Institution of Civil Engineers: Energy*.
310. Li X, Yilmaz S, Patel MK, et al. (2023) Techno-economic analysis of fifth-generation district heating and cooling combined with seasonal borehole thermal energy storage. *Energy* 285: 129382.
311. Todorov O, Alanne K, Virtanen M, et al. (2021) A Novel Data Management Methodology and Case Study for Monitoring and Performance Analysis of Large-Scale Ground Source Heat Pump (GSHP) and Borehole Thermal Energy Storage (BTES) System. *Energies 2021, Vol 14, Page 1523* 14: 1523.
312. Welsch B, Göllner-Völker L, Schulte DO, et al. (2018) Environmental and economic assessment of borehole thermal energy storage in district heating systems. *Appl Energy* 216: 73–90.
313. Hesselbrandt M, Erlström M, Sopher D, et al. (2021) Multidisciplinary approaches for assessing a high temperature borehole thermal energy storage facility at linköping, sweden. *Energies (Basel)* 14: 4379.
314. Sørensen A, Schmidt T (2018) Design and Construction of Large Scale Heat Storages for District Heating in Denmark.
315. Yang L, Entchev E, Rosato A, et al. (2017) Smart thermal grid with integration of distributed and centralized solar energy systems. *Energy* 122: 471–481.

316. Ekmekci E, Ozturk ZF, Sisman A (2023) Collective behavior of boreholes and its optimization to maximize BTES performance. *Appl Energy* 343: 121208.
317. Kumawat PK, Zhou H, Kitz K, et al. (2024) Sensitivity Analysis of Borehole Thermal Energy Storage (BTES): Examining Key Factors for System Optimization. *Energy Storage and Saving*.
318. Desguers T, Friedrich D (2024) Borehole Thermal Energy Storage: Analytical Model and Numerical Validation for Cyclic Energy Recovery Factors and Array Temperatures.
319. Shen H, Wang E (2024) Location effect of borehole for borehole thermal energy storage.
320. Wołoszyn J (2018) Global sensitivity analysis of borehole thermal energy storage efficiency on the heat exchanger arrangement. *Energy Convers Manag* 166: 106–119.
321. Sliwa T, Rosen MA (2017) Efficiency analysis of borehole heat exchangers as grout varies via thermal response test simulations. *Geothermics* 69: 132–138.
322. Pan S, Kong Y, Chen C, et al. (2020) Optimization of the utilization of deep borehole heat exchangers. *Geothermal Energy* 8: 1–20.
323. Brown CS, Cassidy NJ, Egan SS, et al. (2021) Numerical modelling of deep coaxial borehole heat exchangers in the Cheshire Basin, UK. *Comput Geosci* 152: 104752.
324. Wołoszyn J (2018) Global sensitivity analysis of borehole thermal energy storage efficiency on the heat exchanger arrangement. *Energy Convers Manag* 166: 106–119.
325. Ahmadfard M, Bernier M (2023) Simulation of borehole thermal energy storage (BTES) systems using simplified methods. *J Energy Storage* 73: 109240.
326. Malmberg M, Mazzotti W, Acuña J, et al. (2018) High temperature borehole thermal energy storage - A case study. 1–9.
327. Gehlin S, Andersson O, Rosberg J-E (2020) Country Update for Sweden 2020.
328. Rad FM, Fung AS, Rosen MA (2017) An integrated model for designing a solar community heating system with borehole thermal storage. *Energy for Sustainable Development* 36: 6–15.
329. Dincer I, Rosen MA (2007) A unique borehole thermal storage system at university of Ontario Institute of Technology. *Thermal Energy Storage for Sustainable Energy Consumption* 221–228.
330. Li P, Guo F, Yang X (2022) An inversion method to estimate the thermal properties of heterogeneous soil for a large-scale borehole thermal energy storage system. *Energy Build* 263: 112045.
331. Wang R, Ni L, Yang C, et al. (2021) Laboratory study on the thermal performance of vertical U-tube ground heat exchanger during short-term borehole thermal energy storage (BTES) and heat extraction process. *Int J Energy Res* 45: 2043–2057.

332. Yin B, Wu X (2018) Performance analysis on a large scale borehole ground source heat pump in Tianjin cultural centre. *IOP Conf Ser Earth Environ Sci* 121: 052071.
333. Li H, Xu W, Yu Z, et al. (2017) Application analyze of a ground source heat pump system in a nearly zero energy building in China. *Energy* 125: 140–151.
334. Zhang S, Xu W, Liu Z (2014) Research and development of large scale ground source heat pump system.
335. Zhai XQ, Yang Y (2011) Experience on the application of a ground source heat pump system in an archives building. *Energy Build* 43: 3263–3270.
336. Xin-Guo L, Jun Z, Jian W, et al. (2010) Application and Experiment on Solar-Ground Coupled Heat Pump with Heat Storage. *Proceedings World Geothermal Congress* 25–29.
337. Wang H, Qi C (2008) Performance study of underground thermal storage in a solar-ground coupled heat pump system for residential buildings. *Energy Build* 40: 1278–1286.
338. Miedaner O, Mangold D, Sørensen A (2015) Borehole thermal energy storage systems in Germany and Denmark-Construction and operation experiences.
339. Peltola SS, Lund PD, Routti JT (1985) First year operating experience from Kerava solar village. *International Journal of Ambient Energy* 6: 117–122.
340. Korhonen K, Leppäharju N, Hakala P, et al. Simulated temperature evolution of large BTES-case study from Finland.
341. Xue T, Jokisalo J, Kosonen R, et al. (2022) Numerical modeling and validation of a large-scale borehole thermal energy storage system in Finland. *E3S Web of Conferences* 362.
342. Hirvonen J (2020) Seasonal thermal energy storage in Finland. *Decarbonising Heat*.
343. Heliostorage (2020) Seasonal storage of heat is winning ground.
344. Lanini S, Delaleux F, Py X, et al. (2014) Improvement of borehole thermal energy storage design based on experimental and modelling results. *Energy Build* 77: 393–400.
345. Baudoin A (1988) Stockage intersaisonnier de chaleur dans le sol par batterie d'echangeurs baionnette verticaux : modele de predimensionnement.
346. Seib L, Frey M, Bossennec C, et al. (2024) Assessment of a medium-deep borehole thermal energy storage site in the crystalline basement: A case study of the demo site Lichtwiese Campus, Darmstadt. *Geothermics* 119: 102933.
347. Luo J, Rohn J, Xiang W, et al. (2015) Experimental investigation of a borehole field by enhanced geothermal response test and numerical analysis of performance of the borehole heat exchangers. *Energy* 84: 473–484.
348. Sanner B Earth heat pumps and underground thermal energy storage in germany.

349. Reuss M (2015) The use of borehole thermal energy storage (BTES) systems. *Advances in Thermal Energy Storage Systems: Methods and Applications* 117–147.
350. Schmidt T, Mangold D, Müller-Steinhagen H (2004) Central solar heating plants with seasonal storage in Germany. *Solar Energy* 76: 165–174.
351. (PDF) Drilling Engineering Experience Gained from MD-BTES Construction Phase of SKEWS Demo-site Available from: https://www.researchgate.net/publication/371167590_Drilling_Engineering_Experience_Gained_from_MD-BTES_Construction_Phase_of_SKEWS_Demo-site.
352. Seib L, Frey M, Bossennec C, et al. (2024) Assessment of a medium-deep borehole thermal energy storage site in the crystalline basement: A case study of the demo site Lichtwiese Campus, Darmstadt. *Geothermics* 119: 102933.
353. Chicco JM, Mandrone G (2022) Modelling the Energy Production of a Borehole Thermal Energy Storage (BTES) System. *Energies 2022, Vol 15, Page 9587* 15: 9587.
354. Giordano N, Comina C, Mandrone G, et al. (2016) Borehole thermal energy storage (BTES). First results from the injection phase of a living lab in Torino (NW Italy). *Renew Energy* 86: 993–1008.
355. Stølen MS (2010) Heat from the ground and sun An energy-optimizing project at Maere Landbruksskole.
356. Midttømme K, Midttømme K, Hauge A, et al. (2009) Underground thermal energy storage (utes) with heat pumps in Norway.
357. Bäcklund AS (2009) Analys av en grundvärmebaserad värmepumpsanläggning för uppvärmning och kylning av ett sjukhus. *143*.
358. Midttveit HV (2018) Numerisk modellering av varmeoverskudd i grunnvarmeanlegg – Konsekvenser og forebyggende tiltak.
359. Bendea C, Antal C, Rosca M (2015) Geothermal Energy in Romania: Country Update 2010-2014. *Proceedings World Geothermal Congress* 19–25.
360. Olsson S (1984) The Sunclay and Kullavik Projects — Heat Storage in Clay at Low and High Temperature. *Commission of the European Communities, (Report) EUR* 894–898.
361. Lundh M, Dalenbäck JO (2008) Swedish solar heated residential area with seasonal storage in rock: Initial evaluation. *Renew Energy* 33: 703–711.
362. Nordell B (1993) BOREHOLE HEAT STORE DESIGN OPTIMIZATION.
363. Olsson S (1984) The Sunclay and Kullavik Projects — Heat Storage in Clay at Low and High Temperature. *Commission of the European Communities, (Report) EUR* 894–898.
364. Gehlin S (2016) Borehole thermal energy storage. *Advances in Ground-Source Heat Pump Systems* 295–327.
365. Rosenblad G (1983) Seasonal heat storing 1979-83 in Utby ground heat pump project. *International conference on 'Subsurface heat storage - in theory and practice' Stockholm June 6-8* 1983: 670–678.

366. Gehlin S, Andersson O, Bjelm L, et al. (2015) Country Update for Sweden. *Proceedings World Geothermal Congress* 19–25.
367. Lund J, Sanner B, Rybach L, et al. (2004) Geothermal (ground-source) heat pumps a world overview.
368. Andersson O (2007) BTES for heating and cooling of the astronomy house in Lund. *Thermal Energy Storage for Sustainable Energy Consumption* 229–233.
369. Nordell B, Andersson O, Rydell L, et al. (2015) Long-term Performance of the HT-BTES in Emmaboda, Sweden. 19–21.
370. Nordell BO, Hellström G (2000) High temperature solar heated seasonal storage system for low temperature heating of buildings. *Solar Energy* 69: 511–523.
371. Matthey B, Pillonel B (1985) Solar assisted gas heat pump with ground coupled storage for twelve family houses., *van Hattem, D. (Ed.), Proc. 2nd Workshop on Solar Assisted Heat Pumps with Ground Coupled Systems*, Vien, 203–211.
372. Eugster WJ (2007) Road and Bridge Heating Using Geothermal Energy. Overview and Examples. 30.
373. Brown CS, Kolo I, Lyden A, et al. (2024) Assessing the technical potential for underground thermal energy storage in the UK. *Renewable and Sustainable Energy Reviews* 199: 114545.
374. Witte HJL, Van Gelder AJ (2007) Three years monitoring of a borehole thermal energy store of a UK office building. *Thermal Energy Storage for Sustainable Energy Consumption* 205–219.
375. Cullin JR, Spitler JD, Montagud C, et al. (2015) Validation of vertical ground heat exchanger design methodologies. *Sci Technol Built Environ* 21: 137–149.
376. Stiles L (1998) Underground thermal energy storage in the US. *IEA Heat Pump Center Newsletter* 16.
377. Klempa M, Porzer M, Bujok P (2014) The construction of 'Borehole Thermal Energy Storage' in miocene rocks on locality of Green Gas DPB, a.s. in Paskov (Czech Republic).
378. Berta A (2025) BTES Plants Worldwide Distribution, 2025. Available from: https://data.mendeley.com/datasets/gk56yz2pmm/1.
379. Bär K, Rühaak W, Welsch B, et al. (2015) Seasonal High Temperature Heat Storage with Medium Deep Borehole Heat Exchangers. *Energy Procedia* 76: 351–360.
380. Sapinska-Sliwa A, Rosen MA, Gonet A, et al. (2015) Deep Borehole Heat Exchangers-A Conceptual Review. *Proceedings World Geothermal Congress* 19–25.
381. Chen C, Shao H, Naumov D, et al. (2019) Numerical investigation on the performance, sustainability, and efficiency of the deep borehole heat exchanger system for building heating. *Geothermal Energy* 7: 1–26.

382. Gizzi M, Taddia G, Russo S Lo (2021) Reuse of Decommissioned Hydrocarbon Wells in Italian Oilfields by Means of a Closed-Loop Geothermal System. *Applied Sciences 2021, Vol 11, Page 2411* 11: 2411.
383. Welsch B, Rühaak W, Schulte DO, et al. (2016) Characteristics of medium deep borehole thermal energy storage. *Int J Energy Res* 40: 1855–1868.
384. Sadeghi H, Ijaz A, Singh RM (2022) Current status of heat pumps in Norway and analysis of their performance and payback time. *Volume 54* 54.
385. TRONDHEIM KOMMUNE (2021) NYHAVNA SOM NULLUTSLIPPSOMRÅDE.
386. Engen CJ (2024) Høytemperatur termisk energilagring i borhull ved Nyhavna, Trondheim - Berggrunnens mekaniske egenskaper ved syklisk oppvarming, termisk ledningsevne og visuell 3D-modell.
387. Gehlin S, Nordell B (2003) Determining undisturbed ground temperature for thermal response test. *ASHRAE Trans* 109: 151–156.
388. Chaloupsky J (1969) GEOLOGY OF THE HØLONDA-HULSJØEN AREA, TRONDHEIM REGION.
389. Roberts D, Wolff FC (1981) Tectonostratigraphic development of the Trondheim region Caledonides, Central Norway. *J Struct Geol* 3: 487–494.
390. Rise L, Bøe R, Sveian H, et al. (2006) The deglaciation history of Trondheimsfjorden and Trondheimsleia, Central Norway Introduction and geological setting. *Norwegian Journal of Geology* 86: 419–438.
391. Jonatan M, Wiede ES (2024) Høytemperatur borehullsbasert sesongvarmelager på Ladehammerkaia i Trondheim.
392. Geological Survey of Norway (2025) Geologiske kart | NGU, 2025. Available from: https://www.ngu.no/en/geologiske-kart.
393. Ijaz A (2022) Numerical simulation of heat transfer in a partially insulated borehole heat exchanger.
394. Wołoszyn J, Gołaś A (2014) Sensitivity analysis of efficiency thermal energy storage on selected rock mass and grout parameters using design of experiment method. *Energy Convers Manag* 87: 1297–1304.
395. Nordell B, Scorpo AL, Andersson O, et al. (2015) Long-term Long Term Evaluation of Operation and Design of the Emmaboda BTES Operation and Experiences 2010-2015.
396. Nordell B, Scorpo AL, Andersson O, et al. (2016) The HT BTES plant in Emmaboda view of the Emmaboda borehole heat storage during construction div. of architecture and water Luleå university of technology se-97187 luleå, Sweden.
397. Nilsson E, Rohdin P (2019) Empirical Validation and Numerical Predictions of an Industrial Borehole Thermal Energy Storage System. *Energies 2019, Vol 12, Page 2263* 12: 2263.

Appendix A

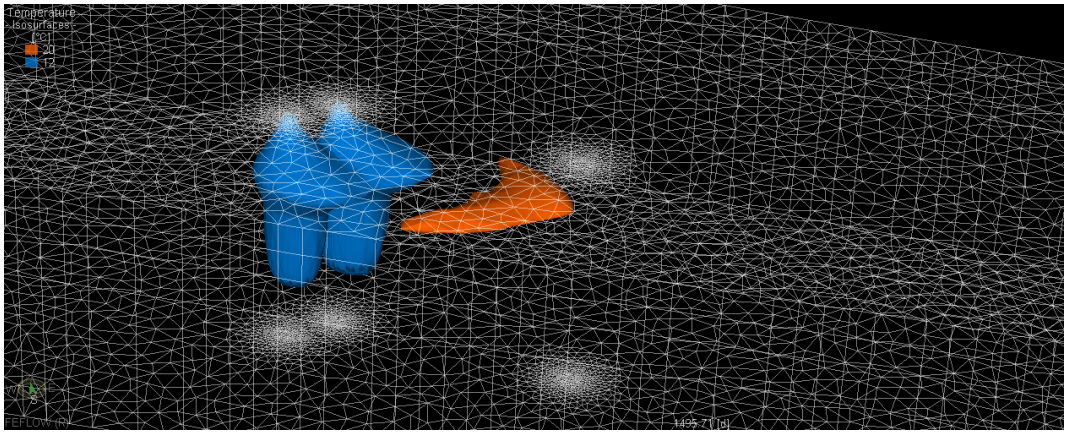

Figure 170. 3D representation of the thermal interference (20°C and 12°C) of the ATES case study 1 after 1495 days of simulation.

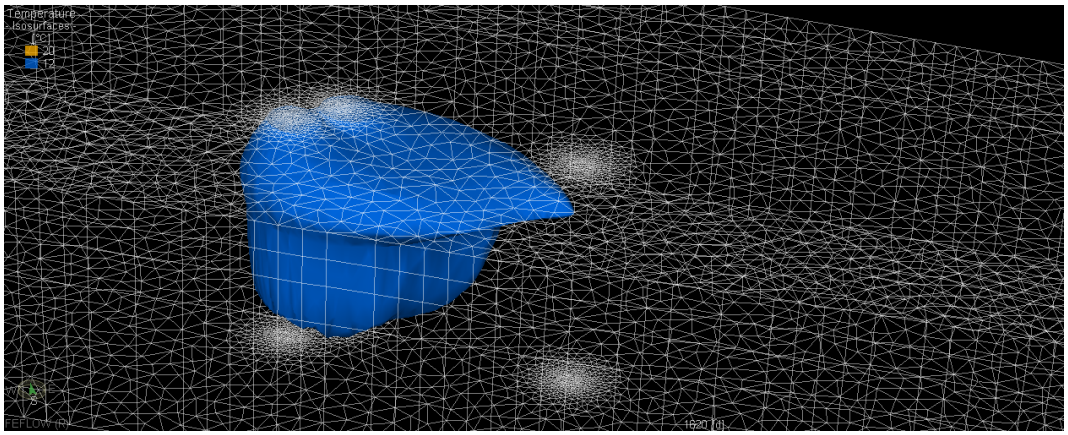

Figure 171. 3D representation of the thermal interference (20°C and 12°C) of the ATES case study 1 after 1620 days of simulation.

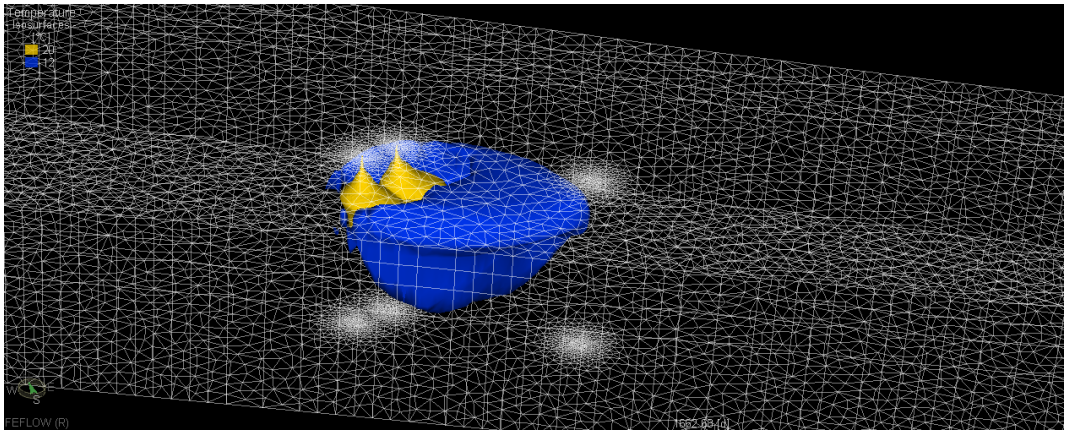

Figure 172. 3D representation of the thermal interference (20°C and 12°C) of the ATES case study 1 after 1662 days of simulation.

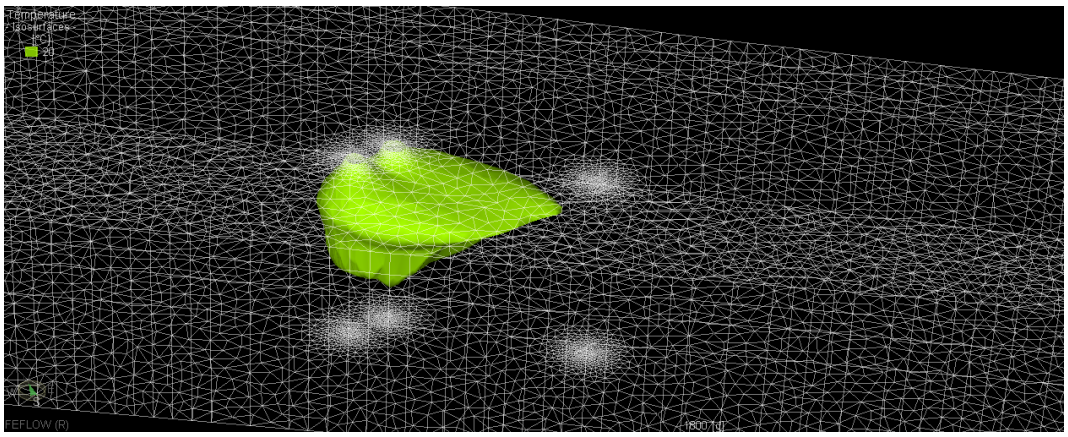

Figure 173. 3D representation of the thermal interference (20°C and 12°C) of the ATES case study 1 after 1800 days of simulation.

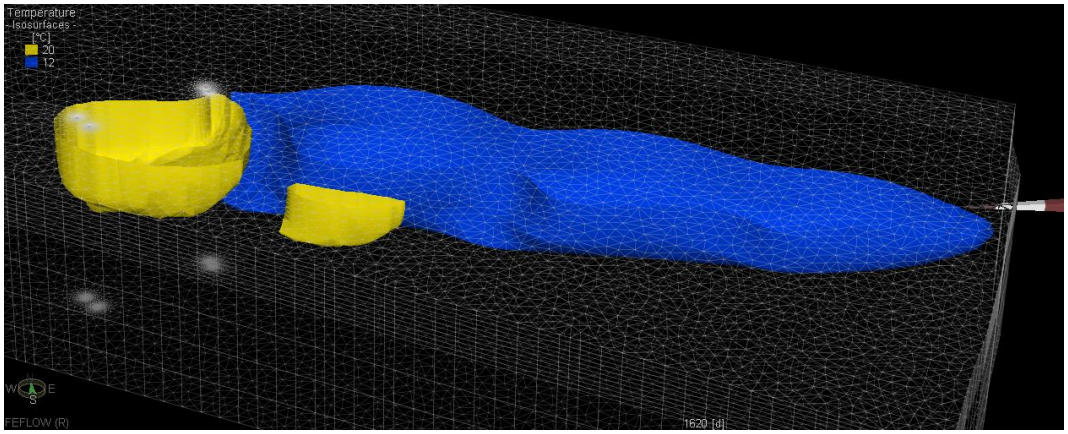

Figure 174. 3D representation of the thermal interference (20°C and 12°C) of the ATES case study 2 after 1620 days of simulation.

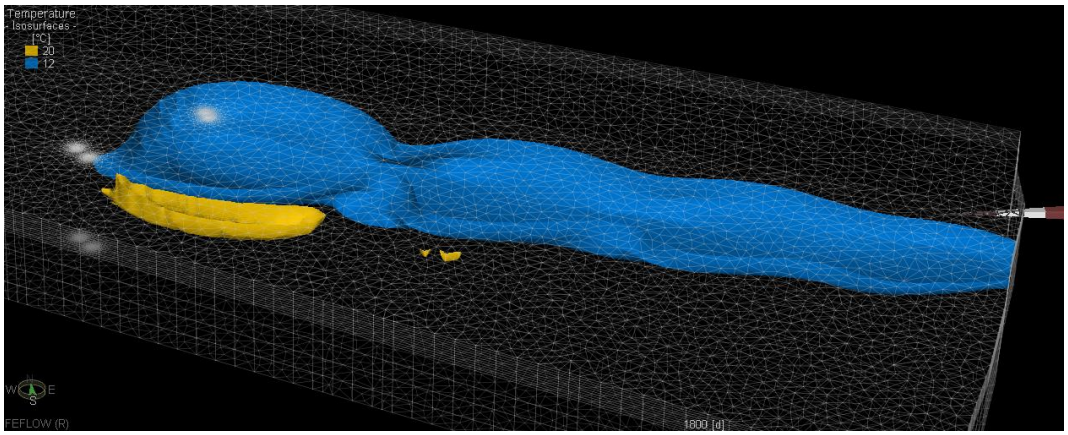

Figure 175. 3D representation of the thermal interference (20°C and 12°C) of the ATES case study 2 after 1800 days of simulation.

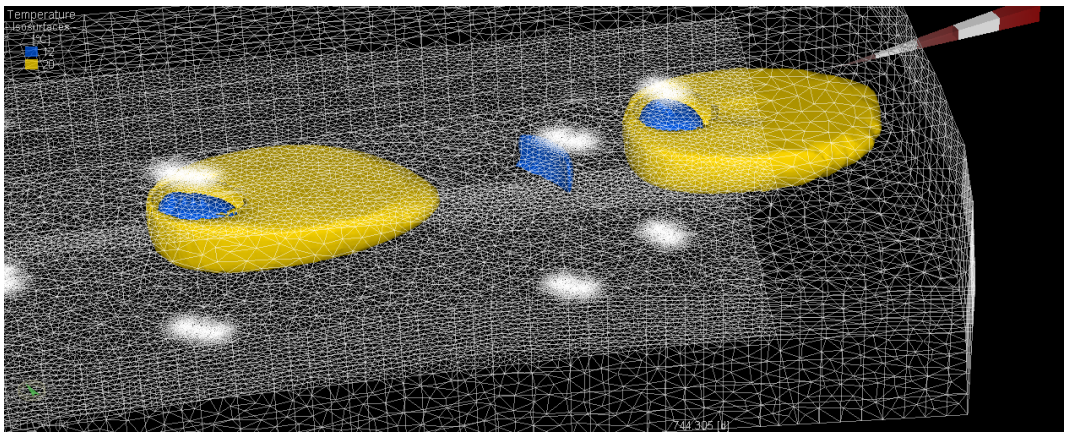

Figure 176. 3D representation of the thermal interference (20°C and 12°C) of the ATES case study 3 after 744 days of simulation (Scenario 1).

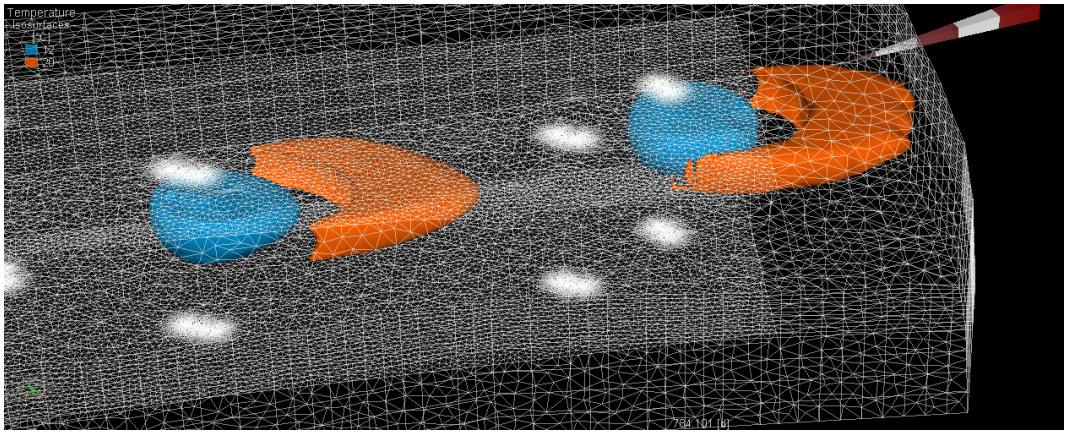

Figure 177. 3D representation of the thermal interference (20°C and 12°C) of the ATES case study 3 after 784 days of simulation (Scenario 1).

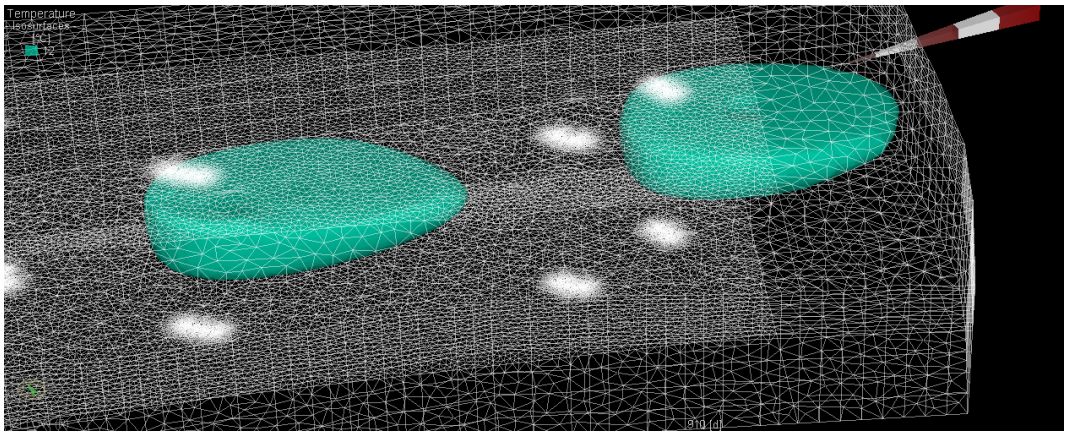

Figure 178. 3D representation of the thermal interference (20°C and 12°C) of the ATES case study 3 after 910 days of simulation (Scenario 1).

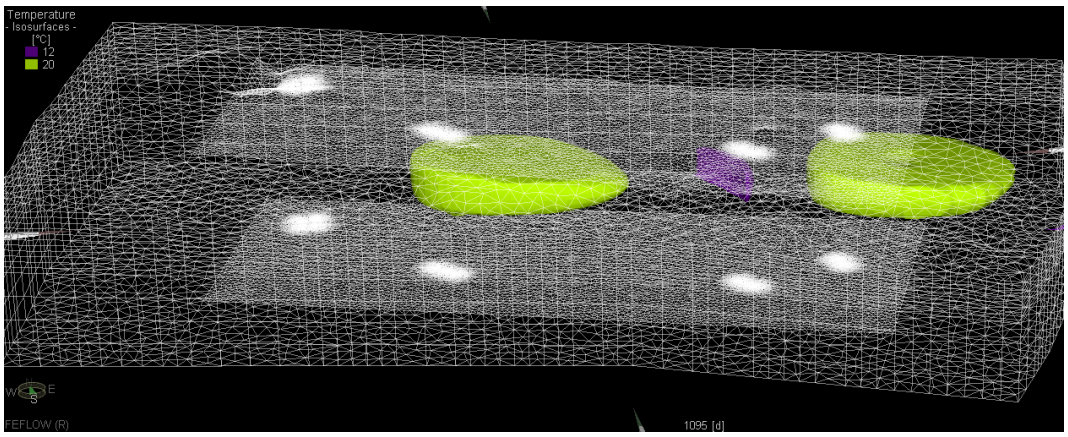

Figure 179. 3D representation of the thermal interference (20°C and 12°C) of the ATES case study 3 after 1095 days of simulation (Scenario 1).

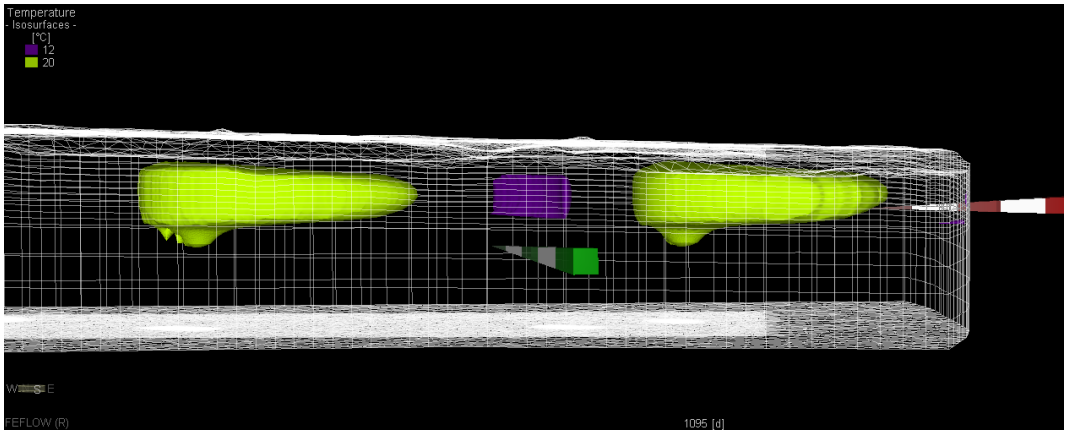

Figure 180. 3D representation of the vertical thermal interference (20°C and 12°C) of the ATES case study 3 after 1095 days of simulation (Scenario 1).

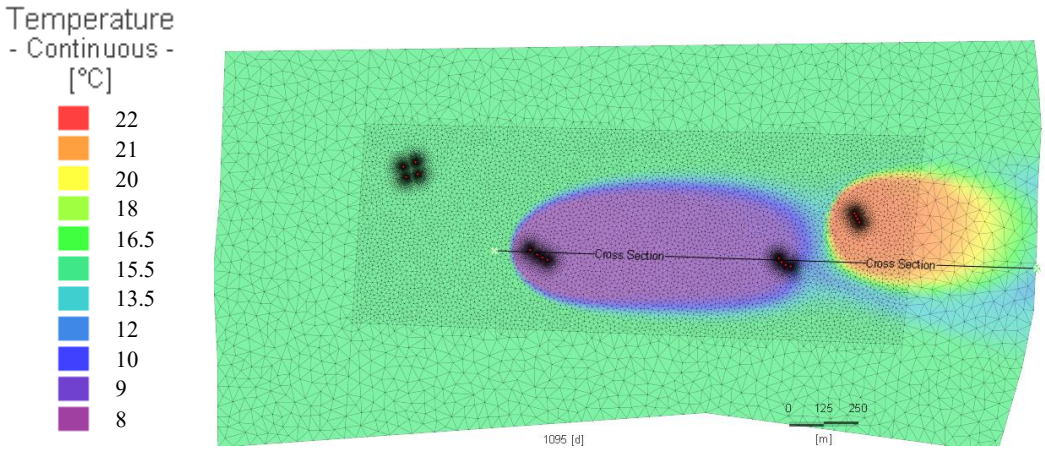

Figure 181. Thermal interference of the ATES case study 3 in horizontal section after 1095 days of simulation (Scenario 2).

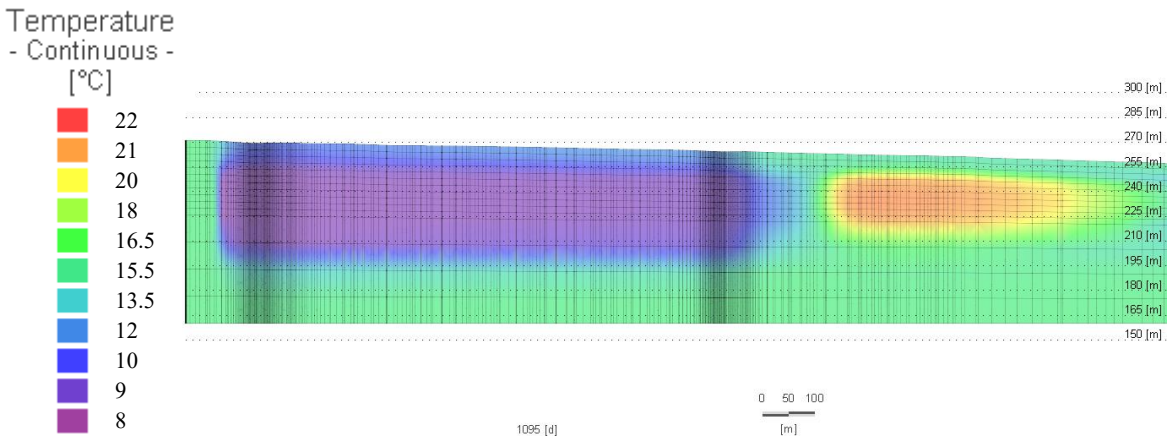

Figure 182. Cross section of the thermal interference of the ATES case study 3 after 1095 days of simulation (Scenario 2).

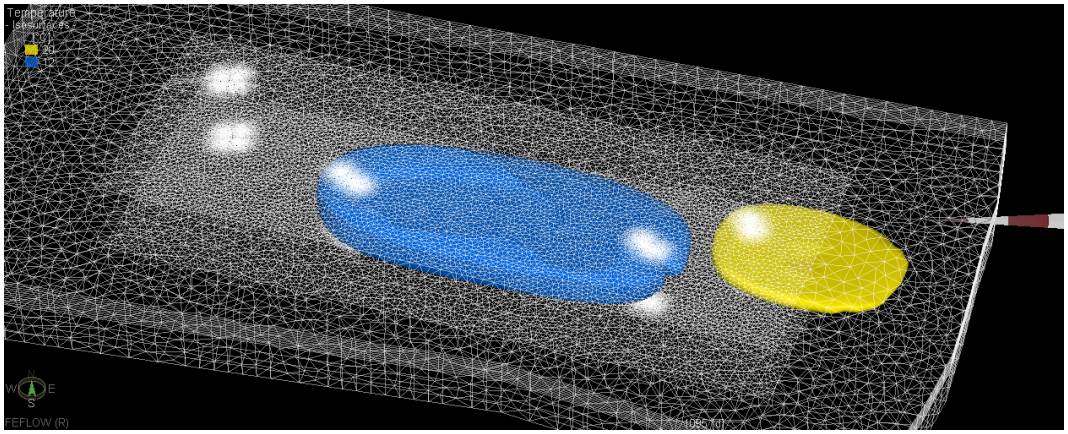

Figure 183. 3D representation of the thermal interference (20°C and 12°C) of the ATES case study 3 after 1095 days of simulation (Scenario 2).

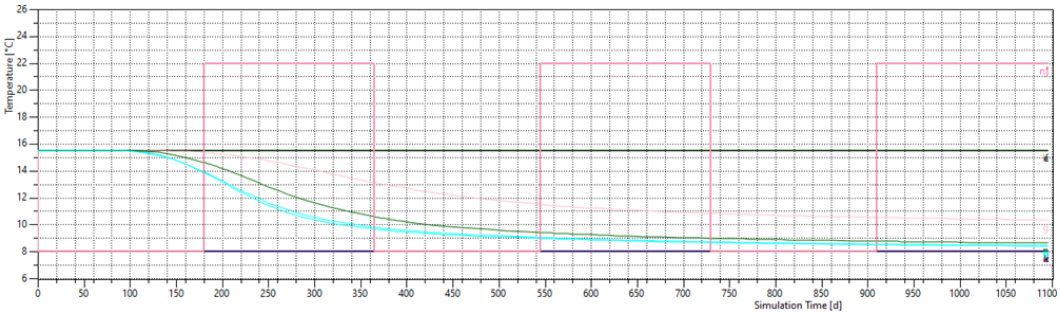

Figure 184. Graph showing temperature trends for each simulated well in Scenario 2 throughout the simulation period. The blue, green and pink lines correspond to the intake wells in the downstream plant.

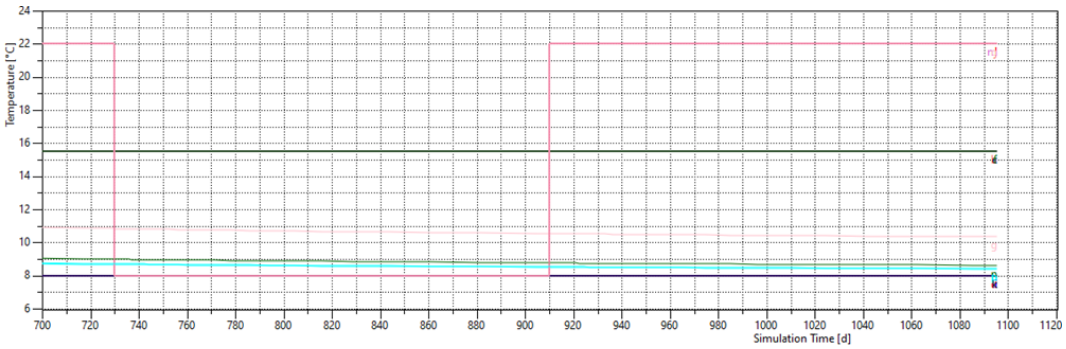

Figure 185. Graph showing temperature trends for each simulated well in Scenario 2 in the last year of simulation. The blue, green and pink lines correspond to the intake wells in the downstream plant.

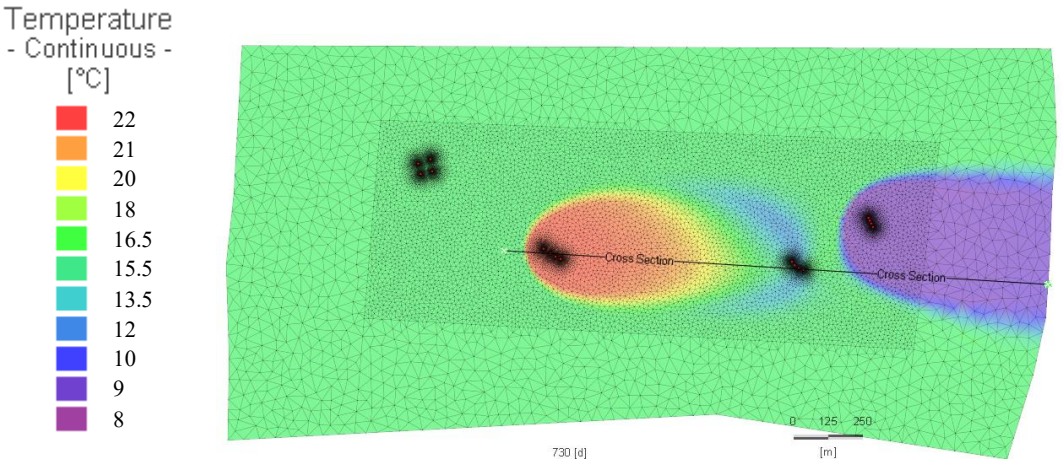

Figure 186. Thermal interference of the ATES case study 3 in horizontal section after 730 days of simulation (Scenario 3).

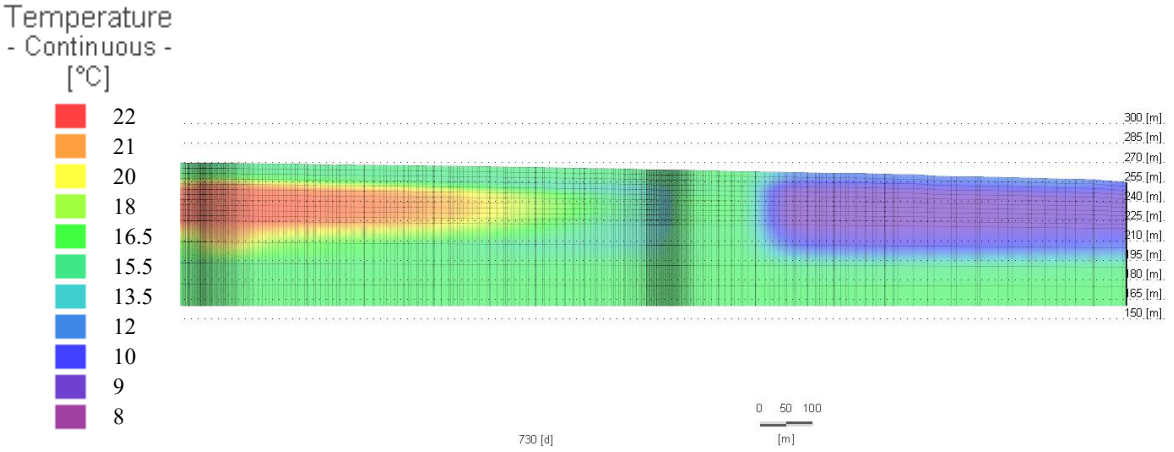

Figure 187. Cross section of the thermal interference of the ATES case study 3 after 730 days of simulation (Scenario 3).

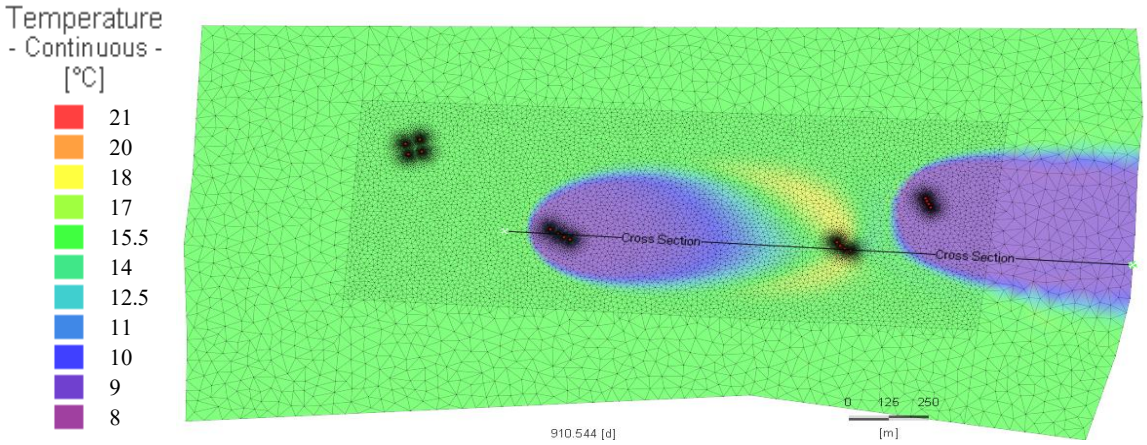

Figure 188. Thermal interference of the ATES case study 3 in horizontal section at after 910 days of simulation (Scenario 3).

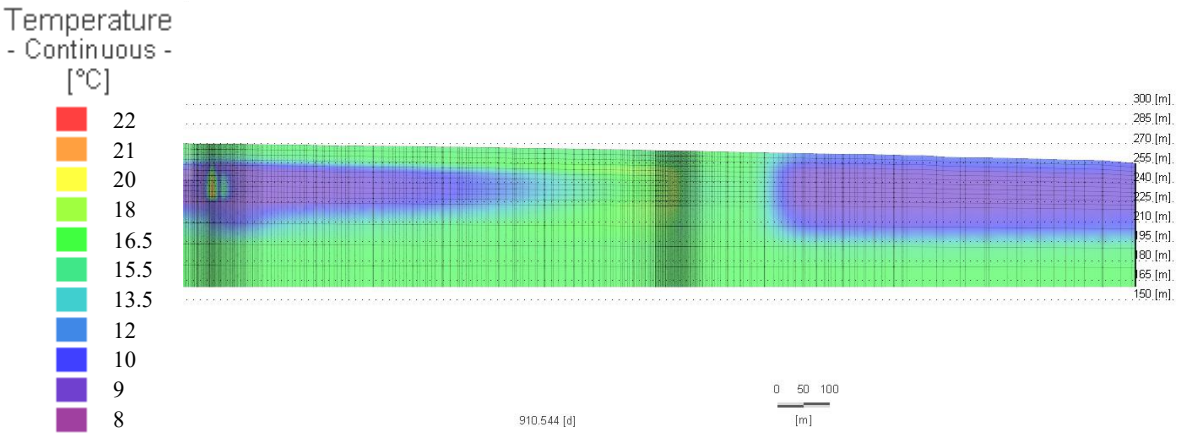

Figure 189. Cross section of the thermal interference of the ATES case study 3 after 910 days of simulation (Scenario 3).

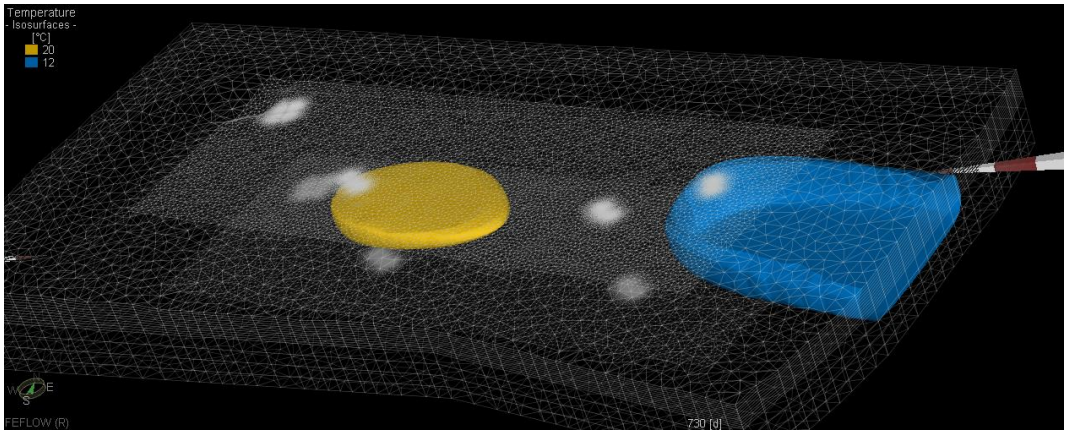

Figure 190. 3D representation of the thermal interference (20°C and 12°C) of the ATES case study 3 after 730 days of simulation (Scenario 3).

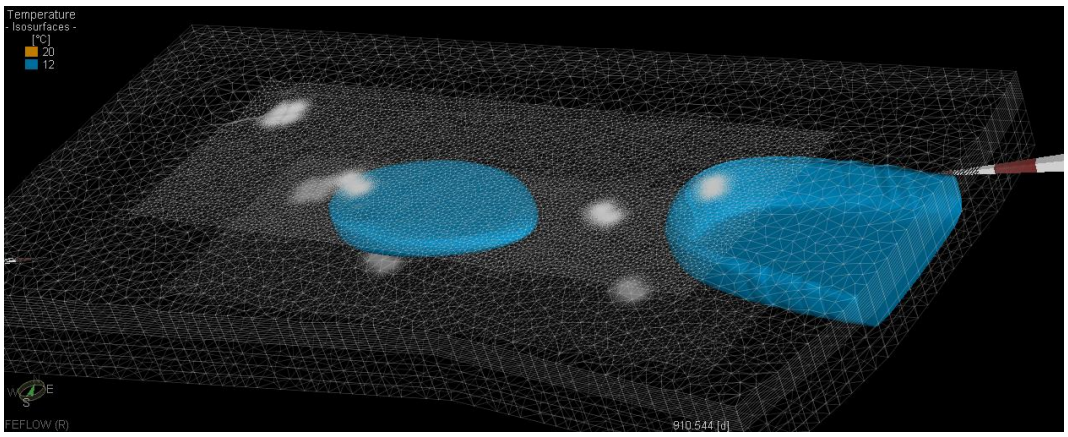

Figure 191. 3D representation of the thermal interference (20°C and 12°C) of the ATES case study 3 after 910 days of simulation (Scenario 3).

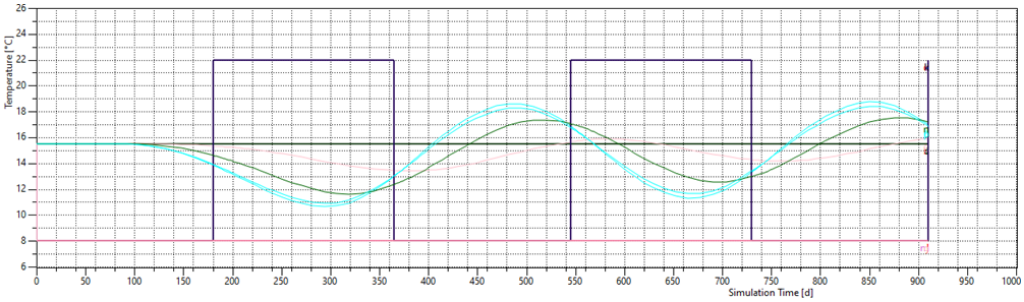

Figure 192. Graph showing temperature trends for each simulated well in Scenario 3 throughout the simulation period. The blue, green and pink lines correspond to the intake wells in the downstream plant.

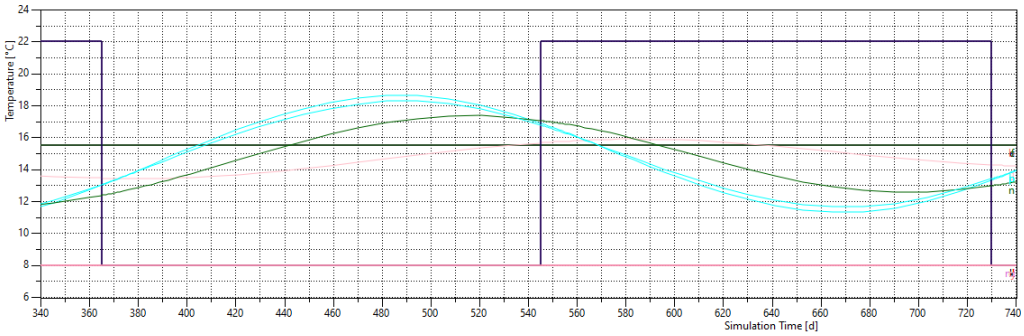

Figure 193. Graph showing temperature trends for each simulated well in Scenario 3 in the last year of simulation. The blue, green and pink lines correspond to the intake wells in the downstream plant.

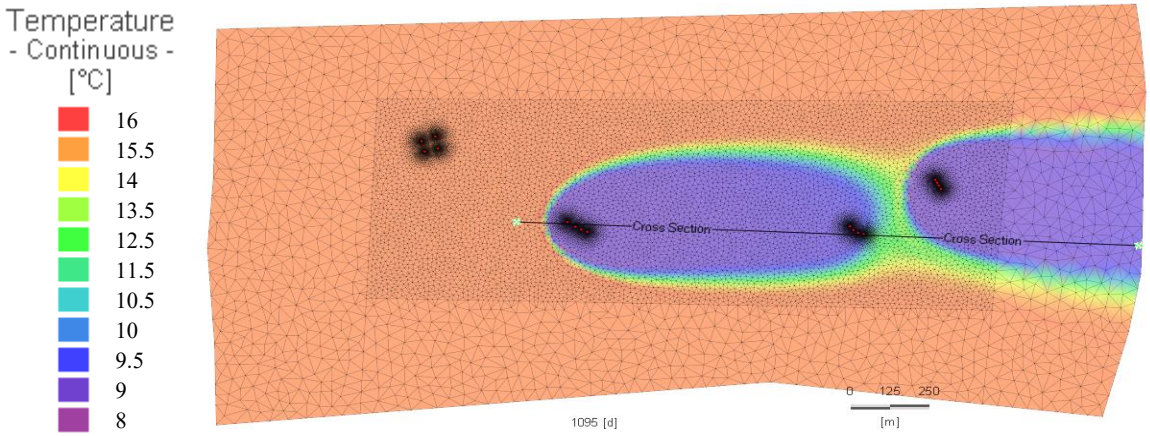

Figure 194. Thermal interference of the ATES case study 3 in horizontal section after 1095 days of simulation (Scenario 4).

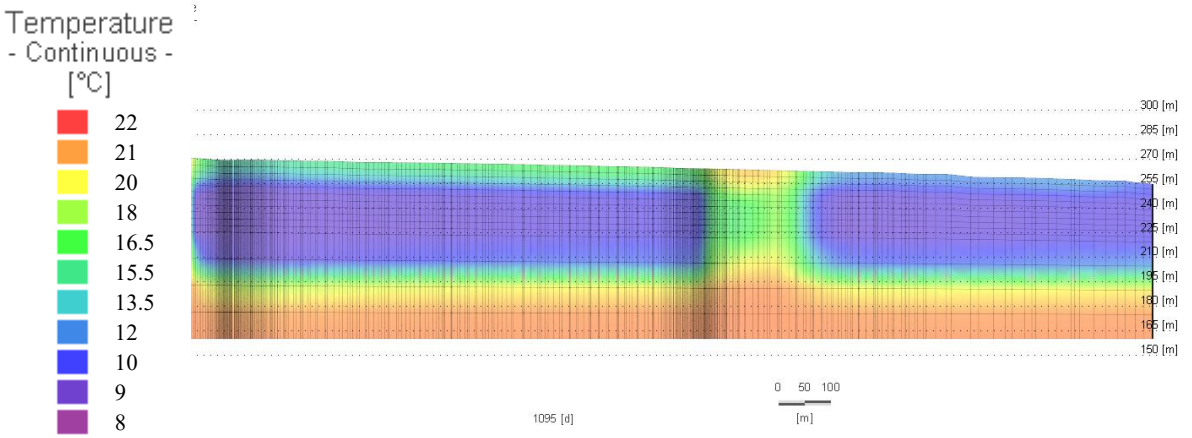

Figure 195. Thermal interference of the ATES case study 3 in horizontal section after 1095 days of simulation (Scenario 4).

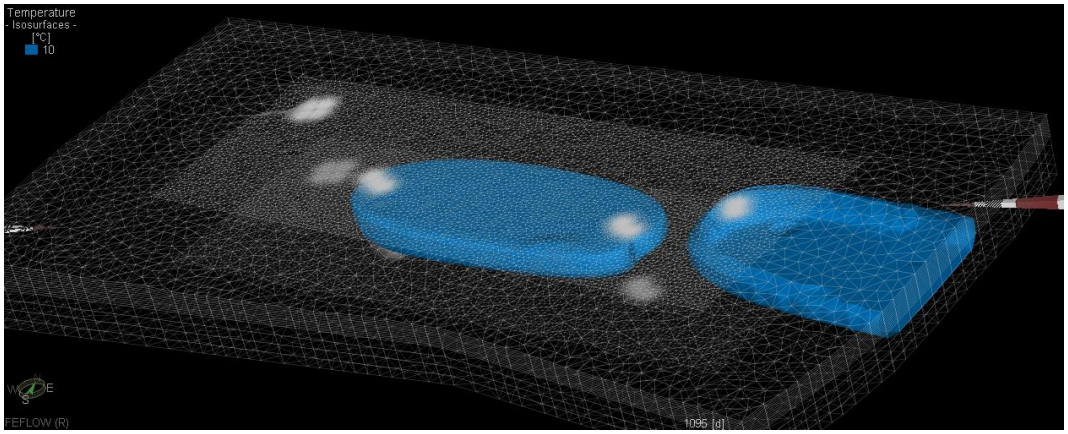

Figure 196. 3D representation of the thermal interference (20°C and 12°C) of the ATES case study 3 after 1095 days of simulation (Scenario 4).

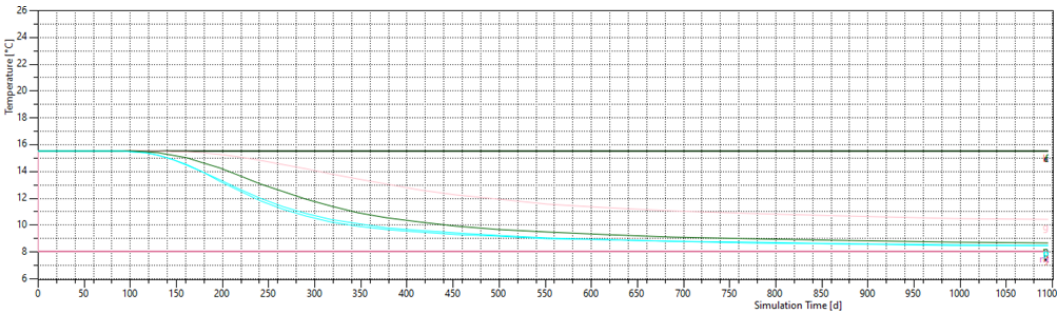

Figure 197. Graph showing temperature trends for each simulated well in Scenario 4 throughout the simulation period. The blue, green and pink lines correspond to the intake wells in the downstream plant.

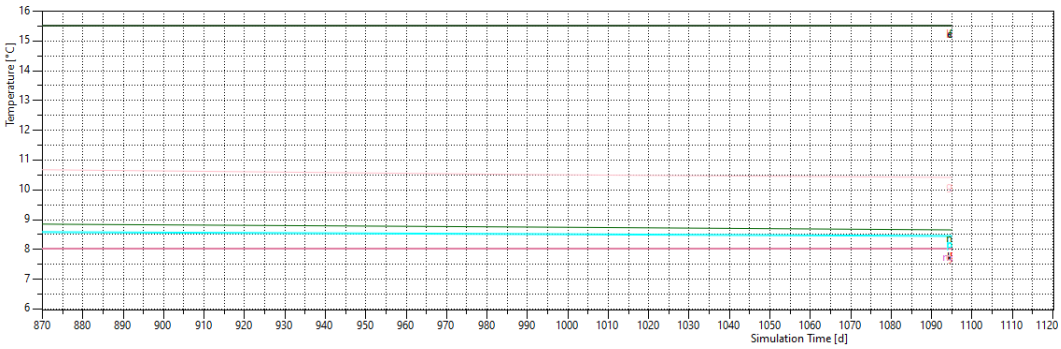

Figure 198. Graph showing temperature trends for each simulated well in Scenario 4 in the last year of simulation. The blue, green and pink lines correspond to the intake wells in the downstream plant.

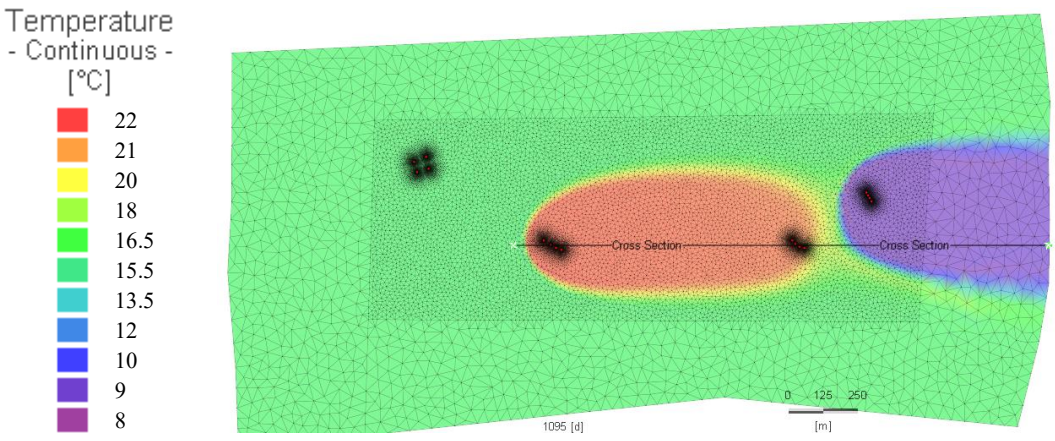

Figure 199. Thermal interference of the ATES case study 3 in horizontal section after 1095 days of simulation (Scenario 5).

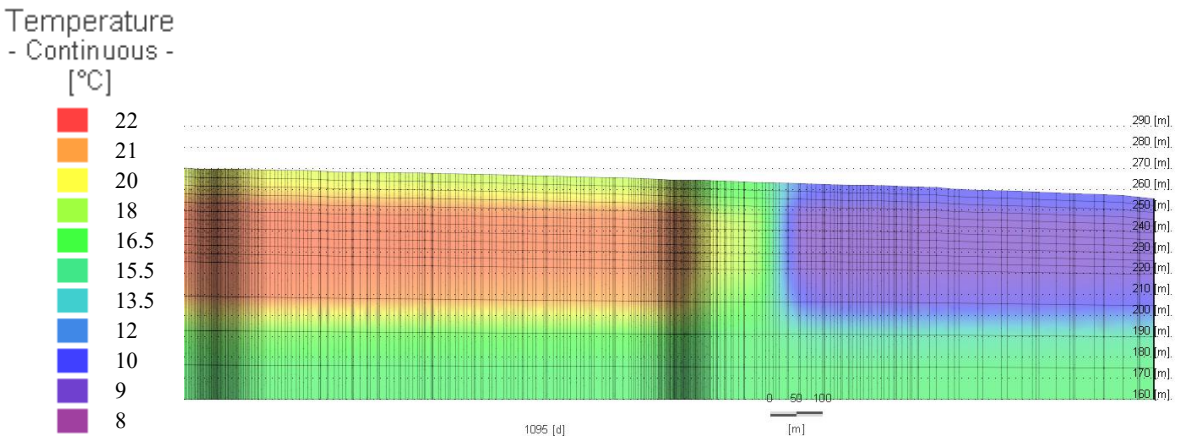

Figure 200. Thermal interference of the ATES case study 3 in horizontal section after 1095 days of simulation (Scenario 5).

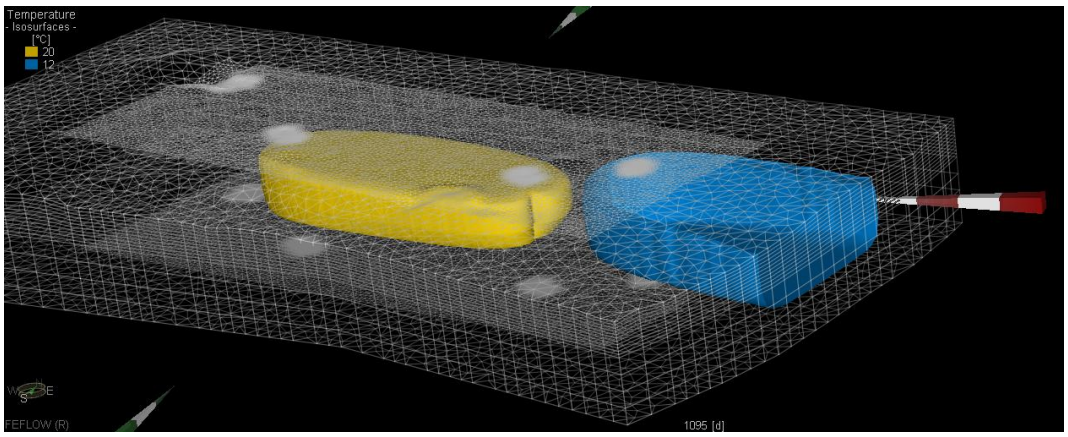

Figure 201. 3D representation of the thermal interference (20°C and 12°C) of the ATES case study 3 after 1095 days of simulation (Scenario 5).

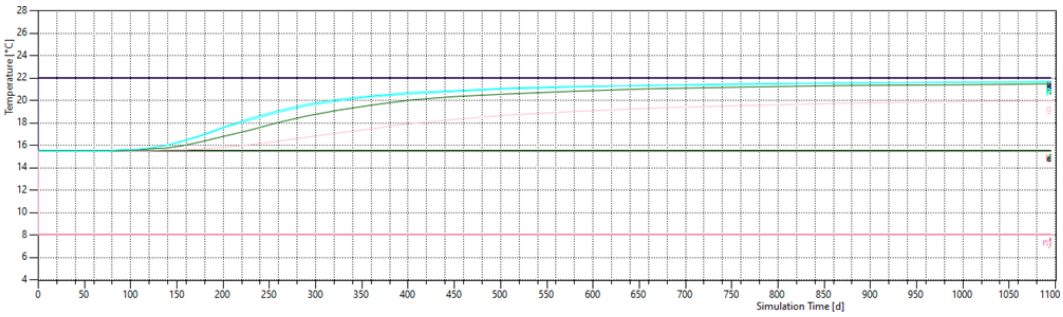

Figure 202. Graph showing temperature trends for each simulated well in Scenario 5 throughout the simulation period. The blue, green and pink lines correspond to the intake wells in the downstream plant.

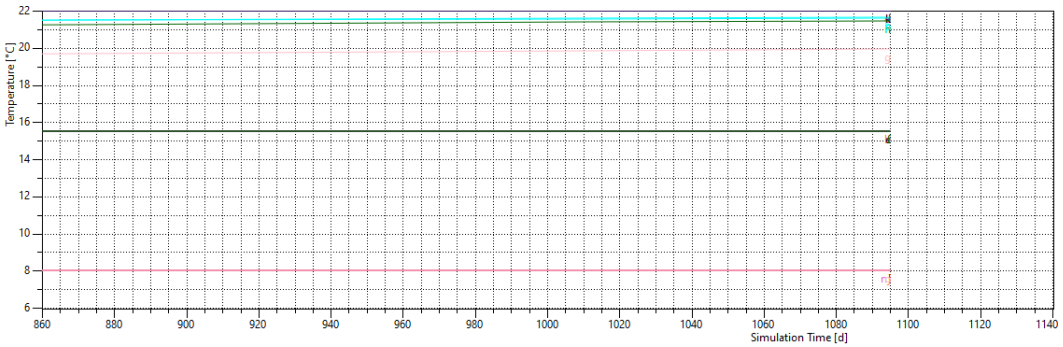

Figure 203. Graph showing temperature trends for each simulated well in Scenario 5 in the last year of simulation. The blue, green and pink lines correspond to the intake wells in the downstream plant.

Appendix B

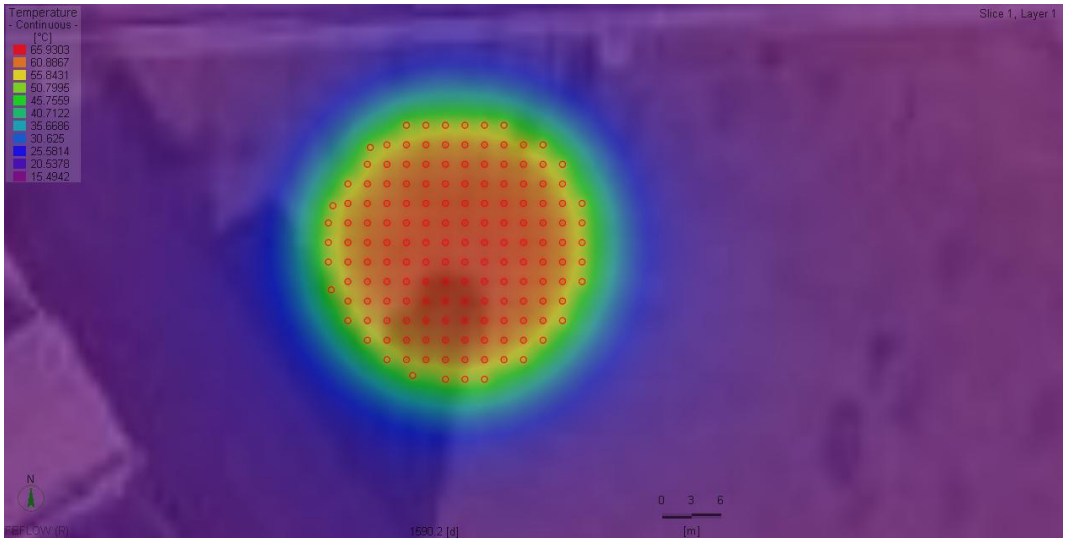

Figure 204. Thermal interference of the BTES system in horizontal section at the end of the fifth charging period (second Scenario).

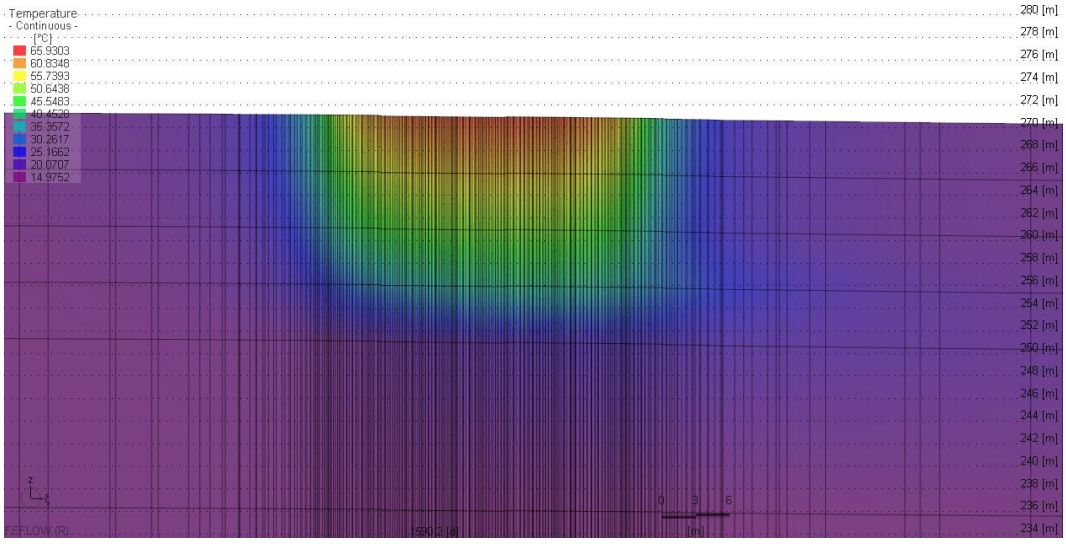

Figure 205. Thermal interference of the BTES system in vertical section at the end of the fifth charging period (second Scenario).

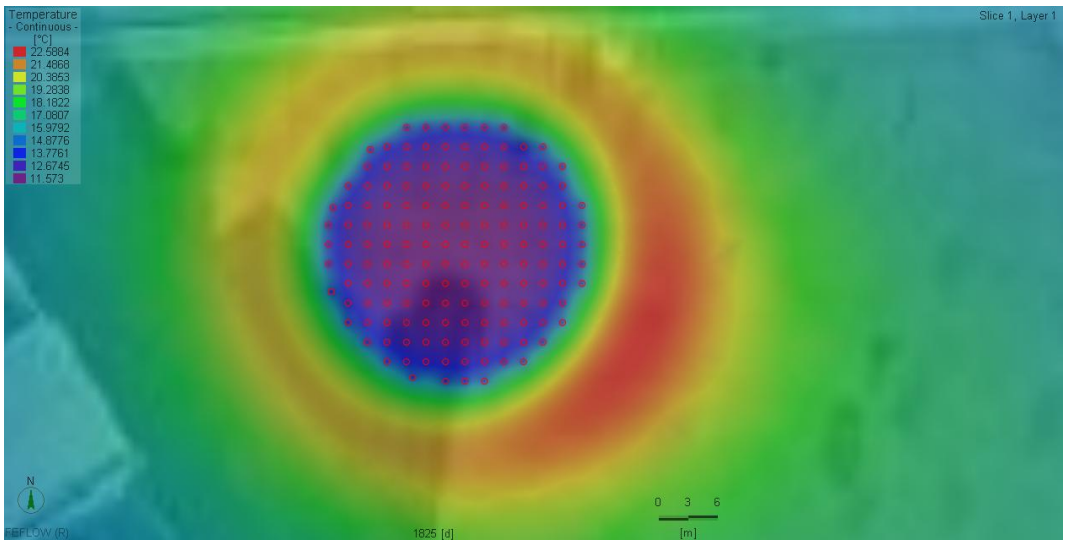

Figure 206. Thermal interference of the BTES system in horizontal section at the end of the fifth discharging period (second Scenario).

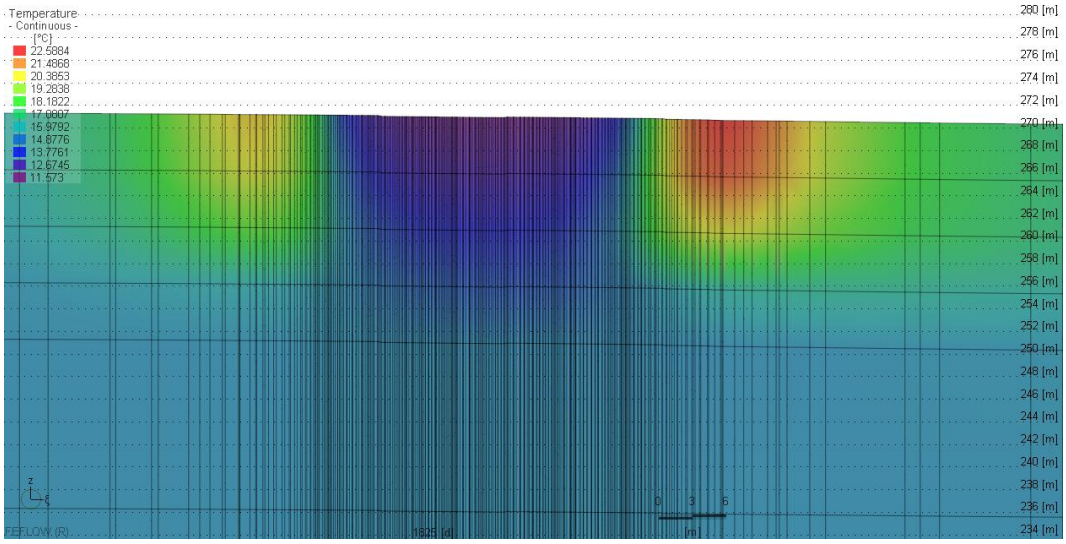

Figure 207. Thermal interference of the BTES system in vertical section at the end of the fifth discharging period (second Scenario).

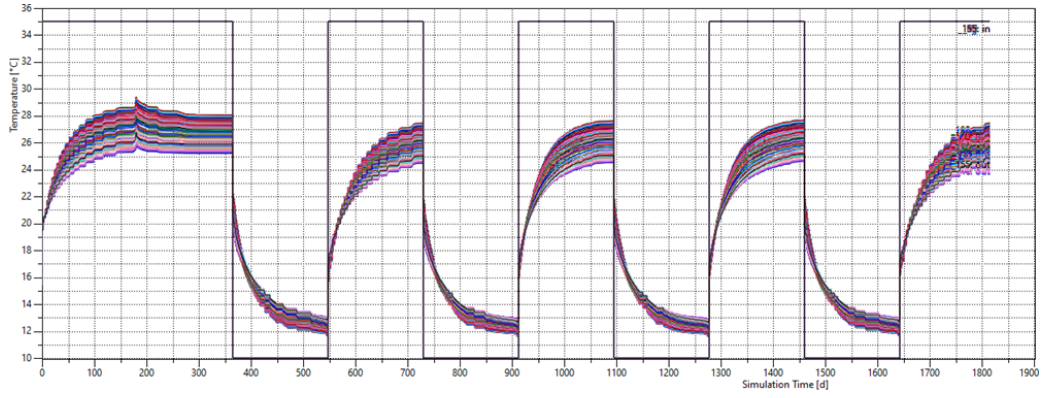

Figure 208. Graph showing the outlet temperatures from each BHEs throughout the entire simulation period (third Scenario).

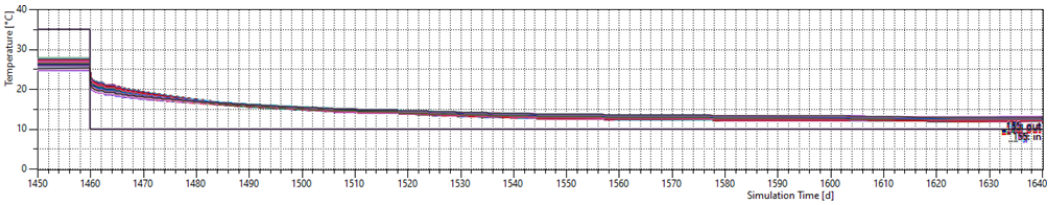

Figure 209. Graph showing the outlet temperatures from each BHEs at the end of the fifth year (third Scenario).

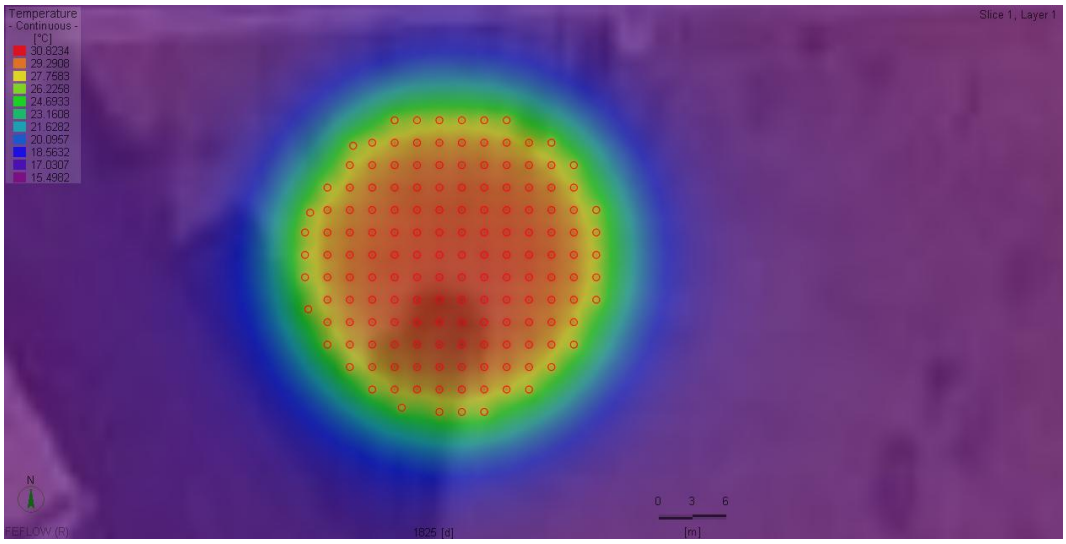

Figure 210. Thermal interference of the BTES system in horizontal section at the end of the fifth charging period (third Scenario).

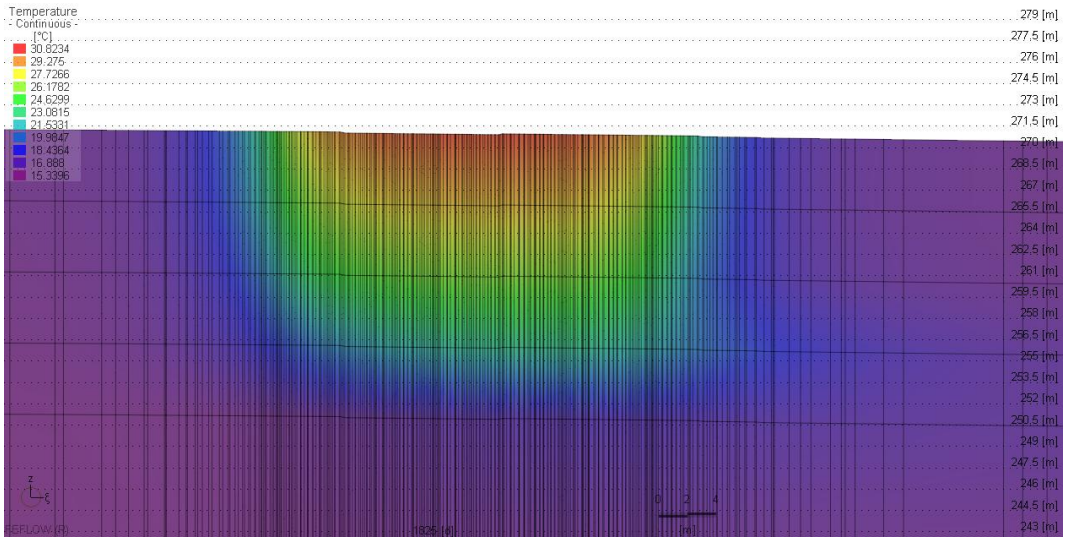

Figure 211. Thermal interference of the BTES system in vertical section at the end of the fifth charging period (third Scenario).

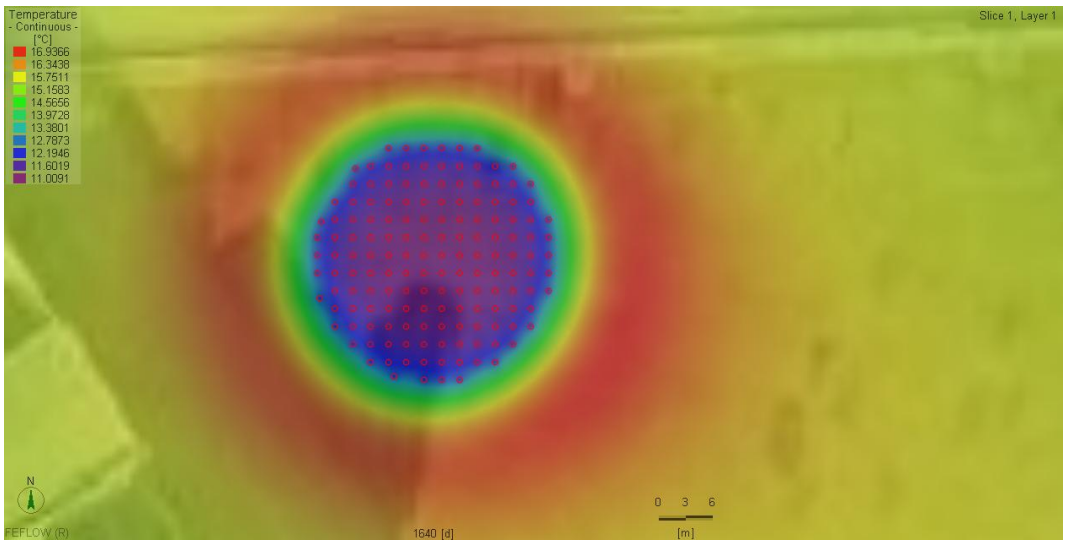

Figure 212. Thermal interference of the BTES system in horizontal section at the end of the fifth discharging period (third Scenario).

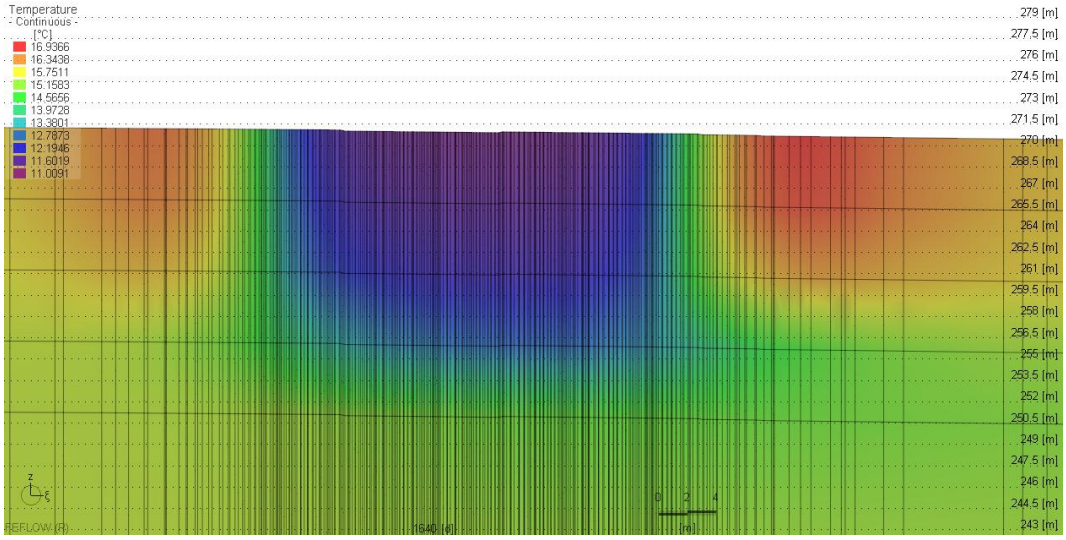

Figure 213. Thermal interference of the BTES system in vertical section at the end of the fifth discharging period (third Scenario).

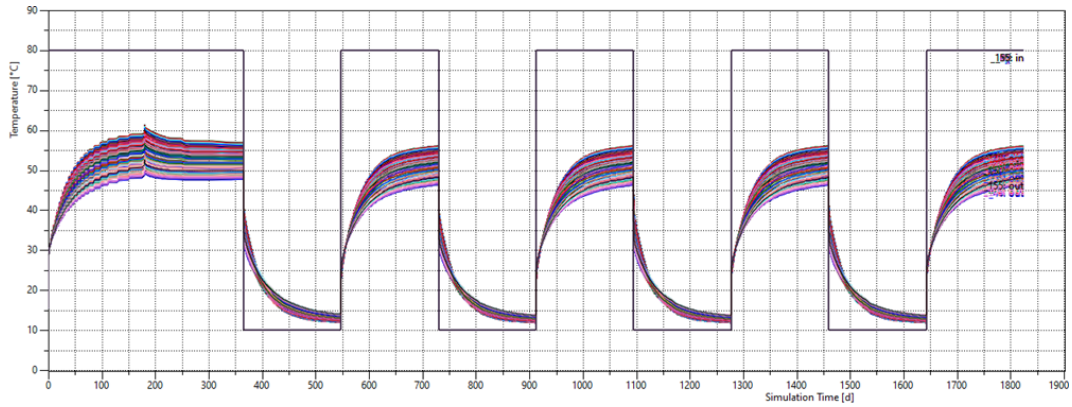

Figure 214. Graph showing the outlet temperatures from each BHEs throughout the entire simulation period (fourth Scenario).

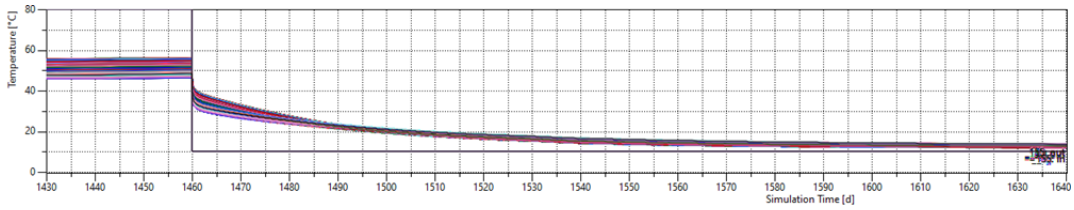

Figure 215. Graph showing the outlet temperatures from each BHEs at the end of the fifth year (fourth Scenario).

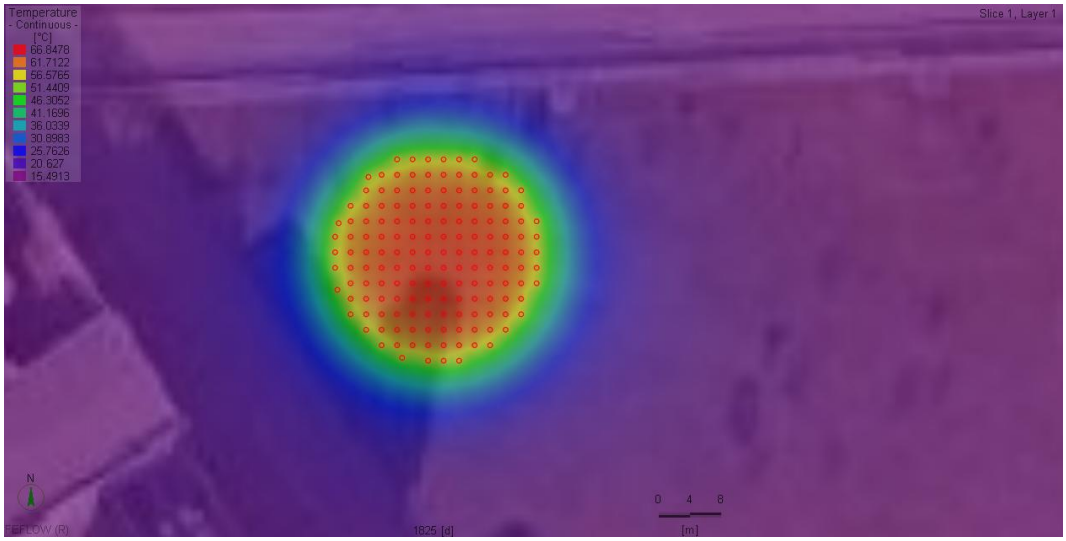

Figure 216. Thermal interference of the BTES system in horizontal section at the end of the fifth charging period (fourth Scenario).

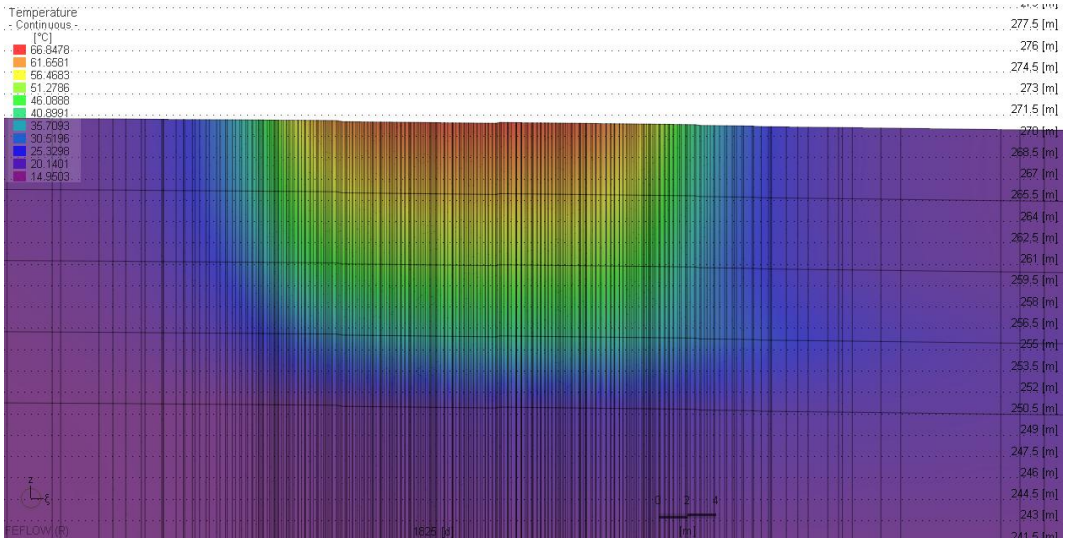

Figure 217. Thermal interference of the BTES system in vertical section at the end of the fifth charging period (fourth Scenario).

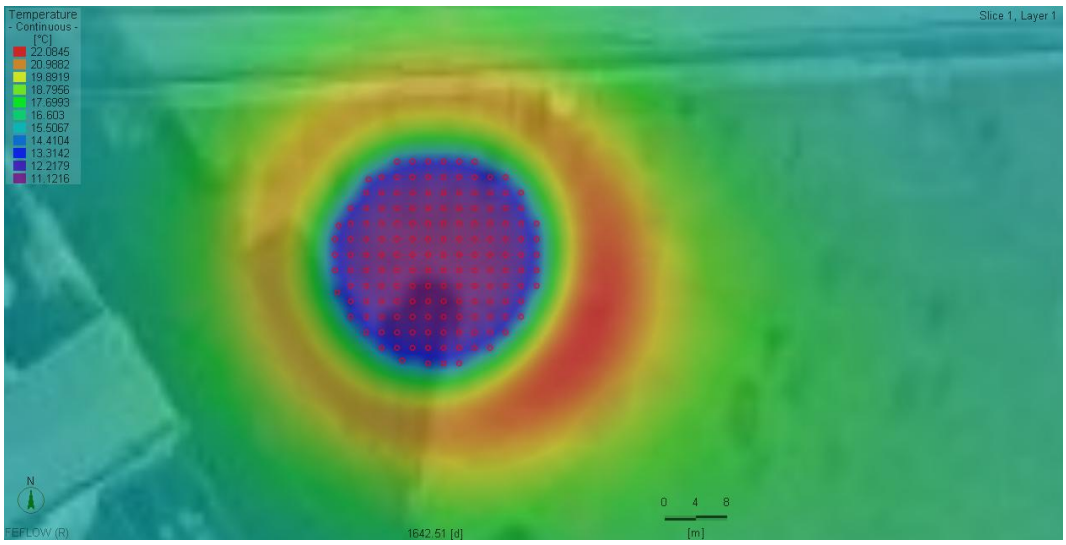

Figure 218. Thermal interference of the BTES system in horizontal section at the end of the fifth discharging period (fourth Scenario).

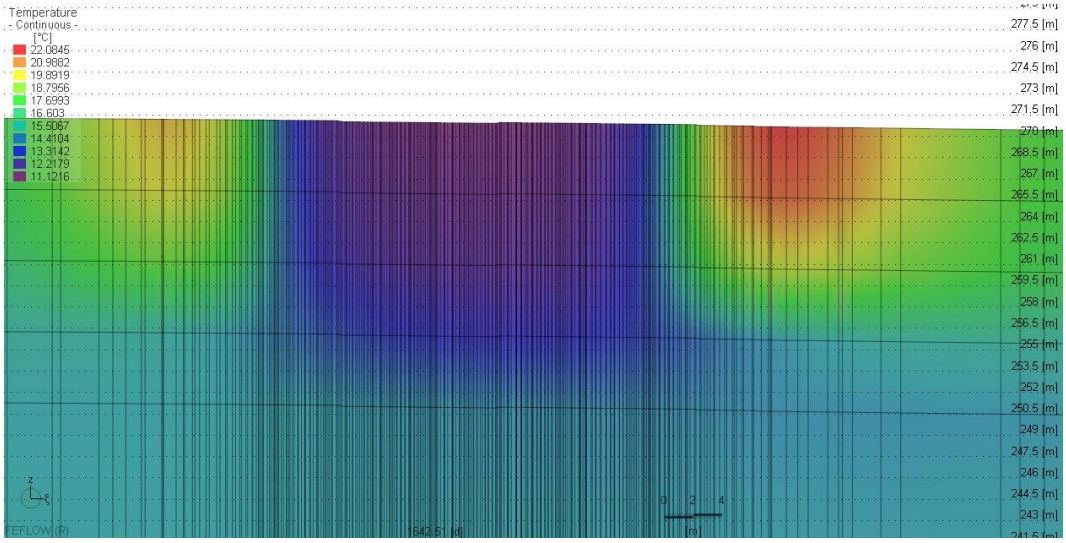

Figure 219. Thermal interference of the BTES system in vertical section at the end of the fifth discharging period (fourth Scenario).

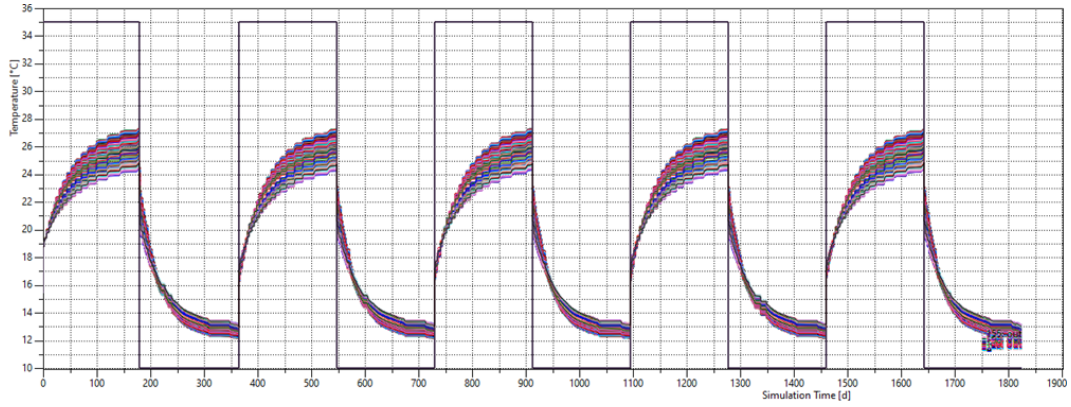

Figure 220. Graph showing the outlet temperatures from each BHEs throughout the entire simulation period (fifth Scenario).

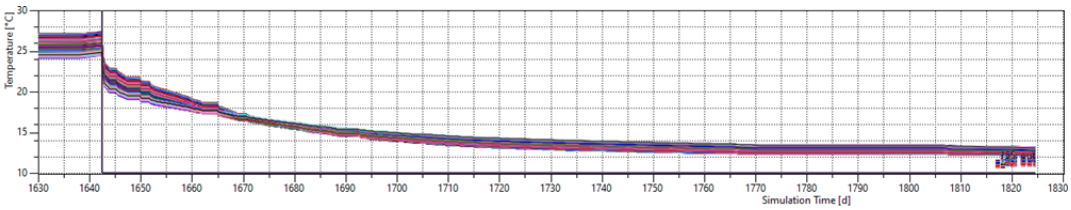

Figure 221. Graph showing the outlet temperatures from each BHEs at the end of the fifth year (fifth Scenario).

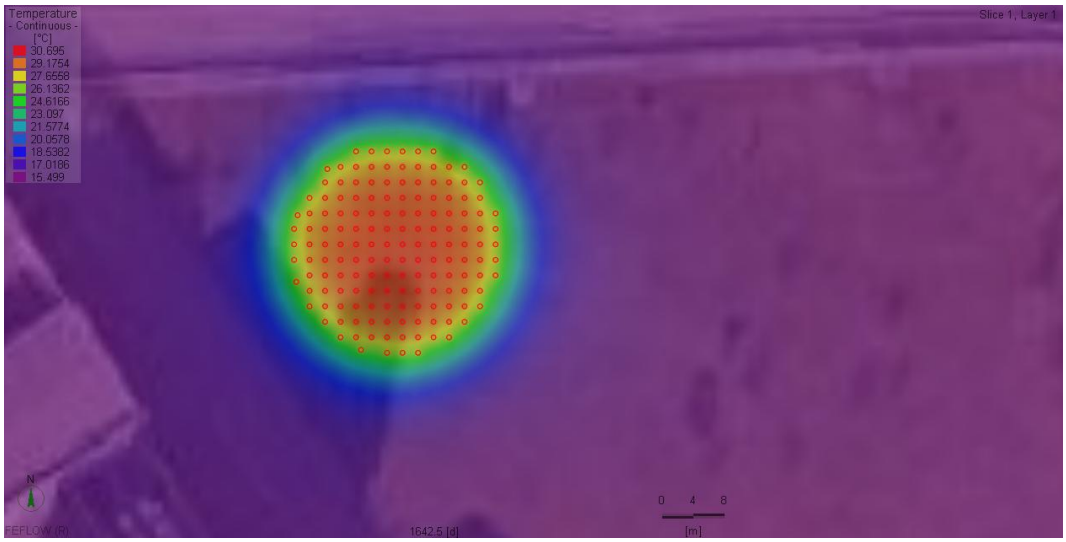

Figure 222. Thermal interference of the BTES system in horizontal section at the end of the fifth charging period (fifth Scenario).

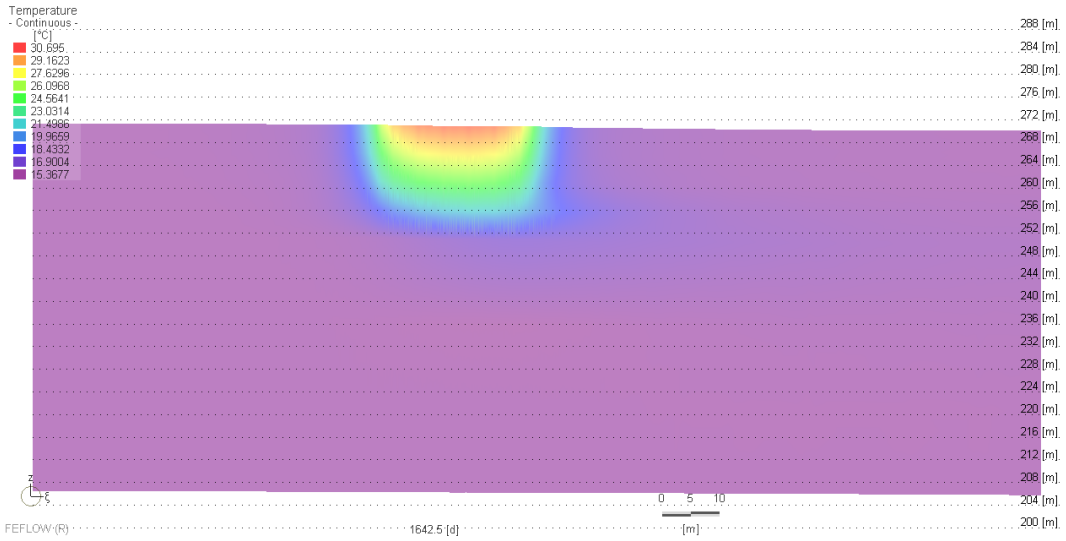

Figure 223. Thermal interference of the BTES system in vertical section at the end of the fifth charging period (fifth Scenario).

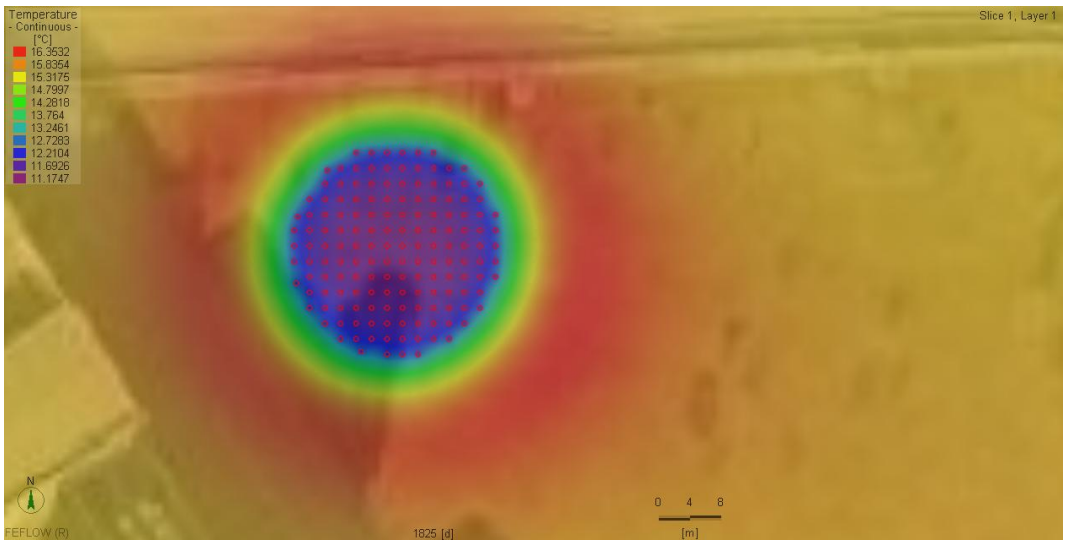

Figure 224. Thermal interference of the BTES system in horizontal section at the end of the fifth discharging period (fifth Scenario).

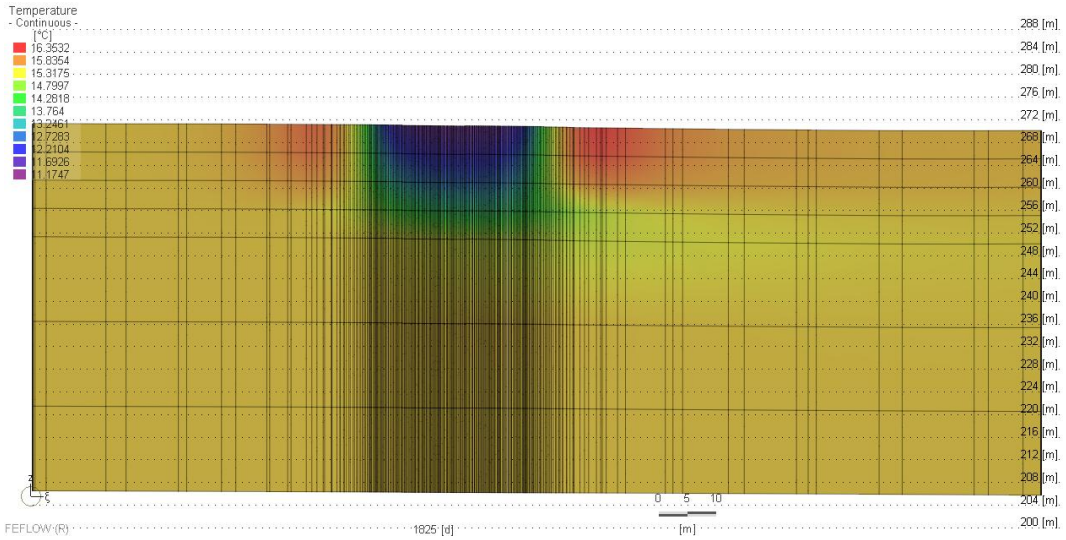

Figure 225. Thermal interference of the BTES system in vertical section at the end of the fifth discharging period (fifth Scenario).